Development of biomimetic photo-responsive artificial carriers for the transmembrane chloride transport

A Thesis

Submitted in Partial Fulfillment of the Requirements
of the Degree of

Doctor of Philosophy

by

Manzoor Ahmad

Roll No.: 20173503

Indian Institute of Science Education and Research Pune

(2022)

Dedicated to

My parents…

CERTIFICATE

Certified that the work incorporated in the thesis entitled "***Development of biomimetic photo-responsive artificial carriers for the transmembrane chloride transport***" submitted by **Mr. Manzoor Ahmad** was carried out by the candidate, under my supervision. The work presented here or any part of it has not been included in any other thesis submitted previously for the award of any degree or diploma from any other university or institution.

Date: 26th July 2022

Prof. Pinaki Talukdar
(Research Supervisor)

Declaration

I declare that this written submission represents my ideas in my own words and wherever others' ideas have been included; I have adequately cited and referenced the original sources. I also declare that I have adhered to all principles of academic honesty and integrity and have not misrepresented or fabricated or falsified any idea/data/fact/source in my submission. I understand that violation of the above will cause disciplinary action by the Institute and can also evoke penal action from the sources which have thus not been properly cited or from whom proper permission has not been taken when needed.

Date: 26th July 2022

Manzoor Ahmad
Roll No.: 20173503

Acknowledgment

The tenure of my Ph.D. degree was an incredible journey for me that has profoundly shaped my intellect and made me an entirely different person with qualities of critical questioning and understanding of surrounding nature. During this beautiful tenure, there were a lot of people who have helped me to achieve and accomplish it and without whom it could have been a very difficult process. I would like to cover all of the related persons without being biased.

First and foremost, I would like to thank my thesis supervisor Prof. Pinaki Talukdar for giving me an opportunity to work in his well-equipped research lab. During all these years he has been well supportive, encouraging, and providing a free environment in the lab to design and execute any sort of research ideas. With his practical guidance, I learned to design and execute research projects, and especially the free environment has helped me to be an independent thinker which will eventually shape me to carry out my future research. Moreover, it has been a friendly relationship and my supervisor has always stood with me in good as well as bad times. The regular lab meetings have helped me to improve the quality of my presentation and communication skills.

I would like to express my profound gratitude to my Research Advisory Committee (RAC) members, Prof. H.N. Gopi sir and Dr. Jayaraj Nithynandhan sir for their valuable time and constructive suggestions during the RAC meetings. These suggestions have helped me a lot to formulate and execute my research experiments. I am really thankful for their time, efforts and positive feedback.

I am deeply grateful to prof. M. Jayakannan (former Chair Chemistry), Prof. H. N. Gopi (former Chair Chemistry), Nirmalya Ballav (current Chair Chemistry), and all the faculty members and staff of the chemistry department for being extremely helpful.

I feel honored to be a part of the Indian Institute of Science Education and Research (IISER), Pune. I would like to spread my gratitude to each and everybody related to IISER Pune, in particular, to them who offered their endless effort to build such a wonderful institute with world-class research facilities. My sincere thank goes to our former Director, Prof. K. N. Ganesh, for providing excellent infrastructure and world-class research facilities, and current director Prof. Jayant Udgaonkar to implement the additions to his efforts at the Indian Institute of science education and research (IISER), Pune, India. The friendly atmosphere of research at IISER Pune always amazed me. I strongly feel that the accessibility of easy discussion among faculty members and students is the key feature of the successful interdisciplinary research at this institute.

My sincere heartful thanks goes out to Dr. Sopan Shinde and Dr. Javid Ahmad Malla. They were the senior members of the lab. My preliminary research/lab training was completed under their guidance and especially it was Dr. Sopan Shinde who shaped me in my initial Ph. D tenure. I always felt encouraged while working with them. I believe that the skills/things/attitude I learned from them will help my life long. It was a great honor to work under their guidance.

I would like to thank my collaborators Prof. Aloke Das and Mr. Surajit Mehta for the theoretical studies. I would also like to thank Dr. Mayurika Lahiri and Dr. Virender Kumar Sharma for the biological studies.

I thank all non-teaching and technical staff for their support, particularly, Mr. Sandip Kennedy, Mr. Mayuresh, Mr. Mahesh, Mr. Ganesh, Mr. Sanjay Kumar Meena, Mr. Nitin, Ms. Dipali and Mr. Chinmay, and Dr. Sandeep Mishra (NMR), Mr. Tushar, Mr. Ravindra (Xrd). It's my pleasure to thank all the lab members; Dr. Arundhati, Dr. Tanmoy Saha, Dr. Debashis, Anjana, Rashmi, Avishikta, Nihar, Abhishek, Avishikta, Sandip, Naveen, Swati, Akram, Umesh and Debarti for making my journey wonderful. It was indeed a great experience of working with them. I would especially like to thank Dr. Debashis for constantly helping and guiding me during my tenure and for his constant support in good and bad times. He has been a good friend which made this journey of Ph. D very easy for me.

I am highly thankful to University Grant Commission (UGC), Government of India, for my research scholarship the financial support during the course of Ph.D. Moreover, I like to thank American Chemical Society (ACS) and John Wiley & Sons, for publishing several research articles produced during the course of my research as well as for giving the permission for a reprint of copyrighted materials.

Finally, I express my profound gratitude to my family members especially to my parents 'Mummy and Papa" for their constant support during the tenure. They have always backed me from the core of their heart and I should undoubtly confess that whatever I am today is all because of their supplications in my favour.

Manzoor Ahmad

Contents

Chapter 1: Introduction to Membrane Transport

1.1. Cell Membrane 1.1

1.2. Membrane Transport 1.2

1.3. Ion Transport across the Cell Membrane 1.3

1.3.1. Gating 1.4

1.3.2. Importance of chloride Transport across the cell membrane 1.7

1.3.3. Non-protein based natural and artificial chloride ion carriers 1.8

1.3.4. Chloride ion transporters in therapeutics 1.10

1.3.5. Light responsive Synthetic Ion Transport Systems 1.11

1.3.6. Techniques Used to Study Synthetic Ion carriers 1.14

1.3.6.1. Fluorescence based assay 1.14

1.3.6.2. Ion Selective Electrode based Assays 1.15

1.4. References 1.15

Chapter 2: A Sandwich Azobenzene-diamide Dimer for Photoregulated Chloride Transport

2.1. Introduction 2.1

2.2. Results and Discussions 2.3

2.2.1. Synthesis 2.3

2.2.2. Chloride Binding analysis by ^{1}H NMR Titration studies 2.4

2.2.3. Ion transport activity 2.6

2.2.4. Theoretical studies

2.2.4.1. Geometry optimization studies 2.9

2.2.4.2. NBO analysis 2.10

2.2.5. Photoisomerization studies 2.11

2.4.6. Photoswitchable ion transport activity across EYPC-LUVs⊃Lucigenin 2.14

2.4.7. Photoswitchable ion transport activity across EYPC-LUVs⊃HPTS 2.15

Contents

2.3. Conclusion 2.16

2.4. Experimental details

2.4.1. General Methods 2.16

2.4.2. Physical Measurements 2.17

2.4.3. Synthetic Procedures 2.18

2.4.4. Anion Binding Studies by ^{1}H NMR 2.24

2.4.5. Ion Transport Studies 2.26

2.4.6. Photoisomerization Studies by ^{1}H NMR and UV-Vis Spectroscopies 2.37

2.4.7. Photoregulated Transport Activity across EYPC-LUVs⊃Lucigenin 2.42

2.4.8. Theoretical Calculations 2.45

2.5. NMR Spectra 2.52

2.6. References 2.66

Chapter 3: Stimuli-Responsive Anion Transport through Acylhydrazone-Based Synthetic Anionophores

3.1. Introduction 3.1

3.2. Results and Discussions

3.2.1. Synthesis 3.3

3.2.2. Anion Binding Study by ^{1}H NMR Titration 3.4

3.2.3. Single crystal X-Ray analysis 3.6

3.2.4. Ion transport activity 3.6

3.2.5. Photoisomerization studies 2.10

3.2.6. Stimuli-Responsive Ion Transport Activity 3.14

3.3. Conclusion 3.16

3.4. Experimental details

3.4.1. General Methods 3.15

3.4.2. Physical Measurements 3.16

3.4.3. Synthetic Procedures 3.17

3.4.4. Anion Binding Studies 3.22

3.4.5. Ion Transport Studies 3.30

Contents

3.4.6. Photoisomerization Studies 3.32

3.4.7. Stimuli-Responsive Ion Transport Activity 3.35

3.4.8. X-Ray measurement 3.36

3.5. NMR Spectra 3.41

3.6. References 3.49

Chapter 4: Reversible Stimuli-Responsive Transmembrane Ion Transport using Phenylhydrazone-Based Photoswitches

4.1. Introduction 4.1

4.2. Results and Discussions

4.2.1. Synthesis 4.3

4.2.2. Crystallographic Studies 4.4

4.2.3. Anion binding studies through ^{1}H NMR studies 4.4

4.2.4. Ion transport activity 4.7

4.2.5. Theoretical studies 4.9

4.2.6. Photoisomerization studies 4.10

4.2.7. Stimuli-Responsive Ion Transport Activity 4.15

4.3. Conclusion 4.16

4.4. Experimental details

4.4.1. General Methods 4.16

4.4.2. Physical Measurements 4.17

4.4.3. Synthetic Procedures 4.17

4.4.4. Anion Binding Studies 4.19

4.4.5. Ion Transport Studies 4.25

4.4.6. Photoisomerization Studies 4.29

4.4.7. X-Ray Crystallographic Studies 4.41

4.4.8. Theoretical Calculations 4.47

4.5. NMR Spectra 4.54

4.6. References 4.58

Contents

Chapter 5: Visible-Light Phototriggered Release of an Apoptosis-Inducing Chloride Anionophore inside the Cancer Cells

5.1. Introduction 5.1

5.2. Results and Discussions

5.2.1. Synthesis 5.3

5.2.2. Chloride binding studies 5.5

5.2.3. Crystallographic studies 5.6

5.2.4. Ion transport studies 5.7

5.2.5. Photocleavable studies 5.11

5.2.6. Photocleavable ion transport studies 5.12

5.2.7. Geometry Optimization and Binding Energy Calculation 5.13

5.2.8. Cellular viability and phototriggered cell death 5.14

5.3. Conclusion 5.18

5.4. Experimental details

5.4.1. General Methods 5.18

5.4.2. Physical Measurements 5.19

5.4.3. Synthetic Procedures 5.20

5.4.4. Anion Binding Studies 5.30

5.4.5. Ion Transport Studies 5.33

5.4.6. Photocleavable Studies 5.35

5.4.7. Phototriggered ion transport across EYPC-LUVs⊃HPTS 5.44

5.4.8. Biological Studies 5.47

5.4.9. X-Ray Crystallographic Studies 5.50

5.4.9. Theoretical Calculations 5.82

5.5. NMR Spectra 5.89

5.6. References 5.106

A

α	Alpha
Å	Angstrom
Ar	Aromatic
Ac	Acetyl
ATP	Adenosine Tri-Phosphate

B

β	Beta
BLM	Black lipid membrane

C

c	Concentration
cm	Centimeter
CF	Carboxyfluorescein
Calc.	Calculated
CFTR	Cystic Fibrosis Transmembrane Conductance Regulator
CLC	Chloride Channel
$CHCl_3$	Chloroform
$CDCl_3$	Deuterated chloroform
CH_3CN	Acetonitrile
CsCl	Cesium chloride
CCDC	Cambridge Crystallographic Data Centre

D

δ	Delta (Chemical shift)
°C	Degree Celsius
d	Doublet
dd	Doublet of doublet
dt	Doublet of triplet
DPhPC	2-diphytanoyl-*sn*-glycero-3-phosphocholine

DMSO	Dimethylsulfoxide
DCM	Dichloromethane
DFT	Density Functional Theory

E

EYPC	L-α-phosphatidylcholine from egg-yolk
EC_{50}	Effective concentration at half maximal activity
EtOAc	Ethylacetate
EtOH	Ethanol
Et_3N	Triethylamine
ESI	Electrospray ionization
EDC·HCl	1-(3-Dimethylaminopropyl)-3-ethylcarbodiimide hydrochloride

F

F_t	Fluorescence intensity at time *t*
FCCP	Carbonyl cyanide-p-trifluoromethoxyphenylhydrazone

G

G_{hyd}	Free energy of hydration

H

Hz	Hertz
h	Hour
HPTS	8-Hydroxypyrene-1,3,6-trisulfonate trisodium salt
HOBt	Hydroxybenzotriazole
HEPES	4-(2-hydroxyethyl)-1-piperazineethanesulfonic acid
HCl	Hydrochloric acid
HPLC	High performance liquid chromatography
HRMS	High Resolution Mass Spectrometry

I

I_F	Normalized Fluorescence Intensity
IR	Infrared spectroscopy
ISE	Ion selective electrode

J

J	Coupling constant

K

k	Rate constant
K_a	Association constant
K_2CO_3	Potassium carbonate
kcal	kilocalorie
KCl	Potassium chloride
KBr	Potassium bromide
KOH	Potassium Hydroxide

L

λ	Lambda
LUV	Large unilamellar vesicle
logP	logarithmic form of a ratio of Partition Coefficient
LiCl	Lithium chloride

M

m	Multiplet
M	Molar
μM	Micromolar
μL	Microliter
M.P.	Melting Point
MHz	Mega hertz
min	Minute(s)
max	Maximum

mg	Milligram(s)
mol	Mole
mmol	Millimole(s)
mM	Millimolar
mL	Milliliter
M. W.	Molecular weight
MeOH	Methanol
Me	Methyl

N

n	Hill coefficient
nm	Nanometer
nM	nanomolar
NMR	Nuclear magnetic resonance
Na_2SO_4	Sodium sulfate
NaF	Sodium fluoride
NaCl	Sodium chloride
NaBr	Sodium bromide
NaI	Sodium iodide
$NaNO_3$	Sodium nitrate
$NaClO_4$	Sodium perchlorate
NaSCN	Sodium thiocyanate
NaOAc	Sodium acetate
NaOH	Sodium hydroxide

O

obs	Observed
ORTEP	Oak Ridge Thermal Ellipsoid plot

P

Ph	Phenyl
ppm	Parts per million

R

rt	Room temperature
RbCl	Rubidium chloride

S

s	singlet
s	Second(s)
SCXRD	Single crystal X-ray diffraction

T

t	Triplet
td	Triplet of doublets
t	Time
Tx	Triton X-100
TLC	Thin Layer Chromatography
THF	Tetrahydrofuran
TBA	Tetrabutyl ammonium

V

Val	Valinomycin

Y

Y	Fractional fluorescence intensity

The thesis entitled **"Development of biomimetic photo-responsive artificial carriers for the transmembrane chloride transport"** comprises five chapters.

Synopsis

The thesis aims to develop various light-responsive synthetic ion transport systems. The transport of ions across the cell membrane through naturally occurring ion carriers and ion channels is crucial for multiple physiological functions. In particular, the transport of chloride ions is known to induce chloride-mediated apoptosis inside the cancer cells. Traditional transporters lack ion selectivity and hence can damage the normal healthy tissues. Stimuli such as voltage, pH, enzymes, ligands, light, etc., have been employed for activating ion transporters inside the cancer cells. Light-responsive ion transport systems, in particular, are important systems because of their spatiotemporal control, remote addressability, and less cytotoxicity.

Herein, we developed several light-responsive synthetic ion carriers, which were manifestly controlled utilizing the external electromagnetic radiations. Initially, the most widely used azobenzene photoswitch was used to generate the light-responsive ion transport systems, and efficient "OFF-ON" photoreguatory ion transport activity was achieved. Acylhydrazone-based photoswitches were employed to enhance the exciting state thermal stability. The reversibly-gated ion transport activity was achieved utilizing light and catalytic acid, respectively, as the external stimuli. Phenylhydrazone-based photoswitches were utilized to enhance the excitation wavelength. These photoswitches function comparatively at higher wavelengths compared to that of acylhydrazone switches. Eventually, we demonstrated an o-nitrobenzyl-based photocaged ion transport system could be selectively activated inside the cancer cells to induce chloride-mediated apoptosis utilizing the external electromagnetic radiations.

Chapter 1: Introduction to Membrane Transport

In cellular biology, membrane transport involves the collection of processes that regulate the movement of solute particles such as ions, small uncharged polar molecules, and bigger charged and uncharged molecules through biological membranes. Biological membranes are made up of lipid molecules, and they provide the protective layers around the cells and cellular organelles. Small nonpolar molecules like O_2 and CO_2 or small polar uncharged molecules like H_2O and NH_3 can easily pass through the membrane by simple diffusion. Ions and large

charged molecules like sugars or amino acids on the other hand cannot pass through the membrane because of the high thermodynamic barrier of the lipid membrane. However, the transport of these molecules is very essential for the smooth functioning of the living cells. Therefore, nature has developed special molecules in the form of ion channels, ion carriers, ion pumps, and ion pores that lead the transport of these important molecules across the lipid bilayer membrane. Ion carriers are those molecules that can shuttle across the membrane and hence drive the transport of ions across it. Ion channels on the other hand provide the static hydrophilic path across the lipid bilayer membrane through which the transport of ions occurs. Furthermore, the transport of ions through ion carriers and ion channels occurs along the concentration gradient without the expenditure of energy in a process called passive ion transport. The ion transport can also occur against the concentration gradient utilizing the energy in the form of ATPs in a process called active transport. This type of ion transport occurs through ion pumps. Moreover, the transport of bigger molecules like carbohydrates, and amino acids occurs through channels of bigger lumen called ion pores.

Chloride is the most abundant among other ions and its transport usually occurs through some specific chloride ion channels, important for maintaining the membrane potential cell volume regulation, Trans epithelial salt transport, cell cycle, apoptosis, etc. Malfunction of chloride channels or the genes which regulate these channels can lead to multiple numbers of life-threatening diseases called ‘channelopathies’, which include cystic fibrosis, barters syndrome, myotonia congenita, etc. Artificial ion carriers in this regard, have shown a good promise to be used in the replacement of these faulty ion channels to cure these diseases in a process called ‘channel replacement therapy’. Moreover, natural ion transporters like prodigiosin, tembjamine, and sphingolipids, have shown good anticancer applications. A significant number of artificial mimics have also been reported that show potential therapeutic applications as anticancer agents. However, one of the drawbacks which are associated with these systems is the lack of selectivity and thereby they can damage the normal healthy tissue as well. To overcome the undesired toxicity of normal cells, various stimuli-responsive ion transport systems have been reported that can regulate the transport of ions and in particular chloride ions across the lipid bilayer membrane and thus can be selectively activated inside the cancer cells. Therefore, Herein, we aimed to design several light-responsive ion transport systems that can be controlled using external electromagnetic radiations.

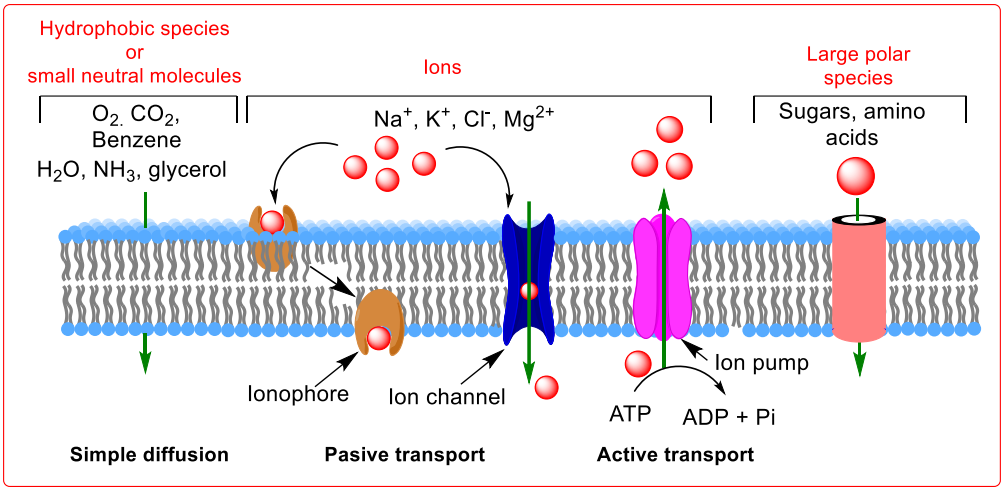

Figure 1. The schematic representation of membrane transport across the phospholipid membrane.

Chapter 2: A Sandwich Azobenzene-diamide Dimer for Photoregulated Chloride Transport

In This section, we designed and demonstrated six azobenzene-diamides as photoregulated anionophores **1a-1c** and **2a-2c**. For **1a-1c**, an ethyl group was linked to one of the amides while, for **2a-2c**, a cyanomethyl group was linked to the same amide moiety for better anion recognition. ^{1}H NMR-based anion binding studies confirmed stronger Cl^- binding cyano-bearing receptor **2b** compared to the non-cyano receptor **1b**. However, the ion transport activity of non-cyano receptors across large unilamellar vesicles (LUVs) was better compared to corresponding cyano congeners primarily due to the better amphiphilicity. Among the six receptors, **1a** showed the most efficient ion transport activity, i.e., EC_{50} = 0.199 μM and Hill coefficient ~ 2, when determined using a well-known HPTS essay. Detailed studies on **1a** unveiled Cl^- selectivity, and the Cl^-/anion antiport was found as the primary ion transport process. The transport activities of anionophores **1a**, **1c**, and **2a** were significantly attenuated upon photoisomerization of the azobenzene subunit from *trans* to *cis* using UV light, which on the other hand, efficiently regained back upon reverse photoisomerization using visible light. Photoregulation was carried out for a number of repeating cycles without any significant loss of efficiency. Importantly, photo-gating was achieved with a significantly short response time, which is highly desirable for its versatile applications. Moreover, the photoisomerized *cis* state showed excellent thermal stability due to the intramolecular hydrogen bonding of one of the amide protons with the nearest azo nitrogen. We strongly believe that with the very slow *cis* → *trans* thermal isomerization and unprecedentedly short response-time of *cis-trans* photoisomerization, the present system can also be incorporated into several supramolecular

artifacts with potential applications, which include soft materials, stimuli-responsive systems and in possible biological applications.

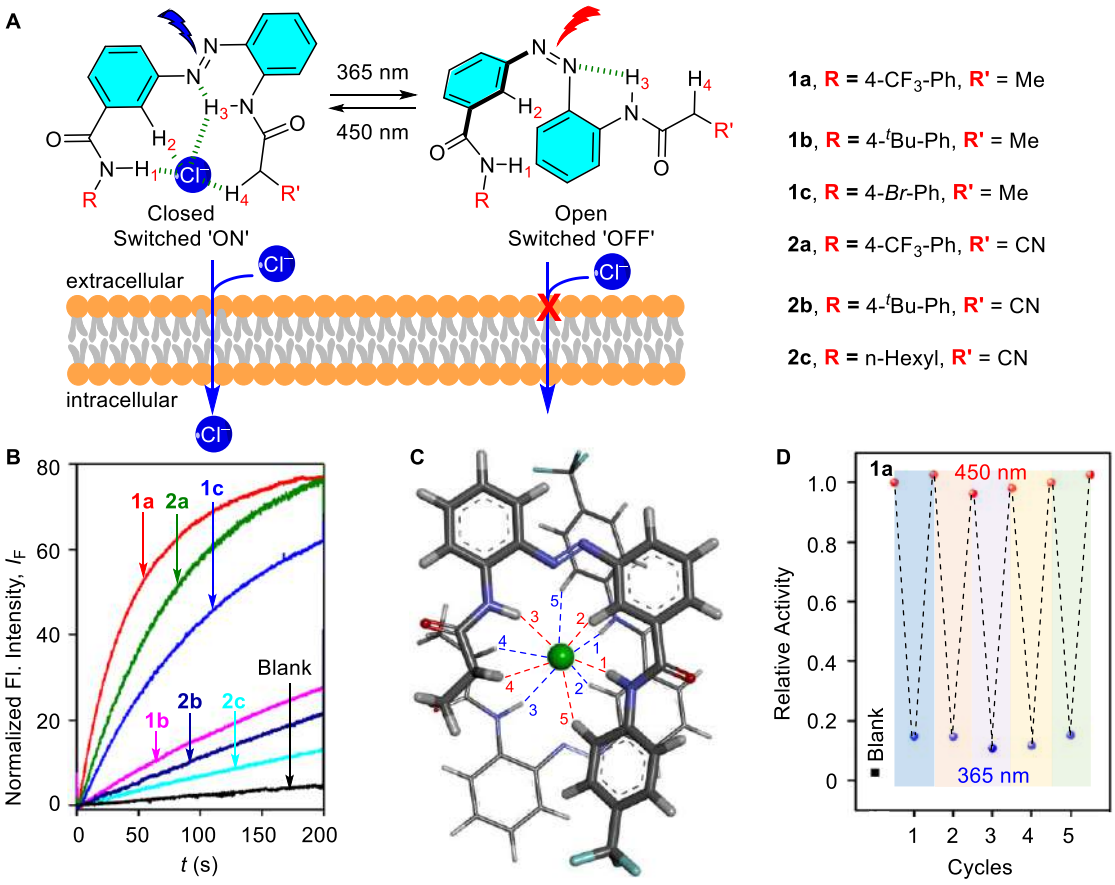

Figure 2. Design and working principle and structures of azobenzene-based light regulatory synthetic ion transporters (**A**). Activity comparison of **1a-1c** and **2a-2c** (0.3 μM each) across EYPC-LUVs⊃HPTS (**B**) geometry-optimized structure of [(**1a**)$_2$+Cl$^-$] complex (**C**). Photoregulated transport activity of **1a** (3 μM) taken at *t* = 280 s under alternating photoirradiation at two different wavelengths of 365 nm and 450 nm across EYPC-LUVs⊃Lucigenin (**D**).

Chapter 3: Stimuli-Responsive Anion Transport through Acylhydrazone-Based Synthetic Anionophores

In this section, we designed 5-(pentyloxy) isophthalic bisamide-based synthetic anions carrier's **1a–1d**, containing an amide linkage at one side and acylhydrazone on the other side, creating an efficient anion binding pocket. The single-crystal X-ray structure and ^{1}H NMR spectroscopic titrations confirmed anion binding in solid as well as in solution states. ^{1}H NMR titration confirmed 1:1 receptor-to-Cl$^-$ binding stoichiometry with the binding sequence of **1a** > **1d** > **1b** > **1c**. This binding sequence corroborated to the pK_a values of amide N–H and

acylhydrazone N–H protons. Single-crystal X-ray structure of **1d** confirmed that two molecules of the receptor create a cavity in which two Cl^- ions are bound. Although, **1d** (a phenyl group linked acylhydrazone) displayed the most efficient ion transport activity (EC_{50} = 0.11 μM and Hill coefficient ~ 2), compound **1a** (EC_{50} = 0.62 μM and Hill coefficient ~ 2) was recognized as a better stimuli-responsive system. Detailed mechanistic studies on **1a** revealed carrier-mediated anion antiport mechanism as the main transport process. Reversible switching between (*Z*)- and (*E*)-form was achieved by application of different stimuli, 312 nm radiation for (*E*)-to-(*Z*) isomerization, and acid catalyst for the back conversion. Such reversible isomerization led to ON-OFF switching of ion transport activity over several cycles, establishing the system as a gated anionophore.

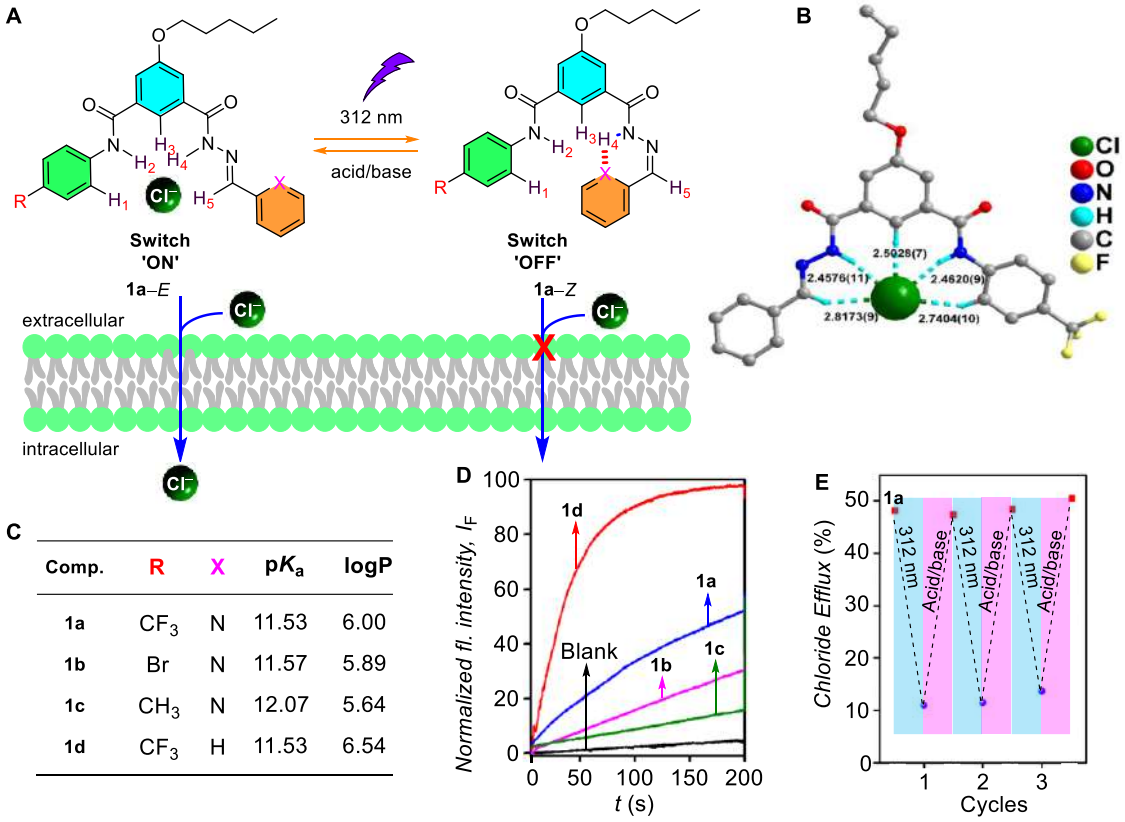

Comp.	R	X	pK_a	logP
1a	CF_3	N	11.53	6.00
1b	Br	N	11.57	5.89
1c	CH_3	N	12.07	5.64
1d	CF_3	H	11.53	6.54

Figure 3. Design and working principle and structures of acylhydrazone-based light regulatory synthetic ion transporters (**A**). X-ray crystal structure of compound **1d** complexed with Cl^- ion in a 1:1 (**1d**:Cl^-) binding pattern (**B**). Table showing R, X, pK_a (N–H_2) and logP values of compound **1a**–**1d** (**C**). Activity comparison of **1a-1d** across EYPC-LUVs⊃HPTS (**D**). Chloride efflux of **1a** in *E* form, after irradiation at 312 nm and after acid/base treatment (5 equiv) (**E**).

Chapter 4: Reversible Stimuli-Responsive Transmembrane Ion Transport using Phenylhydrazone-Based Photoswitches

In this section, we have designed different phenylhydrazone-based synthetic carriers **1a–1d**. The ^{1}H NMR spectroscopic titrations and electrospray ionization mass spectrometric (ESI-MS) studies revealed the anion binding in the solution state. ^{1}H NMR titration confirmed 1:1 receptor-to-Cl^- binding stoichiometry with the binding sequence of **1a** > **1b** > **1d** > **1c**. On the other hand, the mass spectrometric data provided peaks at *m/z* = 330.0620 and 332.0597, which correspond to the [**1a**+Cl^-] complex in the solution state. Compound **1a** (a trifluoromethyl-based) displayed the most efficient ion transport activity (EC_{50} = 2.5 ± 0.1 μM and Hill coefficient ~ 2), among other derivatives. Detailed mechanistic studies on **1a** revealed carrier-mediated anion antiport mechanism as the main transport process. Reversible switching between (*Z*)- and (*E*)-form was achieved by application of different stimuli, 365 nm radiation for (*E*)-to-(*Z*) isomerization, and acid catalyst for the back conversion. The pyridine-based

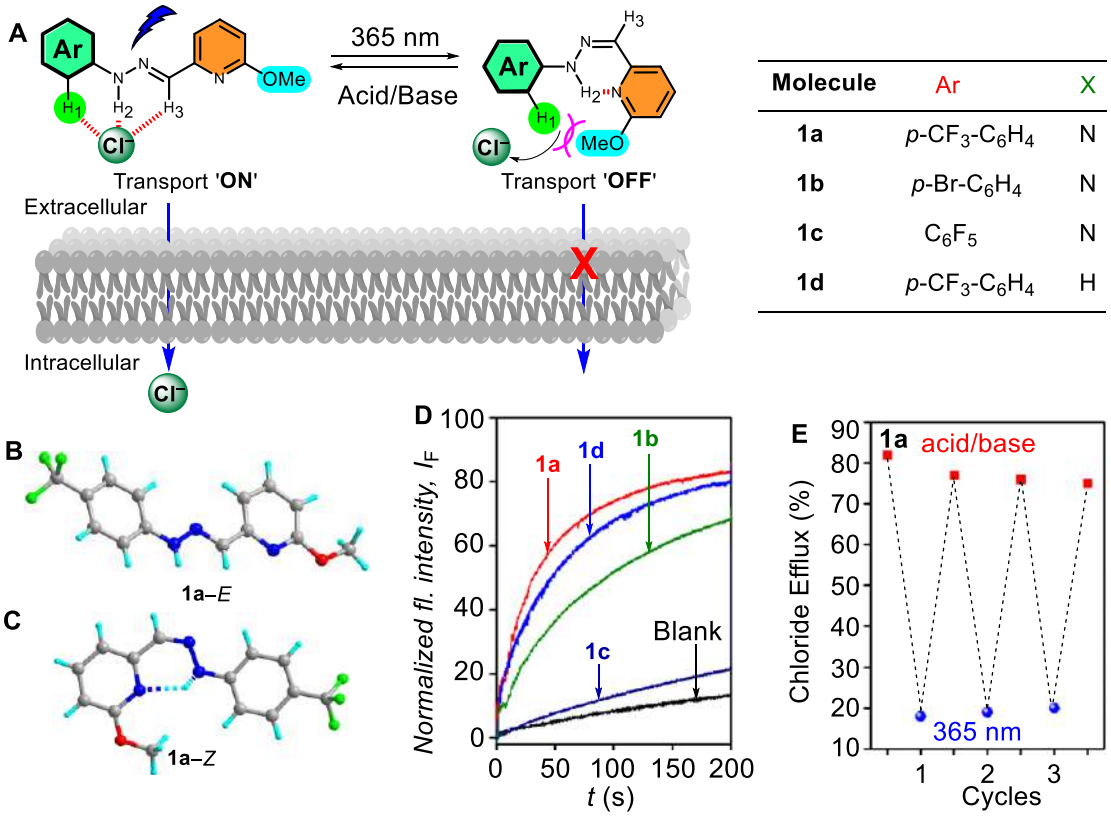

Molecule	Ar	X
1a	*p*-CF_3-C_6H_4	N
1b	*p*-Br-C_6H_4	N
1c	C_6F_5	N
1d	*p*-CF_3-C_6H_4	H

Figure 4. Design and working principle and structures of phenylhydrazone-based light regulatory synthetic ion transporters (**A**). Single crystal X-ray structures of **1a**–*E* (A) and **1a**–*Z* (**B**). Activity comparison of **1a-1d** across EYPC-LUVs⊃HPTS (**D**). Chloride efflux of **1a** in *E* form, after irradiation at 365 nm and after acid/base treatment (10 equiv) (**E**).

compound **1a** was seen to be an efficient photoswitch due to the presence of an intramolecular hydrogen bond in the (*Z*)-form. The phenyl based compound **1d** which lacks such an intramolecular hydrogen bond was poorly photoisomerized as compared to the pyridine-based compound **1a**. Such reversible isomerization led to ON-OFF switching of ion transport activity over several cycles, establishing the system as a stimuli-responsive anionophore.

Chapter 5: Visible-Light Phototriggered Release of an Apoptosis-Inducing Chloride Anionophore Inside the Cancer Cells

In this section, we report 3-substituted indole-2-carboxamide-based synthetic anionophores **2′**–**5′** and a library of *o*-nitrobenzyl-based procarriers **5a–5d** and the incorporation of electron-donating *N*, *N* dimethyl substituent to the *O*NB group enhances the absorption wavelength up to 500 nm. The single-crystal X-ray crystallographic studies and ^{1}H NMR spectroscopic titrations confirmed anion binding in solid and solution states. ^{1}H NMR titration confirmed 1:1 receptor-to-Cl^- binding stoichiometry with the binding sequence of **5′** > **3′** > **2′** > **4′** and the solid state Single-crystal X-ray structure of **5′** with Cl^- ion confirmed 1:1 **5′**:Cl^- binding stoichiometry. Transporter **5′** (a trifluoromethylphenyl-based) displayed the most efficient ion transport activity (EC_{50} = 0.184 ± 0.018 μM and Hill coefficient ~ 2), among other derivatives. Detailed mechanistic studies on **5′** revealed carrier-mediated anion antiport mechanism as the main transport process. The procarriers **5a–5d** displayed efficient photoactivation in artificial liposomes and inside MCF-7 breast cancer cells upon photoirradiation at 400 nm of electromagnetic radiations. On the other hand, *N*, *N* dimethyl-based procarrier **5c** shows photoactivation at 450 nm. This photoactivation at the higher wavelength of electromagnetic radiations is desirable for its practical biological applications. Further mechanistic details confirmed the chloride-mediated intrinsic pathway of apoptosis as the main process of cell death occurring through single-strand DNA cleavage.

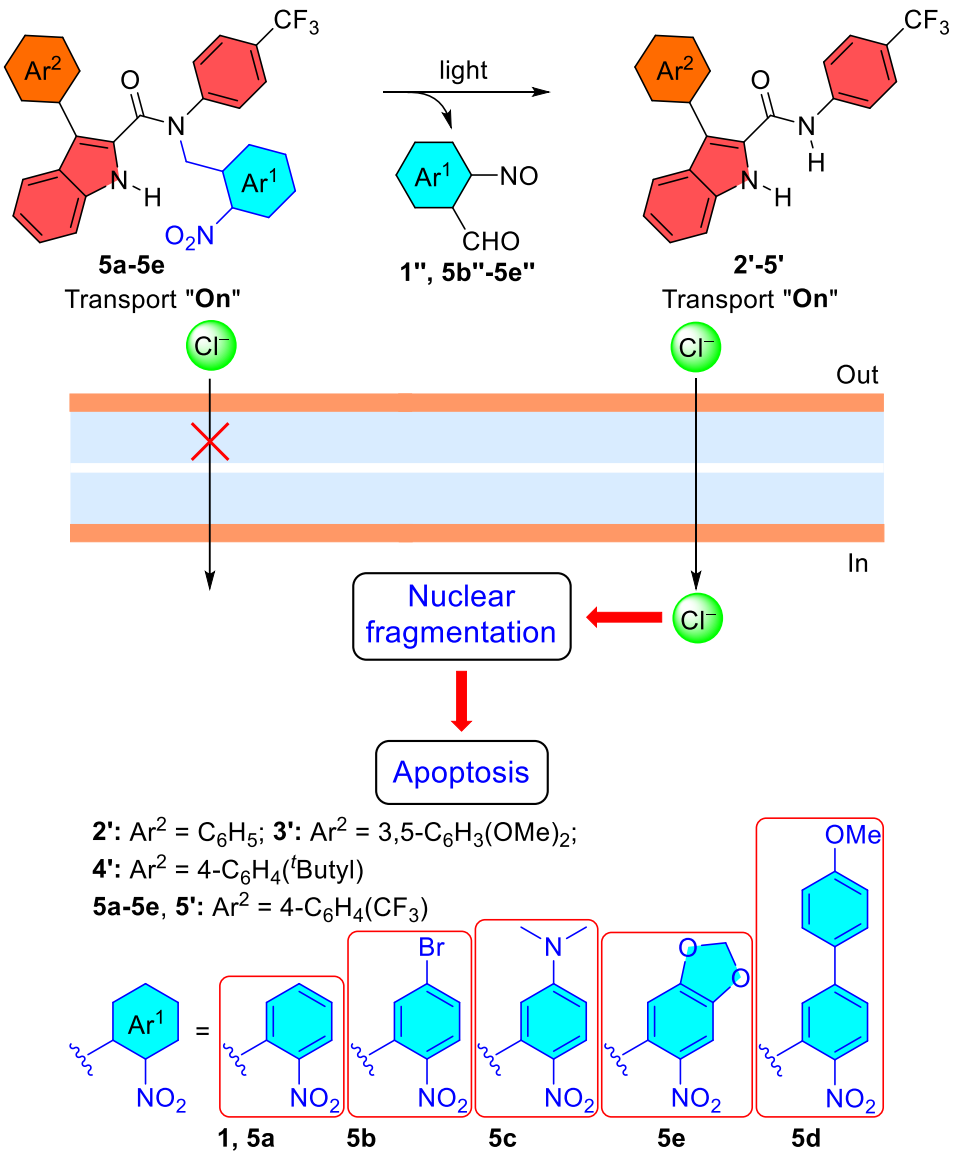

Figure 5. The schematic representation of visible-light photo-triggered release of an active chloride anion carrier for chloride-mediated apoptosis in cancer cells.

Chapter 1

Introduction to Membrane Transport

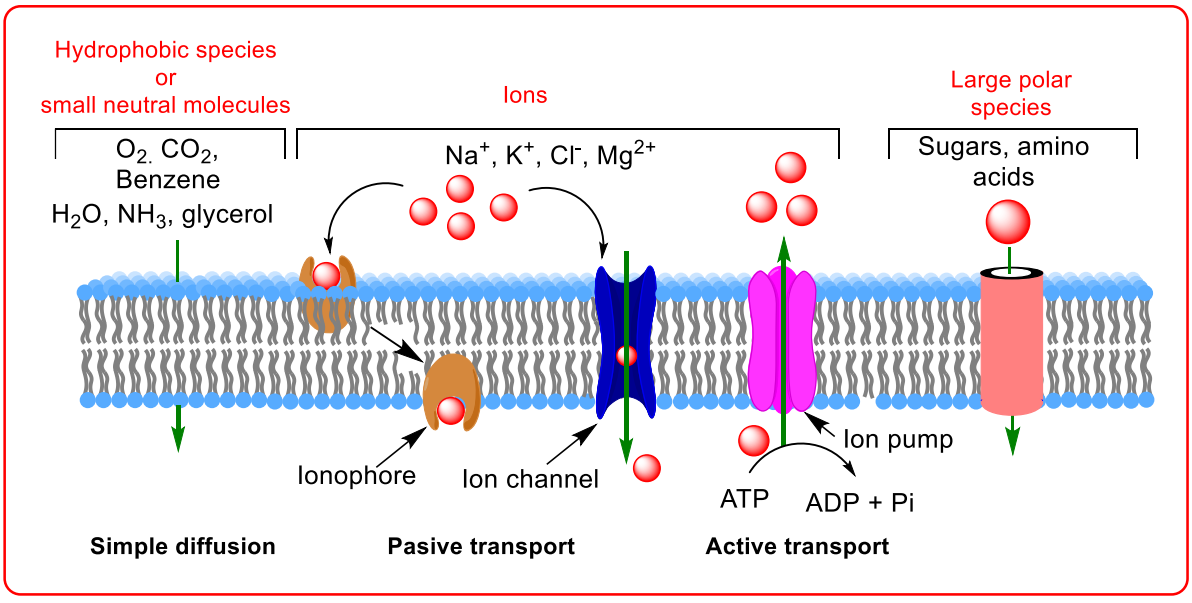

The biological cells are the basic structural and functional building blocks of living organisms that contain the essential and fundamental molecules of life, such as proteins, lipids, carbohydrates, nucleic acids, etc. Every living organism is made up of cells, and some cells, like bacteria or yeast, themselves constitute an organism. However, the cells in the multicellular organisms differentiate into specialized tissues to the execute the vital biochemical processes of the body. The important functions include the production and storage of energy, transfer of genetic information, creation of metabolic reactions, facilitate growth through mitosis, etc. The cell itself is made up of three major compartments: (i) nucleus, (i) cytoplasm, and (iii) cell membrane. The nucleus contains essential genetic information, which is vital for cell growth and reproduction. On the other hand, the cytoplasm is composed of several compartments called cell organelles, and these include mitochondria, Golgi apparatus, lysosomes, ribosomes, endoplasmic reticulum, etc. Every cell organelle is specialized to perform a specific cell function, for example, mitochondria, are important for the production of cell energy, lysosomes are important to digest unwanted substances, and the Golgi apparatus and endoplasmic reticulum are important for internal organization. The nucleus and the entire cytoplasmic constituents are separated from the exterior of the cell by a flexible protective layer of lipid bilayer membrane called as the cell membrane or plasma membrane. The cell membrane is very essential for the survival of the cell as it allows only specific solutes to cross through and restrict others. The cellular sub-organelles are also enveloped within this protective lipid bilayer membrane which separates them from the cytoplasmic compartment.[1]

1.1. Cell Membrane

As already stated above, the cell membrane is a flexible protective layer that separates the cytoplasmic constituents from the exterior of the cell, and on the other hand, it also separates the cellular sub-organelles from the cytoplasmic compartment. In its structure, the cell membrane or plasma membrane of the cell is made up of phospholipid molecules which are made up of two parts: (i) Hydrophilic head group and (ii) hydrophobic alkyl tails. These phospholipid molecules generate a lipid bilayer membrane through self-assembly (Figure 1.1A), and the typical width of this double layer is around 3–4 nm. The lipid bilayer membrane is selectively permeable, allowing certain substances to enter the cell and dastards others. This selective transport is essential for maintaining the ion homeostasis of the cell.[2]

Variation of the hydrophobic tails and the polar head groups constitute a wide variety of phospholipids in our cell membrane (Figure 1.1B), and among all, phosphatidylcholine is the most abundant.

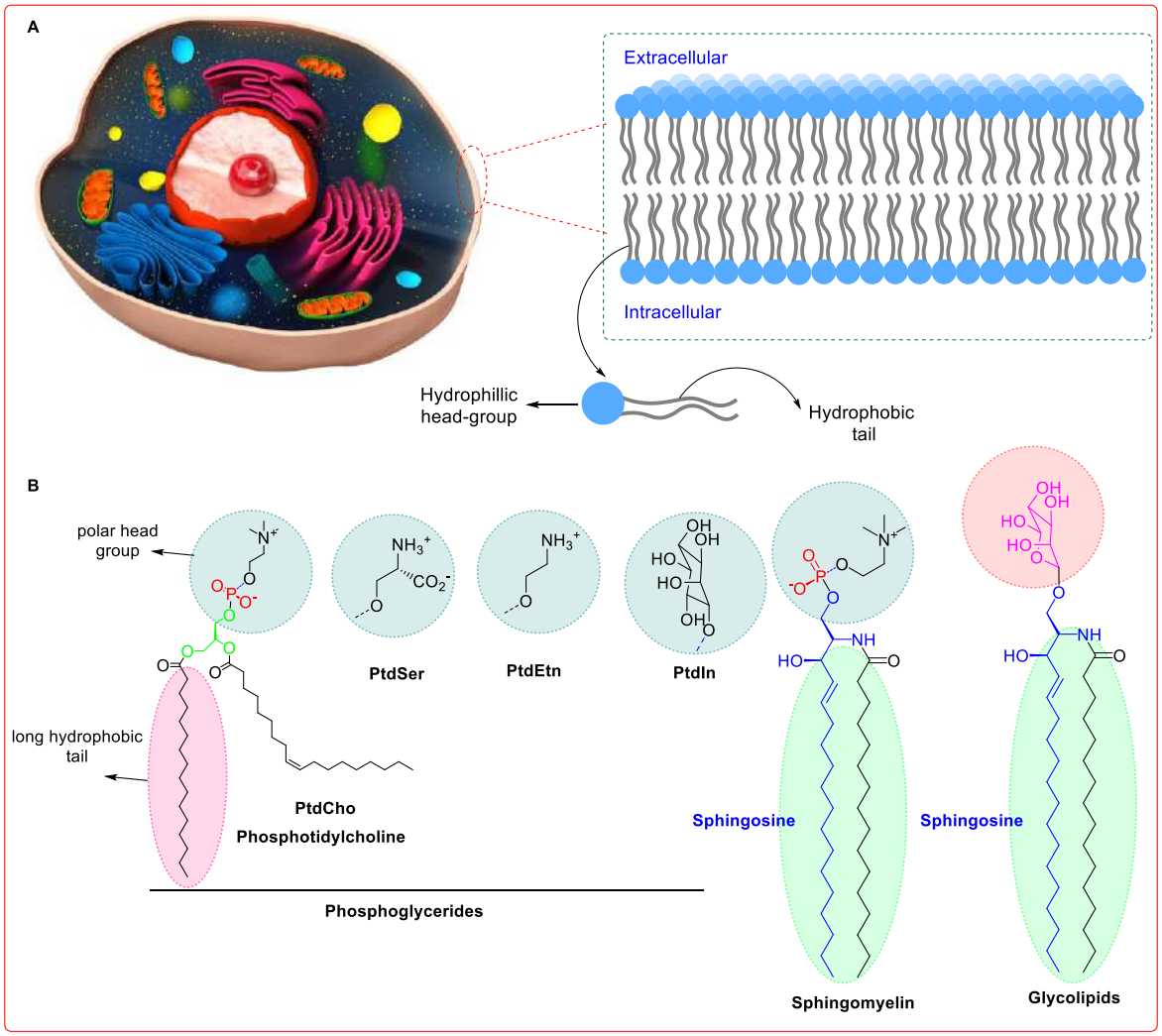

Figure 1.1. Schematic representation of eukaryotic cell and structure of lipid bilayer (**A**). The image has been adapted from https://o.quizlet.com/cI6TJpS6xSK1AiIGhmqpMA_b.jpg. Different types of phospholipids present in the lipid bilayer membrane of the cell (**B**).

1.2. Membrane Transport

As mentioned above, the cell membranes are selectively permeable and allow specific substances to tress pass while retarding others from doing so. This inherited selectivity of the cell membranes is essential for the cell's survival. Most membrane transport occurs through simple diffusion from high concentration to lower concentration. Uncharged molecules like O_2, CO_2, benzene, and N_2 and small hydrophobic molecules like water, ethanol, and NH_3 can quickly diffuse along the concentration gradient. On the other hand, the charged ions and large polar molecules like amino acids and sugars, which are vital for the cell, are not diffused freely due to the hydrophobic barrier of the lipid membrane (Figure 1.2). As these substances are important for various biological functions, they are usually transported across the cell

membrane through specialized molecules, such as protein channels or pores, which provide a static hydrophilic sites to diffuse these polar and charged moieties.[3]

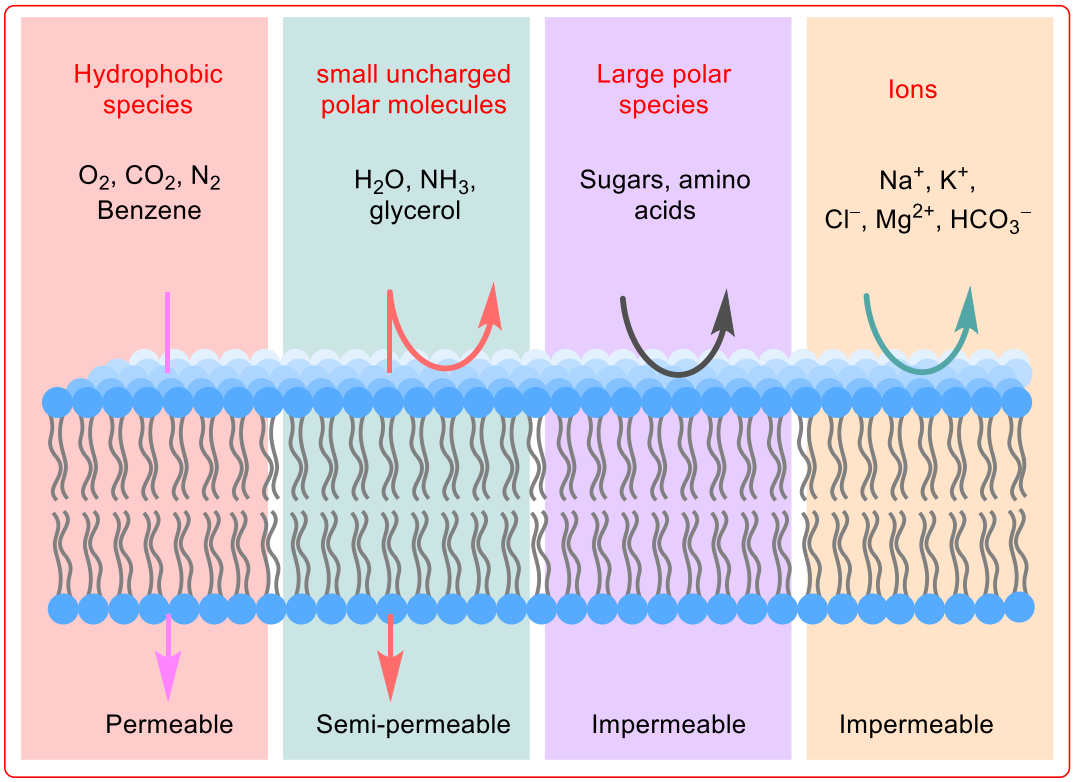

Figure 1.2. Schematic representation of the transport processes of different polar and non-polar solutes across the cell membrane and their relative permeability.

1.3.1. Ion Transport across the Cell Membrane

The transport of ions across the biological membranes is very essential for performing the vital physiological functions of sensory transduction, pH regulation, regulation of cell volume, ionic homeostasis, growth and development, etc.[3] This transport of ions is usually mediated through either ion channels or ion carriers. The ion carriers are relatively small molecules that shuttle through the lipid bilayer membrane to drive the ion transport across the membrane, and on the other hand, ion channels provide the static hydrophilic path across the lipid membrane for the ions to tress pass across the membrane (Figure 1.3A). The transport of ions usually occurs through the process of simple diffusion from high concentration to low concentration without the expenditure of energy and, this process of ion transport is called as passive ion transport. It can also occur against the concentration gradient of ions by utilizing the energy of ATP in a process called as active ion transport. This active transport occurs through some specific molecules called as ion pumps.

Further on the basis of the transport of ions across the cell membrane, the process can be divided into the following categories (Figure 1.3B):

Symport process: In this mode of ion transport, the two oppositely ions are transported in the same direction.

Antiport process: In this mode of ion transport similar ions, cations or anions, are being transported the opposite direction of the lipid bilayer membrane.

Uniport process: In this mode of ion transport, a single ion is transported in a particular direction of the l membrane.

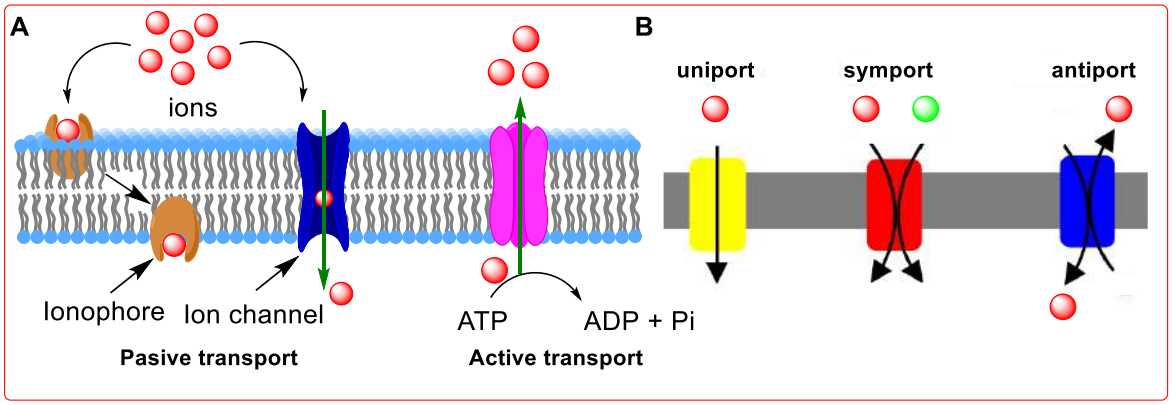

Figure 1.3. Schematic representation of transport process by ion carriers, ion channels, and ion pumps (**A**). Schematic representation of different transport modes across the lipid bilayer membrane (**B**). The image has been adapted from https://upload.wikimedia.org/wikipedia/commons/6/6c/Porters.PNG.

1.3.2. Gating

One of the most important characteristic features of the natural ion transport systems is 'gating', a process through which they can be opened or closed in a very controlled manner. This process is very important for the regulation of multiple physiological functions. Further based on the stimuli to which these ion channels respond, they can be classified into the following categories:

1.3.2.1. Light-Gated Ion channels: They belong to the family of ion channels that are regulated by light irradiation. (Figure 1.4). In nature, these ion channels are very rare due to light penetration issues e.g., channel rhodopsin.[4]

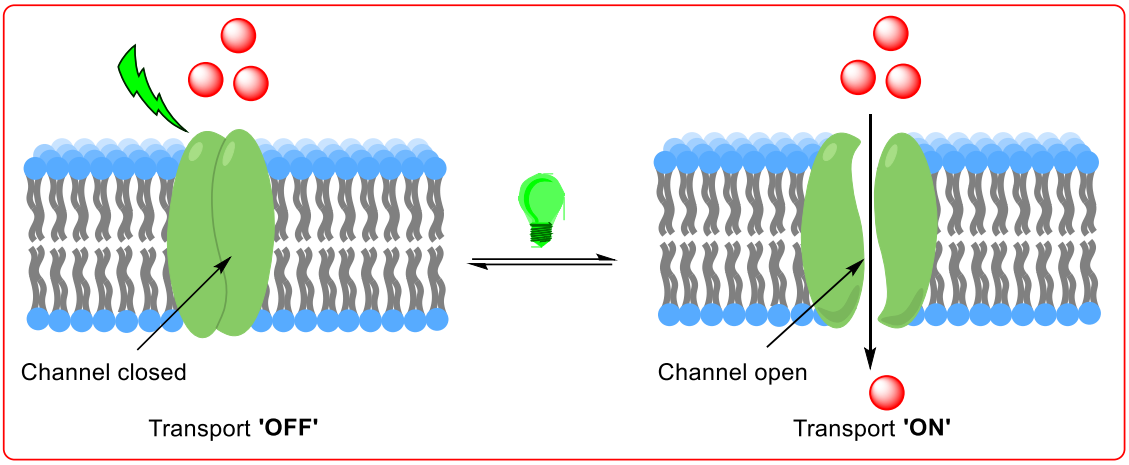

Figure 1.4. Schematic representation of a light-gated ion channel.

1.3.2.2. Ligand-Gated Ion channels: This family of ion channels is regulated by the binding of a specific ligand to the receptor site of the ion channel, which leads to the opening and closing of a particular ion channel. (Figure 1.5). For example, the release of Ca^{2+} ions from the endoplasmic reticulum to cytosol by calcium ion channel governed by inositol triphosphate (IP_3) ligand.[5] Ligand gated are considered to be important in are believed to be targeted for multiple drugs to treat diseases like anxiety, Schizophrenia and Alzimer's, etc.

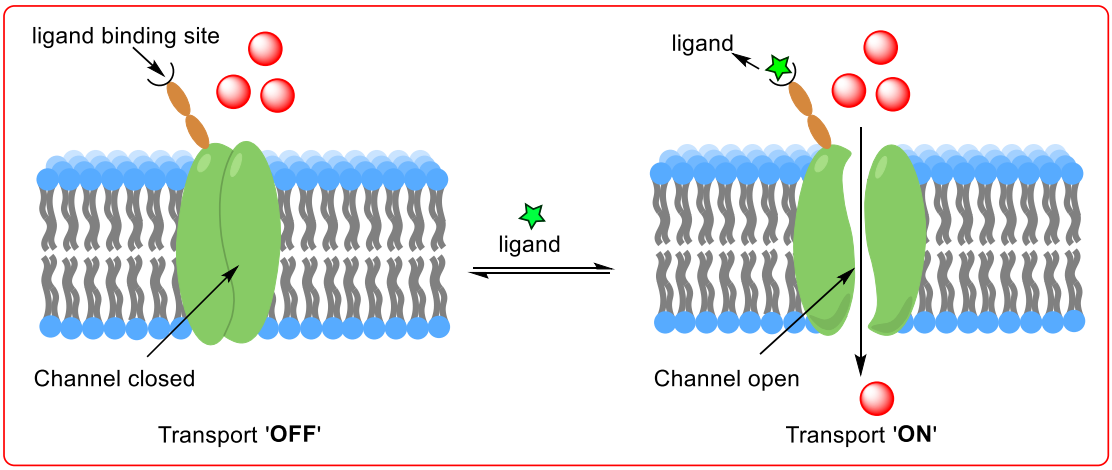

Figure 1.5. Schematic representation of a ligand-gated ion channel.

1.3.2.3. Voltage-Gated Ion channels: The ion channels whose activity is regulated by the change in the cell membrane's electrochemical potential are called voltage-gated ion channels (Figure 1.6). The change in potential change triggers the ion channels' opening and closing and examples include K^+ ion channels that create the membrane potential,[6] and Cl^- ion channels that are responsible for numerous biological applications like cell volume regulation, cell cycle and apoptosis etc.[7]

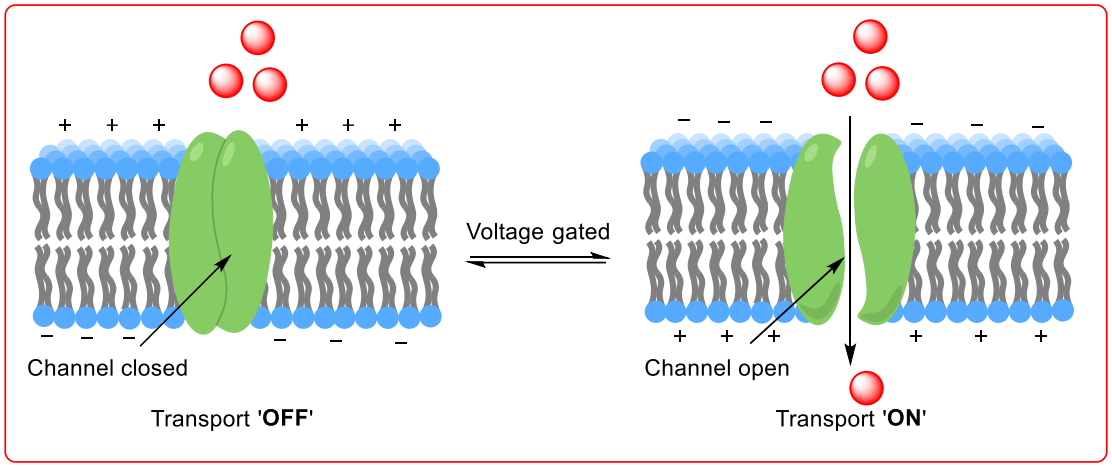

Figure 1.6. Schematic representation of a voltage-gated ion channel.

1.3.2.4. Mechanically-Gated Ion channels: The ion channels opened and closed by the change in the membrane tension are called mechanically gated ion channels or MSCs (Figure 1.7). Membrane tension drives the conformational change in these ion channels that leads to the flow of ions or small molecules, which in turn releases osmotic stress and activates different signaling cascades. For example, the TRPC6 cation channel, expressed in cardiovascular system.[8]

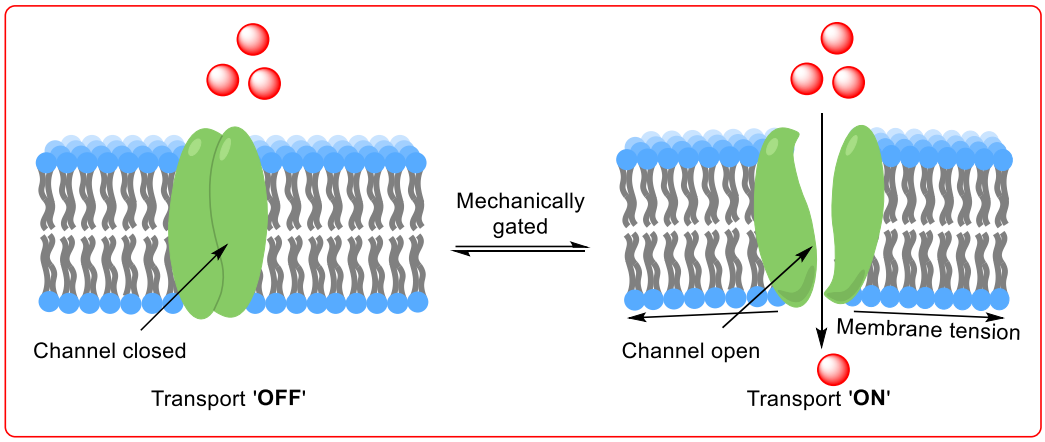

Figure 1.7. Schematic representation of a mechanically-gated ion channel.

1.3.3. Importance of chloride Transport across the cell membrane

The transport of ions across the biological membranes plays a crucial role in maintaining multiple biological functions of sensory transduction,[9] regulation of pH,[10] osmotic stress,[11] cell proliferation,[12] etc. Among all different ions, chloride ions are the most abundant in nature, and the selective transport, which usually occurs through some specific chloride ion channels is very important for the maintenance of membrane potential (30-60 mV in eukaryotic

cells), cell volume regulation, transepithelial transport, cell cycle, and apoptosis, etc.[11, 13] Malfunction of either the chloride channel or any mutation in the genes that regulate these protein channels can trigger multiple life-threatening diseases collectively called as 'channelopathies', like cystic fibrosis, barters syndrome, myotonia congenita, dents syndrome, etc.[14] The various chloride channels present inside the living cells include the CLC family, CFTR, CLIC, CLCA, etc.

Research studies suggest that processes like cancer, metastasis, and drug resistance result from dysregulated chloride ion channels. Regulation of cell volume is necessary for cell proliferation which is regulated by Volume-regulated anion channels (VRAC).[15] VRACs in cancer cells are encoded with CLC-3, which is a voltage-gated ion channel.[16] Cancer cells are characterized by abnormal cell proliferation due to the changes in the cell volume, which usually occurs due to the overexpression of the CLC-3 chloride ion channel. The abnormal cell growth and the drug resistance in cancer cells are attributed to the overexpression of CLC-3 channels.[17] CLC-3, CLC-4, and CLC-5 act as a Cl^-/H^+ antiporters in the intracellular membranes and contribute to the acidification of endosomes and lysosomes. Also, the proton flux regulators, e.g. V-ATPase, and Na^+/H^+ exchangers (NHE), regulate the unusual acidic pH

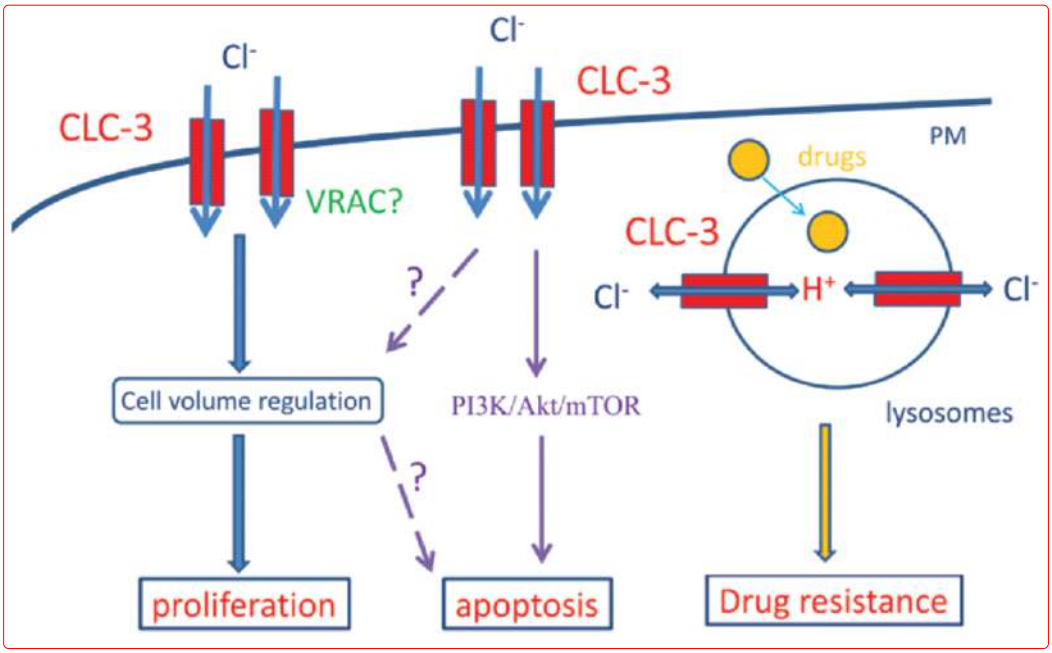

Figure 1.8. Schematic representation of effects of CLC−3 channel in cancer cells. The image has been adapted from https://www.spandidos-publications.com/article_images/or/33/2/OR-33-02-0507-g00.jpg.

in the microenvironment of tumor cells, thereby protect the tumor cells from weak basic drugs.[18] Acidic microenvironment promotes the protonation of weak base drug molecules,

which reduces the effective concentrations of these drugs in the cancer cells (Figure 1.8). Therefore, those molecules that can interfere with the chloride transport inside the biological cells can really be important in treating the cancer cells and thus will have crucial diverse therapeutic applications.

1.3.4. Non-protein-based natural and artificial chloride ion carriers

Most of the ion transport inside the living cells is being carried out through ion channels. Ion channels are usually membrane-bound proteins and typically made up of several self-assembled protein molecules to generate a static hydrophilic path for the transport of ions through them. Ion channels are characterized by selectivity, specificity, as they possess some selectivity filters and 'gating', a process through which they are either switched 'ON' or 'OFF' in response to some electrical or chemical stimuli. Thus, it is obvious that ion channels are complex in nature in terms of their structure and function, and is thus very difficult to mimic them to replace the faulty ion channels in a process called as 'channel replacement therapy'. Ion carriers are another class of ion transport systems that usually shuttle across the membrane to drive the ion transport process. Ion carriers are relatively simpler in terms of structure as compared to the pretentious ion channels. Prodigiosin is one of the examples of natural ion carrier which binds to chloride and can act as Cl^- ion transporter as well as H^+/Cl^- symporter (Figure 1.9A). It is isolated from gram negative bacterium *Serratia marcescens*.[19] Prodigiosin is a tripyrollic-based organic compound and offers a sickle-shaped binding site for chloride. Prodigiosin has a multiple biological number of biological activities which include antibacterial, antimicrobial and antibiotic activities.[20] Tambjamines are another class of naturally occurring ion carriers which are structurally analogous to prodigiosin (Figure 1.9B).[21] Quesada and coworkers investigated the chloride binding properties of these molecules and their synthetic analogs, and it was seen that ^{1}H NMR titration of the protonated form of these molecules lead to a significant shift of NH proton in the presence of TBACl salt, indicating the strong binding of these receptors with chloride. The high pK_a value (~10)[22] makes them weak H^+/Cl^- symporters but they do act as strong Cl^-/NO_3^- or Cl^-/HCO_3^- antiporters.

Sphingolipids are another set of natural ion carriers, for example C-16 ceramide (Figure 1.9 C). M. Colombini and coworkers in 2002 investigated the channel formation of these molecules[23] and later on J.T. Davis and coworkers investigated the ion transport activity of C-2 ceramide and it was observed that it drives the transport process through

Cl^-/NO_3^- mechanism.[24] Further, it was seen that it leaks Carboxyfluorescien only at higher concentrations indicating that it acts as the mobile carrier at the lower concentrations and as a pore at higher concentrations. Ceramides involve OH···A^- interactions during the transport process.

Taking the inspiration from naturally occurring anion carriers like prodigiosin, a lot of strategies have been developed for the successful design of synthetic chloride ion carriers. The general principle for the design of a chloride ion carrier is that there should be a rigid scaffold with multiple anion binding sites for anion recognition. Most of these systems use NH…A^- or OH…A^- hydrogen bonding interactions for anion recognition for example benzimidazole-based anionophores[25] (Figure 1.9D), urea-based anionophores[26] (Figure 1.9E), thiourea-based anionophores[27] (Figure 1.9F), cholapod-based transporters,[28] *trans*-decalins,[29] tripodal anion carriers,[30] squaramides[31] etc. Other interactions involve the use of halogen bond,[32] chalcogen bond,[33] and pnictogen bond.[34]

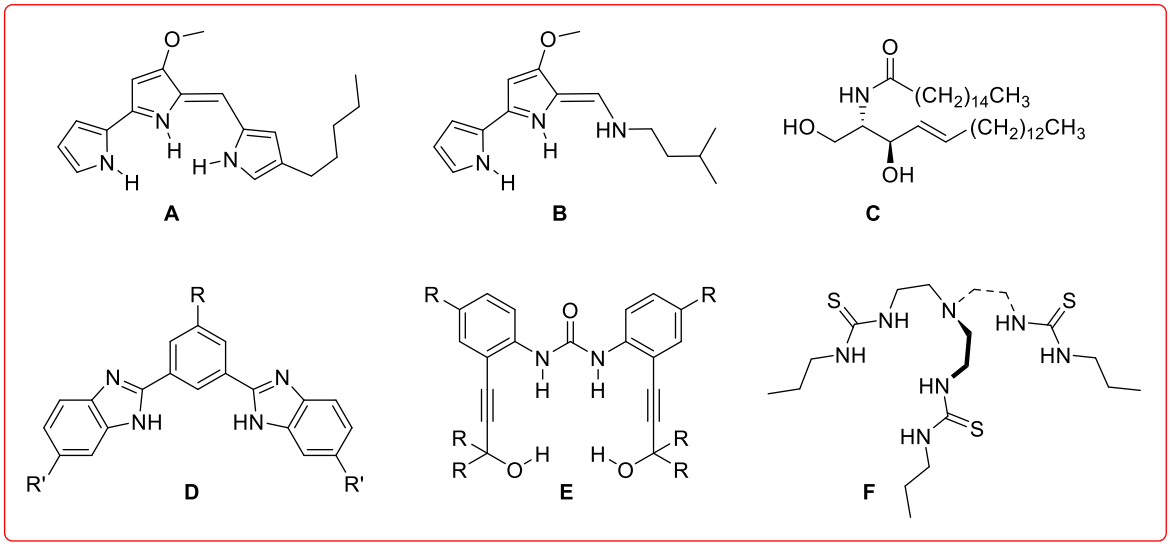

Figure 1.9. Structures of bioactive artificial ion transport systems.

1.3.5. Chloride ion transporters in therapeutics

The development of artificial ion transport systems in the form of ion carriers and ion channels have emerged an important field in the world of supramolecular chemistry. These systems have been studied in a diverse field of sensing, catalysis, waste extraction, porous materials etc.[35] However, they particularly promise their use for the treatment of "channelopathies", diseases which are caused due to the malfunction of either the ion channels or the genes which control a particular ion channels, through a process called as "ion channel replacement therapy".[36] In

this context, bis-(*p*-nitrophenyl)ureidodecalin system was introduced by Davis and coworkers, as an efficient and non-toxic chloride ion carrier in cells, which could find a suitable place in the therapeutics.[29c] Burke and coworkers further enhanced the interest in the ion channel replacement therapy and used amphotericin B, which forms non-selective ion channels in the cystic fibrosis cells, and it was found that these systems can restore host defenses in cystic fibrosis airway epithelia via a mechanism that is independent of CFTR and is therefore independent of genotype.[37] Though a lot of studies are to be needed to remove the unnecessary cytotoxicity emerging from these systems.

Recently studies have shown that these artificial ion transport systems are associated with the apoptosis-inducing activity in cancer cells, which raises a new hope for anticancer drug development. The naturally occurring prodigiosin (Figure 1.10A) is best known to induce apoptosis in the cancer cells in addition to its other valuable biological applications.[38] However, little is known about its mode of action. One hypothesis suggests the inhibition of phosphorylation and activation of JAK-3, a cytoplasmic tyrosine kinase for its immunoresponsive properties.[39] Likewise, as already discussed above that they are known to bind H^+/Cl^- through hydrogen bonding interactions and their ability to depolarize the acidic compartments of cells through H^+/Cl^- symport, or exchange of Cl^-/HCO_3^- across lipid bilayer membranes, is believed to be the reason for their anticancer activity. Similarly, naturally occurring tambjamine analogues also show potential anticancer activities.[40] A wide variety of artificial chloride ion carriers have been designed and well-studied for their anticancer activities. For example, bis-sulfonamides were shown to induce apoptosis in cancer cells (Figure 1.10D),[41] Shin and coworkers for the first time using calix[4]pyrrole showed the caspase-dependent induction of apoptosis by these systems (Figure 1.10B).[42] The same group showed that the squaramide-based carriers (Figure 1.10C), disrupts the autophagy and induces apoptosis by perturbing cellular chloride concentrations in cells.[43]

However, these systems don't show any selectivity towards the cancer cells and thus cannot distinguish the cancer cells from normal cells which could be detrimental as far as their biological applications are concerned. Therefore, it is of great interest to make these systems selective, particularly to the cancer cells, without effecting the normal cells. One of the ways through which this can be achieved is to make these systems stimulus-responsive so that they can only be activated at a particular desired tissue using that external stimuli.

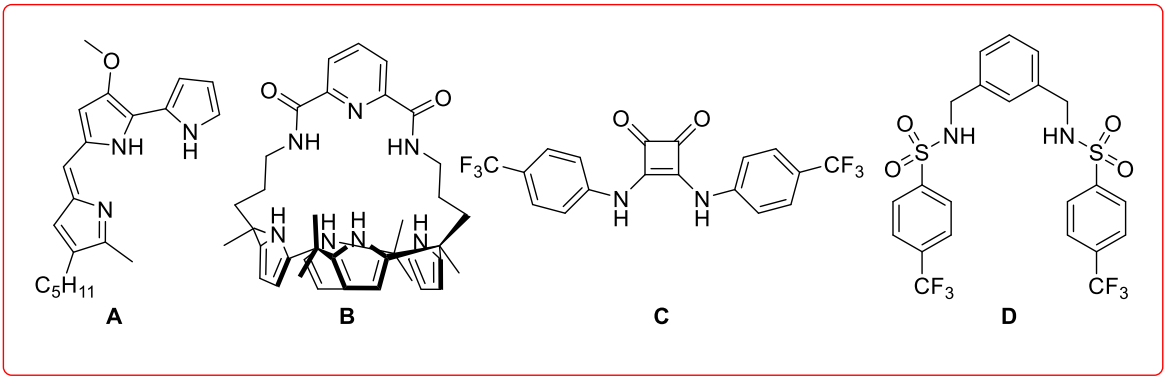

Figure 1.10. Structures of bioactive artificial ion transport systems.

1.3.6. Light responsive Synthetic Ion Transport Systems

As already discussed above, gating is an important process for executing the important biological functions inside the physiological systems. Different stimuli that control this gating behavior inside the physiological systems include membrane potential, pH change, chemical messengers, light etc. Malfunctioning in the natural ion transport systems can lead to various life-threatening biological abnormalities, which are collectively called as "channellopathies". Artificial ion transport systems in this regard have promised potential applications to be used in the replacement of these faulty channels in a process called as 'channel replacement therapy'. Additionally, recent studies have shown that these artificial ion transport systems are associated with the apoptosis inducing activity in the cancer cells, which raises a new hope for anticancer drug development.

Although a lot of synthetic ion transport systems in the form of ion channels and ion carriers have been studied, still the regulatory transport systems which promise the potential practical applications in curing the diseases arising from faulty natural ion channels or which can selectively be used for the treatment of cancer cells are rare. Different kinds of external stimuli that have been utilized for the generation of artificial gated systems involves the use of light, pH, ligand, enzymes, or voltage, etc.[26, 44] Light regulatory systems are of particularly interesting because of their intensity tunability, non-physical contact, high spatiotemporal precision, selectivity, and biocompatibility. Channelorhodopsin is the naturally occurring light-gated ion channel that works upon the application of light (Figure 1.11A).[45] 'Optochemical genetics' is one of the ways to incorporate a photoreceptor to the natural channel protein to attain the photo-regulatory ion transport behavior (Figure 1.11B), however, it involves a complex design strategy, complex fabrication and is often unpredictable.[46] The alternative approach involves the incorporation of a photoswitch to a simple yet all functional synthetic

ion transporter (Figure 1.11D-G).[47] Light-responsive ionophores that have been studied include the use of either photoswitchable (e.g., azobenzene, acylhydrazone, phenylhydrazone, stilbene, spiropyran, etc.)[48] or photocleavable (e.g., o-nitro aromatics)[49] groups.

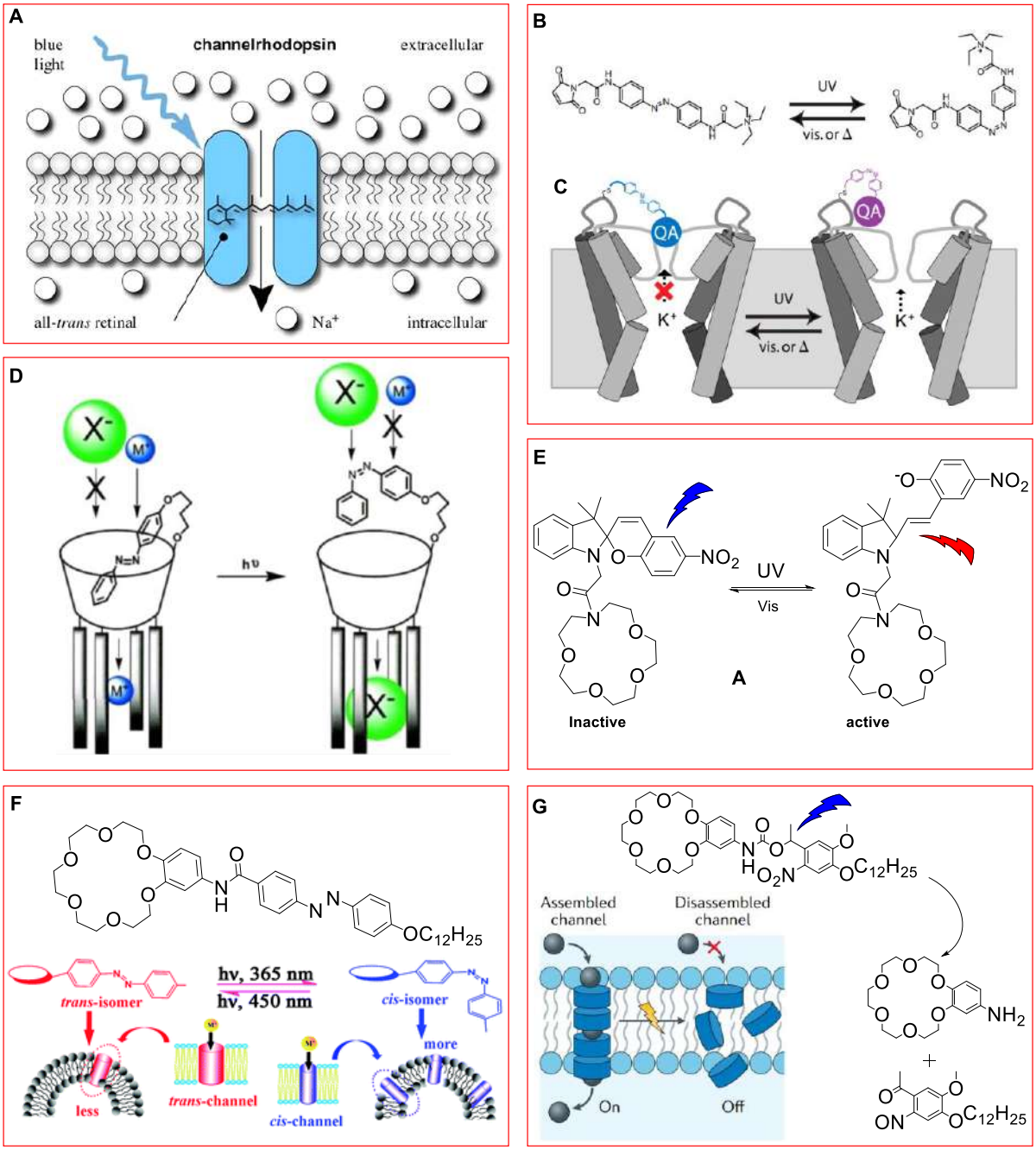

Figure 1.11. Channelrhodopsin, a light-sensitive, membrane-bound cation channel (**A**). Maleimide-azobenzene-quaternary ammonium photoswitch (**B**). Schematic representation of the K^+selective H-SPARK channel (**C**). Schematic diagram of possible anion and cation transport through azobenzene-based ion channel (**D**). Spiraopyran-based light switchable synthetic ion carrier (**E**). The molecular structure of compound, and schematic representation of crown ether-based light-regulated ion channel-transport (**F**). The molecular structures, the proposed channel-like self-assembly, the photolysis mechanism, and the proposed light-deactivated ion transport mechanism of *o*nb-based ion transport system (**G**).

1.4. Techniques Used to Study Synthetic Ion carriers

The study of ion transport using synthetic ion transport systems is usually done by creating the model cell membrane utilizing phospholipids. The ion transport activity is then monitored either by measuring the conductance through planer bilayer membranes (BLM study) or measuring the change in the concentration of a particular ion, sensed through different methods. The former BLM method is employed for ion channels and on the other hand, transport activity by ion carriers is monitored using spherical lipid bilayer membranes. Artificial liposomes provide a greatly reliable method of mimicking the biological membranes and provide a way to carefully control the intra and extra vesicular concentrations during the vesicular preparation. A concentration gradient is created across the liposomal membranes, and the relaxation of this ionic gradient enabled through artificial ion carriers can be studied either fluorescence, NMR, or ion-selective electrode-based assays.

1.4.1. Fluorescence based assay

In this method, spherical vesicles are prepared from phospholipids like 1-palmitoyl-2-oleoyl-sn-glycero-3-phosphocholine (POPC) or egg yolk phosphatidylcholine (EYPC) and are entrapped with a particular suitable dye. The transport activity is then evaluated and quantified by monitoring the change in fluorescence of a particular dye that is sensitive to the change in pH, anion gradient, or electrical potential. The different kinds of dyes which are usually used for the studies include 8-Hydroxypyrene-1,3,6-trisulfonic acid Trisodium salt (HPTS), *N*, *N*′-Dimethyl-9,9′-acridinium dinitrate (Lucigenin), Safranin O and Carboxyfluorescien. HPTS, a highly water-soluble membrane-impermeable dye is a pH indicator with a pK_a value of ~7.3 in aqueous buffers.[50] It can exist either in protonated form with the excitation wavelength of 403 nm or non-protonated form with the excitation wavelength of 460 nm. However, excitation at both of the wavelength gives the emission at same wavelength of 510 nm. The deprotonated form has high emission intensity as compared to the protonated form. During ion transport studies, a pH gradient is created across the lipid vesicles and the dissipation of this pH gradient in the presence of ion transporter is observed as the enhancement of the fluorescence intensity of HPTS dye at 510 nm is the indicative of the ion transport which occurs either via H^+/A^- efflux, i.e., symport or OH^-/A^- exchange process (Figure 1.10A).[50-51] Lucigenin is another kind of a dye where its fluorescence is selectively quenched in the

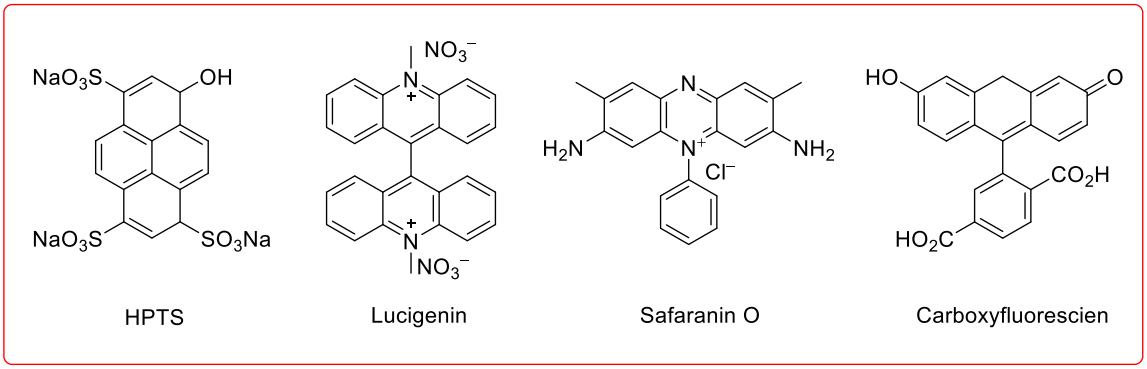

Figure 1.12. Representation of fluorescence-based ion transport assay in spherical vesicles, and the structure of the different dyes used.

presence of halide anions. In this assay, the lucigenin dye is entrapped in lipid vesicles containing a solution of $NaNO_3$. A chloride gradient is created by the addition of sodium chloride solution in the extravesicular solution. The quenching of the fluorescence in the presence of transport molecules is the indication of the chloride influx that occurs through Cl^-/NO_3^- antiport process.[52] Similarly, the safranin O is a dye which is sensitive to the membrane potential and is used to detect the unidirectional lion transport. It is a cationic dye that remains associated with the membrane and the development of membrane potential by the addition of transport molecule will lead to increase in fluorescence of safranin O.[53] Other fluorescent dyes like Carboxyfluorescein and ANTS-DPX are used to distinguish the ion channels from transmembrane pores.

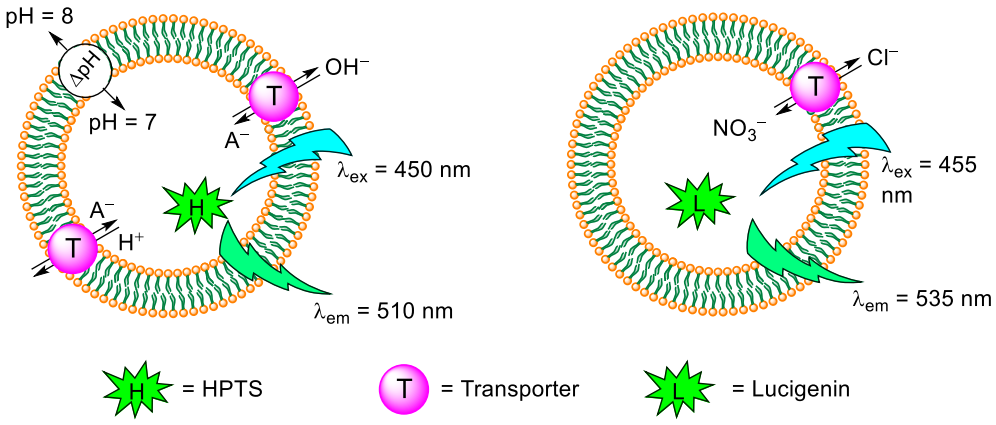

Figure 1.13. Schematic representation of the fluorescence-based ion transport assay in spherical vesicles using HPTS and lucigenin dyes.

1.4.2. Ion Selective Electrode based Assays

The ion selective electrodes are used to study the efflux of a particular ion entrapped inside the lipid vesicles by measuring the changes in conductivity of an external solution.[54] Chloride selective electrode is one of the type of electrode which is used to monitor the conductivity of chloride ions in the external aqueous solution and in this essay, the chloride ions are entrapped within the vesicles and their efflux is triggered by the addition of a transporter molecule (Figure 1.14).

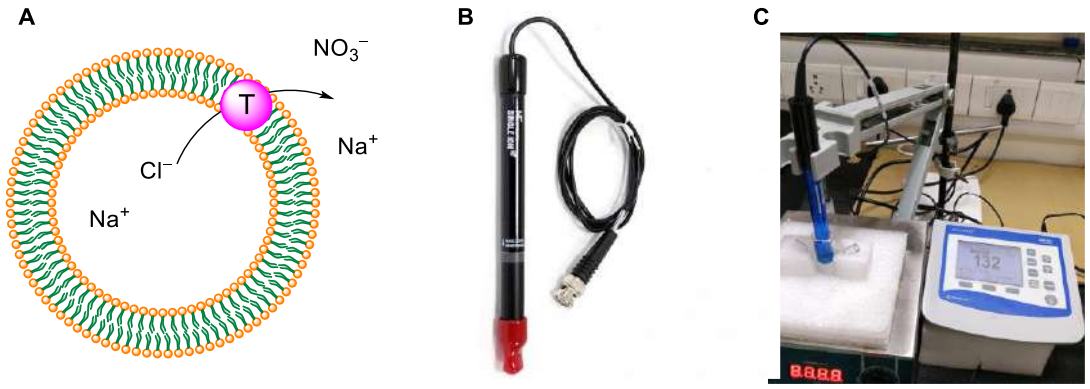

Figure 1.14. Schematic representation of ion transport study using chloride-based ion selective electrode (ISE). Vesicular representation of chloride transport across the membrane (**A**) Chloride-selective electrode (**B**) Complete setup of chloride sensing ion selective electrode (ISE) (**C**).

1.5. REFERENCES:

[1] Y. Z. Li, D., Basics of Molecular Biology. *In Molecular Imaging: Fundamentals and Applications*, J. Tian, Ed. Springer Berlin Heidelberg: Berlin, Heidelberg, 2013; pp 541–601.

[2] (a) H. e. Lodish, et, al., *Molecular Cell Biology, 5th Edition* **2003**, *W. H. Freeman*; (b) D. Metzler, *Biochemistry: The Chemical Reactions of Living Cells, 2nd Edition; Academic Press,* **2003**.

[3] B. Hille, *Ion Channels of Excitable Membranes, 3rd Edition* **2001**, *Sinauer*.

[4] G. Nagel, D. Ollig, M. Fuhrmann, S. Kateriya, A. M. Musti, E. Bamberg, P. Hegemann, *Science* **2002**, *296*, 2395–2395.

[5] F. Hucho, C. Weise, *Angew. Chem. Int. Ed.* **2001**, *40*, 3100–3116.

[6] Z. Sands, A. Grottesi, M. S. P. Sansom, *Curr. Biol.* **2005**, *15*, 44–47.

[7] G. J. A. Dale Purves, David Fitzpatrick, Lawrence C Katz, Anthony-Samuel LaMantia, James O McNamara, and S Mark Williams, *Neuroscience, 2nd edition* **2001**.

[8] R. Peyronnet, J. M. Nerbonne, P. Kohl, *Circ. Res.* **2016**, *118*, 311–329.

[9] O. Martí, A. Armario, *Int. J. Dev. Neurosci.* **1998**, *16*, 241–260.

[10] (a) V. V. Cherny, V. S. Markin, T. E. DeCoursey, *J. Gen. Physiol.* **1995**, *105*, 861–896; (b) I. S. Ramsey, Y. Mokrab, I. Carvacho, Z. A. Sands, M. S. P. Sansom, D. E. Clapham, *Nat. Struct. Mol. Biol.* **2010**, *17*, 869–875; (c) T. E. Decoursey, *Physiol Rev* **2003**, *83*, 475–579.

[11] K. Lange, *J. Cell. Physiol.* **2000**, *185*, 21–35.

[12] (a) S. Y. Chiu, G. F. Wilson, *J. Physiol.* **1989**, *408*, 199–222; (b) L. Nowak, P. Bregestovski, P. Ascher, A. Herbet, A. Prochiantz, *Nature* **1984**, *307*, 462–465.

[13] (a) B. Wang, J. Xie, H. Y. He, E. W. Huang, Q. H. Cao, L. Luo, Y. S. Liao, Y. Guo, *Oncotarget* **2017**, *8*, 63788–63798; (b) R. Benz, R. E. Hancock, *J. Gen. Physiol.***1987**, *89*, 275–295.

[14] (a) A. S. Verkman, L. J. Galietta, *Nat. Rev. Drug Discov.* **2009**, *8*, 153–171; (b) J. C. Edwards, C. R. Kahl, *FEBS letters* **2010**, *584*, 2102–2111.

[15] (a) V. Lehen'kyi, G. Shapovalov, R. Skryma, N. Prevarskaya, *Am. J. Physiol. Cell Physiol.* **2011**, *301*, 1281–1289; (b) J. Mao, L. Chen, B. Xu, L. Wang, W. Wang, M. Li, M. Zheng, H. Li, J. Guo, W. Li, T. J. C. Jacob, L. Wang, *Biochem. Pharmacol.* **2009**, *77*, 159–168; (c) B. Nilius, J. Eggermont, T. Voets, G. Droogmans, *Gen. Pharmacol.* **1996**, *27*, 1131–1140.

[16] D. D. Duan, *Acta Pharmacol. Sin.* **2011**, *32*, 675–684.

[17] S. Hong, M. Bi, L. Wang, Z. Kang, L. Ling, C. Zhao, *Oncol. Rep.* **2015**, *33*, 507–514.

[18] R. Martinez-Zaguilan, R. M. Lynch, G. M. Martinez, R. J. Gillies, *Am. J. Physiol. Cell Physiol.* **1993**, *265*, 1015–1029.

[19] F. Wrede, O. Hettche, *Ber. Dtsch. Chem. Ges. B*, **1929**, *62*, 2678–2687.

[20] (a) N. R. Williamson, P. C. Fineran, T. Gristwood, S. R. Chawrai, F. J. Leeper, G. P. Salmond, *Future Microbiol.* **2007**, *2*, 605–618; (b) R. A. Manderville, *Curr. Med. Chem. Anticancer Agents* **2001**, *1*, 195–218; (c) R. Pérez-Tomás, B. Montaner, E. Llagostera, V. Soto-Cerrato, *Biochem. Pharmacol.* **2003**, *66*, 1447–1452.

[21] (a) P. I. Hernández, D. Moreno, A. A. Javier, T. Torroba, R. Pérez-Tomás, R. Quesada, *Chem. Commun.* **2012**, *48*, 1556–1558; (b) V. Saggiomo, S. Otto, I. Marques, V. Félix,

T. Torroba, R. Quesada, *Chem. Commun.* **2012**, *48*, 5274–5276; (c) N. J. Knight, E. Hernando, C. J. E. Haynes, N. Busschaert, H. J. Clarke, K. Takimoto, M. García-Valverde, J. G. Frey, R. Quesada, P. A. Gale, *Chem. Sci.* **2016**, *7*, 1600–1608.

[22] M. S. Melvin, D. C. Ferguson, N. Lindquist, R. A. Manderville, *J. Org. Chem.* **1999**, *64*, 6861–6869.

[23] (a) L. J. Siskind, M. Colombini, *J. Biol. Chem.* **2000**, *275*, 38640–38644; (b) L. J. Siskind, R. N. Kolesnick, M. Colombini, *J. Biol. Chem.* **2002**, *277*, 26796–26803.

[24] J. W. A. Harrell, M. L. Bergmeyer, P. Y. Zavalij, J. T. Davis, *Chem. Commun.* **2010**, *46*, 3950–3952.

[25] M. G. J. Baud, M. R. Bauer, L. Verduci, F. A. Dingler, K. J. Patel, D. Horil Roy, A. C. Joerger, A. R. Fersht, *Eur. J. Med. Chem.* **2018**, *152*, 101–114.

[26] Y. R. Choi, B. Lee, J. Park, W. Namkung, K.-S. Jeong, *J. Am. Chem. Soc.* **2016**, *138*, 15319–15322.

[27] M. J. Spooner, H. Li, I. Marques, P. M. R. Costa, X. Wu, E. N. W. Howe, N. Busschaert, S. J. Moore, M. E. Light, D. N. Sheppard, V. Félix, P. A. Gale, *Chem. Sci.* **2019**, *10*, 1976–1985.

[28] (a) S. J. Edwards, H. Valkenier, N. Busschaert, P. A. Gale, A. P. Davis, *Angew. Chem. Int. Ed.* **2015**, *54*, 4592–4596; (b) A. P. Davis, *Coord. Chem. Rev.* **2006**, *250*, 2939–2951.

[29] (a) S. Hussain, P. R. Brotherhood, L. W. Judd, A. P. Davis, *J. Am. Chem. Soc.* **2011**, *133*, 1614–1617; (b) H. Valkenier, L. W. Judd, H. Li, S. Hussain, D. N. Sheppard, A. P. Davis, *J. Am. Chem. Soc.* **2014**, *136*, 12507–12512; (c) H. Li, H. Valkenier, L. W. Judd, P. R. Brotherhood, S. Hussain, J. A. Cooper, O. Jurček, H. A. Sparkes, D. N. Sheppard, A. P. Davis, *Nat. Chem.* **2016**, *8*, 24–32.

[30] (a) D. Mondal, A. Sathyan, S. V. Shinde, K. K. Mishra, P. Talukdar, *Org. Biomol. Chem.* **2018**, *16*, 8690–8694; (b) A. Roy, D. Saha, A. Mukherjee, P. Talukdar, *Org. Lett.* **2016**, *18*, 5864–5867; (c) A. Roy, T. Saha, M. L. Gening, D. V. Titov, A. G. Gerbst, Y. E. Tsvetkov, N. E. Nifantiev, P. Talukdar, *Chem. Eur. J.* **2015**, *21*, 17445–17452; (d) N. Busschaert, P. A. Gale, C. J. E. Haynes, M. E. Light, S. J. Moore, C. C. Tong, J. T. Davis, J. W. A. Harrell, *Chem. Commun.* **2010**, *46*, 6252–6254.

[31] (a) X. Bao, X. Wu, S. N. Berry, E. N. W. Howe, Y.-T. Chang, P. A. Gale, *Chem. Commun.* **2018**, *54*, 1363–1366; (b) N. Busschaert, I. L. Kirby, S. Young, S. J. Coles, P. N. Horton, M. E. Light, P. A. Gale, *Angew. Chem. Int. Ed.* **2012**, *51*, 4426–4430; (c) S. Zhang, Y. Wang, W. Xie, E. N. W. Howe, N. Busschaert, A. Sauvat, M. Leduc, L.

C. Gomes-da-Silva, G. Chen, I. Martins, X. Deng, L. Maiuri, O. Kepp, T. Soussi, P. A. Gale, N. Zamzami, G. Kroemer, *Cell Death Discov.* **2019**, *10*, 242.

[32] A. Vargas Jentzsch, D. Emery, J. Mareda, P. Metrangolo, G. Resnati, S. Matile, *Angew. Chem. Int. Ed.* **2011**, *50*, 11675–11678.

[33] S. Benz, M. Macchione, Q. Verolet, J. Mareda, N. Sakai, S. Matile, *J. Am. Chem. Soc.* **2016**, *138*, 9093–9096.

[34] L. M. Lee, M. Tsemperouli, A. I. Poblador-Bahamonde, S. Benz, N. Sakai, K. Sugihara, S. Matile, *J. Am. Chem. Soc.* **2019**, *141*, 810–814.

[35] (a) L. Steller, M. Kreir, R. Salzer, *Anal. Bioanal. Chem.* **2012**, *402*, 209–230; (b) R. Natarajan, L. Bridgland, A. Sirikulkajorn, J.-H. Lee, M. F. Haddow, G. Magro, B. Ali, S. Narayanan, P. Strickland, J. P. H. Charmant, A. G. Orpen, N. B. McKeown, C. G. Bezzu, A. P. Davis, *J. Am. Chem. Soc.* **2013**, *135*, 16912–16925; (c) L. Travaglini, L. N. Bridgland, A. P. Davis, *Chem. Commun.* **2014**, *50*, 4803-4805; (d) N. Busschaert, C. Caltagirone, W. Van Rossom, P. A. Gale, *Chem. Rev.* **2015**, *115*, 8038-8155; eS. Blake, R. Capone, M. Mayer, J. Yang, *Bioconjug.Chem.* **2008**, *19*, 1614–1624.

[36] (a) C. Cossu, M. Fiore, D. Baroni, V. Capurro, E. Caci, M. Garcia-Valverde, R. Quesada, O. Moran, *O. Front. Pharmacol.* **2018**, *9*; (b) J. R. S. Broughman, L. P.; Takeguchi, W.; Schultz, B. D. Iwamoto, T. Mitchell, K. E. Tomich, *Biochemistry* **2002**, *41*, 7350–7358.

[37] K. A. Muraglia, R. S. Chorghade, B. R. Kim, X. X. Tang, V. S. Shah, A. S. Grillo, P. N. Daniels, A. G. Cioffi, P. H. Karp, L. Zhu, M. J. Welsh, M. D. Burke, *Nature* **2019**, *567*, 405–408.

[38] (a) S. Cheung, D. Wu, H. C. Daly, N. Busschaert, M. Morgunova, J. C. Simpson, D. Scholz, P. A. Gale, D. F. O'Shea, *Chem.* **2018**, *4*, 879–895; (b) J. L. Sessler, L. R. Eller, W. S. Cho, S. Nicolaou, A. Aguilar, J. T. Lee, V. M. Lynch, D. J. Magda, *Angew. Chem. Int. Ed.* **2005**, *44*, 5989–5992.

[39] E. A. Sudbeck, F. M. Uckun, *IDrugs* **1999**, *2*, 1026–1030.

[40] E. Hernando, V. Soto-Cerrato, S. Cortés-Arroyo, R. Pérez-Tomás, R. Quesada, *Org. Biomol. Chem.* **2014**, *12*, 1771–1778.

[41] T. Saha, M. S. Hossain, D. Saha, M. Lahiri, P. Talukdar, *J. Am. Chem. Soc.* **2016**, *138*, 7558–7567.

[42] S.-K. Ko, S. K. Kim, A. Share, V. M. Lynch, J. Park, W. Namkung, W. Van Rossom, N. Busschaert, P. A. Gale, J. L. Sessler, I. Shin, *Nat. Chem.* **2014**, *6*, 885–892.

[43] N. Busschaert, S.-H. Park, K.-H. Baek, Y. P. Choi, J. Park, E. N. W. Howe, J. R. Hiscock, L. E. Karagiannidis, I. Marques, V. Félix, W. Namkung, J. L. Sessler, P. A. Gale, I. Shin, *Nat. Chem.* **2017**, *9*, 667–675.

[44] (a) Y. Kobuke, K. Morita, *Inorg. Chim. Acta* **1998**, *283*, 167–174; (b) N. Sakai, K. C. Brennan, L. A. Weiss, S. Matile, *J. Am. Chem. Soc.* **1997**, *119*, 8726–8727; (c) M. M. Tedesco, B. Ghebremariam, N. Sakai, S. Matile, *Angew. Chem. Int. Ed.* **1999**, *38*, 540–543; (d) E. K. Shea, R. Rutkowski, W. F. Stafford, P. S. Kim, *Science* **1989**, *245*, 646–648; (e) C. P. Wilson, S. J. Webb, *Chem. Commun.* **2008**, 4007–4009; (f) E. N. W. Howe, N. Busschaert, X. Wu, S. N. Berry, J. Ho, M. E. Light, D. D. Czech, H. A. Klein, J. A. Kitchen, P. A. Gale, *J. Am. Chem. Soc.* **2016**, *138*, 8301–8308.

[45] J. Abilez, J. Wong, R. Prakash, K. Deisseroth, K. Zarins, E. Kuhl, *Biophys. J.* **2011**, *101*, 1326–1334.

[46] (a) Y.-H. Tsai, S. Essig, J. R. James, K. Lang, J. W. Chin, *Nat. Chem.* **2015**, *7*, 554–561; (b) T. Fehrentz, F. M. E. Huber, N. Hartrampf, T. Bruegmann, J. A. Frank, N. H. F. Fine, D. Malan, J. G. Danzl, D. B. Tikhonov, M. Sumser, P. Sasse, D. J. Hodson, B. S. Zhorov, N. Klöcker, D. Trauner, *Nat. Chem. Biol.* **2018**, *14*, 764–767.

[47] P. V. Jog, M. S. Gin, *Org. Lett.* **2008**, *10*, 3693–3696.

[48] (a) R. F. Khairutdinov, J. K. Hurst, *Langmuir* **2004**, *20*, 1781–1785; (b) A. Kerckhoffs, Z. Bo, S. E. Penty, F. Duarte, M. J. Langton, *Org. Biomol. Chem.* **2021**, *19*, 9058–9067; (c) A. Kerckhoffs, M. J. Langton, *Chem. Sci.* **2020**, *11*, 6325–6331; (d) Y. R. Choi, G. C. Kim, H.-G. Jeon, J. Park, W. Namkung, K.-S. Jeong, *chem. commun.* **2014**, *50*, 15305–15308; (e) C. Wang, S. Wang, H. Yang, Y. Xiang, X. Wang, C. Bao, L. Zhu, H. Tian, D.-H. Qu, *Angew. Chem. Int. Ed.* **2021**, *60*, 14836–14840; (f) Y. Zhou, Y. Chen, P.-P. Zhu, W. Si, J.-L. Hou, Y. Liu, *Chem. Commun.* **2017**, *53*, 3681–3684; (g) C. Li, H. Chen, X. Yang, K. Wang, J. Liu, *Chem. Commun.* **2021**, *57*, 8214–8217; (h) W.-Z. Wang, L.-B. Huang, S.-P. Zheng, E. Moulin, O. Gavat, M. Barboiu, N. Giuseppone, *J. Am. Chem. Soc.* **2021**, *143*, 15653–15660; (i) T. Liu, C. Bao, H. Wang, Y. Lin, H. Jia, L. Zhu, *Chem. Commun.* **2013**, *49*, 10311–10313; (j) R.-Y. Yang, C. Bao, Q.-N. Lin, L.-Y. Zhu, *Chin. Chem. Lett.* **2015**, *26*, 851–856.

[49] C. Bao, M. Ma, F. Meng, Q. Lin, L. Zhu, *New J. Chem.* **2015**, *39*, 6297–6302.

[50] K. Kano, J. H. Fendler, *Biochimica. et. biophysica. acta.* **1978**, *509*, 289–299.

[51] (a) E. V. Anslyn, *J. Org. Chem.* **2007**, *72*, 687–699; (b) N. Sakai, S. Matile, *J. Phys. Org. Chem.* **2006**, *19*, 452–460.

[52] B. A. McNally, A. V. Koulov, B. D. Smith, J.-B. Joos, A. P. Davis, *Chem. Commun.* **2005**, 1087–1089.

[53] G. A. Woolley, M. K. Kapral, C. M. Deber, *FEBS Lett.* **1987**, *224*, 337–342.

[54] (a) P. H. Schlesinger, A. Gross, X.-M. Yin, K. Yamamoto, M. Saito, G. Waksman, S. J. Korsmeyer, *Proc. Natl. Acad. Sci.* **1997**, *94*, 11357–11362; (b) A. Silberstein, T. Mirzabekov, W. F. Anderson, Y. Rozenberg, *Biochimica. et. biophysica. acta.* **1999**, *1461*, 103–112.

Chapter 2

A sandwich azobenzene-diamide dimer for photoregulated chloride transport

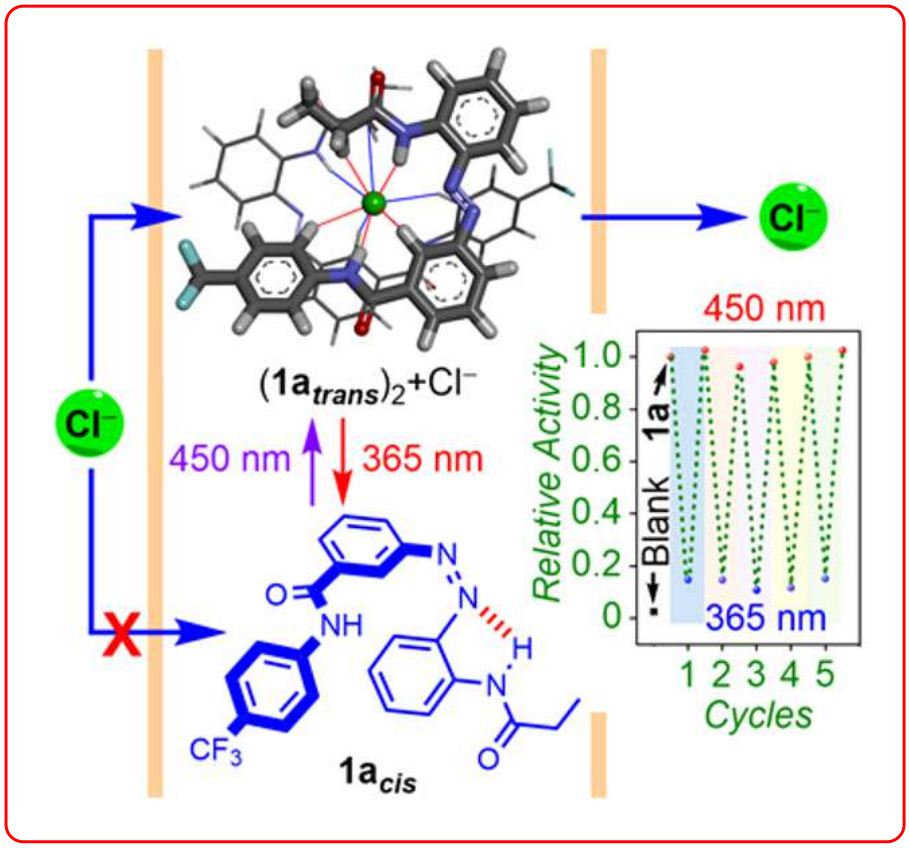

2.1. Introduction

As already disused in chapter 1, the transport of chloride across the biological membranes is essential for performing vital biological functions which include osmotic regulation, nerve transmission, muscle excitation, ionic homeostasis, growth, and development.[1] This process is efficiently carried out through natural protein channels and ion carriers.[2] One of the important characteristic features associated with natural transport systems is 'gating', a process through which they can be switched 'On' or 'OFF' to control the transport of ions through these systems.[3] This 'gating' behaviour is important for the necessary biological functions. The natural ion transport systems are environmentally sensitive and the Stimuli like membrane potential, pH, chemical messengers, and light can trigger their gating behaviour.[4] As we know, any misregulation in the transport process, particularly, chloride ions can lead to different dreadful diseases.[5] A lot of artificial ion transport systems have been developed with the aim to use them in the replacement of faulty ion channels in a process called as 'channel replacement therapy'.[6] Additionally, recent research studies have shown that these systems have potential applications in cancer therapy.[7] Stimulus-responsive ion transport systems promise better applications in terms of their utility in 'ion channel replacement therapy' or their use as target-specific moieties in cancer therapeutics.[8] Artificial gated systems usually involve the use of pH, light, voltage, ligands, enzymes, etc., as external stimuli.[9] Light is one of the important external stimuli due to its high Spatio-temporal control, intense tenability, and less toxicity.[10] Light-responsive ionophores that have been studied include the use of either photoswitchable (e.g., azobenzene, acylhydrazone, spiropyran, etc.)[5a, 11] or photocleavable (e.g., *o*-nitro aromatic) groups. Azobenzene is one of the important photoswitches that has been incorporated into the artificial ion transport systems to achieve the gating behavior because of the facts that it is easy to design, has modular synthesis, has good addressability, less toxicity, efficient reversibility, and a significant change in the length and dipole moment upon *trans* to *cis* photoisomerization.[12] The *trans* → *cis* isomerization occurs upon exposure to UV light (~ 365 nm), while the *cis* → *trans* isomerization takes place by visible light (~ 450 nm). Moreover, the *cis* → *trans* isomerization also occurs thermally owing to the thermodynamic stability of the *trans* isomer resulting in spontaneous *cis* → *trans* even in dark (Figure 2.1A). the *trans* conformation of azobenzene was incorporated for achieving the active state of the bioengineered protein and self-assembled synthetic channels.[4c, 10, 11e, 13] On the other hand, azobenzene-urea-based light-responsive chloride carriers were generated by Ye Rin Choi et al. in 2014.[14] The

transporters were inactive in the *Trans* form and photoisomerization into the *cis* form at 365 nm generated the active transporter by bringing the two urea groups in close proximity for better chloride binding (Figure 2.1B). However, the thermal stability of the anionophores in the excited *cis* state is expected to delimit its practical applications.

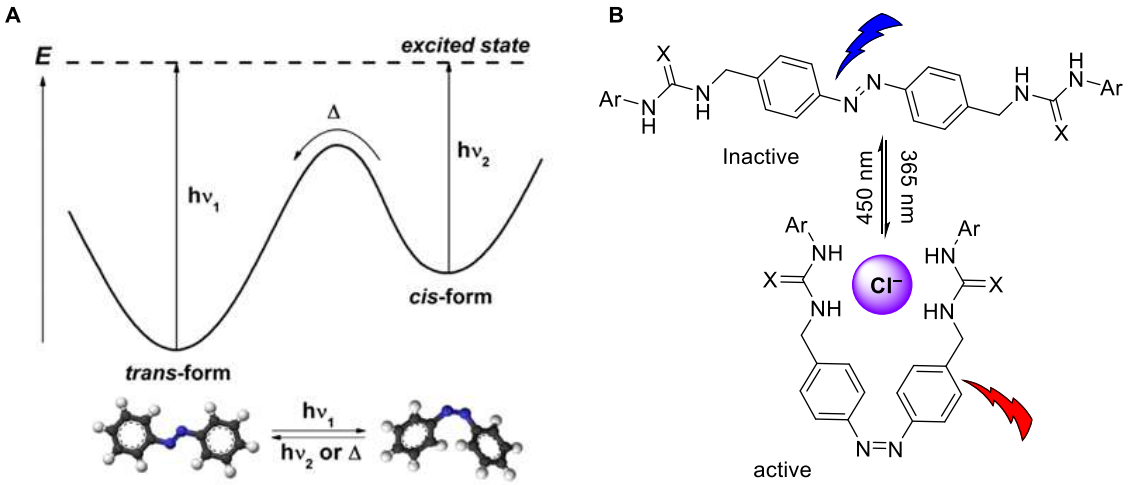

Figure 2.1. Energy diagram of Photo and thermal *trans-cis* photoisomerization of azobenzene subunit (**A**). Azobenzene-urea-based synthetic photoresponsive chloride carrier (**B**).

We envisaged that an adequately designed *trans*-azobenzene can provide an anion binding cavity involving its aryl C–H that is *ortho* to the azo group. Herein, we report an intramolecular-hydrogen bonded *trans*-azobenzene-diamide system that forms an efficient photoswitchable chloride carrier and offers a thermally stable inactive state in the *cis*-conformation. The structure of the *trans*-azobenzene-diamide-based anion receptor system is illustrated in Figure 2.2A. In the receptor, the amide N–H_1, and C_{Ar}–H_2 create the anion binding site. In this site, the presumed repulsion between the anion and the nearest azo nitrogen is masked by the intramolecular six-membered $N_{azo}\cdots H_3$–N hydrogen bond using a second amide moiety. Interestingly, that the N–H_3 moiety would also provide an additional hydrogen bond for anion recognition. The possibility of a further anion recognition through C_{Alk}–$H_4\cdots$anion hydrogen bond was also envisaged. In the lipid bilayer membrane, the receptor would facilitate the transport of anions. The *trans* to *cis* photoisomerization of the receptor at 365 nm would drastically change the planarity and proximity of the anion recognizing groups leading to poor anion binding and transport.[15] We envisaged that in the *cis*-conformation, the N–H_3 group would be involved in an intramolecular five-membered $N_{azo}\cdots H_3$–N hydrogen bond providing significant thermal stability to the *cis* isomer.[16] Therefore, the *cis* to *trans* isomerization can be achieved entirely by light at 450 nm to regain

the active state back and hence, a photoregulated artificial ion transport system will be generated out. Structural modification in terms of lipophilicity, as per Lipinski rule[17] was expected to influence the permeability as well as the transport affinity of these anionophores.[18] The logP and pK_a values of these compounds were calculated using the Marvin Sketch program (Figure 2.2B).[19]

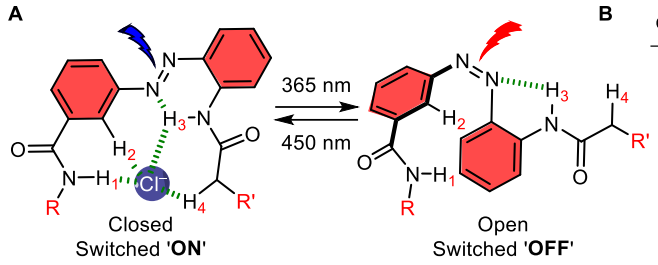

comp.	R	R'	pK_a(H_1)	pK_a(H_2)	logP
1a	4-CF_3-Ph	Me	11.44	12.24	6.29
1b	4-^{t}Bu-Ph	Me	11.76	12.38	6.95
1c	4-*Br*-Ph	Me	11.48	12.25	6.18
2a	4-CF_3-Ph	CN	11.30	11.92	5.54
2b	4-^{t}Bu-Ph	CN	12.17	11.52	6.20
2c	n-Hexyl	CN	14.29	11.69	4.85

Figure 2.2. Design and working principle of light regulatory synthetic ion transporter (**A**). Chemical structures, pK_a values of N-H_1 and N-H_2 protons, logP values of compounds **1a-1c** and **2a-2c** (**B**).

2.2. Results and discussions

2.2.1. Synthesis

The synthesis of the anionophores **1a-1c** were achieved by reducing the nitro derivate **3** into the corresponding aniline derivative **4** using sodium borohydride. The aniline derivative **4** was oxidized into the nitroso compound **5** which was subsequently coupled with 3-aminobenzoic acid to synthetize acid derivative **6**. The acid derivative **6** was finally coupled with different aniline derivatives to furnish the final compounds **1a-1c** in good yields (Scheme 2.1).

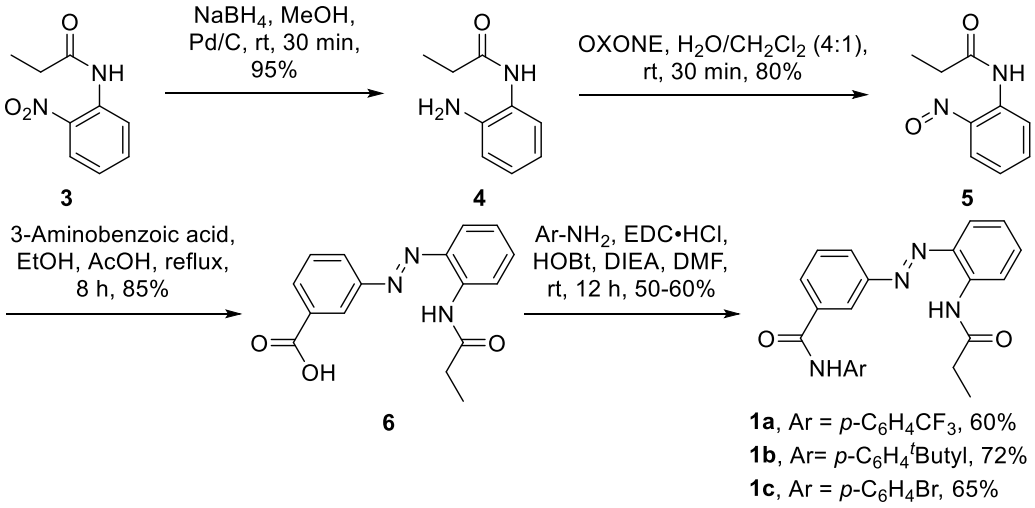

Scheme 2.1. Synthetic scheme for the compounds **1a-1c**.

The synthesis of the derivatives **2a-2c** was achieved by converting the mono-Boc protected aniline derivative **7** into the corresponding nitroso derivative **8** which was subsequently reacted with 3-aminobenzoic acid to get the acid derivative **9**. Compound **9** was coupled with different aniline derivatives to obtain the mono-Boc derivatives **10a-10c** which were deprotected to get the aniline derivatives **11a-11c**. Finally, aniline derivatives **11a-11c** were coupled with 2-cyanoacetic acid to furnish the final compounds **2a-2c** in excellent yields (Scheme 2.2).

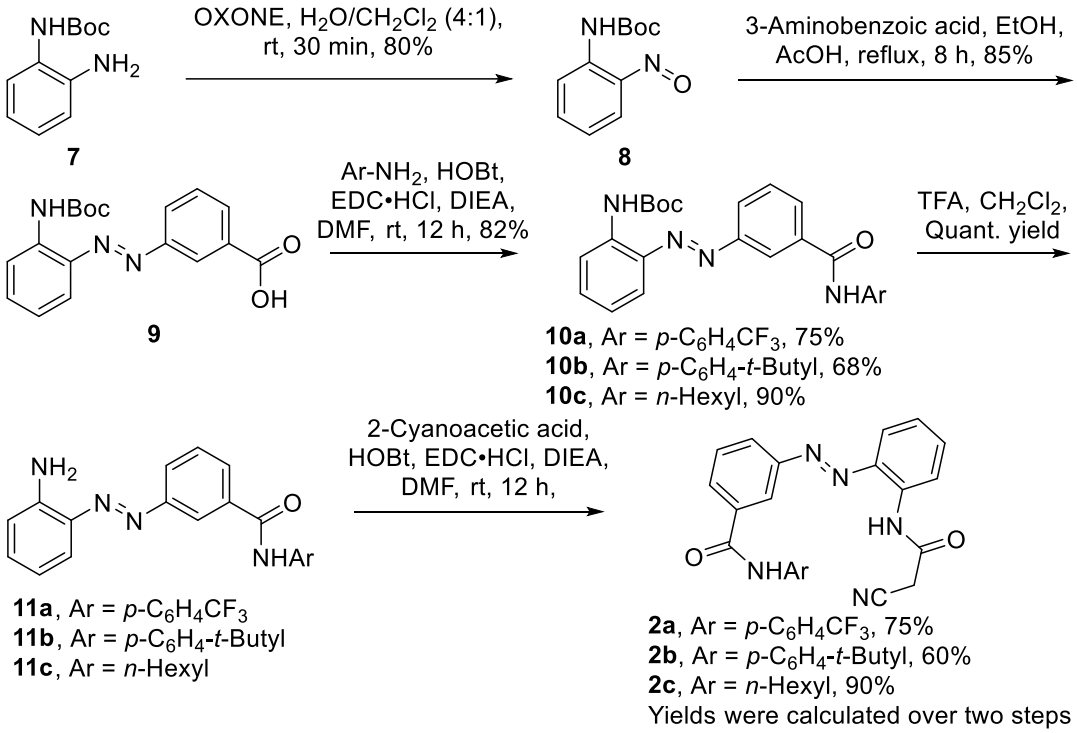

Scheme 2.2. Synthetic scheme for the compounds **2a-2c**.

2.2.2. Chloride binding analysis by ^{1}H NMR titration studies

The Cl^- binding studies of **1b** was investigated through ^{1}H NMR titration by titrating TBACl into a solution of host **1b** in CD_3CN at 298 K. Upon the gradual addition of TBACl, the downfield shift of protons H_1, H_2, H_3, H_4, and H_5 were observed, indicating the involvement of $N–H_1\cdots Cl^-$, $C_{Ar}–H_2\cdots Cl^-$, $N–H_3\cdots Cl^-$, $C_{Alk}–H_4\cdots Cl^-$ and $C_{Ar}–H_5\cdots Cl^-$ hydrogen bond interactions in the recognition of the anion (Figure 2.3A). Further analysis of the data by Bindfit program[20] gave a 1:1 (Host:Guest) binding stoichiometry with Cl^-binding constant ($K_{a(1:1)}$ = 110 ± 3.3 M^{-1}, Figure 2.3B). The ^{1}H NMR titration of **2b** with TBACl showed a similar binding interaction mode with a higher Cl^- binding constant ($K_{a(1:1)}$ value of 515 ±

12.7 M^{-1} (Figure 2.17). The stronger binding of **2b** with the anion was rationalized based on the stronger hydrogen bonding interaction between its H_4 proton and the Cl^- ion than that between the H_4 proton of **1b** and the anion. The larger downfield shift for H_4 proton of **2b** than that of **1b** is a consequence of the stronger hydrogen bonding. Binding studies of the *cis* form for **1b** furnished Cl^- binding constant $K_{a(1:1)}$ = 88 ± 0.4 M^{-1} (Figure 2.18), which is lower as compared to the *trans* form of **1b**.

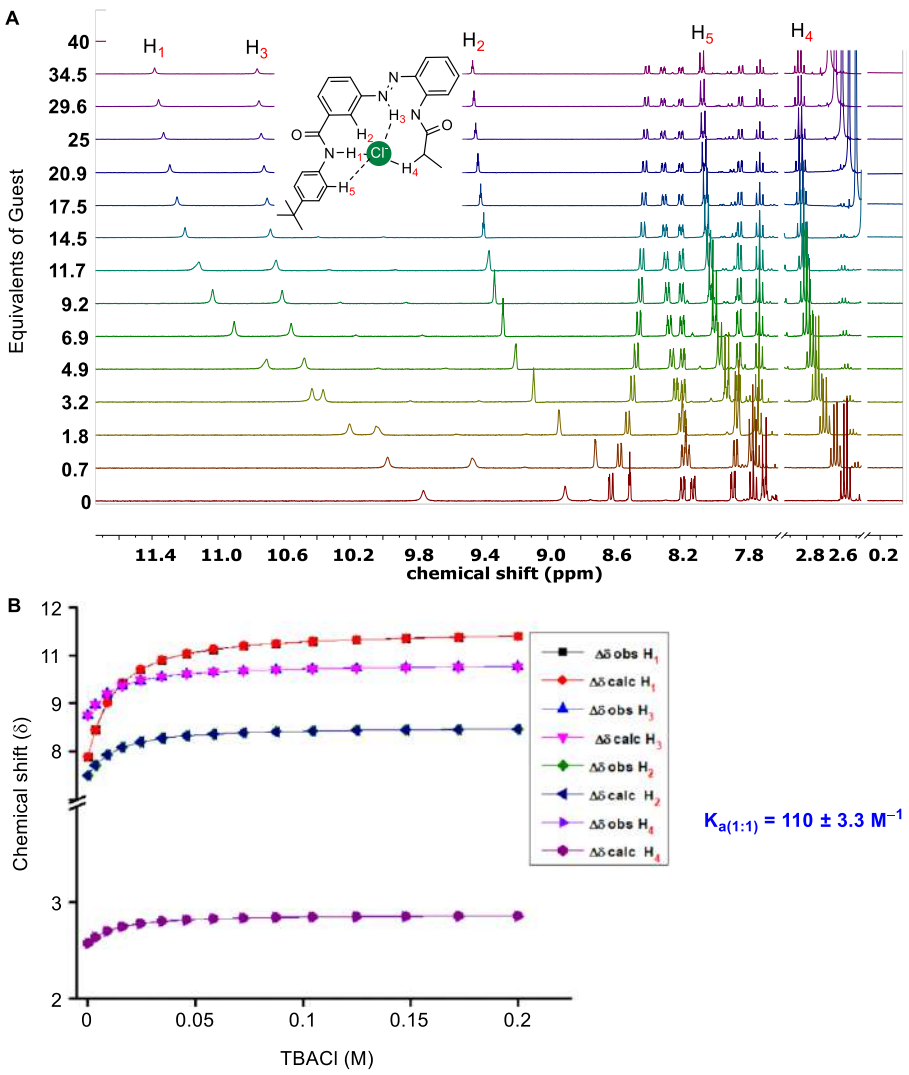

Figure 2.3. Stacked ^1H NMR titration spectra for **1b** (5 mM) with stepwise addition of TBACl in CD_3CN. The equivalents of added TBACl are shown on the stacked spectra (**A**). The plot of chemical shift (δ) of H_1, H_2, H_3 and H_4 protons *vs* concentration of TBACl added, fitted to 1:1 binding model of BindFit v0.5, the binding constant obtained is the mean of the three independent experiments (**B**).

2.2.3. Ion transport activity

The ion transport activities of compounds **1a-1c** and **2a-2c** were examined across large unilamellar vesicles (LUVs), prepared from egg-yolk phosphatidylcholine (EYPC) lipid entrapped with 8-hydroxypyrene-1,3,6-trisulfonic acid trisodium salt (HPTS, 1 mM) containing 10 mM of HEPES buffer and 100 mM of NaCl (see the experimental details).[21] During the fluorescent studies, a pH gradient of 0.8 (pH_{in} = 7 and pH_{out} = 7.8) was created with NaOH and the collapse of pH gradient was monitored by fluorescence at λ_{em} = 510 nm (λ_{ex} = 450 nm) after addition of each compound. All the anionophores exhibited efficient transport activity with the activity sequence of **1a** > **2a** > **1c** > **1b** > **2b** > **2c** (Figure 2.4A). From dose-responsive plots, using Hill analysis, the half-maximal effective concentration (EC_{50}) values comes out to be **1a** = 0.198 ± 0.002 μM, **2a** = 0.277 ± 0.032 μM, **1c** = 0.419 ± 0.050 μM, **1b** = 0.912 ± 0.113 μM, **2b** = 1.5 ± 0.056 μM and **2c** = 1.554 ± 0.102 μM (Figures 2.20–2.25). The Hill coefficient values of $n \sim 2$ for all compounds indicate the involvement of two molecules in catalyzing the ion transport process. Compound **1b**, possessing lower binding affinity showed better transport activity as compared to the cyano-bearing compound **2b**, most probably because of poor lipid bilayer permeation of hydrophilic cyano group. Similarly, **1a** showed better transport as compared to **2a**. Compound **2c** containing an aliphatic side chain connected to amide N-H_1 showed the least activity plausibly due to the absence of (C_{Ar}–H_5···anion) interactions.

Anion selectivity was investigated using EYPC-LUVs⊃HPTS. Variation of extravesicular as well as intravesicular anions using different NaX salt solutions (X^- = Cl^-, Br^-, I^-, NO_3^-, and ClO_4^-) makes a significant change in the transport rate, confirming the involvement of anions in the transport process,[22] with an activity sequence of Cl^- > Br^- > I^- > NO_3^- > ClO_4^- (Figure 2.4B).

Subsequently, the Cl^- leakage for compounds **1a-1c** and **2a** was monitored across EYPC-LUVs⊃lucigenin at λ_{em} = 535 nm (λ_{ex} = 455 nm) by creating a Cl^-/NO_3^- gradient across the lipid membrane. All of them showed a significant Cl^- transport across the lipid

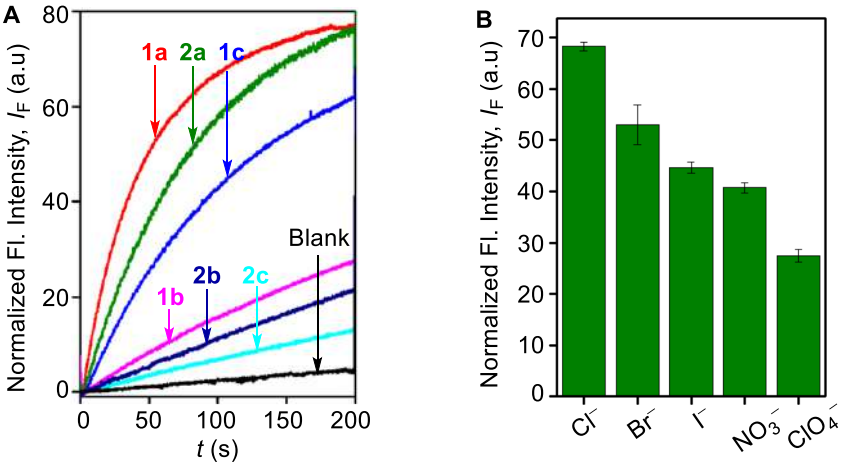

Figure 2.4. Activity comparison of **1a-1c** and **2a-2c** (0.3 μM each) across EYPC-LUVs⊃HPTS (**A**). Anion selectivity of **1a** (0.3 μM) by varying external as well as internal anions across EYPC-LUVs⊃HPTS, (**B**)

membrane.[23] Dose-responsive Cl^- leakage for compound **1a** is shown in Figure 2.5A. Hill analysis for the compounds **1a**, **1b**, **1c**, and **2a** furnish the EC_{50} of 1.26 ± 0.092 μM, 4.76 ± 0.136 μM, 2.83 ± 0.207 μM and 2.53 ± 0.114 μM (Figure 2.27–2.30), and Hill coefficient n = 2 confirming the involvement of two molecules in the anion transport process. Compounds **2b** and **2c** could not be evaluated due to precipitation in the buffer at higher concentrations. Further, variation in the extravesicular MCl (M^+ = Li^+, Na^+, K^+, Rb^+, and Cs^+) salt solutions did not make any significant change in the transport activity of **1a** (c = 3 μM), which rules out any involvement of cations in an overall ion transport process (Figure 2.5B).

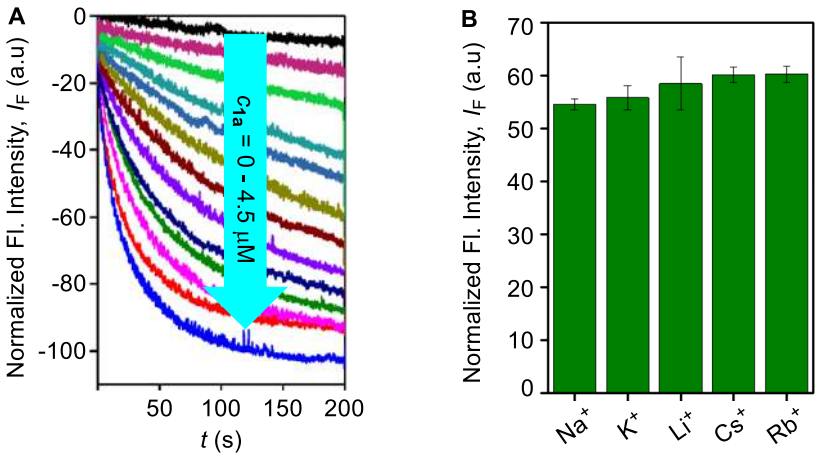

Figure 2.5. The concentration-dependent activity of compound **1a** across EYPC-LUVs⊃Lucigenin (**A**). Cation selectivity of **1a** (3.0 μM) by varying external cations across EYPC-LUVs⊃lucigenin (**B**)

The operative mechanism was further analysed through modified lucigenin essay. The transport activity of **1a** was monitored in the presence of iso-osmolar Na_2SO_4 and $NaNO_3$

salts. Significant transport activity only in the presence of NO_3^- ions suggests the operation of antiport mechanism (Figure 2.6A).[22] Efflux of Cl^- ions, and on the other hand, SO_4^{2-} being more hydrophilic is not transported easily, suggesting the operation of antiport mechanism.The antiport process was further confirmed through ISE studies. EYPC-LUVs entrapped with KCl (300 mM) were prepared and suspended in an external potassium gluconate solution. Cl^- efflux using a Cl^- sensitive electrode was monitored in the presence and absence of monensin (a H^+/K^+ antiporter) and valinomycin (a highly selective K^+ transporter).[24] No considerable change in Cl^- efflux was observed in presence of monensin (Figure 2.6B), and on the other hand, a significant increment in the activity was observed in the presence of valinomycin (Figure 2.6C).

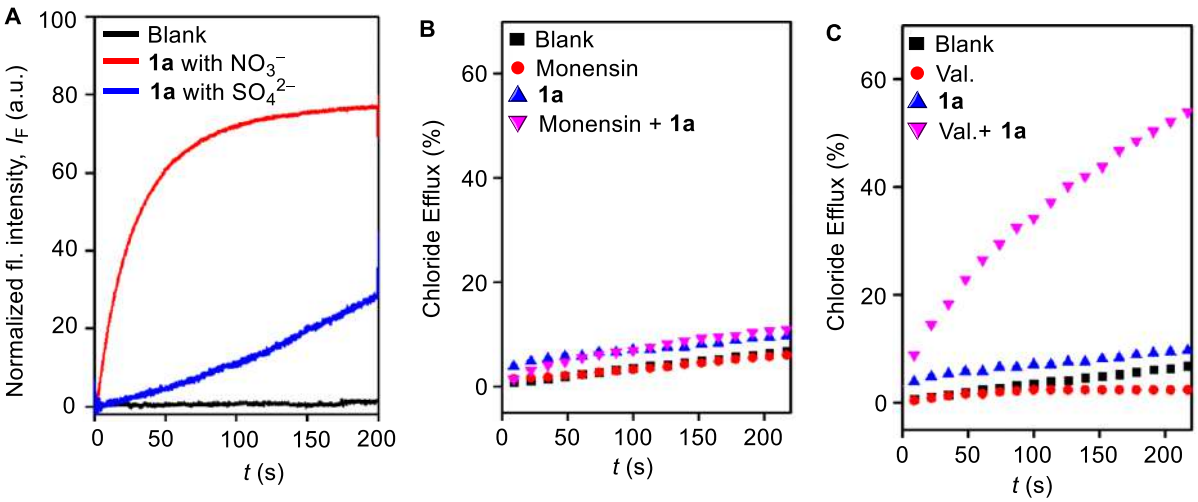

Figure 2.6. Efflux of Cl^- ion by **1a** (5.0 μM) in the presence of either extravesicular SO_4^{2-} or extravesicular NO_3^- ion with iso-osmolar intravesicular Cl^- (**A**). Normalized chloride efflux of **1a** in the presence and absence of Monensin (**B**), and in the presence and absence of Valinomycin (**C**).

Additionally, the evidence of the carrier mode of ion transport by **1a** was obtained by performing the classic U-tube experiment.[25] Significant chloride transport was observed from one of the arms of the U-tube (source arm, containing 500 mM NaCl) to the other arm (receiver arm, containing 500 mM $NaNO_3$) using chloride selective electrode (Figure 2.7).

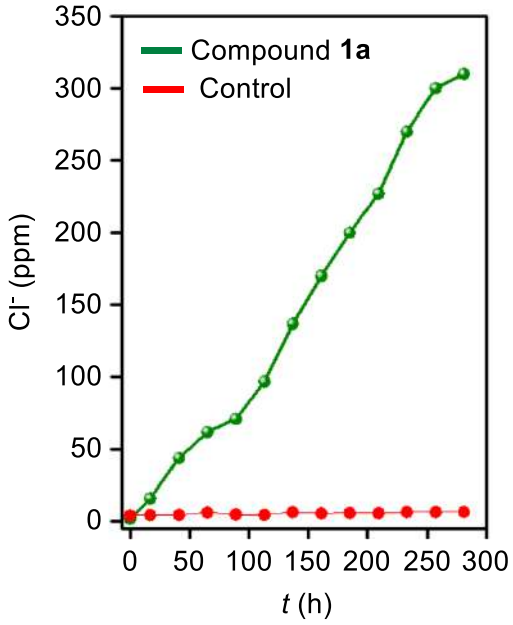

Figure 2.7. Change of chloride ion concentration in a U-tube experiment with and without compound **1a** (1.0 mM).

2.2.4. Theoretical studies (carried out in collaboration with Surajit Metya and Aloke Das from IISER Pune).

2.2.4.1. Geometry optimization studies

Based on the experimentally determined Hill coefficient value of $n \sim 2$ and chloride-anion antiport mechanism, the geometry-optimized structure of the [(**1a**)$_2$+Cl$^-$] complex was obtained first by generating the most probable sandwich conformation by using CONFLEX 8 program (Figure 2.8),[26] and subsequently optimizing the generated conformation by Gaussian 09 program[27] using B3LYP functional and 6-311G(d,p) basis set.[18] The geometry

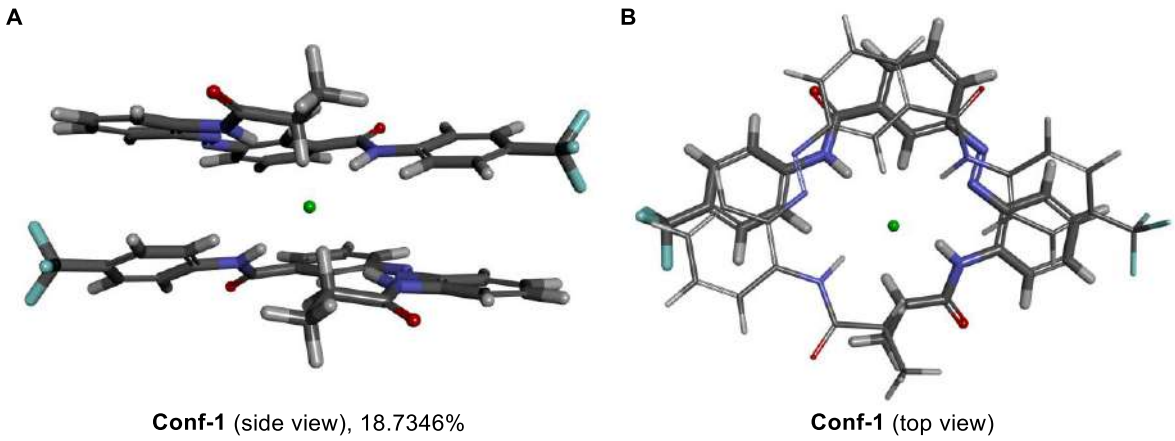

Figure 2.8. Initial highest populated geometry of **Conf-1** for [(**1a**)$_2$+Cl$^-$] in the side view (**A**) and top view (**B**) obtained after optimization by CONFLEX 8 software using MMFF94s force field.

optimized structure of [(**1a**)$_2$+Cl$^-$] complex indicated that two receptor molecules are oriented in an anti-parallel fashion to form a sandwich structure around the central Cl$^-$ ion (Figure 2.9). The structure confirmed that each receptor participates in the anion recognition through N−H$_1$···Cl$^-$ (H$_1$···Cl$^-$ = 2.42 Å), C$_{Ar}$−H$_2$···Cl$^-$ (H$_2$···Cl$^-$ = 2.80 Å), N−H$_3$···Cl$^-$ (H$_3$···Cl$^-$ = 2.86 Å), C$_{Alk}$−H$_4$···Cl$^-$ (H$_4$···Cl$^-$ = 2.79 Å), and C$_{Ar}$−H$_5$···Cl$^-$ (H$_5$···Cl$^-$ = 2.70 Å) hydrogen bonding interactions.

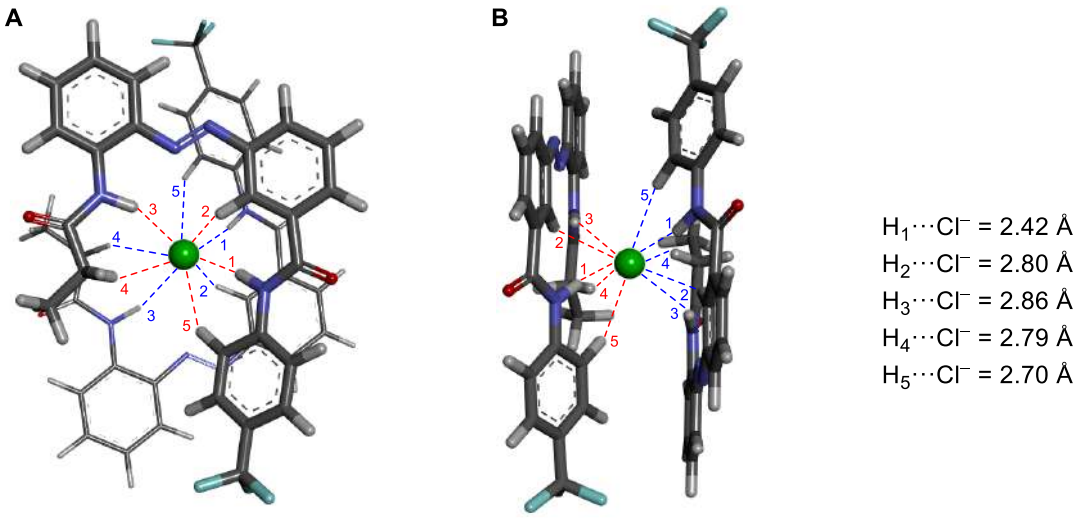

Figure 2.9. Top (**A**) and side (**B**) views of the geometry-optimized structure of [(**1a**)$_2$+Cl$^-$] complex.

2.2.4.2. NBO analysis

The existence, as well as strength of various hydrogen-bonding interactions between the Cl$^-$ and N-H/C-H groups of each of the two receptor molecules in the [(**1a**)$_2$+Cl$^-$] complex, was further confirmed through natural bond orbital (NBO) analysis. The NBO calculations, which determine the second-order perturbation energy ($E^{(2)}_{n\rightarrow\sigma^*}$) between the filled lone pair orbitals (n) of the anion and the vacant σ* orbitals of the N−H/C−H groups, are performed at the B3LYP/6-311G(d,p) level of theory using NBO 6.0 software.[28] The NBO overlap between the lone pair and σ* orbitals for all the five hydrogen-bond interactions are shown in Figure 2.10 and different components of the total NBO interaction value of a specific interaction are listed in Table 2.4. It has been found that the N−H$_1$···Cl$^-$ hydrogen bonding interaction is much stronger than the other four hydrogen-bonding interactions present there.

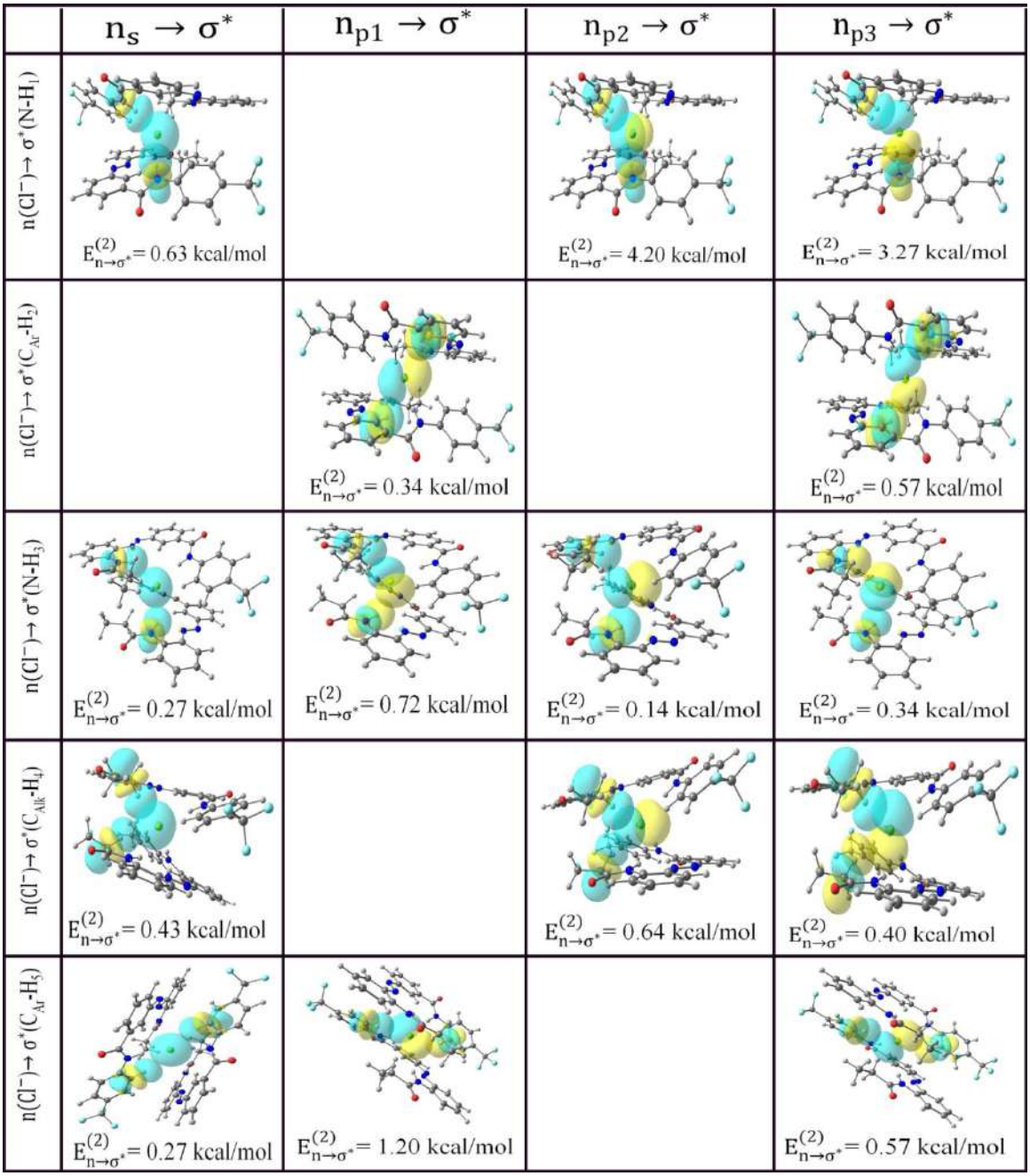

Figure 2.10. NBO view of the orbital overlap between the four lone pairs of Cl^- with the N–H and C-H antibonding orbitals of both the receptor units. Second-order perturbative energy ($E^{(2)}_{i\rightarrow j^*}$) is given here for contribution of individual lone pair orbital of Cl^- to the σ^* orbital of the N–H or C–H bonds of a single receptor.

2.2.5. Photoisomerization studies

The photoisomerization studies of the compounds **1a**, **1c**, **2a**, and **2c** were carried through UV-Vis and ^{1}H NMR spectroscopy. Fresh solutions of these compounds in acetonitrile showed an intense absorption peak at 380 nm (corresponding to π-π* transition) and a relatively weak absorption peak at 450 nm (corresponding to *n*-π* transition). The UV

irradiation of these compounds at 365 nm led to a substantial decrease in the π-π* absorption band, and on the other hand, the intensity of the *n*-π* transition band increases slightly (Figures 2.11, 2.39–2.41). These changes were consistent with *trans* → *cis* photoisomerization of an azobenzene subunit.[29] Meanwhile, the reverse photoisomerization, *cis* → *trans* was achieved by irradiating the samples at 450 nm. Photoregulation, through the process of alternating photoirradiation at two different wavelengths of 365 nm and 450 nm was carried out for several repeating cycles without the loss of efficiency. Photoisomerization behavior of these compounds was also studied through ^{1}H NMR spectroscopy. The photoirradiation of these samples in DMSO-d_6 at 365 nm significantly changes the proton signals indicative of *trans* → *cis* photoisomerization (Figures 2.12, 2.36–2.38). compound **1a** showed good thermal stability (half-life of 32 ± 1.04 h) in the photoisomerized *cis* form likely due to intramolecular hydrogen bonding of amide N-H_3 with one of the azo nitrogen (Figure 2.13).[16, 30]

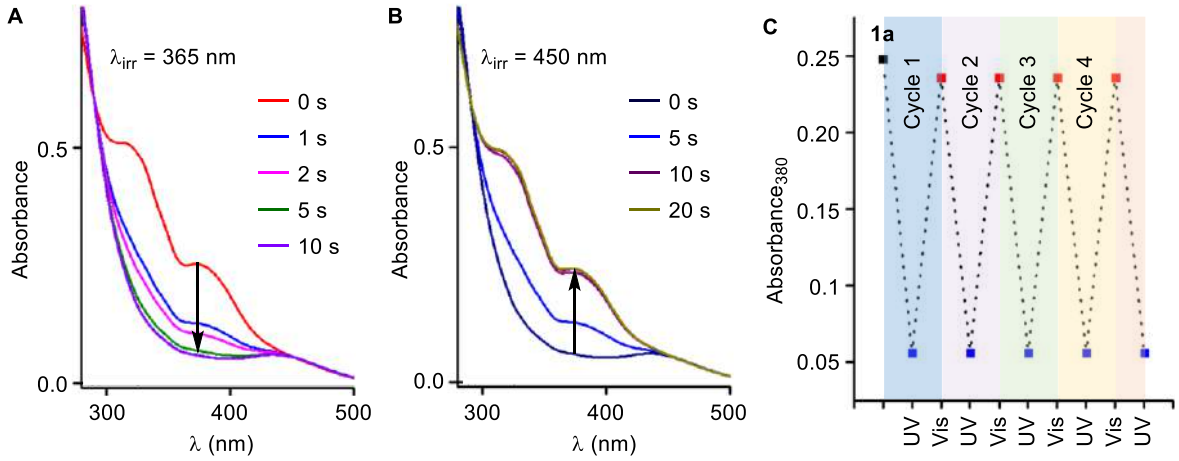

Figure 2.11. UV-visible spectral changes for **1a** (20 μM) upon irradiation with 365 nm light (3 × 3 Watt LEDs) (**A**). UV-visible spectral changes for **1a** (20 μM) upon irradiation with 450 nm light (3 × 3 Watt) (**B**). Switching cycles for **1a** (20 μM) under alternating irradiation with 365 nm and 450 nm lights (**C**). The absorbance at 380 nm was monitored for the switching study. All data were recorded in CH_3CN.

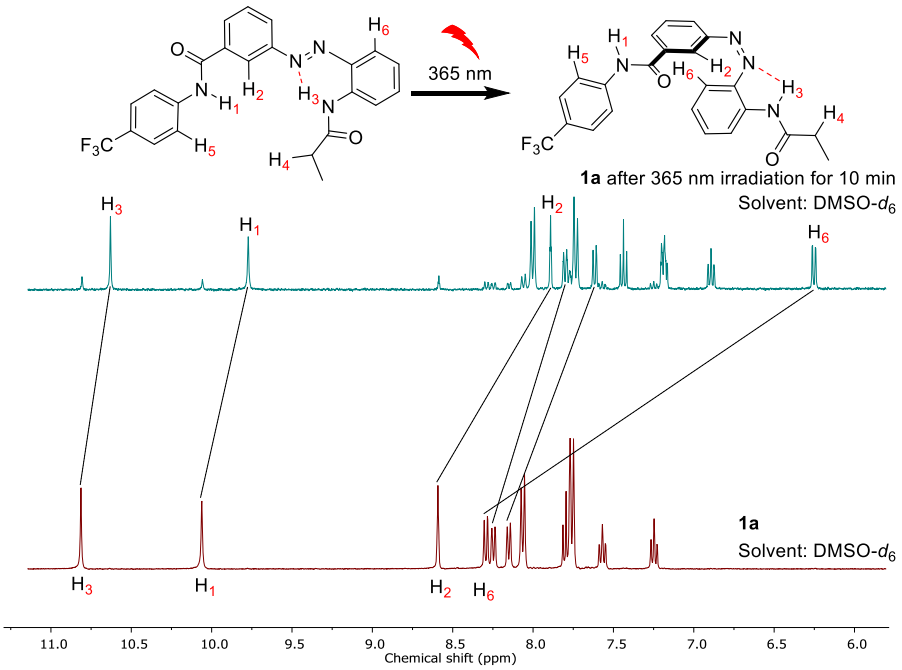

Figure 2.12. Partial 400 MHz ^{1}H NMR spectrum of **1a** (4.0×10^{-3} M, down) in DMSO-d_6 at 25 °C, and that of photo-irradiated sample of **1a** (up) by 365 nm light for 10 min. The *trans* to *cis* ratio after photo-irradiation is 15:85.

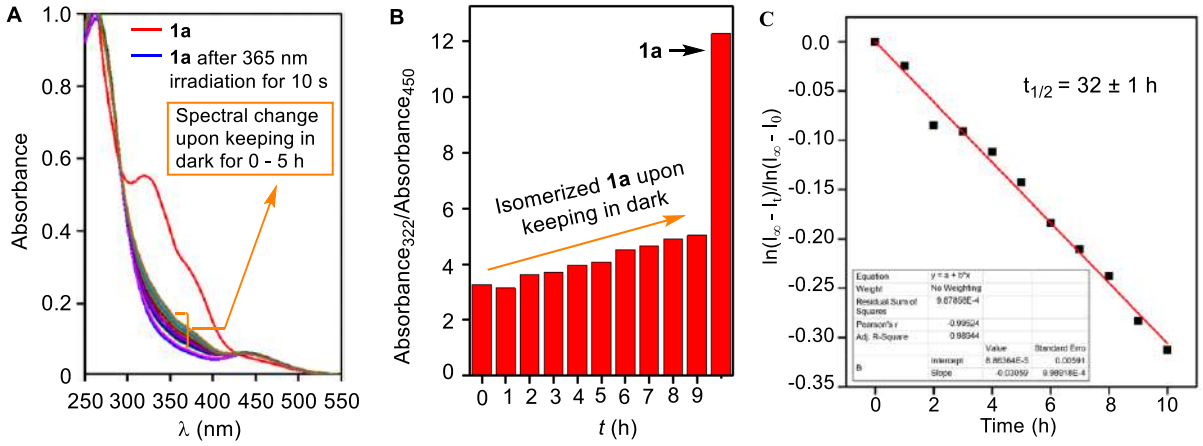

Figure 2.13. UV-visible spectral change for **1a** (20 μM) upon irradiation with 365 nm light (3 × 3 Watt LEDs) and upon keeping in dark for 9 h (**A**). Change in ratiometric absorption at (A_{322}/A_{450}) of **1a** (20 μM) upon keeping in dark for 9 h (**B**). Plot of $[\ln(I_\infty - I_t) / \ln(I_\infty - I_0)]$ as a function of time to determine the half-life for thermal *cis* to *trans* isomerisation for **1a**. The half-life comes out to be 32 ± 1 h, which has been calculated from three independent experiments (**C**).

The similar behavior was reflected in the lucigenin activity of **1a** in its *cis* form. No significant increment in the transport activity was observed while keeping the sample in dark and monitored for 5 h of time (Figure 2.14).

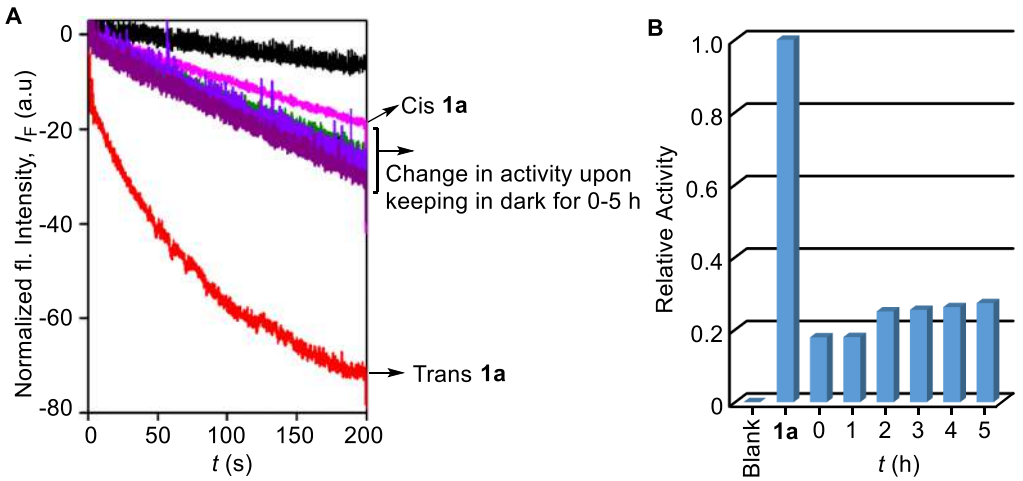

Figure 2.14. Change in transport activity for **1a** (c = 3.5 μM) upon keeping the in the dark for 5 h (**A**). Transport activity of **1a** (3.5 μM) in *trans* and *cis* form across EYPC-LUVs⊃Lucigenin (**B**).

2.2.6. Photoswitchable ion transport activity across EYPC-LUVs⊃lucigenin

After analysing the photoisomerization behavior of these anionophores, photoswitchable ion transport of **1a**, **1c,** and **2a** were investigated using lucigenin essay. The ion transport activity of anionophores **1a**, **1c** and **2a** (c = 3.0 μM, ACN:MeOH (4:1)), was drastically reduced upon photoirradiation of the samples at 365 nm, due to *trans* to *cis* photoisomerizatio n which was efficiently regained back upon 450 nm irradiation. The reason for less activity of *cis* form can be due to less binding affinity as compared to the *trans* form, however, the change in the conformation and planarity can effect the formation of active receptor-anion complex for the necessary ion transport process. Also, the effect due to the change in the lipid permeation and mobility of the *cis* form cannot be ruled out as the reason for less activity of the *cis* form. Potoregulatory behavior in the transport activity was efficiently carried out for several repeating cycles (Figures 2.15, 2.42–2.43). The ratio of the transport rates for the anionophores in the corresponding active *trans* form to that of inactive *cis* form comes out to be 100:18 for **1a**, 100:6 for **1c**, 100:31 for **2a**.

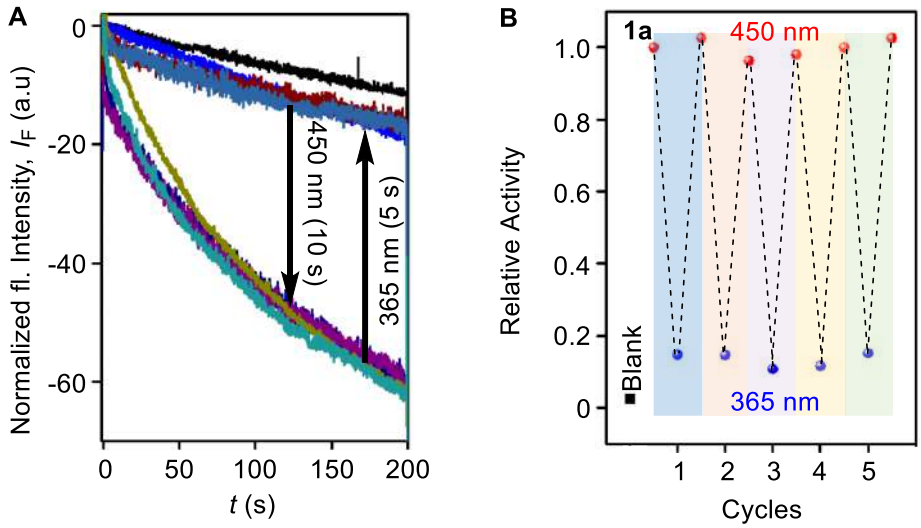

Figure 2.15. Transport activity of **1a** (3.5 μM) in *trans* and *cis* form across EYPC-LUVs⊃lucigenin (**A**). Photo regulated transport activity of **1a** (3 μM) taken at t = 280 s under alternating photo irradiation at two different wavelengths of 365 nm and 450 nm across EYPC-LUVs⊃lucigenin (**B**).

2.2.7. Photoswitchable ion transport activity across EYPC-LUVs⊃HPTS

Photo regulatory transport activity was also achieved *in situ* in the presence of EYPC-LUVs⊃HPTS.[5m] The transport activity of **1a** got decreased by photoirradiation at 365 nm for 2 min, which on the other hand was regained back through photo irradiation at 450 nm for 5 min (Figure 2.16).

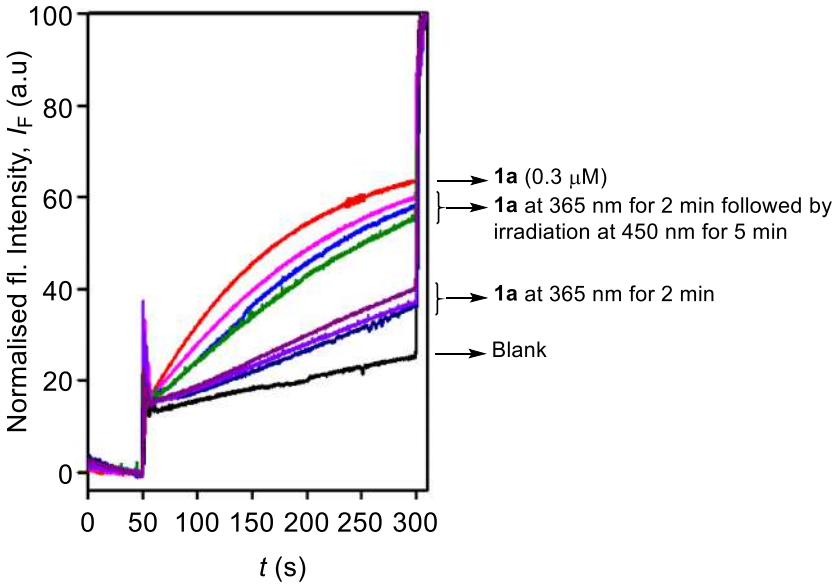

Figure 2.16. Normalized ion transport activity of **1a** across HPTS vesicles upon alternative photoirradiation at 365 nm and 450.

2.3. Conclusion

In summary, we have developed a *trans*-azobenzene-diamide-based synthetic photoswitchable anionophoric system that forms a sandwich complex with a chloride ion for its transport across the lipid membrane. The most active transporter **1a**, decorated with a 4-(trifluoromethyl) phenyl aminoformyl and a propionamide groups, provided EC_{50} = 0.199 μM and Hill coefficient of $n \sim 2$ when measured across EYPC-LUVs⊃HPTS. Detailed mechanistic studies confirmed that **1a** functions as an anion carrier with Cl^-/anion antiport as the main operative process. Photoirradiation of the *trans*-isomer at 365 nm resulted in the very fast conversion to its *cis*-isomer, which was thermally stable at ambient temperature and amenable to very rapid back conversion exclusively by photoirradiation at 450 nm. Such *cis-trans* reversible photoisomerization behavior of the anionophore was utilized to achieve very efficient light-gated off-on Cl^- transport over several cycles. Beyond this photoswitchable transport activity, the very slow *cis* → *trans* thermal isomerization and short response-time of *cis-trans* photoisomerization, the present system can also be incorporated into several supramolecular artifacts with potential applications, which include soft materials,[31] stimuli-responsive systems[32] and in possible biological applications.

2.4. Experimental details

2.4.1. General Methods

All chemical reactions were performed under nitrogen atmosphere. All reagents and solvents for synthesis were purchased from commercial sources (Sigma-Aldrich, Spectrochem) and used further without purification. The column chromatography was carried out using Merck silica (100-200/ 230-400 mesh size). The thin layer chromatography was performed on E. Merck silica gel 60-F254 plates. Egg yolk phosphatidylcholine (EYPC) as a solution of chloroform (25 mg/ mL), mini extruder, polycarbonate membrane of 100 nm and 200 nm were purchased from Avanti Polar Lipid. HEPES, HPTS, lucigenin, NaOH, Triton X-100, FCCP, valinomycin and all inorganic salts were obtained as molecular biology grade from Sigma Aldrich.

2.4.2. Physical Measurements

The ^1H NMR spectra were recorded at 400 MHz whereas ^{13}C spectra at 101 MHz. The residual solvent signals were considered as an internal reference (δ_H = 7.26 ppm for $CDCl_3$, δ_H = 2.50 for DMSO-d_6, and δ_H = 1.94 for CD_3CN) to calibrate spectra. The chemical shifts were reported in ppm. Following abbreviations were used to indicate multiplicity patterns m:

multiplet, s: singlet, d: doublet, t: triplet, q: quartet, dd: doublet of doublets, td: triplet of doublets. Coupling constants were measured in Hz. Infra-red (IR) spectra were measured in cm^{-1} using FT–IR spectrophotometer. Melting points were measured on micro melting point apparatus. High-resolution mass spectra (HRMS) were recorded on electrospray ionization time-of-flight (ESI-TOF). Fluorescence experiments were recorded on Fluoromax-4 from Jobin Yvon Edison equipped with injector port and magnetic stirrer in microfluorescence cuvette. All buffer solutions were prepared from the autoclaved water. Adjustment of pH of buffer solutions was made using Helmer pH meter. The extravesicular dye was removed by performing gel chromatography using Sephadex. The fluorescence studies were proceed using OriginPro 8.5. ChemBio Draw 15 Ultra software was used for drawing structures and processing figures. UV-vis spectra were recorded on a Varian Cary 5000 spectrophotometer.

2.4.3. Synthetic procedures

Synthetic procedures for the synthesis of compounds 1a-1c

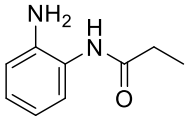

***N*-(2-aminophenyl) propionamide (4):** In a 50 mL round bottom flask, to a stirred solution of Compound **3** (0.5 g) and 10 % Pd-C (10 wt%, 20 mg) in MeOH (10 mL) was added $NaBH_4$ (4 equiv.) in portion wise using solid addition funnel or dispenser. A septum with an empty (deflated) balloon was placed to avoid the loss of generated hydrogen and overpressure in the flask. After completion of reaction (monitored by TLC, 3-10 min), reaction mixture was filtered through celite and filtrate was evaporated to dryness to afford crude amine **4** which upon purification using column chromatography over silica gel (Eluent: 3% MeOH in $CHCl_3$) afforded pure amine as a white solid (359 mg, 85%). **M.P.:** 135.0 °C; **^{1}H NMR (400 MHz, Chloroform-*d*):** δ 7.30 (s, 1H), 7.15 (d, *J* = 7.4 Hz, 1H), 7.05 (t, *J* = 7.6 Hz, 1H), 6.82 – 6.74 (m, 2H), 3.84 (s, 2H), 2.40 (q, *J* = 7.6 Hz, 2H), 1.24 (t, *J* = 7.6 Hz, 3H); **^{13}C NMR (101 MHz, Chloroform-*d*):** δ 172.66, 140.93, 127.27, 125.36, 124.51, 119.69, 118.36, 30.16, 10.07; **IR (Neat, ν/cm^{-1}):** 3732, 3391, 3322, 3020, 2931, 1739, 1638, 1522, 1494, 1364, 1216; **HRMS (ESI):** Calc. for $C_9H_{12}N_2OH^+$ $[M+H]^+$: 165.1022, found 165.1028.

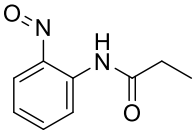

***N*-(2-nitrosophenyl) propionamide (5):** In a 100 mL round bottom flask, Aniline **4** (1.83 mmol, 0.3 g, and 1 eq) in dichloromethane (5 mL) was added oxone (3.65 mmol, 2.25 g, 2 eq) dissolved in water (20 mL) The reaction was stirred for 0.5 h and extracted with CH_2Cl_2 (3 × 30 mL). The organic layer was dried with anhydrous sodium sulphate, filtered and concentrated under reduced pressure to give

crude product. The residue was then purified by silica gel column chromatography (Eluent: 2% EtOAc in pet ether) to give product **5** as a green solid (292 mg, yield 90%). **M.P.:** 115.0 °C; **^{1}H NMR (400 MHz, Chloroform-*d*):** δ 10.85 (s, 1H), 8.90 (d, *J* = 8.5 Hz, 1H), 7.86 – 7.66 (m, 1H), 7.44 (s, 1H), 7.25 – 7.12 (m, 1H), 2.61 (q, *J* = 7.5 Hz, 2H), 1.35 (t, *J* = 7.5 Hz, 3H); **^{13}C NMR (101 MHz, Chloroform-*d*):** δ 173.35, 156.12, 139.19, 122.54, 120.99, 31.54, 9.38; **IR (Neat, ν/cm^{-1}):** 3833, 3725, 3623, 2972, 2312, 1738, 1674, 1583, 1459, 1366, 1218; **HRMS (ESI):** Calc. for $C_9H_{10}N_2O_2H^+$ $[M+H]^+$: 179.0815, found 179.0820.

(*E*)-3-((2-propionamidophenyl) diazenyl) benzoic acid (6): In a 50 mL round bottom flask, *N*-(2-nitrosophenyl)propionamide **5** (250 mg, 1.4 mmol, 1.0 eq.) and 3-aminobenzoicacid (192 mg, 1.4 mmol, 1.0 equiv) were dissolved in 10 mL of glacial acetic acid and heated at reflux. After 6 h, the mixture was cooled to room temperature and EtOAc (30 mL) was added. The solution was then washed with water (3 × 100 mL), dried over Na_2SO_4 and concentrated. The residue was then purified by silica gel column chromatography (Eluent: 5% MeOH in $CHCl_3$) provided **6** (320 mg, 77 %) as an orange solid. **M.P.:** 210.0 °C; **^{1}H NMR (400 MHz, DMSO-*d*$_6$):** δ 13.29 (s, 1H), 10.09 (s, 1H), 8.47 (s, 1H), 8.31 – 8.18 (m, 2H), 8.13 (d, *J* = 7.6 Hz, 1H), 7.75 (ddd, *J* = 10.1, 7.0, 2.6 Hz, 2H), 7.56 (t, *J* = 8.6 Hz, 1H), 7.27 (s, 1H), 2.51 (dd, *J* = 4.6, 2.6 Hz, 5H), 1.15 (t, *J* = 7.5 Hz, 3H); **^{13}C NMR (101 MHz, DMSO-*d*$_6$):** δ 172.91, 167.22, 152.64, 141.73, 137.68, 133.18, 132.66, 132.33, 130.28, 127.03, 124.57, 124.49, 123.30, 117.33, 30.22, 10.14; **IR (Neat, ν/cm^{-1}):** 3732, 3443, 3298, 2973, 2558, 1739, 1588, 1520, 1425, 1425, 1366, 1216; **HRMS (ESI):** Calc. for $C_{16}H_{15}N_3O_3H^+$ $[M+H]^+$: 298.1186, found 298.1191.

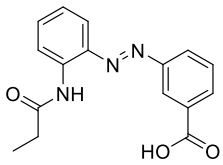

General procedure for synthesizing azobenzene diamide derivatives (1a-1c)

General method A: In a 25 mL round bottom flask, (*E*)-3-((2-propionamidophenyl) diazenyl)benzoic acid **6** (100 mg, 0.336 mmol, 1 equiv) EDC·HCl (128 mg, 0.4 mmol, 1.2 equiv), and HOBt (54 mg, 0.4 mmol, 1.2 equiv) were dissolved in DMF (10 mL). The resulted solution was stirred at room temperature for 30 min. After 30 min, *para*-substituted aniline derivatives (0.336 mmol, 1 equiv) and *N*, *N*-diisopropylethylamine (65 mg, 0.5 mmol, 1.5 equiv) were added. The reaction mixture was stirred at room temperature for an additional 12 h. After completion of the reaction, the reaction mixture was quenched with water (10 mL), extracted with ethyl acetate (3 × 20 mL), washed with brine (2 × 20 mL), the organic layer was dried over Na_2SO_4 and concentrated under reduced pressure. The crude product was purified using silica gel chromatography to give pure **1a-1c**.

(*E*)-3-((2-propionamidophenyl)diazenyl)-*N*-(4-(trifluoromethyl)phenyl)benzamide (1a):

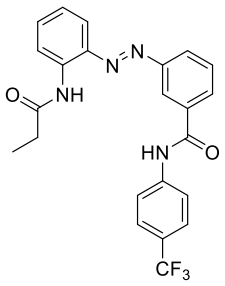

Eluent for column chromatography: The crude product was purified by column chromatography over silica gel (EtOAc : petroleum ether 3:7 v/v) to furnish **1a** as an orange solid (88 mg, 60%). **M.P.:** 242.0 °C; **^{1}H NMR (400 MHz, DMSO-*d*$_6$):** δ 10.82 (s, 1H), 10.07 (s, 1H), 8.60 (s, 1H), 8.30 (d, *J* = 8.2 Hz, 1H), 8.25 (d, *J* = 8.0 Hz, 1H), 8.16 (d, *J* = 7.8 Hz, 1H), 8.07 (d, *J* = 8.6 Hz, 2H), 7.79 (dd, *J* = 18.1, 8.2 Hz, 4H), 7.58 (t, *J* = 8.4 Hz, 1H), 7.25 (t, *J* = 7.1 Hz, 1H), 2.58 – 2.52 (m, 2H), 1.15 (t, *J* = 7.5 Hz, 3H); **^{13}C NMR (101 MHz, DMSO-*d*$_6$):** δ 172.26, 165.13, 151.77, 142.52, 140.61, 137.34, 135.49, 132.66, 130.45, 129.50, 125.80, 125.76, 125.69, 123.67, 122.43, 122.38, 119.89, 115.99, 39.52, 29.54, 9.41, quartet (125.6-122.8); **IR (Neat, ν/cm^{-1}):** 3726, 3266, 3014, 1738, 1653, 1593, 1523, 1217, 1110; **HRMS (ESI):** Calc. for $C_{23}H_{19}F_3N_4O_2H^+$ $[M+H]^+$: 441.1533 found 441.1538.

(*E*)-*N*-(4-(tert-butyl)phenyl)-3-((2-propionamidophenyl)diazenyl)benzamide (1b): The crude product was purified by column chromatography over silica gel (EtOAc : petroleum ether 2:8 v/v) to furnish **1b** as an orange solid (108 mg, 72%). **M.P.:** 199.0 °C; **^{1}H NMR (400 MHz, DMSO-*d*$_6$):** δ 10.41 (s, 1H), 10.07 (s, 1H), 8.57 (s, 1H), 8.31 (d, *J* = 8.3 Hz, 1H), 8.22 (d, *J* = 7.9 Hz, 1H), 8.14 (d, *J* = 7.7 Hz, 1H), 7.76 (q, *J* = 8.2 Hz, 4H), 7.56 (d, *J* = 8.1 Hz, 1H), 7.40 (d, *J* = 8.6 Hz, 2H), 7.25 (t, *J* = 7.7 Hz, 1H), 2.55 (d, *J* = 7.5 Hz, 2H), 1.30 (s, 9H), 1.15 (t, *J* = 7.5 Hz, 4H); **^{13}C NMR (101 MHz, DMSO-*d*$_6$):** δ 172.98, 165.10, 152.49, 138.03, 137.02, 136.73, 133.34, 131.06, 130.11, 125.95, 125.81, 124.39, 123.06, 120.59, 116.74, 34.61, 31.74, 30.26, 10.16; **IR (Neat, ν/cm^{-1}):** 3833, 3725, 3623, 2972, 1738, 1674, 1583, 1459, 1366, 1218; **HRMS (ESI):** Calc. for $C_{26}H_{28}N_4O_2H^+$ $[M+H]^+$: 429.2285, found 429.2298.

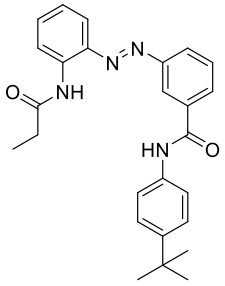

(*E*)-*N*-(4-bromophenyl)-3-((2-propionamidophenyl)diazenyl)benzamide (1c): The crude product was purified by column chromatography over silica gel (EtOAc : petroleum ether 3:7 v/v) to furnish **1c** as an orange solid (97 mg, 65%). **M.P.:** 264.0 °C; **^{1}H NMR (400 MHz, DMSO-*d*$_6$):** δ 10.60 (s, 1H), 10.06 (s, 1H), 8.57 (s, 1H), 8.30 (d, *J* = 8.3 Hz, 1H), 8.23 (d, *J* = 7.9 Hz, 1H), 8.13 (d, *J* = 7.6 Hz, 1H), 7.82 (d, *J* = 8.9 Hz, 2H), 7.79 – 7.74 (m, 2H), 7.61 – 7.54 (m, 3H), 7.25 (t, *J* = 7.7 Hz, 1H), 2.59 – 2.51 (m, 2H), 1.14 (t, *J* = 7.5 Hz, 4H); **^{13}C NMR (101 MHz, DMSO-*d*$_6$):** δ 172.99, 165.46, 152.49, 141.35, 139.00, 138.05, 136.44, 133.38, 132.05, 131.09, 130.19, 126.19, 124.41, 123.12, 122.67, 116.71,

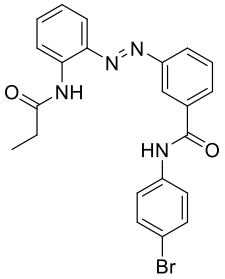

116.06, 30.26, 10.15; **IR (Neat, v/cm^{-1}):** 3726, 3262, 3014, 2962, 1738, 1656, 1588, 1216, 1099; **HRMS (ESI):** Calc. for $C_{22}H_{19}BrN_4O_2H^+$ $[M+H]^+$: 451.0764, found 451.0774.

Synthetic procedures for the synthesis of compounds 2a-2c

***tert*-Butyl (2-nitrosophenyl)carbamate (8):** In a 100 mL round bottom flask, Aniline **7** (2.4 mmol, 0.5 g, 1 equiv) in dichloromethane (10 mL) was added oxone (4.8 mmol, 2.95 g, 2 equiv) dissolved in water (50 mL). The reaction was stirred for 0.5 h and then extracted with CH_2Cl_2 (3×50 mL). The organic layer was dried with anhydrous sodium sulfate and concentrated under reduced pressure. The mixture was then purified by silica gel column chromatography (Eluent: 2% EtOAc in pet ether) to give product **8** as a green liquid (320 mg, yield 60%). **^{1}H NMR (400 MHz, Chloroform-*d*):** δ 10.22 (s, 1H), 8.61 (d, *J* = 9.3 Hz, 1H), 7.68 (t, *J* = 8.7 Hz, 1H), 7.39 (s, 1H), 7.09 (t, *J* = 8.1 Hz, 1H), 1.59 (s, 9H); **^{13}C NMR (101 MHz, Chloroform-*d*):** δ 156.35, 152.35, 138.86, 121.26, 119.63, 81.83, 28.22; **HRMS (ESI)**: Calc. for $C_{11}H_{13}N_2O_3H^+$ $[M+H]^+$: 222.0999, Found: 221.9978.

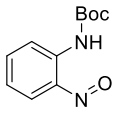

(*E*)-3-((2-((tert-butoxycarbonyl)amino)phenyl)diazenyl)benzoic acid (9): In a 50 mL round bottom flask, tert-butyl (2-nitrosophenyl)carbamate **8** (300 mg, 1.35mmol, 1.0 equiv) and 3-aminobenzoic acid (185 mg, 1.35 mmol, 1.0 equiv) were dissolved in 10 mL of glacial acetic acid and heated at reflux. After 6 h, the mixture was cooled to room temperature and EtOAc (30 mL) was added. The solution was then washed with water (3×100 mL), dried over Na_2SO4, and concentrated. The residue was then purified by silica gel column chromatography (Eluent: 2 % MeOH in CH_2Cl_2) provided **9** (368 mg, 80%) as an orange solid. **M.P.:** 175.0 °C; **^{1}H NMR (400 MHz, DMSO-d_6):** δ 13.23 (s, 1H), 9.44 (s, 1H), 8.42 (t, *J* = 1.7 Hz, 1H), 8.19 (s, 1H), 8.12 (d, *J* = 7.9 Hz, 1H), 8.02 (s, 1H), 7.75 (d, *J* = 7.9 Hz, 1H), 7.73 – 7.68 (m, 1H), 7.56 – 7.51 (m, 1H), 7.22 (s, 1H), 1.49 (s, 9H); **^{13}C NMR (101 MHz, DMSO-d_6):** δ 167.19, 153.13, 152.57, 141.57, 137.68, 133.14, 132.59, 132.17, 130.24, 127.42, 123.81, 123.73, 122.11, 118.17, 80.36, 28.45; **IR (Neat, v/cm^{-1}):** 3240, 3000, 2980, 1722, 1740 1588, 1520, 1441, 1392, 1245, 1150; **HRMS (ESI)**: Calc. for $C_{18}H_{18}N_3O_4H^+$ $[M+H]^+$: 342.1400, Found: 342.1454.

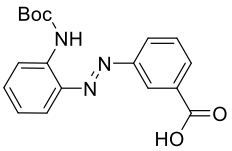

General procedure for synthesizing Boc-protected amide derivatives (10a-10c)

General method B: In a 25 mL round bottom flask, (*E*)-3-((2-((tert-butoxycarbonyl)amino) phenyl) diazenyl) benzoic acid **9** (100 mg, 0.292 mmol, 1 equiv) EDC·HCl (128 mg, 0.4 mmol, 1.2 equiv), and HOBt (67 mg, 0.351 mmol, 1.2 equiv), were dissolved in DMF (10 mL). The resulted solution was stirred at room temperature for 30 min. After 30 min, *para*-substituted aniline derivatives (0.292 mmol, 1 equiv) and *N*, *N*-diisopropylethylamine (56 mg, 0.439 mmol, 1.5 equiv) were added. The reaction mixture was stirred at room temperature for an additional 12 h. After completion of the reaction, the reaction mixture was quenched by water (10 mL), extracted with ethyl acetate (3 × 20 mL), washed with brine (2 × 20 mL), the organic layer dried over Na_2SO_4 and concentrated under reduced pressure. The purification of the crude product was done by using silica gel chromatography to give pure **10a-10c**.

tert-butyl(*E*)-(2-((3-((4-(trifluoromethyl)phenyl)carbamoyl)phenyl)diazenyl)phenyl)-carbamate (10a): Eluent for column chromatography: The crude product was purified by column chromatography over silica gel (EtOAc:petroleum ether 3:7 v/v) to furnish **10a** as an orange solid (115 mg, 82%). **M.P:** 210.0 °C; **^{1}H NMR (400 MHz, Chloroform-*d*):** δ 9.20 (s, 1H), 8.38 (d, *J* = 8.4 Hz, 1H), 8.30 (t, *J* = 1.7 Hz, 1H), 8.19 (s, 1H), 8.06 – 7.98 (m, 2H), 7.85 – 7.79 (m, 3H), 7.71 – 7.61 (m, 3H), 7.45 (t, *J* = 8.5 Hz, 1H), 7.10 (s, 1H), 1.56 (s, 9H); **^{13}C NMR (101 MHz, DMSO-*d*$_6$):** δ 165.89, 153.12, 152.46, 143.18, 141.21, 138.05, 136.18, 133.40, 131.03, 130.23, 126.49, 123.75, 122.61, 121.84, 20.68, 117.63, 80.51, 28.48; **IR (Neat, ν/cm^{-1}):** 3726, 3266, 3014, 1722, 1653, 1593, 1523, 1217, 1110; **HRMS (ESI):** Calc. for $C_{25}H_{22}F_3N_4O_3H^+$ $[M+H]^+$: 485.1800, Found: 485.1800.

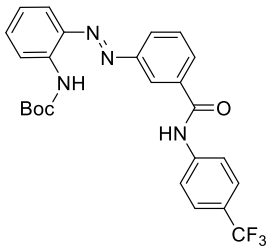

***tert*-butyl(*E*)-(2-((3-((4-(tert butyl)phenyl)carbamoyl)phenyl)diazenyl)phenyl)carbamate (10b):** The crude product was purified by column chromatography over silica gel (EtOAc:petroleum ether 2:8 v/v) to furnish **10b** as an orange solid (124 mg, 90%). **M.P.:** 160.0 °C; **^{1}H NMR (400 MHz, Chloroform-*d*):** δ 9.22 (s, 1H), 8.41 (d, *J* = 8.4 Hz, 1H), 8.30 (s, 1H), 8.01 (d, *J* = 7.8 Hz, 2H), 7.97 (s, 1H), 7.82 (d, *J* = 8.1 Hz, 1H), 7.66 (d, *J* = 7.8 Hz, 1H), 7.61 (s, 2H), 7.48 (s, 1H), 7.42 (s, 2H), 7.11 (s, 1H), 1.57 (s, 9H), 1.34 (s, 9H); **^{13}C NMR (101 MHz, Chloroform-*d*):** δ164.97, 152.57, 147.95, 138.72, 137.19, 135.17, 133.50, 129.87, 129.67, 126.07, 125.42, 122.23, 121.36, 120.72, 120.16, 118.92, 34.55, 31.46, 28.44; **IR (Neat, ν/cm^{-1}):** 3833, 3725,

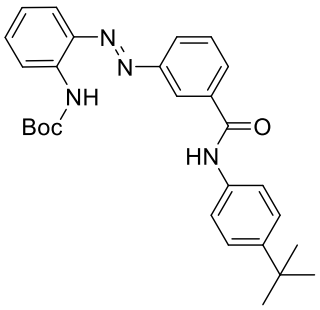

3623, 3266, 3014, 1722, 1670, 1593, 1523, 1217, 1110; **HRMS (ESI):** Calc. for $C_{28}H_{31}N_4O_3H^+$ $[M+H]^+$: 472.2469, Found: 472.2450.

tert-butyl (*E*)-(2-((3-(hexylcarbamoyl)phenyl)diazenyl)phenyl)carbamate (10c): The crude product was purified by column chromatography over silica gel (EtOAc:petroleum ether 2:8 v/v) to furnish **10c** as a yellow solid (111 mg, 90%). **M.P.:** 148.0 °C; **^{1}H NMR (400 MHz, Chloroform-*d*):** δ 9.25 (s, 1H), 8.42 (d, *J* = 8.3 Hz, 1H), 8.22 (t, *J* = 1.7 Hz, 1H), 7.99 (ddd, *J* = 7.9, 1.8, 1.1 Hz, 1H), 7.94 (dt, *J* = 7.7, 1.2 Hz, 1H), 7.83 (dd, *J* = 8.1, 1.5 Hz, 1H), 7.62 (t, *J* = 7.8 Hz, 1H), 7.52 – 7.43 (m, 1H), 7.11 (ddd, *J* = 8.3, 7.3, 1.3 Hz, 1H), 6.35 (s, 1H), 3.54 (s, 2H), 1.67 (p, *J* = 8.0, 7.5 Hz, 2H), 1.59 (s, 9H), 1.39 (dtd, *J* = 25.6, 7.3, 2.6 Hz, 6H), 1.05 – 0.84 (m, 3H); **^{13}C NMR (101 MHz, Chloroform-*d*):** δ 166.74, 152.49, 152.37, 137.0, 136.13, 33.27, 129.55, 129.48, 124.99, 122.12, 121.11, 120.62, 118.83, 80.97, 40.31, 31.52, 29.66, 28.36, 26.70, 22.57, 14.04; **IR (Neat, ν/cm^{-1}):** 3726, 3266, 3014, 1738, 1656, 1593, 1523, 1217, 1110; **HRMS (ESI):** Calc. for $C_{24}H_{31}N_4O_3H^+$ $[M+H]^+$: 425.2500, Found: 425.2552.

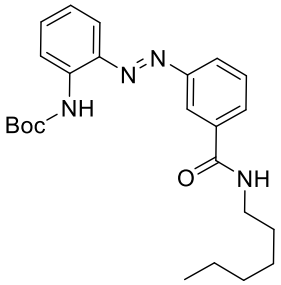

General procedure for synthesizing Amine derivatives (11a-11c)

General method C: The N-Boc derivative **10a-c** (100 mg each) were dissolved in 2 mL of CH_2Cl_2 in a 10 mL of round bottom flask equipped with a gas bubbler. To this solution 0.4 mL of trifluoroacetic acid were added and the resulting mixture was stirred for 5 h. After this time, it was poured into a pre-cooled sodium bicarbonate solution, extracted with CH_2Cl_2 (3 × 10 mL), dried over Na_2SO_4 and evaporated to dryness to furnish compounds **11a-11c**. All the compounds were obtained as an orange oil in quantitative yield (~100%). These compounds were used in the next step without any further purification.

General procedure for synthesizing azobenzene diamide derivatives (2a-c)

General Method D: Aniline derivatives **11a-11c** (100mg, 1 equiv), 2-cyanoacetic acid (2 equiv), EDC·HCl (1.2 equiv), HOBt (1.2 equiv) and *N*, *N*-diisopropylethylamine (2 equiv) were dissolved in DMF (10 mL). The reaction mixture was stirred at room temperature for 12 h. After completion of the reaction, the reaction mixture was quenched by water (10 mL), extracted with ethyl acetate (3 × 20 mL), washed with brine (2 × 20 mL), the organic layer dried over Na_2SO_4 and concentrated under reduced pressure. The purification of the crude product was done by using silica gel chromatography to give pure **2a-2c**.

(*E*)-3-((2-(2-cyanoacetamido)phenyl)diazenyl)-*N*-(4(trifluoromethyl)phenyl)benzamide (2a): The crude product was purified by column chromatography over silica gel (EtOAc:petroleum ether 3:7 v/v) to furnish **2a** as an orange solid (70 mg, 75%). **M.P.:** 230.0 °C; **^{1}H NMR (400 MHz, DMSO-*d*$_6$):** δ 10.79 (s, 1H), 10.43 (s, 1H), 8.66 (t, *J* = 1.7 Hz, 1H), 8.29 (d, *J* = 7.9 Hz, 1H), 8.24 (d, *J* = 7.7 Hz, 1H), 8.17 (d, *J* = 7.8 Hz, 1H), 8.08 (d, *J* = 8.5 Hz, 2H), 7.84 – 7.73 (m, 4H), 7.62 (t, *J* = 7.1 Hz, 1H), 7.35 (s, 1H), 4.18 (s, 2H); **^{13}C NMR (101 MHz, DMSO-*d*$_6$):** δ 165.72, 162.28, 152.38, 143.14, 141.70, 137.13, 136.13, 133.46, 131.39, 130.17, 126.46, 126.42, 126.29, 125.44, 123.57, 123.26, 120.62, 116.43, 116.29, 27.40, quartet (126-123.6); **IR (Neat, ν/cm^{-1}):** 3726, 3266, 3014, 2230, 1738, 1653, 1593, 1523, 1217, 1110; **HRMS (ESI):** Calc. for $C_{23}H_{16}F_3N_5O_2H^+$ $[M+H]^+$: 452.1329, Found: 452.1334.

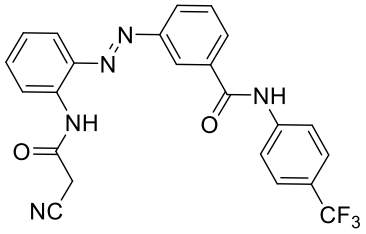

(*E*)-N-(4-(*tert*-butyl)phenyl)-3-((2-(2-cyanoacetamido)phenyl)diazenyl)benzamide (2b): The crude product was purified by column chromatography over silica gel (EtOAc:petroleum ether 3:7 v/v) to furnish **2b** as an orange solid (94 mg, 80%). **M.P.:** 196.0 °C; **^{1}H NMR (400 MHz, Chloroform-*d*):** δ 10.90 (s, 1H), 8.59 (d, *J* = 8.3 Hz, 2H), 8.37 (s, 1H), 8.27 (d, *J* = 7.8 Hz, 1H), 8.19 (d, *J* = 7.9 Hz, 1H), 7.91 (d, *J* = 8.1 Hz, 1H), 7.70 (s, 1H), 7.63 (s, 2H), 7.55 (s, 1H), 7.39 (d, *J* = 8.8 Hz, 2H), 7.31 – 7.24 (m, 2H), 3.69 (s, 2H), 1.33 (s, 9H); **^{13}C NMR (101 MHz, Chloroform-*d*):** δ 164.66, 158.32, 151.74, 147.60, 139.57, 135.48, 135.24, 133.46, 132.39, 130.59, 130.09, 125.78, 125.03, 121.03, 120.02, 119.56, 115.95, 115.54, 34.52, 31.48, 27.30; **IR (Neat, ν/cm^{-1}):** 3833, 3725, 3623, 2972, 2230, 1738, 1674, 1583, 1459, 1366, 1218; **HRMS (ESI)**: Calc. for $C_{26}H_{25}N_5O_2H^+$ $[M+H]^+$: 440.2081, Found: 440.2060.

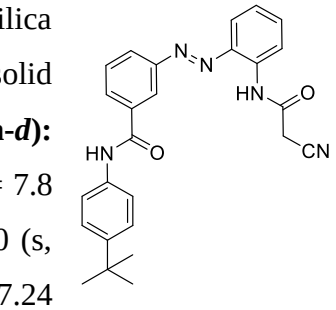

(*E*)-3-((2-(2-cyanoacetamido)phenyl)diazenyl)-*N*-hexylbenzamide (2c): The crude product was purified by column chromatography over silica gel (EtOAc:petroleum ether 2:8 v/v) to furnish **2c** as an orange solid (108 mg, 90%). **M.P.:** 198.0 °C; **^{1}H NMR (400 MHz, Chloroform-*d*):** δ 10.39 (s, 1H), 8.63 (t, *J* = 5.5 Hz, 1H), 8.48 (t, *J* = 1.7 Hz, 1H), 8.23 (d, *J* = 8.0 Hz, 1H), 8.18 (d, *J* = 7.9 Hz, 1H), 8.04 (dt, *J* = 7.7, 1.2 Hz, 1H), 7.74 (d, *J* = 8.1 Hz, 1H), 7.69 (t, *J* = 7.8 Hz, 1H), 7.60 (t, *J* = 8.5 Hz, 1H), 7.31 (t, *J* = 8.3 Hz, 1H), 4.15 (s, 2H), 3.30 (q, *J* = 6.9 Hz, 2H), 1.56 (p, *J* = 7.2

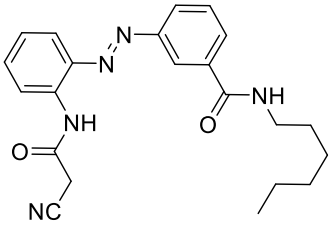

Hz, 2H), 1.44 – 1.19 (m, 7H), 0.97 – 0.65 (m, 3H); **^{13}C NMR (101 MHz, DMSO-d_6):** δ 165.72, 162.22, 152.39, 141.70, 137.01, 136.39, 133.27, 130.81, 129.85, 125.36, 125.06, 123.33, 123.16, 116.39, 116.33, 31.52, 29.46, 27.37, 26.66, 22.53, 14.42; **IR (Neat, ν/cm^{-1}):** 3726, 3262, 3014, 2962, 2230, 1738, 1656, 1588, 1216, 1099; **HRMS (ESI)**: Calc. for $C_{22}H_{25}N_5O_2H^+$ $[M+H]^+$: 392.2100, Found: 392.2086.

2.4.4. Anion Binding Studies by ^{1}H NMR

^{1}H NMR titration was carried out at room temperature on Bruker 400 MHz spectrometer. The residual solvent signal (CD_3CN, δ_H = 1.94) was considered as an internal reference to calibrate spectra. Both the TBACl salt and receptor were dried in high vacuum before use. The titrations were performed by addition of aliquots from the Tetrabutylammonium chloride (TBACl) solution (1 M in CD_3CN) to the solution of either **1b** (0.005 M in CD_3CN) or **2b** (0.005 M in CD_3CN). All NMR data were processed using MestReNova 6.0 and collected data were fitted in different binding modes using BindFit v0.5.

In order to get the binding affinity of the *cis* isomer, the 0.002 M solution of **1b** in acetonitrile-d_3 was irradiated with 365 nm of electromagnetic radiations and subsequently, titration was carried out against TBACl. It is to be noted that upon irradiation **1b** exists as 90:10 *cis*:*trans* PSS and at equilibrium some of the chloride ions will also be bound to the 10% of *trans* form as well. Hence, in order to get the binding constant for the pure *cis* form from the mixture, the chloride concentration which will be bound to the 10% of trans form was deducted from the actual concentration of TBACl used in the titration studies and the concentration of chloride which will be bound to the 10% of *trans* form was calculated using the below equation.[33]

$$[C] = \frac{\left([H]_0 + [G]_0 + \frac{1}{K}\right) \pm \sqrt{\left([H]_0 + [G]_0 + \frac{1}{K}\right)^2 - 4 \cdot [H]_0 \cdot [G]_0}}{2}$$

[C] is the concentration of chloride bound to the *trans* form, H_0 is the concentration of the trans form present in the mixture and G_0 is the concentration of TBACl used as the guest. Binding constant (K) = 110 M^{-1}, which was already obtained for the pure form of the *trans* **1b**.

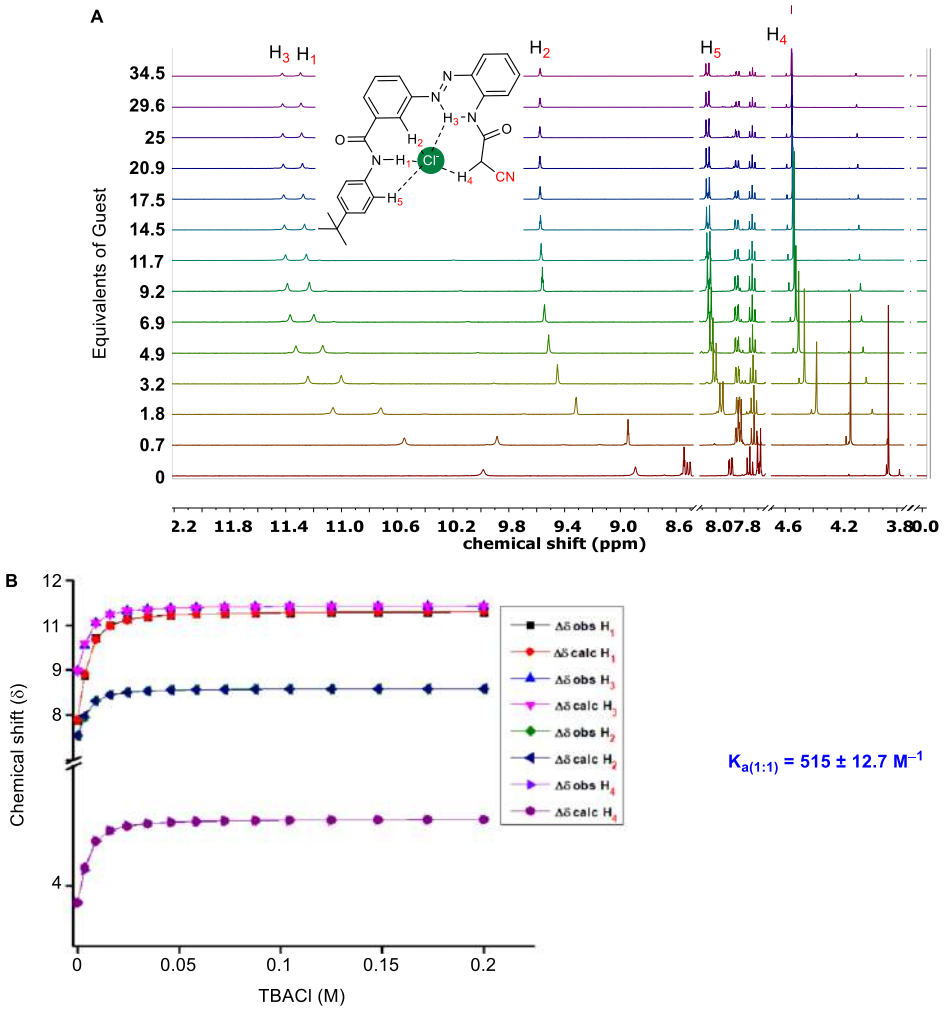

Figure 2.17. ^{1}H NMR titration spectra for **2b** (5 mM) with stepwise addition of TBACl in CD_3CN. The equivalents of added TBACl are shown on the stacked spectra (**A**). The plot of chemical shift (δ) of H_1, H_2, H_3 and H_4 protons *vs* concentration of TBACl added, fitted to 1:1 binding model of BindFit v0.5, the binding constant obtained is the mean of the three independent experiments (**B**).

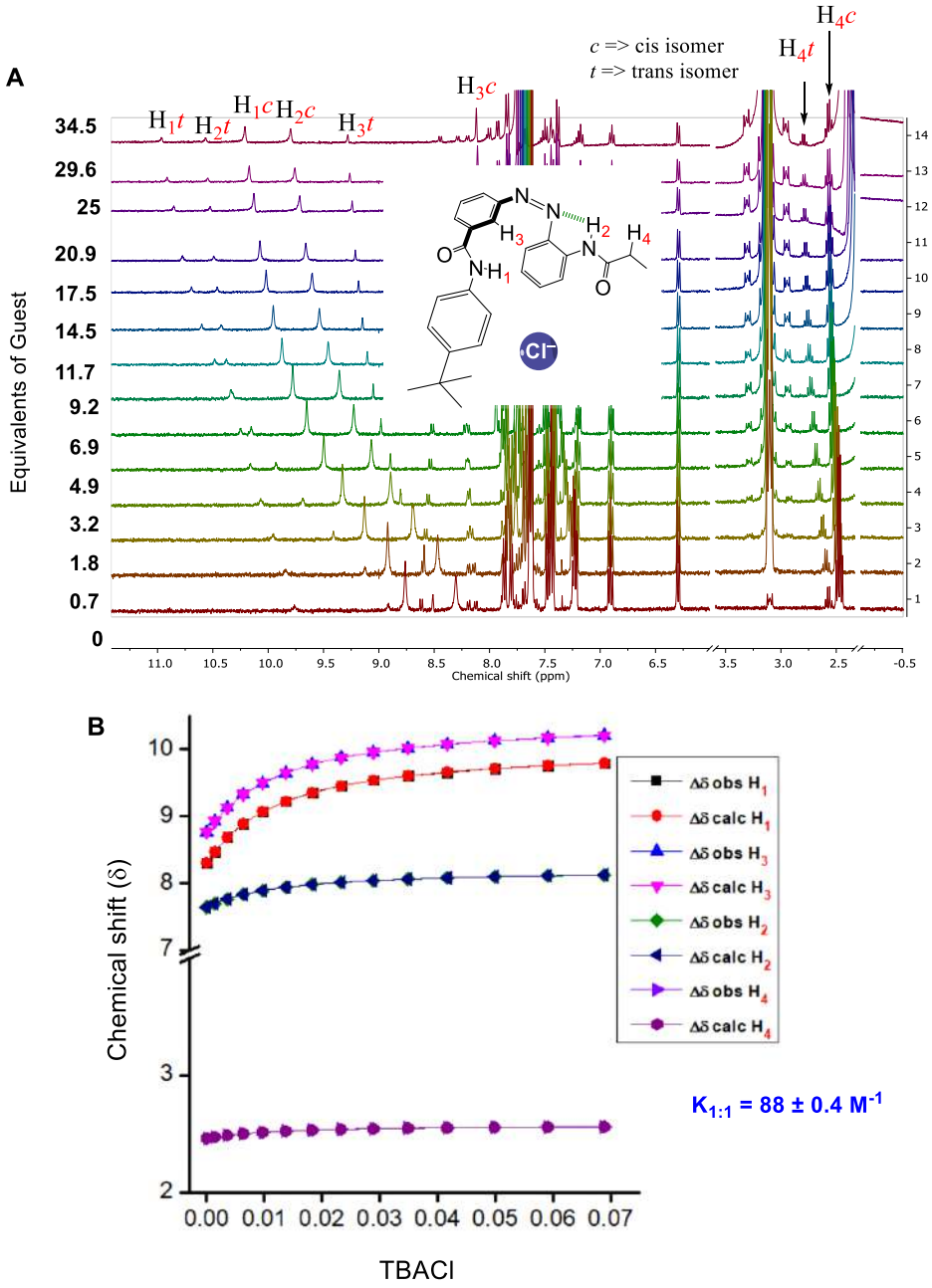

Figure 2.18. ^{1}H NMR titration and binding data for the *cis* form of compound **1b** with TBACl in CD_3CN. The equivalents of added TBACl are shown on the stacked spectra (**A**). The plot of chemical shift (δ) of H_1, H_2, H_3 and H_4 protons *vs* concentration of TBACl added, fitted to 1:1 binding model of BindFit v0.5 (**B**).

2.4.5. Ion Transport Studies [34]

2.4.5.1. Ion transporting activity studies across EYPC-LUVs⊃HPTS:

Preparation of HEPES buffer and stock solutions: The HEPES buffer of pH = 7.0 was prepared by dissolving an appropriate amount of solid HEPES (10 mM) and NaCl (100 mM) in autoclaved water. The pH was adjusted to 7.0 by addition aliquots from 0.5 M NaOH solution. The stock solution of all carriers was prepared using HPLC grade DMSO.

Preparation of EYPC-LUVs⊃HPTS in NaCl: In 10 mL clean and dry round bottom flask thin transparent film of egg yolk phosphatidylcholine (EYPC) was formed using a 1 mL EYPC lipid (25 mg/mL in $CHCl_3$) by providing continuous rotation and purging nitrogen gas. The transparent thin film was completely dried under high vacuum for 4-5 h. After that transparent thin film was hydrated with 1 mL HEPES buffer (1 mM HPTS, 10 mM HEPES, 100 mM NaCl, pH = 7.0) and resulting suspension was vortexed at 10 min intervals during 1 h. This hydrated suspension was subjected to 15 cycles of freeze-thaw (N_2 gas, 55 °C) followed by extrusion through 100 nm (pore size) polycarbonate membrane for 21 times, to obtain the vesicles of an average 100 nm diameter. The unentrapped HPTS dyes were removed by size exclusion chromatography using Sephadex G-50 (Sigma-Aldrich) with eluting of HEPES buffer (10 mM HEPES, 100 mM NaCl, pH = 7.0). Finally, collected vesicles were diluted to 6 mL to get EYPC-LUVs⊃HPTS. *Final conditions:* ~ 5 mM EYPC, Inside: 1 mM HPTS, 10 mM HEPES, 100 mM NaCl, pH = 7.0, Outside: 10 mM HEPES, 100 mM NaCl, pH = 7.0.

Ion transport activity by HPTS assay: In clean and dry fluorescence cuvette, 1975 µL of HEPES buffer (10 mM HEPES, 100 mM NaCl, pH =7.0) and 25 µL of EYPC−LUVs⊃HPTS vesicle was added. The cuvette was placed in the fluorescence instrument equipped with magnetic stirrer (t = 0 s). The time-dependent HPTS emission intensity monitored at λ_{em} = 510 nm (λ_{ex} = 450 nm) by creating pH gradient between intra- and extra- vesicular system by addition of 0.5 M NaOH (20 µL) at t = 20 s. Then different concentrations of transporter molecules in DMSO were added at t = 100 s. Finally, the vesicles were lysed by adding 10% Triton X-100 (25 µL) at t = 300 s to disturbed pH gradient.

The time axis was normalized using Equation S1 and fluorescence intensity using Equation S2:

$$t = t - 100 \qquad \text{Equation S1}$$

$$I_F = [(I_t - I_0) / (I_\infty - I_0)] \times 100 \qquad \text{Equation S2}$$

Where, I_0 is the initial intensity, I_t is the intensity at time t, and I_∞ is the final intensity after addition of Triton X-100.

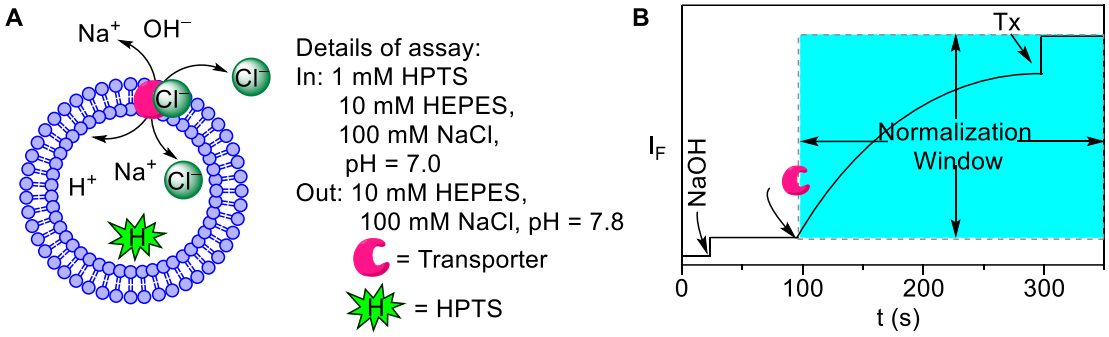

Figure 2.19. Schematic Representation of HPTS-based ion transport assay (**A**), Representation of ion transport kinetics (**B**).

Dose-response activity: The fluorescence kinetics of each transporter at different concentration was studied as a course of time. The concentration profile data were evaluated at t = 290 s to get effective concentration, EC_{50} (i.e. the concentration of transporter needed to achieve 50% chloride efflux)[35] using Hill equation (Equation S3):

$$Y = Y_\infty + (Y_0 - Y_\infty) / [1 + (c/EC_{50})^n] \qquad \text{Equation S3}$$

where, Y_0 = fluorescence intensity just before the transporter addition (at t = 0 s), Y_∞ = fluorescence intensity with excess transporter concentration, c = concentration of transporter compound, and n = Hill coefficient (i.e. indicative for the number of monomers needed to form an active supramolecule).[36]

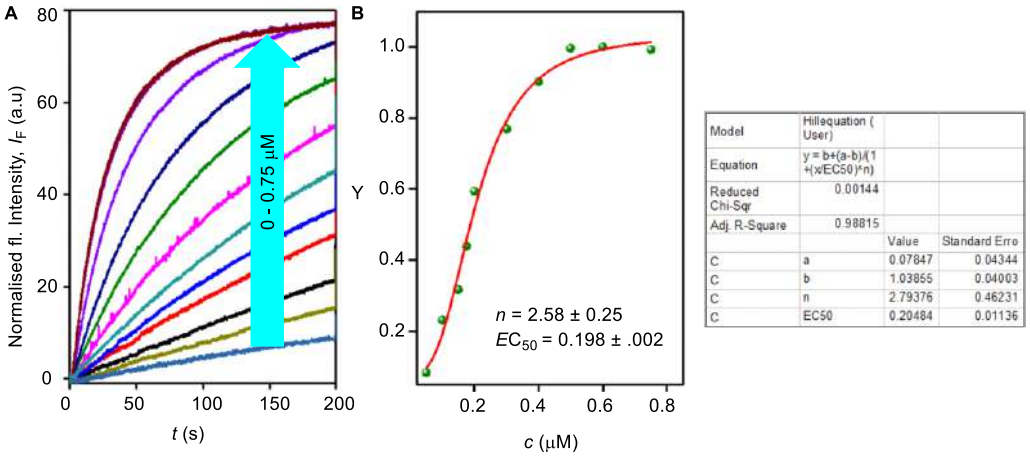

Figure 2.20. Concentration-dependent activity of **1a** across EYPC-LUVs⊃HPTS (**A**). Dose-response plot of **1a** at 280 s after addition of compound (**B**).

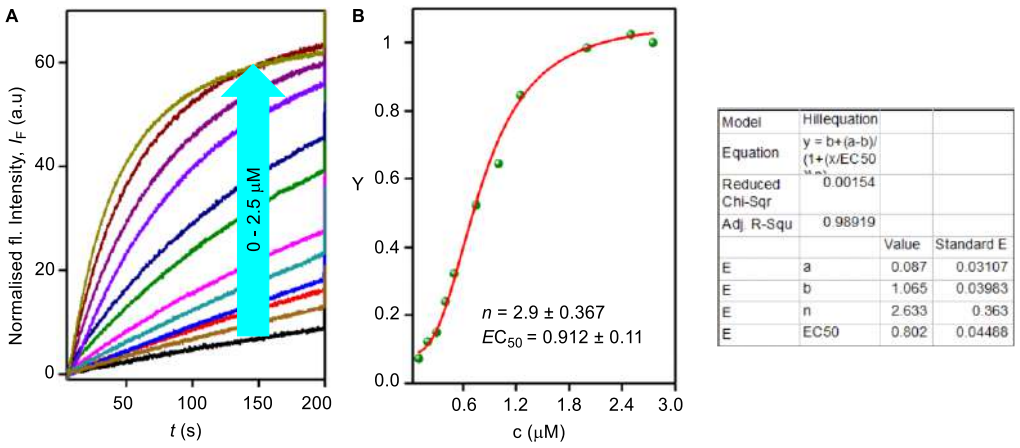

Model	Hillequation		
Equation	y = b+(a-b)/(1+(x/EC50		
Reduced Chi-Sqr	0.00154		
Adj. R-Squ	0.98919		
		Value	Standard E
E	a	0.087	0.03107
E	b	1.065	0.03983
E	n	2.633	0.363
E	EC50	0.802	0.04488

Figure 2.21. Concentration-dependent activity of **1b** across EYPC-LUVs⊃HPTS (**A**). Dose-response plot of **1b** at 280 s after addition of compound (**B**).

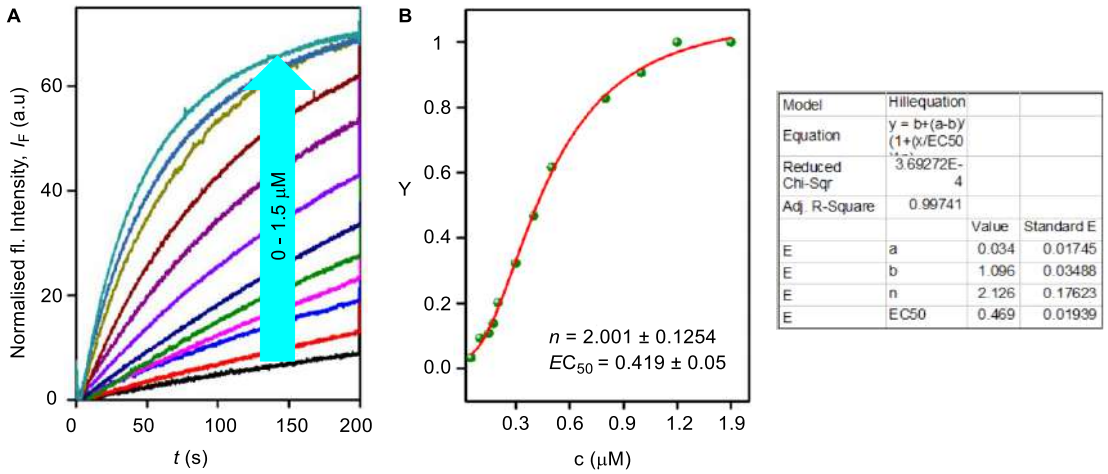

Model	Hillequation		
Equation	y = b+(a-b)/(1+(x/EC50		
Reduced Chi-Sqr	3.69272E-4		
Adj. R-Square	0.99741		
		Value	Standard E
E	a	0.034	0.01745
E	b	1.096	0.03488
E	n	2.126	0.17623
E	EC50	0.469	0.01939

Figure 2.22. Concentration-dependent activity of **1c** across EYPC-LUVs⊃HPTS (**A**). Dose-response plot of **1c** at 280 s after addition of compound (**B**).

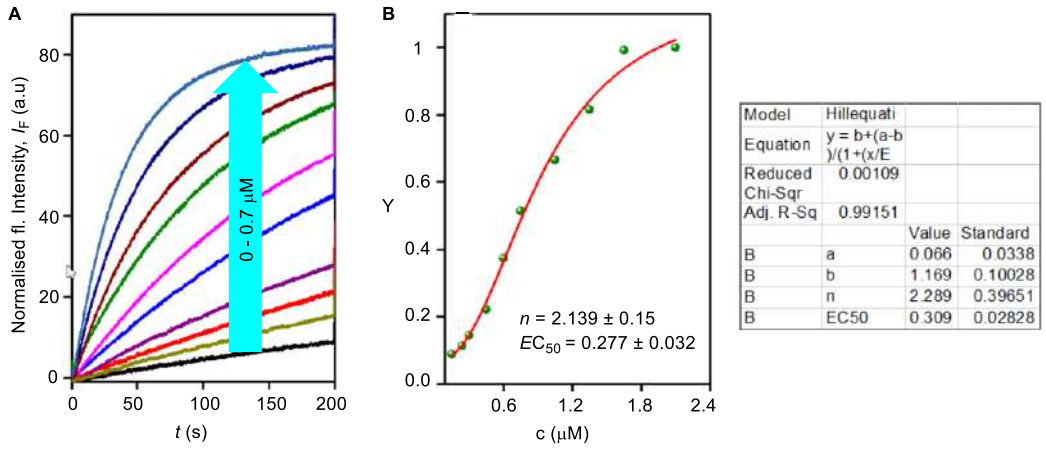

Model	Hillequati		
Equation	y = b+(a-b)/(1+(x/E		
Reduced Chi-Sqr	0.00109		
Adj. R-Sq	0.99151		
		Value	Standard
B	a	0.066	0.0338
B	b	1.169	0.10028
B	n	2.289	0.39651
B	EC50	0.309	0.02828

Figure 2.23. Concentration-dependent activity of **2a** across EYPC-LUVs⊃HPTS (**A**). Dose-response plot of **2a** at 280 s after addition of compound (**B**).

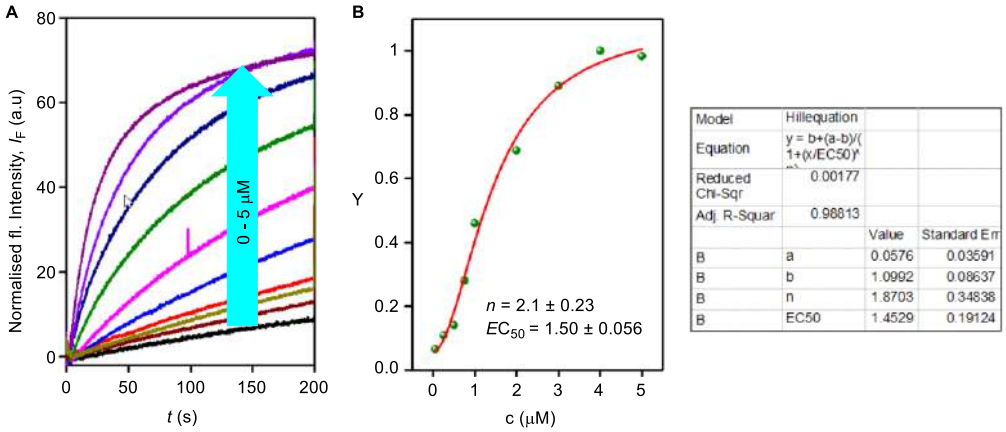

Figure 2.24. Concentration-dependent activity of **2b** across EYPC-LUVs⊃HPTS (**A**). Dose-response plot of **2b** at 280 s after addition of compound (**B**).

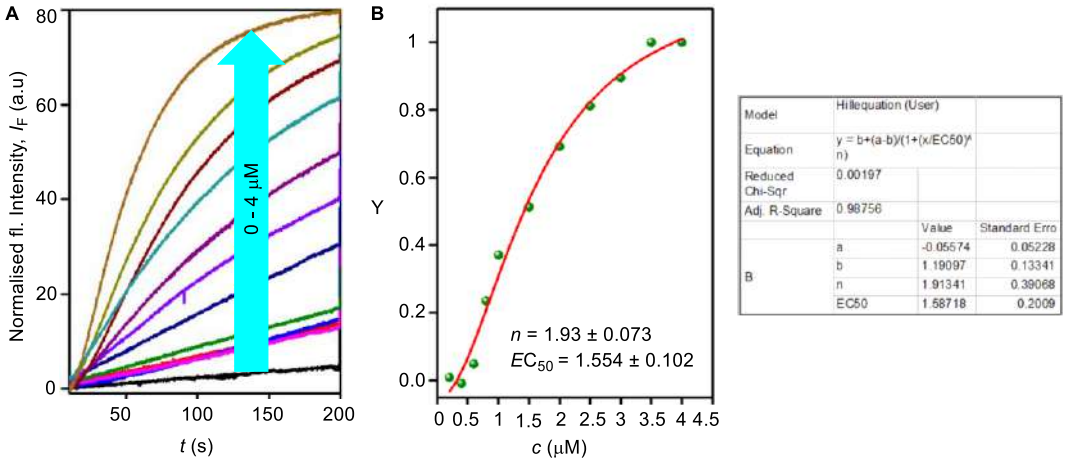

Figure 2.25. Concentration-dependent activity of **2c** across EYPC-LUVs⊃HPTS (**A**). Dose-response plot of **2c** at 280 s after addition of compound (**B**).

2.4.5.2. Ion transport activity by Lucigenin assay:

In a fluorescence cuvette, 200 mM $NaNO_3$ (1975 µL) and lucigenin-based vesicles (25 µL) were taken and kept in a fluorescence instrument under stirring. The fluorescence of the lucigenin was monitored (λ_{em} = 535 nm and λ_{ex} = 455 nm) with time. The chloride gradient was created using 2.0 M NaCl (33.3 µL) at t = 20 s, followed by addition of transporter at t = 100 s. Finally, vesicles were lysed using10% Triton X-100 (25 µL) at t = 300 s for the complete destruction of chloride gradient.

The fluorescent data was normalized using Equation S4, and time axis was normalized using Equation S1.

$$I_F = [(I_t - I_0) / (I_\infty - I_0)] \times 100 \qquad \text{Equation S4}$$

where, I_0 is the initial intensity, I_t is the intensity at time t, and I_∞ is the final intensity after addition of Triton X-100.

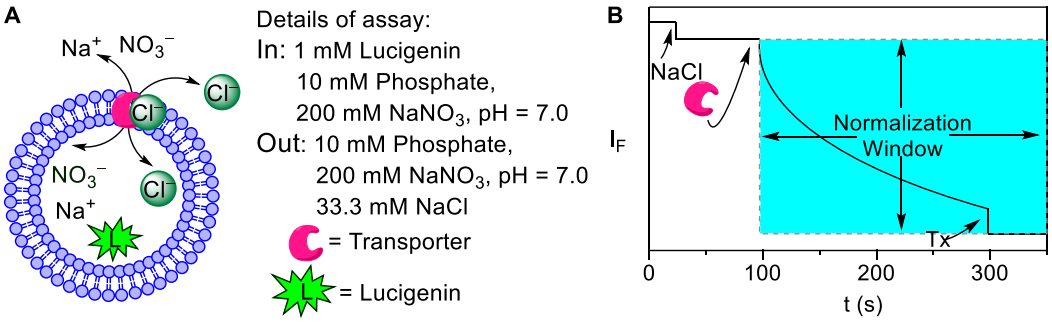

Figure 2.26. Schematic representation of lucigenin-based ion transport assay (**A**) Graphical representation of kinetic study (**B**).

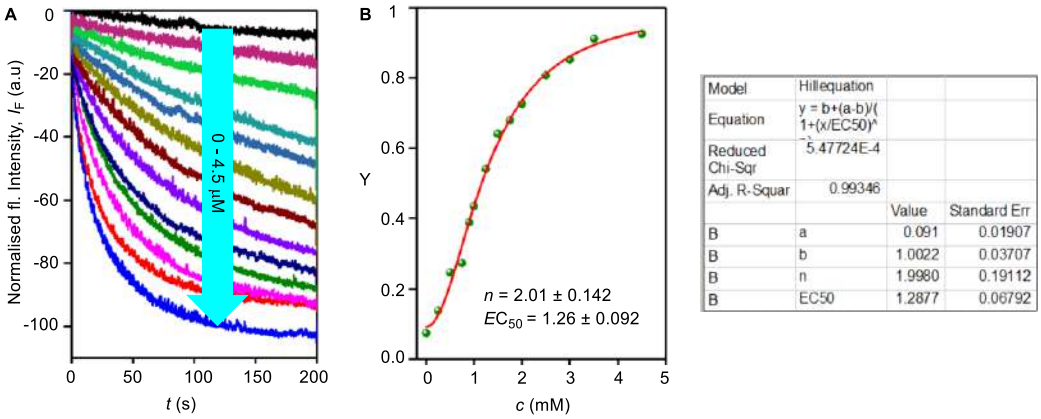

Figure 2.27. Concentration dependent activity of **1a** across EYPC-LUVs⊃HPTS (**A**). Dose-response plot of **1a** at 280 s after addition of compound (**B**).

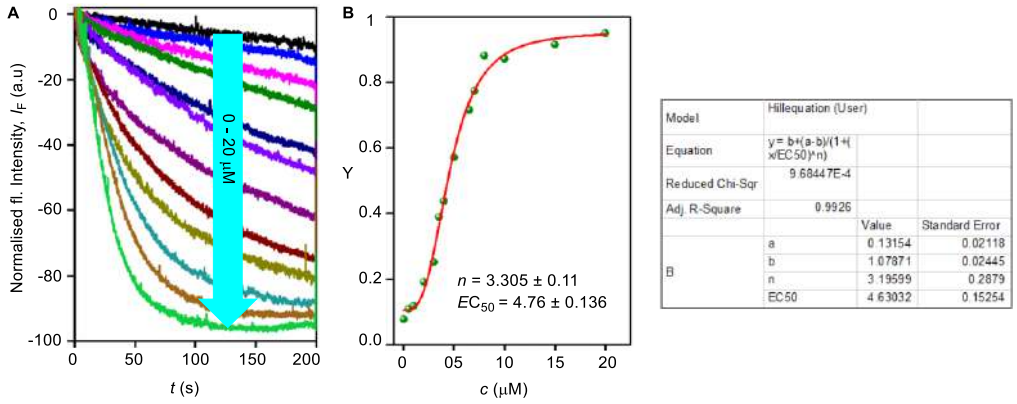

Figure 2.28. Concentration dependent activity of **1b** across EYPC-LUVs⊃HPTS (**A**). Dose-response plot of **1b** at 280 s after addition of compound (**B**).

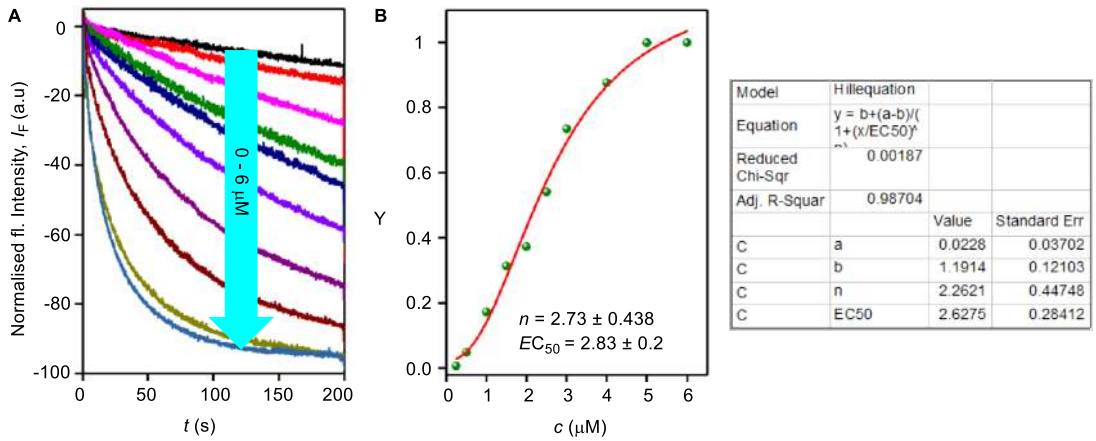

Model	Hillequation		
Equation	y = b+(a-b)/(1+(x/EC50)^		
Reduced Chi-Sqr	0.00187		
Adj. R-Squar	0.98704		
		Value	Standard Err
C	a	0.0228	0.03702
C	b	1.1914	0.12103
C	n	2.2621	0.44748
C	EC50	2.6275	0.28412

Figure 2.29. Concentration dependent activity of **1c** across EYPC-LUVs⊃HPTS (**A**). Dose-response plot of **1c** at 280 s after addition of compound (**B**).

Figure 2.30. Concentration dependent activity of **2a** across EYPC-LUVs⊃HPTS (**A**). Dose-response plot of **2a** at 280 s after addition of compound (**B**).

2.4.5.3. Anion selectivity studies:

Preparation of EYPC-LUVs⊃HPTS for anion selectivity: EYPC-LUVs⊃HPTS (~ 5.0 mM EYPC, inside: 1 mM HPTS, 10 mM HEPES, 100 mM NaX, pH = 7.0 and outside: 10 mM HEPES, 100 mM NaX, pH = 7.0; where, X^- = Cl^-, Br^-, ClO_4^-, NO_3^- and I^-) were prepared following reported protocol.[37]

Anion Selectivity Assay: In a fluorescence cuvette, 1975 μL buffer containing 10 mM of HEPES, 100 mM of NaX; where, X^- = Cl^-, Br^-, ClO_4^-, NO_3^- and I^- and 25 μL of vesicle were kept in a fluorescent instrument with stirring. The fluorescence emission monitored for HPTS (λ_{em} = 510 nm and λ_{ex} = 450 nm). A pH gradient was created using NaOH solution. The compound **1a** was added at t = 100 s and at t = 300 s, 25 μL of 10% Triton X-100 was added

to lyze the vesicles for 100 % activity. Time axis and fluorescent data were normalized using Equations S1 and S2, respectively.

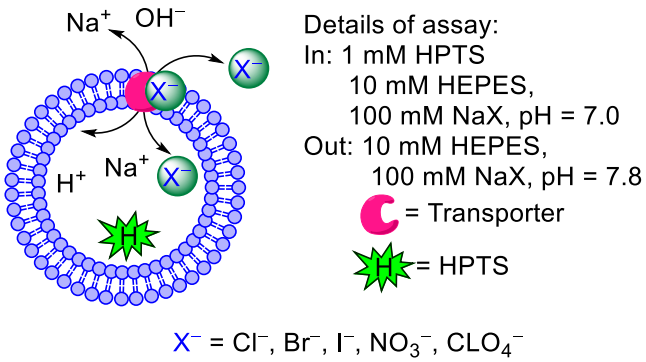

Figure 2.31. Schematic representation of anion-selective assay by changing intravesicular as well as extravesicular anions.

2.4.5.4. Cation selectivity assay across EYPC-LUVs⊃lucigenin vesicles:

The vesicles were prepared by following the same protocol as stated above. In this particular assay, unlike normal lucigenin assay, the chloride gradient was created by adding salts of different cations MCl (M = Li^+, Na^+, K^+, Rb^+, and Cs^+) before the transporter addition. Other experimental steps are same as the normal lucigenin-based assay.

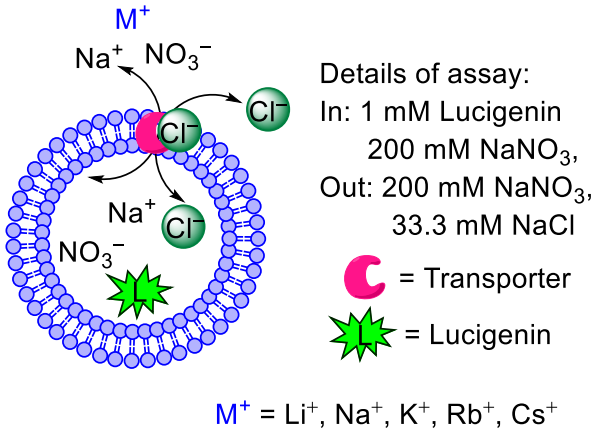

Figure 2.32. Schematic representations of fluorescence-based cation selectivity assay.

Preparation of EYPC-LUVs⊃lucigenin for antiport study: Vesicles were prepared encapsulated 200 mM NaCl buffered at pH = 7.0.

Determination of antiport mechanism by lucigenin assay: In a cuvette, 50 μL of the above lipid solution and 1950 μL of an iso-osmolar solution of different NaX salts were taken. The fluorescent intensity of lucigenin was monitored with time.

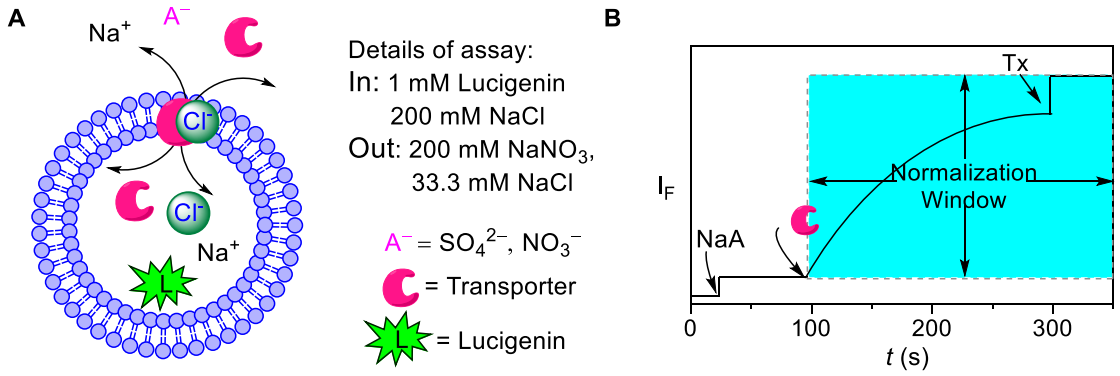

Figure 2.33. Representation of fluorescence-based antiport assay using EYPC-LUVs⊃lucigenin (**A**) Representation of ion transport kinetics showing normalization window (**B**).

2.4.5.5. Ion transport mechanism by ISC studies

Preparation of ISE vesicles: A chloroform solution (1 mL) of 1-palmitoyl-2-oleoylphosphatidylcholine (EYPC) (25 mg) was evaporated under reduced pressure to give a thin film. The lipid film was dried under high vacuum for 4 hours. The thin film was rehydrated by vortexing with a sodium chloride solution (300 mM KCl, 5 mM phosphate buffer at pH = 7.2,). The lipid suspension was then subjected to fifteen freeze–thaw cycles and was allowed to age for 1 h at room temperature. The suspension was extruded twenty-three times through a 200 nm polycarbonate membrane using extruder (Avanti, The Mini-Extruder set) to obtain unilamellar vesicles containing KCl (300 mM in 5 mM phosphate buffer at pH = 7.2). Non-encapsulated KCl salts were removed by dialysing the vesicles three times in a potassium gluconate solution (300 mM, 5 mM phosphate buffer at pH = 7.2,).

Ion transport activity in the presence of Valinomycin and Monensin

In a glass vial, 50 μL of lipid solution and 1950 μL of 300 mM Kgluconate were taken in a fluorescent instrument with magnetic stirrer and chloride efflux was monitored with time. Transporter molecule **1a** as DMSO solution was added at t = 50 s, Monensin and Valinomycin as DMSO solutions were added at t = 10 s and finally at t = 300 s, 25 μL of 10% Triton X-100 was added to lyse those vesicles for 100% chloride influx. The chloride efflux for **1a** was monitored in presence and absence of Monensin and Valinomycin following the above sequence of addition of components. The value at 50 seconds was set at 0% chloride efflux and the final chloride reading at 300 s was set as 100% chloride efflux. The time axis was normalized using the Equation S5.

$t = t - 50$ Equation S5

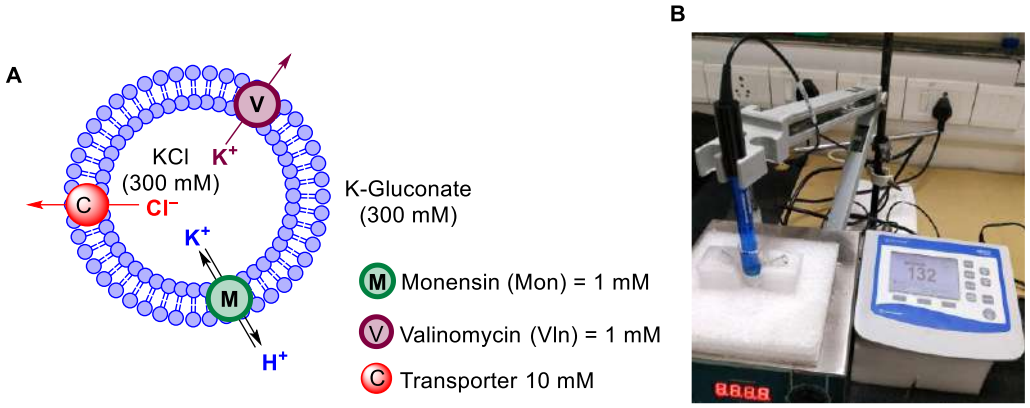

Figure 2.34. Schematic representation of ISE-based Valinomycin and Monensin essay (**A**). ISE assembly (**B**).

2.4.5.6. U-tube experiments for checking Cl^- transport

In this experiment we have checked whether the chloride ion is transporting via mobile carrier mechanism or ion channel formation by transporter molecule. For that we have set up an experiment using a U-tube where left arm (Source arm) of the tube was filled with 7.5 mL of 500 mM NaCl solution buffered to pH 7.0 using 5mM phosphate buffer and the right arm (receiver arm) of the tube was filled with 7.5 mL of 500 mM $NaNO_3$ solution buffered to pH 7.0 using 5mM phosphate buffer. Two different salts solution in two different arm were separated by 15 mL solution of compound **1a** in $CHCl_3$ (1 mM compound **1a**, 1 mM Tetrabutylammonium hexafluorophosphate) in such a way that two salts solution never come contact with each other. Here transport of chloride ion is only possible via mobile carrier mechanism due to the long length of $CHCl_3$ layer, which does not allow the formation ion channel. For checking transport activity via carrier mechanism, chloride ion concentration in the receiver arm was measured by chloride ion selective electrode. The gradual increase of chloride ion concentration was measured in a fixed time interval for the time period of 8 days, gave evidence in support of mobile carrier mechanism. In a control experiment no increase in chloride ion concentration was observed when we omitted transporter molecule **1a** keeping other conditions same.

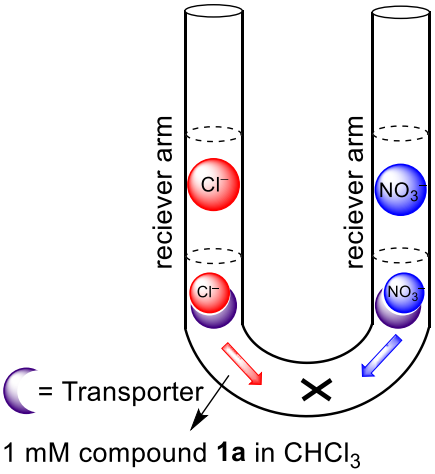

Figure 2.35. Schematic representation of the U-tube experiment.

2.4.6. Photoisomerization Studies by ^{1}H NMR and UV-Vis Spectroscopies

2.4.6.1. ^{1}H NMR studies

***trans* to *cis* Isomerization:** For monitoring the *trans* to *cis* isomerization by ^{1}H NMR, either a sample of **1a**, **1b**, **1c**, **2a** (4.0×10^{-3} M) in DMSO-d_6 or **2c** (4.0×10^{-3} M) in chloroform-*d* in was prepared in an NMR tube and then irradiated at λ = 365 nm using LEDs (3 × 3 Watt) for 5 min and then the ^{1}H NMR data before and after photoirradiation were compared. The *trans* to *cis* ratio after photo-irradiation for **1a**, **1b**, **1c**, **2a** and **2c** were 15:85, 15:85, 17:83, 10:90 and 10:90, respectively.

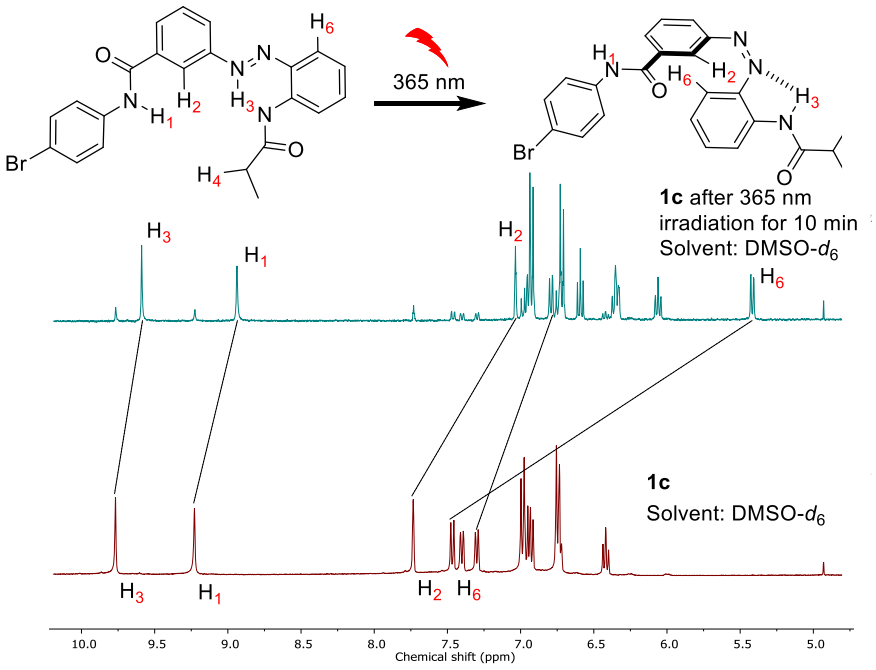

Figure 2.36. Partial 400 MHz ^{1}H NMR spectrum of **1c** (4.0×10^{-3} M, down) in DMSO-d_6 at 25 °C, and that of photo-irradiated sample of **1c** (up) by 365 nm light for 10 min. The *trans* to *cis* ratio after photo-irradiation is 17:83.

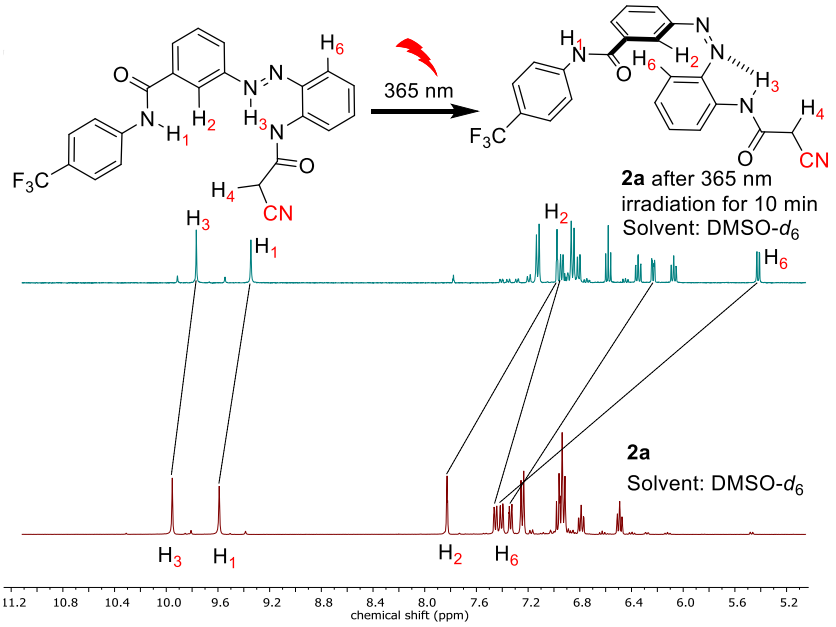

Figure 2.37. Partial 400 MHz ^{1}H NMR spectrum of **2a** (4.0×10^{-3} M, down) in DMSO-d_6 at 25 °C, and that of photo-irradiated sample of **2a** (up) by 365 nm light for 10 min. The *trans* to *cis* ratio after photo-irradiation is 10:90.

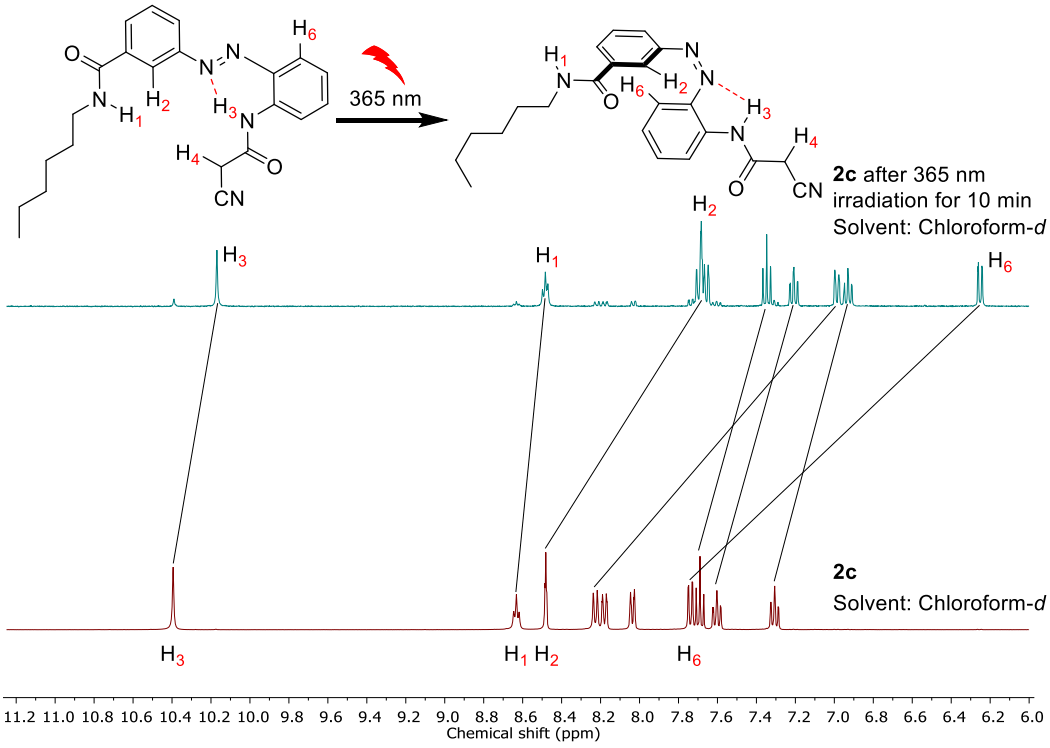

Figure 2.38. Partial 400 MHz ^{1}H NMR spectrum of **2c** (4.0×10^{-3} M, down) in chloroform-*d* at 25 °C, and that of photoirradiated sample of **2c** (up) by 365 nm light for 10 min. The *trans* to *cis* ratio after photo-irradiation is 10:90.

Proof of intramolecular hydrogen bonding in *trans* and *cis* forms: In the compound **2c**, the amide N-H_1 is connected to the aliphatic chain which distinguishes it from the other amide N-H_3 on the basis of its splitting pattern (Figure 2.38). In the *trans* isomer of **2c** in $CDCl_3$, the amide N-H_1 showed a triplet peak at 8.65 ppm. For amide N-H_3 the appearance of a singlet at 10.4 ppm clearly suggests the presence of intramolecular hydrogen bonding possibly with the rarest azo nitrogen forming a 6-member ring.[30, 38] In the photoirradiated sample, the amide N-H_3 showed a little up-field shift suggesting the presence of hydrogen bond, which is probably with the nearest azo nitrogen forming a 5-member ring.[16, 39]

2.4.6.2. UV-Vis studies

Photoisomerization of compounds **1a**, **1c**, **2a** and **2c** were carried out in CH_3CN. Initially, stock solutions of these compounds (2 mM in DMSO) were prepared in different vials, and covered with an aluminium foil.

For **1a** and **1c:** In a 3 mL UV cuvette was placed either 1980 μL of CH_3CN and 20 μL of either **1a** (2 mM in DMSO) or **1c** (2 mM in DMSO) were added to get the final concentration of 20 μM.

For **2a** and **2c:** In a 3 mL UV cuvette was placed either 1950 μL of CH_3CN and 50 μL of either **2a**, or **2c** (2 mM in DMSO) were added to get the final concentration of 50 μM.

The cuvette was placed in a UV-vis spectrometer and the UV-vis spectrum was recorded.

***trans* to *cis* Isomerization:** Subsequently, each of these samples was irradiated at λ = 365 nm using LEDs (3 × 3 Watt) for varied time intervals to isomerize the azobenzene moiety. After each irradiation, the UV-vis spectrum was recorded. The complete *trans* to *cis* isomerization was achieved within 10 s.

***cis* to *trans* Isomerization:** The back-conversion from *cis* to *trans* form was carried out by irradiating the sample at λ = 450 nm using LEDs (3 × 3 Watt) for varied time intervals till 20 s. No spectral change was observed after 10 s irradiation.

***trans-cis* Isomerization cycle:** For monitoring the reversibility of the *trans-cis* isomerization process, the *trans*-to-*cis* isomerization was carried out by irradiating each sample at λ = 365 nm using LEDs (3 × 3 Watt) for 10 s, and the *cis*-to-*trans* isomerization was carried out by irradiating each sample at λ = 450 nm using LEDs (3 × 3 Watt) for 20 s. The process was repeated several times.

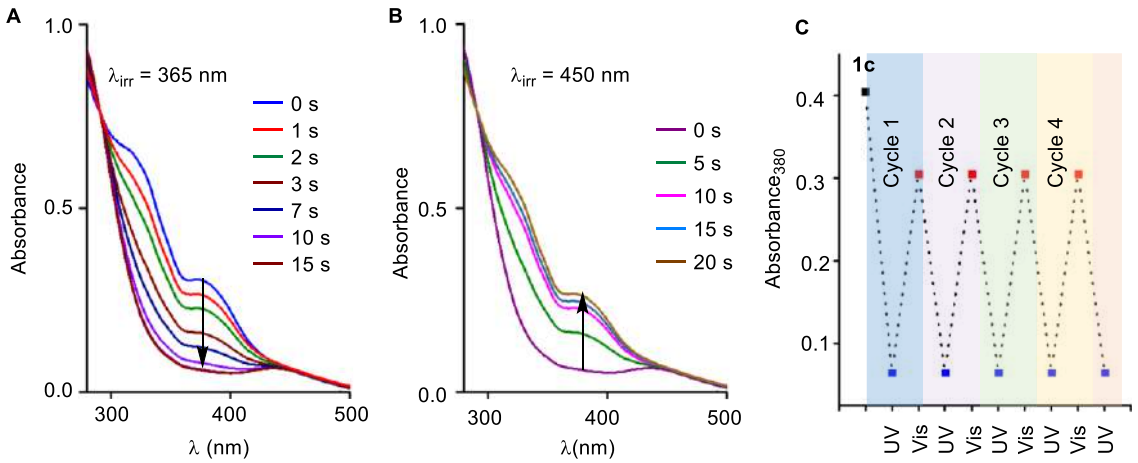

Figure 2.39. UV-visible spectral changes for **1c** (20 μM) upon irradiation with 365 nm light (3 × 3 Watt LEDs) (**A**). UV-visible spectral changes for **1c** (20 μM) upon irradiation with 450 nm light (3 × 3 Watt) (**B**). Switching cycles for **1c** (20 μM) under alternating irradiation with 365 nm and 450 nm lights (**C**). The absorbance at 380 nm was monitored for the switching study. All data were recorded in CH_3CN.

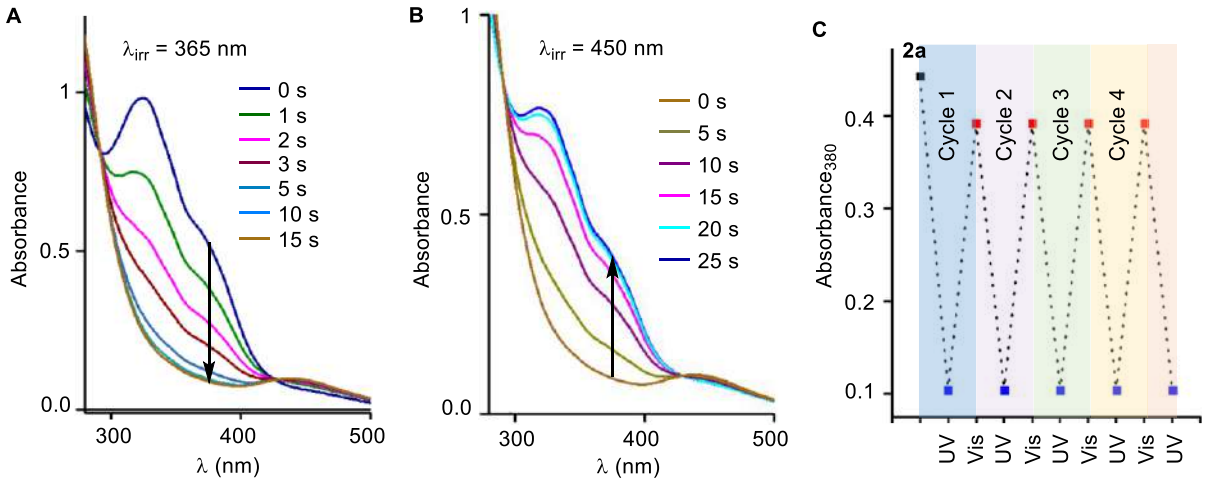

Figure 2.40. UV-visible spectral changes for **2a** (50 μM) upon irradiation with 365 nm light (3 × 3 Watt LEDs) (**A**). UV-visible spectral changes for **2a** (50 μM) upon irradiation with 450 nm light (3 × 3 Watt) (**B**). Switching cycles for **2a** (50 μM) under alternating irradiation with 365 nm and 450 nm lights (**C**). The absorbance at 380 nm was monitored for the switching study. All data were recorded in CH_3CN.

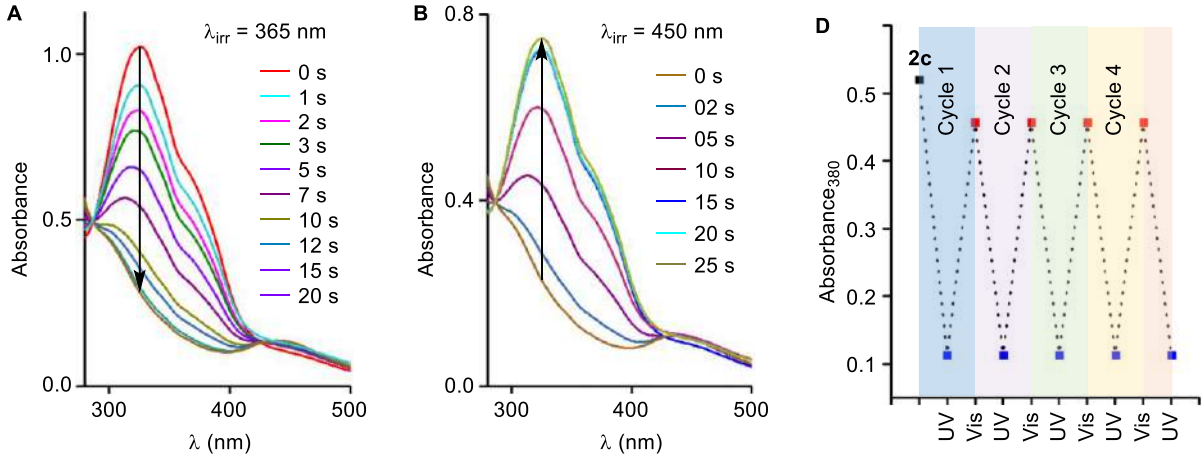

Figure 2.41. UV-visible spectral changes for **2c** (50 μM) upon irradiation with 365 nm light (3 × 3 Watt LEDs) (A). UV-visible spectral changes for **2c** (50 μM) upon irradiation with 450 nm light (3 × 3 Watt) (**B**). Switching cycles for **2c** (50 μM) under alternating irradiation with 365 nm and 450 nm lights (**D**). The absorbance at 380 nm was monitored for the switching study. All data were recorded in CH_3CN.

2.4.6.3. Thermal stability

In order to check the thermal stability of photoisomerized *cis* form, in a 3 mL UV cuvette was placed 1980 μL of acetonitrile and 20 μL of **1a** (2 mM in DMSO) was added to get the final concentration of 20 μM. Initially, the UV-Vis absorbance was recorded for the *trans* form. Subsequently, the sample was irradiated at λ = 365 nm using LEDs (3 × 3 Watt) for 10 s to achieve *trans* to *cis* photoisomerization and absorbance was again recorded. The photoisomerized *cis* sample was then kept in dark and UV-Vis absorbance was recorded after each 1 h. The process was repeated for a total of 9 h.

2.4.7. Photoregulated Transport Activity across EYPC-LUVs⊃Lucigenin

In the lucigenin-based vesicles, Initially, the transport activity of either of the compound **1a, 1c** or **2a** (3 μM, using stock solution of 0.5 mM in ACN/MeOH (4:1)) was recorded. Subsiquently, the stock samples were irradiated at λ = 365 nm using LEDs (3 × 3 Watt) for 5 s to photoisomerize the azobenzene subunit and the transport activity using these photoisomerized samples for each compound was recorded. Photoisomerization leads to a substantial decrease in the transport activity. After that, these photoisomerized samples were irradiated at λ = 450 nm using LEDs (3 × 3 Watt) for 10 s and the transport activity for each compound was recorded again and it was observed that the initial transport activity of the

anionophores was regenerated efficiently. This photo-regulatory activity behaviour of the transporters **1a, 1c** and **2a** was repeated several times.

Furthermore, the transport activity of 1a (c = 3.5 μM) was monitored by keeping the sample in dark in the *cis* photoisomerised form. There was hardly any increment in the transport activity during this time of 5 h (Figure S63), which showed its better thermal stability.

The time-dependent data were normalized to percent change in fluorescence intensity using Equation S4:

$$I_F = [(I_t - I_0) / (I_\infty - I_0)] \times (-100) \qquad \text{Equation S4}$$

where, I_0 is the initial intensity, I_t is the intensity at time t, and I_∞ is the final intensity after addition of Triton X-100.

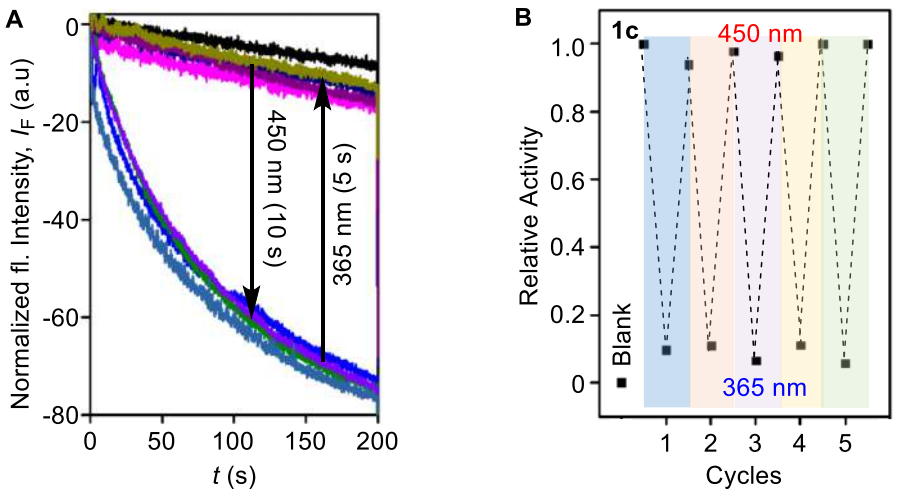

Figure 2.42. Transport activity of **1c** (3 μM) in *trans* and *cis* form across EYPC-LUVs⊃Lucigenin (**A**). Photo regulated transport activity of **1c** (3.5 μM) taken at t = 280 s under alternating photo irradiation at two different wavelengths of 365 nm and 450 nm across EYPC-LUVs⊃Lucigenin (**B**).

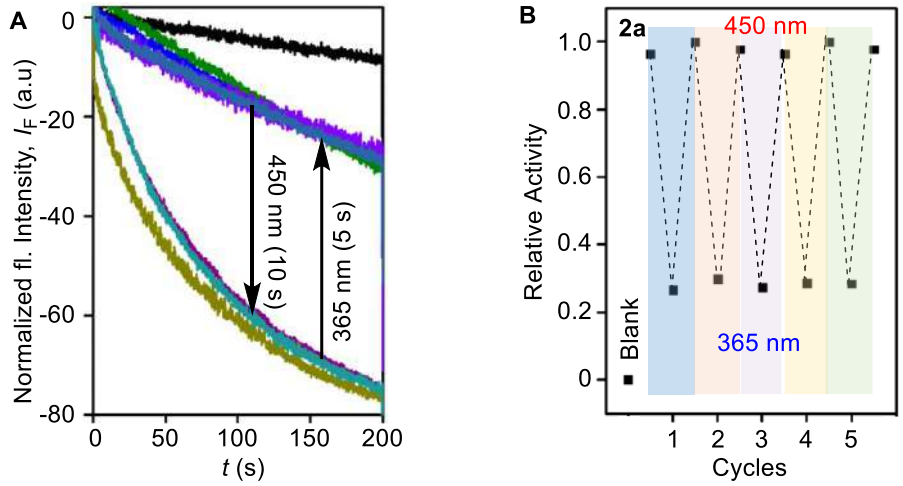

Figure 2.43. Transport activity of **2a** (3 μM) in *trans* and *cis* form across EYPC-LUVs⊃Lucigenin (**A**). Photo regulated transport activity of **2a** (3.5 μM) taken at t = 280 s under alternating photo irradiation at two different wavelengths of 365 nm and 450 nm across EYPC-LUVs⊃Lucigenin (**B**).

2.4.8. Photoregulated ion transport process inside the lipid membrane

Preparation of HEPES buffer and stock solutions: The HEPES buffer of pH = 7.0 was prepared by dissolving an appropriate amount of solid HEPES (10 mM) and NaCl (100 mM) in autoclaved water. The pH was adjusted to 7.0 by addition aliquots from 0.5 M NaOH solution using pH meter.

Preparation of EYPC-LUVs⊃HPTS: The vesicles were prepared by the following protocol as stated above.

Photoregulation and ion transport assay in LUVs: In clean and dry fluorescence cuvette, 1975 μL HEPES buffer (10 mM HEPES, 100 mM NaCl, pH = 7.0) and 25 μL EYPC-LUVs⊃HPTS vesicles were placed. To this suspension, compound **1a** (0.3 μM, as DMSO solution) was added. The initial activity was recorded. Further, the same solution was first irradiated for 2 min with 365 nm wavelength UV (using three 3 W LEDs each placed at a distance of 2 cm) and subsequently the transport activity was monitored. A significant decrease in the transport activity confirms the photoisomerisation of *trans* to *cis* form. The reverse photoisomerisation process was operated by photoirridiating the samle initially with 365 nm to convert *trans* to *cis* form, and subsequently with 450 nm to isomerise it back *cis* to *trans* form. The activity was regained back confirming the back photoisomerisation process of *cis* to *trans* from inside the lipid membrane. The fluorescence intensity of HPTS at λ_{em} =

510 nm (λ_{ex} = 450 nm) of each sample was monitored as a course of time *t*. At *t* = 100 s, a pH gradient was created by the addition of 20 μL NaOH (0.5 M). Finally, at *t* = 300 s vesicles were lysed by the addition of 10% Triton X-100 (25 μL) to get the complete destruction of the applied pH gradient. Each, time-dependent fluorescence data was normalized using Equation S2. A sample containing 1975 μL HEPES buffer (10 mM HEPES, 100 mM NaCl, pH = 7.0), 25 μL EYPC-LUVs⊃HPTS and 20 μL DMSO was also subjected to 5 min irradiation with same UV LEDs. The ion transport activity of this sample was measured by

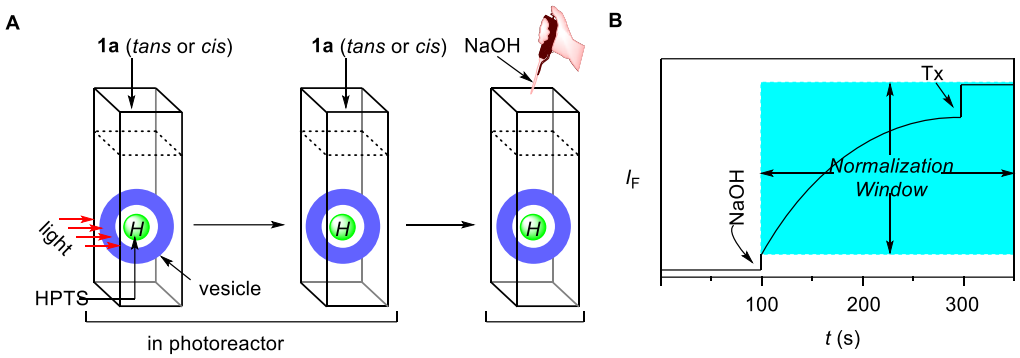

Figure 2.44. Description of photoisomerisation process of **1a** in the presence of unilamellar vesicles followed by ion transport measurement (**A**). Illustration of ion transport kinetics showing normalization window (**B**).

adding 20 μL NaOH (0.5 M) at *t* = 100 s of the kinetics experiment, and this data was used as a control data. The time axis was normalized according to Equation S1. The time-dependent data were normalized to percent change in fluorescence intensity using Equation S2.

2.4.7. Theoretical Calculations

2.4.7.1. Conformational studies and geometry optimization

To compare the ^{1}H NMR-based Cl^- binding interactions of **1a** and **2a**, the initial conformations of [**1a**+Cl^-] and [**2a**+Cl^-] complexes were generated using the CONFLEX 8 software package using MMFF94s force field. The [**1a**+Cl^-] complex provided 246 conformations. The Boltzmann populations of top four conformations **Conf-1** – **Conf-4** were 36.5015% (Figure 2.45 A), 36.3414% (Figure 2.45 B), 10.7435% (Figure 2.45 D), and 10.6886% (Figure 2.45 E), respectively. Rest of the conformations were less than 3% in population, therefore, were not considered further calculation. The conformations **Conf-1** and **Conf-2** differed only at the rotated positions of the CF_3 group (Figure 2.45 C).

The [**2a**+Cl^-] complex provided 75 conformations. The Boltzmann populations of top two conformations (i.e., **Conf-1** and **Conf-2**) were 50.18% (Figure 2.46 A) and 49.7898% (Figure

2.46 B), respectively. Rest of the conformations were less than 1% in population, therefore, were not considered further calculation. The conformations **Conf-1** and **Conf-2** differed only at the rotated positions of the CF_3 group (Figure 2.46 C). Therefore, the most populated

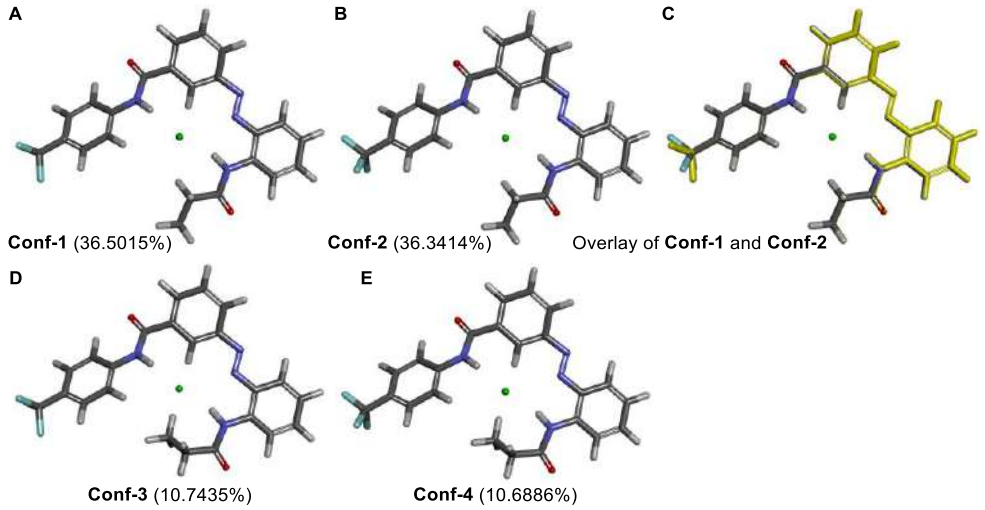

Figure 2.45. The top four initial geometries **Conf-1 - Conf-4** (**A**, **B**, **D** and **E**) for [**1a**+Cl^-], optimized by CONFLEX 8 software using MMFF94s force field. The Boltzmann populations of these conformations are also provided in next to the conformation names. Figure **C** represents the overlay images of **Conf-1** and **Conf-2** with **Conf-1** shown in yellow colour.

conformations [**1a**+Cl^-] and [**2a**+Cl^-] complexes were optimized separately by Gaussian 09 program package using B3LYP functional and 6-311++G(d,p) basis set. The geometry optimized structures of [**1a**+Cl^-] and [**2a**+Cl^-] complexes are represented in Figure 2.47.

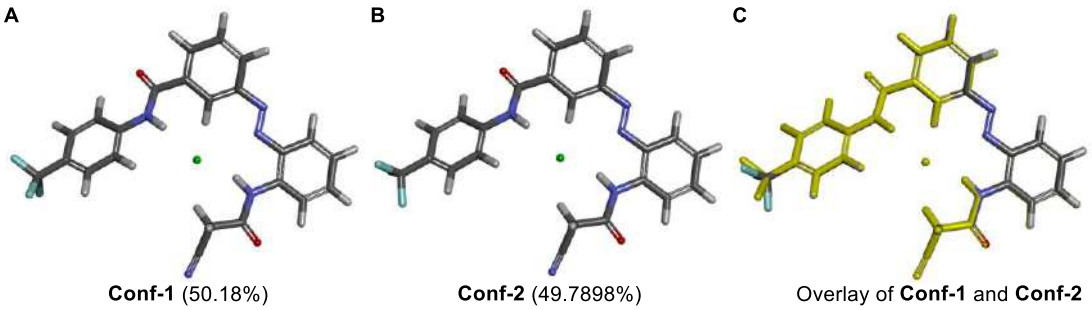

Figure 2.46. The top four initial geometries **Conf-1 - Conf-4** (**A** and **B**) for [**2a**+Cl^-], optimized by CONFLEX 8 software using MMFF94s force field. The Boltzmann populations of these conformations are also provided in next to the conformation names. Figure **C** represents the overlay images of **Conf-1** and **Conf-2** with **Conf-1** shown in yellow color.

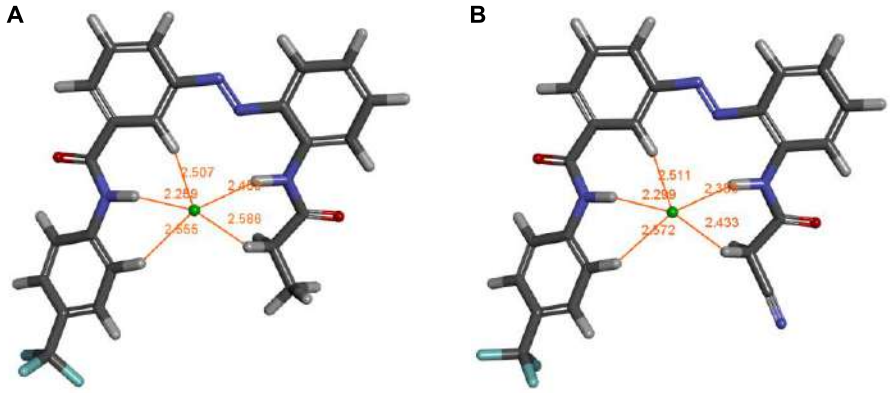

Figure 2.47. Geometry-optimized images of [**1a**+Cl^-] (**A**) and [**2a**+Cl^-] (**B**) complexes.

Table 2.1. Atomic coordinates of [**1a**+Cl^-] after geometry optimization by Gaussian 09 program using B3LYP functional and 6-311++G(d,p) basis set.

Charge = –1		Multiplicity = 1		
Atom #	Atom Type	x	y	Z
1	C	0.323192	4.567481	-0.276226
2	C	0.094107	3.182005	-0.235406
3	C	1.173318	2.307826	-0.116296
4	C	2.476122	2.822089	-0.020861
5	C	2.691287	4.203542	-0.03233
6	C	1.612913	5.073618	-0.16829
7	N	3.639218	2.025979	0.125648
8	N	3.475742	0.794515	-0.050045
9	C	4.630233	-0.002645	0.094718
10	C	4.450349	-1.407613	-0.007953
11	C	5.590463	-2.231623	0.061687
12	C	6.849983	-1.67819	0.240338
13	C	7.022134	-0.294489	0.35999
14	C	5.914174	0.53079	0.28844
15	N	3.158541	-1.920621	-0.147742
16	H	2.392638	-1.303852	0.139587
17	C	2.80537	-3.175408	-0.603248
18	O	3.615562	-4.038746	-0.915846
19	C	1.303734	-3.384758	-0.733245
20	C	0.905643	-4.859226	-0.685949
21	C	-1.344717	2.742923	-0.362979
22	N	-1.646074	1.474043	0.062357
23	O	-2.177341	3.521685	-0.820652
24	C	-2.903806	0.850745	0.028507
25	C	-2.995609	-0.431464	0.605506
26	C	-4.197845	-1.117889	0.607093
27	C	-5.339878	-0.549568	0.032139
28	C	-5.254378	0.719854	-0.53739

29	C	-4.052963	1.420833	-0.547089
30	H	-0.906867	0.906358	0.504718
31	H	1.043593	1.233905	-0.057248
32	H	0.782429	-2.799144	0.028876
33	H	-3.995761	2.402048	-0.988697
34	C	-6.645277	-1.272598	0.09033
35	F	-6.509304	-2.616101	-0.058843
36	F	-7.519989	-0.863018	-0.864348
37	F	-7.292917	-1.10131	1.282047
38	H	-0.529607	5.224554	-0.390368
39	H	3.70723	4.569806	0.062116
40	H	1.778049	6.145412	-0.186065
41	H	5.464192	-3.298125	-0.032349
42	H	7.710085	-2.337777	0.292635
43	H	8.011135	0.127128	0.502678
44	H	6.005224	1.606404	0.364904
45	H	1.012368	-2.94695	-1.697194
46	H	-0.169541	-4.964333	-0.854701
47	H	1.438282	-5.43915	-1.442112
48	H	1.13693	-5.295056	0.289872
49	H	-2.105797	-0.872128	1.043908
50	H	-4.245541	-2.104801	1.051775
51	H	-6.131058	1.169982	-0.987059
52	Cl	0.408992	-0.669339	1.446856

Table 2.2. Atomic coordinates of [**2a**+Cl^-] after geometry optimization by Gaussian 09 program using B3LYP functional and 6-311++G(d,p) basis set.

Charge = –1		Multiplicity = 1		
Atom #	Atom Type	x	y	Z
1	C	0.262777	4.667322	-0.279065
2	C	0.045679	3.279926	-0.231991
3	C	1.133661	2.41588	-0.117734
4	C	2.432328	2.943311	-0.0349
5	C	2.635229	4.326641	-0.054119
6	C	1.548203	5.186199	-0.183981
7	N	3.606492	2.162728	0.102532
8	N	3.459391	0.926695	-0.051099
9	C	4.633432	0.15439	0.08557
10	C	4.481437	-1.253853	0.018461
11	C	5.633592	-2.057072	0.090963
12	C	6.886527	-1.477679	0.234254
13	C	7.034024	-0.08911	0.31427
14	C	5.910445	0.715161	0.242208
15	N	3.192339	-1.795851	-0.08583
16	H	2.41495	-1.196023	0.218228

17	C	2.876398	-3.058877	-0.517601
18	O	3.678987	-3.906818	-0.865523
19	C	1.359754	-3.303613	-0.580789
20	C	1.017129	-4.718268	-0.559423
21	C	-1.392919	2.833494	-0.346449
22	N	-1.68403	1.557967	0.065576
23	O	-2.234639	3.614295	-0.781768
24	C	-2.942941	0.932444	0.051875
25	C	-3.02126	-0.357037	0.610417
26	C	-4.22496	-1.043205	0.634831
27	C	-5.381314	-0.46058	0.108772
28	C	-5.307568	0.815739	-0.448982
29	C	-4.106647	1.514841	-0.481535
30	H	-0.935145	0.985521	0.476357
31	H	1.015502	1.340519	-0.057602
32	H	0.840422	-2.767646	0.225222
33	H	-4.061088	2.504977	-0.903947
34	C	-6.672146	-1.213311	0.083554
35	F	-6.880728	-1.864447	-1.098888
36	F	-7.753085	-0.404311	0.24805
37	F	-6.747639	-2.163039	1.047587
38	H	-0.597085	5.315768	-0.388604
39	H	3.648698	4.701941	0.029545
40	H	1.70302	6.259288	-0.20748
41	H	5.527979	-3.128113	0.027244
42	H	7.758785	-2.120398	0.288752
43	H	8.017321	0.353825	0.427927
44	H	5.983833	1.793596	0.290898
45	H	0.989136	-2.866577	-1.515052
46	N	0.701825	-5.827234	-0.535781
47	H	-2.123736	-0.806291	1.022232
48	H	-4.263863	-2.033084	1.072353
49	H	-6.197993	1.279046	-0.857335
50	Cl	0.422368	-0.651563	1.350554

To get an idea about the conformation of [(**1a**)$_2$+Cl$^-$], several initial geometries of the complex were generated using the CONFLEX 8 software package using MMFF94s force field. The calculation provided 10319 conformers. The Boltzmann population of the highest populated conformation (**Conf-1**) was 18.7346% (Figure 2.48A). The populations of second to ninth highest conformers (**Conf-2** – **Conf-9**) were 5.43059%, 5.16218%, 4.81526%, 4.50659%, 4.49147, 4.27749, 4.24343 and 4.02775, respectively (Figure 2.48 A-H). Subsequently, **Conf-1** was optimized by Gaussian 09 program package using B3LYP functional and 6-311G(d,p) basis set. The geometry optimized structure is provided above.

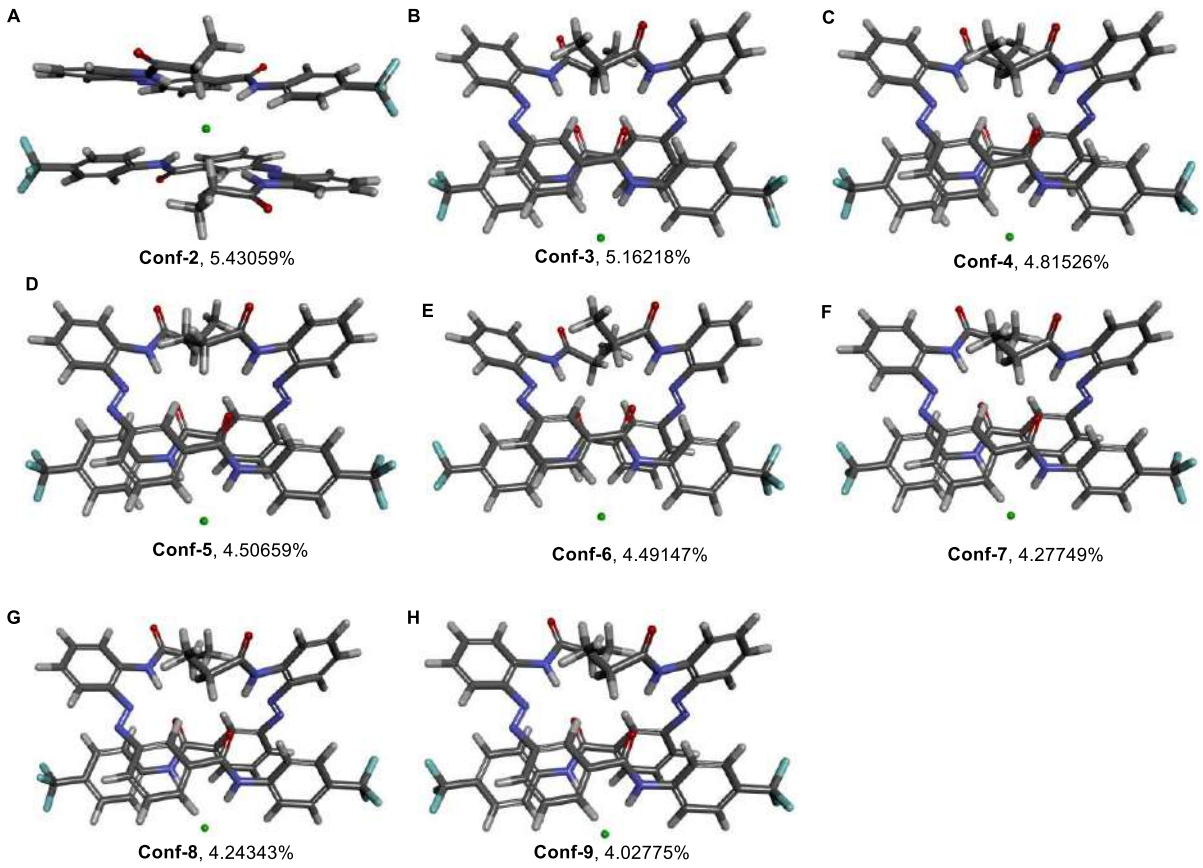

Figure 2.48. Other initial geometries **Conf-2 - Conf-9** (**A-H**) for [(**1a**)$_2$+Cl$^-$], optimized by CONFLEX 8 software using MMFF94s force field. The Boltzmann populations of conformations **Conf-2 - Conf-9** are also provided in next to the conformation names.

Table 2.3. Atomic coordinates of [(**1a**)$_2$+Cl$^-$] after geometry optimization by Gaussian 09 program using B3LYP functional and 6-311++G(d,p) basis set.

Charge = –1		Multiplicity = 1		
Atom #	Atom Type	x	y	z
1	C	1.295626	-4.162609	2.986991
2	C	0.639851	-2.94617	2.738393
3	C	1.386354	-1.782718	2.575654
4	C	2.786252	-1.832796	2.658535
5	C	3.429526	-3.053714	2.879566
6	C	2.682078	-4.216262	3.043454
7	N	3.639028	-0.710278	2.531419
8	N	3.057339	0.396397	2.413534
9	C	3.892519	1.522996	2.295226
10	C	3.233756	2.772054	2.140579
11	C	4.01381	3.940129	2.073309
12	C	5.397576	3.85581	2.133067
13	C	6.047695	2.6229	2.257817
14	C	5.293657	1.466173	2.338809

15	N	1.841689	2.774591	2.051643
16	H	1.425723	1.854979	1.936202
17	C	0.980194	3.854235	2.10255
18	O	1.350352	5.014886	2.166772
19	C	-0.490285	3.453923	2.104196
20	C	-1.42717	4.633566	1.854622
21	C	-0.86744	-2.981157	2.743967
22	N	-1.502521	-1.953038	2.089689
23	O	-1.452924	-3.890613	3.317417
24	C	-2.885971	-1.713473	2.025908
25	C	-3.307917	-0.597217	1.280287
26	C	-4.652787	-0.28854	1.175602
27	C	-5.611184	-1.081552	1.813912
28	C	-5.197434	-2.185826	2.554363
29	C	-3.849178	-2.508005	2.667634
30	H	-0.935443	-1.321561	1.519706
31	H	0.921514	-0.826861	2.380723
32	H	-0.644695	2.653155	1.373936
33	H	-3.534284	-3.367597	3.235714
34	C	-7.061213	-0.756561	1.650196
35	F	-7.516788	-1.03115	0.397858
36	F	-7.323979	0.558108	1.857009
37	F	-7.853412	-1.451246	2.502137
38	H	0.691006	-5.04793	3.136248
39	H	4.512103	-3.061714	2.9217
40	H	3.181804	-5.162384	3.218079
41	H	3.513644	4.890042	1.973764
42	H	5.979916	4.769077	2.072272
43	H	7.129951	2.5724	2.288369
44	H	5.754679	0.492646	2.441056
45	H	-0.697628	3.004606	3.084304
46	H	-2.468144	4.315231	1.950611
47	H	-1.239023	5.437756	2.568123
48	H	-1.291652	5.044085	0.85186
49	H	-2.565181	0.010573	0.776391
50	H	-4.958733	0.573794	0.595705
51	H	-5.932838	-2.805438	3.051895
52	Cl	0.000252	0.314303	-0.000021
53	C	-1.295852	-4.162713	-2.98673
54	C	-0.640035	-2.94628	-2.738208
55	C	-1.386514	-1.782838	-2.575293
56	C	-2.786424	-1.832924	-2.657927
57	C	-3.429739	-3.053836	-2.878869
58	C	-2.682314	-4.216373	-3.042936
59	N	-3.639165	-0.710404	-2.530635
60	N	-3.057417	0.396272	-2.413052

61	C	-3.892501	1.522965	-2.294862
62	C	-3.233629	2.771995	-2.140476
63	C	-4.013584	3.940139	-2.073301
64	C	-5.397363	3.855931	-2.132923
65	C	-6.04759	2.623056	-2.25743
66	C	-5.293649	1.466258	-2.33832
67	N	-1.841551	2.774453	-2.051649
68	H	-1.425611	1.854847	-1.936044
69	C	-0.980017	3.854049	-2.102912
70	O	-1.350148	5.014695	-2.167422
71	C	0.490455	3.453702	-2.104685
72	C	1.427377	4.633302	-1.855027
73	C	0.867255	-2.981293	-2.744014
74	N	1.50245	-1.953225	-2.089766
75	O	1.452628	-3.890772	-3.317543
76	C	2.885925	-1.713768	-2.026029
77	C	3.307978	-0.597776	-1.280054
78	C	4.652858	-0.289192	-1.175374
79	C	5.611184	-1.08203	-1.814037
80	C	5.197334	-2.185996	-2.554864
81	C	3.849046	-2.50809	-2.668128
82	H	0.935469	-1.321765	-1.51966
83	H	-0.921656	-0.826977	-2.380412
84	H	0.644905	2.652847	-1.374534
85	H	3.534087	-3.367478	-3.236476
86	C	7.061184	-0.756788	-1.65056
87	F	7.853699	-1.453887	-2.500201
88	F	7.516091	-1.027893	-0.397234
89	F	7.324228	0.557298	-1.860915
90	H	-0.691249	-5.048022	-3.136124
91	H	-4.512324	-3.061839	-2.920797
92	H	-3.182066	-5.162493	-3.217504
93	H	-3.513327	4.890024	-1.973943
94	H	-5.97962	4.769256	-2.072206
95	H	-7.129853	2.57264	-2.287891
96	H	-5.754756	0.492751	-2.440375
97	H	0.69772	3.004515	-3.08487
98	H	2.468338	4.314995	-1.951251
99	H	1.239097	5.43763	-2.568337
100	H	1.292023	5.043623	-0.85216
101	H	2.565303	0.009868	-0.775891
102	H	4.958867	0.572933	-0.595192
103	H	5.932675	-2.80548	-3.052642

2.4.7.2. NBO analysis of the [(1a)$_2$+Cl$^-$] complex

The strength of individual non-covalent interaction i.e. hydrogen bond present in molecules or weakly bound complexes can be determined by calculating the second-order perturbative energy ($E^{(2)}_{i\rightarrow j^*}$) through NBO analysis where i and j^* represent donor and acceptor orbitals, respectively, involved in the non-covalent interaction. According to the NBO formalism, the lone pair electrons in donor orbitals are delocalized into an antibonding acceptor orbital and $E^{(2)}_{i\rightarrow j^*}$ is given by the following:

$$E^{(2)}_{i\rightarrow j^*} = q_i \frac{(F_{i,j})^2}{E_j - E_i}$$

Where q_i is the occupancy of the donor orbital, E_i and E_j are the orbital energies of the donor and acceptor orbitals, respectively while $F_{i,j}$ is the off-diagonal element of NBO-Fock matrix. N–H and C–H groups of both the receptor units in the [(**1a**)$_2$+Cl$^-$] complex form hydrogen-bonds with the Cl$^-$ ion. In this complex, the electron density from the trapped Cl$^-$ ion gets delocalized into the N-H and C-H antibonding orbitals of both the receptor units. Cl$^-$ ion has four lone pairs denoted as s, p1, p2, and p3, which contribute to the electronic delocalization. The second-order perturbation energy ($E^{(2)}_{i\rightarrow j^*}$, kcal/mol) values for individual hydrogen bonding interaction from different lone-pairs of the Cl$^-$ ion to the N–H/C–H antibonding orbitals, and the total interaction energy for a specific hydrogen bonding interaction of a single receptor unit in the complex are listed in Table 2.4. Individual hydrogen bond interaction energy for each of the receptors is same. NBO view of the overlap of the orbitals for different interactions by the four lone pairs of Cl$^-$ to the N–H and C–H antibonding orbitals of both the receptor-units are provided in Figure 2.10.

Table 2.4. Contribution of the NBO interaction energies ($E^{(2)}_{n\rightarrow\sigma^*}$, kcal/mol) for delocalization of s-type and p-type lone-pairs of Cl$^-$ ion into different acceptor orbitals of one receptor unit in the [(**1a**)$_2$+Cl$^-$] complex calculated at the B3LYP/6-311G(d,p) level of theory.

Interactions	$n_s \rightarrow \sigma^*$	$n_{p1} \rightarrow \sigma^*$	$n_{p2} \rightarrow \sigma^*$	$n_{p3} \rightarrow \sigma^*$	Total $E^{(2)}_{n\rightarrow\sigma^*}$ (kcal/mol)
N–H$_1$···Cl$^-$	0.63	-	4.20	3.27	8.00
C$_{Ar}$–H$_2$···Cl$^-$	-	0.34	-	0.57	0.91
N–H$_3$···Cl$^-$	0.27	0.72	0.14	0.34	1.47
C$_{Alk}$–H$_4$···Cl$^-$	0.43	-	0.64	0.40	1.47
C$_{Ar}$–H$_5$···Cl$^-$	0.27	1.20	-	0.57	2.04

2.5. NMR Spectra

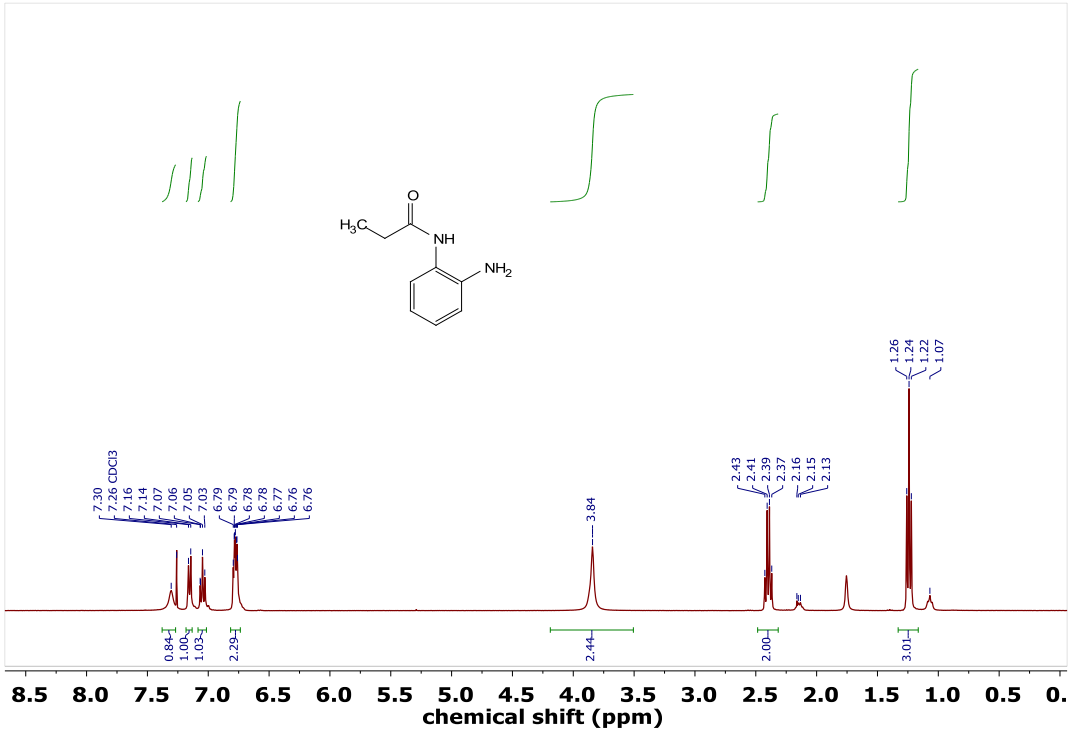

Figure 2.49. ^{1}H NMR spectrum (400 MHz) of **3** in $CDCl_3$ at room temperature.

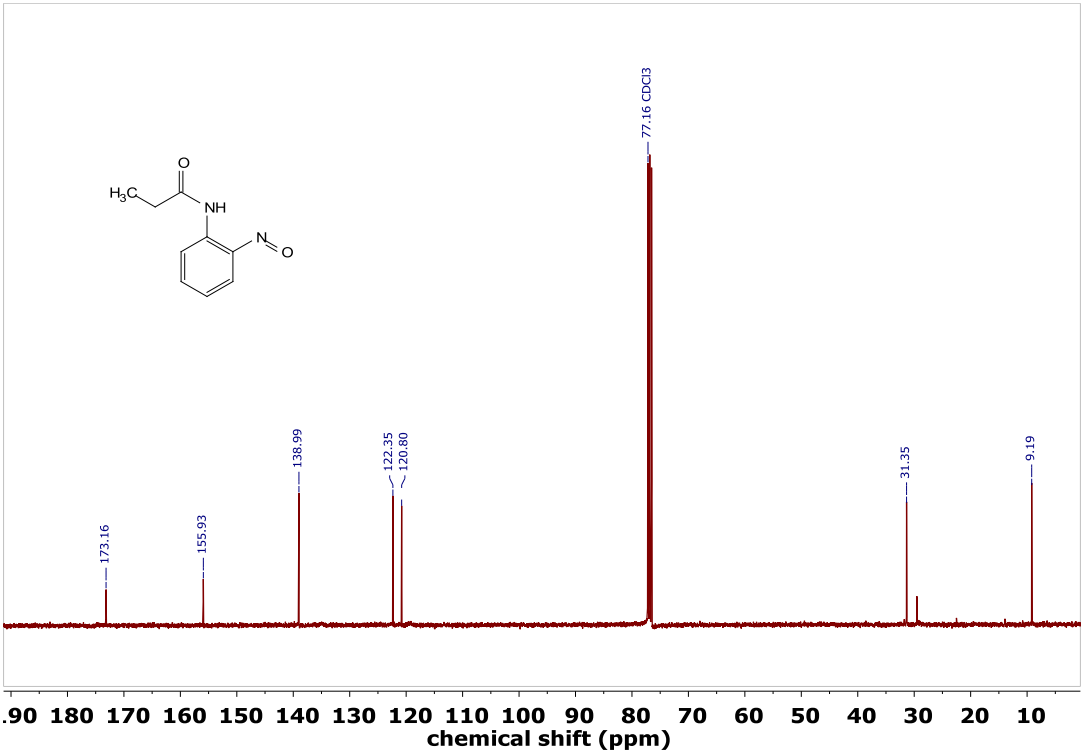

Figure 2.50. ^{13}C NMR spectrum (101 MHz) of **3** in $CDCl_3$ at room temperature.

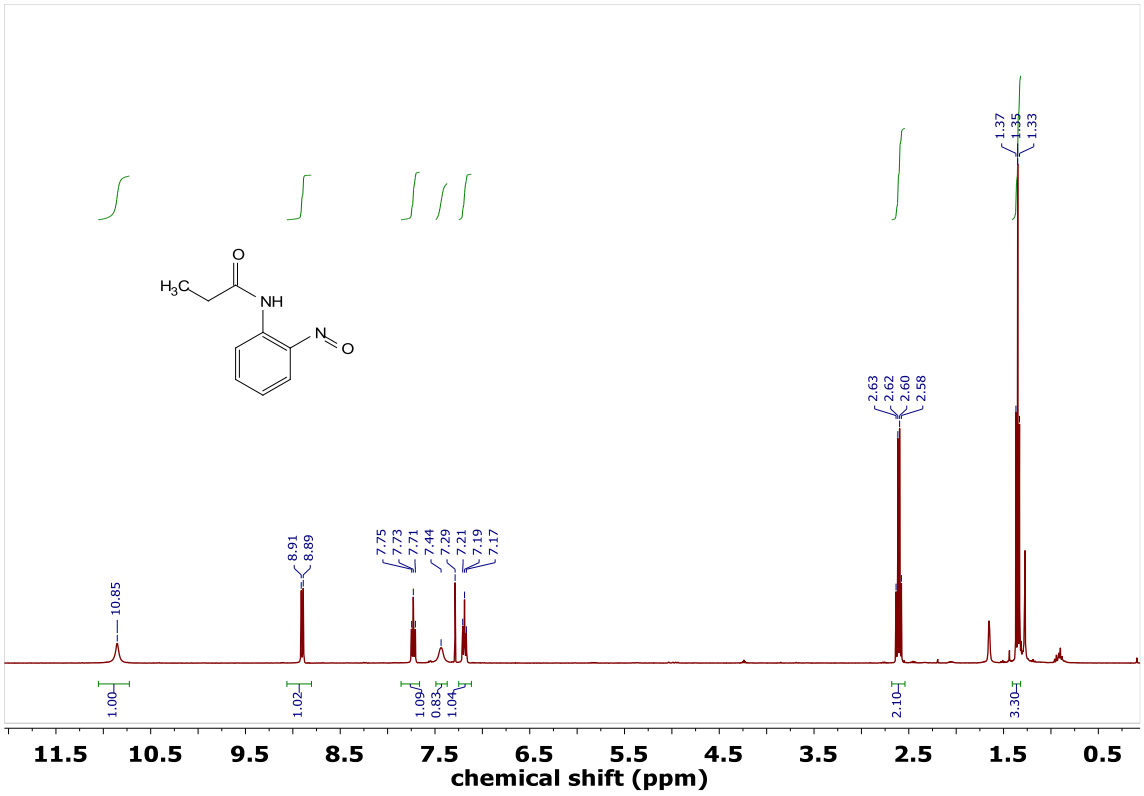

Figure 2.51. ^{1}H NMR spectrum (400 MHz) of **4** in $CDCl_3$ at room temperature.

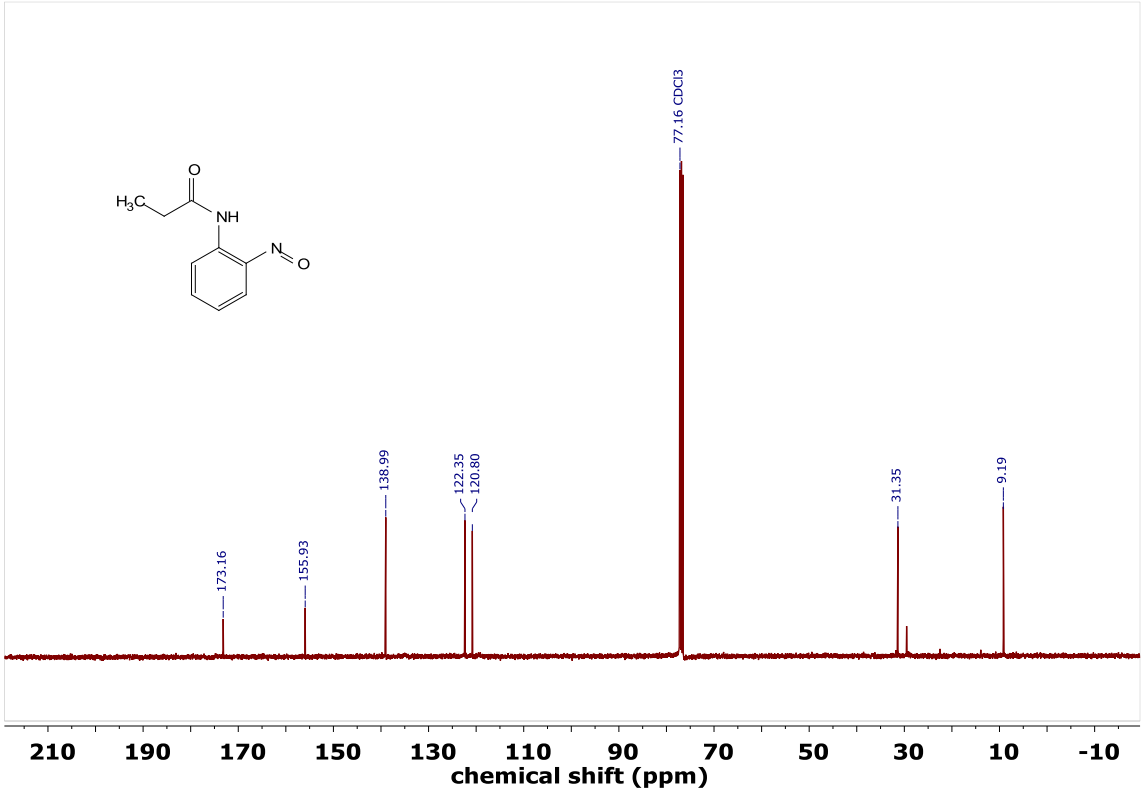

Figure 2.52. ^{13}C NMR spectrum (101 MHz) of **4** in $CDCl_3$ at room temperature.

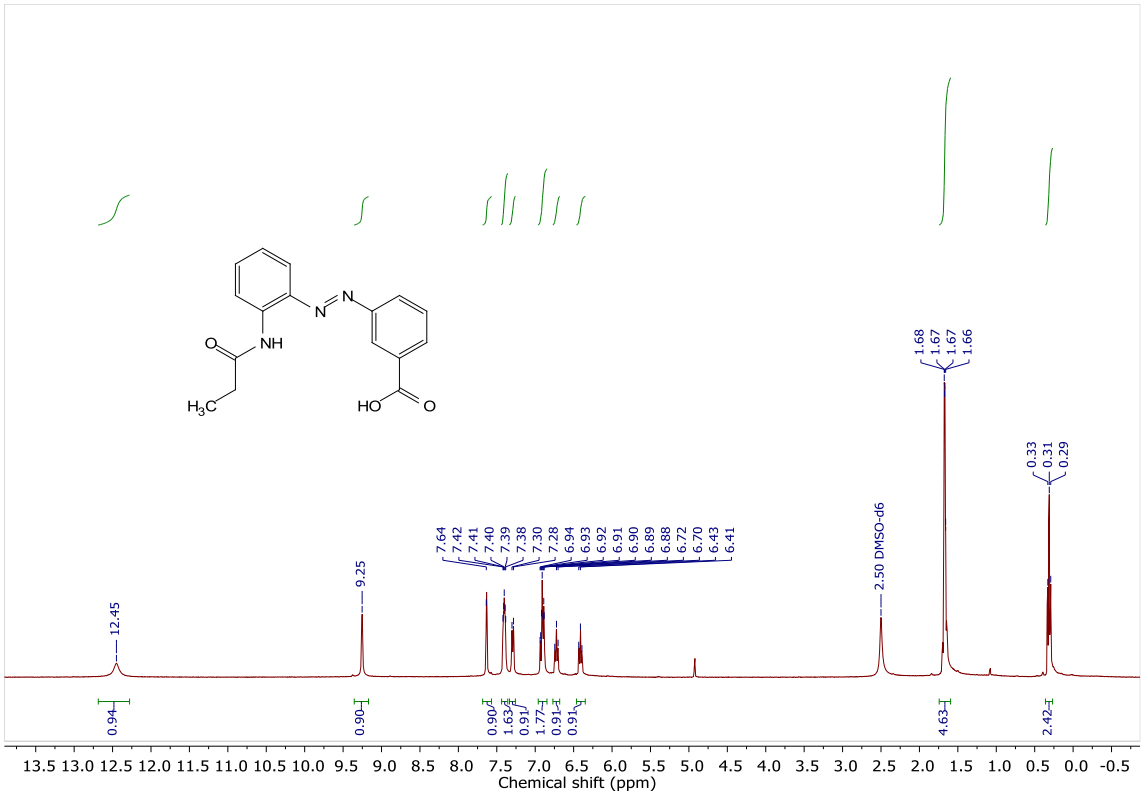

Figure 2.53. ^{1}H NMR spectrum (400 MHz) of **5** in DMSO-d_6 at room temperature.

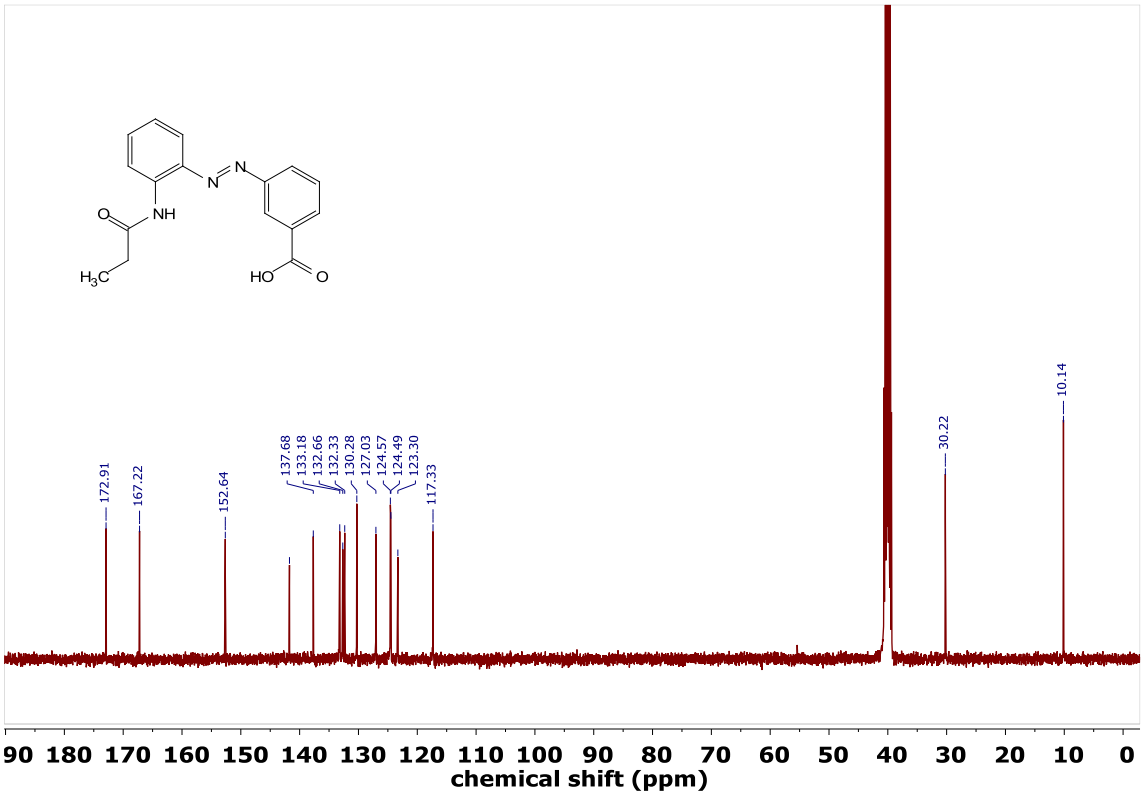

Figure 2.54. ^{13}C NMR spectrum (101 MHz) of **5** in DMSO-d_6 at room temperature.

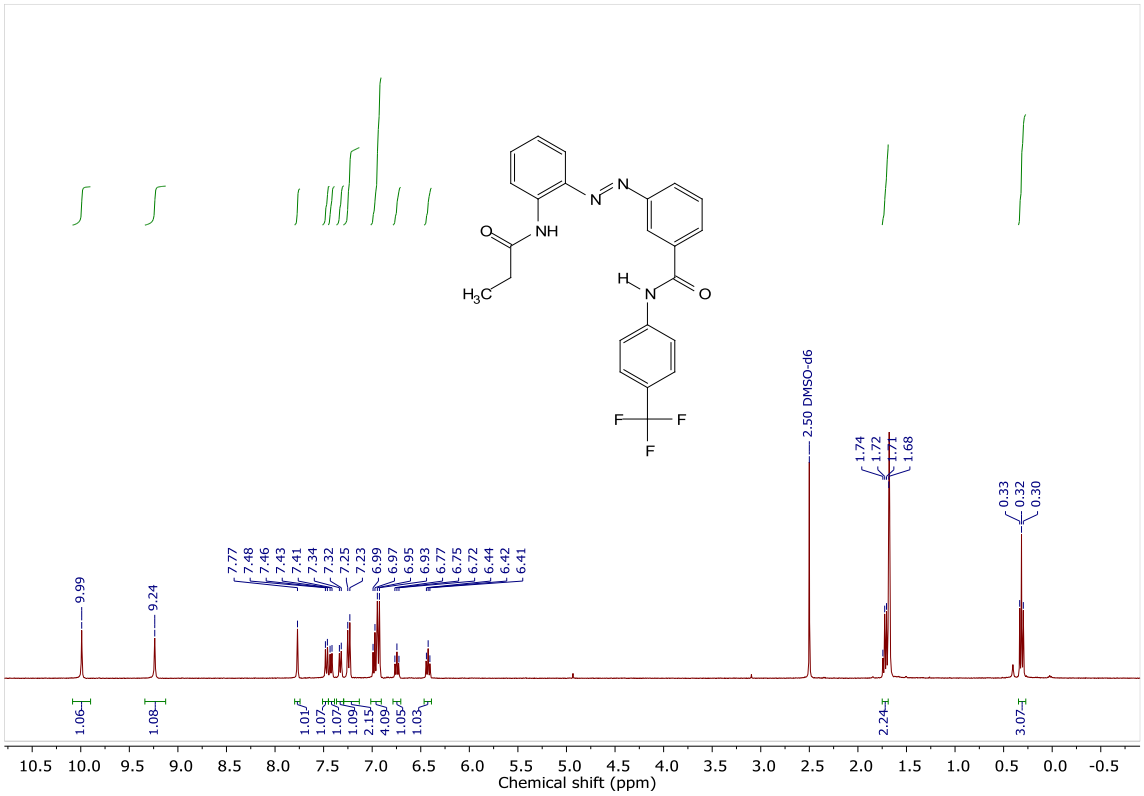

Figure 2.55. ^{1}H NMR spectrum (400 MHz) of **1a** in DMSO-d_6 at room temperature.

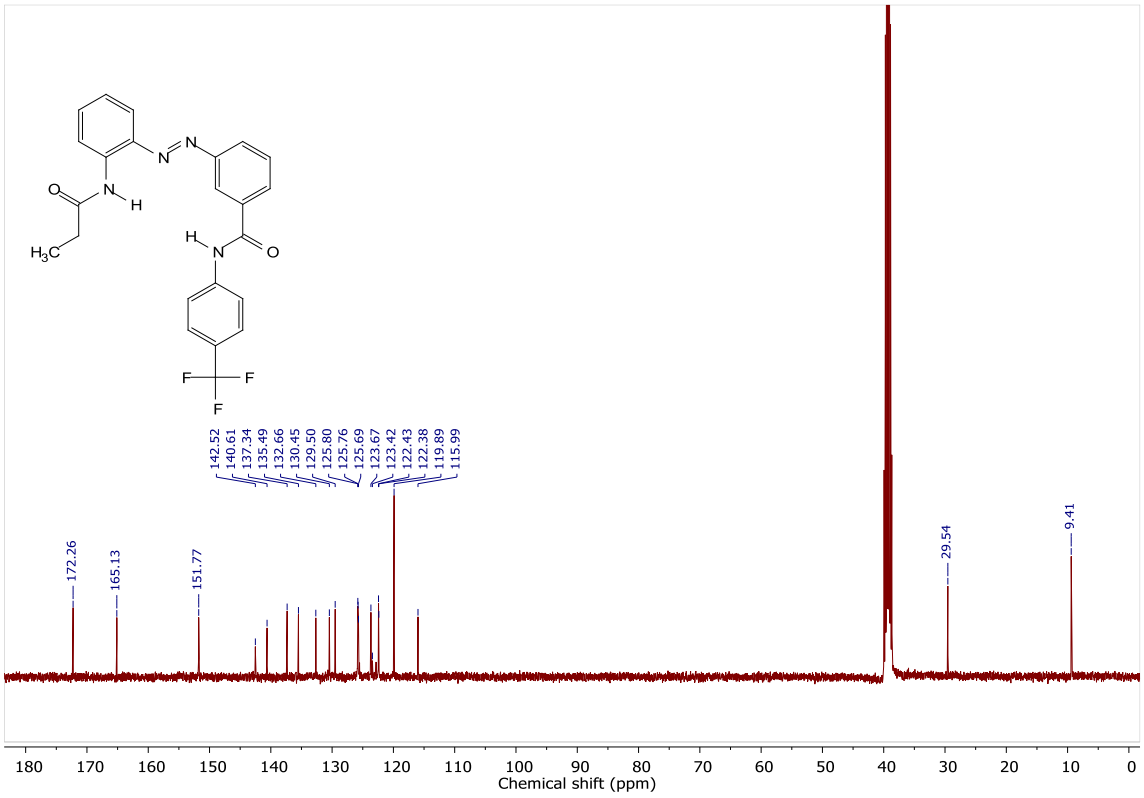

Figure 2.56. ^{13}C NMR spectrum (101 MHz) of **1a** in DMSO-d_6 at room temperature.

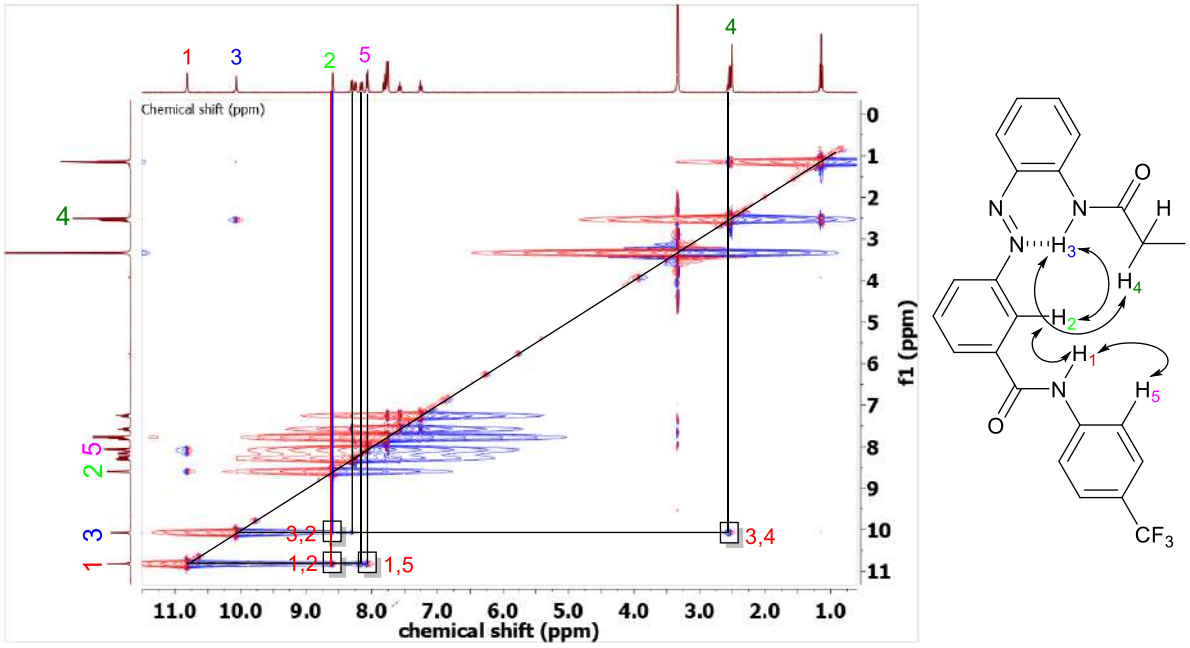

Figure 2.57. ^{1}H ^{1}H NOESY of **1a** in DMSO-d_6.

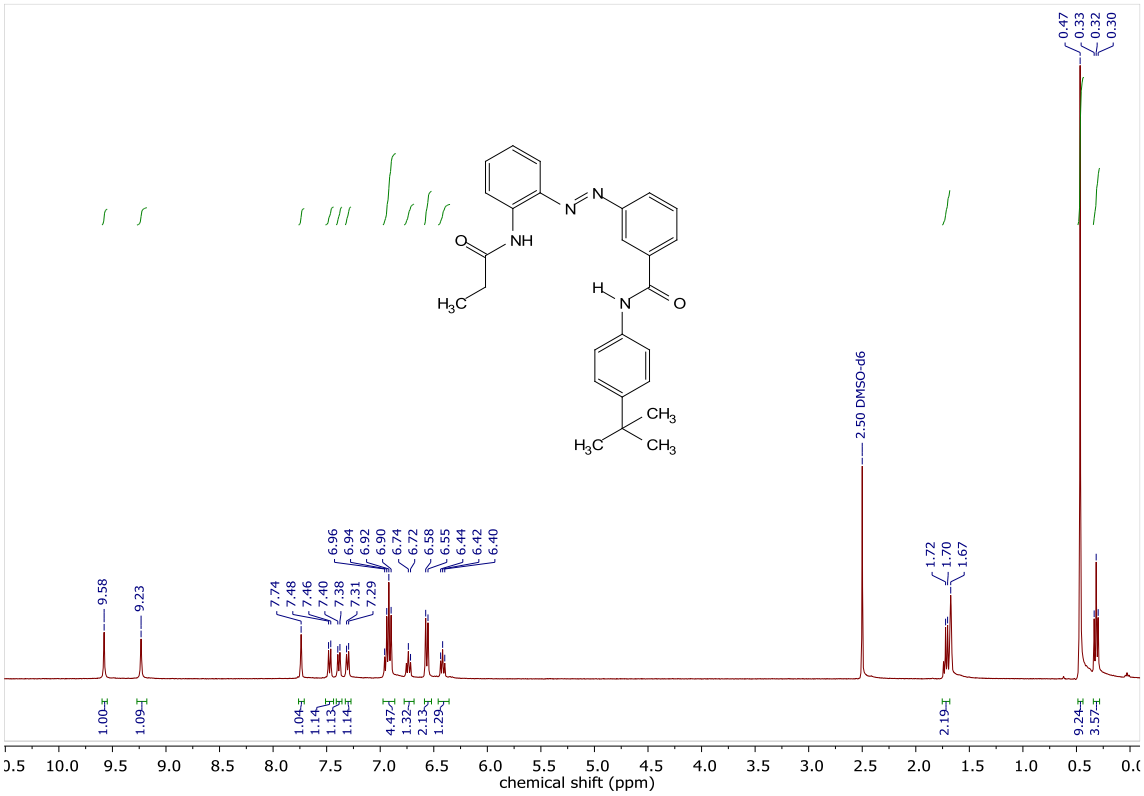

Figure 2.58. ^{1}H NMR spectrum (400 MHz) of **1b** in DMSO-d_6 at room temperature.

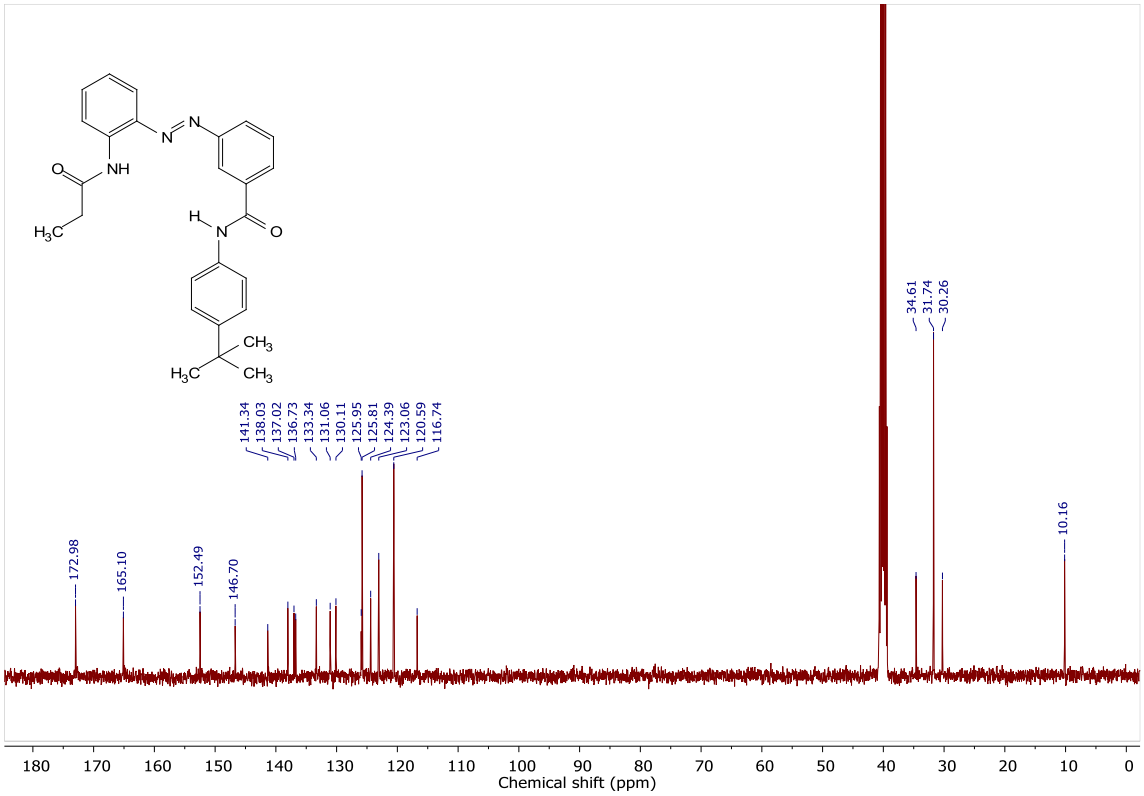

Figure 2.59. ^{13}C NMR spectrum (101 MHz) of **1b** in DMSO-d_6 at room temperature.

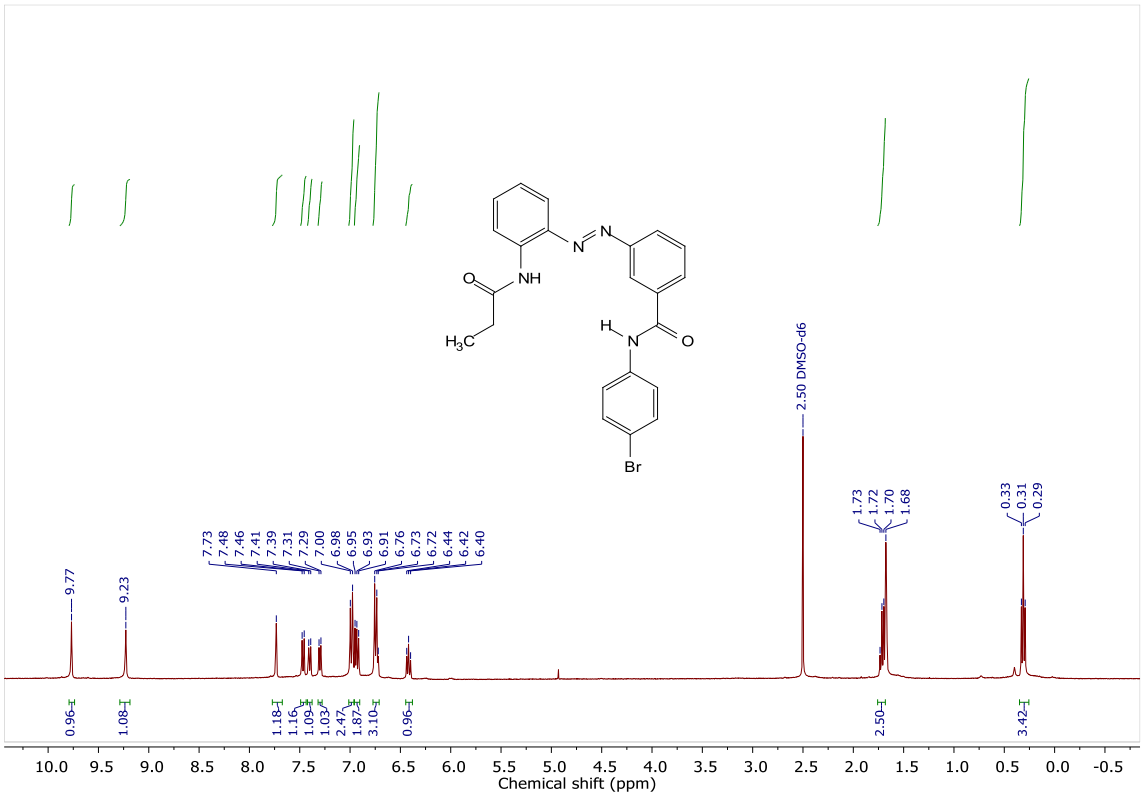

Figure 2.60. ^{1}H NMR spectrum (400 MHz) of **1c** in DMSO-d_6 at room temperature.

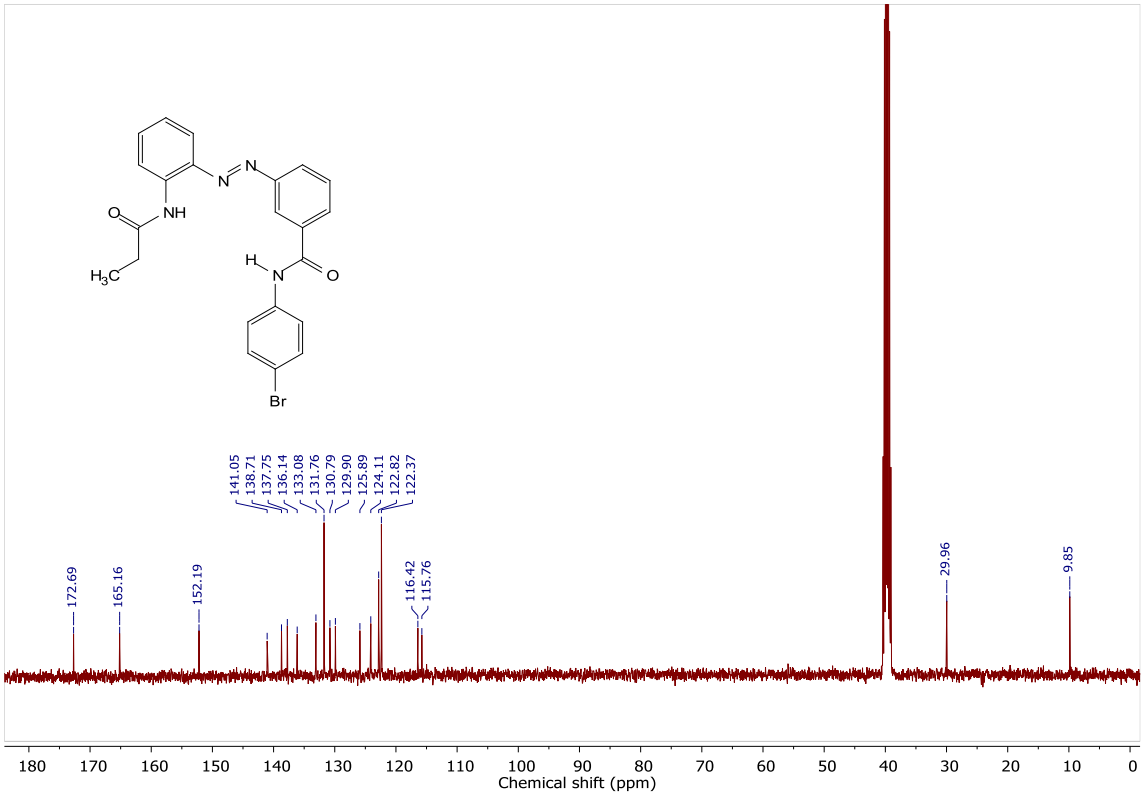

Figure 2.61. ^{13}C NMR spectrum (101 MHz) of **1C** in DMSO-d_6 at room temperature.

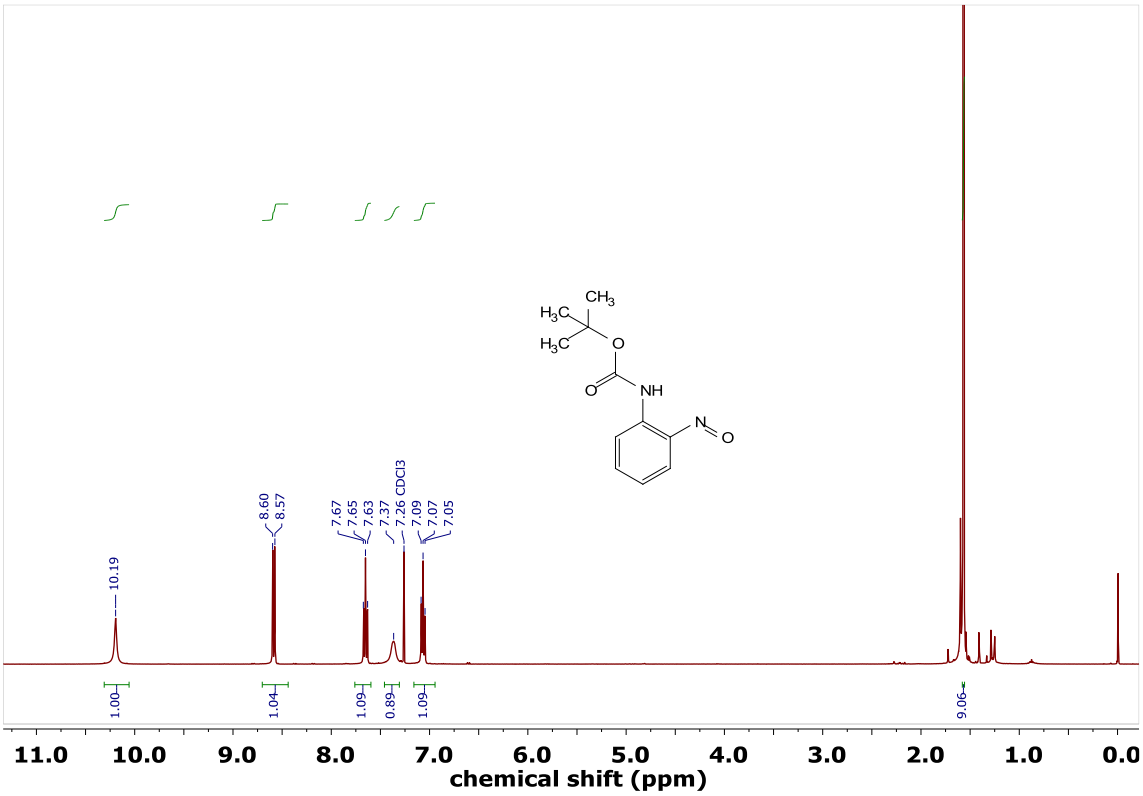

Figure 2.62. ^{1}H NMR spectrum (400 MHz) of **8** in $CDCl_3$ at room temperature.

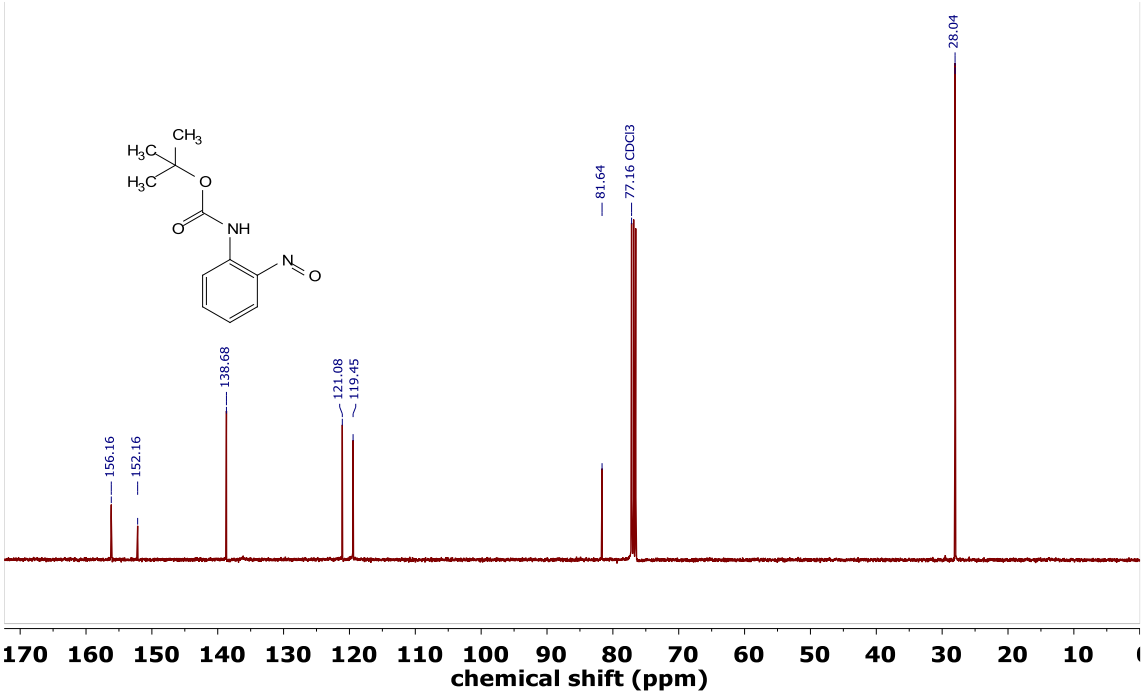

Figure 2.63. ^{13}C NMR spectrum (101 MHz) of **8** in $CDCl_3$ at room temperature.

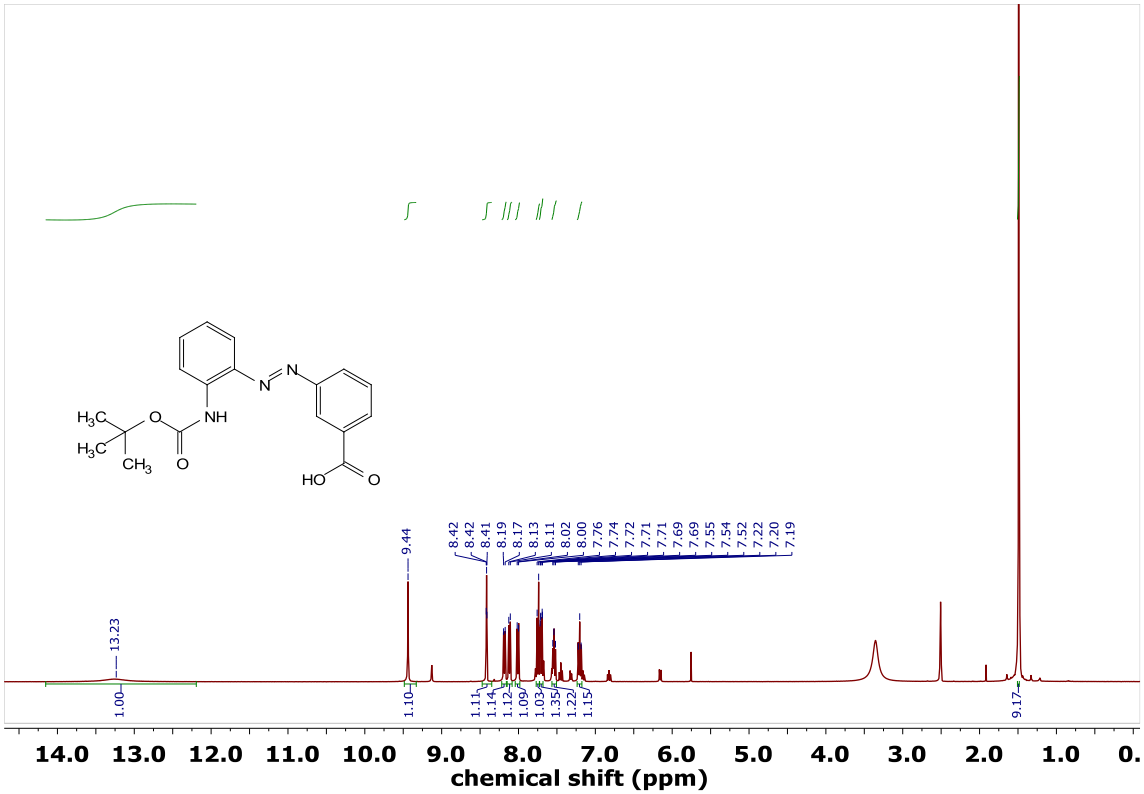

Figure 2.64. ^{1}H NMR spectrum (400 MHz) of **9** in DMSO-d_6 at room temperature.

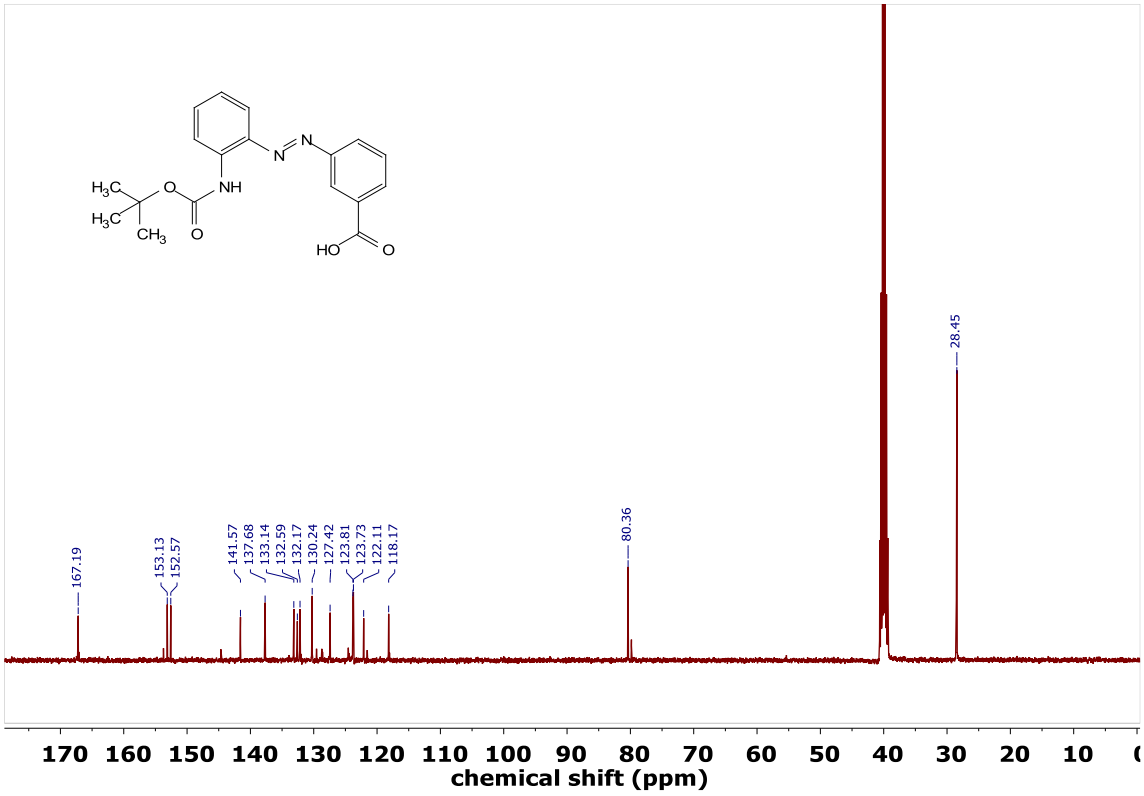

Figure 2.65. ^{13}HC NMR spectrum (101 MHz) of **9** in DMSO-d_6 at room temperature.

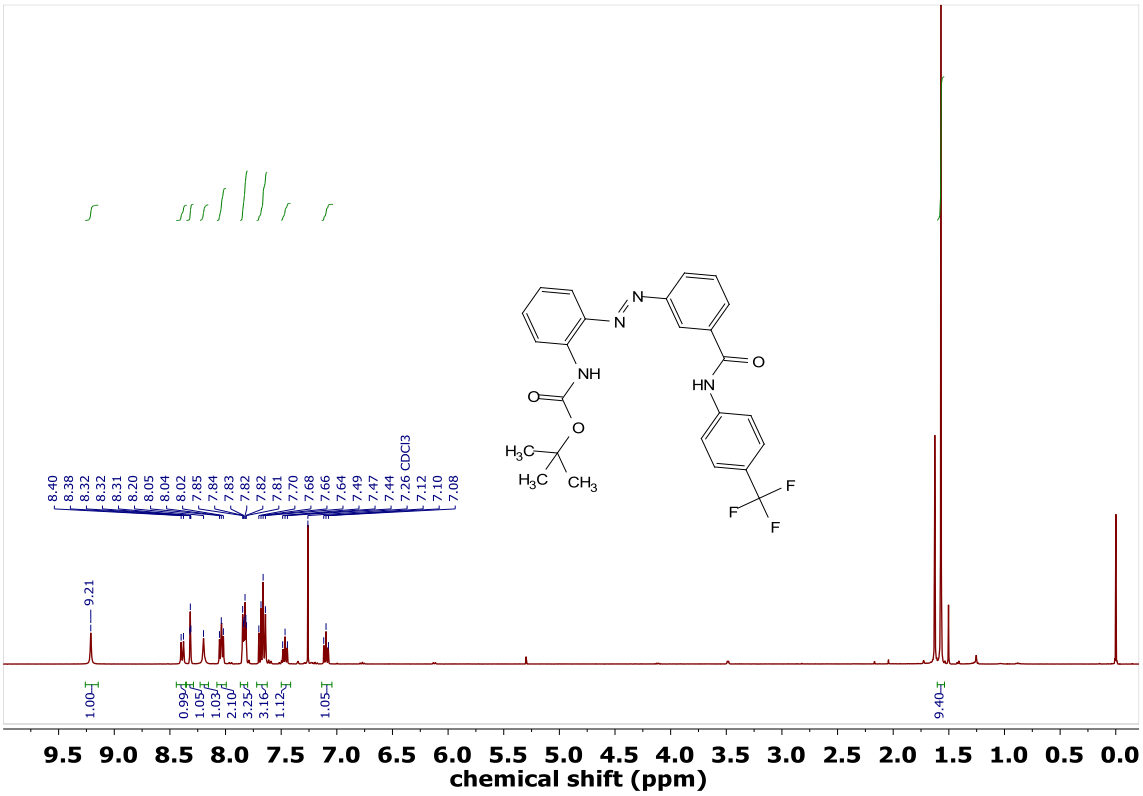

Figure 2.66. ^{1}H NMR spectrum (400 MHz) of **10a** in $CDCl_3$ at room temperature.

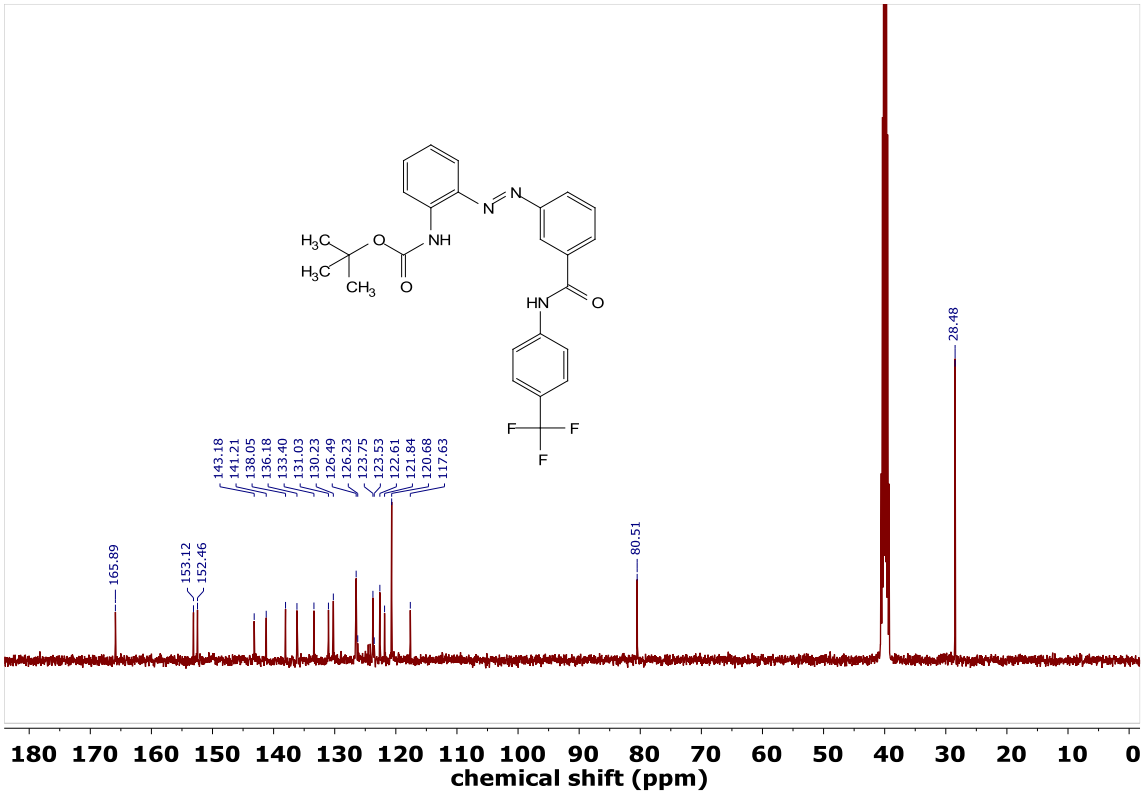

Figure 2.67. ^{13}C NMR spectrum (101 MHz) of **10a** in $CDCl_3$ at room temperature.

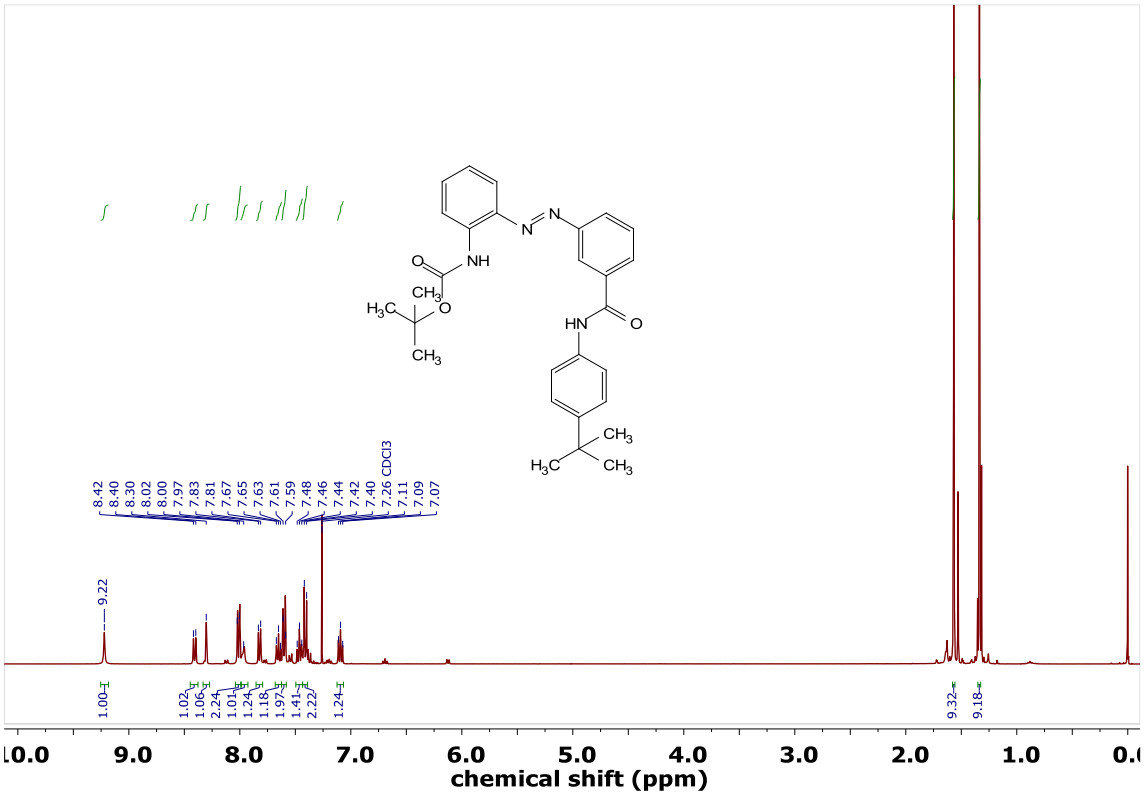

Figure 2.68. ^{1}H NMR spectrum (400 MHz) of **10b** in $CDCl_3$ at room temperature.

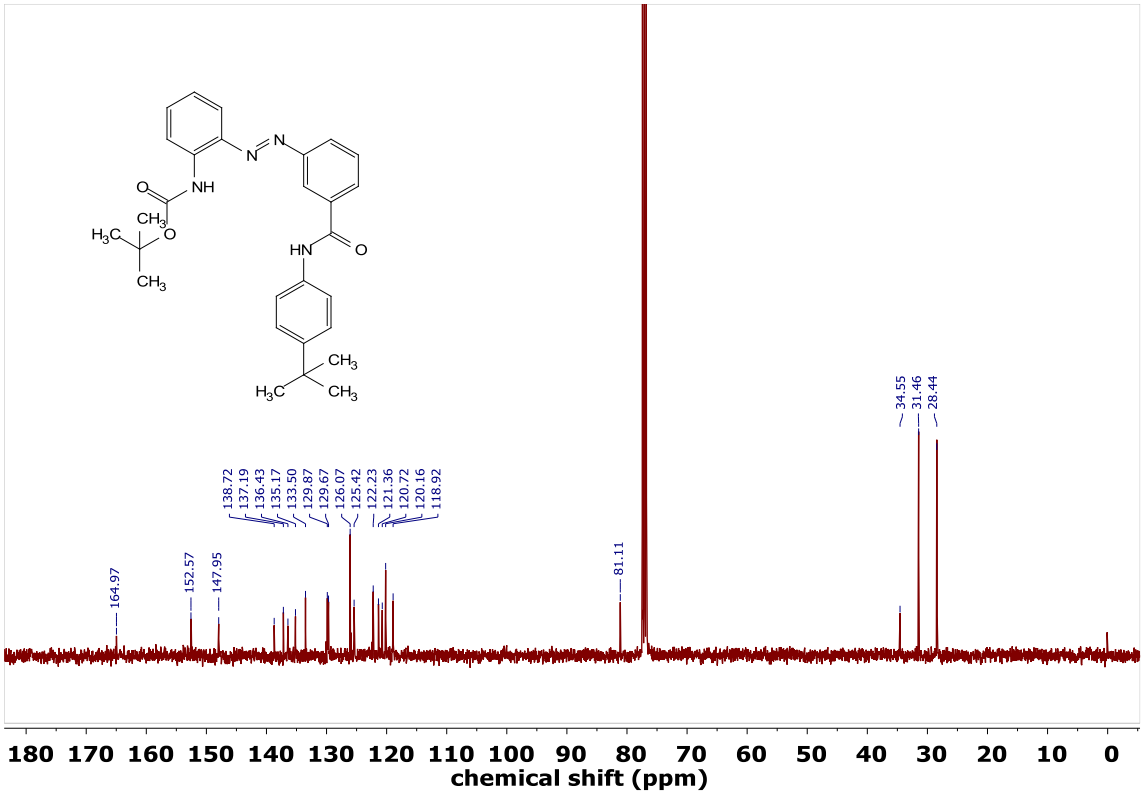

Figure 2.69. ^{13}C NMR spectrum (101 MHz) of **10b** in $CDCl_3$ at room temperature.

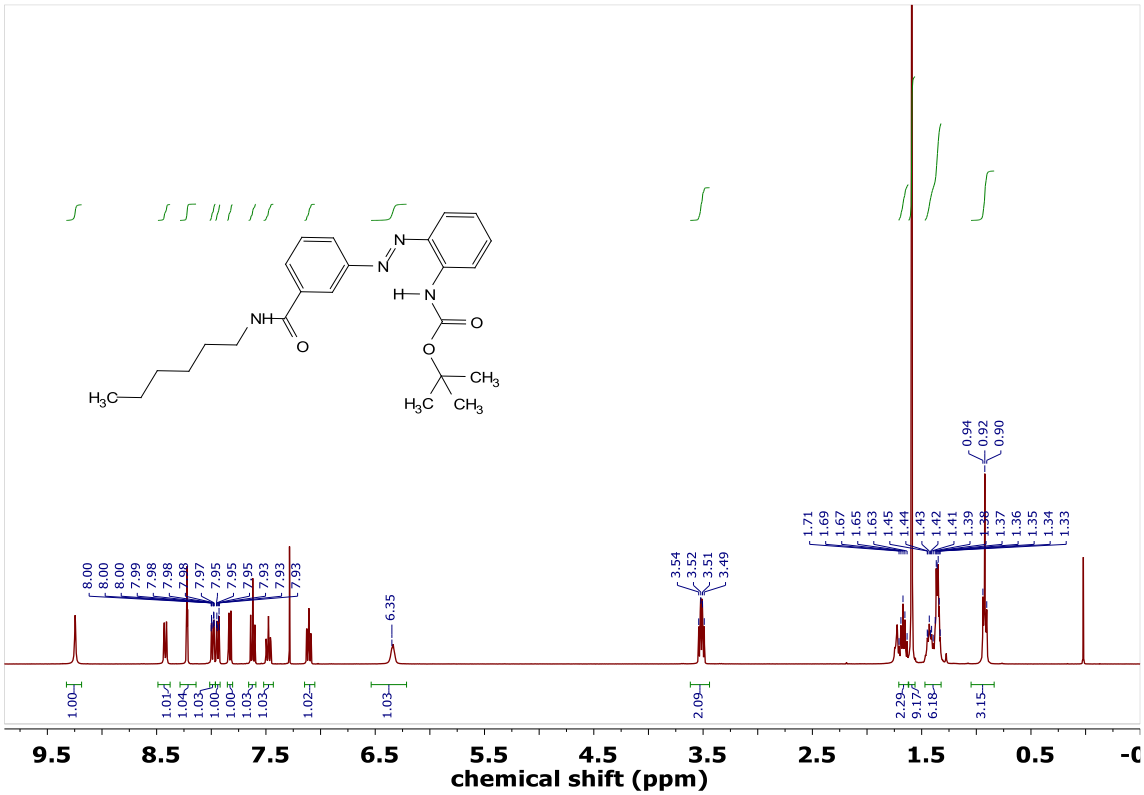

Figure 2.70. ^{1}H NMR spectrum (400 MHz) of **10c** in $CDCl_3$ at room temperature.

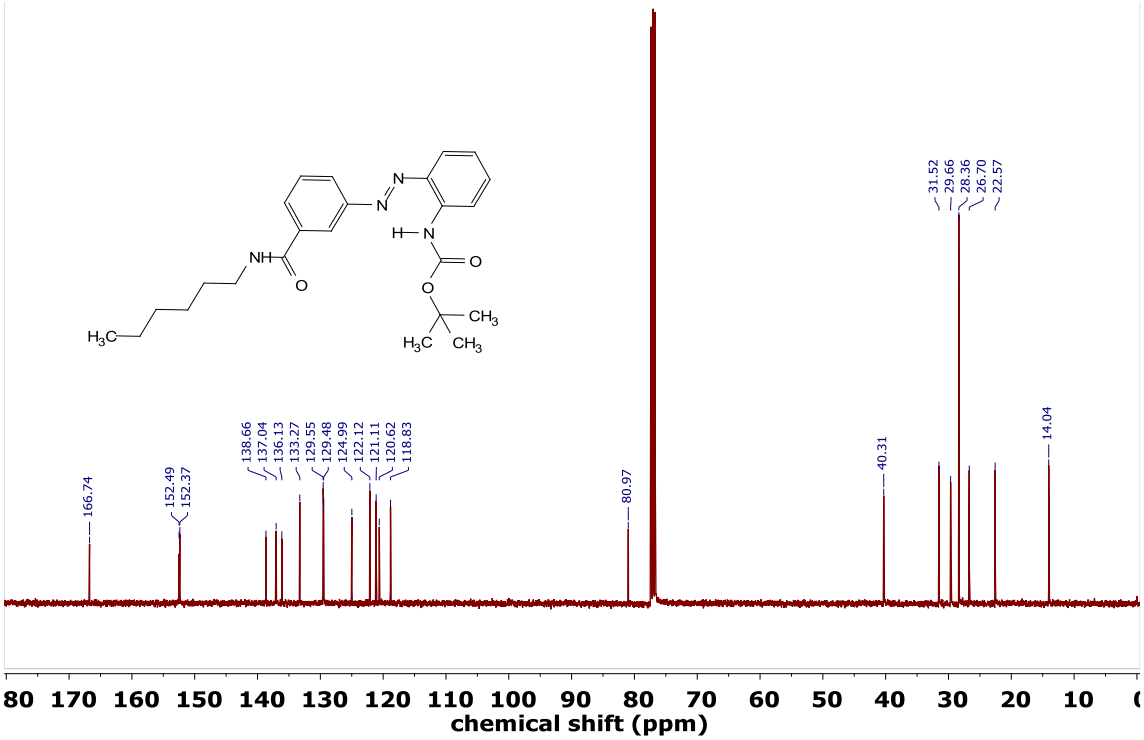

Figure 2.71. ^{13}C NMR spectrum (101 MHz) of **10c** in $CDCl_3$ at room temperature.

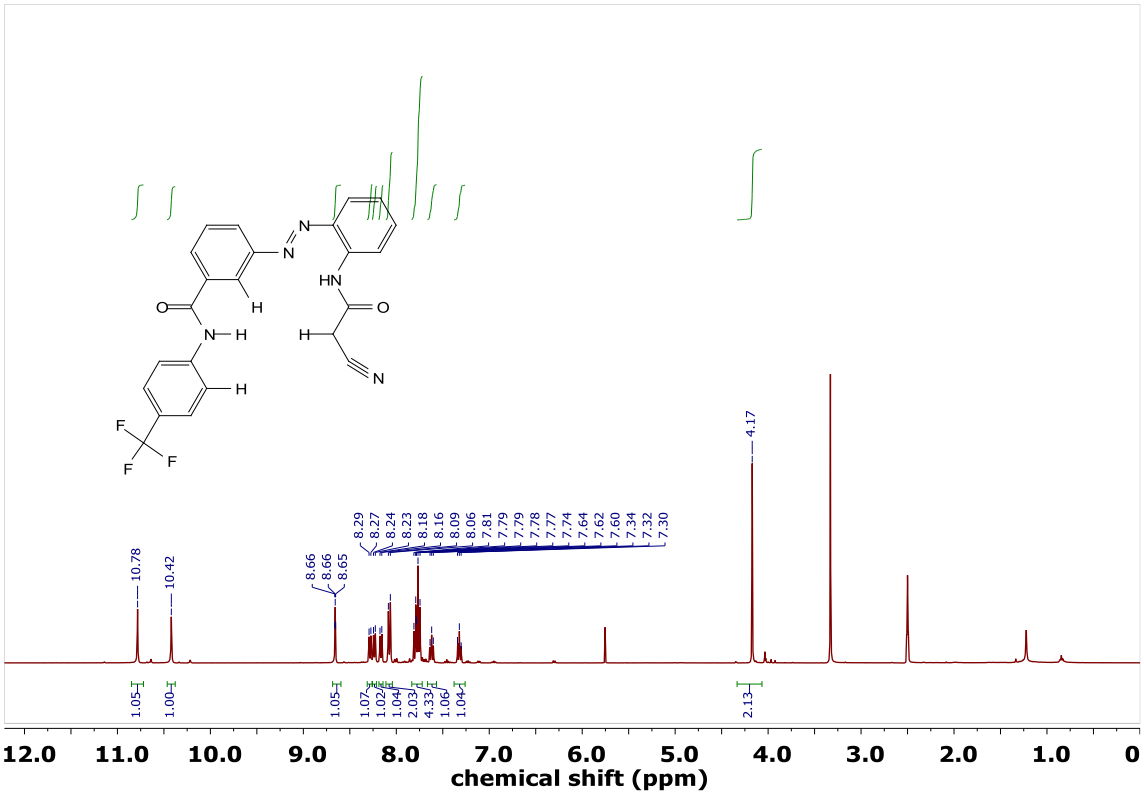

Figure 2.72. ^{1}H NMR spectrum (400 MHz) of **2a** in DMSO-d_6 at room temperature.

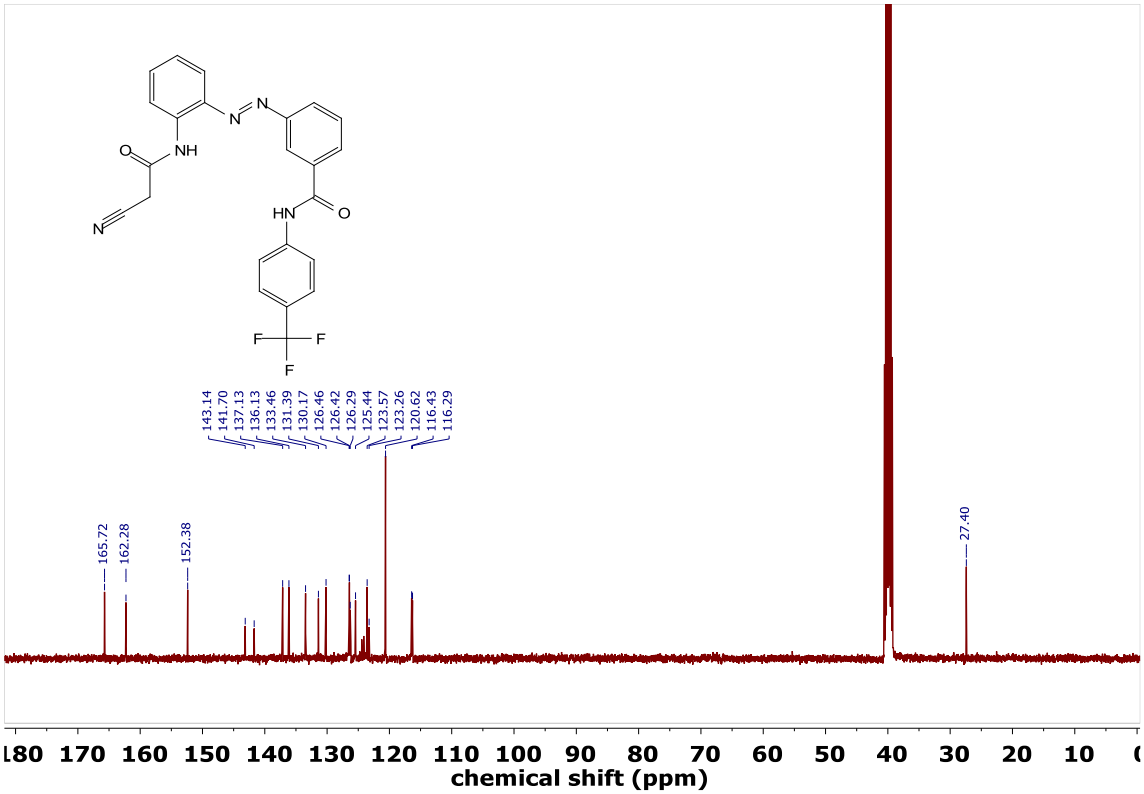

Figure 2.73. ^{13}C NMR spectrum (101 MHz) of **2a** in DMSO-d_6 at room temperature.

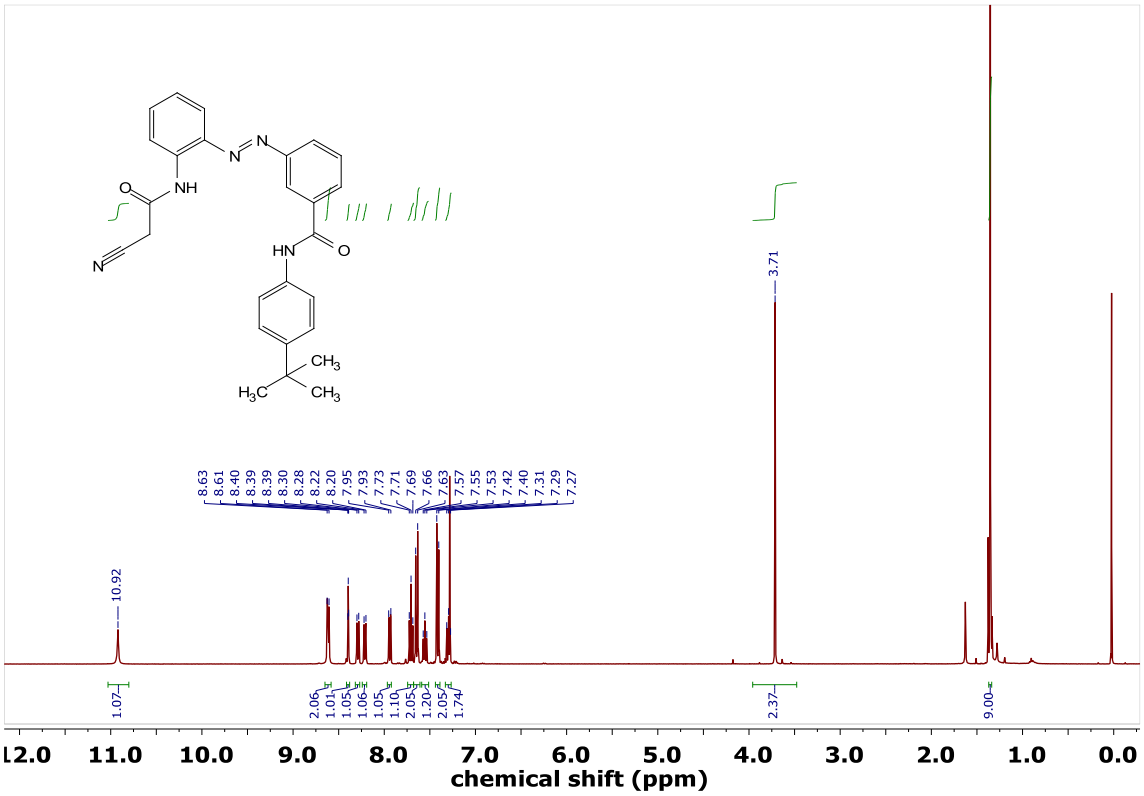

Figure 2.74. ^{1}H NMR spectrum (400 MHz) of **2b** in $CDCl_3$ at room temperature.

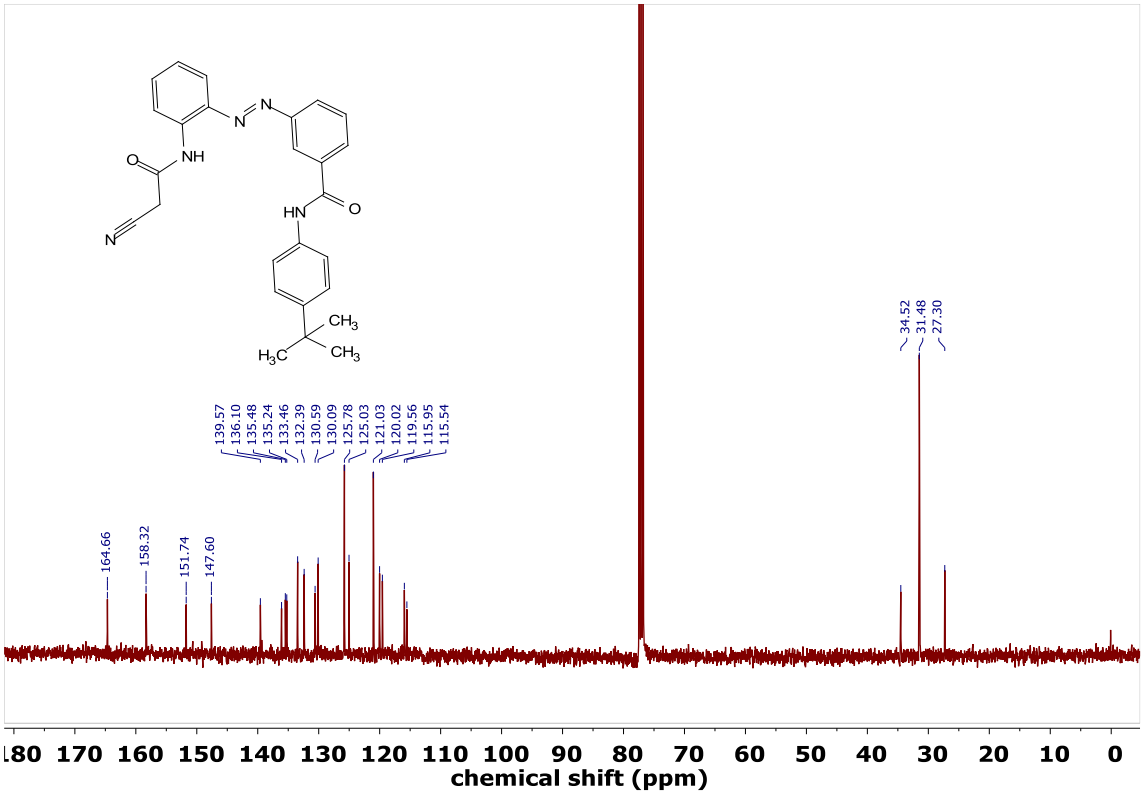

Figure 2.75. ^{13}C NMR spectrum (101 MHz) of **2b** in $CDCl_3$ at room temperature.

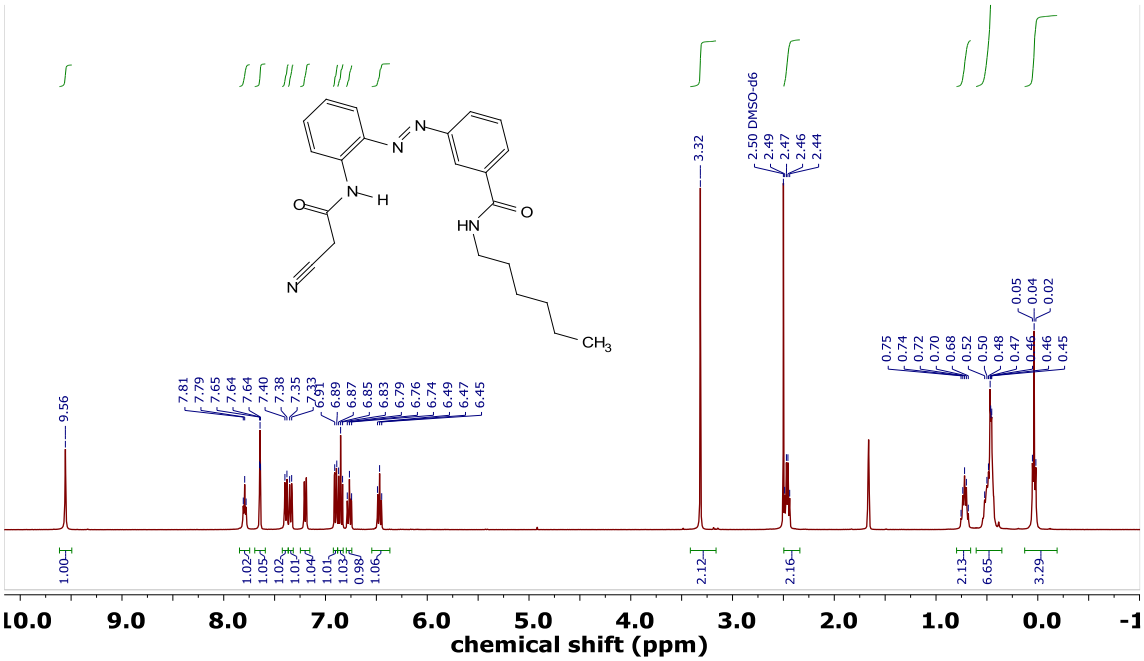

Figure 2.76. ^{1}H NMR spectrum (400 MHz) of **2C** in DMSO-d_6 at room temperature.

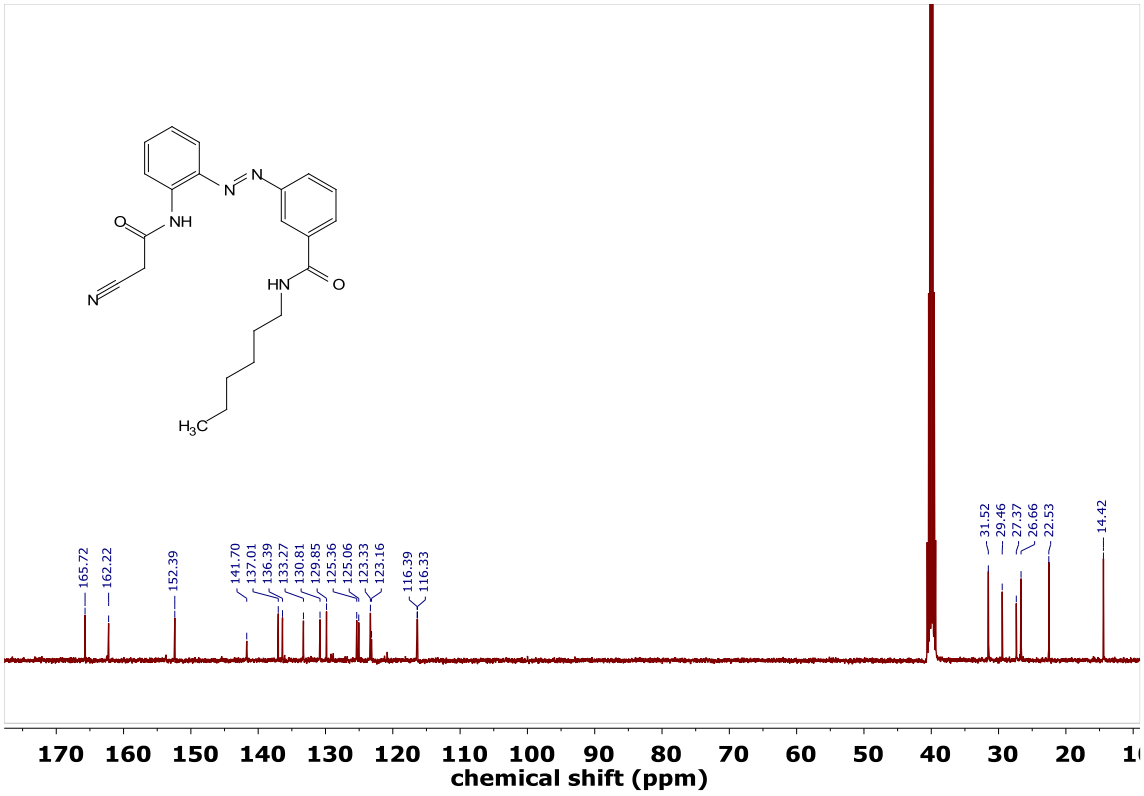

Figure 2.77. ^{13}C NMR spectrum (101 MHz) of **2C** in DMSO-d_6 at room temperature.

2.6. References

[1] (a) M. Tagliazucchi, I. Szleifer, *Mater. Today* **2015**, *18*, 131–142; (b) P. Agre, *Angew. Chem. Int. Ed.* **2004**, *43*, 4278–4290; (c) A. Arcangeli, O. Crociani, E. Lastraioli, A. Masi, S. Pillozzi, A. Becchetti, *Curr. Med. Chem.* **2009**, *16*, 66–93; (d) O. Murillo, I. Suzuki, E. Abel, C. L. Murray, E. S. Meadows, T. Jin, G. W. Gokel, *J. Am. Chem. Soc.* **1997**, *119*, 5540–5549.

[2] (a) M. Lisbjerg, H. Valkenier, B. M. Jessen, H. Al-Kerdi, A. P. Davis, M. Pittelkow, *J. Am. Chem. Soc.* **2015**, *137*, 4948–4951; (b) T. Saha, A. Gautam, A. Mukherjee, M. Lahiri, P. Talukdar, *J. Am. Chem. Soc.* **2016**, *138*, 16443–16451.

[3] (a) A. Kuo, J. M. Gulbis, J. F. Antcliff, T. Rahman, E. D. Lowe, J. Zimmer, J. Cuthbertson, F. M. Ashcroft, T. Ezaki, D. A. Doyle, *Science* **2003**, *300*, 1922–1926; (b) D. A. Doyle, J. M. Cabral, R. A. Pfuetzner, A. Kuo, J. M. Gulbis, S. L. Cohen, B. T. Chait, R. MacKinnon, *Science* **1998**, *280*, 69–77.

[4] (a) G. Nagel, D. Ollig, M. Fuhrmann, S. Kateriya, A. M. Musti, E. Bamberg, P. Hegemann, *Science* **2002**, *296*, 2395–2398; (b) W. A. Catterall, *Annu. Rev. Biochem.*

1995, *64*, 493–531; (c) S. R. Frolova, O. Gaiko, V. A. Tsvelaya, O. Y. Pimenov, K. I. Agladze, *PLoS One* **2016**, *11*, e0152018.

[5] (a) J. Y. Choi, D. Muallem, K. Kiselyov, M. G. Lee, P. J. Thomas, S. Muallem, *Nature* **2001**, *410*, 94–97; (b) R. D. Vaughan-Jones, K. W. Spitzer, P. Swietach, *J. Mol. Cell. Cardiol.* **2009**, *46*, 318–331.

[6] C. Cossu, M. Fiore, D. Baroni, V. Capurro, E. Caci, M. Garcia-Valverde, R. Quesada, O. Moran, *Front. Pharmacol.* **2018**, *9*.

[7] (a) T. Saha, M. S. Hossain, D. Saha, M. Lahiri, P. Talukdar, *J. Am. Chem. Soc.* **2016**, *138*, 7558–7567; (b) S.-K. Ko, S. K. Kim, A. Share, V. M. Lynch, J. Park, W. Namkung, W. Van Rossom, N. Busschaert, P. A. Gale, J. L. Sessler, I. Shin, *Nat. Chem.* **2014**, *6*, 885–892; (c) N. Busschaert, S.-H. Park, K.-H. Baek, Y. P. Choi, J. Park, E. N. W. Howe, J. R. Hiscock, L. E. Karagiannidis, I. Marques, V. Félix, W. Namkung, J. L. Sessler, P. A. Gale, I. Shin, *Nat. Chem.* **2017**, *9*, 667–675.

[8] S. B. Salunke, J. A. Malla, P. Talukdar, *Angew. Chem. Int. Ed.* **2019**, *58*, 5354–5358.

[9] (a) E. N. W. Howe, N. Busschaert, X. Wu, S. N. Berry, J. Ho, M. E. Light, D. D. Czech, H. A. Klein, J. A. Kitchen, P. A. Gale, *J. Am. Chem. Soc.* **2016**, *138*, 8301–8308; (b) N. Busschaert, R. B. P. Elmes, D. D. Czech, X. Wu, I. L. Kirby, E. M. Peck, K. D. Hendzel, S. K. Shaw, B. Chan, B. D. Smith, K. A. Jolliffe, P. A. Gale, *Chem. Sci.* **2014**, *5*, 3617–3626; (c) A. Roy, O. Biswas, P. Talukdar, *Chem. Comm.* **2017**, *53*, 3122–3125; (d) S. V. Shinde, P. Talukdar, *Org. Biomol. Chem.* **2019**, *17*, 4483–4490; (e) S. V. Shinde, P. Talukdar, *Angew. Chem. Int. Ed.* **2017**, *56*, 4238–4242; (f) Y. R. Choi, B. Lee, J. Park, W. Namkung, K.-S. Jeong, *J. Am. Chem. Soc.* **2016**, *138*, 15319–15322; (g) E. B. Park, K.-S. Jeong, *Chem. Commun.* **2015**, *51*, 9197–9200; (h) M. M. Tedesco, B. Ghebremariam, N. Sakai, S. Matile, *Angew. Chem. Int. Ed.* **1999**, *38*, 540–543; (i) P. Talukdar, G. Bollot, J. Mareda, N. Sakai, S. Matile, *Chem. Eur. J.* **2005**, *11*, 6525–6532; (j) T. Kiwada, K. Sonomura, Y. Sugiura, K. Asami, S. Futaki, *J. Am. Chem. Soc.* **2006**, *128*, 6010-6011; (k) G. A. Woolley, B. A. Wallace, *Biochemistry* **1993**, *32*, 9819–9825; (l) L. Lien, D. C. J. Jaikaran, Z. Zhang, G. A. Woolley, *J. Am. Chem. Soc.* **1996**, *118*, 12222–12223; (m) Y. Kobuke, K. Ueda, M. Sokabe, *J. Am. Chem. Soc.* **1992**, *114*, 7618–7622; (n) W. Si, Z.-T. Li, J.-L. Hou, *Angew. Chem. Int. Ed.* **2014**, *53*, 4578–4581; (o) M. Fares, X. Wu, D. Ramesh, W. Lewis, P. A. Keller, E. N. W. Howe, R. Pérez-Tomás, P. A. Gale, *Angew. Chem. Int.*

Ed. **2020**, *59*, 17614–17621; (p) N. Akhtar, N. Pradhan, A. Saha, V. Kumar, O. Biswas, S. Dey, M. Shah, S. Kumar, D. Manna, *Chem. Commun.* **2019**, *55*, 8482–8485.

[10] M. R. Banghart, M. Volgraf, D. Trauner, *Biochemistry* **2006**, *45*, 15129–15141.

[11] (a) R. F. Khairutdinov, J. K. Hurst, *Langmuir* **2004**, *20*, 1781–1785; (b) A. Kerckhoffs, M. J. Langton, *Chem. Sci.* **2020**, *11*, 6325–6331; (c) Y. Zhou, Y. Chen, P.-P. Zhu, W. Si, J.-L. Hou, Y. Liu, *Chem. Commun.* **2017**, *53*, 3681–3684; (d) T. Liu, C. Bao, H. Wang, Y. Lin, H. Jia, L. Zhu, *Chem. Commun.* **2013**, *49*, 10311–10313; (e) R.-Y. Yang, C. Bao, Q.-N. Lin, L.-Y. Zhu, *Chin. Chem. Lett.* **2015**, *26*, 851–856.

[12] (a) H. Fliegl, A. Köhn, C. Hättig, R. Ahlrichs, *J. Am. Chem. Soc.* **2003**, *125*, 9821–9827; (b) S. Spörlein, H. Carstens, H. Satzger, C. Renner, R. Behrendt, L. Moroder, P. Tavan, W. Zinth, J. Wachtveitl, *Proc. Natl. Acad. Sci. U.S.A.* **2002**, *99*, 7998–8002.

[13] (a) R. J. Mart, R. K. Allemann, *Chem. Commun.* **2016**, *52*, 12262–12277; (b) M. Banghart, K. Borges, E. Isacoff, D. Trauner, R. H. Kramer, *Nat. Neurosci.* **2004**, *7*, 1381–1386; (c) P. Leippe, J. A. Frank, *Curr. Opin. Struct. Biol.* **2019**, *57*, 23–30; (d) M. Izquierdo-Serra, M. Gascón-Moya, J. J. Hirtz, S. Pittolo, K. E. Poskanzer, È. Ferrer, R. Alibés, F. Busqué, R. Yuste, J. Hernando, P. Gorostiza, *J. Am. Chem. Soc.* **2014**, *136*, 8693–8701; (e) Y. Kobuke, A. Ohgoshi, *Colloids and Surfaces A: Physicochem. Eng. Aspects* **2000**, *169*, 187–197.

[14] Y. R. Choi, G. C. Kim, H.-G. Jeon, J. Park, W. Namkung, K.-S. Jeong, *Chem. Commun.* **2014**, *50*, 15305–15308.

[15] A. A. Beharry, G. A. Woolley, *Chem. Soc. Rev.* **2011**, *40*, 4422–4437.

[16] A. M. Kolpak, J. C. Grossman, *Nano Lett.* **2011**, *11*, 3156–3162.

[17] C. A. Lipinski, F. Lombardo, B. W. Dominy, P. J. Feeney, *Adv. Drug Deliv. Rev.* **1997**, *23*, 3–25.

[18] A. D. McLean, G. Chandler, *J. Chem. Phys.* **1980**, *72*, 5639–5648.

[19] Marvin 5.8.0, *ChemAxon*, **2012**, *(http://www.chemaxon.com).*

[20] http://app.supramolecular.org/bindfit/

[21] A. Roy, T. Saha, M. L. Gening, D. V. Titov, A. G. Gerbst, Y. E. Tsvetkov, N. E. Nifantiev, P. Talukdar, *Chem. Eur. J.* **2015**, *21*, 17445–17452.

[22] J. A. Malla, A. Roy, P. Talukdar, *Org. Lett.* **2018**, *20*, 5991–5994.

[23] B. L. Schottel, H. T. Chifotides, K. R. Dunbar, *Chem. Soc. Rev.* **2008**, *37*, 68–83.

[24] (a) X. Wu, E. N. W. Howe, P. A. Gale, *Acc. Chem. Res.* **2018**, *51*, 1870–1879; (b) J. T. Davis, P. A. Gale, R. Quesada, *Chem. Soc. Rev.* **2020**, *49*, 6056–6086; (c) L. Chen, S. N. Berry, X. Wu, E. N. W. Howe, P. A. Gale, *Chem.* **2020**, *6*, 61–141.

[25] (a) N. Busschaert, M. Wenzel, M. E. Light, P. Iglesias-Hernández, R. Pérez-Tomás, P. A. Gale, *J. Am. Chem. Soc.* **2011**, *133*, 14136–14148; (b) N. Busschaert, I. L. Kirby, S. Young, S. J. Coles, P. N. Horton, M. E. Light, P. A. Gale, *Angew. Chem. Int. Ed.*, **2012**, *51*, 4426–4430; (c) P. A. Gale, C. C. Tong, C. J. E. Haynes, O. Adeosun, D. E. Gross, E. Karnas, E. M. Sedenberg, R. Quesada, J. L. Sessler, *J. Am. Chem. Soc.* **2010**, *132*, 3240–3241.

[26] (a) S. O. H. Goto, N. Nakayama, K. Ohta, CONFLEX 8, *CONFLEX Corporation, Tokyo, Japan*,, **2012**; (b) H. Goto, E. Osawa, *J. Am. Chem. Soc.* **1989**, *111*, 8950–8951.

[27] M. J. Frisch, G. W. Trucks, H. B. Schlegel, G. E. Scuseria, M. A. Robb, J. R. Cheeseman, G. Scalmani, V. Barone, B. Mennucci, G. A. Petersson, H. Nakatsuji, M. Caricato, X. Li, H. P. Hratchian, A. F. Izmaylov, J. Bloino, G. Zheng, J. L. Sonnenberg, M. Hada, M. Ehara, K. Toyota, R. Fukuda, J. Hasegawa, M. Ishida, T. Nakajima, Y. Honda, O. Kitao, H. Nakai, T. Vreven, J. A. Montgomery, J. E. Peralta, F. Ogliaro, M. Bearpark, J. J. Heyd, E. Brothers, K. N. Kudin, V. N. Staroverov, T. Keith, R. Kobayashi, J. Normand, K. Raghavachari, A. Rendell, J. C. Burant, S. S. Iyengar, J. Tomasi, M. Cossi, N. Rega, J. M. Millam, M. Klene, J. E. Knox, J. B. Cross, V. Bakken, C. Adamo, J. Jaramillo, R. Gomperts, R. E. Stratmann, O. Yazyev, A. J. Austin, R. Cammi, C. Pomelli, J. W. Ochterski, R. L. Martin, K. Morokuma, V. G. Zakrzewski, G. A. Voth, P. Salvador, J. J. Dannenberg, S. Dapprich, A. D. Daniels, O. Farkas, J. B. Foresman, J. V. Ortiz, J. Cioslowski, D. J. Fox, Gaussian 09, Revision B.01; Gaussian, Inc.: Wallingford, CT, 2010.

[28] (a) E. D. Glendening, C. R. Landis, F. Weinhold, *J. Comput. Chem.* **2013**, *34*, 1429–1437; (b) C. L. F. Weinhold, Valency and Bonding: A Natural Bond Orbital Donor-Acceptor Perspective; Cambridge university press: Cambridge, U.K., **2011.**

[29] H. M. D. Bandara, S. C. Burdette, *Chem. Soc. Rev.* **2012**, *41*, 1809–1825.

[30] H. M. D. Bandara, T. R. Friss, M. M. Enriquez, W. Isley, C. Incarvito, H. A. Frank, J. Gascon, S. C. Burdette, *J. Org. Chem.* **2010**, *75*, 4817–4827.

[31] X. Ji, R.-T. Wu, L. Long, C. Guo, N. M. Khashab, F. Huang, J. L. Sessler, *J. Am. Chem. Soc.* **2018**, *140*, 2777–2780.

[32] (a) S. Yagai, A. Kitamura, *Chem. Soc. Rev.* **2008**, *37*, 1520–1529; (b) X. Yao, T. Li, J. Wang, X. Ma, H. Tian, *Adv. Opt. Mater.* **2016**, *4*, 1322–1349.

[33] Hirose, K. (**2007**) Determination of Binding Constants. In: Schalley, C., Ed., Analytical Methods in Supramolecular Chemistry, Wiley-VCH Verlag GmbH & Co. KGaA, Weinheim, 17-54.

[34] (a) T. Saha, S. Dasari, D. Tewari, A. Prathap, K. M. Sureshan, A. K. Bera, A. Mukherjee, P. Talukdar, *J. Am. Chem. Soc.* **2014**, *136*, 14128–14135; (b) P. Talukdar, G. Bollot, J. Mareda, N. Sakai, S. Matile, *J. Am. Chem. Soc.* **2005**, *127*, 6528–6529; (c) V. Gorteau, G. Bollot, J. Mareda, A. Perez-Velasco, S. Matile, *J. Am. Chem. Soc.* **2006**, *128*, 14788–14789.

[35] A. Vargas Jentzsch, D. Emery, J. Mareda, P. Metrangolo, G. Resnati, S. Matile, *Angew. Chem. Int. Ed.* **2011**, *50*, 11675–11678.

[36] S. Bhosale, S. Matile, *Chirality* **2006**, *18*, 849–856.

[37] C. Ren, X. Ding, A. Roy, J. Shen, S. Zhou, F. Chen, S. F. Yau Li, H. Ren, Y. Y. Yang, H. Zeng, *Chem. Sci.* **2018**, *9*, 4044–4051.

[38] (a) E. Procházková, L. Čechová, J. Kind, Z. Janeba, C. M. Thiele, M. Dračínský, *Chem. Eur. J.* **2018**, *24*, 492–498; (b) C. Tie, J. C. Gallucci, J. R. Parquette, *J. Am. Chem. Soc.* **2006**, *128*, 1162–1171.

[39] M. Li, Y. Feng, E. Liu, C. Qin, W. Feng, *Sci. China Tech. Sci.* **2016**, *59*, 1383–1390.

Chapter 3

Stimuli-responsive anion transport through acylhydrazone-based synthetic anionophores

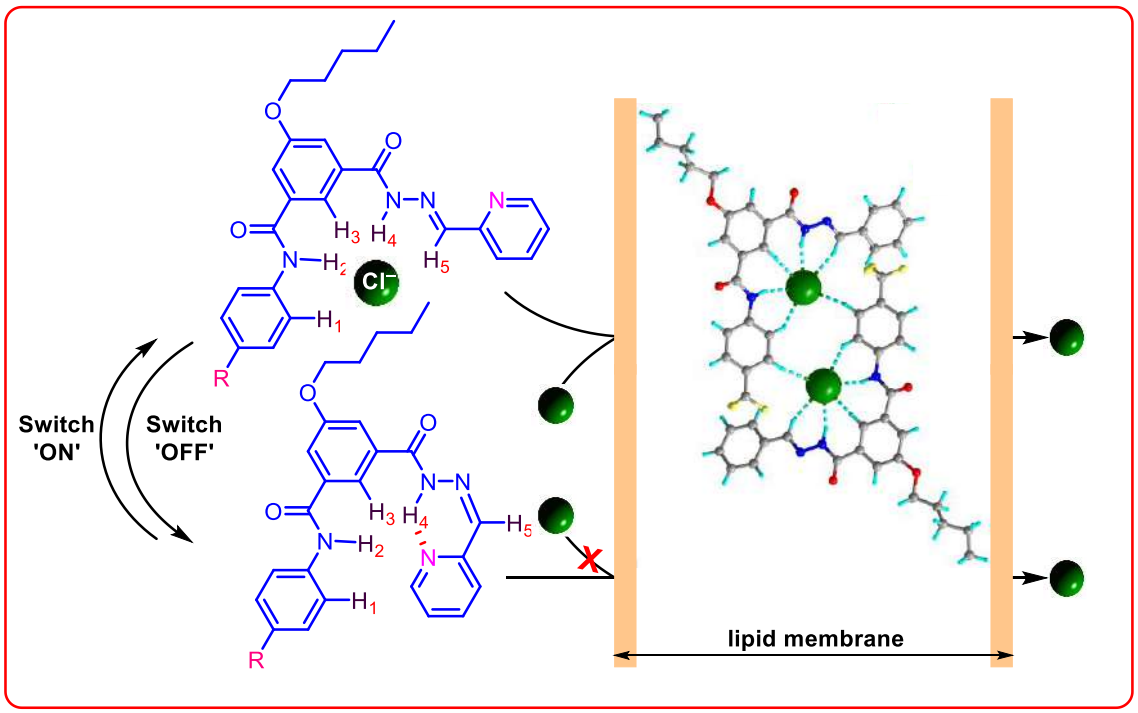

3.1. Introduction

As discussed in chapter 2, 'Gating', the controlled 'ON-OFF' ion transport process is very essential for performing the vital functions inside the physiological systems.[1] Artificial ion transport systems especially stimulus-responsive systems promise a better replacement of the faulty natural ion channels or their use as target-specific moieties in cancer therapeutics.[2] Light-responsive ionophores, in particular, are attractive targets because of their intensity tunability and high spatiotemporal control.[3] Different light switches (e.g. azobenzene, spiropyran, acylhydraone, etc.) or photocleavable (e.g. *o*-nitro aromatics)[2a, 4] groups have been employed for generating light-responsive ion transport systems. In the previous chapter, we chose azobenzene as the photoswitch because of its short-responsive nature, less toxicity, and significant change in its dipole moment upon *trans* to *cis* photoisomerization process.[5] We successfully achieved the photo-gated ion transport activity using the azobenzene-based ion carriers across the artificial liposomes. However, the spontaneous *cis* to *trans* thermal relaxation is one of the main drawbacks associated with this photoswitch which delimits potential applications under the biological temperature ranges. In this regard, acylhydrazone-based photoswitches are found to be highly tunable that can be controlled through the application of either light,[6] redox,[7] thermal[8] or pH changes[9] (Figure 3.1A). Especially, (*E*)-acylhydrazones based on 2-pyridinecarboxaldehyde, which upon photoisomerization of the C=N double bond, gives the (*Z*)-form with more thermal stability due to intramolecular hydrogen bond formation (Figure 3.1B).[10] Therefore, acylhydrazones have been well explored in different fields, e.g., ion-pair recognition,[11] supramolecular self-assemblies,[8] photo-regulated molecular shuttles,[12] etc.

In 2017, Zhou *et al*. introduced acylhydrazone as a switch to design a crown ether-based cation-selective ion channel.[13] The self-assembled channel structure was disassembled

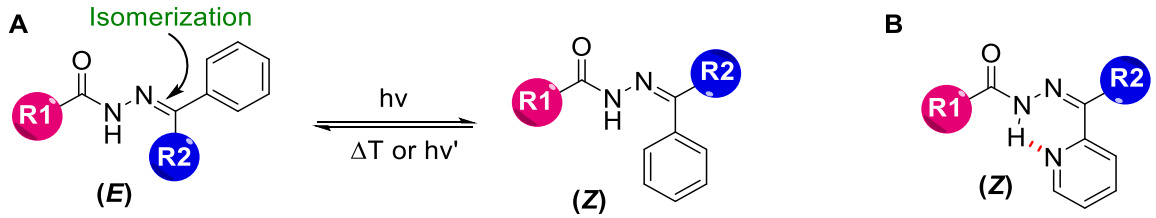

Figure 3.1. *E* to *Z* photoisomerization process of acylhydrazone subunit across C=N double bond (**A**). Hydrogen bonding stabilized Z state of pyridine-based acylhydrazone motif (**B**). Note: R1 and R2 groups represent a wide variety of organic substituents.

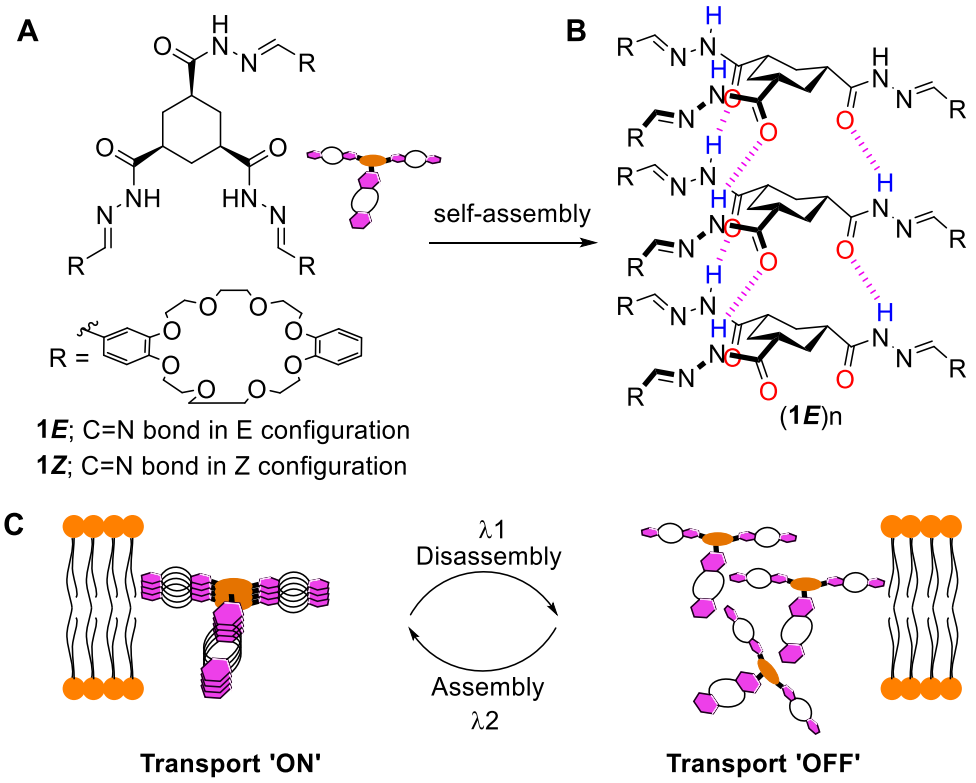

Figure 3.2. The structure of 1*E* and 1*Z*. (**A**) Schematic representation for the assembly of 1*E*. (**B**) Working principle of photoregulatory ion transport (**C**).

upon photoirradiation at 300 nm and then regenerated back upon photoirradiation at 365 nm, leading to the reversible "OFF-ON" ion channel activity (Figure 3.2). Zoran Kokan and Michal J. Chmielewski in 2018 designed a 2-pyridyl acyclhydrazone-based light switchable heteroditopic ion-pair receptor with 2,6-pyridine bisamide as an anion recognition site (Figure 3.3).[11] The ion-pair receptor can be efficiently switched OFF using the electromagnetic radiations of 312 nm and the excited Z state was seen as kinetically stable over several days. The back isomerization was achieved less effectively using a different set of radiations 365 nm or more effectively by the acid-catalyzed reactivation process.

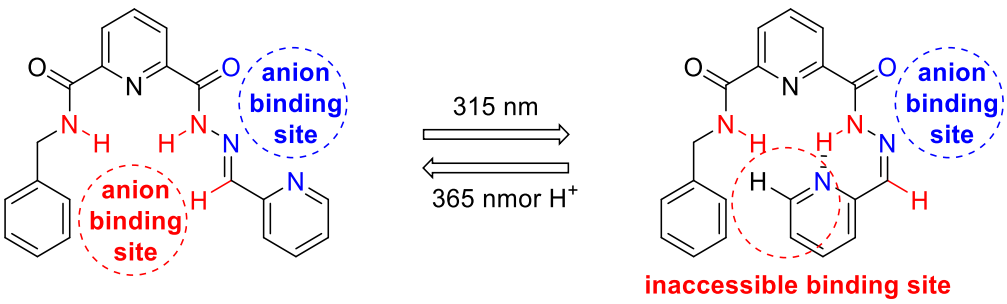

Figure 3.3. An arylhydrazones-based photoswitchable heteroditopic ion-pair receptor.

We realized that 2-pyridinecarboxaldehyde-based acylhydrazone system can be tuned easily to design a stimuli-responsive anion transporter by creating a cavity that can offer multivalent and strong anion recognition. Although, a cation binding domain in the receptor, the site may not bind and transport cation as this cationic domain would be exposed to the hydrophobic domains of the lipid membrane, which will be thermodynamically unfavourable. Based on this understanding, we designed a class of acylhydrazone-based anion carriers **1a-1d** (Figure 3.4A). Our motif contains 5-(pentyloxy)isophthalic biscarboxyamide as a cavity for strong anion recognition and 2-pyridyl acylhydrazone as a stimuli-responsive switch. Photoisomerization from (*E*)- to (*Z*)-forms across C=N double bond using electromagnetic radiation would block the anion binding site due to intramolecular hydrogen bonding. On the other hand, the inactive (*Z*)-form can be converted back to the (*E*)-form through an acid-catalyzed reactivation process. We also designed a molecule **1d** that has a phenyl ring instead of pyridyl ring and was not expected to be an efficient stimuli-responsive switch. Different aromatic moieties were connected to the amide linkage to fine-tune the binding affinity and lipophilicity of the molecules.[14] The pK_a and LogP values were calculated using Marvin Sketch Program (Figure 3.4B).[15]

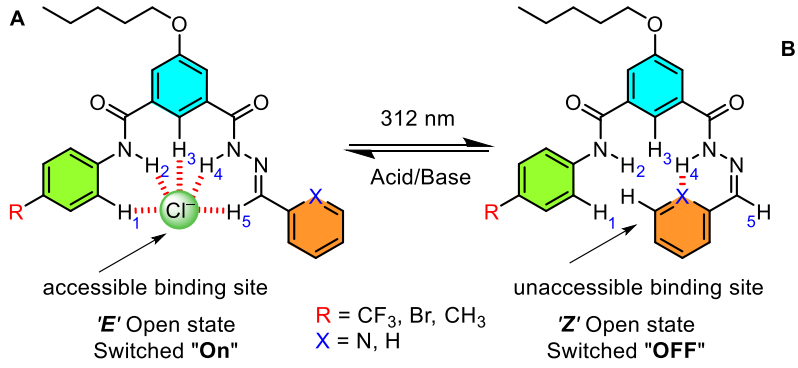

B

Comp.	R	X	pK_a	logP
1a	CF_3	N	11.53	6.00
1b	Br	N	11.57	5.89
1c	CH_3	N	12.07	5.64
1d	CF_3	H	11.53	6.54

Figure 3.4. Design of light regulatory acylhydrazone-based synthetic ion transporters (**A**). Description of logP and pK_a values of the transporters **1a-1d** (**B**).

3.2. Results and discussion

3.2.1. Synthesis

The synthesis of the desired compounds **1a-1d** was achieved from compound **2**, which was prepared from 5-hydroxyisopthalic acid following a reported protocol.[16] Mono-hydrolysis of compound **2** using sodium hydroxide under reflux conditions furnished compound **3**, which upon coupling with different aromatic amines using EDC·HCl gave monoamide derivatives

4a-4c in excellent yield (Scheme 3.1). These monoamide ester derivatives upon reacting with hydrazine hydrate followed by coupling with pyridine-2-carboxaldehyde furnish the desired final compounds **1a-1c** in excellent yields. On the other hand, compound **1d** was synthesized by reacting **4a** with hydrazine hydrate followed by coupling with benzaldehyde.

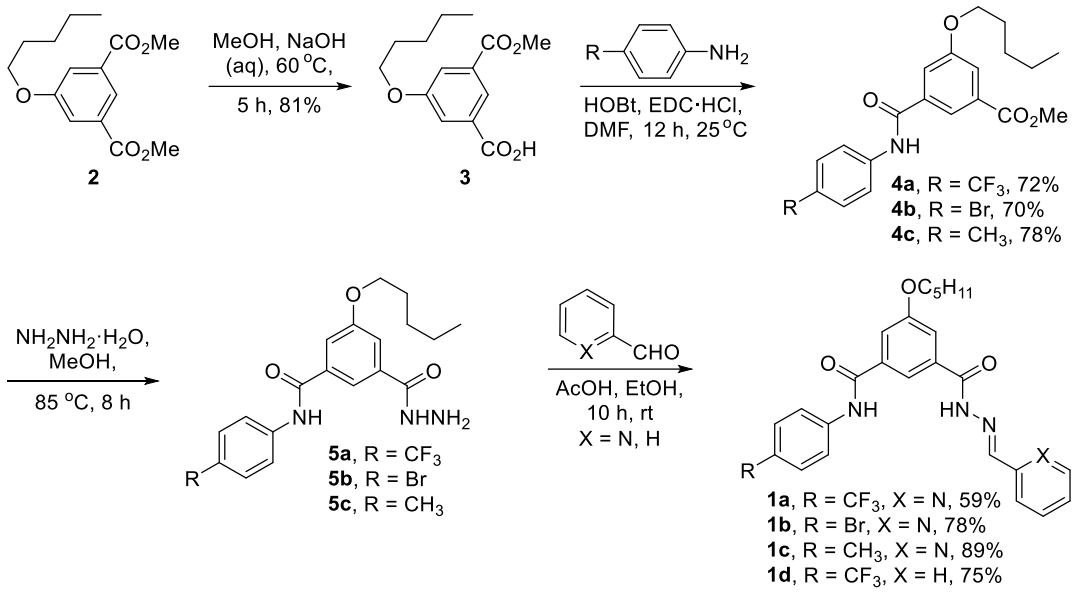

Scheme 3.1. Synthetic Scheme for the compounds **1a-1d.**

3.2.2. Anion Binding Study by ^{1}H NMR Titration

Initial evidence of the anion binding of these anionic receptors **1a–1d** was obtained from ^{1}H NMR studies in acetonitrile–d_3. Upon titration with TBACl in acetonitrile–d_3, significant shifts of N–H_1, N–H_2, C_{Ar}–H_3, C_{Ar}–H_4, and C_{imine}–H_5 were observed, which indicated the involvement of these protons in an overall anion binding process through N–H···Cl^- and C–H···Cl^- hydrogen bonding interactions (Figure 3.5, 3.23, 3.25, 3.27). ^{1}H NMR titration data of **1a** with TBACl is shown the figure 2. Further binding analysis using BindFit program[17] (Figure 3.6, 3.24, 3.26, and 3.28) revealed 1:1 binding stoichiometry with the binding affinity sequence of **1a** > **1b** > **1d** > **1c** and the binding constants ($K_{a(1:1)}$/Cl^- obtained are 11168 ± 675 M^{-1}, for **1a**, 7934 ± 573 M^{-1} for **1b**, 4201 ± 257 M^{-1} for **1c** and 6037 ± 385 M^{-1} for **1d** respectively (Table 3.1). This sequence is an outcome of the pK_a values of these receptors. Binding studies of **1a** were also done with Br^-, I^-, and ClO_4^- anions, respectively (Figure 3.19, 3.21), and the study provided $K_{a(1:1)}$/Br^- = 2596 ± 289 M^{-1} and $K_{a(1:1)}$/I^- = 69 ± 17 M^{-1} (Figure 3.20, 3.22). No change in the chemical shift was observed upon the addition of ClO_4^- anion. The observed binding sequence: Cl^- > Br^- > I^- > ClO_4^- may be attributed to the high charge density of Cl^- and its perfect fitting to the binding cavity of the receptor. Furthermore, **1a** in its

(*Z*)–form showed a weak Cl^- binding with TBACl (Figure 3.30), with the association constant of $K_{a(1:1)}/Cl^- = 53 \pm 11\ M^{-1}$ (Figure 3.31), which indicates the blockage of the binding site due to photoisomerization across C=N bond.

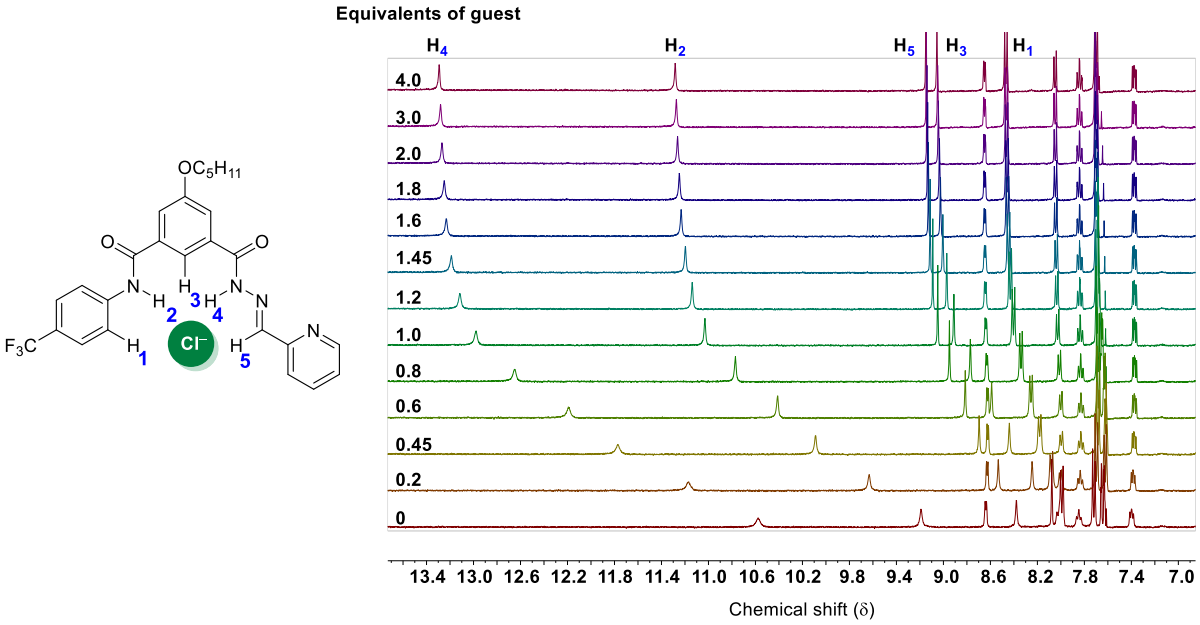

Figure 3.5. ^{1}H NMR titration spectra for **1a** (5 mM) with stepwise addition of TBACl in CD_3CN. The equivalents of added TBACl are shown on the stacked spectra.

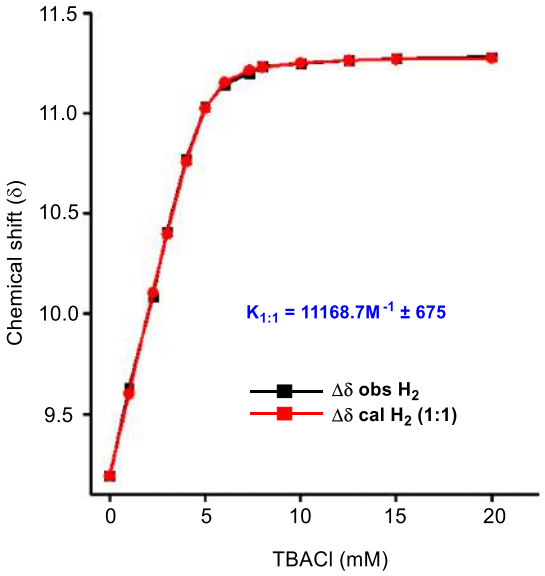

Figure 3.6. The plot of chemical shift (δ) of H_2 protons *vs* concentration of TBACl added, fitted to 1:1 binding model of BindFit v0.5.

3.2.3. Single crystal X-Ray analysis

Among all synthesized compounds, cocrystals were obtained for only **1d** with TBACl in acetonitrile. The single crystal X-ray diffraction data revealed a $(\mathbf{1d})_2(Cl^-)_2$ binding mode. In the cavity created by two molecules of **1d**, two Cl^- ions were encapsulated, and each anion formed five hydrogen bonds with one molecule and one hydrogen bond with the second one (Figure 3.7). The distance between two Cl^- ions was 5.672 Å that indicating no repulsion between these anions. The solid-state Cl^- ion binding pattern is in good agreement with that in the solution phase Cl^- binding by ^1H NMR spectroscopy binding (i.e. 1:1 receptor–to–Cl^- ratio).

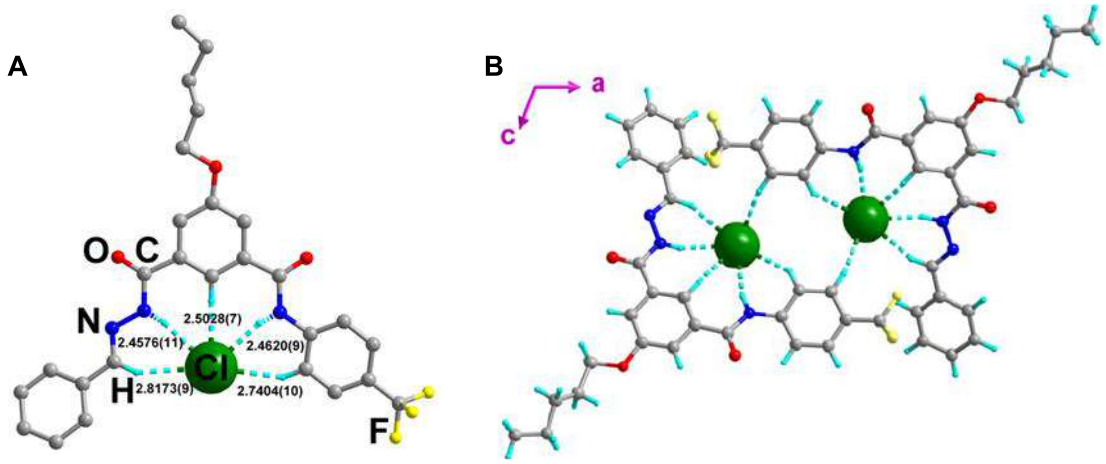

Figure 3.7. X–ray crystal structure of compound **1d** complexed with Cl^- ion, Hydrogen bonds are shown by cyan colour lines, The TBA^+ cations, hydrogen atoms other than hydrogen bonds were omitted for clarity (**A**) X–ray crystal structure of compound **1d** complexed with Cl^- ion in a 2:2 (**1d**:Cl^-) binding pattern (**B**).

3.2.4. Ion transport activity

The ion transport activity of compounds **1a–1d** was examined across large unilamellar vesicles (LUVs) entrapped with 8-hydroxy-1,3,6-pyrenetrisulfonate (HPTS) buffered at pH_{in}= 7 using 10 mM of HEPES and 100 mM of NaCl. A pH gradient, ΔpH = 0.8 (pH_{in} = 7.0 and pH_{out} = 7.8) was created by adding aqueous sodium hydroxide in the extravesicular buffer[18] (see ESI). The equilibration of the applied pH gradient by either influx of OH^- ions or efflux of H+ ions, in the presence of each compound, was monitored by measuring fluorescence intensity of HPTS at λ = 510 nm (λ_{ex} = 450 nm). Eventually, using triton-100 vesicles were lysed completely to get the maximum intensity. All the ionophores, **1a–1d** showed a significant increment in the fluorescent intensity with the activity sequence of **1d** > **1a** > **1b** > **1c** (Figure

3.8A). This sequence is explained based on collective involvement of binding affinity and membrane permeability of the anionophores involved in the transport process. From the dose-dependent activity data, Hill analyses were done to get EC_{50} values of 0.62, 1.58, 2.08, and 0.11 μM for **1a**, **1b**, **1c**, and **1d**, respectively (Figure 3.32 – 3.35). For each compound, the Hill coefficient of n ~ 2 is indicative of the involvement of two molecules in generating the active ion transport system and data is in synergy to that observed in the crystal structure of **1d** with Cl^- ion. Anion selectivity was investigated using EYPC-LUVs⊃HPTS. When the anions in the extravesicular buffer of LUVs entrapped with HPTS were varied by using different NaX (X^- = Cl^-, Br^-, I^-, $ClO_4^-$and NO_3^-) salt solutions,[19] the activity sequence of $Cl^- > Br^- > NO_3^- > I^- > ClO_4^-$ was obtained (Figure 3.8B), suggesting the involvement of anions in the transport process. The above sequence may be attributed to the combinative effects of the anion binding affinity, lipophilicity and membrane permeability of the transporting molecule.

Subsequently, the influx of Cl^- ions by **1a**–**1d** was monitored across LUVs, entrapping a lucigenin dye and 200 mM $NaNO_3$.[20] Subsequently, NaCl pulse was applied in the extravesicular solution to create a Cl^-/NO_3^- gradient across the vesicles. The influx of Cl^- ions was monitored by measuring the fluorescence intensity at λ = 455 nm (λ_{ex} = 535 nm, for lucigenin). The dose-response Cl^- influx activity of **1a** and **1d** are shown in Figures 3.9A, and Figures 3.36. Hill analysis furnished EC_{50} values of 5.70 and 0.50 μM for **1a** and **1d**,

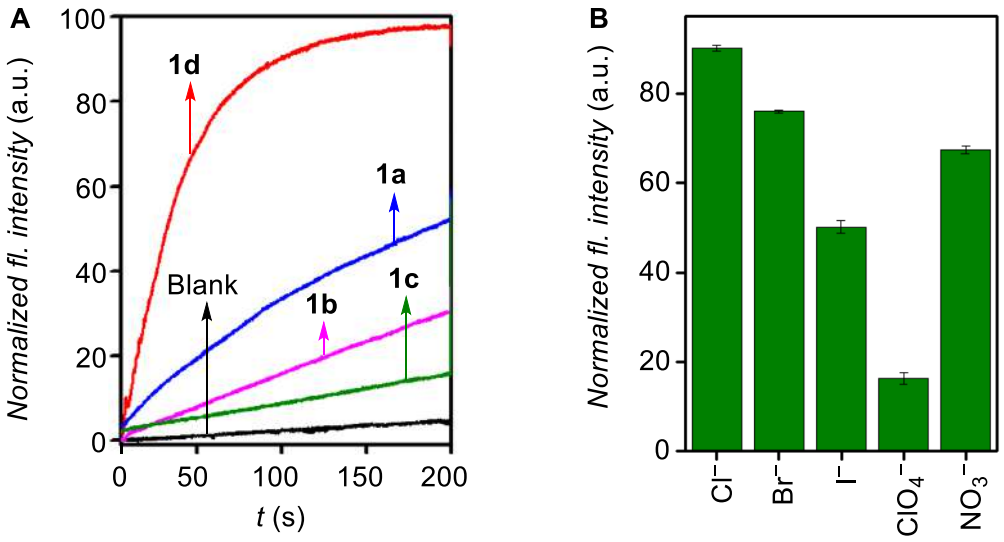

Figure 3.8. Activity comparison of **1a-1d** (0.3 μM each) across EYPC-LUVs⊃HPTS (**A**). Anion selectivity of **1a** (0.3 μM) by varying external anions across EYPC-LUVs⊃HPTS, each bar graph represents mean ion transport activity calculated from three independent experiments (**B**).

Table 3.1. ^{1}H NMR titration studies of compounds **1a-1d** with different salts of TBACl, TBABr, TBAI and $TBAClO_4$ salts in acetonitrile-d_3.

			Association constant, $K_a \times 10^3$ (M^{-1}) in CD_3CN				Transport activity
Comp.	logP	pK_a	Cl^-	Br^-	I^-	ClO_4^-	EC_{50}
1a–*E*	6	11.53	11.16	2.59	0.069	– [b]	0.62
1b	5.89	11.57	7.9	– [a]	– [a]	– [a]	1.58
1c	5.64	12.07	4.2	– [a]	– [a]	– [a]	2.08
1d	6.54	11.53	6.02	– [a]	– [a]	– [a]	0.11
1a–*Z*	–	–	0.053	– [a]	– [a]	– [a]	–

[a] = ^{1}H NMR titration was not done with these systems, and [b] = Binding constant couldn't be determined due to the absence of any chemical shift in ^{1} H NMR titration of **1a** with ClO_4^-.

respectively. The dose-dependent Cl^- influx activities of **1b** and **1c** are shown in Figure 3.37. Hill analysis could not be done with these compounds due to the precipitation issues at higher concentrations. Furthermore, no change in the transport activity was observed by changing the extravesicular cations (M^- = Li^+, Na^{-+}, K^+, Rb^+, Cs^+), which rules out any involvement of cations in the transport process (Figure 3.9B).

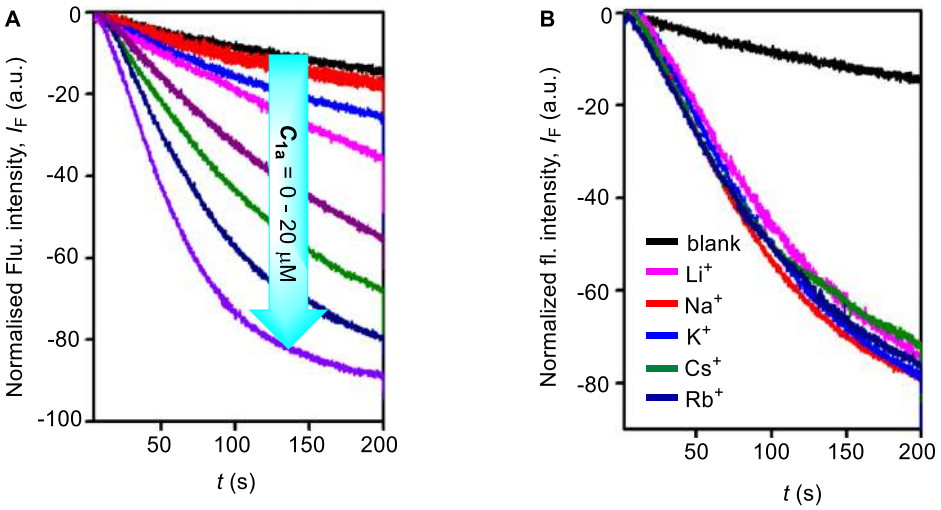

Figure 3.9. Concentration-dependent activity of **1a** across EYPC-LUVs⊃lucigenin (**A**). Cation selectivity of **1a** (1.25 μM) measured by varying external cations (M^+ = Li^+, Na^+, K^+, Rb^+, Cs^+) across EYPC-LUVs⊃Lucigenin (**B**).

The antiport mechanism was initially confirmed by monitoring the efflux of Cl^- ions by **1a** from EYPC LUVs via the fluorescence intensity enhancement of entrapped lucigenin dye. With NaCl in the intravesicular matrix, the Cl^- efflux ability by **1a** was significantly higher when iso-osmolar NaNO3 was present in the extravesicular matrix compared to that with iso-osmolar Na_2SO_4 in the extravesicular matrix (Figure 3.10A).[21] The results corroborate the antiport mechanism as NO_3^-, a lipophilic anion, participates better in the anion exchange process with Cl^- compared to highly hydrophilic SO_4^{2-}. To get further mechanistic insights for ion transport, chloride efflux from LUVs by **1a** in the presence and absence of either valinomycin (a highly selective K^+ transporter) or monensin (an H^+/K^+ antiporter) was monitored by a chloride Ion-selective Electrode (ISE). With intravesicular KCl (300 mM) and extravesicular potassium gluconate, a significant enhancement in the Cl^- efflux rate was observed for **1a** in the presence of valinomycin compared to that with **1a** alone (Figure 3.10B), and on the other hand, no significant change in the Cl^- efflux was observed in the presence of monensin (Figure 3.10C). The KCl efflux only under electrogenic potassium transporter is the evidence of an electrogenic chloride transport by **1a**.[22]

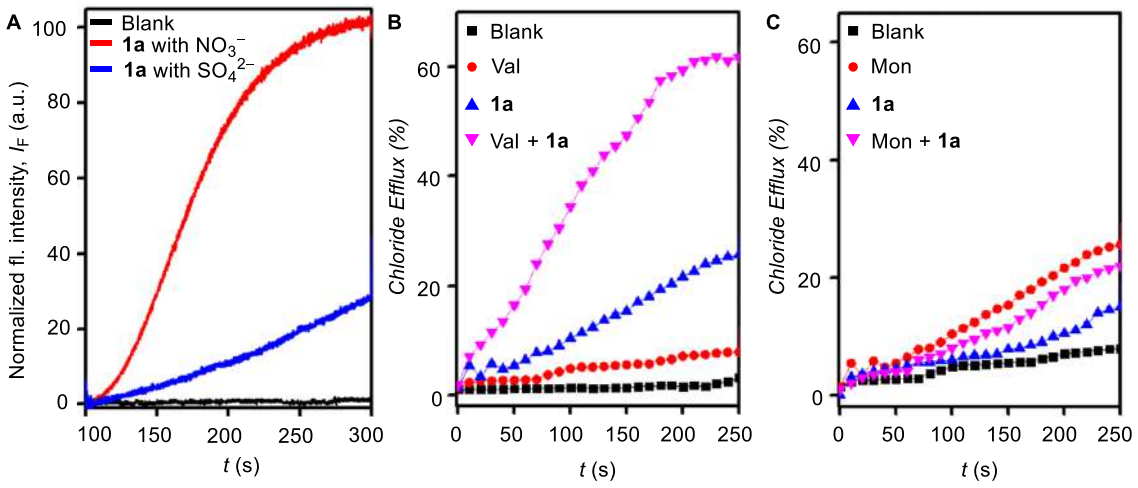

Figure 3.10. Efflux of Cl^- ion by **1a** (10 μM) in the presence of either extravesicular SO_4^{2-} or extravesicular NO_3^- ion with iso-osmolar intravesicular Cl^- (**A**). Normalized chloride efflux of **1a** in the presence and absence of valinomycin (**B**), and the presence and absence of monensin (**C**).

Furthermore, U-tube experiment showed an efficient transport Cl^- ions from the source-arm to the receiver-arm of the U-tube, when the Cl^- concentration in the receiver-arm was monitored using a chloride-based ion selective electrode (Figure 3.11). This result confirms that **1a** acts as a mobile carrier of anions.[23]

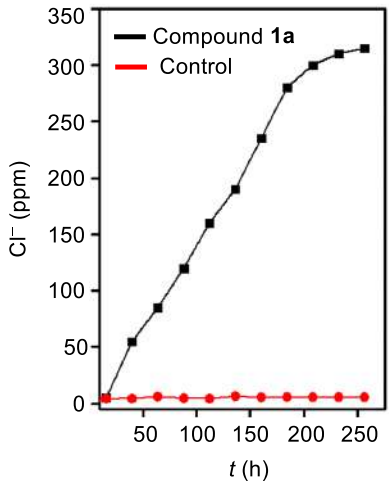

Figure 3.11. Change of chloride ion concentration in a U-tube experiment with and without compound **1a** (1.0 mM).

3.2.5. Photoisomerization studies

3.2.5.1. UV-vis and ^{1}H NMR studies

Photoisomerization studies of the compounds **1a–1d** were monitored by UV–vis absorption and ^{1}H NMR spectroscopy. UV band at 300 nm corresponding to π-π* transition got substantially decreased upon irradiation with 312 nm light, and the N–H proton connected to each (*E*)-acylhydrazone shifted significantly to the up field region upon photoisomerization to the (*Z*)-form (Figure 3.12, 3.38–3.40).[10a]

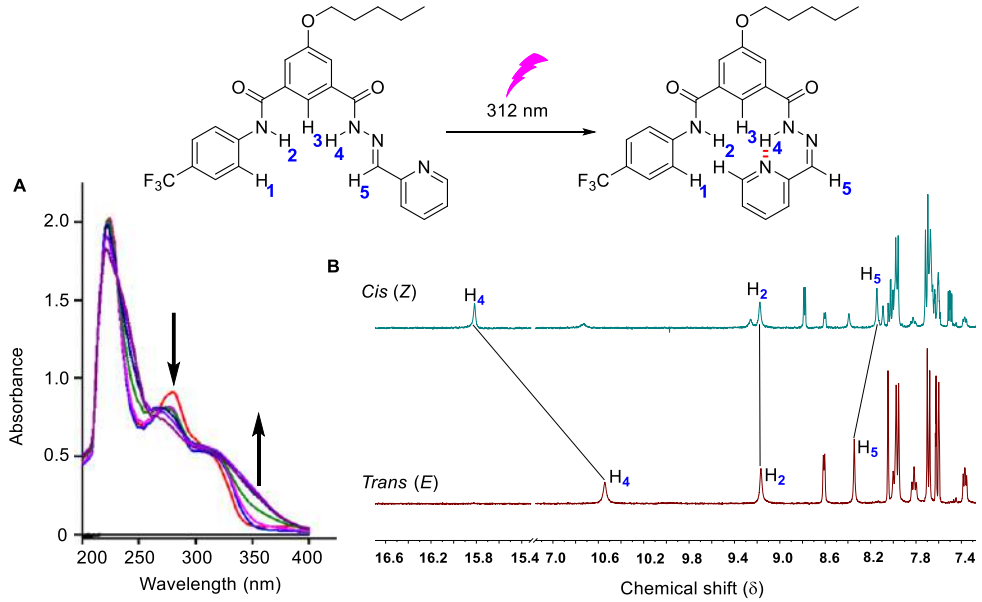

Figure 3.12. UV-visible spectral changes for **1a** (100 μM) upon irradiation with 312 nm using UV tubes (8 × 3 Watt) (**A**). Partial 400 MHz ^{1}H NMR spectrum of **1a** (4.0×10^{-3} M, down) in CD_3CN at 25 °C, and that of photo-irradiated sample of **1a** (up) by 312 nm light for 30 min (**B**).

3.2.5.2. Acid-catalyzed reversible photoisomerization studies

Initially, ^{1}H NMR was recorded for **1a**–*E* in acetonitrile-d_3. The sample was irradiated with 312 nm of light using UV tubes (8 × 3 Watt) for 35 min to convert **1a**–***E*** to **1a**–***Z***. After that, the **1a**–***Z*** sample was first treated with 5 equiv. of TFA followed by the addition of 5 equiv. of TEA to generate the initial **1a**–***E*** form (Figure 3.13). This process of photoirradiation and acid/base reactivation process was repeated for a number of cycles without the loss of efficiency (Figure 3.2).

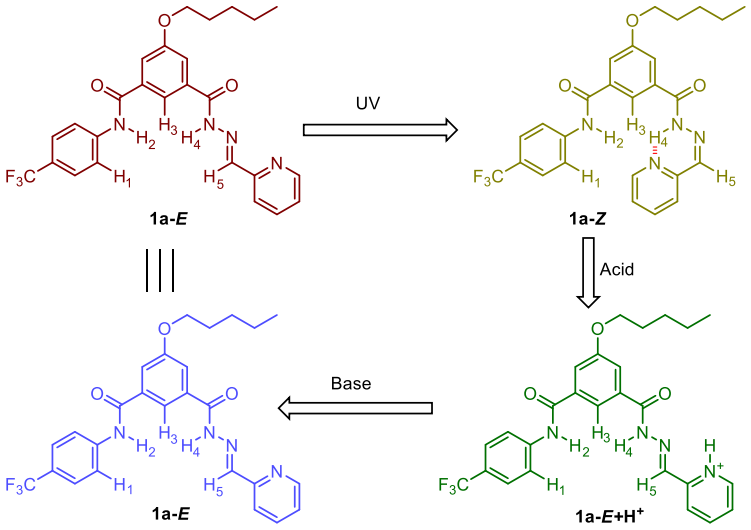

Scheme 3.2. Proposed photo and acid-induced switching cycle of the receptor **1a** between the binding *E* and non-binding *Z* isomers.

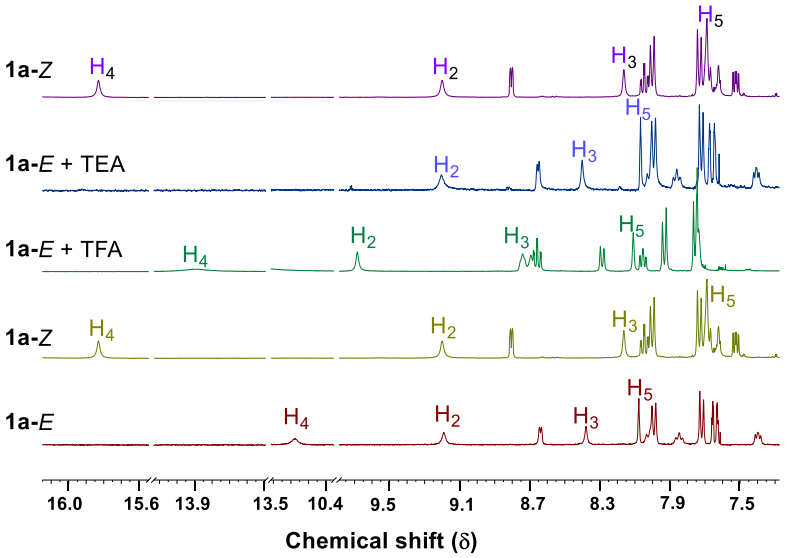

Figure 3.13. ^{1}H NMR (acetonitrile-d_3) spectra of one photo/acid switching cycle (bottom to top) in the *E*/*Z* isomerization of **1a**-***E*** (2 mM).

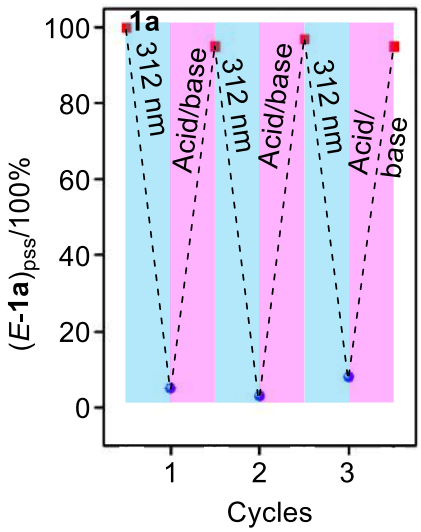

Figure 3.14. Switching between *E*-**1a** and *Z*-**1a** in acetonitrile-d_3 (2 mM) after UV irradiation and triflic acid/DIPEA addition (1 equiv).

3.2.5.3. Thermal stability

In order to find the stability of **1a** and **1d** in photoisomerized *Z* state, $\mathbf{1a}_E$ and $\mathbf{1d}_E$ in CD_3CN was irradiated at 312 nm to photoisomerize them into $\mathbf{1a}_Z$ and $\mathbf{1d}_Z$ form. After that the photoisomerized samples were kept in the dark and ^1H NMR was recorded with time. No, significant change was observed for $\mathbf{1a}_Z$ during 30 days while kept it in the dark Figure 3.15. On the other hand, compound $\mathbf{1d}_E$ was poorly photoisomerized into the $\mathbf{1d}_Z$ state with 62:38 *E*:*Z* at the PSS. In addition to this, the photoisomerized $\mathbf{1d}_Z$ state got thermally relaxed back fully within one-day Figure 3.16. These results are the outcome of the presence of intramolecular hydrogen bonding in the photoisomerized *Z* state of **1a** between the pyridine nitrogen and acylhydrazone N–H_3, which shall stabilize it. The lack of this intramolecular hydrogen bonding in **1d** leads to its poor photoisomerization and low thermal stability.

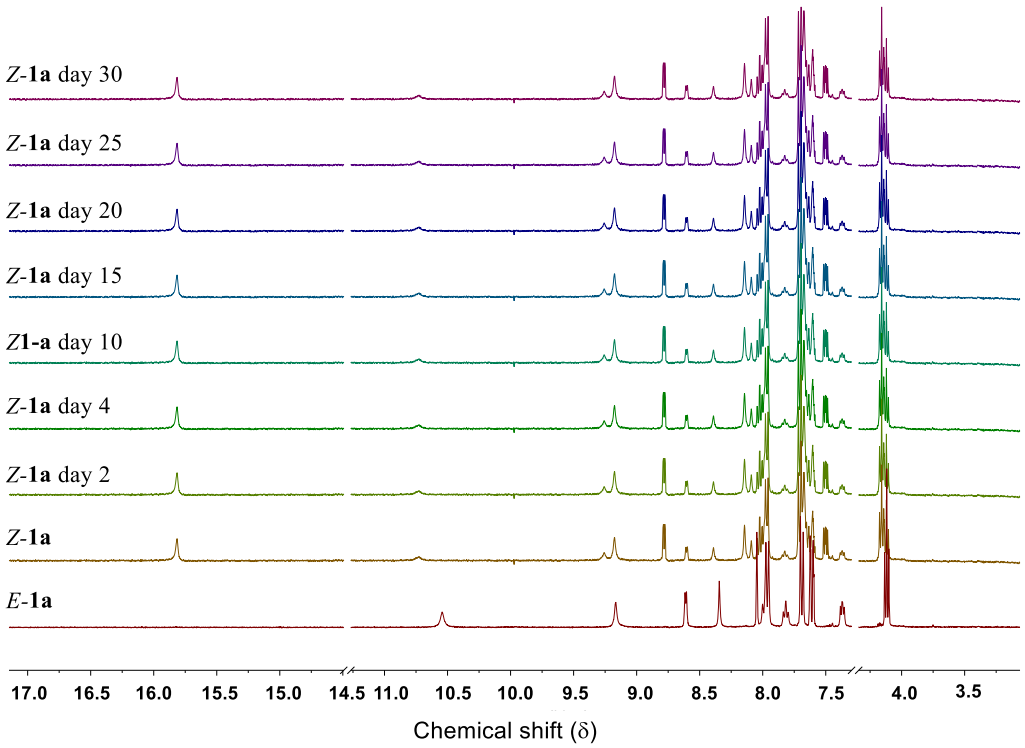

Figure 3.15. Overlapped ^{1}H NMR spectra of *Z*-**1a** in acetonitrile-d_3 after 1 and 30 days of standing in the dark. No significant changes were observed in the spectra within the investigated time.

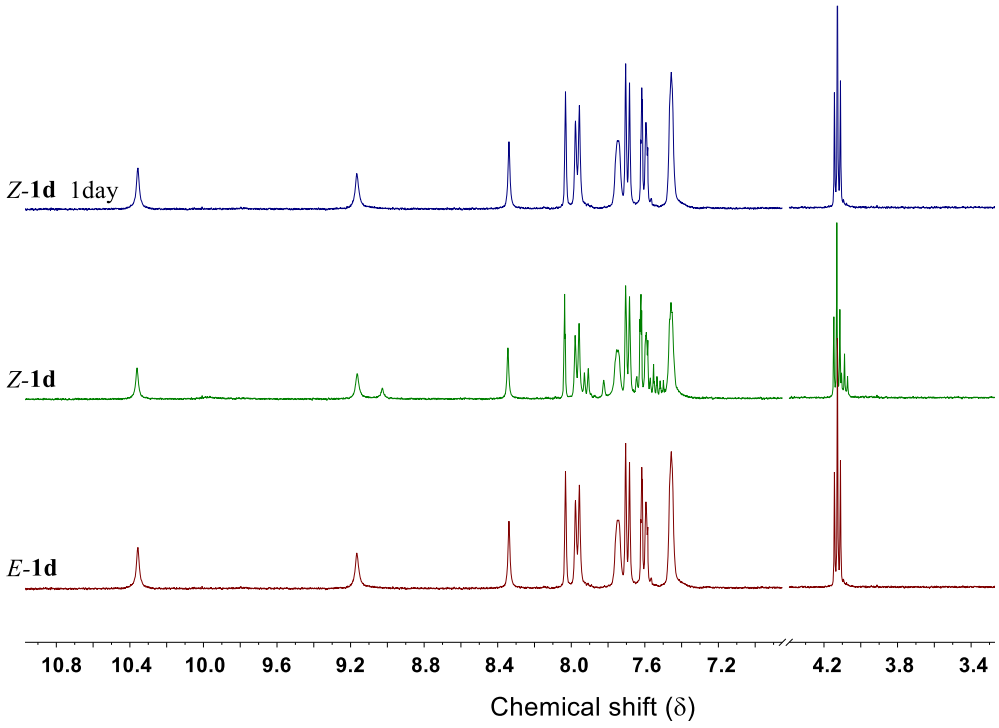

Figure 3.16. Stacked ^{1}H NMR spectra of *Z*-**1d** in acetonitrile-d_3 after day of standing in the dark. No significant changes were observed in the spectra within the investigated time.

3.2.6. Stimuli-Responsive Ion Transport Activity

3.2.5.1. Photo deactivation of ion transport through EYPC-LUVs⊃HPTS assay

Subsequently, the highest active compound 1a was used to study the photoisomerized transport activity across the lipid bilayer membrane and it was done through HPTS based vesicles. The transport activity was significantly attenuated upon the photoirradiation of **1a** in acetonitrile at 312 nm (Figure 3.17A). This reduced activity is attributed to the loss of anion binding site due to *E* to *Z* photoisomerization. No significant change in the transport activity was observed while keeping the sample in dark for 10 h owning to its higher thermal stability in this photoisomerized Z state. (Figure 3.17B).

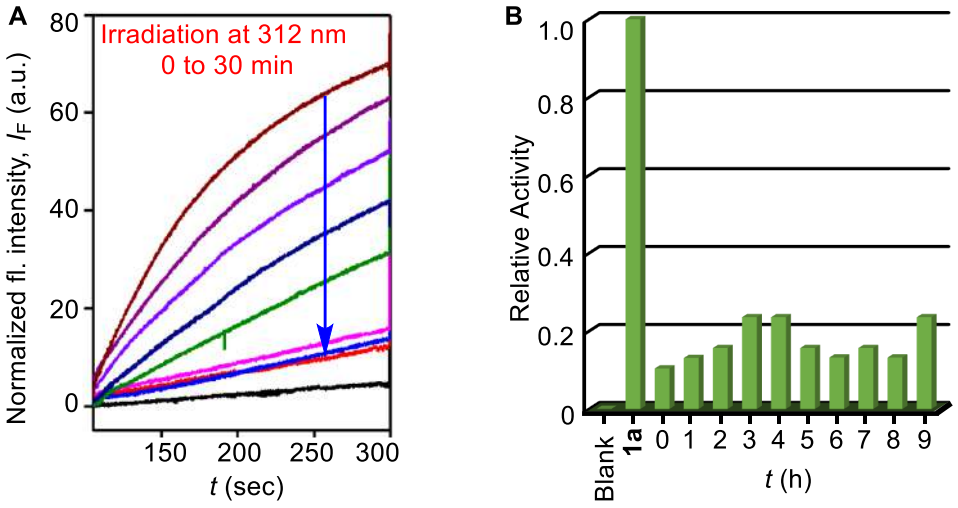

Figure 3.17. Transport activity of **1a** after irradiation at 312 nm for 0-30 min (**A**) Ion transport activity of **1a**-*Z* while keeping in the dark for 9 h **(B).**

3.2.5.2. Stimuli-responsive reversible ion transport activity through ISE studies

Reversible switching of ion transport activity using different stimuli of light and acid/base treatment were studied by monitoring the chloride efflux from LUVs. There was 82% of decrease in the chloride efflux upon photoirradiation of **1a** as acetonitrile solution, which was efficiently regained back by applying acid/base treatment to the photoisomerized solution of **1a** (Figure 3.18A). This process of de-activation and re-activation was successfully carried out for three repeated cycles without the loss of efficiency (Figure 3.18B).

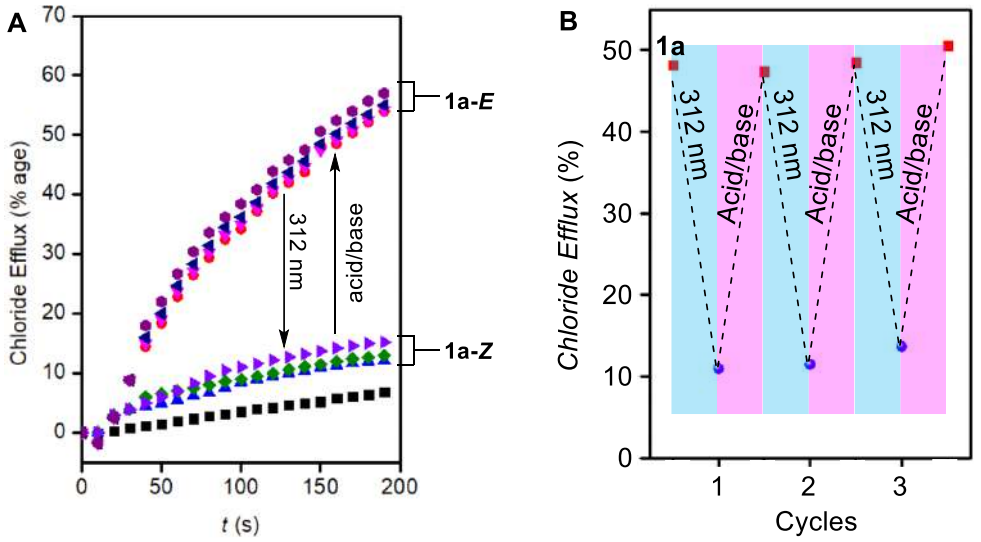

Figure 3.18. Chloride efflux of **1a** in *E* and *Z* forms (**A**). Chloride efflux of **1a** in *E* form, after irradiation at 312 nm and after acid/base treatment (5 equiv.) (**B**).

3.3. Conclusion

In conclusion, we have demonstrated the photo-responsive acylhydrazone based synthetic anionophores **1a–1d**. The anion binding particularly chloride was confirmed through solid state single crystal XRD and solution phase ^{1}H NMR spectroscopic studies. Both studies revealed 1:1 (Cl^- Receptor) binding pattern. Anionophore **1a** provided the *E*C50 = 0.199 μM and Hill coefficient of n ~ 2 across EYPC-LUVs⊃HPTS, confirming the involvement of two molecules in the ion transport process. Presence of intramolecular hydrogen bonding in the Z excited state greatly enhance the photoconversion and stability of **1a**, as compared to the **1d** (only 40% of conversion). Transport activity of **1a** was greatly reduced upon photoisomerization at 312 nm. The reversible photoisomerization through the application of alternating UV light followed by acid/base treatment was achieved through several repeated cycles. Importantly, the simple modular synthesis may allow its easy incorporation into several supramolecular artefacts with the potential applications, in stimuli-responsive systems, soft materials and in possible biological applications.

3.4. Experimental details

3.4.1. General Methods

All reagents and solvents for chemical synthesis were purchased from different commercial sources (Sigma-Aldrich, Spectrochem) and used further without purification. The column

chromatography was carried out using Merck silica (100-200/ 230-400 mesh size). The thin layer chromatography was performed on E. Merck silica gel 60-F254 plates. Egg yolk phosphatidylcholine (EYPC) as a solution of chloroform (25 mg/ mL), mini extruder, polycarbonate membrane of 100 nm and 200 nm were purchased from Avanti Polar Lipid. HEPES, HPTS, lucigenin, NaOH, Triton X-100, valinomycin and all inorganic salts were obtained as molecular biology grade from Sigma Aldrich.

3.4.2. Physical Measurements

The ^{1}H NMR spectra were recorded at 400 MHz whereas ^{13}C spectra at 101 MHz. The residual solvent signals were considered as an internal reference (δ_H = 7.26 ppm for $CDCl_3$, δ_H = 2.50 for DMSO-d_6, and δ_H = 1.94 for CD_3CN) to calibrate spectra. The chemical shifts were reported in ppm. Following abbreviations were used to indicate multiplicity patterns m: multiplet, s: singlet, d: doublet, t: triplet, q: quartet, dd: doublet of doublets, td: triplet of doublets. Coupling constants were measured in Hz. Infra-red (IR) spectra were measured in cm^{-1} using FT–IR spectrophotometer. Melting points were measured on micro melting point apparatus. High-resolution mass spectra (HRMS) were recorded on electrospray ionization time-of-flight (ESI-TOF). Fluorescence experiments were recorded on Fluoromax-4 from Jobin Yvon Edison equipped with injector port and magnetic stirrer in microfluorescence cuvette. All buffer solutions were prepared from the autoclaved water. Adjustment of pH of buffer solutions was made using Helmer pH meter. The extravesicular dye was removed by performing gel chromatography using Sephadex. The fluorescence studies were proceed using OriginPro 8.5. ChemBio Draw 15 Ultra software was used for drawing structures and processing figures. UV-vis spectra were recorded on a Varian Cary 5000 spectrophotometer. The single-crystal X-ray diffraction (SCXRD) analysis was performed on a Bruker Smart Apex Duo diffractometer using Mo Kα radiation (λ = 0.71073Å). The crystal structures were solved using intrinsic methods and then refined by full-matrix least-squares against F^2 using all data by using SHELXL-2014/7 built in the Apex-3 package.

3.4.3. Synthetic Procedure

3-(Methoxycarbonyl)-5-(pentyloxy)benzoic acid (3): A suspension of **2** (2.0 g, 7.13 mmol) in a solution of NaOH (260 mg, 6.49 mmol) in MeOH (150 mL) and H_2O (25 mL) was heated under reflux for 5 h. After cooling the reaction mixture to room temperature, it was poured into cold water (60 mL) and the pH of the solution was adjusted to 1 with concentrated HCl. The crude product was then extracted with EtOAc (2 x 100 mL) and the combined organic phase was washed with water. It was then dried over Na_2SO_4, and solvent was removed under vacuum. Compound was purified by column chromatography (1.2% MeOH/$CHCl_3$) to get white solid (1.41 g, 81%).**M.P.:** 198.0 °C;**^{1}H NMR** (400 MHz, $CDCl_3$) δ 8.33 (s, 1H), 7.79 (s, 2H), 4.04 (t, *J* = 6.4 Hz, 2H), 3.94 (s, 3H), 1.82 (p, *J* = 6.5 Hz, 2H), 1.50 – 1.35 (m, 4H), 0.94 (t, *J* = 7.1 Hz, 3H). ^{13}C NMR (101 MHz, $CDCl_3$) δ 170.95 (s), 166.13 (s), 159.31 (s), 131.87 (s), 130.79 (s), 123.37 (s), 120.68 (s), 120.28 (s), 68.69 (s), 52.47 (s), 28.77 (s), 28.12 (s), 22.42 (s), 14.01 (s). **IR (Neat, ν/cm^{-1}):** 3726, 3262, 3014, 2962, 2230, 1738, 1656, 1588, 1216, 1099; **HRMS (ESI):** Calculated for $C_{14}H_{18}O_5H^+$ $(M+H)^+$: 267.1227; Found: 267.1278.

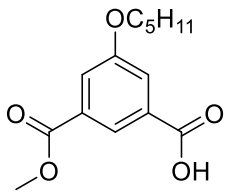

Methyl-3-(pentyloxy)-5-((4-(trifluoromethyl)phenyl)carbamoyl)benzoate (4a): In a 10 mL round bottom flask, **3** (150 mg, 0.563 mmol, 1 eq) was dissolved in DMF (2 mL). To the clear solution EDC.HCl (131.17 mg, 0.845 mmol , 1.5 eq), HOBt (191.33 mg, 0.676 mmol, 1.2 eq) and Triethyl amine (94 µL, 0.676 mmol, 1.2 eq), was added and the solution was stirred at room temperature for 15 min. 4-(trifluoromethyl)aniline (70 µL, 0.569 mmol, 1 eq), was added and then continuously stirred at rt for 12 h. After reaction completion, the solution was transferred to a separating funnel with EtOAc (25 mL) and washed with aqueous $NaHCO_3$ (25 mL). The aqueous layer was extracted with EtOAc (25 mL). Combined organic layer was dried over Na_2SO_4 and the solvent was evaporated under reduced pressure. The crude residue was further purified by column chromatography (5% EtOAC/PE) to get white solid pure product. Yield: 165.7 mg (71.85%). **M.P.:** 184.0 °C; **^{1}H NMR** (400 MHz, $CDCl_3$) δ 8.05 (s, 1H), 8.02 (t, *J* = 1.4 Hz, 1H), 7.80 (d, *J* = 8.5 Hz, 2H), 7.74 (dd, *J* = 2.6, 1.3 Hz, 1H), 7.68 – 7.65 (m, 2H), 7.63 (s, 1H), 4.06 (t, *J* = 6.5 Hz, 2H), 3.96 (s, 3H), 1.88 – 1.77 (m, 2H), 1.51 – 1.34 (m, 5H), 0.94 (t, *J* = 7.2 Hz, 4H). **^{13}C NMR** (101 MHz, $CDCl_3$) δ 166.24, 164.88, 159.83, 140.88, 135.99, 131.91, 126.46, 126.43, 119.93, 119.23, 119.16, 118.37, 68.78, 52.64, 28.82, 28.17,

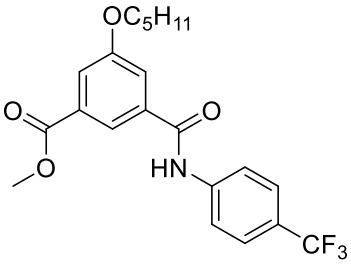

22.48, 14.07. **IR (Neat, ν/cm^{-1}):** 3726, 3262, 3014, 2962, 2230, 1738, 1656, 1588, 1216, 1099; **HRMS (ESI):** Calculated for $C_{21}H_{22}F_3NO_4H^+$ $(M+H)^+$: 410.1574; Found: 410.1578.

Methyl 3-((4-bromophenyl) carbamoyl)-5-(pentyloxy)benzoate (4b): In a 10 mL round bottom flask, **3** (150 mg, 0.563 mmol, 1 eq) was dissolved in DMF (2 mL). To the clear solution

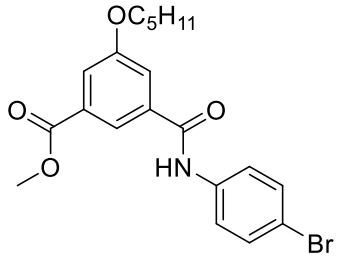

EDC.HCl (131.17 mg, 0.845 mmol , 1.5 eq), HOBt (191.33 mg, 0.676 mmol, 1.2 eq) and Triethyl amine (94 µL, 0.676 mmol, 1.2 eq), was added and the solution was stirred at rt for 20 min. 4-bromoaniline (96.9 mg, 0.563 mmol, 1 eq), was added and then continuously stirred at rt for 12 h. After completion of the reaction, the solution was transferred to a separating funnel with EtOAc (25 mL) and washed with aqueous $NaHCO_3$ (25 mL). The aqueous layer was extracted with EtOAc (25 mL). The combined organic layer was dried over Na_2SO_4 and the solvent was then evaporated under reduced pressure. Crude residue was purified by column chromatography (4% EtOAC/PE) to get white solid pure product. Yield: 163.73 mg (70 %). **M.P.:** 225.0 °C;**^{1}H NMR** (400 MHz, $CDCl_3$) δ 8.12 (s, 1H), 7.97 (t, *J* = 1.4 Hz, 1H), 7.67 (dd, *J* = 2.6, 1.3 Hz, 1H), 7.62 – 7.60 (m, 1H), 7.57 (d, *J* = 8.8 Hz, 2H), 7.47 (d, *J* = 8.8 Hz, 2H), 4.01 (t, *J* = 6.5 Hz, 2H), 3.92 (s, 3H), 1.80 (p, *J* = 6.6 Hz, 2H), 1.46 – 1.36 (m, 4H), 0.93 (t, *J* = 7.1 Hz, 3H). **^{13}C NMR** (101 MHz, $CDCl_3$) δ 166.29, 164.75, 159.75, 136.91, 136.21, 132.14, 131.79, 121.93, 119.24, 118.97, 118.31, 117.47, 68.74, 52.61, 28.84, 28.18, 22.49, 14.10. **IR (Neat, ν/cm^{-1}):** 3726, 3262, 3014, 2962, 2230, 1738, 1656, 1588, 1216, 1099; **HRMS (ESI):** Calculated for $C_{20}H_{22}BrNO_4H^+$ $(M+H)^+$: 420.0805; Found: 420.0778.

Methyl 3-(pentyloxy)-5-(*p*-tolylcarbamoyl) benzoate (4c): In a 20 mL round bottom flask, **3**

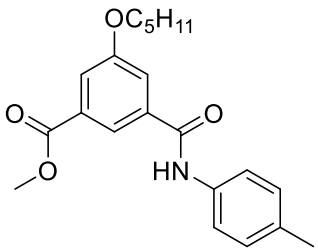

(150 mg, 0.563 mmol, 1 eq) was dissolved in DMF (2 mL). To the clear solution EDC.HCl (131.17 mg, 0.845 mmol , 1.5eq), HOBt (191.33 mg, 0.676 mmol, 1.2 eq) and Triethyl amine (94 µL, 0.676 mmol, 1.2 eq), was added and the solution was stirred at rt for 15 min. p-toluidine (60.36 mg, 0.563 mmol, 1 eq), was added and then continuously stirred at rt for 12 h. After the reaction completion, the solution was transferred to a separating funnel with EtOAc (25 mL) and washed with aqueous $NaHCO_3$ (25 mL). The aqueous layer was extracted with EtOAc (25 mL).Combined organic layer was dried over Na_2SO_4 and the solvent was then evaporated under reduced pressure. Crude residue was further purified by column chromatography (4% EtOAC/PE) to get white solid pure product. Yield:

156.81 mg (68 %). **M.P.:** 236.0 °C; **^{1}H NMR** (400 MHz, $CDCl_3$) δ 8.00 (t, *J* = 1.4 Hz, 1H), 7.88 (s, 1H), 7.70 (dd, *J* = 2.6, 1.3 Hz, 1H), 7.66 (dd, *J* = 2.4, 1.7 Hz, 1H), 7.53 (d, *J* = 8.4 Hz, 2H), 7.18 (d, *J* = 8.3 Hz, 2H), 4.05 (t, *J* = 6.5 Hz, 2H), 3.95 (s, 3H), 2.35 (s, 3H), 1.86 – 1.77 (m, 2H), 1.48 – 1.36 (m, 4H), 0.94 (t, *J* = 7.1 Hz, 3H). **^{13}C NMR** (101 MHz, $CDCl_3$) δ 166.37, 164.53, 159.76, 136.69, 135.18, 131.80, 129.71, 120.40, 119.17, 118.79, 118.32, 68.73, 52.59, 28.85, 28.19, 22.49, 21.01, 14.10. **IR (Neat, ν/cm^{-1}):** 3726, 3262, 3014, 2962, 2230, 1738, 1656, 1588, 1216, 1099; **HRMS (ESI):** Calculated for $C_{21}H_{25}NO_4H^+$ $(M+H)^+$: 356.1856; Found: 356.1878.

3-(Hydrazinecarbonyl)-5-(pentyloxy)-*N*-(4-(Bromo) phenyl)benzamide (5a): In a 25 mL round bottom flask **4a** (150 mg, 0.366 mmol, 1 eq) was dissolved in methanol (10 mL). Hydrazine monohydrate (356 µL, 7.33 mmol, 20 eq) was added, and the solution was refluxed for 8 hours at 60 °C. After the completion of reaction monitored through TLC, the solvent was evaporated under reduced pressure. The residue was extracted with EtOAc (2 × 20 mL) , washed with brine solution and dried over Na_2SO_4. Solvent was evaporated and crude product was directly used for the next reaction step.

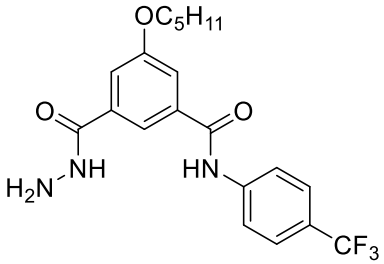

(*E*)-3-(pentyloxy)-5-(2-(pyridin-2-ylmethylene)hydrazine-1-carbonyl)-*N*-(4-(trifluoromethyl)phenyl)benzamide(1a): In a 20 mL round bottom flask, **5a** (150 mg, 0.366 mmol, 1 eq) was dissolved in absolute ethanol (6 mL). picolinaldehyde (35 µL, 0.366 mmol, 1 eq) and acetic acid (2 mL) were added and the solution was stirred at room temperature for 12 hours. The solvent was removed under reduced pressure. The residue was extracted with EtOAc (3 × 20 mL), washed with brine solution and dried over Na_2SO_4. The compound was further purified by column chromatography (1.5% methanol/chloroform). Yield: 111.41 mg (61%), white powder. **M.P.:** 245.0 °C; **^{1}H NMR** (400 MHz, DMSO-d_6) δ 12.18 (s, 1H), 10.72 (s, 1H), 8.63 (d, *J* = 4.7 Hz, 1H), 8.51 (s, 1H), 8.11 (s, 1H), 8.02 (t, *J* = 9.7 Hz, 3H), 7.90 (t, *J* = 7.1 Hz, 1H), 7.75 (d, *J* = 8.7 Hz, 2H), 7.73 (s, 1H), 7.69 (s, 1H), 7.48 – 7.40 (m, 1H), 4.15 (t, *J* = 6.4 Hz, 2H), 1.79 (m, *J* = 6.6 Hz, 2H), 1.51 – 1.31 (m, 5H), 0.92 (t, *J* = 7.1 Hz, 3H). **^{13}C NMR** (101 MHz, DMSO- d_6) δ 165.61 (s), 162.91 (s), 159.16 (s), 153.63 (s), 150.04 (s), 148.96 (s), 143.08 (s), 137.38 (s), 136.66 (s), 135.23 (s),

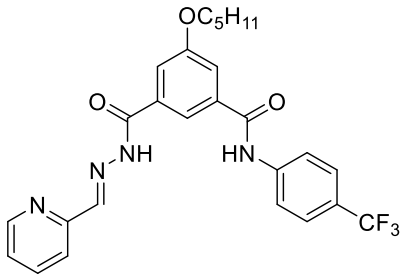

126.35 (t, *J* = 13.5 Hz), 126.09 – 125.78 (m), 124.98 (s), 124.45 (s), 123.49 (s), 120.92 – 120.79 (m), 120.61 (d, *J* = 25.7 Hz), 119.84 (s), 117.33 (d, *J* = 19.9 Hz), 115.07 (s), 68.64 (s), 28.77 (s), 28.17 (s), 22.35 (s), 14.39 (s). **IR (Neat, ν/cm^{-1}):** 3726, 3262, 3014, 2962, 2230, 1738, 1656, 1588, 1216, 1099; **HRMS (ESI):** Calculated for $C_{26}H_{25}F_3N_4O_3H^+$ $(M+H)^+$: 499.1952; Found:499.1957.

***N*-(4-Bromophenyl)-3-(hydrazinecarbonyl)-5-(pentyloxy)benzamide (5b):** In a 25 mL round bottom flask, **4b** (150 mg, 0.356 mmol, 1 eq) was dissolved in absolute methanol (10 mL). Hydrazine monohydrate (346 µL, 7.14 mmol, 20 eq) was added, and the solution was refluxed for 8 hours at 60 °C. After the completion of reaction monitored through TLC, the solvent was evaporated under reduced pressure. The residue was extracted with EtOAc (2 × 20 mL) , washed with brine solution and dried over Na_2SO_4. Solvent was evaporated and crude product was directly used for the next reaction step.

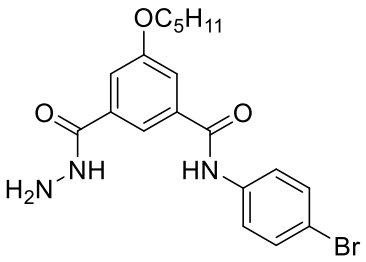

(*E*)-*N*-(4-bromophenyl)-3-(pentyloxy)-5-(2-(pyridin-2-ylmethylene)hydrazine carbonyl)benzamide (1b): In a 20 mL round bottom flask, **5b** (150 mg, 0.357 mmol, 1 eq) was dissolved in absolute ethanol (6 mL). picolinaldehyde (34 µL, 0.357 mmol, 1 eq) and acetic acid(2 mL) were added and the solution was stirred at room temperature for 12 hours. The solvent was removed under reduced pressure. The residue was extracted with EtOAc (3 × 20 mL), washed with brine solution and dried over Na_2SO_4. The compound was purified by column chromatography (3% methanol/dichloromethane). Yield: 141.81 mg (78%), white powder. **M.P.:** 255.0 °C; **^{1}H NMR** (400 MHz, DMSO-d_6) δ 12.12 (s, 1H), 10.46 (s, 1H), 8.59 (d, *J* = 4.4 Hz, 1H), 8.47 (s, 1H), 8.05 (s, 1H), 7.96 (d, *J* = 7.9 Hz, 1H), 7.86 (t, *J* = 7.5 Hz, 1H), 7.74 (d, *J* = 8.8 Hz, 3H), 7.64 (d, *J* = 11.4 Hz, 2H), 7.52 (d, *J* = 8.8 Hz, 2H), 7.42 – 7.34 (m, 1H), 4.09 (t, *J* = 6.3 Hz, 2H), 1.73 (q, *J* = 6.6 Hz, 2H), 1.37 (dp, *J* = 21.0, 7.4, 6.9 Hz, 5H), 0.87 (t, *J* = 7.1 Hz, 4H). **^{13}C NMR** (101 MHz, DMSO-d_6) δ 165.27 , 163.02 , 159.20 , 153.70 , 150.09 , 149.00 , 138.88 , 137.43 , 136.93 , 132.01 , 125.03 , 122.87 , 120.54 , 119.81 , 117.12 , 116.13 , 68.67 , 28.83 , 28.23 , 22.42 , 14.46 . **IR (Neat, ν/cm^{-1}):** 3726, 3262, 3014, 2962, 2230, 1738, 1656, 1588, 1216, 1099; **HRMS (ESI):** Calculated for $C_{25}H_{25}BrN_4O_3H^+$ $(M+H)^+$: 509.1183; Found: 509.1178.

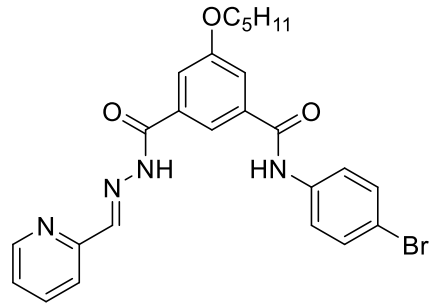

3-(Hydrazinecarbonyl)-5-(pentyloxy)-*N*-(p-tolyl)benzamide(5c): In a 25 mL round bottom flask, **4c** (150 mg, 0.422 mmol, 1 eq) was dissolved in absolute methanol (10 mL). Hydrazine monohydrate (410 µL, 8.44 mmol, 20 eq) was added, and the solution was refluxed for 8 hours at 60 °C. After the completion of reaction monitored through TLC, the solvent was evaporated under reduced pressure. The residue was extracted with EtOAc (2 × 20 mL) , washed with brine solution and dried over Na_2SO_4. Solvent was evaporated and crude product was directly used for the next reaction step.

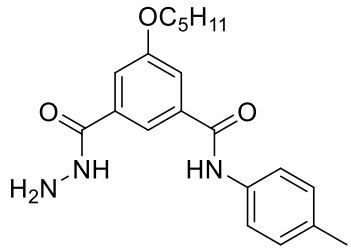

(E)-3-(pentyloxy)-5-(2-(pyridin-2-ylmethylene)hydrazine-1-carbonyl)-N-(p-tolyl)benzamide(1c): In a 25 mL round bottom flask, **5c** (150 mg, 0.422 mmol, 1 eq) was dissolved in absolute ethanol (6 mL). picolinaldehyde (40 µL, 0.422 mmol, 1 eq) and acetic acid(2 mL) were added and the solution was stirred at room temperature for 12 hours. The solvent was removed under reduced pressure. The residue was extracted with ethylacetate (3 × 20 mL), washed with brine solution and dried over Na_2SO_4. Compound was further purified by column chromatography (1.5% methanol/dichloromethane). Yield: 167.68 mg (78%), white powder. **M.P.:** 236.0 °C; **^{1}H NMR** (400 MHz, DMSO-d_6) δ 12.15 (s, 1H), 10.30 (s, 1H), 8.63 (d, *J* = 4.4 Hz, 1H), 8.51 (s, 1H), 8.09 (s, 1H), 8.00 (d, *J* = 7.9 Hz, 1H), 7.90 (t, *J* = 7.5 Hz, 1H), 7.69 (d, *J* = 9.0 Hz, 2H), 7.66 (s, 2H), 7.47 – 7.41 (m, 1H), 7.19 (s, 1H), 7.16 (s, 1H), 4.14 (t, *J* = 6.3 Hz, 2H), 1.78 (q, *J* = 6.6 Hz, 2H), 1.42 (ddd, *J* = 27.0, 14.8, 7.5 Hz, 4H), 0.92 (t, *J* = 7.1 Hz, 3H). **^{13}C NMR** (101 MHz, DMSO-d_6) δ 164.95, 153.72, 150.10, 148.96, 137.45, 137.29, 136.94, 133.39, 129.57, 125.04, 121.03, 120.53, 119.76, 117.26, 116.93, 68.66, 28.84, 28.24, 22.43, 21.05, 14.48. **IR (Neat, ν/cm^{-1}):** 3726, 3262, 3014, 2962, 2230, 1738, 1656, 1588, 1216, 1099; **HRMS (ESI):** Calculated for $C_{26}H_{28}N_4O_3H^+$ $(M+H)^+$: 445.2234; Found:445.2278.

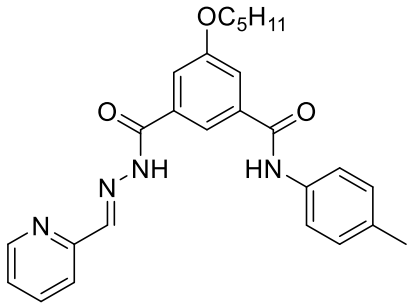

(E)-3-(2-benzylidenehydrazine-1-carbonyl)-5-(pentyloxy)-N-(4-(trifluoromethyl)phenyl)benzamide(1d):

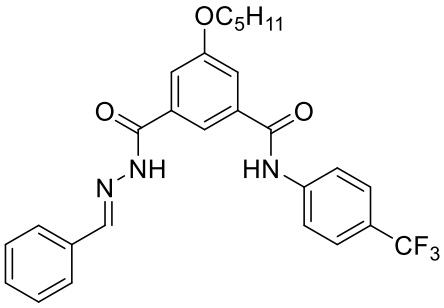

In a 25 mL round bottom flask, **5a** (150 mg, 0.422 mmol, 1 eq) was dissolved in absolute ethanol (6 mL). Benzaldehyde (40 µL, 0.422 mmol, 1 eq) and acetic acid (2 mL) were added and the solution was stirred at room temperature for 12 hours. The solvent was removed under reduced pressure. The residue was extracted with ethyl acetate (3 × 20 mL), washed with brine solution and dried over Na_2SO_4. Compound was further purified by column chromatography (1.5% methanol/dichloromethane). Yield: 167.68 mg (78%), white powder. **M.P.:** 212.0 °C**;** **^{1}H NMR** (400 MHz, DMSO-d_6) δ 11.98 (s, 1H), 10.71 (s, 1H), 8.49 (s, 1H), 8.10 (s, 1H), 8.03 (d, *J* = 8.5 Hz, 2H), 7.75 (d, *J* = 8.2 Hz, 4H), 7.69 (d, *J* = 12.0 Hz, 2H), 7.47 (q, *J* = 4.8 Hz, 3H), 4.14 (t, *J* = 6.4 Hz, 2H), 1.79 (p, *J* = 6.6 Hz, 2H), 1.50 – 1.32 (m, 5H), 0.92 (t, *J* = 7.1 Hz, 3H). **^{13}C NMR** (101 MHz, DMSO-d_6) δ 162.69, 159.13 , 148.73 , 143.09 , 136.60 , 135.46 , 134.69 , 130.67 , 129.33 , 127.63 , 126.45 , 126.41 , 120.72 , 119.80 , 117.26 , 117.13 , 68.61 , 28.78 , 28.17 , 22.36 , 14.40 . **IR (Neat, ν/cm^{-1}):** 3726, 3262, 3014, 2962, 2230, 1738, 1656, 1588, 1216, 1099; **HRMS (ESI):** Calculated for $C_{26}H_{25}F_3N_4O_3H^+$ $(M+H)^+$: 499.1952; Found: 499.1957.

3.4.4. Anion binding studies

^{1}H NMR titration was carried out at room temperature on Bruker 400 MHz spectrometer. The residual solvent signal (CD_3CN, δ_H = 1.94) was considered as an internal reference to calibrate spectra. Both the TBACl salt and receptor were dried in high vacuum before use. The titrations were performed by addition of aliquots from the tetrabutylammonium chloride (TBACl) solution (1 M in CD_3CN) to the solution of either **1b** (0.005 M in CD_3CN) or **2b** (0.005 M in CD_3CN). All NMR data were processed using MestReNova 6.0 and collected data were fitted in different binding modes using BindFit v0.5.

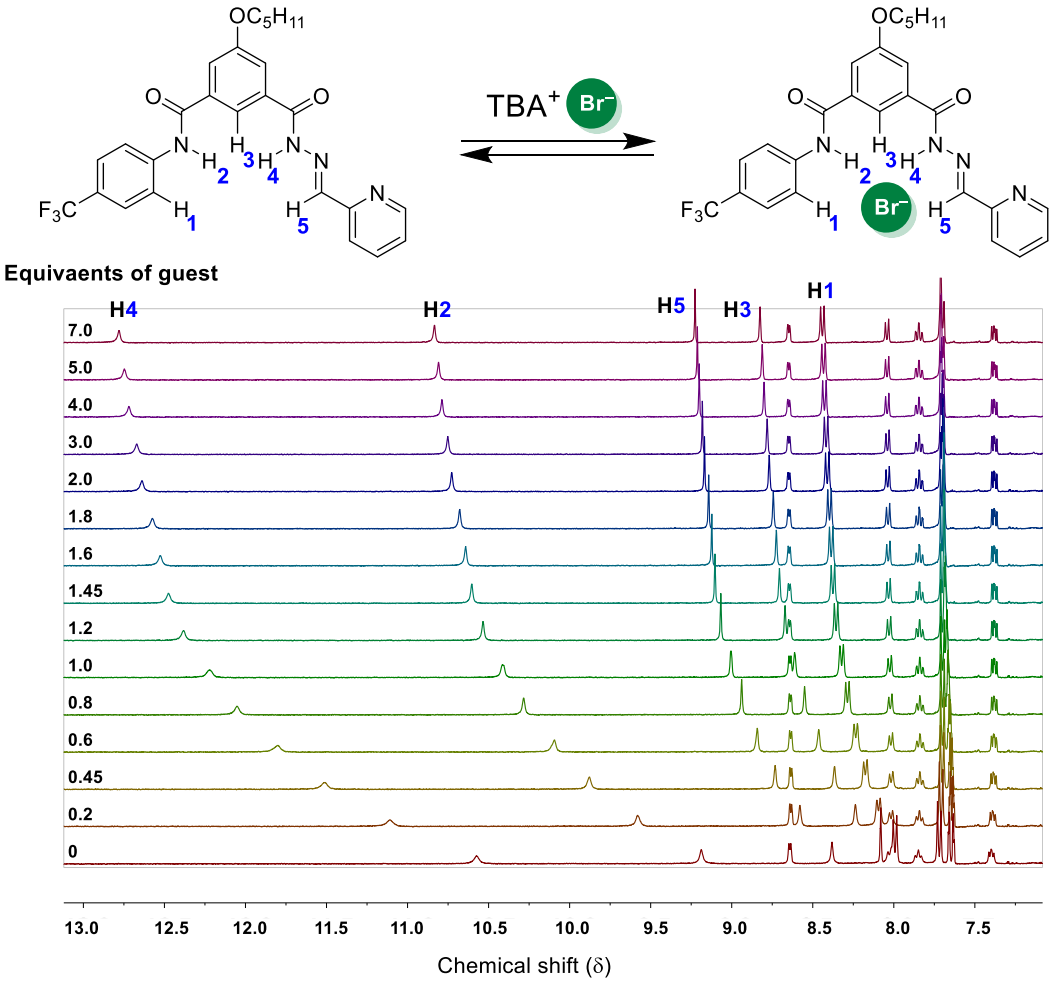

Figure 3.19. ^{1}H NMR titration spectra for **1a** (5 mM) with stepwise addition of TBABr in CD_3CN. The equivalents of added TBABr are shown on the stacked spectra.

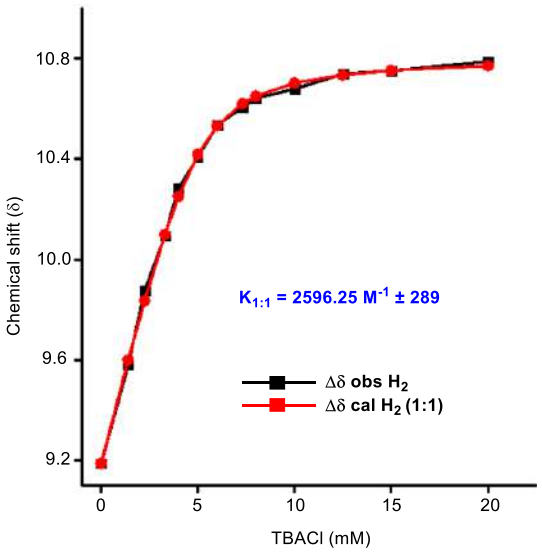

Figure 3.20. The plot of chemical shift (δ) of H_2 protons *vs* concentration of TBACl added, fitted to 1:1 binding model of BindFit v0.5.

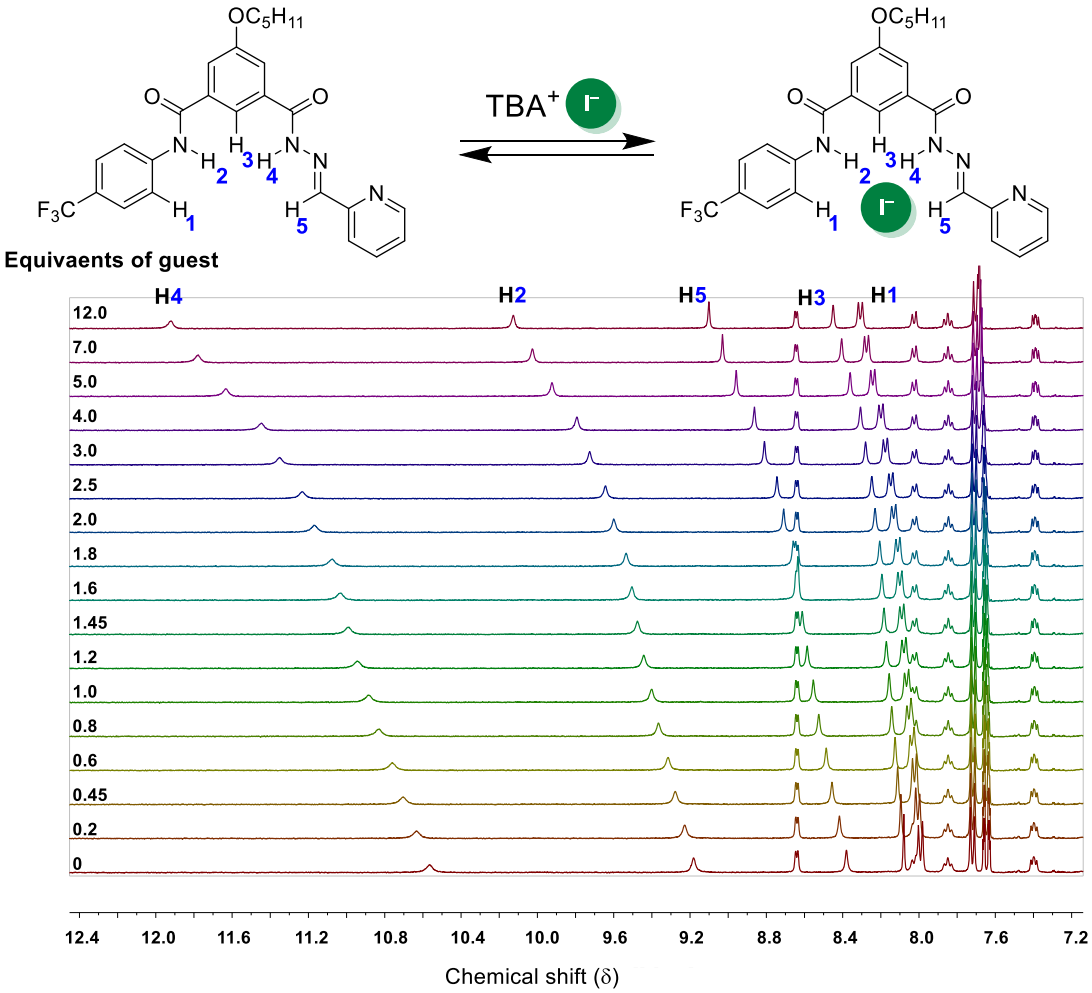

Figure 3.21. ^{1}H NMR titration spectra for **1a** (5 mM) with stepwise addition of TBAI in CD_3CN. The equivalents of added TBAI are shown on the stacked spectra.

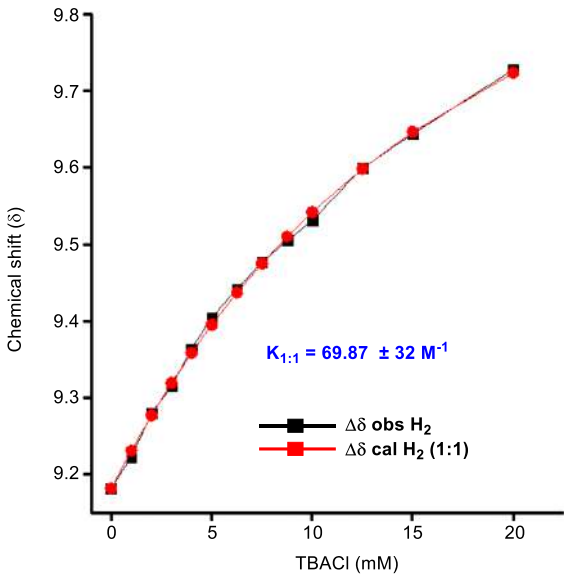

Figure 3.22. The plot of chemical shift (δ) of H_2 protons *vs* concentration of TBACl added, fitted to 1:1 binding model of BindFit v0.5.

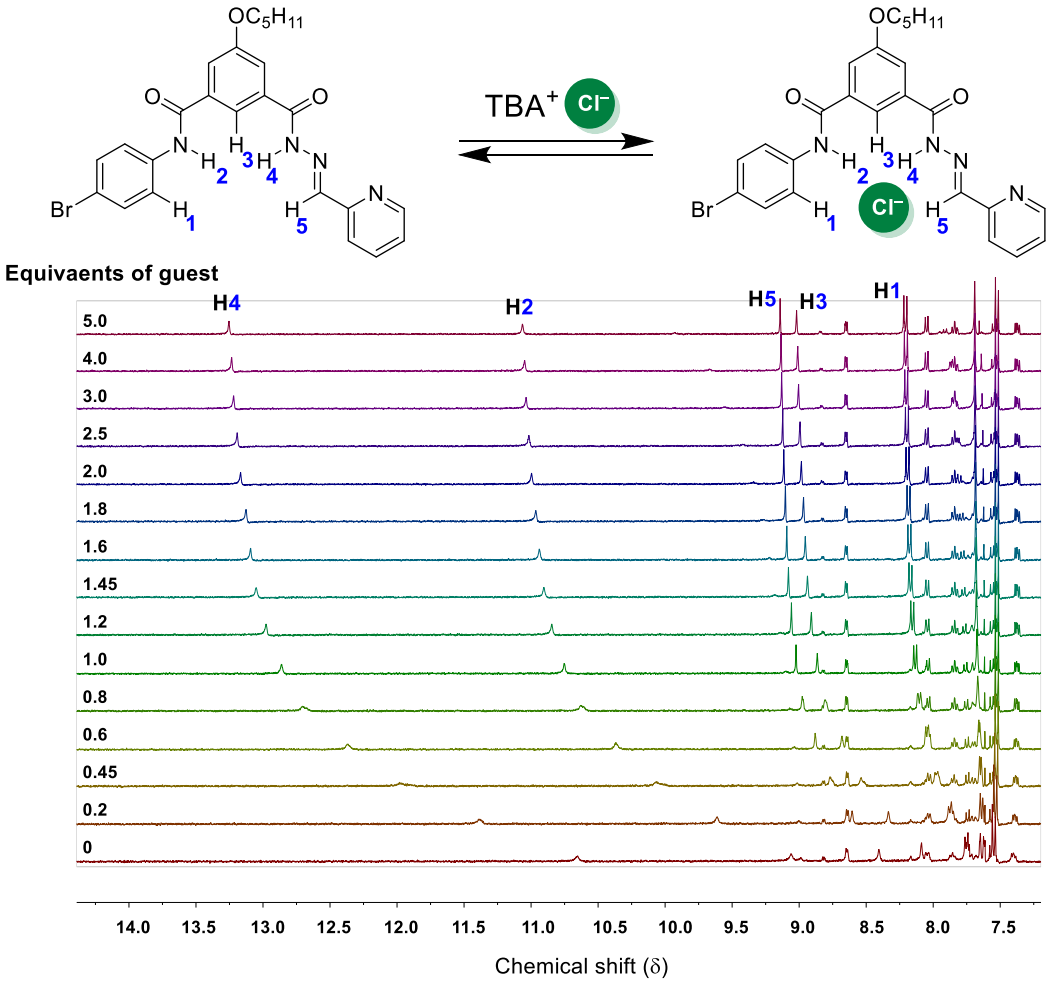

Figure 3.23. ^{1}H NMR titration spectra for **1b** (5 mM) with stepwise addition of TBACl in CD_3CN. The equivalents of added TBACl are shown on the stacked spectra.

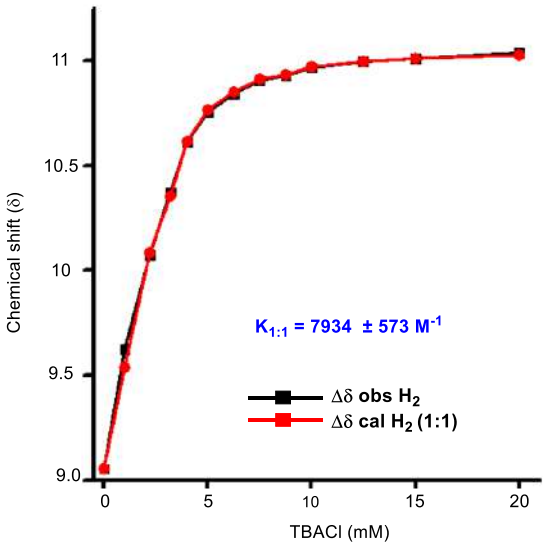

Figure 3.24. The plot of chemical shift (δ) of H_2 protons *vs* concentration of TBACl added, fitted to 1:1 binding model of BindFit v0.5.

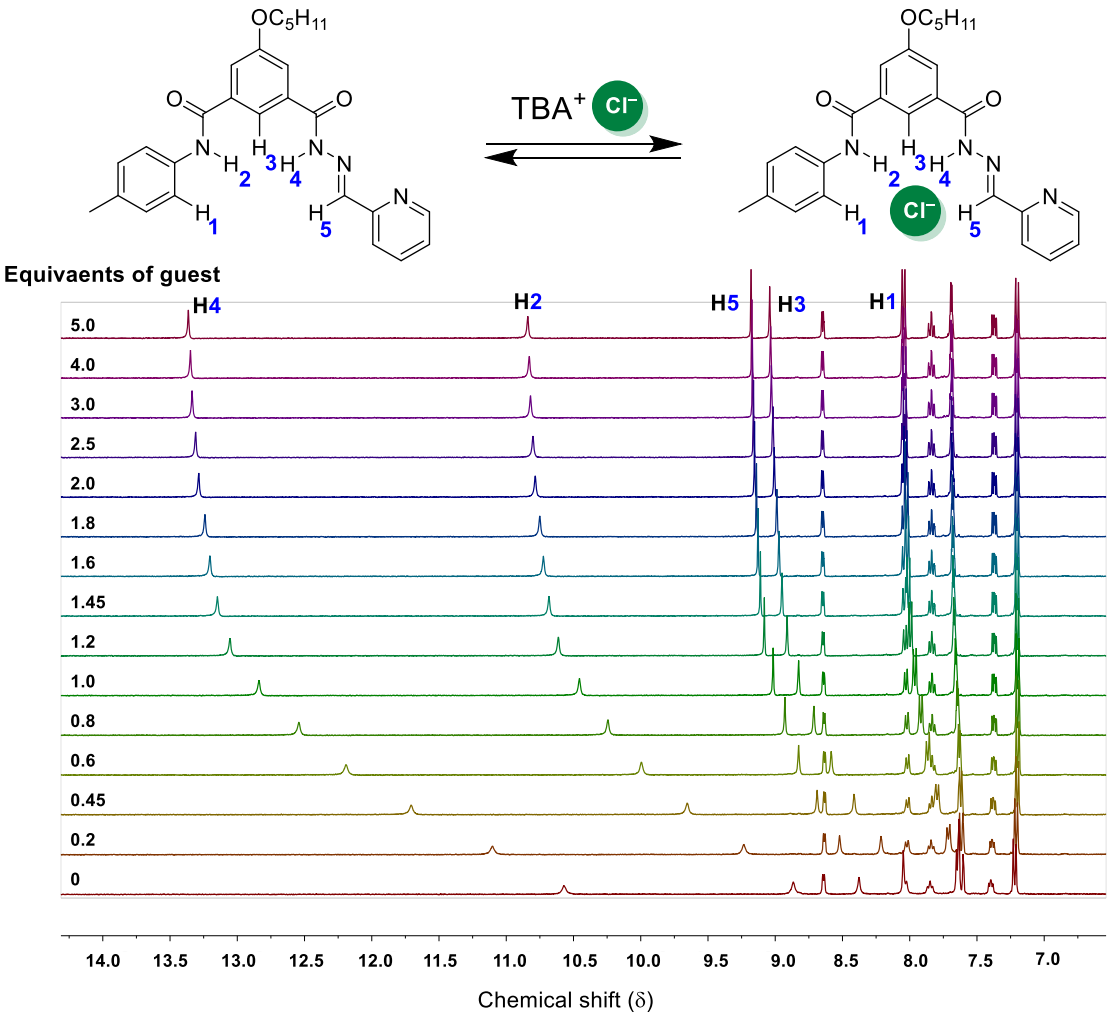

Figure 3.25. ^{1}H NMR titration spectra for **1c** (5 mM) with stepwise addition of TBACl in CD_3CN. The equivalents of added TBACl are shown on the stacked spectra.

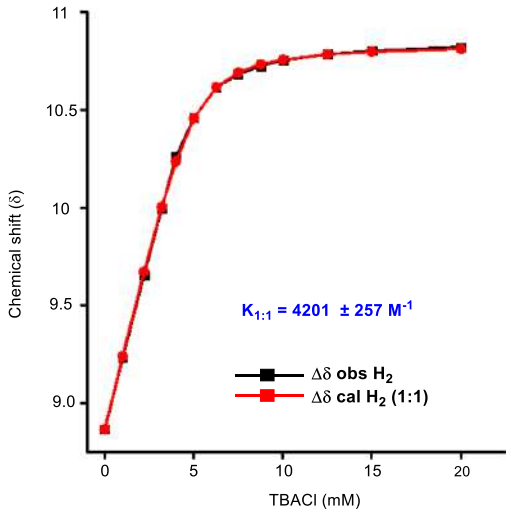

Figure 3.26. The plot of chemical shift (δ) of H_2 protons *vs* concentration of TBACl added, fitted to 1:1 binding model of BindFit v0.5.

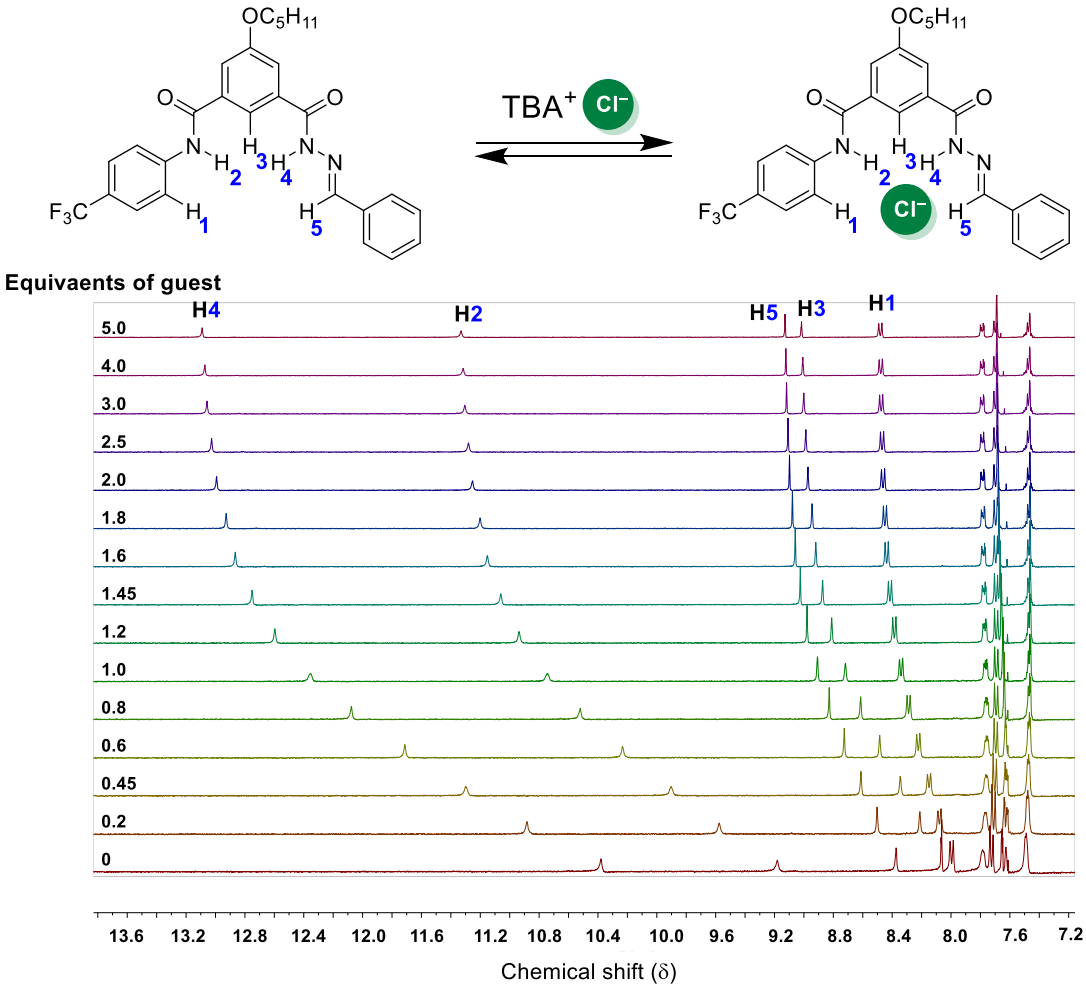

Figure 3.27. ^{1}H NMR titration spectra for **1d** (5 mM) with stepwise addition of TBACl in CD_3CN. The equivalents of added TBACl are shown on the stacked spectra.

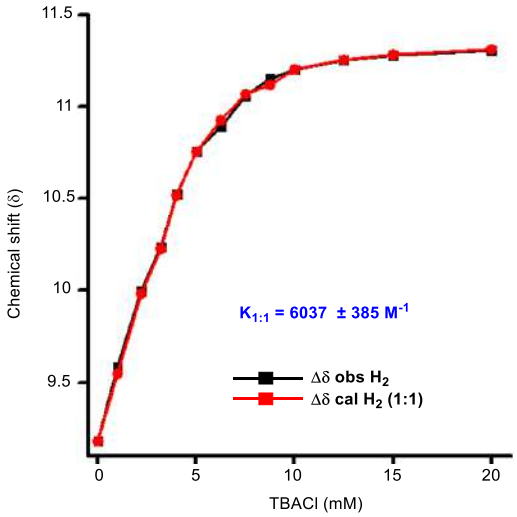

Figure 3.28. The plot of chemical shift (δ) of H_2 protons *vs* concentration of TBACl added, fitted to 1:1 binding model of BindFit v0.5.

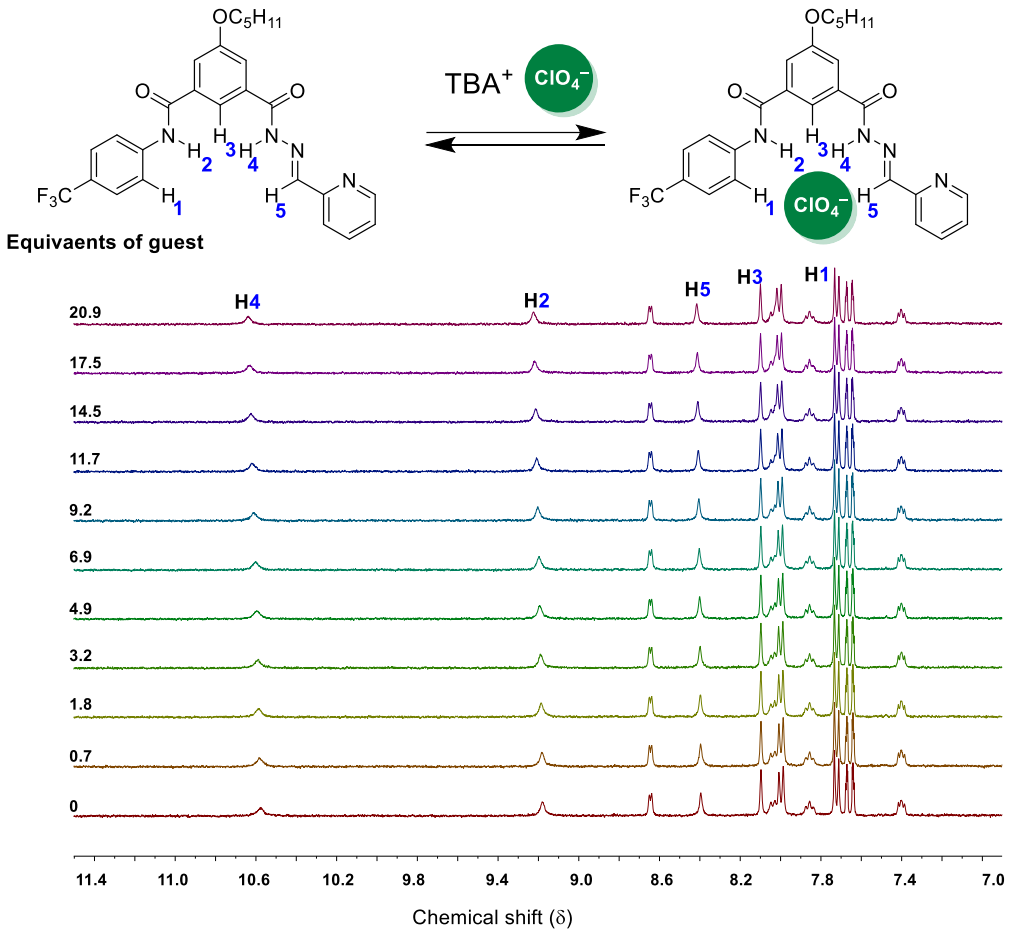

Figure 3.29. ^{1}H NMR titration spectra for **1a** (5 mM) with stepwise addition of $TBAClO_4$ in CD_3CN. The equivalents of added $TBAClO_4$ are shown on the stacked spectra.

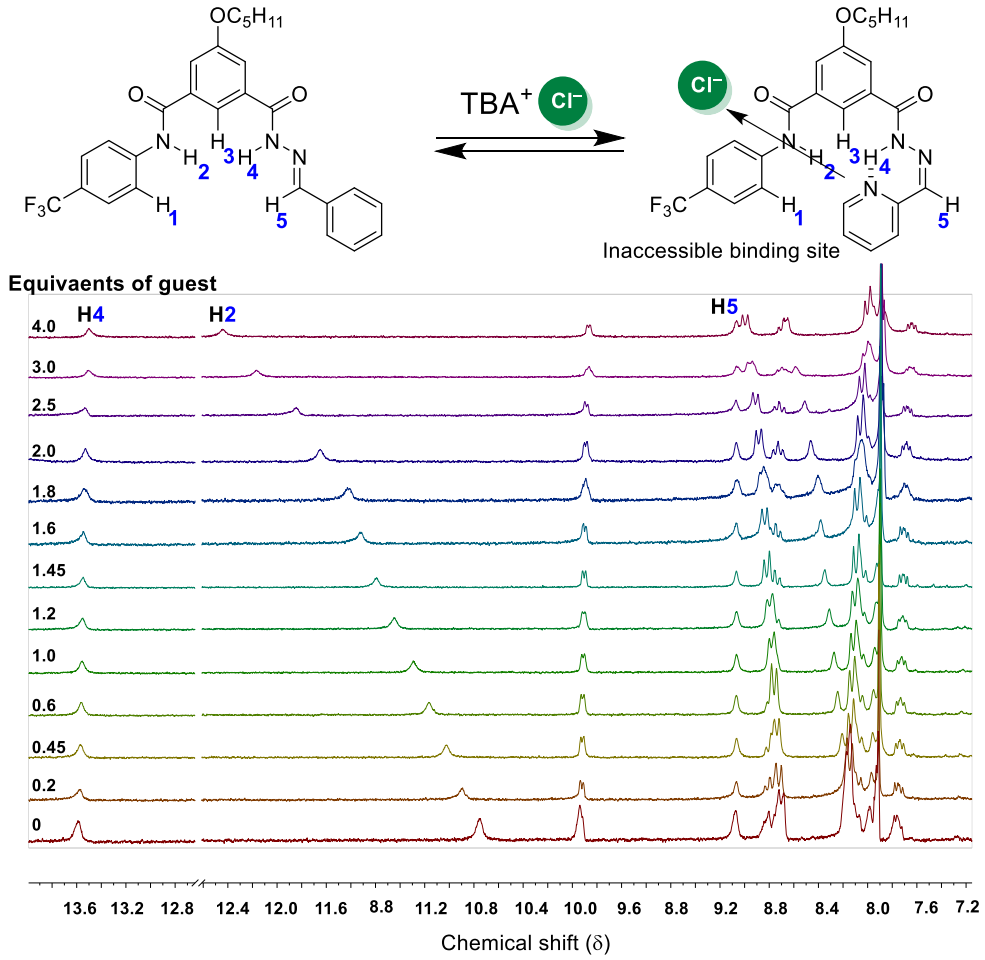

Figure 3.30. ^{1}H NMR titration spectra for **1a** (*cis*) (5 mM) with stepwise addition of TBACl in CD_3CN. The equivalents of added TBACl are shown on the stacked spectra.

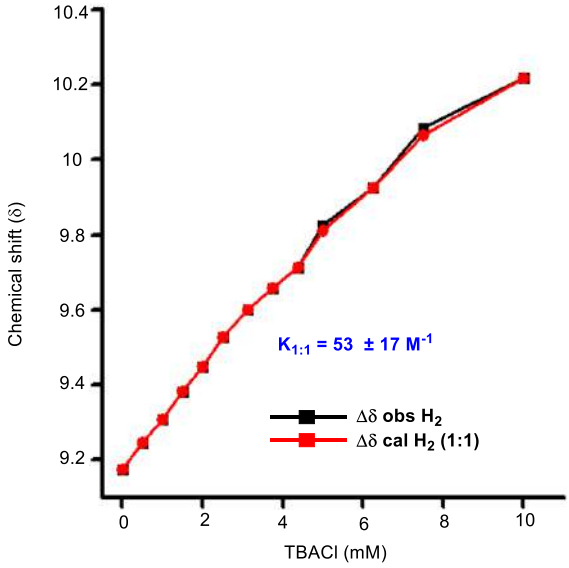

Figure 3.31. The plot of chemical shift (δ) of H_2 protons *vs* concentration of TBACl added, fitted to 1:1 binding model of BindFit v0.5.

3.4.5. Ion transport studies

3.4.5.1. Dose-dependent ion transport activity across HPTS-based vesicles

The dose-dependent ion transport studies of the compounds **1a-1d** across EYPC-LUVs⊃HPTS was performed following the same procedure reported in the chapter 2.

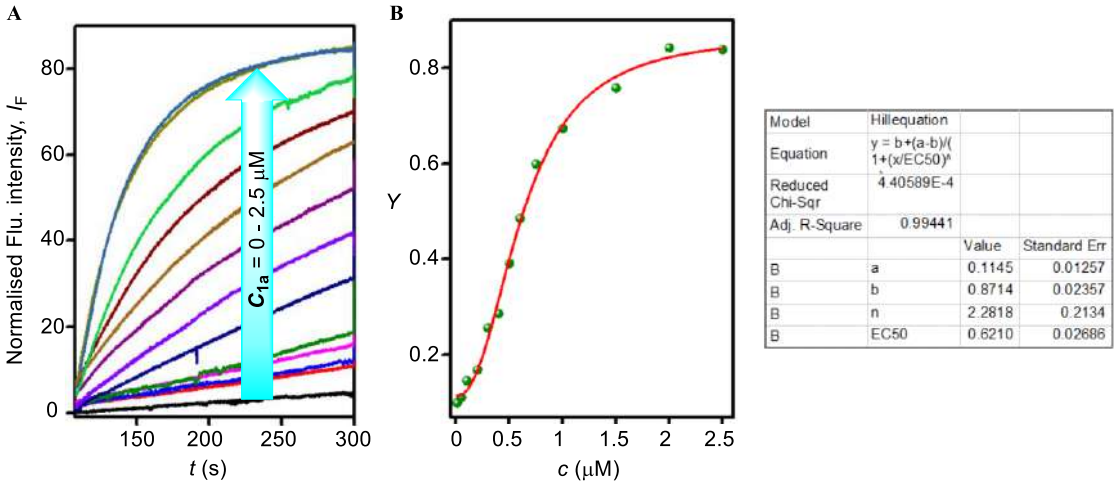

Model	Hillequation		
Equation	y = b+(a-b)/(1+(x/EC50)^		
Reduced Chi-Sqr	4.40589E-4		
Adj. R-Square	0.99441		
		Value	Standard Err
B	a	0.1145	0.01257
B	b	0.8714	0.02357
B	n	2.2818	0.2134
B	EC50	0.6210	0.02686

Figure 3.32. Concentration dependent activity of **1a** across EYPC-LUVs⊃HPTS (**A**). Dose-response plot of **1a** at 280 s after addition of compound (**B**).

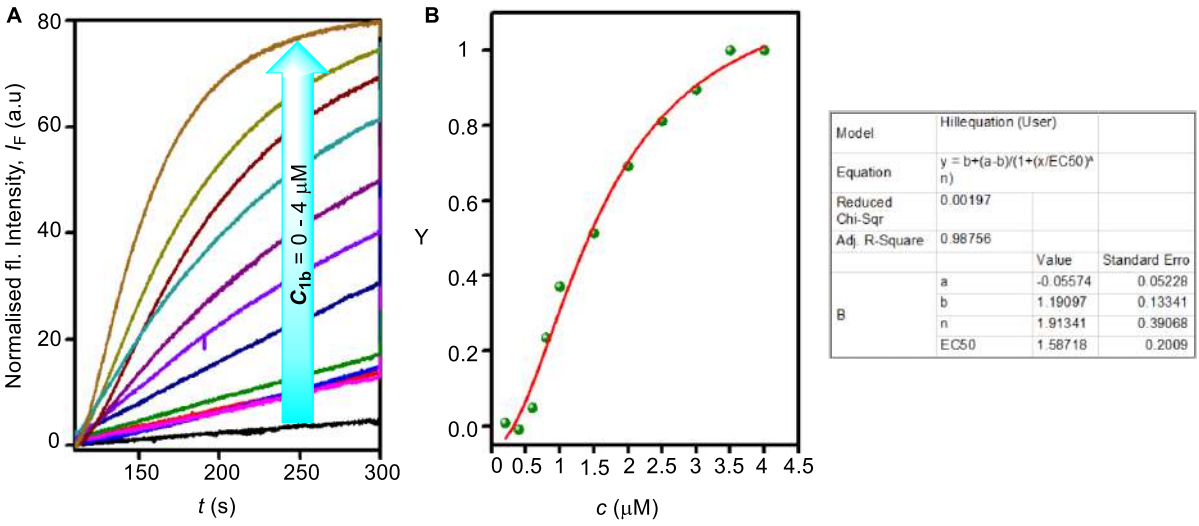

Model	Hillequation (User)		
Equation	y = b+(a-b)/(1+(x/EC50)^n)		
Reduced Chi-Sqr	0.00197		
Adj. R-Square	0.98756		
		Value	Standard Erro
B	a	-0.05574	0.05228
	b	1.19097	0.13341
	n	1.91341	0.39068
	EC50	1.58718	0.2009

Figure 3.33. Concentration dependent activity of **1b** across EYPC-LUVs⊃HPTS (**A**). Dose-response plot of **1b** at 280 s after addition of compound (**B**).

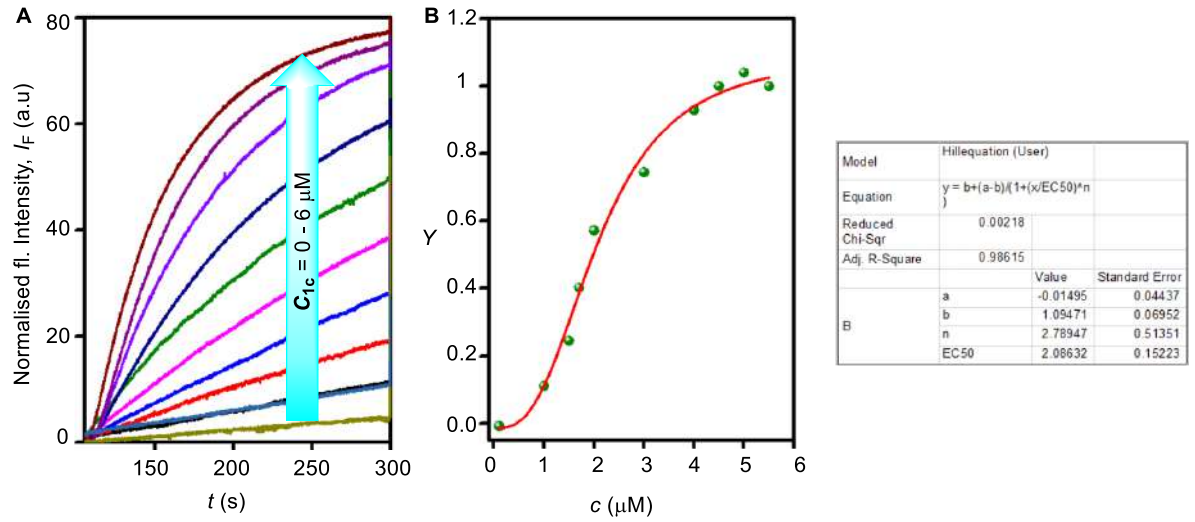

Figure 3.34. Concentration dependent activity of **1c** across EYPC-LUVs⊃HPTS (**A**). Dose-response plot of **1c** at 280 s after addition of compound (**B**).

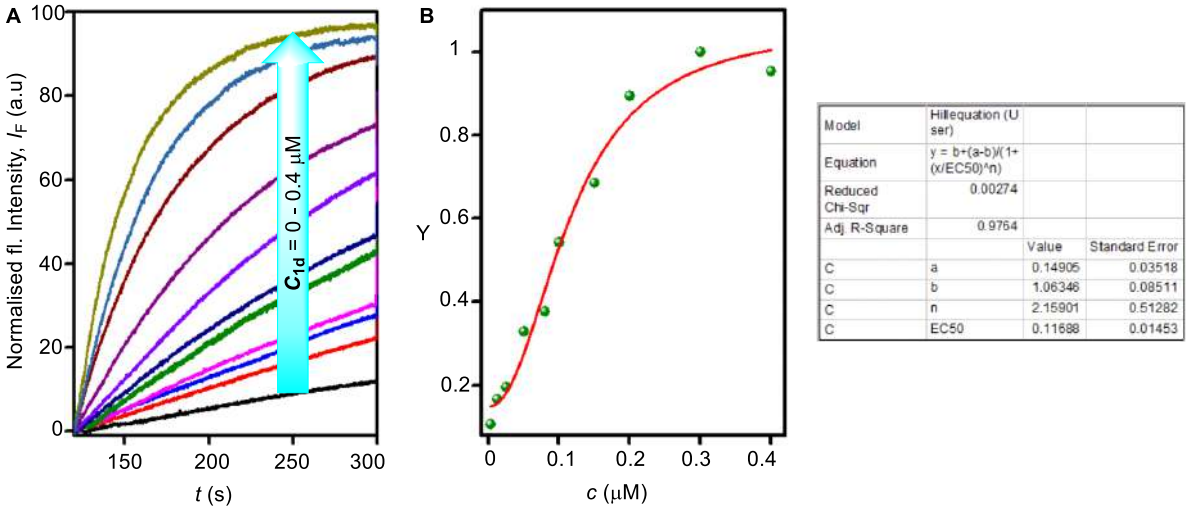

Figure 3.35. Concentration dependent activity of **1d** across EYPC-LUVs⊃HPTS (**A**). Dose-response plot of **1d** at 280 s after addition of compound (**B**).

3.4.5.2. Dose-dependent ion transport activity across EYPC-LUVs⊃lucigenin

The dose-dependent ion transport studies of the compounds **1a-1d** across EYPC-LUVs⊃lucigenin was performed following the same procedure reported in the chapter 2.

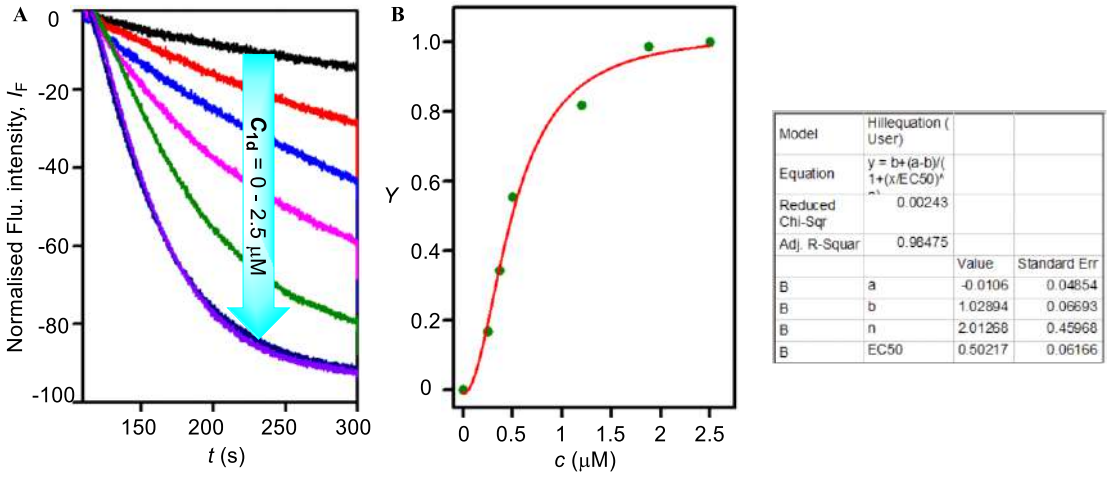

Figure 3.36. Concentration dependent activity of **1d** across EYPC-LUVs⊃lucigenin (**A**). Dose-response plot of **1d** at 280 s after addition of compound (**B**).

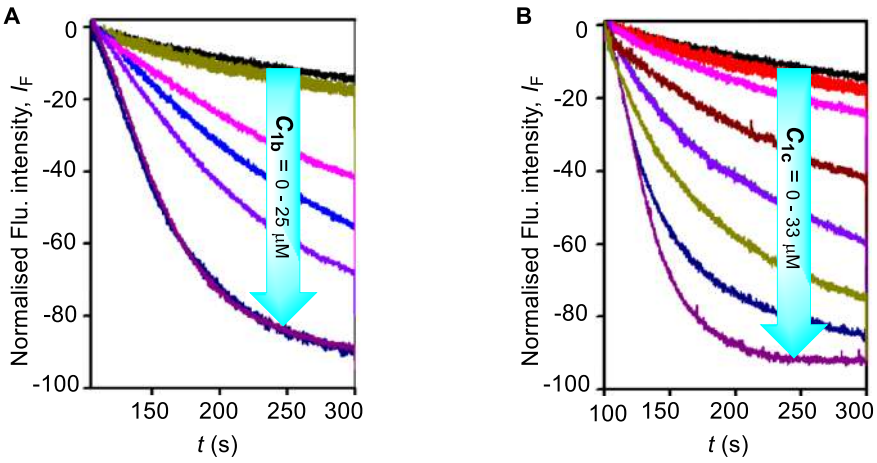

Figure 3.37. Concentration dependent activity of **1b** (**A**) and **1c** (**B**) across EYPC-LUVs⊃lucigenin.

3.4.6. Photo isomerisation studies

3.4.6.1. ^{1}H NMR studies

***trans* to *cis* Isomerization:** For monitoring the *trans* to *cis* isomerization by ^{1}H NMR, either a sample of **1a**, **1b**, **1c**, **1d** (4.0×10^{-3} M) in CD_3CN was prepared in an NMR tube and then irradiated at λ = 365 nm using UV tubes (3 × 3 Watt) for 30 min and then the ^{1}H NMR data before and after photoirradiation were compared. The *trans* to *cis* ratio after photo-irradiation for **1a**, **1b**, **1c**, and **1d** were 15:85, 10:90, 17:83, and 62:38 respectively.

3.4.6.2. UV-Vis studies

Photoisomerization of compounds **1a**, **1b**, **1c** and **1d** were carried out in CH_3CN. Initially, stock solutions of these compounds (2 mM in CH_3CN) were prepared in different vials, and covered with an aluminium foil.

In a 2 mL UV cuvette, was placed either 1900 μL of CH_3CN and 100 μL of either **1a**, **1b**, **1c** or **1d** (2 mM in CH_3CN) was added to get the final concentration of 100 μM.

The cuvette was placed in a UV-vis spectrometer and the UV-vis spectrum was recorded.

***trans* to *cis* Isomerization:** Subsequently, each of these samples was irradiated at λ = 312 nm using UV tubes (3 × 3 Watt) for varied time intervals to isomerize the acylhydrazone moiety. After each irradiation, the UV-vis spectrum was recorded.

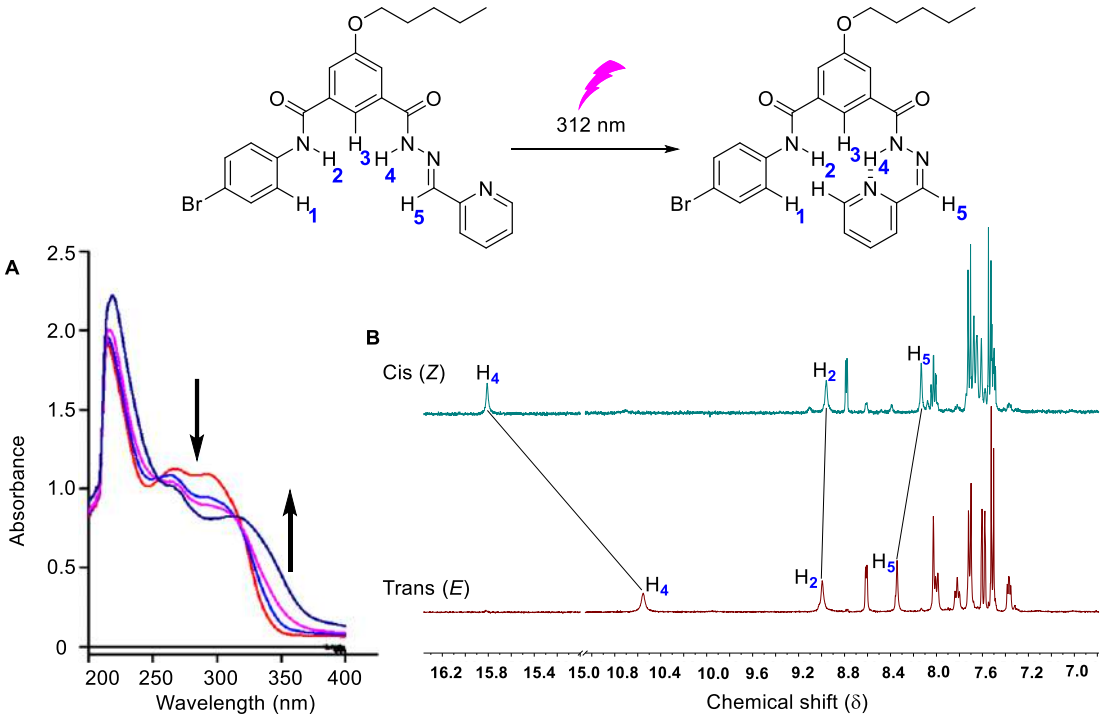

Figure 3.38. UV-visible spectral changes for **1b** (100 μM) upon irradiation with 312 nm using UV tubes (8 × 3 Watt) (**A**). Partial 400 MHz ^{1}H NMR spectrum of **1b** (4.0×10^{-3} M, down) in CD_3CN at 25 °C, and that of photo-irradiated sample of **1b** (up) by 312 nm light for 30 min (**B**).

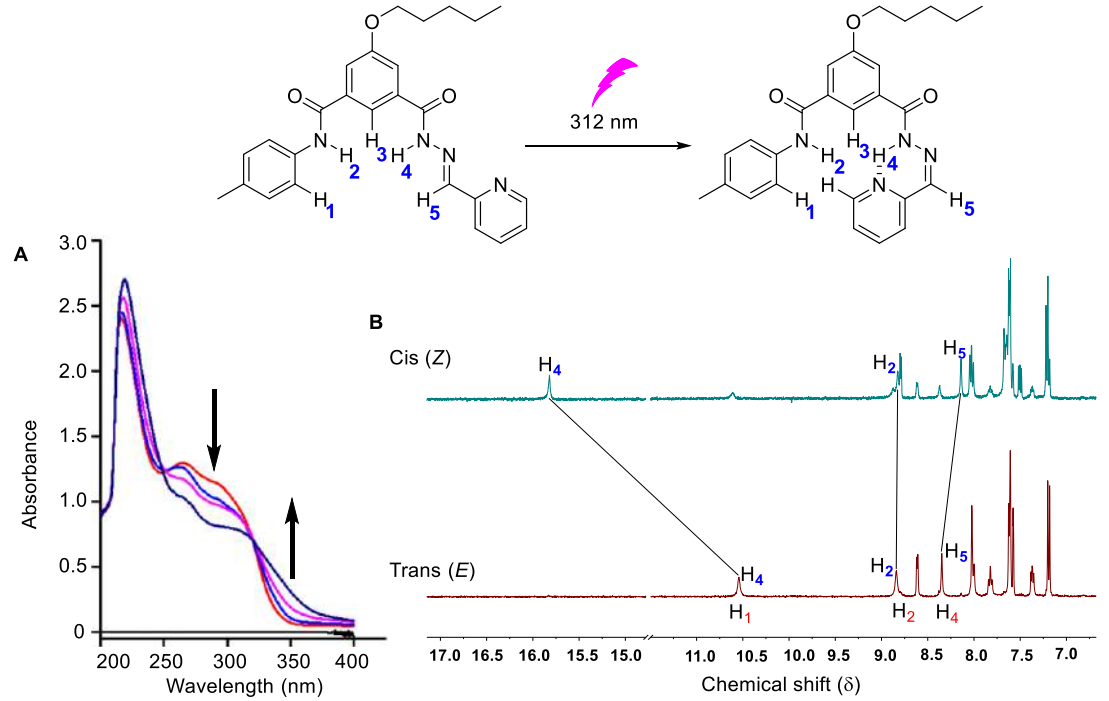

Figure 3.39. UV-visible spectral changes for **1c** (100 μM) upon irradiation with 312 nm light using UV tubes (8 × 3 Watt) (**A**). Partial 400 MHz ^{1}H NMR spectrum of **1c** (4.0×10^{-3} M, down) in CD_3CN at 25 °C, and that of photo-irradiated sample of **1c** (up) by 312 nm light for 30 min (**B**).

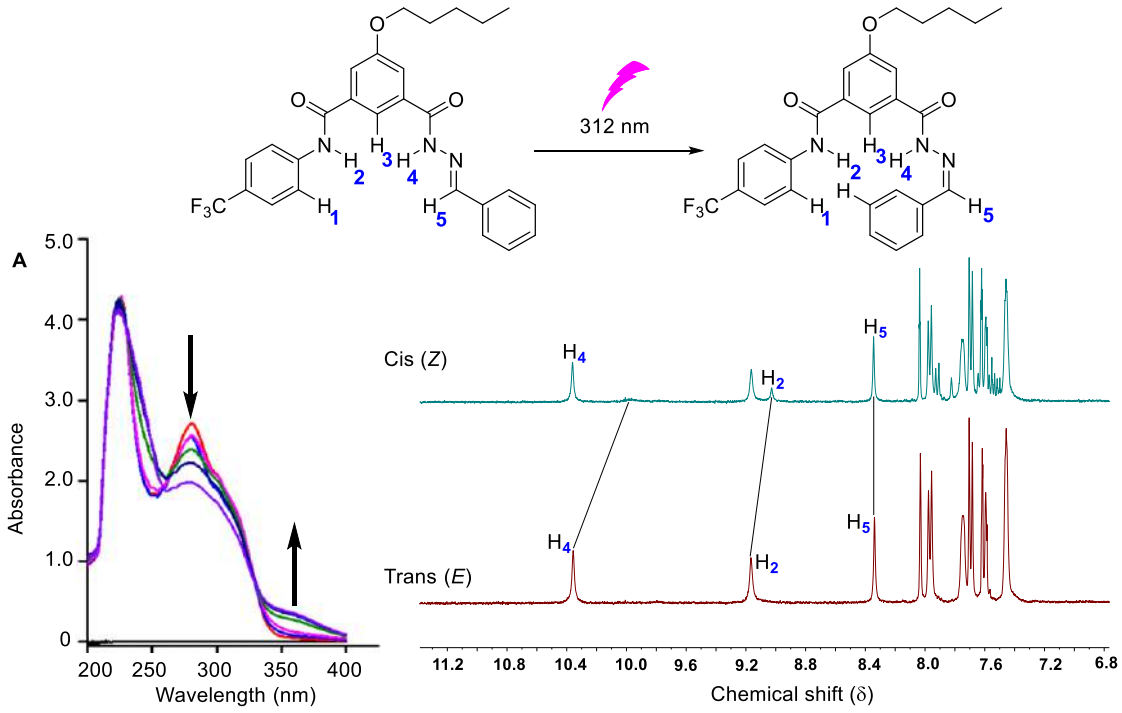

Figure 3.40. UV-visible spectral changes for **1d** (100 μM) upon irradiation with 312 nm light using UV tubes (8 × 3 Watt) (**A**). Partial 400 MHz ^{1}H NMR spectrum of **1d** (4.0×10^{-3} M, down) in CD_3CN at 25 °C, and that of photo-irradiated sample of **1d** (up) by 312 nm light for 30 min (**B**).

3.4.7. Stimuli-Responsive Ion Transport Activity

3.4.7.1. Photo deactivation of ion transport through EYPC-LUVs⊃HPTS assay

The EYPC-LUVs⊃HPTS vesicles were initially prepared. In a clean and dry fluorescence cuvette, 100 mM NaCl (1975 µL) and EYPC-LUVs⊃HPTS (25 µL) were taken. This suspension was placed in a fluorescence instrument with constant stirring. The HPTS fluorescence was monitored at λ_{em} = 510 nm (λ_{ex} = 450 nm) as a course of time. The pH gradient was created by the addition of 2.0 M NaOH (25 µL) at *t* = 20 s followed by the addition of transporter **1a** at *t* = 100 s. The vesicles were eventually lysed using 10% Triton X-100 (25 µL) at *t* = 300 s for the complete destruction of the pH gradient. Initially, the transport activity of the compound **1a** (0.3 µM, using a stock solution of 1 mM in acetonitrile was recorded. Subsequently, the stock sample was irradiated at λ = 312 nm using UV tubes (8 × 3 Watt) for 0 to 30 min to photoisomerize the acylhydrazone subunit, and the transport activity using each photoisomerized sample was recorded at different time intervals. Photoisomerization leads to a substantial decrease in transport activity.

Furthermore, the transport activity of **1a** was monitored by keeping the sample in the dark in the *cis* photoisomerized form. There was no significant increment in the transport activity during this time of 9 h, which showed its better thermal stability.

The time axis was normalized using Equation S1, and fluorescence intensity was normalized using Equation S2.

3.4.7.2. Stimuli-responsive reversible ion transport activity through ISE studies

Preparation of ISE vesicles: A chloroform solution (1 mL) of 1-palmitoyl-2-oleoylphosphatidylcholine (EYPC) (25 mg) was evaporated under reduced pressure to give a thin film. The lipid film was dried under a high vacuum for 4 hours. The thin film was rehydrated by vortexing with a sodium chloride solution (500 mM NaCl, 10 mM phosphate buffer at pH = 7.0). The suspension was subjected to fifteen freeze-thaw cycles and was allowed to age for 1 h at room temperature. The suspension was extruded twenty-three times through a 200 nm polycarbonate membrane using an extruder (Avanti, The Mini-Extruder set) to obtain unilamellar vesicles containing NaCl (500 mM in 10 mM phosphate buffer at pH = 7). Non-encapsulated NaCl salts were removed by dialyzing the vesicles three times in a sodium nitrate solution (500 mM, 10 mM phosphate buffer at pH = 7.0).

Switchable ion transport studies using ion selective electrode

In a glass vial, 50 μL of above lipid solution and 1950 μL of 500 mM $NaNO_3$ were taken with constant stirring conditions using a magnetic stirrer. Transporter molecule **1a** as acetonitrile solution was added at t = 50 s, at t = 250 s, 25 μL of 10% Triton X-100 was added to lyse the vesicles for 100% chloride influx. Initially, the chloride efflux was recorded for **1a** (30 μM) using the stock solution of 5 mM of **1a**. Subsequently, the stock solution was photoirridiated for 30 min using 312 nm UV tubes and ion transport activity was recorded. The ion transport activity of **1a** was greatly reduced upon photoirradiation at 312 nm, likely due to the photoisomerization of **1a-*E*** form to **1a-*Z*** form. Eventually, to this photoisomerized stock solution was added triflic acid (5 equiv.) and the solution was kept for 30 min to get the **1a-*E*** form back. After 30 min, triethylamine (TEA, 5 equiv.) was added to neutralize the solution and the chloride efflux was recorded again. The activity was significantly regained back upon the treatment of acid and base. This process of alternative photoirradiation and acid/base reactivation process was repeated for three cycles. Finally, the value at 50 seconds was set at 0% chloride efflux and the final chloride reading at 250 s was set as 100% chloride efflux. The time axis was normalized using the Equation 5.

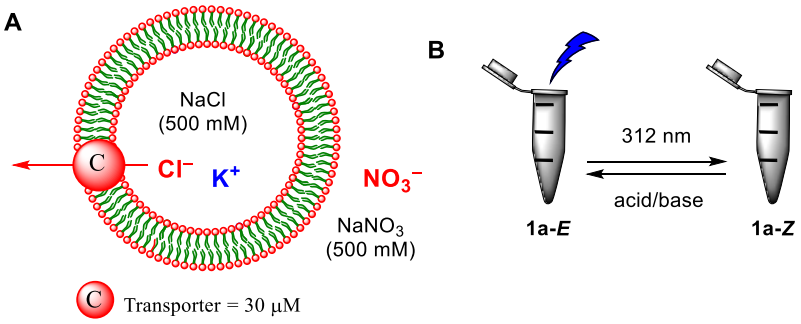

Figure 3.41. Schematic representation of ISE vesicles (**A**). **1a-*E*** to **1a-*Z*** Photoisomerization and acid/base reactivation process of **1a** acetonitrile solution (5 mM). Chloride efflux of **1a** in *E* and *Z* forms (**B**).

3.4.8. X-ray measurement

3.4.8.1. General procedure for crystallization

The solution of *E*-**1a** (10 mg) in acetonitrile was heated with TBACl salt (5 eq.) in a 5 mL of glass vial and then filtered to separate any undissolved component. The solution was then left in a stable place to evaporate slowly. After few days, colourless needle-like crystalline material precipitated from the vial. Suitable crystals were chosen for the X-ray measurement.

3.4.8.2. X-ray Single Crystal Diffraction Analysis

The single-crystal X-ray diffraction (SCXRD) analysis of compound **1a** was performed on a Bruker Smart Apex Duo diffractometer using Mo Kα radiation (λ= 0.71073Å). The crystal structures were solved using intrinsic methods and then refined by full-matrix least-squares against F^2 using all data by using SHELXL-2014/7 built in the Apex-3 package.[24] The crystallographic refinement data for compound **1** are listed in **(Table S1)**. All the non-hydrogen atoms were refined anisotropically if not stated otherwise. Hydrogen atoms were constructed in geometric positions to their parent atoms,[25] Some of the atom positions (CF_3 group) disordered sites and their occupancies were modeled using the different crystallographic constrain commands. The DIAMOND-3.1 software was used to describe the bond length, bond angles and various structural illustrations of compound **1**.

Table 3.2. Crystallographic data for compound **1** at 100 K.

Crystallographic details	**Compound 1**
Chemical formula	$C_{43}H_{62}ClF_3N_4O_4$
Formula weight (g/mol)	791.41
Temperature	100(2)K
Crystal system	Monoclinic
Space group	*P* 2/*n*
a (Å); α (°)	20.366(9); 90
b (Å); β (°)	8.237(4); 110.575(9)
c (Å); γ (°)	27.647(12); 90
V ($Å^3$); Z	4342.(3); 4
ρ (calc.) g cm^{-3}	1.211
μ(Mo K_α) mm^{-1}	0.145
$2\theta_{max}$ (°)	46.5
R(int)	0.2887
Completeness to θ	99.4
Data / param.	6200/494
GOF	1.028
R1 [F>4σ(F)]	0.0987
wR2 (all data)	0.2971
max. peak/hole (e.$Å^{-3}$)	0.995/-0.628

Table 3.3. Crystallographic data for compound **1** at 100 K.

D-H…A	d(D-H)	d(H…A)	d(D-A)	<DHA	Symmetry operations
N(1)-H(1)…Cl(1)	0.8800(4)	2.4576(11)	3.3062(15)	162.127 (75)	x, y, z
N(3)-H(3)…Cl(1)	0.8800(3)	2.4620(9)	3.3151(11)	163.470(45)	x, y, z
C(1)-H(1A)…Cl(1)	0.9500(4)	2.8173(9)	3.6590(13)	148.196(56)	x, y, z
C(12P)-H(12P)…Cl(1)	0.9500(3)	2.5028(7)	3.4454(10)	171.587(50)	x, y, z
C(17P)-H(17P)…Cl(1)	0.9500(4)	2.8074(10)	3.7202(14)	161.406(45)	x, y, z
C(18P)-H(18P)…Cl(1)	0.9500(3)	2.7404(10)	3.5484(12)	143.379(49)	x, y, z

Table 3.4. Selected bond lengths [Å] and angles [°] for compound **1** at 100 K.

Bond length	Bond length	Bond angle	Bond angle
N1-N2: 1.384(7)	C3P-C4P: 1.39	N2-N1-C2: 118.3(6)	H13A-C13C-H13B: 108.0
N1-H1: 0.88	C4P-C5P: 1.39	C2-N1-H1: 120.8	C13C-C14C-H14A: 108.4
N3-C8: 1.381(9)	C5P-H5P: 0.95	C8-N3-C13P: 126.3(5)	C13C-C14C-H14B: 108.4
N3-H3: 0.88	C7P-C8P: 1.39	C13P-N3-H3: 116.8	H14A-C14C-H14B: 107.5
O1-C3: 1.433(12)	C8P-C9P: 1.39	N2-C1-C4P: 121.7(6)	C16C-C15C-H15A: 108.3
O3-C2: 1.183(7)	C9P-C10P: 1.39	C4P-C1-H1A: 119.1	C16C-C15C-H15B: 108.3
C1-H1A: 0.95	C10P-H10P: 0.95	O3-C2-C7P: 123.0(7)	H15A-C15C-H15B: 107.4
C3-C4: 1.525(13)	C12P-H12P: 0.95	O1-C3-C4: 100.6(9)	C15C-C16C-H16A: 109.4
C3-H3B: 0.99	C13P-C18P:1.39	C4-C3-H3A: 111.6	C15C-C16C-H16B: 109.4
C4-H4A: 0.99	C14P-H14P: 0.95	C4-C3-H3B: 111.6	H16A-C16C-H16B: 108.0
C5-C6: 1.513(14)	C15P-H15P: 0.95	C5-C4-C3: 132.7(12)	C18C-C17C-H17A: 108.5
C5-H5B: 0.99	C16P-C9: 1.461(9)	C3-C4-H4A: 104.1	C18C-C17C-H17B: 108.5
C6-H6A: 0.99	C17P-H17P: 0.95	C3-C4-H4B: 104.1	H17A-C17C-H17B: 107.5
C7-H7A: 0.98	N1C-C24C: 1.515(7)	C4-C5-C6: 121.4(12)	C17C-C18C-H18B: 109.5
C7-H7C: 0.98	N1C-C25C: 1.517(7)	C6-C5-H5A: 107.0	C17C-C18C-H18C: 109.5
C1P-C2P: 1.39	C11C-C12C: 1.486(10)	C6-C5-H5B: 107.0	H18B-C18C-H18C: 109.5
C1P-H1P: 0.95	C11C-H11B: 0.98	C7-C6-C5: 106.8(11)	C15C-N2C-C14C: 110.5(3)
C2P-H2P: 0.95	C12C-C13C: 1.515(9)	C5-C6-H6A: 110.4	C15C-N2C-C14C: 111.3(4)
C3P-H3P: 0.95	C12C-H12B: 0.99	C5-C6-H6B: 110.4	C14C-N2C-C14C: 106.7(6)
C5P-C6P: 1.39	C13C-H13A: 0.99	C6-C7-H7A: 109.5	C22C-C21C-H21B: 109.5
C6P-H6P: 0.95	C14C-N2C: 1.520(7)	H7A-C7-H7B: 109.5	C22C-C21C-H21C: 109.5

C7P-C12P: 1.39	C14C-H14B: 0.99	H7A-C7-H7C: 109.5	H21B-C21C-H21C: 109.5
C8P-H8P: 0.95	C15C-N2C: 1.518(7)	O2-C8-N3: 121.9(8)	C21C-C22C-H22A: 109.0
C10P-C11P: 1.39	C15C-H15B: 0.99	N3-C8-C11P: 117.5(6)	C21C-C22C-H22B: 109.0
C11P-C12P: 1.39	C16C-H16A: 0.99	C2P-C1P-H1P: 120.0	H22A-C22C-H22B: 107.8
C13P-C14P: 1.39	C17C-C18C: 1.493(11)	C1P-C2P-C3P: 120.0	C24C-C23C-H23A: 109.5
C14P-C15P: 1.39	C17C-H17B: 0.99	C3P-C2P-H2P: 120.0	C24C-C23C-H23B: 109.5
C15P-C16P: 1.39	C18C-H18B: 0.98	C4P-C3P-H3P: 120.0	H23A-C23C-H23B: 108.1
C16P-C17P: 1.39	N2C-C15C:1.518(7)	C3P-C4P-C5P: 120.0	C23C-C24C-H24A: 108.3
C17P-C18P: 1.39	C21C-C22C: 1.500(9)	C5P-C4P-C1: 118.4(4)	C23C-C24C-H24B: 108.3
C18P-H18P: 0.95	C21C-H21B: 0.98	C6P-C5P-H5P: 120.0	H24A-C24C-H24B: 107.4
N1C-C24C: 1.515(7)	C22C-C23C: 1.505(9)	C5P-C6P-C1P: 120.0	C26C-C25C-H25A: 108.2
N1C-C25C: 1.517(7)	C22C-H22B: 0.99	C1P-C6P-H6P: 120.0	C26C-C25C-H25B: 108.2
C11C-H11A: 0.98	C23C-H23A: 0.99	C8P-C7P-C2: 115.8(4)	H25A-C25C-H25B: 107.4
C11C-H11C: 0.98	C24C-H24A: 0.99	C9P-C8P-C7P: 120.0	C25C-C26C-H26A: 109.8
C12C-H12A: 0.99	C25C-C26C: 1.511(8)	C7P-C8P-H8P: 120.0	C25C-C26C-H26B: 109.8
C13C-C14C: 1.517(8)	C25C-H25B: 0.99	O1-C9P-C8P: 124.9(5)	H26A-C26C-H26B: 108.2
C13C-H13B: 0.99	C26C-H26A: 0.99	C9P-C10P-C11P: 120.0	C26C-C27C-H27A: 109.0
C14C-H14A: 0.99	C27C-C28C: 1.540(9)	C11P-C10P-H10P: 120.0	C26C-C27C-H27B: 109.0
C15C-C16C: 1.510(9)	C27C-H27B: 0.99	C10P-C11P-C8: 116.0(4)	H27A-C27C-H27B: 107.8
C15C-H15A: 0.99	C28C-H28B: 0.98	C11P-C12P-C7P: 120.0	C27C-C28C-H28B: 109.5
C16C-C17C: 1.511(10)	C9-F3': 1.274(16)	C7P-C12P-H12P: 120.0	C27C-C28C-H28C: 109.5
C16C-H16B: 0.99	C9-F1: 1.303(11)	C14P-C13P-N3: 123.2(4)	H28B-C28C-H28C: 109.5
C17C-H17A: 0.99	C9-F3: 1.364(10)	C15P-C14P-C13P: 120.0	F3'-C9-F2': 107.7(13)
C18C-H18A: 0.98	N1-C2: 1.388(8)	C13P-C14P-H14P: 120.0	F1-C9-F3: 107.1(9)
C18C-H18C: 0.98	N2-C1: 1.261(8)	C14P-C15P-H15P: 120.0	F2-C9-C16P: 111.2(8)
N2C-C14C: 1.520(7)	N3-C13P: 1.398(6)	C15P-C16P-C17P: 120.0	F2'-C9-C16P: 122.1(9)
C21C-H21A: 0.98	O1-C9P: 1.371(6)	C17P-C16P-C9: 119.4(5)	F3'-C9-F1': 98.4(12)
C21C-H21C: 0.98	O2-C8: 1.218(9)	C18P-C17P-H17P: 120.0	C16P-C9-F1': 109.3(8)
C22C-H22A: 0.99	C1-C4P: 1.454(7)	C17P-C18P-C13P: 120.0	C27C-C26C-H26B: 109.8
C23C-C24C: 1.504(8)	C2-C7P: 1.476(7)	C13P-C18P-H18P: 120.0	C26C-C27C-C28C: 112.8(6)

C23C-H23B: 0.99	C3-H3A: 0.99	C24C-N1C-C25C: 110.9(3)	C28C-C27C-H27A: 109.0
C24C-H24B: 0.99	C4-C5: 1.252(11)	C24C-N1C-C25C: 110.8(3)	C28C-C27C-H27B: 109.0
C25C-H25A: 0.99	C4-H4B: 0.99	C25C-N1C-C25C: 106.5(6)	C27C-C28C-H28A: 109.5
C26C-C27C: 1.515(9)	C5-H5A: 0.99	C12C-C11C-H11B: 109.5	H28A-C28C-H28B: 109.5
C26C-H26B: 0.99	C6-C7: 1.386 (15)	C12C-C11C-H11C: 109.5	H28A-C28C-H28C: 109.5
C27C-H27A: 0.99	C6-H6B: 0.99	H11B-C11C-H11C: 109.5	F2-C9-F1: 112.4(10)
C28C-H28A: 0.98	C7-H7B: 0.98	C11C-C12C-H12A: 108.7	F2-C9-F3: 104.5(10)
C28C-H28C: 0.98	C8-C11P: 1.480(9)	C11C-C12C-H12B: 108.7	F3'-C9-C16P: 120.1(11)
C9-F2: 1.279(11)	C1P-C6P: 1.39	H12A-C12C-H12B: 107.6	F1-C9-C16P: 112.7(9)
C9-F2': 1.341(16)	C2P-C3P: 1.39	C12C-C13C-H13A: 109.4	F3-C9-C16P: 108.4(7)
C9-F1': 1.490(16)		C12C-C13C-H13B: 109.4	F2'-C9-F1': 92.8(11)

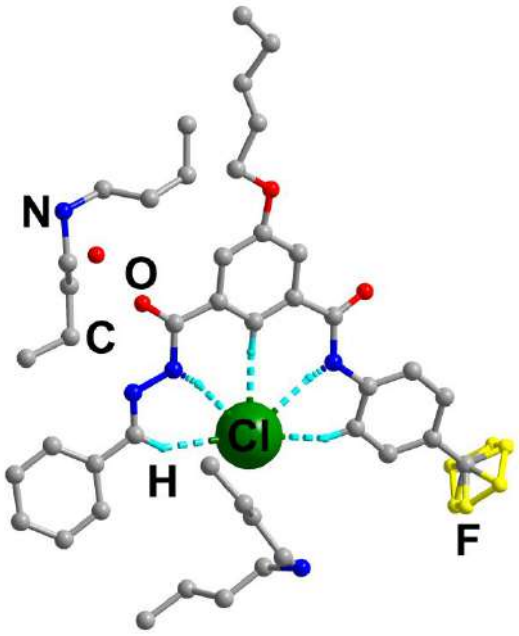

Figure 3.42. The asymmetric unit of **1a** (Here the H-atoms are removed for structure clarity).

3.5. NMR Spectra

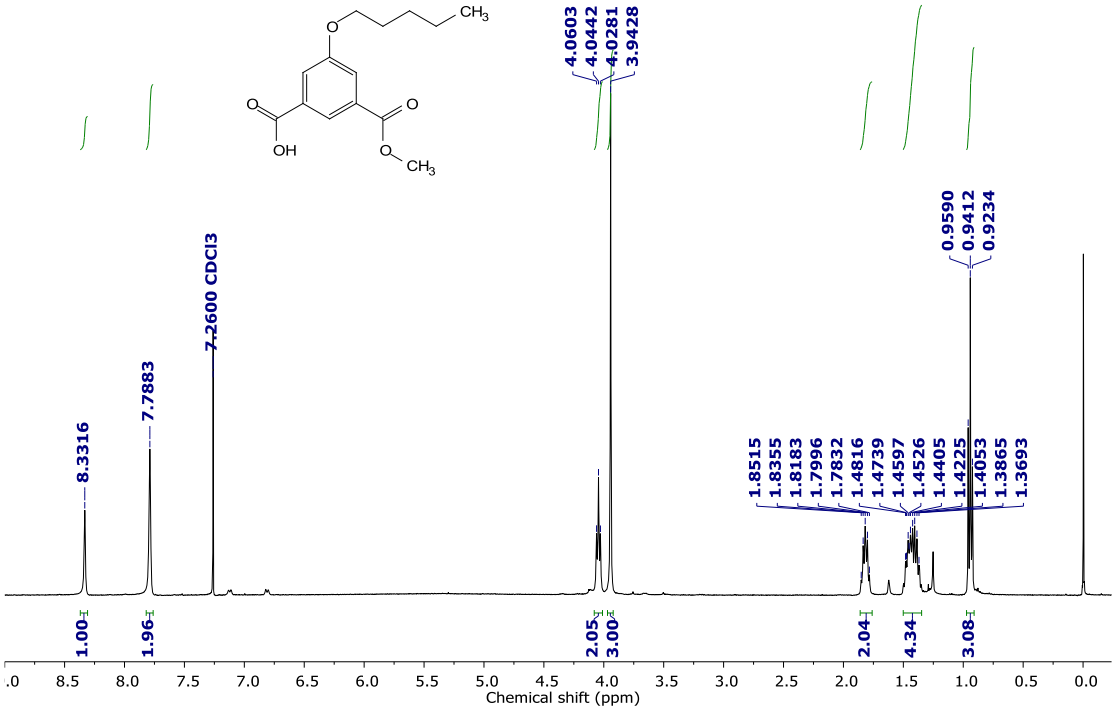

Figure 3.43. ^{1}H NMR spectrum (400 MHz) of **3** in $CDCl_3$ at room temperature.

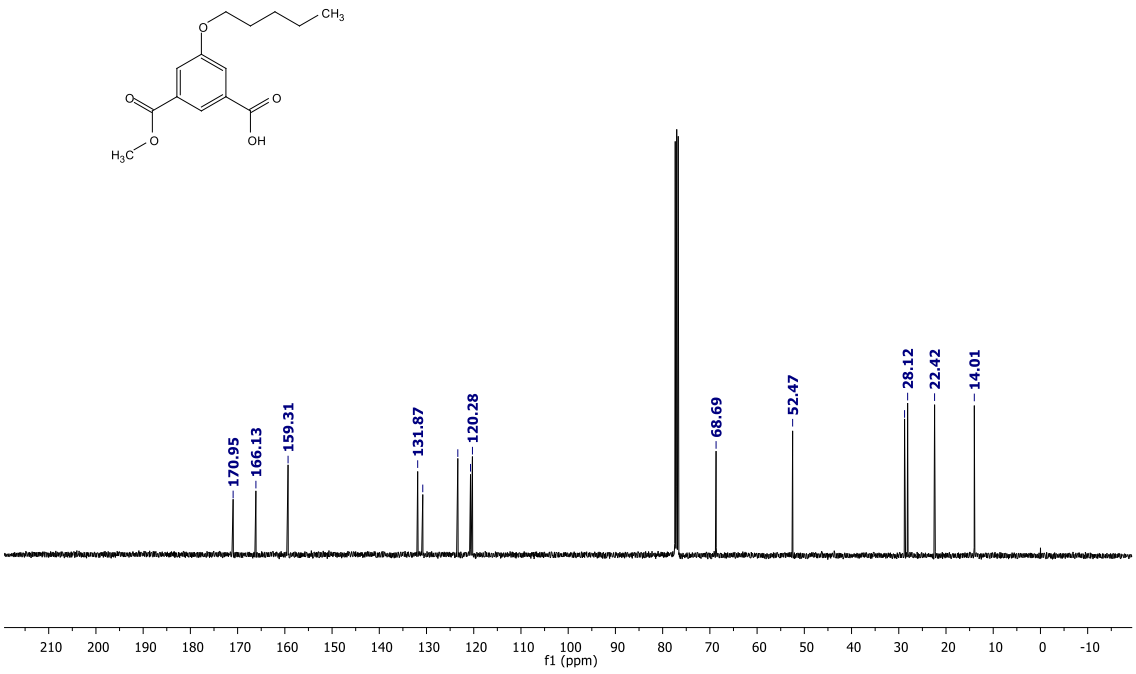

Figure 3.44. ^{13}C NMR spectrum (101 MHz) of **3** in $CDCl_3$ at room temperature.

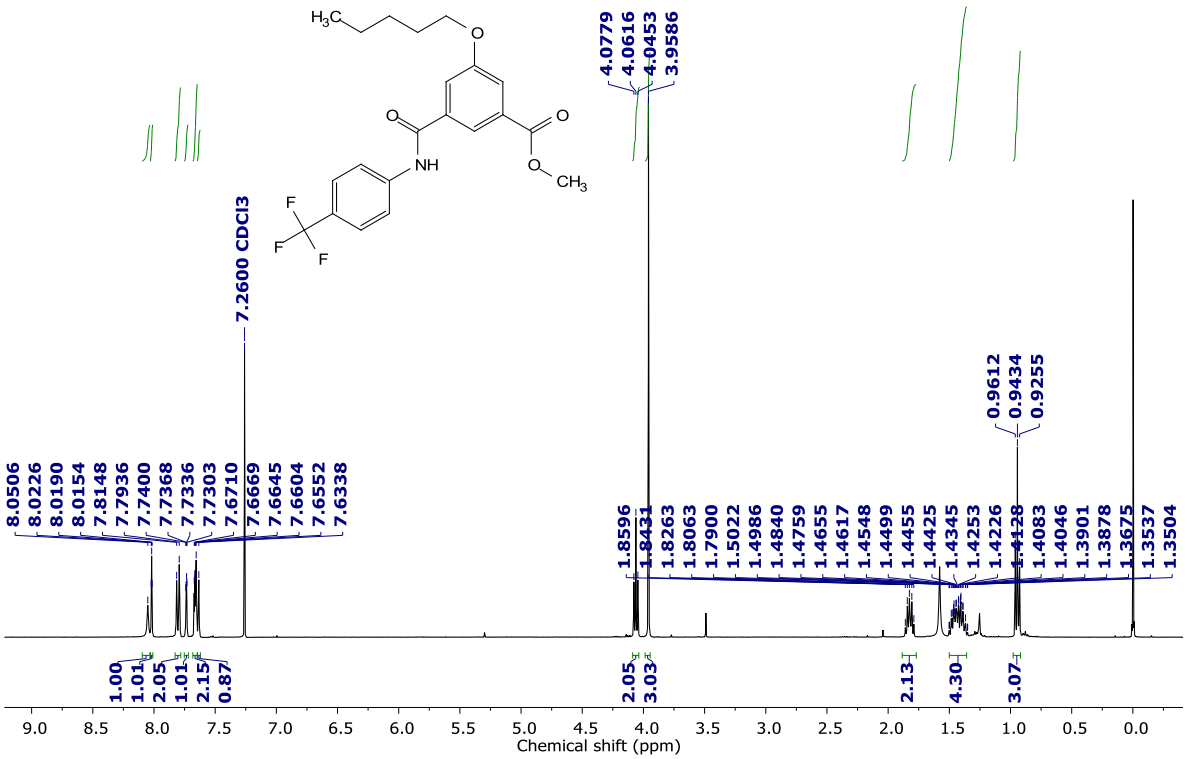

Figure 3.45. ^{1}H NMR spectrum (400 MHz) of **4a** in $CDCl_3$ at room temperature.

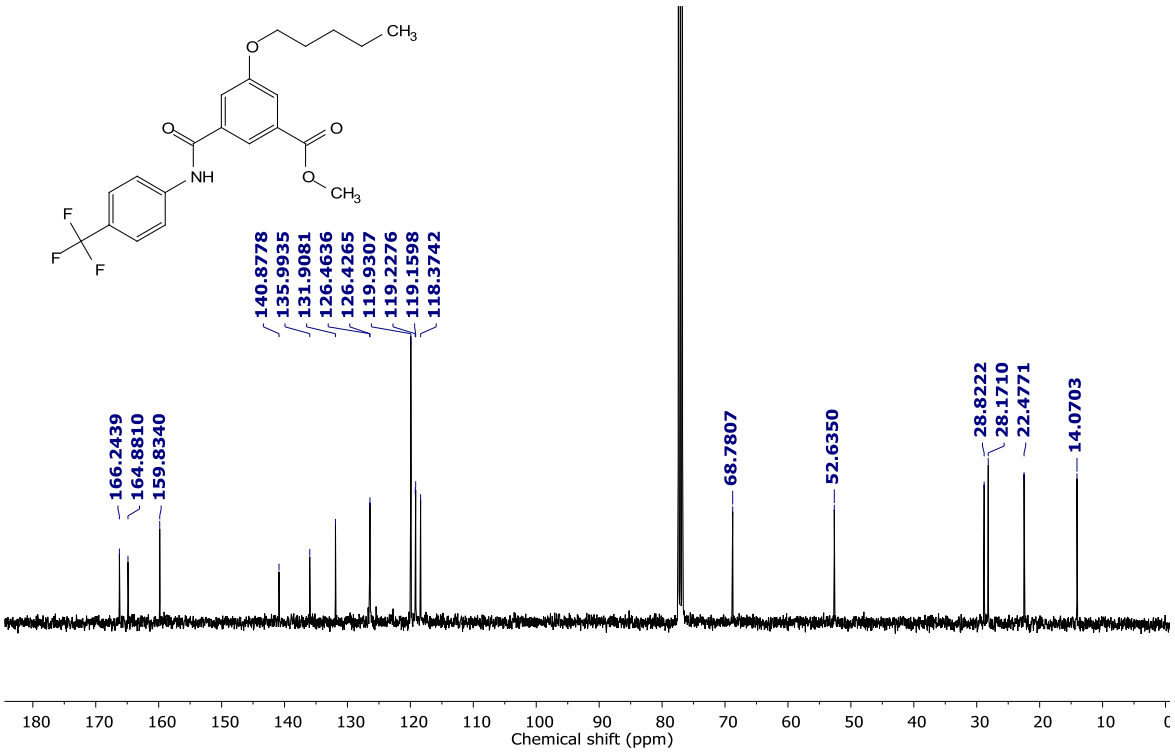

Figure 3.46. ^{13}C NMR spectrum (101 MHz) of **4a** in $CDCl_3$ at room temperature.

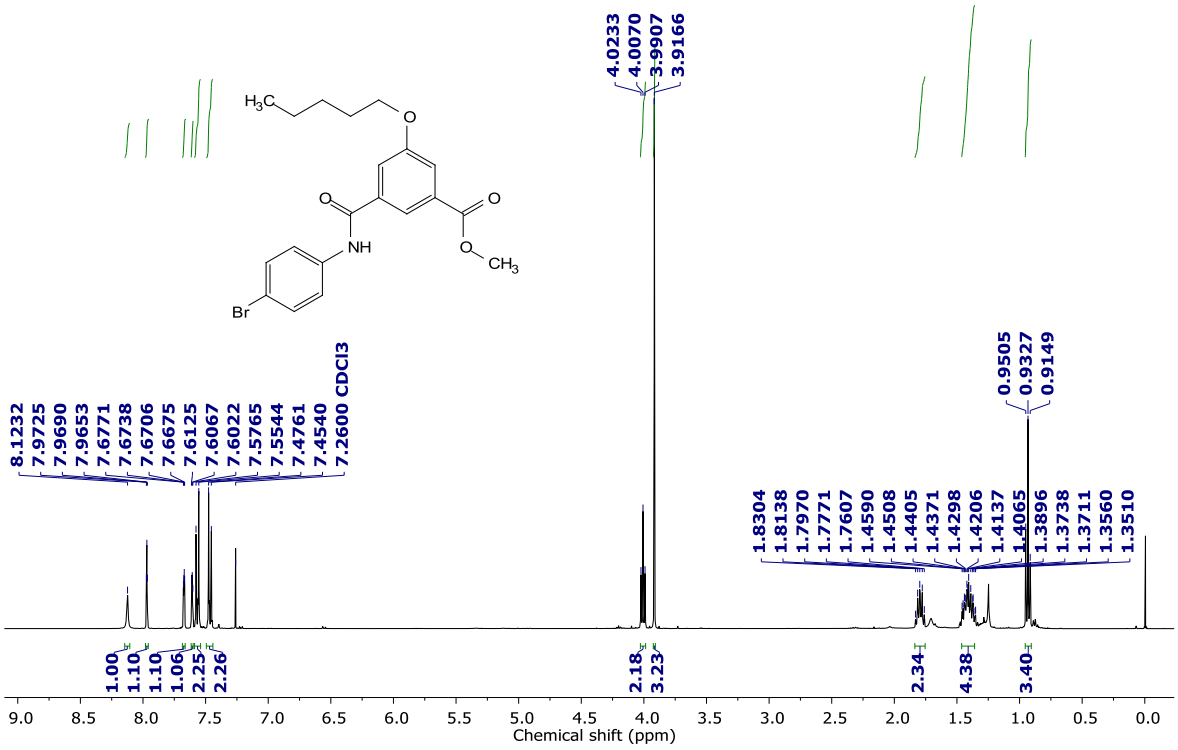

Figure 3.47. ^{1}H NMR spectrum (400 MHz) of **4b** in $CDCl_3$ at room temperature.

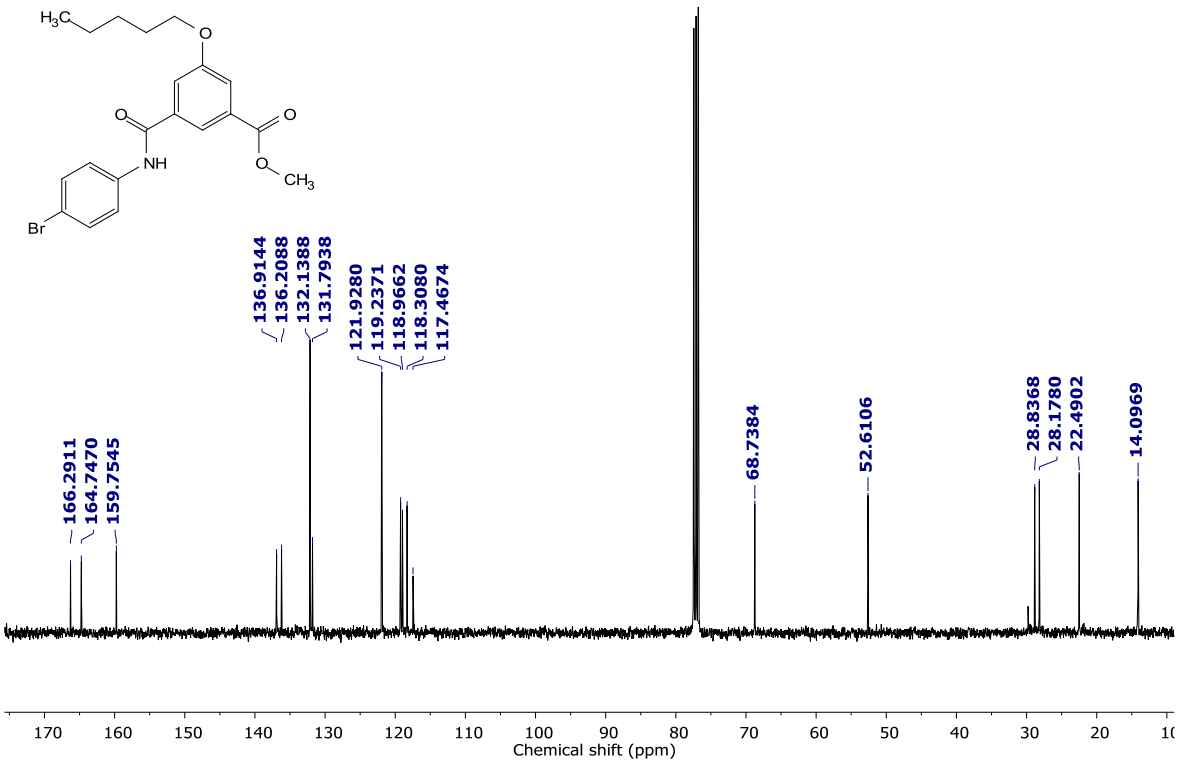

Figure 3.48. ^{13}C NMR spectrum (101 MHz) of **4b** in $CDCl_3$ at room temperature.

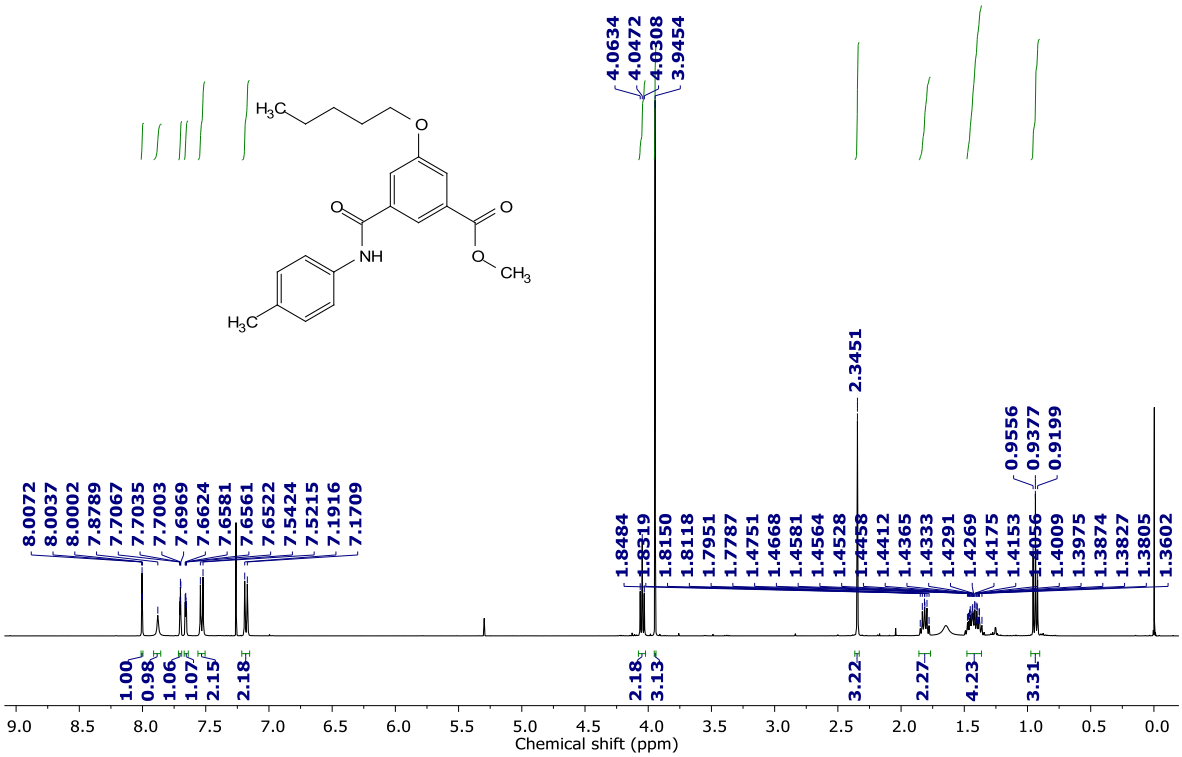

Figure 3.49. ^{1}H NMR spectrum (400 MHz) of **4c** in $CDCl_3$ at room temperature.

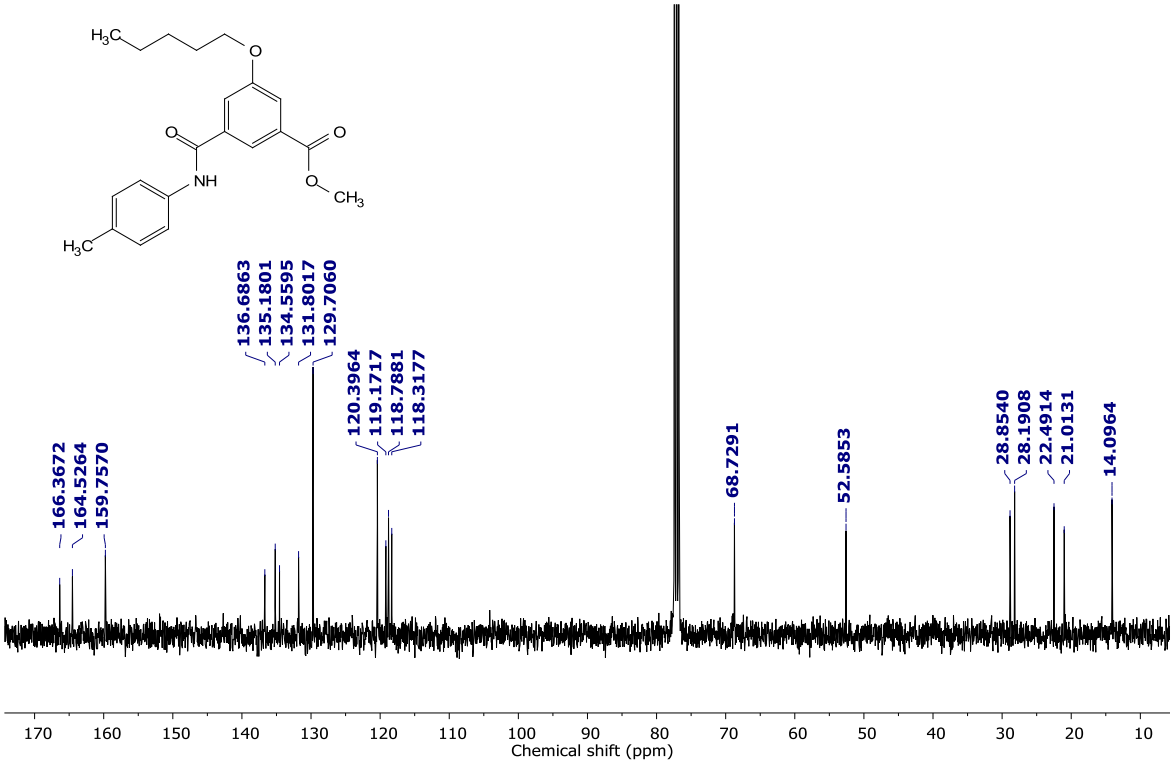

Figure 3.50. ^{13}C NMR spectrum (101 MHz) of **4c** in $CDCl_3$ at room temperature.

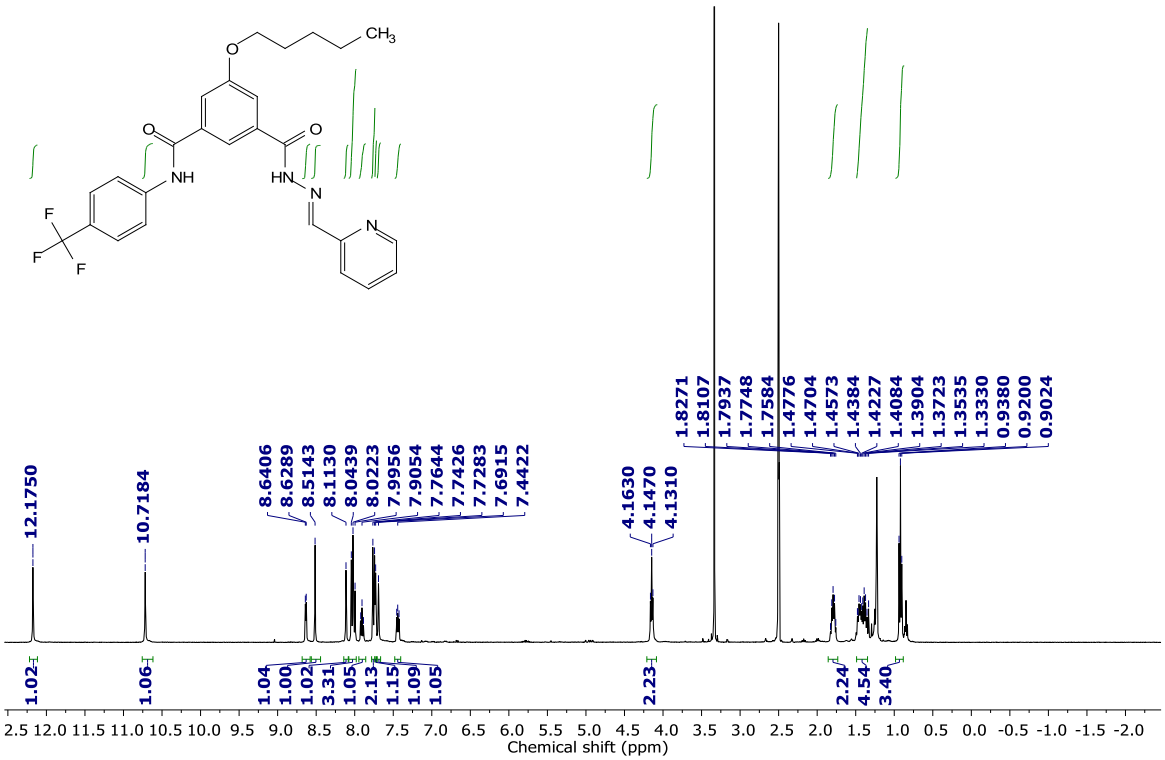

Figure 3.51. ^{1}H NMR spectrum (400 MHz) of **1a** in DMSO-d_6 at room temperature.

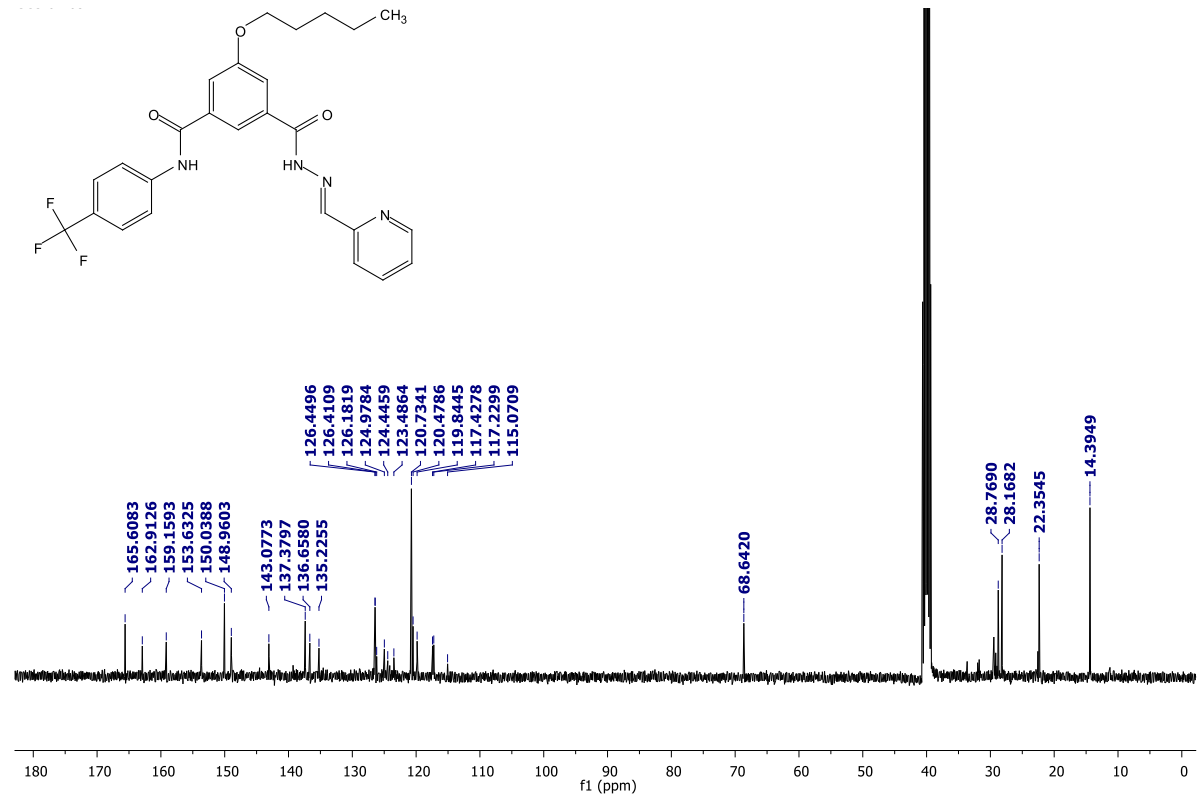

Figure 3.52. ^{13}C NMR spectrum (101 MHz) of **1a** in DMSO-d_6 at room temperature.

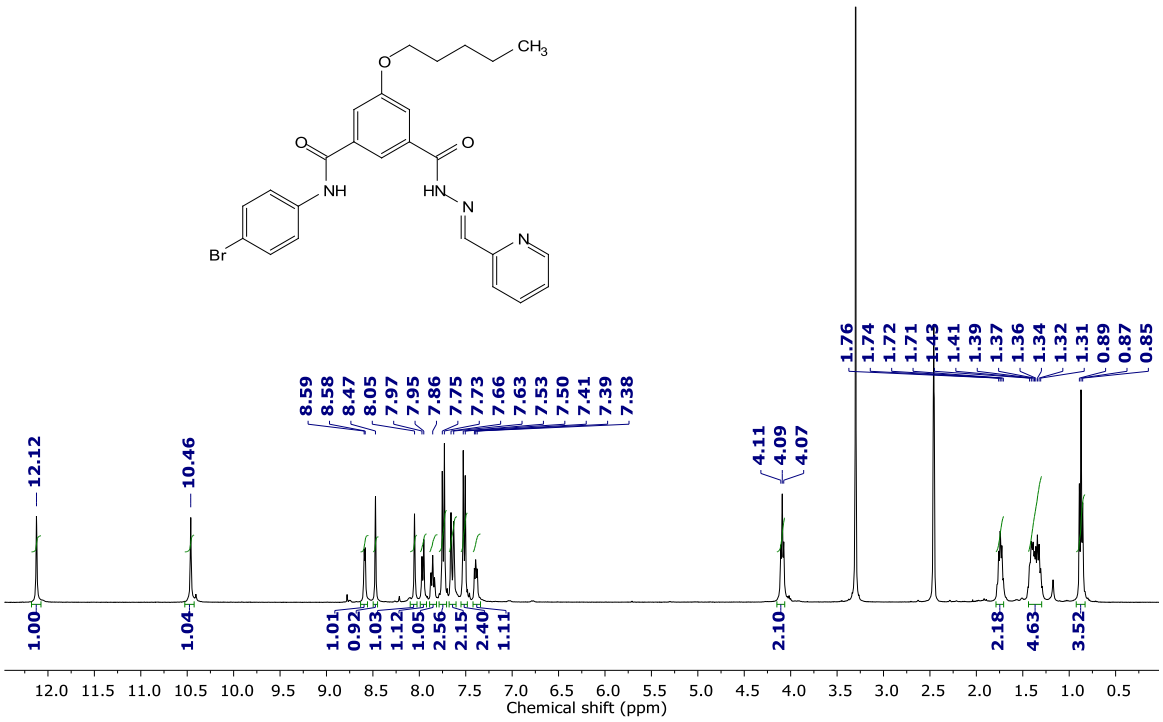

Figure 3.53. ^{1}H NMR spectrum (400 MHz) of **1b** in DMSO-d_6 at room temperature.

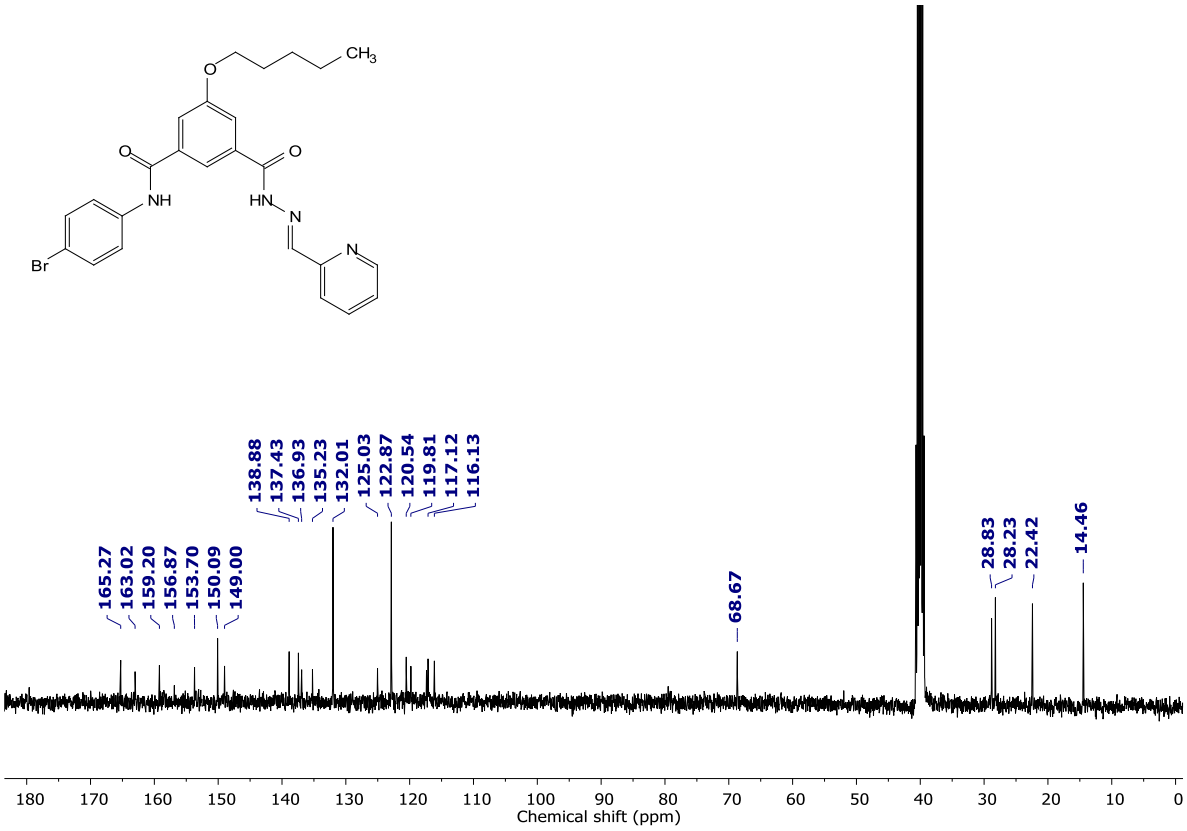

Figure 3.54. ^{13}C NMR spectrum (101 MHz) of **1b** in DMSO-d_6 at room temperature.

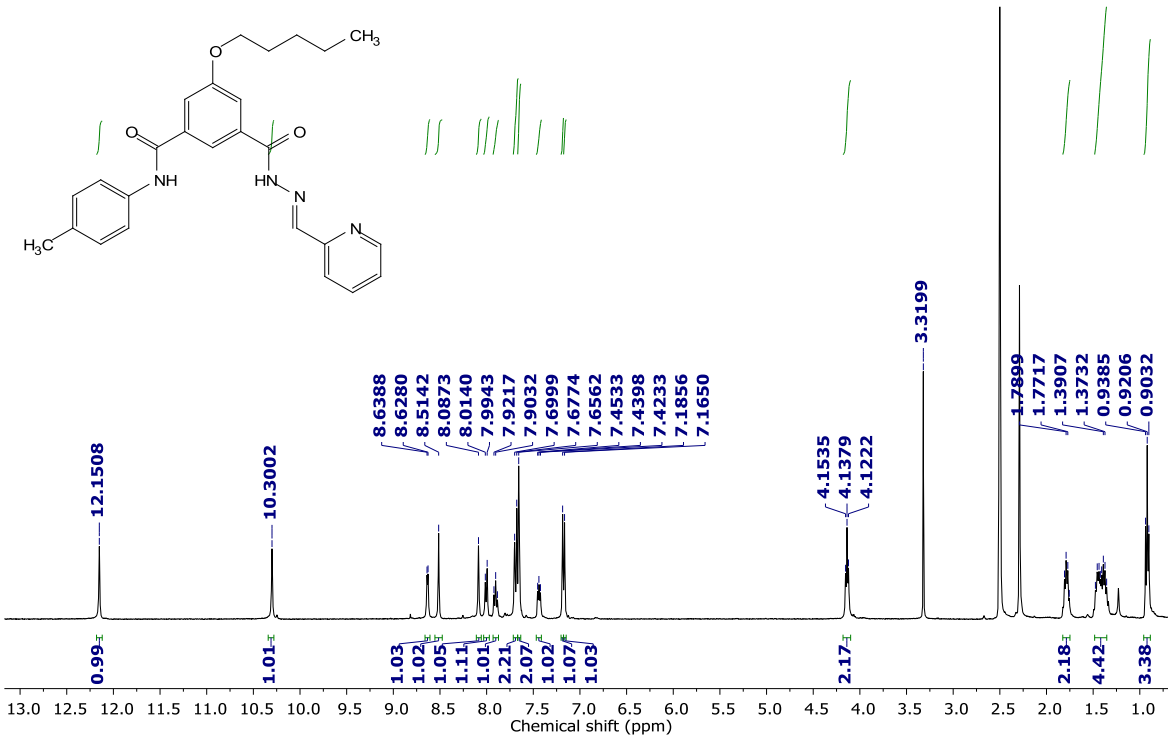

Figure 3.55. ^{1}H NMR spectrum (400 MHz) of **1c** in DMSO-d_6 at room temperature.

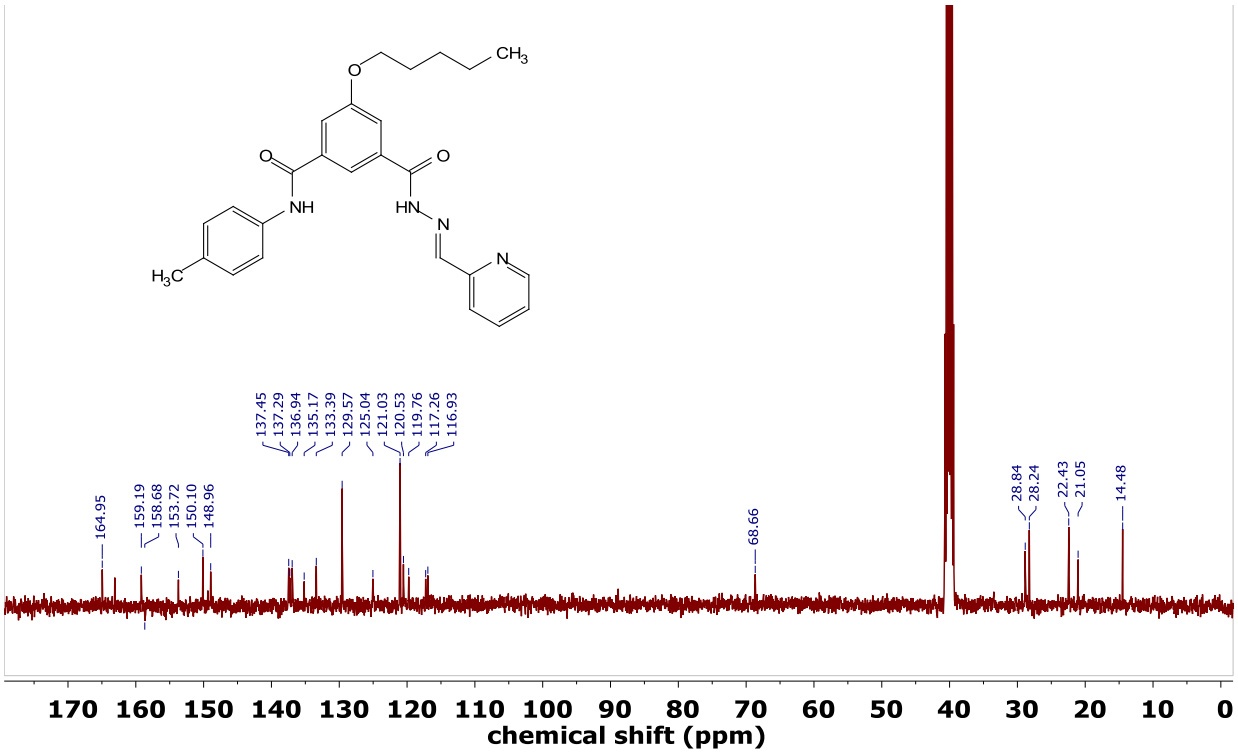

Figure 3.56. ^{13}C NMR spectrum (101 MHz) of **1c** in DMSO-d_6 at room temperature.

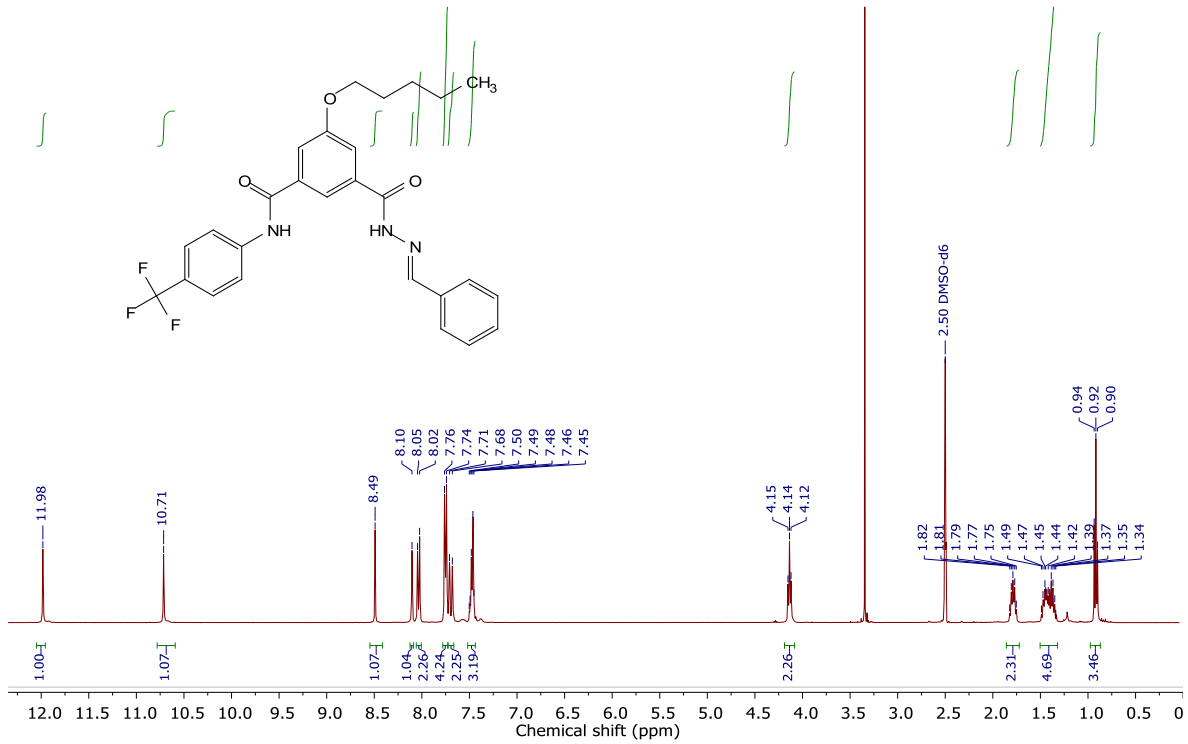

Figure 3.57. ^{1}H NMR spectrum (400 MHz) of **1d** in DMSO-d_6 at room temperature.

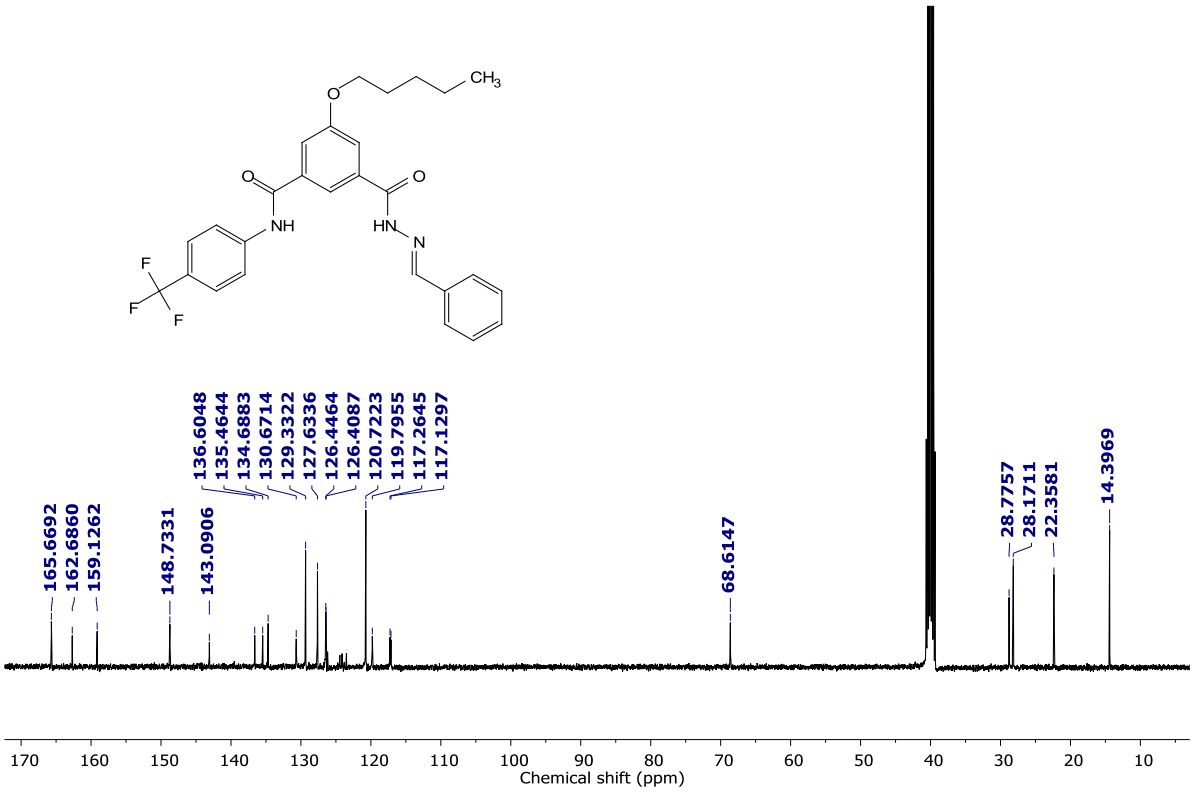

Figure 3.58. ^{13}C NMR spectrum (101 MHz) of **1d** in DMSO-d_6 at room temperature.

3.6. References

[1] (a) M. Tagliazucchi, I. Szleifer, *Mater. Today* **2015**, *18*, 131–142; (b) P. Agre, *Angew. Chem. Int. Ed.* **2004**, *43*, 4278–4290; (c) A. Kuo, J. M. Gulbis, J. F. Antcliff, T. Rahman, E. D. Lowe, J. Zimmer, J. Cuthbertson, F. M. Ashcroft, T. Ezaki, D. A. Doyle, *Science* **2003**, *300*, 1922–1998; (d) D. A. Doyle, J. M. Cabral, R. A. Pfuetzner, A. Kuo, J. M. Gulbis, S. L. Cohen, B. T. Chait, R. MacKinnon, *Science* **1998**, *280*, 69–77.

[2] (a) S. B. Salunke, J. A. Malla, P. Talukdar, *Angew. Chem. Int. Ed.* **2019**, *58*, 5354–5358; (b) J. A. Malla, R. M. Umesh, S. Yousf, S. Mane, S. Sharma, M. Lahiri, P. Talukdar, **2020**, *59*, 7944–7952; (c) I. F. Tannock, D. Rotin, *Cancer Res.* **1989**, *49*, 4373–4384; (d) W. Van Rossom, D. J. Asby, A. Tavassoli, P. A. Gale, *Org. Biomol. Chem.* **2016**, *14*, 2645–2650; (e) N. Busschaert, C. Caltagirone, W. Van Rossom, P. A. Gale, *Chem. Rev.* **2015**, *115*, 8038–8155.

[3] M. R. Banghart, M. Volgraf, D. Trauner, *Biochemistry.* **2006**, *45*, 15129–15141.

[4] (a) A. Kerckhoffs, M. J. Langton, *Chem. Sci.* **2020**, *11*, 6325–6331; (b) R. F. Khairutdinov, J. K. Hurst, *Langmuir* **2004**, *20*, 1781–1785; (c) T. Liu, C. Bao, H. Wang, Y. Lin, H. Jia, L. Zhu, *Chem. Commun.* **2013**, *49*, 10311–10313; (d) Y. Zhou, Y. Chen, P.-P. Zhu, W. Si, J.-L. Hou, Y. Liu, *Chem. Commun.* **2017**, *53*, 3681–3684.

[5] (a) H. Fliegl, A. Köhn, C. Hättig, R. Ahlrichs, *J. Am. Chem. Soc.* **2003**, *125*, 9821–9827; (b) S. Spörlein, H. Carstens, H. Satzger, C. Renner, R. Behrendt, L. Moroder, P. Tavan, W. Zinth, J. Wachtveitl, *Proc. Natl. Acad. Sci. U.S.A.* **2002**, *99*, 7998–8002.

[6] D. J. van Dijken, P. Kovaříček, S. P. Ihrig, S. Hecht, *J. Am. Chem. Soc.* **2015**, *137*, 14982–14991.

[7] I. Cvrtila, H. Fanlo-Virgós, G. Schaeffer, G. Monreal Santiago, S. Otto, *J. Am. Chem. Soc.* **2017**, *139*, 12459–12465.

[8] G. Vantomme, J.-M. Lehn, *Angew. Chem. Int. Ed.* **2013**, *52*, 3940–3943.

[9] S. M. Landge, I. Aprahamian, *J. Am. Chem. Soc.* **2009**, *131*, 18269–18271.

[10] (a) X. Su, I. Aprahamian, *Chem. Soc. Rev.* **2014**, *43*, 1963-1981; (b) M. N. Chaur, D. Collado, J. M. Lehn, *Chem. Eur. J.* **2011**, *17*, 248-258; cI. Aprahamian, *Chem. Commun.* **2017**, *53*, 6674–6684.

[11] Z. Kokan, M. J. Chmielewski, *J. Am. Chem. Soc.* **2018**, *140*, 16010–16014.

[12] D. A. Leigh, V. Marcos, T. Nalbantoglu, I. J. Vitorica-Yrezabal, F. T. Yasar, X. Zhu, *J. Am. Chem. Soc.* **2017**, *139*, 7104–7109.

[13] Y. Zhou, Y. Chen, P.-P. Zhu, W. Si, J.-L. Hou, Y. Liu, *Chem. Commun.* **2017**, *53*, 3681–3684.

[14] C. A. Lipinski, F. Lombardo, B. W. Dominy, P. J. Feeney, *Adv. Drug Deliv. Rev.* **1997**, *23*, 3–25.

[15] Marvin 5.8.0, *ChemAxon*, **2012**, *(http://www.chemaxon.com)*.

[16] (a) D. Nakatake, Y. Yokote, Y. Matsushima, R. Yazaki, T. Ohshima, *Green Chem.* **2016**, *18*, 1524–1530; (b) H. Hu, J. Zhu, F. Yang, Z. Chen, M. Deng, L. Weng, Y. Ling, Y. Zhou, *Chem. Commun.* **2019**, *55*, 6495–6498.

[17] http://app.supramolecular.org/bindfit/ **(**accessed July **2017)**.

[18] A. Roy, T. Saha, M. L. Gening, D. V. Titov, A. G. Gerbst, Y. E. Tsvetkov, N. E. Nifantiev, P. Talukdar, *Chem. Eur. J.* **2015**, *21*, 17445–17452.

[19] D. Mondal, A. Sathyan, S. V. Shinde, K. K. Mishra, P. Talukdar, *Org. Biomol. Chem.* **2018**, *16*, 8690–8694.

[20] B. L. Schottel, H. T. Chifotides, K. R. Dunbar, *Chem. Soc. Rev.* **2008**, *37*, 68–83.

[21] J. A. Malla, A. Roy, P. Talukdar, *Org. Lett.* **2018**, *20*, 5991–5994.

[22] (a) X. Wu, E. N. W. Howe, P. A. Gale, *Acc. Chem. Res.* **2018**, *51*, 1870–1879; (b) J. T. Davis, O. Okunola, R. Quesada, *Chem. Soc. Rev.*, **2010**, *39*, 3843–3862; (c) L. Chen, S. N. Berry, X. Wu, E. N. W. Howe, P. A. Gale, *Chem.* **2020**, *6*, 61–141.

[23] (a) N. Busschaert, I. L. Kirby, S. Young, S. J. Coles, P. N. Horton, M. E. Light, P. A. Gale, *Angew. Chem. Int. Ed.*, **2012**, *51*, 4426–4430; (b) P. A. Gale, C. C. Tong, C. J. E. Haynes, O. Adeosun, D. E. Gross, E. Karnas, E. M. Sedenberg, R. Quesada, J. L. Sessler, *J. Am. Chem. Soc.* **2010**, *132*, 3240–3241.

[24] G. Sheldrick, *Acta crystallographica.* **2008**, *64*, 112–122.

[25] A. Spek, *Acta Crystallographica* **2009**, *65*, 148–155.

Chapter 4

Reversible stimuli-responsive transmembrane anion transport using phenylhydrazone-based photoswitches

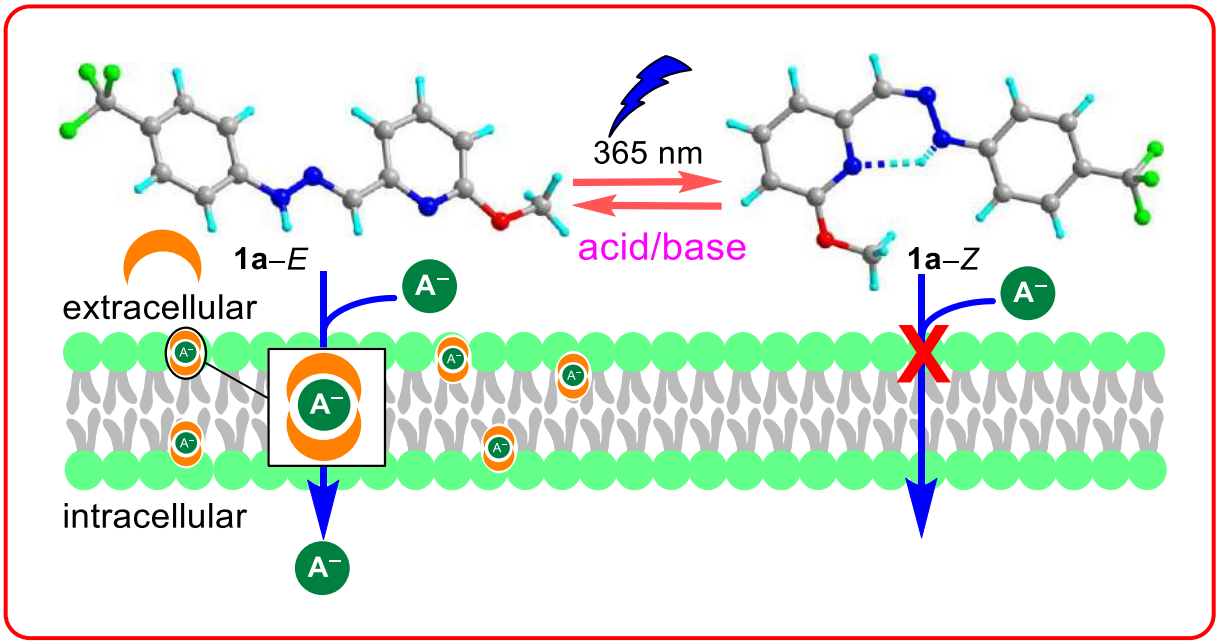

4.1. Introduction

As discussed in the previous chapters that artificial ion transport systems have emerged as an important class of attractive molecules that mimic the natural systems for the transport of ions across the biological membranes, and are relatively simpler as compared to the complex natural systems.[1] Small molecule ion carriers, in particular have been the key targets because of their diverse therapeutic applications[2] and in particular, the stimuli-responsive systems that are controlled by some external stimuli of light, voltage, pH, ligand, enzymes, etc. promise the real biological applications.[3] Light is one of the important external stimuli that has been utilized because of its spatial and temporal control, remote addressability, intense tenability, less toxicity, etc.[4] In chapter 2, we used azobenzene as a photo switch because of its short-responsive time, efficient photo-reversibility, substantial change of conformation, and dipole moment upon *t*rans to *c*is photo-isomerization. The transporters designed demonstrated efficient photo-gated ion transport activities across the artificial liposomes. However, fast thermal *c*is to *t*rans reversible isomerization was considered to be their limitation, which delimits their use as therapeutics under the biological temperatures. To overcome the stability issues in the photoisomerized excited state, in chapter 3, we designed acylhdrazone-based ion transporters. The designed acylhydrazone-based ion transport systems and in particular acylhydrazone systems based on pyridine moiety possess tremendously high thermal stability in the photoisomerized *Z* state due to the presence of intramolecular hydrogen bonding. The ion transporters also showed efficient stimuli-responsive ion transport properties across the artificial liposomes by the application of electromagnetic radiations to drive the *E* to *Z* photoisomerization followed by acid-catalyzed reverse isomerization. However, acylhydrazones require bio-incompatible harmful UV radiations (~300 nm) for *E* to *Z* photoisomerization process. The use of ultraviolet radiation delimits their potential biological applications because the use of ultraviolet radiations can lead to phototoxic cell damage or death.[5] Phenylhydrazones are another set of photoswitches that can exist either in *E* or *Z* forms in the solution phase due to the configurational photoisomerization across the C=N double bond[6] and possess acidic protons which can sense for anions and on the other hand contains cation binding nitrogen atoms (Figure 4.1A). Phenylhydrazones derived from pyridine-2-aldehyde are particularly more efficient photoswitches because of hydrogen bond stabilized *Z* state (Figure 4.1B).[7] Reverse isomerization occurs in the presence of acid

as a catalyst Due to the presence of versatile and multifaceted (C–N–N=CH) functionality, with acidic N–H proton and nucleophilic imine bond, they found applications in different fields of supramolecular chemistry and especially in sensing (Figure 4.1C).[8] Unlike acylhydrazones, photoisomerization of phenylhydrazones across the C–N double bond occurs comparatively at a higher wavelength.[9] Therefore, phenylhydrazone can be an interesting system for designing photo–responsive ion transport system.

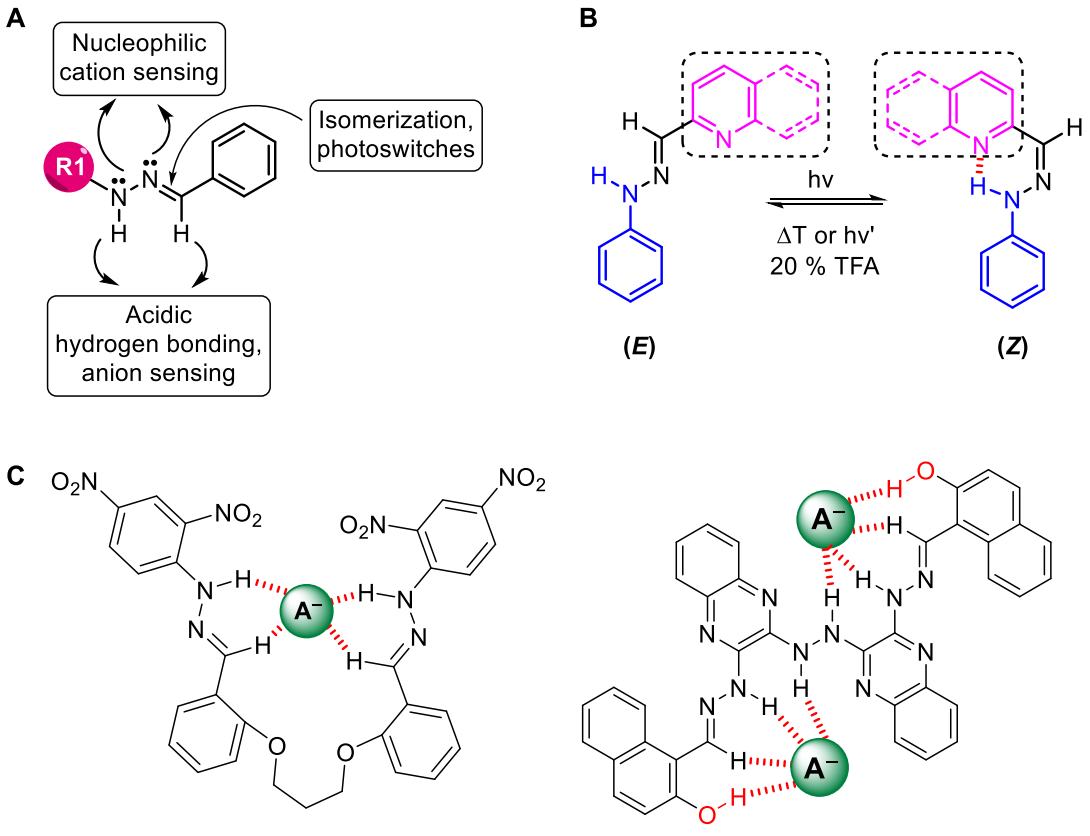

Figure 4.1. Phenylhydrazone-based photoswitch possessing different functional properties (**A**). Representation of a pyridine-based phenylhydrazone photoswitch showing intramolecular hydrogen bonding between NH and pyridine nitrogen (**B**). Examples of Phenylhydrazone-based anion sensing molecular stuffs (**C**).

To achieve such a goal, we designed phenylhydrazone–based anion receptors **1a**–**1d** (Figure 4.2A). We envisaged that the acidic N–H_2, –N–C–H_3 and C_{Ar}–H_1 protons would be responsible for anion binding through N–H_2···Cl^-, –N–C–H_3···Cl^- and C_{Ar}–H_1···Cl^- noncovalent interactions, which would eventually lead to the transport of the bound anion across the lipid bilayer membrane (Figure. 1B). On the other hand, photoisomerization of the C–N bond at 365 nm would lead to the formation of a closed

Z–form with no possibility of anion binding, and hence no ion transport would occur (Figure 4.2B). Furthermore, the incorporation of the methoxy group next to pyridine nitrogen was expected to further block the binding cavity of the photoisomerized *Z*–state. The active *E*–form would be regenerated back by an acid-catalyzed re-activation process Different aromatic moieties were incorporated to tune the lipophilicity and the binding affinity of the anionophores.[10] The logP and pK_a values of these compounds were calculated using the MarvinSketch program.[11]

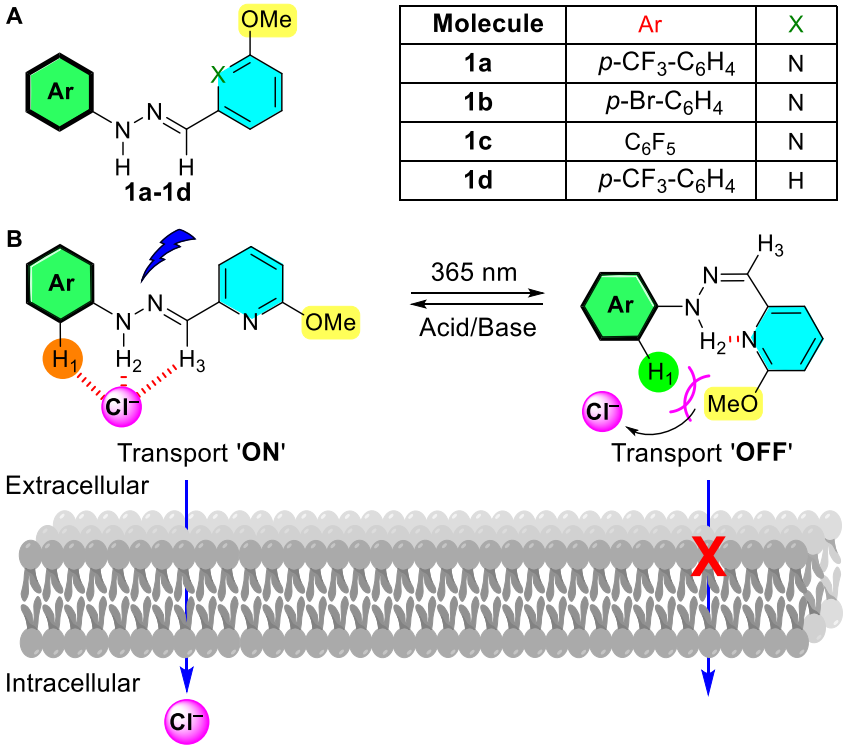

Molecule	Ar	X
1a	*p*-CF_3-C_6H_4	N
1b	*p*-Br-C_6H_4	N
1c	C_6F_5	N
1d	*p*-CF_3-C_6H_4	H

Figure 4.2. Chemical structure of compounds **1a**–**1d** (**A**). Design and working principle of stimuli–responsive phenylhydrazone–based transporters (**B**).

4.2. Results and discussions

4.2.1. Synthesis

The synthesis of the desired compounds **1a**–**1d** was achieved by reacting an appropriate arylhydrazine among **2a**–**2c** with 3-methoxy–2–pyridine carboxyaldehyde or 3–methoxy benzaldehyde (Scheme 4.1).

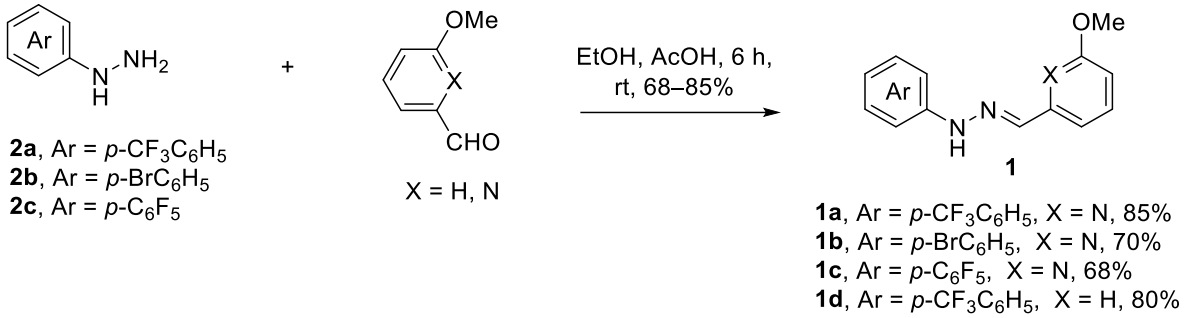

Scheme 4.1. Synthetic scheme for the compounds **1a-1d**.

4.2.2. Crystallographic Studies

The single crystal X-ray crystal structure of as-synthesized **1a** confirmed the *E*–stereochemistry across the C–N bond, and an open molecular geometry with N–H_2, N–C–H_3, and C_{Ar}–H_1 groups adapting a *syn–syn* conformation that is necessary for the anion binding process (Figure 4.3A). On the other hand, the *Z* isomer of **1a**, obtained by photoisomerizing as-synthesized **1a** at 365 nm, exhibited a 'closed' conformation due to the formation of six-membered intramolecular hydrogen bond (Figure 4.3B). Moreover, a significant steric effect by the attached methoxy group at the proposed anion binding site is also evident.

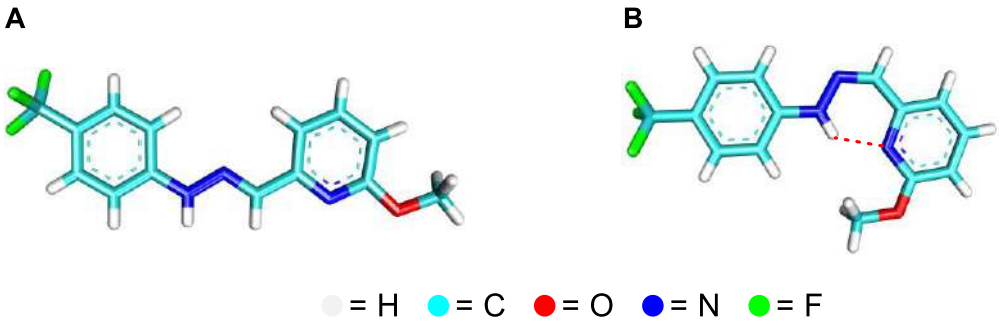

Figure 4.3. Single crystal X-ray structures of **1a**–*E* (**A**) and **1a**–*Z* (**B**). (Red dotted line shows the intramolecular hydrogen bonding).

4.2.3. Anion binding studies through ^{1}H NMR studies

Initial evidence of Cl^- binding by **1a**–**1d** was obtained by ^{1}H NMR titration studies in acetonitrile–d_3. In the presence of Tetrabutylammonium chloride (TBACl), significant downfield shifts were observed for N–H_2, N–C–H_3 and C_{Ar}–H_1 protons indicating the involvement of N–H_2···Cl^-, N–C–H_3···Cl^- and C_{Ar}–H_1···Cl^- hydrogen bonding interactions (Figure 4.4, 4.23, 4.25, 4.27). Further analysis using BindFit program[12] furnished a 1:1 (Host : Guest) binding stoichiometry with the association constant values ($K_{a(1:1)}$/Cl^-) of 160 M^{-1} ±

8.2 for **1a**, 136 M^{-1} ± 5.2 for **1b**, 30 M^{-1} ± 3.4 for **1c**, and 50 M^{-1} ± 3.8 for **1d**, respectively (Figure 4.5, 4.24, 4.26, 4.28, Table 4.1), with the binding affinity sequence of **1a** > **1b** > **1d** > **1c**. Binding studies of **1a** with Br^- and I^- ions were also done using Tetrabutylammonium bromide (TBABr) and Tetrabutylammonium iodide (TBAI) salts, respectively (Figure 4.19, 4.21). The association constants obtained were $K_{a(1:1)}/Br^-$ = 22 M^{-1} ± 4.5 and $K_{a(1:1)}/I^-$ = 6 M^{-1} ± 0.8, respectively (Figure 4.20, 4.22). The photoisomerized Z–isomer of **1a** on the other hand, did not show any Cl^- binding plausibly due to the disruption of the anion binding site and hence validating the proposed design (Figure 4.29).

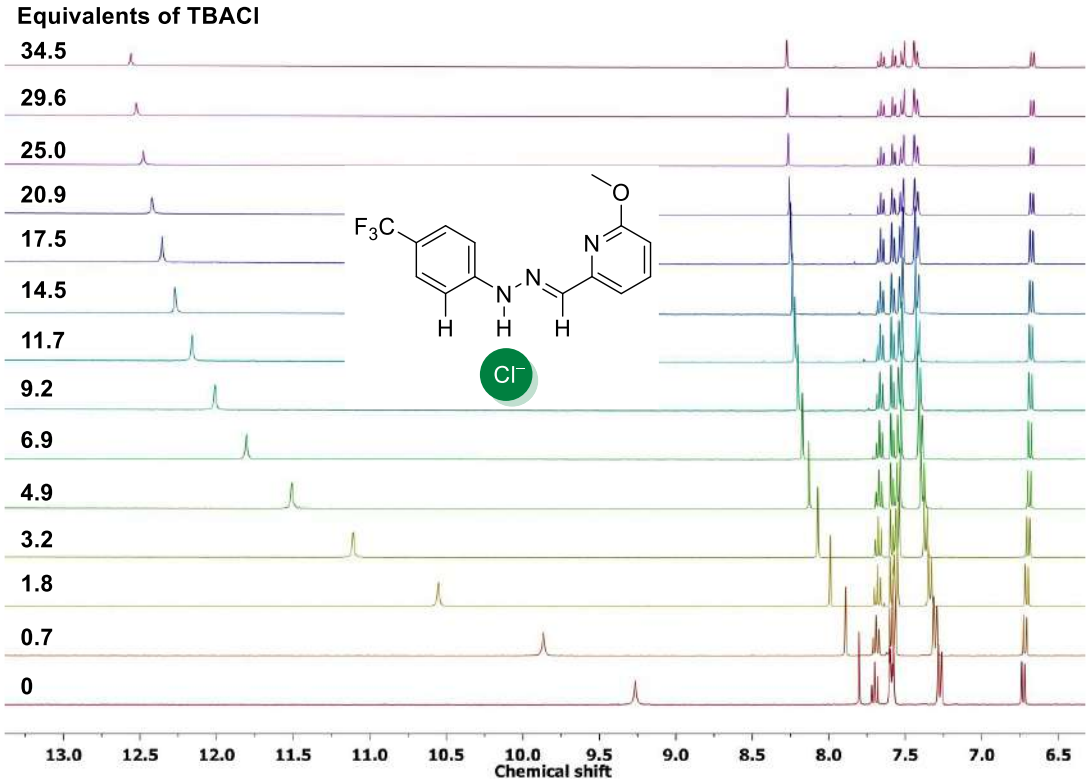

Figure 4.4. ^1H NMR titration spectra for **1a** (5 mM) with stepwise addition of TBACl in CD_3CN. The equivalents of added TBACl are shown on the stacked spectra.

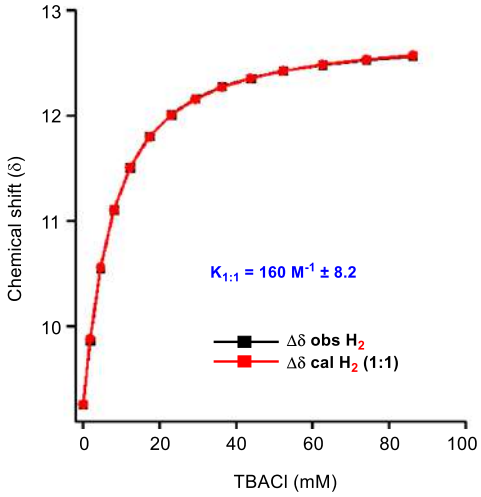

Figure 4.5. The plot of chemical shift (δ) of H_2 protons *vs* concentration of TBACl added, fitted to 1:1 binding model of BindFit v0.5.

The direct evidence of chloride binding by **1a** was obtained by high resolution mass spectrometric data (electrospray ionization) and it provided peaks at m/z = 330.0620 and 332.0597, corresponding to the [**1a**+Cl^-] complex in the solution state (Figure 4.6). Moreover, the presence of a [(**1a**)$_2$+Cl^-] complex at *m/z* = 625.1566 and 627.1387 was also evident.

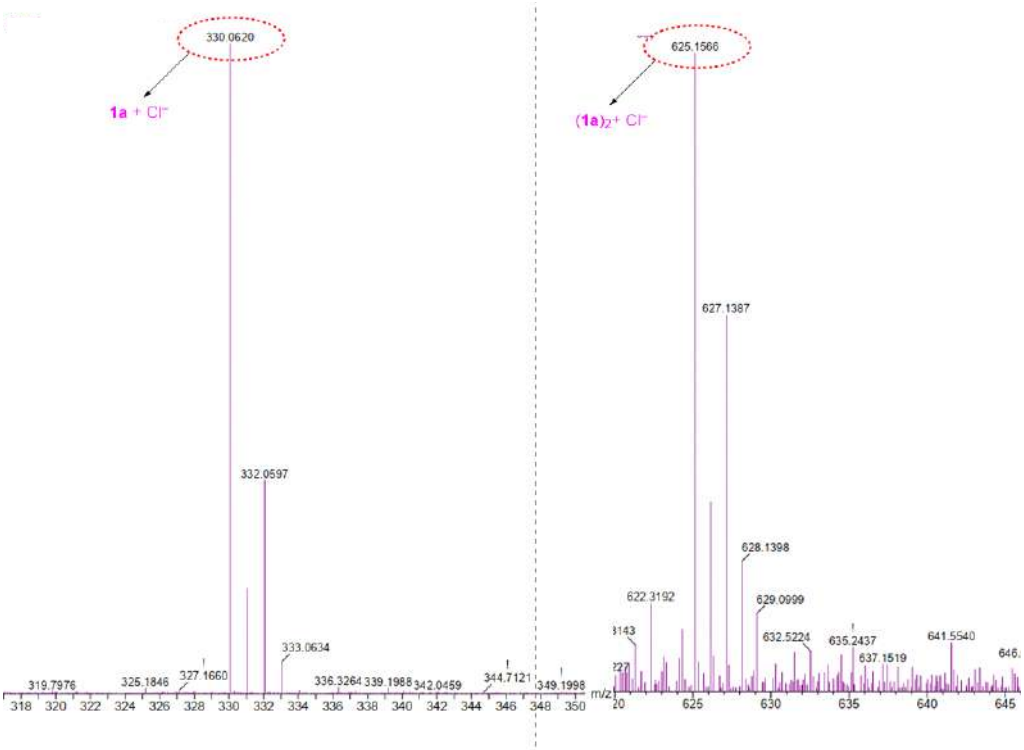

Figure 4.6. ESI-MS spectrum of 2:1 mixture of **1a** and TMACl recorded in CH_3CN. The data confirms the presence of both 1:1 and 2:1 **1a**-Cl^- complexes.

4.2.4. Ion transport activity

Next, the ion transport activity of the compounds **1a**–**1d** across large unilamellar vesicles (LUVs) was evaluated. 8-Hydroxy pyrene-1,3,6-trisulfonic acid trisodium salt (HPTS, 1 mM) was entrapped within the vesicles containing 100 mM of NaCl and 10 mM of HEPES buffer.[13] A pH gradient (pH_{in} = 7.0 and pH_{out} = 7.8) was created across the lipid vesicles by adding NaOH solution to the extravesicular solution. Subsequently, the compounds **1a**–**1d** were added, and the collapse of the pH gradient was monitored by recording the change of fluorescence intensity at λ_{em} = 510 nm (λ_{ex} = 450 nm). The ion transport activity sequence of **1a** > **1d** > **1b** > **1c** was derived from the study (Figure. 4.7A). The dose–responsive plots furnished the half-maximal effective concentration (EC_{50}) values of 2.5 ± 0.1 µM, 3.4 ± 0.4 µM, 10.5 ± 2.3 µM, and 2.7 ± 0.2 µM, for **1a**, **1b**, **1c**, and **1d**, respectively (Figures 4.30–4.33). For each compound, the Hill coefficient (n) ~ 2 indicates the involvement of two molecules catalyzing the ion transport process.

Mechanistically, the disruption of the pH gradient across the lipid bilayer membrane can occur through the following modes: (a) OH^-/X^- antiport, (b) H^+/X^- symport, (c) H^+/M^+ antiport, and (d) OH^-/M^+ symport. To identify the preferential iontransport mechanism, the ion transport activity of **1a** was checked across EYPC-LUVs⊃HPTS by varying either cations or anions in the extravesicular buffer.Variation of the external cations (M^+ = Li^+, Na^+, K^+, Rb^+, and Cs^+) in the external buffer did not provide any significant change in the ion

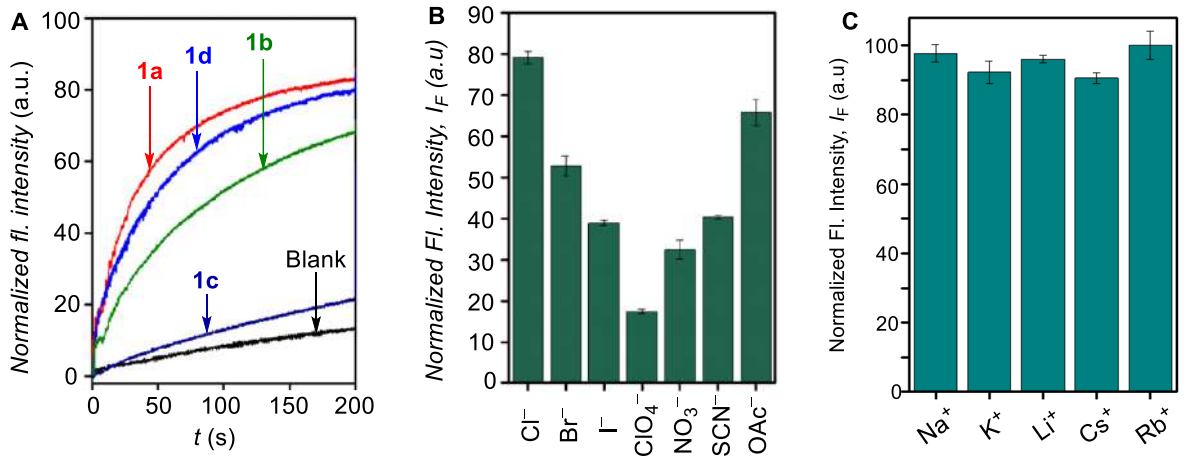

Figure 4.7. Activity comparison of **1a–1d** (4.0 µM each) across EYPC–LUVs⊃HPTS. (**A**). Anion selectivity of **1a** (3.5 µM) by varying the external anions across EYPC–LUVs⊃HPTS. (**B**). Cation selectivity of **1a** (3.0 µM) measured by varying external cations (M^+ = Li^+, Na^+, K^+, Rb^+, Cs^+) across EYPC-LUVs⊃HPTS (**C**).

transport rate, (Figure 4.7C). However, changing the external anions (X = F^-, Cl^-, Br^-, OAc^-, and NO_3^-) in the external buffer provided a significant enhancement in the ion transport activity (Figure 4.7B), indicating the role of anions in an overall transport process. These results indicate that H^+/M^+ antiport and OH^-/M^+ symport mechanisms are not operational, and hence the transport mechanism can be operated through either OH^-/X^- antiport or H^+/X^- symport mode.[14]

Table 4.1. Summary of pK_a (N–H_2), logP, chloride association K_a (M^{-1}) recorded in acetonitrile–d_3, EC_{50} (μM), and Hill coefficient (n) values of compounds **1a–1d**.

Comp.	logP[a]	pK_a[a]	K_a[b] (M^{-1})/ Cl^-	EC_{50} (μM)	n
1a	4.57	15.81	160 ± 8.2	2.5 ± 0.1	2.1 ± 0.2
1b	4.46	15.81	136 ± 5.2	3.4 ± 0.4	2.3 ± 0.2
1c	4.41	10.43	30 ± 3.4	10.5 ± 2.3	2.6 ± 0.5
1d	4.14	15.89	50 ± 3.8	2.7 ± 0.2	2.6 ± 0.4

[a] Calculator plugin of the Marvin Sketch program was used for calculating logP and pK_a values. [b] Association constants were obtained based on the 1:1 binding model for NH protons.

Subsequently, Cl^- leakage for **1a** across EYPC–LUVs⊃lucigenin was monitored. Vesicles were prepared in $NaNO_3$ (200 mM) by entrapping the lucigenin dye and then creating a Cl^-/NO_3^-gradient by adding NaCl solution to the exterior of the vesicles.[15] The rate of change in fluorescence intensity (λ_{ex} = 455 nm and λ_{em} = 535 nm) was monitored after the addition of **1a**. The dose-dependent Cl^- influx by **1a** is seen in Figure 4.8A. The Hill coefficient value of $n \sim 2$ further indicates the involvement of two molecules in catalyzing the ion transport process (Figure 4.34). The transport of chloride ions in the above lucigenin assay can occur either through Cl^-/NO_3^- antiport mode or H^+/Cl^- symport mode as the role of metal ions has been nullified in the above cation selectivity assay. To obtain the more mechanistic insights, a lucigenin-based coupled assay in the presence and absence of valinomycin (a highly selective K^+ transporter) was performed, with intravesicular $NaNO_3$ (200 mM) and extravesicular KCl (200 mM). A significant enhancement in the Cl^- efflux rate was observed for **1a** in the presence of valinomycin compared to that with **1a** alone (Figure 4.8B). This experiment illustrates that there is a significant synergistic effect on chloride transport by adding the compound **1a** and cationophore together as compared to the compound or cationophore alone, and this synergistic effect between the two is evidence for a co-transport process. This cooperativity between the

two is only possible if the transport process by an anionophore **1a** occurs through an electrogenic mode and hence can be accelerated by the presence of cationophore like valinomycin. Hence, these results suggest that the transport process in lucigenin assay occurs through Cl^-/NO_3^- antiport mode.[16]

Furthermore, U-tube experiment showed an efficient transport Cl^- ions from the source-arm to the receiver-arm of the U-tube, when the Cl^- concentration in the receiver-arm was monitored using a chloride-based ion selective electrode (Figure 4.8C). This result confirms that **1a** acts as a mobile carrier of anions.[17]

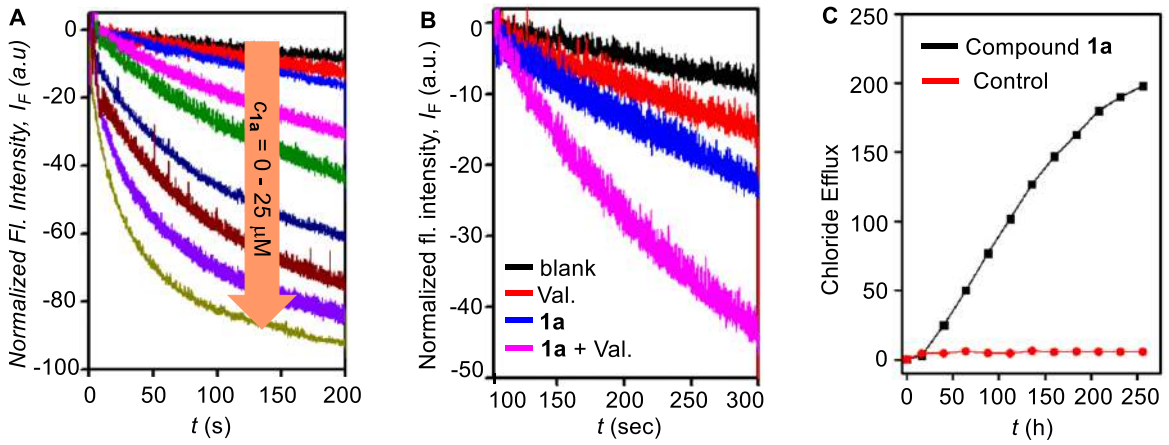

Figure 4.8. Concentration dependent activity of **1d** across EYPC-LUVs⊃Lucigenin (**A**). Comparison of Cl^- influx activity of **1a** (1.25 mm) in the absence and in the presence of valinomycin (1.25 mm) (**B**). Change of chloride ion concentration in a U-tube experiment with and without compound **1a** (1.0 mM) (**C**).

4.2.5. Theoretical studies

Based on the experimentally determined Hill coefficient value of $n \sim 2$ and Cl^- selectivity, the geometry-optimized structure of [(**1a**)$_2$+Cl^-] complex was obtained first by generating the most probable conformation by using CONFLEX 8 program[18] (Figure 4.60), and subsequently, optimizing the generated conformation by Gaussian 09 program[19] using B3LYP functional and 6-311++G(d,p) basis set,[20] The geometry optimized structure of [(**1a**)$_2$+Cl^-] complex indicated that two receptor molecules are involved in the binding of a Cl^- ion (Figure 4.9). The structure confirmed that each receptor participates in the anion recognition through N–H_1···Cl^- (H_1···Cl^- = 2.42 Å), C_{Ar}–H_2···Cl^- (H_2···Cl^- = 2.80 Å), N–H_3···Cl^- (H_3···Cl^- = 2.86 Å), hydrogen bonding interactions. Further, the binding energy of –47.89 kcal mol^{-1} was calculated for the [(**1a**)$_2$+Cl^-] complex.

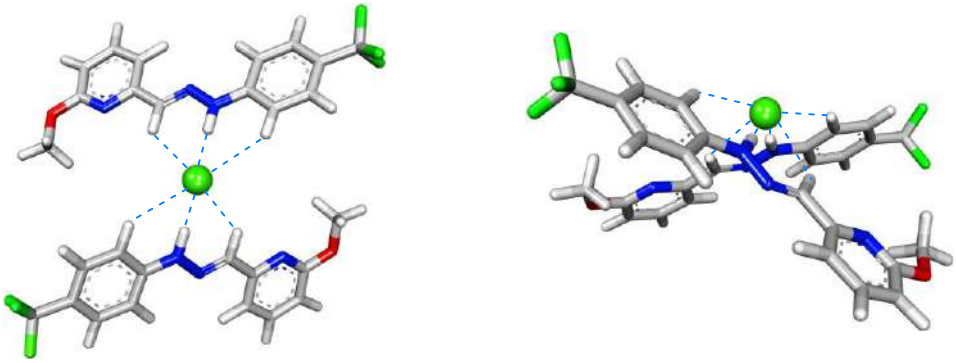

Figure 4.9. Two different geometry–optimized structures of [(**1a**)$_2$+Cl$^-$] complex

4.2.6. Photoisomerization studies

4.2.6.1. Photo conversion through UV-Vis and ^{1}H NMR studies

The photoisomerization studies for the anionpohores **1a**–**1d** were carried through ^{1}H NMR and UV–Vis absorption studies. Photoirradiation at 365 nm in acetonitrile led to the bathochromic shift of the absorption spectra (Figure 4.10, 4.37–4.39), and on the other hand, the chemical shift of phenylhydrazone N–H proton was significantly downfield shifted (Figures 4.11, 4.40–4.42). These changes are consistent with the photoisomerization process of phenylhydrazone moiety across the C–N double bond.[8a] Photo conversion was quantitative for the compounds **1a** and **1b**. Moreover, **1a** showed excellent thermal stability while keeping in the dark for several days (Figure 4.12). Such exceptional thermal stability is the consequence of six membered intramolecular hydrogen bonding in the photoisomerized *Z* state. Compound **1d** that lacks such intramolecular hydrogen bonding was photoisomerized only up to 45%, and showed lower thermal stability while keeping in the dark (Figure 4.13). Compound **1c** was photoisomerized only up to 52%, more likely due to the steric hindrance caused by fluorine atom with the methoxy group in the *Z* state.

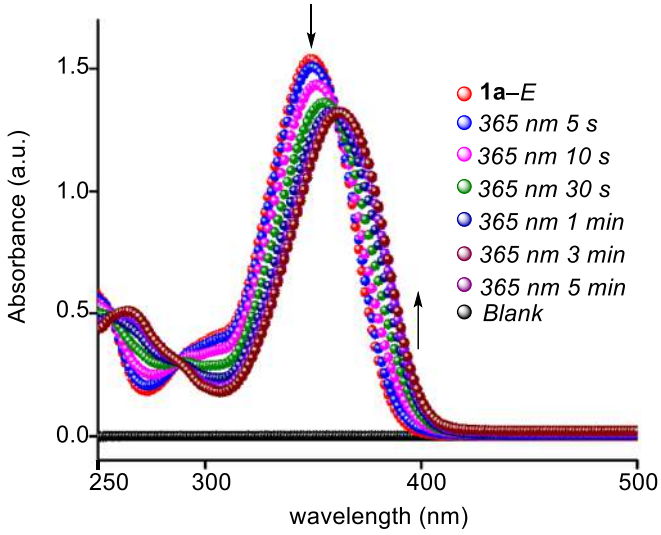

Figure 4.10. UV-visible spectral changes for **1a** (100 μM) upon irradiation with 312 nm light (3 × 3 Watt LEDs).

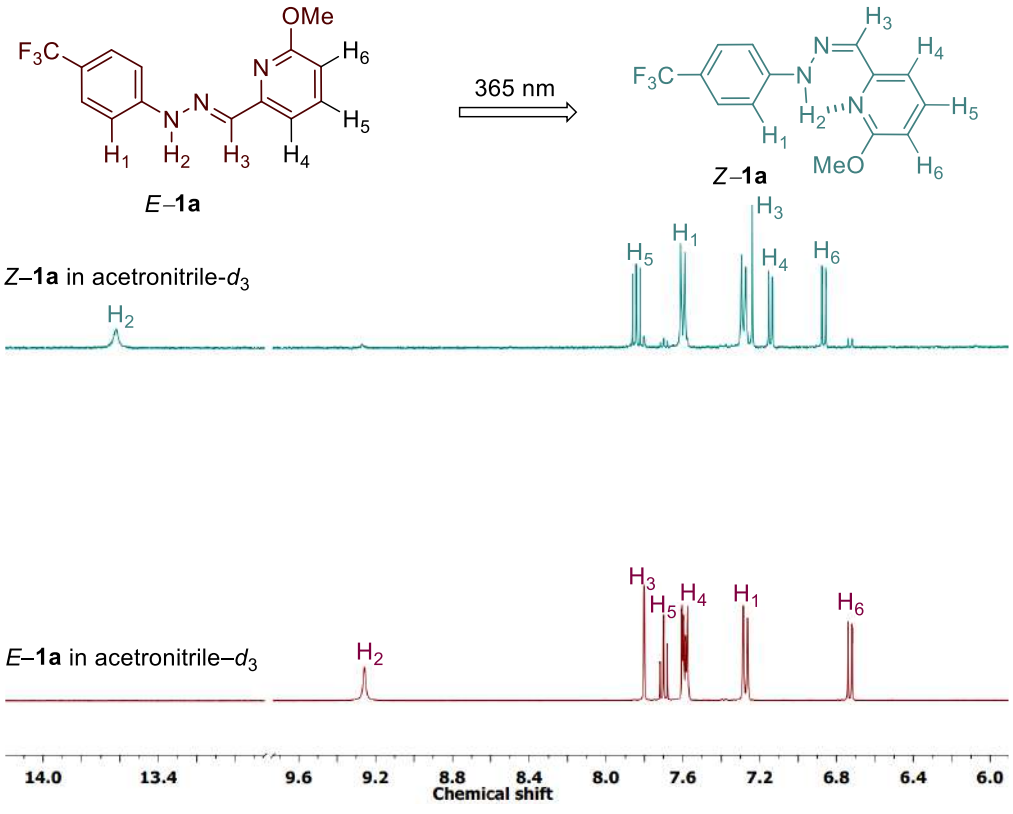

Figure 4.11. Partial 400 MHz ^{1}H NMR spectrum of **2a** in acetonitrile at 25 °C, and that of photo-irradiated sample of **2a** (up) by 365 nm light for 10 min. The *trans* to *cis* ratio after photo-irradiation is 10:90.

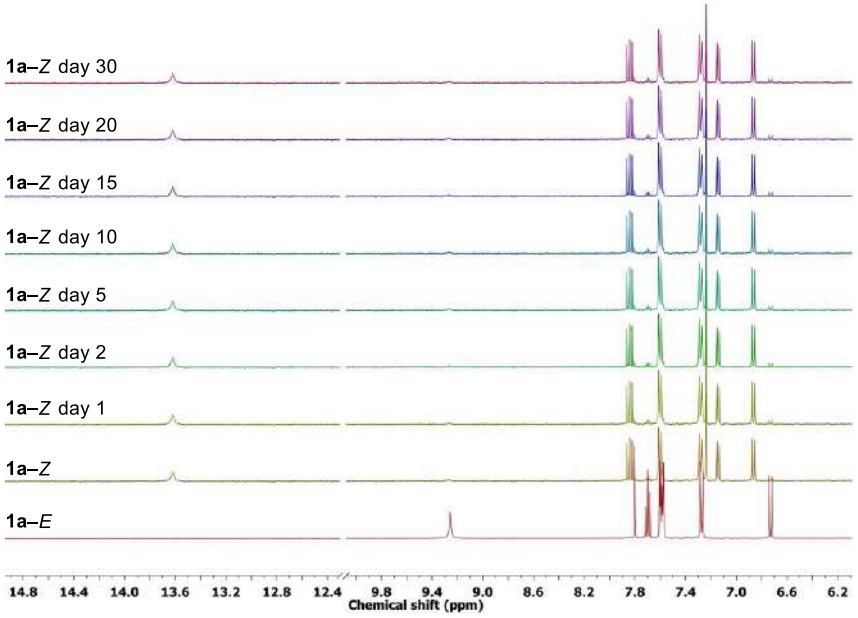

Figure 4.12. Overlapped ^{1}H NMR spectra of **1a**–*Z* in acetonitrile-d_3 after 1 and 30 days of standing in the dark. No significant changes were observed in the spectra within the investigated time.

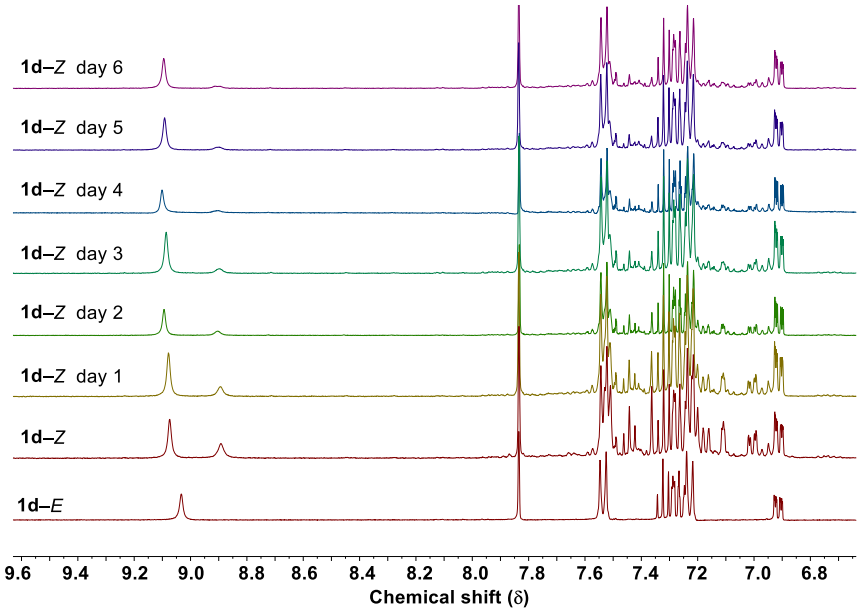

Figure 4.13. Overlapped ^{1}H NMR spectra of **1d**–*Z* in acetonitrile-d_3 after 1 and 6 days of standing in the dark. The photo-irradiated sample significantly relaxed back thermally within the investigated time.

4.2.6.2. Acid-catalysed reversible photoisomerization studies in absence of chloride ions

Initially, ^{1}H NMR was recorded for **1a**–*E* in acetonitrile-d_3. This sample was then irradiated with 365 nm of light using LEDs for 35 min to covert **1a**–*E* to **1a**–*Z* and ^{1}H NMR was recorded. This photoisomerized sample (**1a**–*Z*) was subsequently treated with 10 equiv of triflic acid (TFA) to isomerize **1a**–*Z* form to the protonated **1a**–*E* form. After keeping this acidic solution

for almost 1 h, 10 equiv of triethylamine (TEA) was added to neutralize this acidic solution to regenerate the initial **1a**–*E* form back (Figure 4.14). This reversible isomerization using different stimuli of light and acid catalysed reactivation process was done for three repeated cycles without the loss of efficiency (Figure 4.16A).

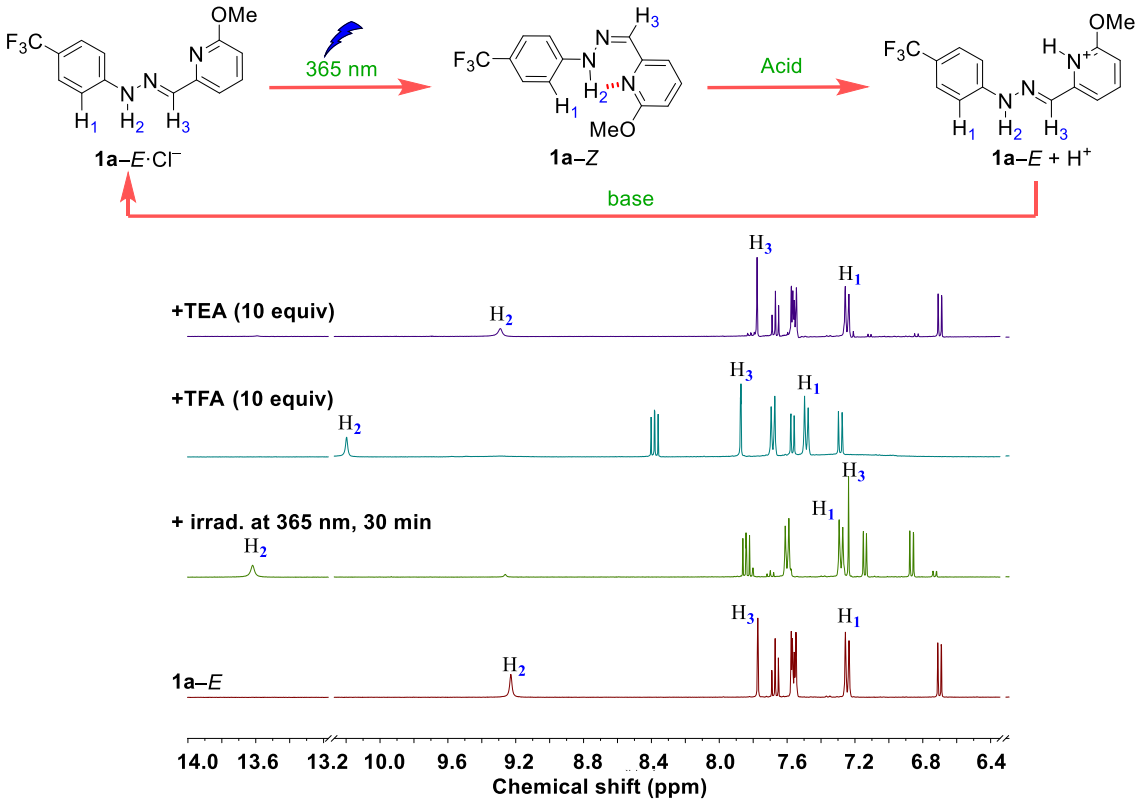

Figure 4.14. ^{1}H NMR (acetonitrile-d3) spectra of one photo/acid switching cycle (bottom to top) in the *E*/*Z* isomerization of *E*-**1a** (2 mM). One cycle involves 3 steps: 1) photo-isomerization of *E*-**1a** to *Z*-**1a** (312 nm, 30 min, 90% PSS); 2) acid-induced quantitative back-isomerization to protonated *E*-**1a**; 3) neutralization of the protonated *E*-**1a** with DIPEA restoring the non-protonated *E*-**1a**.

4.2.6.3. Acid catalysed reversible photoisomerization studies in presence of chloride ions

Initially, ^{1}H NMR was recorded for **1a**–*E* in acetonitrile-d_3 in the presence of chloride ions using Tetrabutylammonium chloride (TBACl, 5 equiv) to form **1a**–*E*·Cl$^-$. This sample was then irradiated with 365 nm of light using LEDs for 35 min to covert **1a**–*E* to **1a**–*Z* and ^{1}H NMR was recorded. This photoisomerized sample (**1a**–*Z*) was subsequently treated with 10 equiv of triflic acid (TFA) to isomerize **1a**–*Z* form to the protonated **1a**–*E* form. After keeping this acidic solution for almost 1 h, 10 equiv of Triethylamine (TEA) was added to neutralize this acidic solution to regenerate the initial **1a**–*E*·Cl$^-$ form back (Figure 4.15). This reversible isomerization using different stimuli of light and acid catalysed reactivation process in the

presence of chloride ions was done for three repeated cycles without the loss of efficiency (Figure 4.16B).

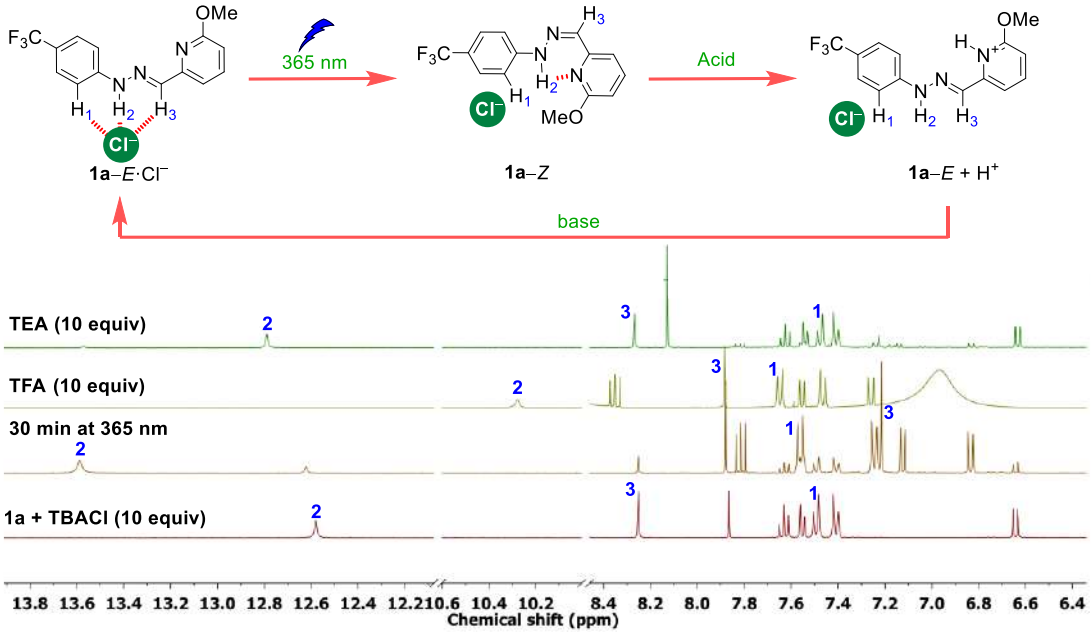

Figure 4.15. ^{1}H NMR spectra of photo/acid switching cycle of **1a**–*E* in acetonitrile–d_3 for *E*/*Z* isomerization process. One cycle involves three steps: 1) Photoisomerization of **1a**–*E* to **1a**–*Z* (365 nm, 30 min); 2) Acid–induced quantitative back–isomerization to protonated **1a**–*E*; 3) Neutralization of the protonated **1a**–*E* with TEA restoring the non-protonated **1a**–*E*.

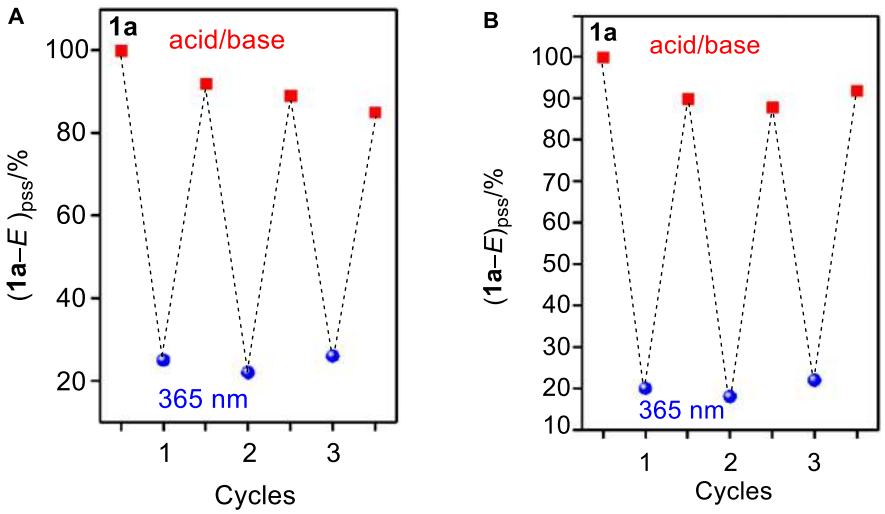

Figure 4.16. Reversible *E* to *Z* switching of **1a** upon photoirradiation at 365 nm and acid/base treatment in the absence of chloride ions acetonitrile–d_3 (**A**). Reversible *E* to *Z* switching of **1a** upon photoirradiation at 365 nm and acid/base treatment in the presence of chloride ions acetonitrile–d_3 (**B**).

4.2.7. Stimuli-Responsive Ion Transport Activity

4.2.7.1. Photodeactivation of ion transport by EYPC-LUVs⊃HPTS assay

Subsequently, the highest active compound **1a** was used to study the photoisomerized transport activity across the lipid bilayer membrane and it was done through HPTS-based vesicles. The transport activity was significantly attenuated upon the photoirradiation of **1a** in acetonitrile at 312 nm. This reduced activity is attributed to the loss of the anion binding site due to *E* to *Z* photoisomerization (Figure 4.17).

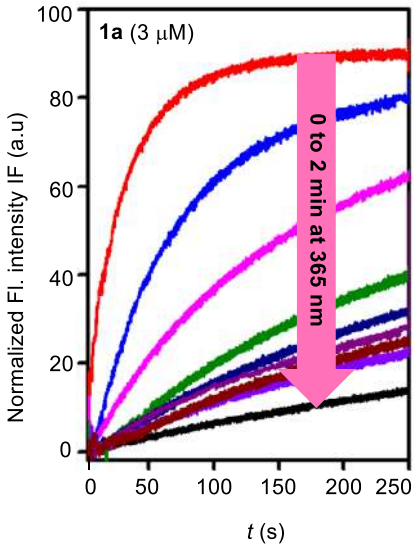

Figure 4.17. Normalized ion transport activity data of **1a** upon photoirradiation at 365 nm for 0-2 min.

4.2.7.2. Stimuli-responsive reversible ion transport activity by ISE studies

Reversible switching of ion transport activity using different stimuli of light and acid/base treatment were studied by monitoring the chloride efflux from LUVs. There was an 82% of decrease in the chloride efflux upon photoirradiation of **1a** as acetonitrile solution, which was efficiently regained back by applying acid/base treatment to the photoisomerized solution of **1a** (Figure 4.18A). This process of de-activation and re-activation was successfully carried out for three repeated cycles without the loss of efficiency (Figure 4.18B).

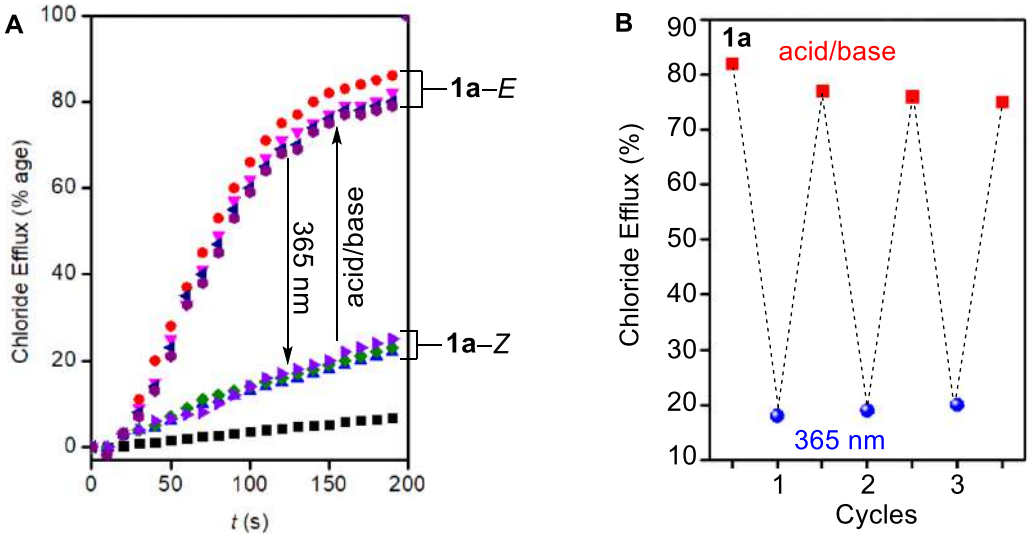

Figure 4.18. Chloride efflux of **1a** in *E* and *Z* forms (**A**). Chloride efflux of **1a** in *E* form, after irradiation at 312 nm and after acid/base treatment (5 equiv) (**B**).

4.3. Conclusion

In conclusion, we have demonstrated photo–responsive anionophoric activities of phenylhydrazones **1a**–**1d**. Anion binding by *E*–form of the system was confirmed by ^{1}H NMR spectroscopic studies. The most active transporter **1a** provided EC_{50} = 2.5 ± 0.1 μM and the Hill coefficient ~ 2, indicating the involvement of two molecules for the formation of an active transporter. The mechanistic studies confirmed a carrier-mediated anion antiport as the primary transport process. The gated ion transport by **1a** was established through the reversible *E*–*Z* isomerization.

4.4. Experimental details

4.4.1. General Methods

All chemical reactions were performed under a nitrogen atmosphere. All reagents and solvents for synthesis were purchased from commercial sources (Sigma-Aldrich, Spectrochem) and used further without purification. The column chromatography was carried out using Merck silica (100-200/ 230-400 mesh size). The thin-layer chromatography was performed on E. Merck silica gel 60-F254 plates. Egg yolk phosphatidylcholine (EYPC) as a solution of chloroform (25 mg/ mL), mini extruder, and polycarbonate membrane of 100 nm and 200 nm were purchased from Avanti Polar Lipid. HEPES, HPTS, lucigenin, NaOH, Triton X-100, FCCP, valinomycin, and all inorganic salts were obtained as molecular biology grades from Sigma Aldrich.

4.4.2. Physical Measurements

The ^{1}H NMR spectra were recorded at 400 MHz whereas the ^{13}C spectra at 101 MHz. The residual solvent signals were considered as an internal reference (δ_H = 7.26 ppm for $CDCl_3$, δ_H = 2.50 for DMSO-d_6, and δ_H = 1.94 for CD_3CN) to calibrate spectra. The chemical shifts were reported in ppm. Following abbreviations were used to indicate multiplicity patterns m: multiplet, s: singlet, d: doublet, t: triplet, q: quartet, dd: doublet of doublets, td: triplet of doublets. Coupling constants were measured in Hz. Infra-red (IR) spectra were measured in cm^{-1} using FT–IR spectrophotometer. Melting points were measured on micro melting point apparatus. High-resolution mass spectra (HRMS) were recorded on electrospray ionization time-of-flight (ESI-TOF). Fluorescence experiments were recorded on Fluoromax-4 from Jobin Yvon Edison equipped with an injector port and a magnetic stirrer in microfluorescence cuvette. All buffer solutions were prepared from the autoclaved water. Adjustment of pH of buffer solutions was made using the Helmer pH meter. The extravesicular dye was removed by performing gel chromatography using Sephadex. The fluorescence studies were proceeded using OriginPro 8.5. ChemBio Draw 15 Ultra software was used for drawing structures and processing figures. UV-vis spectra were recorded on a Varian Cary 5000 spectrophotometer.

4.4.3. General procedure for the synthesis of compounds 1a–1d

In a 25 mL oven-dried round bottom flask, compound **2a–2c** (100 mg, 1 equiv) and appropriate aldehyde (1 equiv) were dissolved in ethanol (10 mL). The reaction mixture was stirred at room temperature for 6 h. After the completion of the reaction, monitored through TLC, the excess solvent was removed under reduced pressure through a rotary evaporator. The crude mixture was then extracted with dichloromethane (3 × 30 mL). The organic layer was dried with anhydrous sodium sulphate, filtered, and concentrated under reduced pressure to give the crude product. The residue was then purified by column chromatography over 100–200 mesh silica gel.

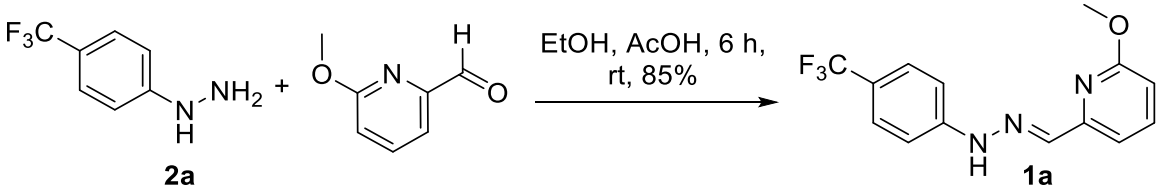

Scheme 4.2. Synthesis of **1a**.

(*E*)-2-methoxy-6-((2-(4-(trifluoromethyl)phenyl)hydrazineylidene)methyl) pyridinebenzamide, $C_{14}H_{12}F_3N_3O$ (1a): Synthesized by reacting *(4-(trifluoromethyl)phenyl)hydrazine* **2a** with *6-methoxypicolinaldehyde*. The crude product was purified by column chromatography over 100–200 mesh silica gel (*Eluent*: EtOAc : petroleum ether 1:9 v/v) to furnish **1a** as yellow solid (141 mg, 85%). **M.P.:** 225.0–227.0 ˚C; **^{1}H NMR (400 MHz, $CDCl_3$):** δ 8.02 (s, 1H), 7.75 (s, 1H), 7.64 – 7.55 (m, 2H), 7.52 (d, *J* = 8.6 Hz, 2H), 7.18 (d, *J* = 8.5 Hz, 2H), 6.68 (dd, *J* = 7.8, 1.1 Hz, 1H), 3.96 (s, 3H).; **^{13}C NMR (101 MHz, $CDCl_3$):** δ 163.8, 151.4, 146.6, 139.3, 138.9, 126.7 (q, *J* = 3.9 Hz), 125.96 (q, *J* = 272.2 Hz), 122 (q, *J* = 32.3 Hz), 112.7, 112.4, 109.8, 53.4; **IR (Neat, ν/cm^{-1}):** 3782, 3701, 3390, 2989, 2354, 1566, 1449, 1343, 1270; **HRMS (ESI) *m/z*:** $[M+H]^+$ Calcd. for $C_{14}H_{12}F_3N_3OH^+$ 296.1005; Found 296.0997.

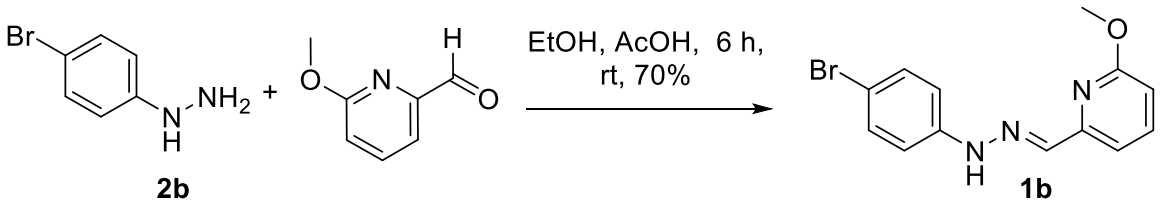

Scheme 4.3. Synthesis of **1b**.

(*E*)-2-((2-(4-bromophenyl)hydrazineylidene)methyl)-6-methoxypyridine, $C_{13}H_{12}BrN_3O$ (1b): Synthesized by reacting *(4-bromophenyl)hydrazine* **2b** with *6-methoxypicolinaldehyde***.** The crude product was purified by column chromatography over 100–200 mesh silica gel (*Eluent*: EtOAc: petroleum ether 2:8 v/v) to furnish **1b** as an orange solid (114 mg, 70%). **M.P.:** 237.0–239.0 ˚C; **^{1}H NMR (400 MHz, DMSO-d_6):** δ 10.75 (s, 1H), 7.80 (s, 1H), 7.70 (t, *J* = 7.8 Hz, 1H), 7.52 (d, *J* = 7.5 Hz, 1H), 7.40 (d, *J* = 8.6 Hz, 2H), 7.06 (d, *J* = 8.6 Hz, 2H), 6.71 (d, *J* = 8.1 Hz, 1H), 3.88 (s, 3H).; **^{13}C NMR (101 MHz, DMSO-d_6):** δ 163.7, 152.5, 144.4, 139.7, 137.8, 132.3, 114.6, 112.3, 110.7, 109.5, 53.4; **IR (Neat, ν/cm^{-1}):** 3781, 3702, 3160, 2990, 2936, 2351, 1567, 1449, 1346, 1272; **HRMS (ESI) *m/z*:** $[M+H]^+$ Calcd. for $C_{13}H_{12}BrN_3OH^+$ 306.0236; Found 306.0235.

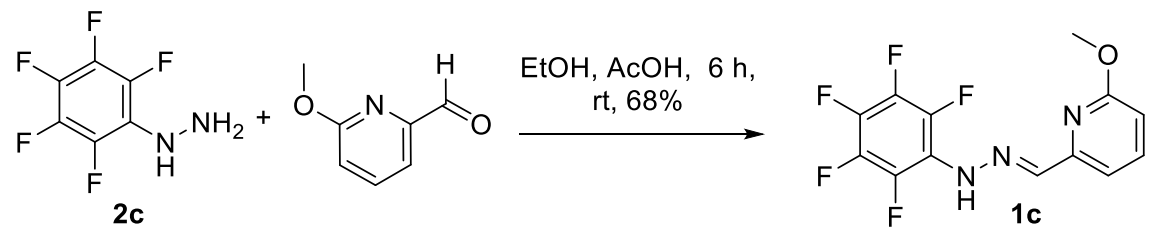

Scheme 4.4. Synthesis of **1c**.

(*E*)-2-methoxy-6-((2-(perfluorophenyl)hydrazineylidene)methyl)pyridine, $C_{13}H_8F_5N_3O$ (1c): Synthesized by reacting *(perfluorophenyl)hydrazine* **2c** with *6-methoxypicolinaldehyde*. The crude product was purified by column chromatography over 100–200 mesh silica gel (*Eluen*t: EtOAc: petroleum ether 1:9 v/v) to furnish **1c** as white solid (97 mg, 68%). **M.P.:** 187.0–189.0 ˚C; **^{1}H NMR (400 MHz, $CDCl_3$):** δ 7.83 (s, 1H), 7.61 (t, *J* = 7.8 Hz, 1H), 7.52 (d, *J* = 7.4 Hz, 1H), 7.47 (s, 1H), 6.72 (d, *J* = 8.1 Hz, 1H), 3.97 (s, 3H).; **^{13}C NMR (101 MHz, $CDCl_3$):** δ 163.8, 150.6, 143.3, 139.2 (m), 138.9, 137.4 (m), 136.7 (m), 135.1 (m), 113.0, 110.6, 55.4.; **IR (Neat, v/cm^{-1}):** 3779, 3704, 3390, 3169, 2948, 2355, 1570, 1515, 1454, 1280; **HRMS (ESI) *m/z*:** $[M+H]^+$ Calcd. for $C_{13}H_8F_5N_3OH^+$ 318.0660; Found 318.0670.

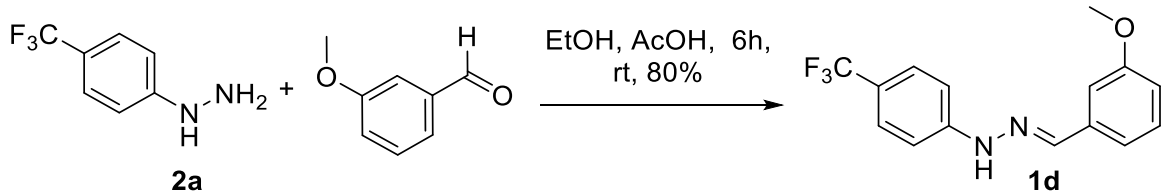

Scheme 4.5. Synthesis of **1d**.

(*E*)-1-(3-methoxybenzylidene)-2-(4-(trifluoromethyl)phenyl)hydrazine, $C_{15}H_{13}F_3N_2O$ (1d): Synthesized by reacting *(4-(trifluoromethyl)phenyl)hydrazine* **2a** with *3-methoxybenzaldehyde*. The crude product was purified by column chromatography over 100–200 mesh silica gel (*Eluent*: EtOAc : petroleum ether 1:9 v/v) to furnish **1d** as white solid (113 mg, 80%). **M.P.:** 207.0–209.0 ˚C; **^{1}H NMR (400 MHz, $CDCl_3$):** δ 7.76 (s, 1H), 7.68 (s, 1H), 7.50 (d, *J* = 8.6 Hz, 2H), 7.32 – 7.24 (m, 2H), 7.19 (d, *J* = 7.6 Hz, 1H), 7.14 (d, *J* = 8.6 Hz, 2H), 6.89 (dd, *J* = 8.0, 2.5 Hz, 1H), 3.86 (s, 3H).; **^{13}C NMR (101 MHz, $CDCl_3$):** δ 159.9, 147.1, 138.9, 136.1, 129.7, 126.6 (q, *J* = 3.9 Hz), 124.4(q, *J* = 272.2 Hz), 121.7(q, *J* = 32.3 Hz), 119.5, 115.1, 112.2, 110.9, 55.3; **IR (Neat, v/cm^{-1}):** 3780, 3703, 3313, 2990, 2352, 1596, 1528, 1477, 1427, 1324; **HRMS (ESI) *m/z*:** $[M+H]^+$ Calcd. for $C_{15}H_{13}F_3N_2OH^+$ 295.1052; Found 295.1046.

4.4.4. Anion Binding Studies

4.4.4.1. Anion Binding by ^{1}H NMR titration Studies

^{1}H NMR titration was carried out at room temperature on a Bruker 400 MHz spectrometer. The residual solvent signal (CD_3CN, δ_H = 1.94) was considered as an internal reference to calibrate spectra. The TBACl, TBABr and TBAI salts and receptors were dried in a high vacuum before use. The titrations were performed by the addition of aliquots from either TBACl, TBABr or

TBAI solutions (0.5 M in CD_3CN) to the solution of either **1a**, **1b**, **1c**, **1d**, or **1a–*Z***, (0.0025 M in CD_3CN). All NMR data were processed using MestreNova 6.0 and collected data were fitted in different binding modes using BindFit.

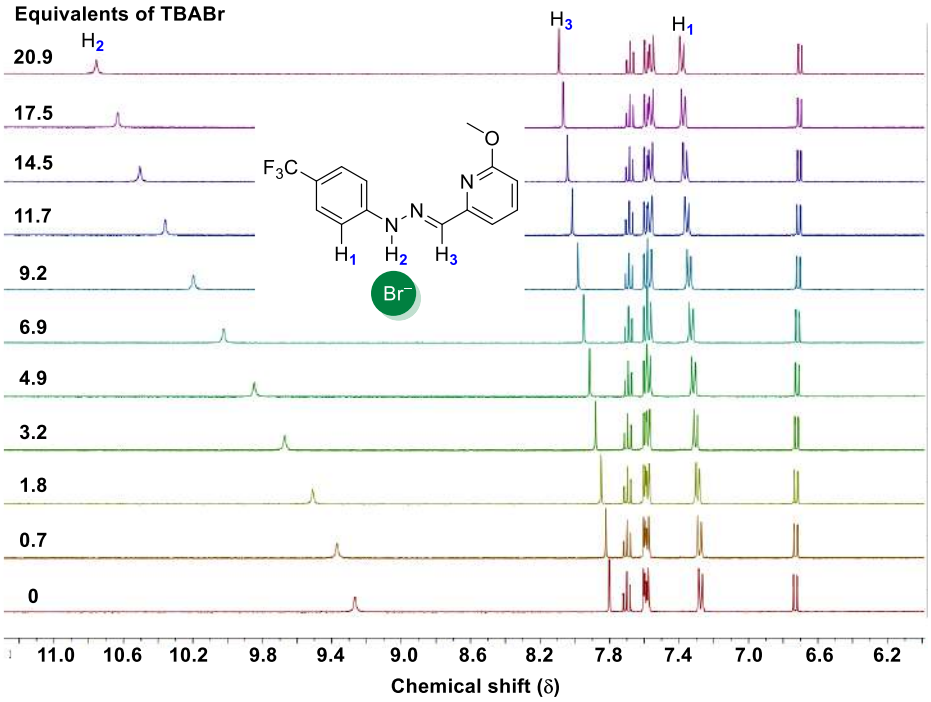

Figure 4.19. ^1H NMR titration spectra for **1a** (2.5 mM) with stepwise addition of TBABr in CD_3CN. The equivalents of added TBABr are shown on the stacked spectra.

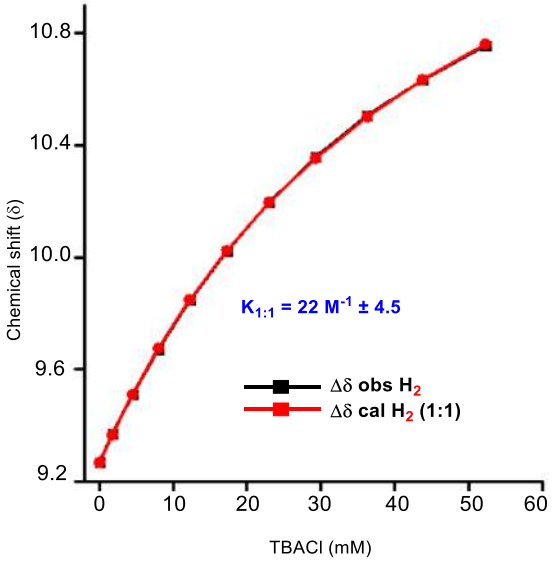

Figure 4.20. The plot of chemical shift (δ) of H_2 protons *vs* concentration of TBABr added, fitted to 1:1 binding model of BindFit v0.5. The binding constant obtained is the mean of the three independent experiments.

http://app.supramolecular.org/bindfit/view/ac216a3a-8c27-4632-9b84-49f8eab7ffe1 (**1a** with TBABr).

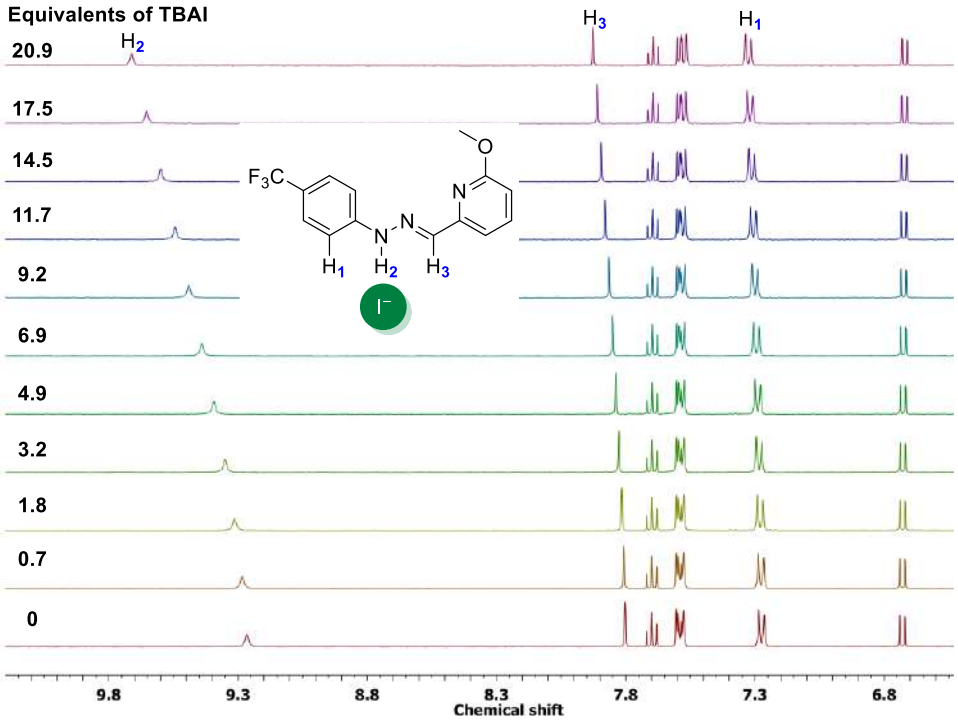

Figure 4.21. ^{1}H NMR titration spectra for **1a** (2.5 mM) with stepwise addition of TBAI in CD_3CN. The equivalents of added TBAI are shown on the stacked spectra.

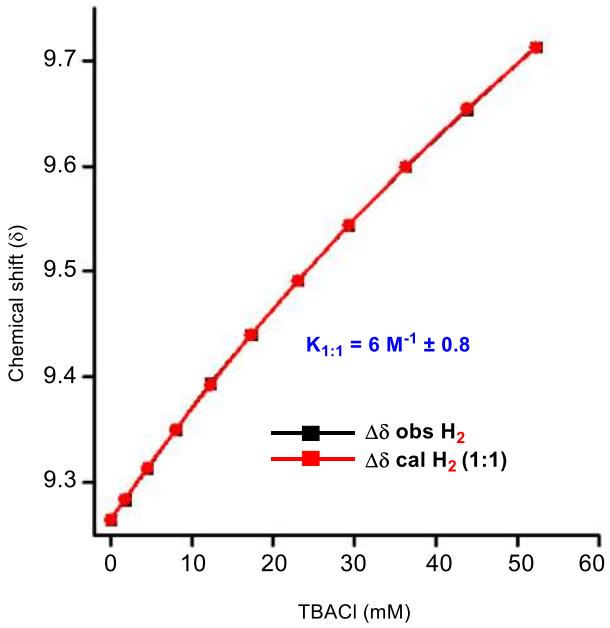

Figure 4.22. The plot of chemical shift (δ) of H_2 protons *vs* concentration of TBAI added, fitted to 1:1 binding model of BindFit v0.5. The binding constant obtained is the mean of the three independent experiments.

http://app.supramolecular.org/bindfit/view/806b331d-b456-4af1-9040-cf60a3492e2b (**1a** with TBAI).

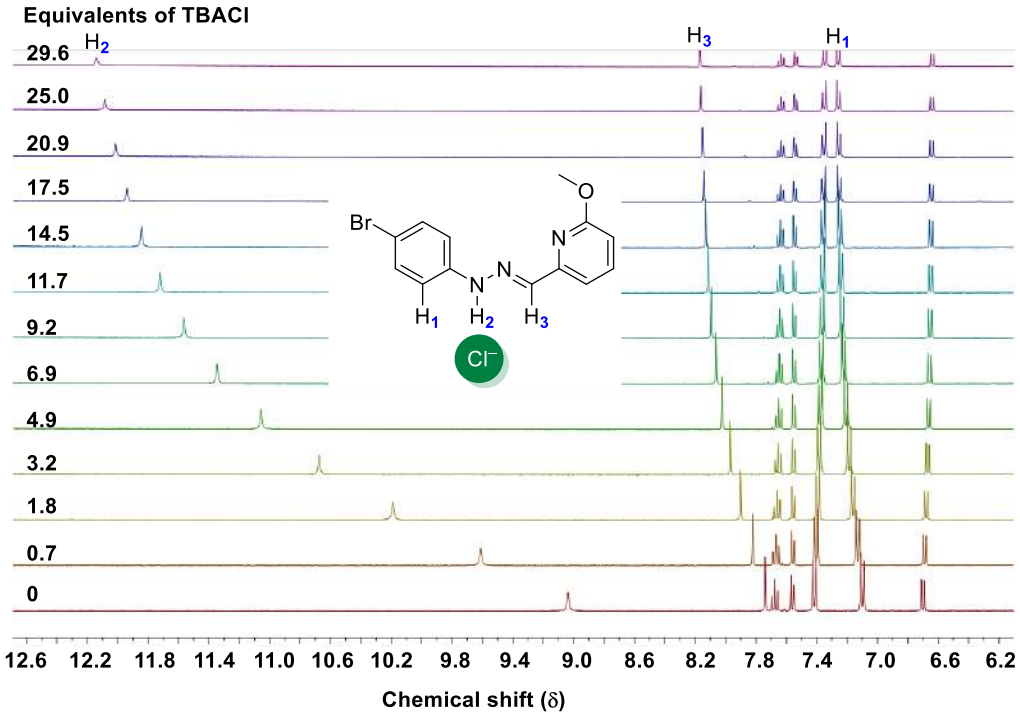

Figure 4.23. ^{1}H NMR titration spectra for **1b** (2.5 mM) with stepwise addition of TBACl in CD_3CN. The equivalents of added TBACl are shown on the stacked spectra.

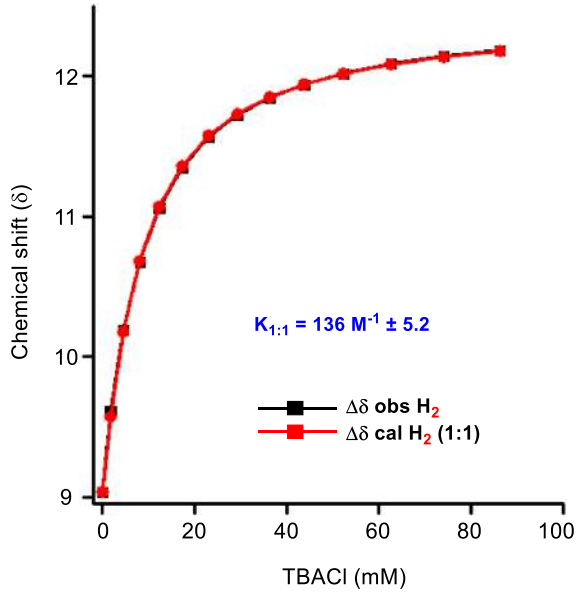

Figure 4.24. The plot of chemical shift (δ) of H_2 protons *vs* concentration of TBACl added, fitted to 1:1 binding model of BindFit v0.5. The binding constant obtained is the mean of the three independent experiments.

http://app.supramolecular.org/bindfit/view/5bd0dd77-06ec-4691-a7dd-0d4079452344 (**1b** with TBACl).

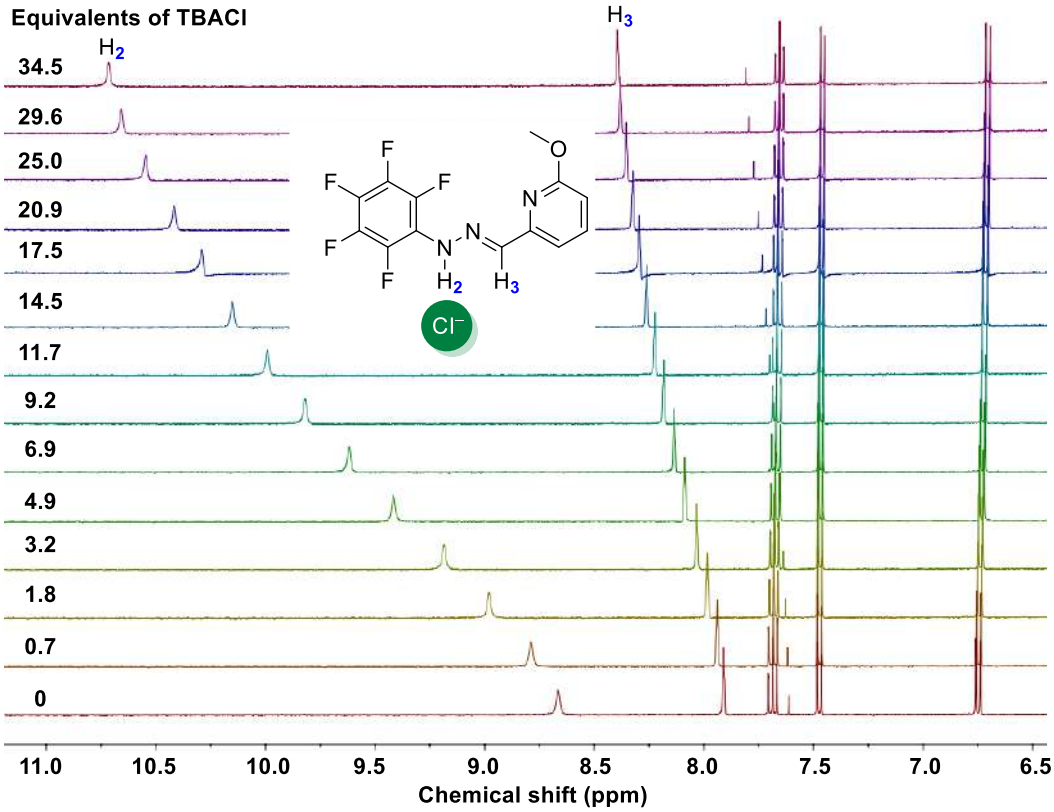

Figure 4.25. ^{1}H NMR titration spectra for **1c** (2.5 mM) with stepwise addition of TBACl in CD_3CN. The equivalents of added TBACl are shown on the stacked spectra.

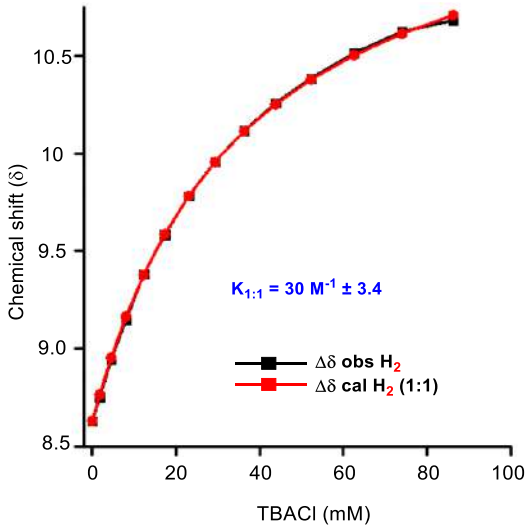

Figure 4.26. The plot of chemical shift (δ) of H_2 protons *vs* concentration of TBACl added, fitted to 1:1 binding model of BindFit v0.5. The binding constant obtained is the mean of the three independent experiments.

http://app.supramolecular.org/bindfit/view/907a4d5d-0171-4d09-8f36-5f6079480e51 (**1c** with TBACl).

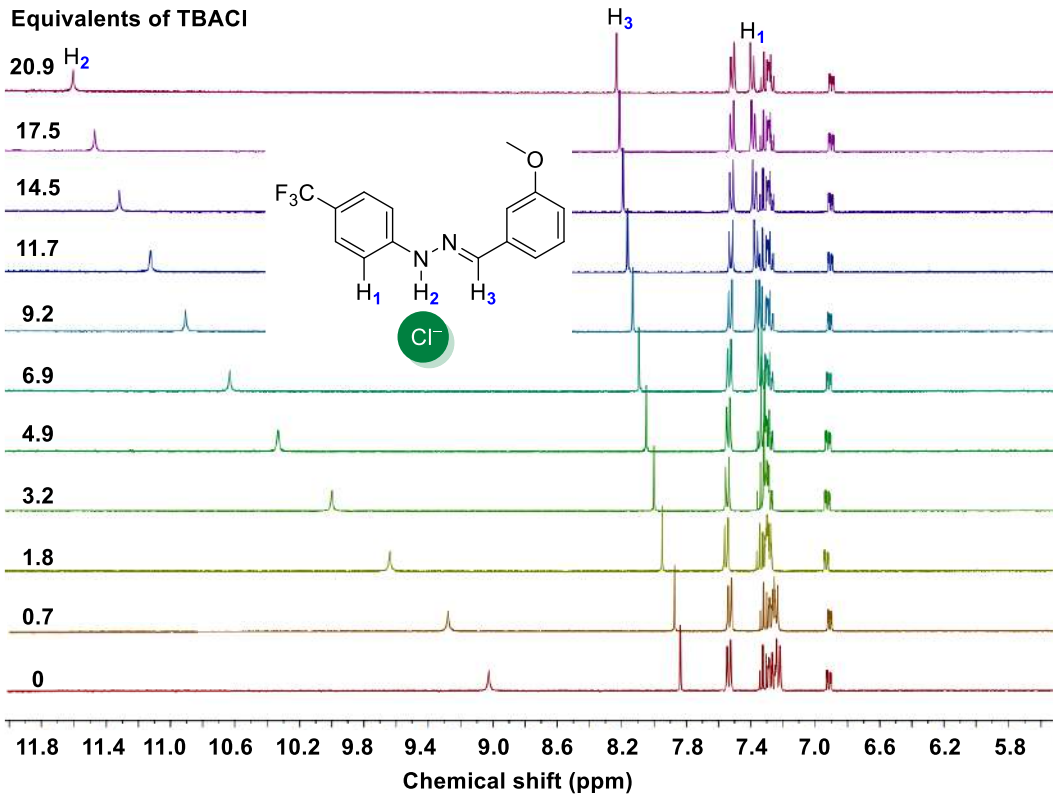

Figure 4.27. ^{1}H NMR titration spectra for **1d** (2.5 mM) with stepwise addition of TBACl in CD_3CN. The equivalents of added TBACl are shown on the stacked spectra.

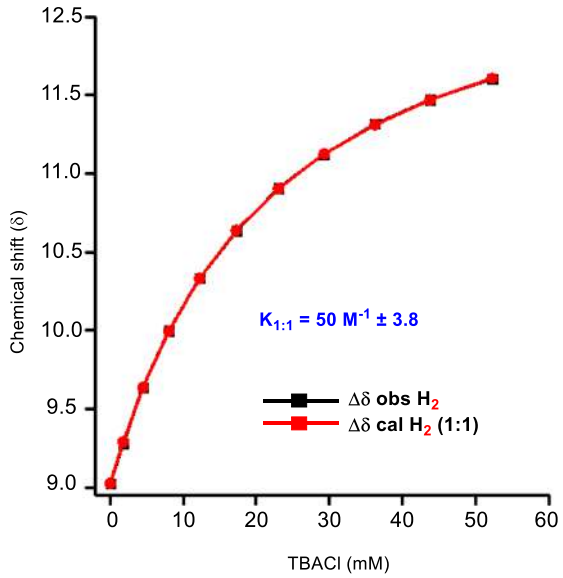

Figure 4.28. The plot of chemical shift (δ) of H_2 protons *vs* concentration of TBACl added, fitted to 1:1 binding model of BindFit v0.5. The binding constant obtained is the mean of the three independent experiments.

http://app.supramolecular.org/bindfit/view/79300945-7f51-445b-87dd-a86c9f089e0c (**1d** with TBACl).

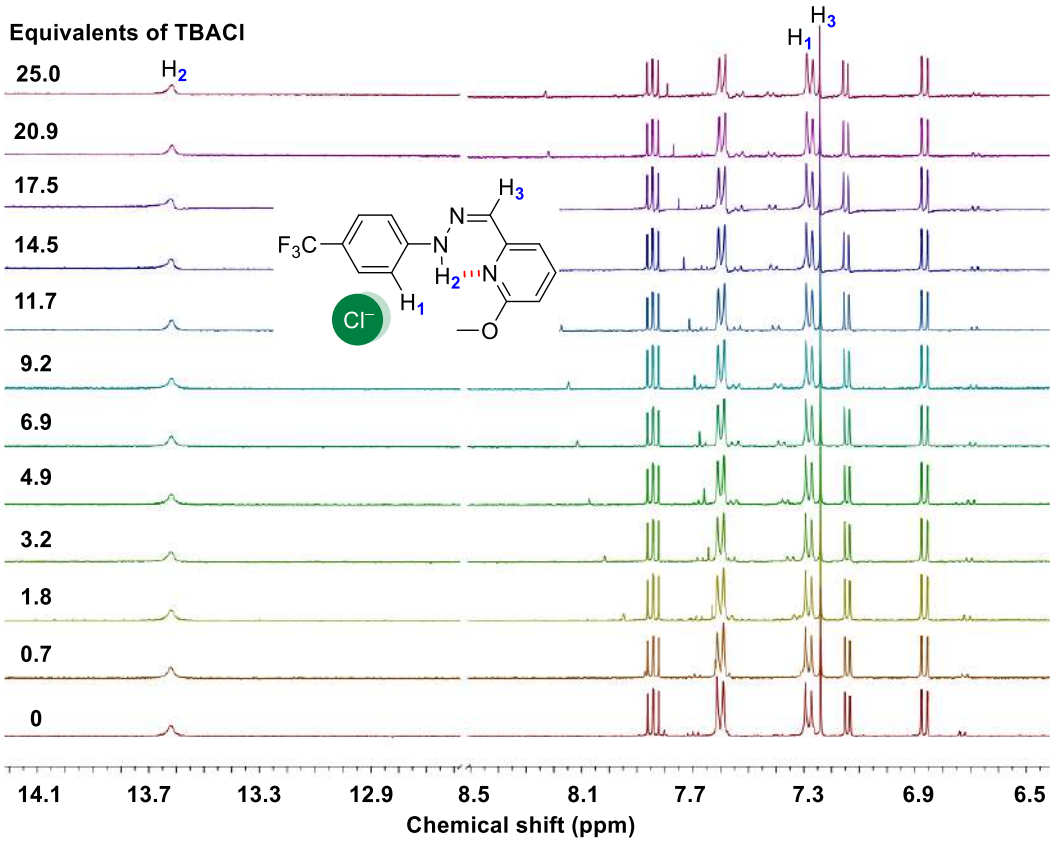

Figure 4.29. ^{1}H NMR titration spectra for **1a–*Z*** (2.5 mM) with stepwise addition of TBACl in CD_3CN. The equivalents of added TBACl are shown on the stacked spectra.

4.4.4.2. Mass Spectrometric Studies

Compound **1a** and TMACl (Tetramethylammonium chloride) (1 mM each) were mixed in the ratio of **1a:**TMACl as 2:1 in CH_3CN. The solution was electrosprayed at a flow rate of 5.0 μL/min. A constant spray and highest intensities were achieved with a capillary voltage of 2500 V at a source temperature of 80 °C. The parameters for sample cone (20 V) and extractor cone voltage (5 V) were optimized for maximum intensities of the desired complexes. Figure S14 represents the ESI-MS data recorded from CH_3CN solution of **1a** with TMACl prepared in 2:1 molar ratio.

4.4.5. Ion transport studies

4.4.5.1. Dose-responsive studies across EYPC-LUVs⊃HPTS vesicles

The dose-responsive studies for the compounds **1a–1d** were carried out across EYPC-LUVs⊃HPTS vesicles following the reported procedure explained in chapter 2.

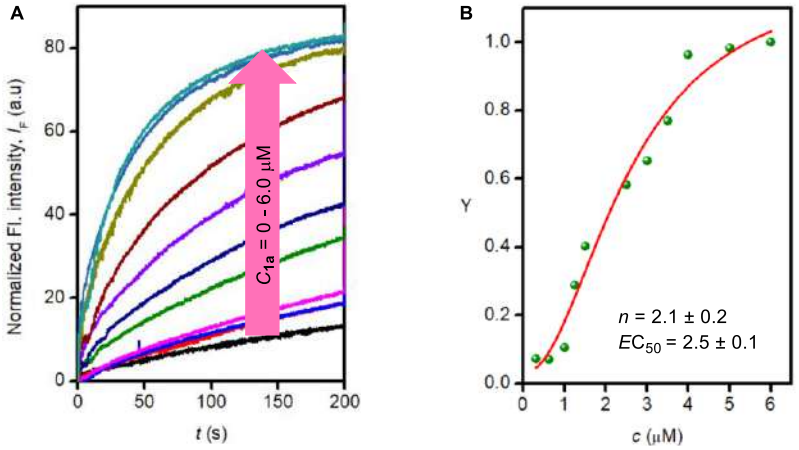

Figure 4.30. Concentration-dependent activity of **1a** across EYPC-LUVs⊃HPTS (**A**). Dose-response plot of **1a** at 180 s after addition of compound (**B**).

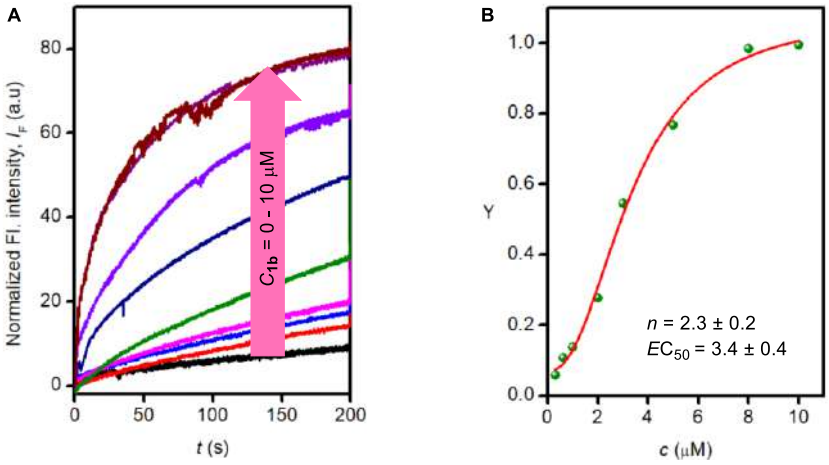

Figure 4.31. Concentration-dependent activity of **1b** across EYPC-LUVs⊃HPTS (**A**). Dose-response plot of **1b** at 180 s after addition of compound (**B**).

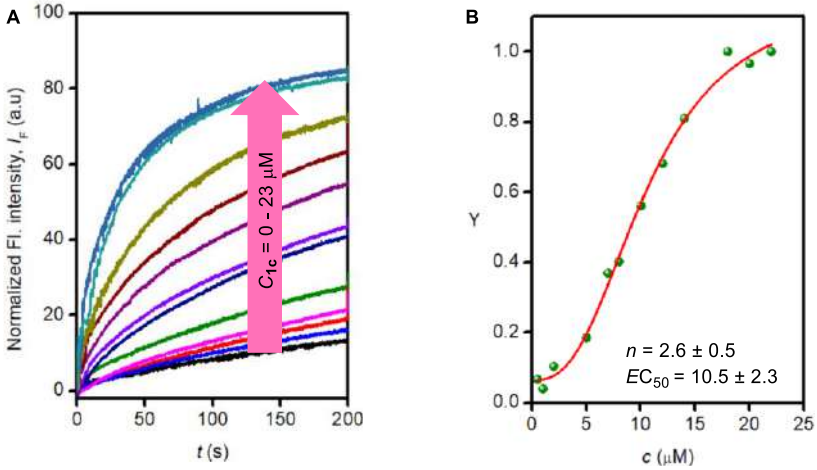

Figure 4.32. Concentration-dependent activity of **1c** across EYPC-LUVs⊃HPTS (**A**). Dose-response plot of **1c** at 180 s after addition of compound (**B**).

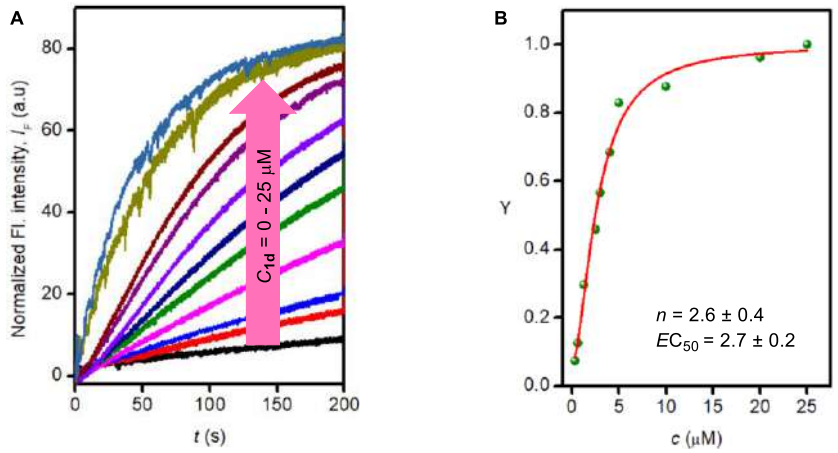

Figure 4.33. Concentration-dependent activity of **1d** across EYPC-LUVs⊃HPTS (**A**). Dose-response plot of **1d** at 280 s after addition of compound (**B**).

4.4.5.2. Dose-responsive studies across EYPC-LUVs⊃lucigenin vesicles

The dose-responsive studies for the compounds **1a** was carried out across EYPC-LUVs⊃lucigenin vesicles following the reported procedure explained in chapter 2.

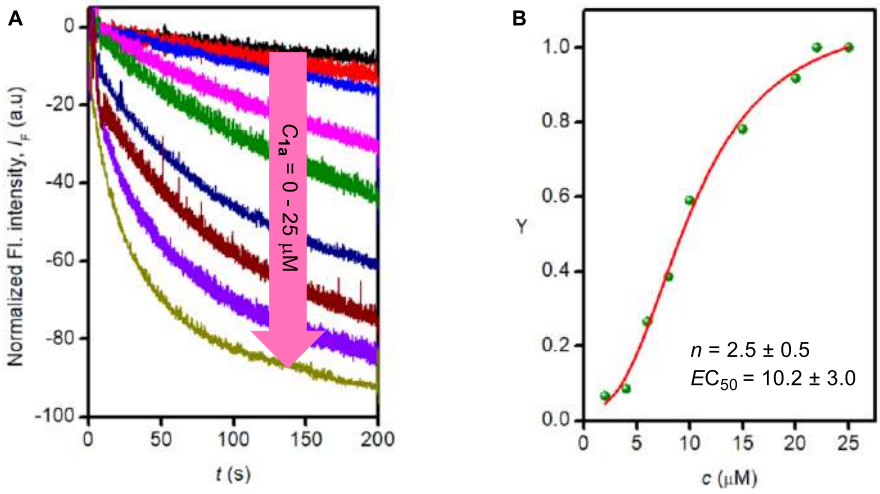

Figure 4.34. Concentration-dependent activity of **1a** across EYPC-LUVs⊃lucigenin (**A**). Dose-response plot of **1a** at 180 s after addition of compound (**B**).

4.4.5.3. Cation selectivity studies across EYPC-LUVs⊃HPTS

Preparation of EYPC-LUVs⊃HPTS for cation selectivity: EYPC-LUVs⊃HPTS (~ 5.0 mM EYPC, inside: 1 mM HPTS, 10 mM HEPES, 100 mM NaCl, pH = 7.0 and outside: 10 mM HEPES, 100 mM MCl, pH = 7.0; where, (M = Li^+, Na^+, K^+, Rb^+, and Cs^+), were prepared.

Cation selectivity assay: In a clean fluorescence cuvette, 1975 µL of HEPES buffer (10 mM HEPES, 100 mM MCl, (M = Li^+, Na^+, K^+, Rb^+, and Cs^+), at pH = 7.0; was added followed by the addition of 25 µL of EYPC-LUVs⊃HPTS vesicle in slowly stirring condition by a magnetic stirrer equipped with the fluorescence instrument (at t = 0 s). HPTS fluorescence emission intensity (F_t) was monitored with time at λ_{em} = 510 nm (λ_{ex} = 450 nm). 20 µL of 0.5 M NaOH was added to the cuvette at t = 20 s to make the pH gradient between the intra- and extravesicular system. The compound **1a** was added at t = 100 s and at t = 300 s, 25 µL of 10% Triton X-100 was added to lyze all vesicles for the complete destruction of the pH gradient. For data analysis and comparison, time (X-axis) was normalized using Equation S1. Fluorescence intensities (F_t) were normalized to fractional emission intensity I_F using Equation S2.

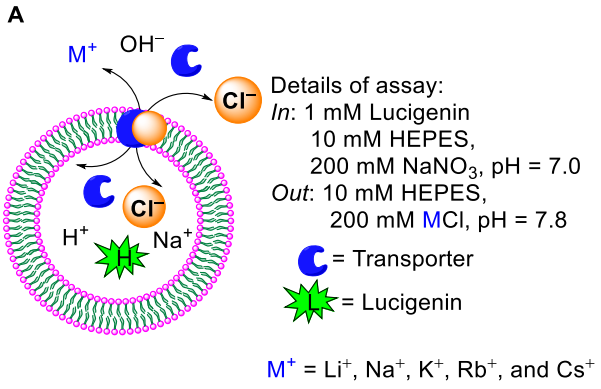

Figure 4.35. Schematic representations of fluorescence-based cation selectivity assay

4.4.5.4. Ion transport activity across EYPC-LUVs⊃lucigenin in the presence of valinomycin

The antiport mechanism (i.e., simultaneous transport of two different ions, in opposite directions, across the membrane)[14] of **1a** was experimentally confirmed by lucigenin assay in the presence of valinomycin. The ion transport activity of **1a** was monitored in a vesicle entrapped with lucigenin (1 mM) and $NaNO_3$ (200 nM) suspended in KCl (2 M) solution with and without valinomycin. The remarkable enhancement in ion transport activity of **1a** in the presence of valinomycin gave a direct experimental insight into the antiport mechanism of ion transport.

Preparation of EYPC-LUVs⊃lucigenin: The vesicles were prepared by the following protocol as stated above.

Antiport mechanism: In a clean and dry fluorescence cuvette, 1975 µL 200 mM $NaNO_3$ solution and 25 µL EYPC-LUVs⊃lucigenin vesicles were taken, and slowly stirred in a fluorescence instrument equipped with a magnetic stirrer (at t = 0 s). The time-dependent fluorescence intensity of lucigenin was monitored at λ_{em} = 535 nm (λ_{ex} = 455 nm). A solution of 2 M KCl (33.3 µL) was added at *t* = 20 s to create a chloride gradient between intra and extra vesicular system, followed by the addition of valinomycin (1.25 µM) at *t* = 50 s and transporter **1a** (3 µM) at *t* = 100 s. Finally, the destruction of the chloride gradient was done by the addition of 10 % Triton X-100 (25 µL) at *t* = 300 s. The time axis was normalized according to Equation S1, and the time-dependent data were normalized to percent change in fluorescence intensity using Equation S4.

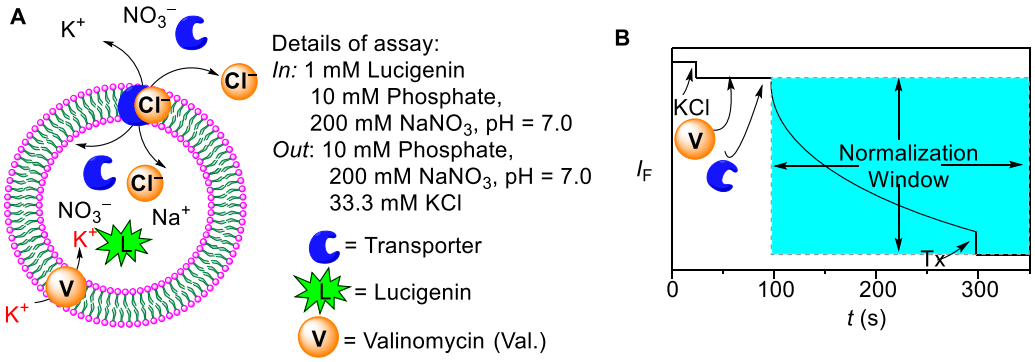

Figure 4.36. Schematic representations of fluorescence-based cation selectivity assay (**A**), and illustration of ion transport kinetics showing normalization window (**B**).

4.4.6. Photoisomerization Studies

4.4.6.1. UV-Vis studies

Photoisomerization studies of compounds **1a**, **1b**, **1c**, and **1d** were carried out in CH_3CN. Initially, stock solutions of these compounds (2 mM in CH_3CN) were prepared in different vials and covered with an aluminium foil.

In a 2 mL UV cuvette, was placed 1900 µL of CH_3CN and 100 µL of either **1a**, **1b**, **1c**, or **1d** was added to get the final concentration of 100 µM.

The cuvette was placed in a UV-Vis spectrometer, and the UV-Vis spectrum was recorded.

***trans* to *cis* Isomerization:** Subsequently, each of these samples was irradiated at λ = 365 nm using LEDs (3 × 1 W) for varied time intervals to isomerize the phenylhydrazone moiety. After each irradiation, the UV-Vis spectrum was recorded.

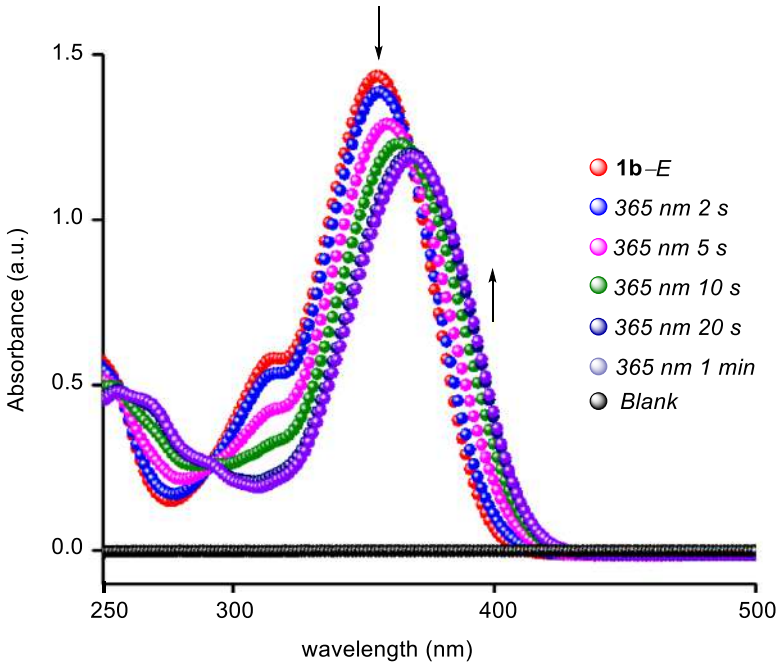

Figure 4.37. UV-Vis spectral changes for **1b** (100 μM) upon irradiation with 365 nm light (3 × 1 W LEDs).

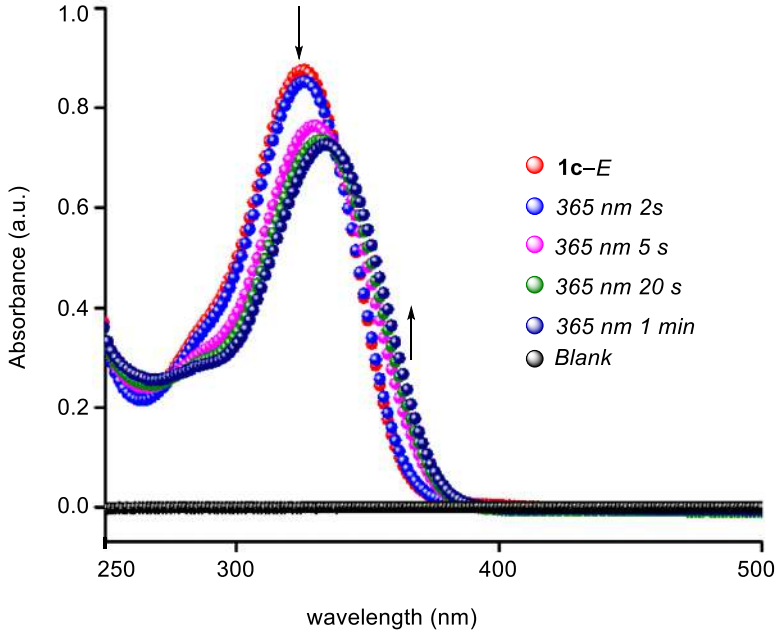

Figure 4.38. UV-Vis spectral changes for **1c** (100 μM) upon irradiation with 365 nm light (3 × 1 W LEDs).

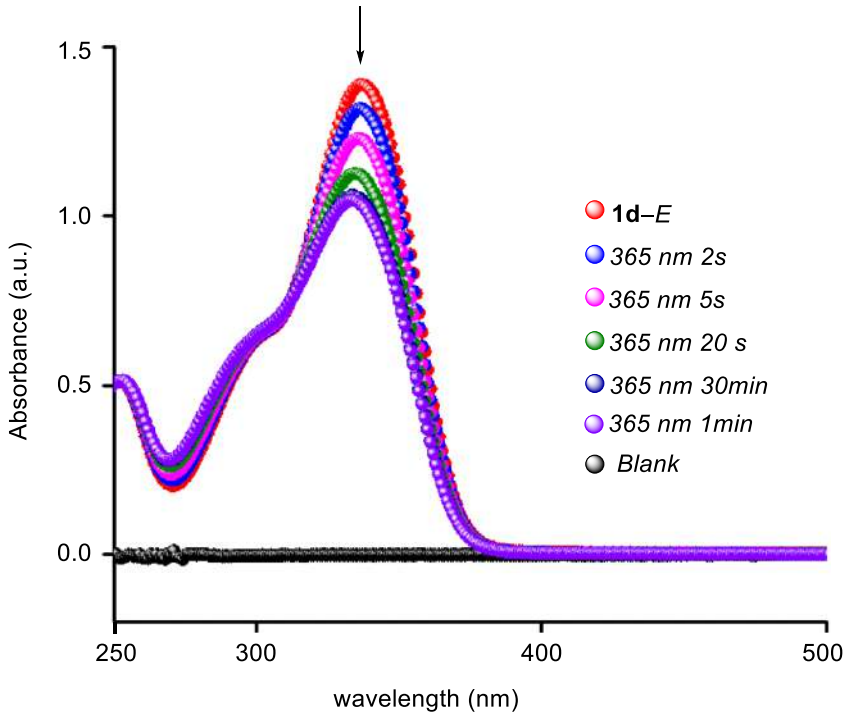

Figure 4.39. UV-Vis spectral changes for **1d** (100 μM) upon irradiation with 365 nm light (3 × 1 W LEDs).

4.4.6.2. ^{1}H NMR studies

***trans* to *cis* Isomerization:** For monitoring the *trans* to *cis* isomerization by ^{1}H NMR, samples of **1a**, **1b**, **1c**, or **1d** (4.0×10^{-3} M) in CD_3CN were prepared in different NMR tubes, and ^{1}H NMR was recorded for each sample. Then each sample was irradiated at λ = 365 nm using LEDs (3 × 1 W) for 30 min. ^{1}H NMR data before and after photoirradiation were compared. The *trans* to *cis* ratio after photo-irradiation for **1a**, **1b**, **1c**, and **1d** were found to be 17:83, 10:90, 47:53, and 48:52, respectively at the photostationary state (PSS).

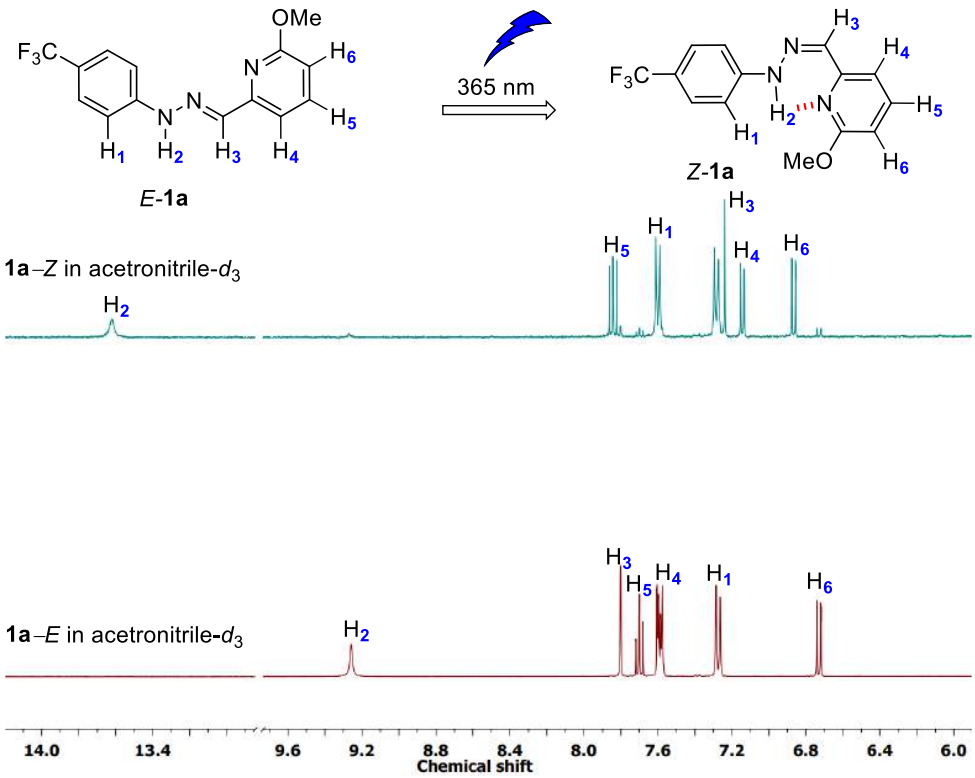

Figure 4.40. Partial 400 MHz ^{1}H NMR spectrum of **1a** (lower plot) in acetonitrile-d_3 at 25 °C, and that of the photo-irradiated (by 365 nm light for 30 min) sample of **1a** (upper plot).

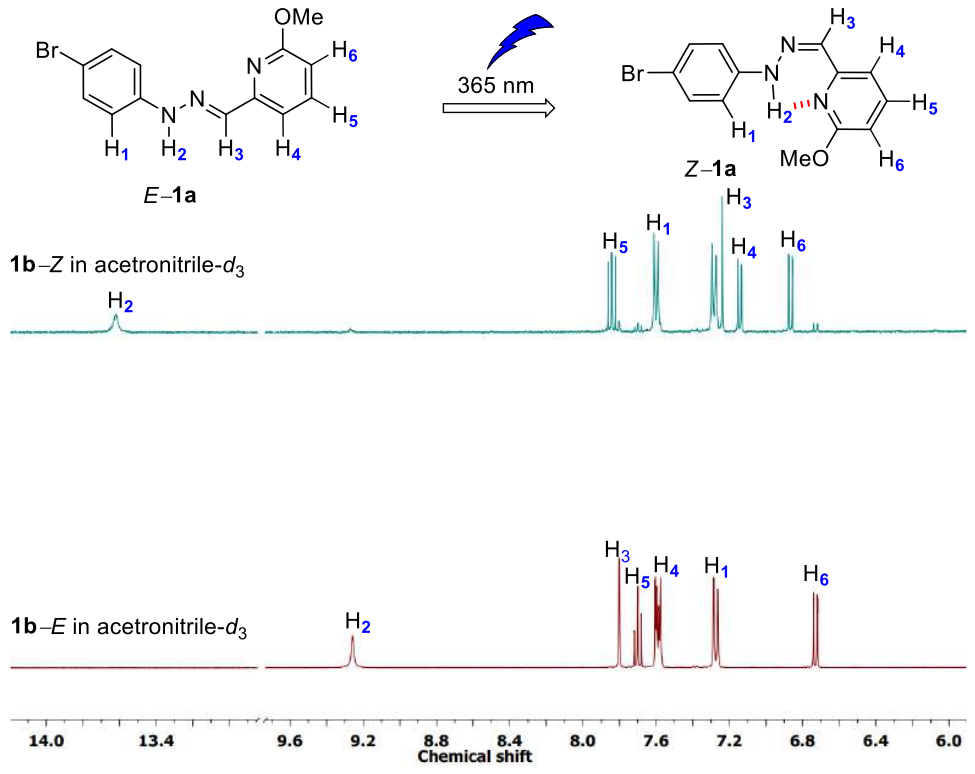

Figure 4.41. Partial 400 MHz ^{1}H NMR spectrum of **1b** (lower plot) in acetonitrile-d_3 at 25 °C, and that of the photo-irradiated (by 365 nm light for 30 min) sample of **1b** (upper plot).

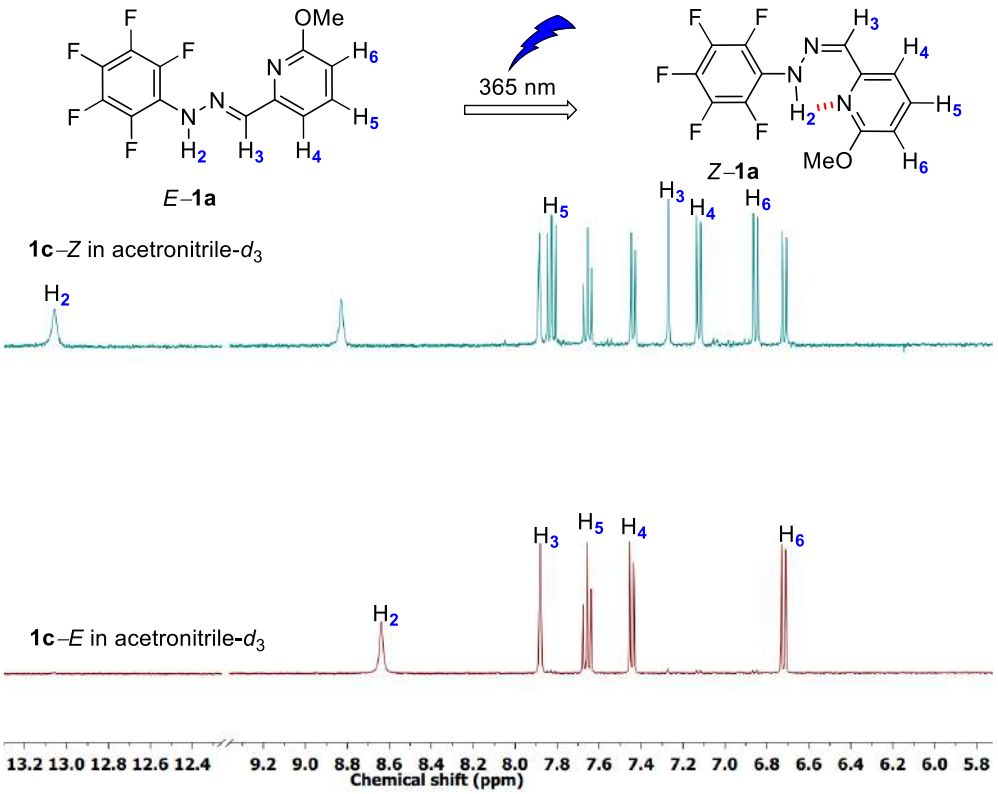

Figure 4.42. Partial 400 MHz ^{1}H NMR spectrum of **1c** (lower plot) in acetonitrile-d_3 at 25 °C, and that of the photo-irradiated (by 365 nm light for 30 min) sample of **1c** (upper plot).

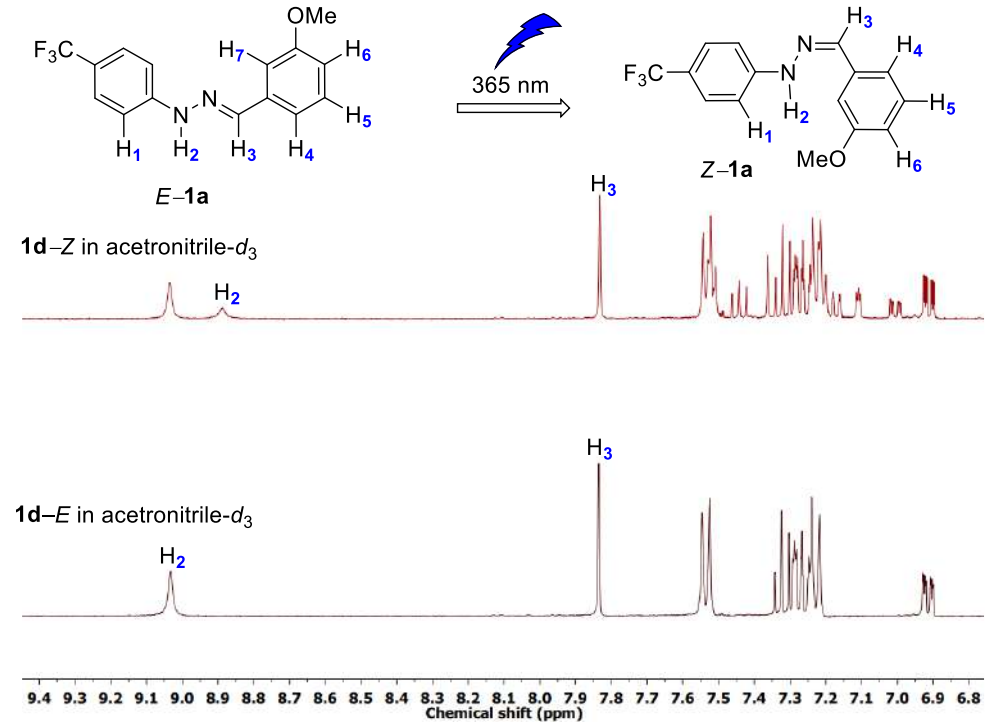

Figure 4.43. Partial 400 MHz ^{1}H NMR spectrum of **1d** (lower plot) in acetonitrile-d_3 at 25 °C, and that of the photo-irradiated (by 365 nm light for 30 min) sample of **1d** (upper plot).

4.4.6.3. Actinometry and Quantum yield determination

Ferrioxalate actinometry and quantum yield determinations were done according to the established procedures.[21] All samples were irradiated in 1 cm quartz cuvettes under controlled conditions (365 nm using 3 × 1 W LEDs). as the light source. The quantum yields ($\Phi_{E\rightarrow Z}$) thus obtained were found to be 0.028, 0.024, 0.007, and 0.047 for the compounds **1a**, **1b**, **1c**, and **1d**, respectively.

For a given photoreaction:

$$A \xrightarrow{h\nu} B$$

The quantum yield, Φ, is given by

$$\Phi = \frac{n_B}{n_{h\nu}}$$

where n_B is the number of moles of the formed product B and $n_{h\nu}$ is the number of moles of photons absorbed by the solution during the irradiation period within which low conversions are obtained (< 5%). Under the same experimental conditions and when all incident light is absorbed (absorbance > 2), two different photoreactions will absorb the same amount of photons, $n_{h\nu}$. Therefore, it is possible to calculate the quantum yield of one reaction if the quantum yield of the other reaction is known:

$$\Phi_1 = \frac{n_{B1}}{n_{h\nu}} \quad \text{and} \quad \Phi_2 = \frac{n_{B2}}{n_{h\nu}} \quad \text{give} \quad \Phi_1 = \frac{n_{B1}}{n_{h\nu}} \Phi_2$$

Or, in terms of the rates of formation:

$$\Phi_1 = \frac{n_{B1}}{n_{h\nu}} \Phi_2 = \frac{\frac{\Delta n_{B1}}{\Delta t} t}{\frac{\Delta n_{B2}}{\Delta t} t} \Phi_2 = \frac{\frac{\Delta c_{B1}}{\Delta t} V_1 t}{\frac{\Delta c_{B2}}{\Delta t} V_1 t} \Phi_2,$$

In the case presented herein, we used a well-known ferrioxalate photoreduction reaction as a reference standard, in which the concentration of the Fe^{2+} product can be easily followed spectrophotometrically and the quantum yield is known to be 1.24.[21] Thus:

$$\Phi_{E_{1a} \rightarrow Z_{1a}} = \frac{\text{rate of } Z_{1a} \text{ formation}}{\text{rate of } Fe^{2+} \text{ formation}} \times \Phi_{Fe^{3+} \rightarrow Fe^{2+}} = \frac{0.76 \times 10^{-6}}{26.80 \times 10^{-6}} \times 1.24 = 0.028$$

$$\Phi_{E_{1b} \rightarrow Z_{1b}} = \frac{\text{rate of } Z_{1b} \text{ formation}}{\text{rate of } Fe^{2+} \text{ formation}} \times \Phi_{Fe^{3+} \rightarrow Fe^{2+}} = \frac{0.65 \times 10^{-6}}{26.80 \times 10^{-6}} \times 1.24 = 0.024$$

$$\Phi_{E_{1c} \rightarrow Z_{1c}} = \frac{\text{rate of } Z_{1c} \text{ formation}}{\text{rate of } Fe^{2+} \text{ formation}} \times \Phi_{Fe^{3+} \rightarrow Fe^{2+}} = \frac{0.19 \times 10^{-6}}{26.80 \times 10^{-6}} \times 1.24 = 0.007$$

$$\Phi_{E_{1d} \rightarrow Z_{1d}} = \frac{\text{rate of } Z_{1d} \text{ formation}}{\text{rate of } Fe^{2+} \text{ formation}} \times \Phi_{Fe^{3+} \rightarrow Fe^{2+}} = \frac{1.28 \times 10^{-6}}{26.80 \times 10^{-6}} \times 1.24 = 0.047$$

For detailed procedures, see below.

Actinometry

Freshly made solution of triply-recrystallized potassium ferrioxalate trihydrate (0.06 M) in H_2SO_4 (0.05 M, prepared from Milli-Q water) was weighted into six 1 cm quartz cuvettes (3 mL into each). Five samples were irradiated using (3 × 1 W LEDs) as the light source for a specific period of time: 2, 4, 6, 8, and 10 s respectively with stirring. One sample was not irradiated ("blank"). Immediately after irradiation, 0.5 mL of the 0.1 % phenanthroline buffer solution (1.65 M CH_3COONa in 0.5 M H_2SO_4) was added and, after exactly 1 h, UV-Vis spectrum was recorded with respect to pure water in the reference beam. From the measured absorbances at 510 nm the concentrations of the Fe^{2+}–phenanthroline complex were calculated (ε_{510} = 11100 M^{-1} cm^{-1}). The Fe^{2+} concentrations thus obtained were corrected for dilution with phenanthroline buffer (that is multiplied by the factor 3.5 mL/3 mL) to yield the Fe^{2+} concentrations in the irradiated samples, which were then plotted versus time and fitted to the linear equation. The obtained slope represents the rate of formation of ferrous ions from which the quantum yields of *E* to *Z* photoisomerisation for the compounds **1a**, **1b**, **1c** and **1d** (performed under the same conditions) were calculated using the known quantum yield of the ferrioxalate actinometer:[21] Φ = 1.24.

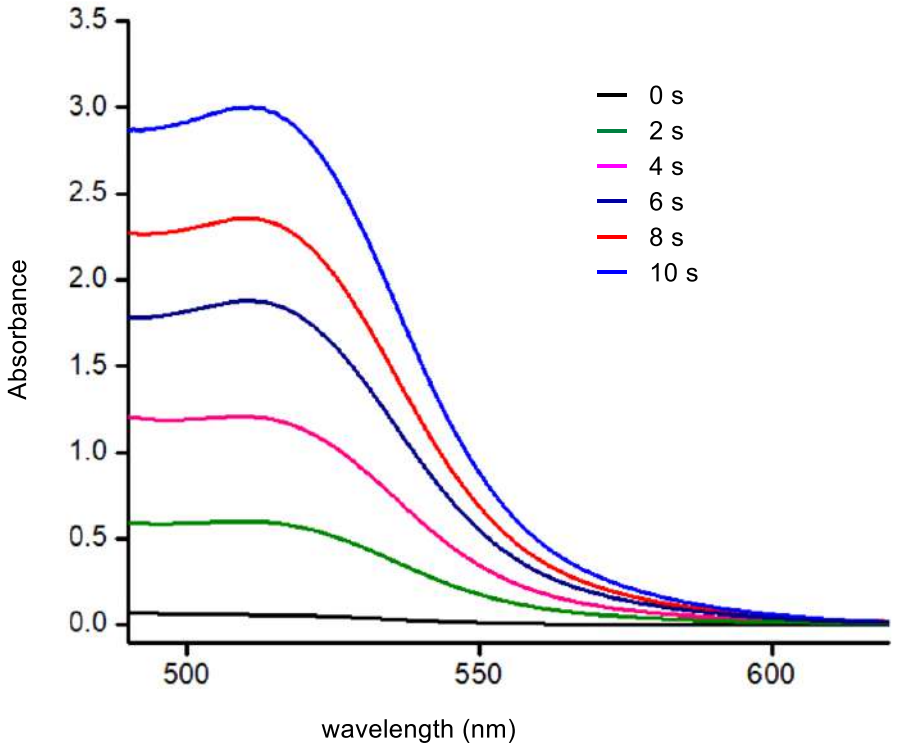

Figure 4.44. UV-Vis spectra acquired during the ferrioxalate actinometry measurements. The absorbance at 510 nm is proportional to the concentration of the formed phenanthroline complex with ferrous ions.

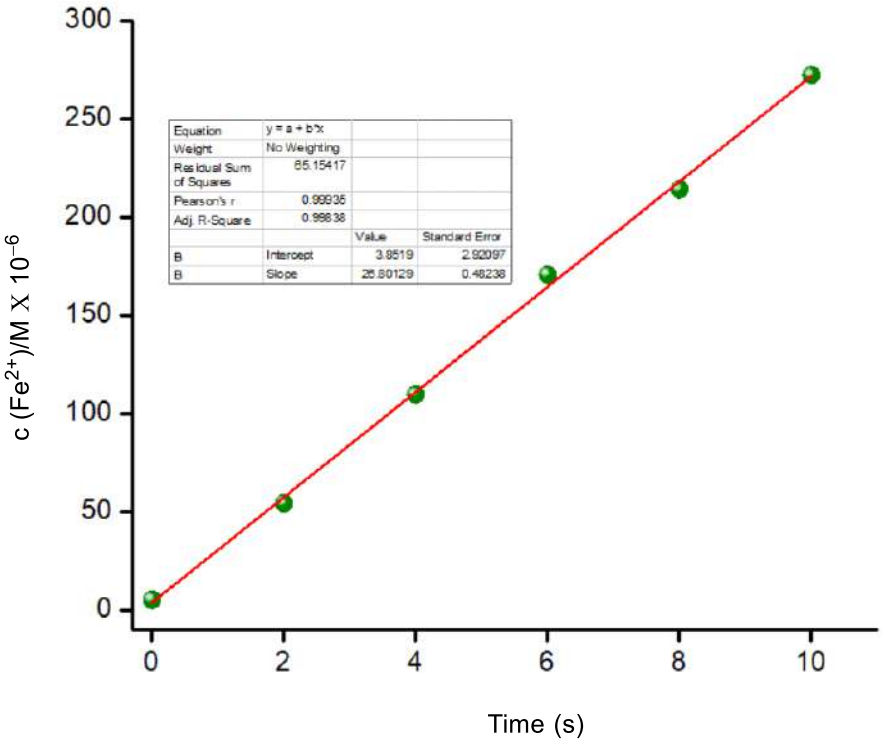

Figure 4.45. Concentration vs. time plot for the formation of ferrous ions during the irradiation at 365 nm using (3 × 1 W LEDs).

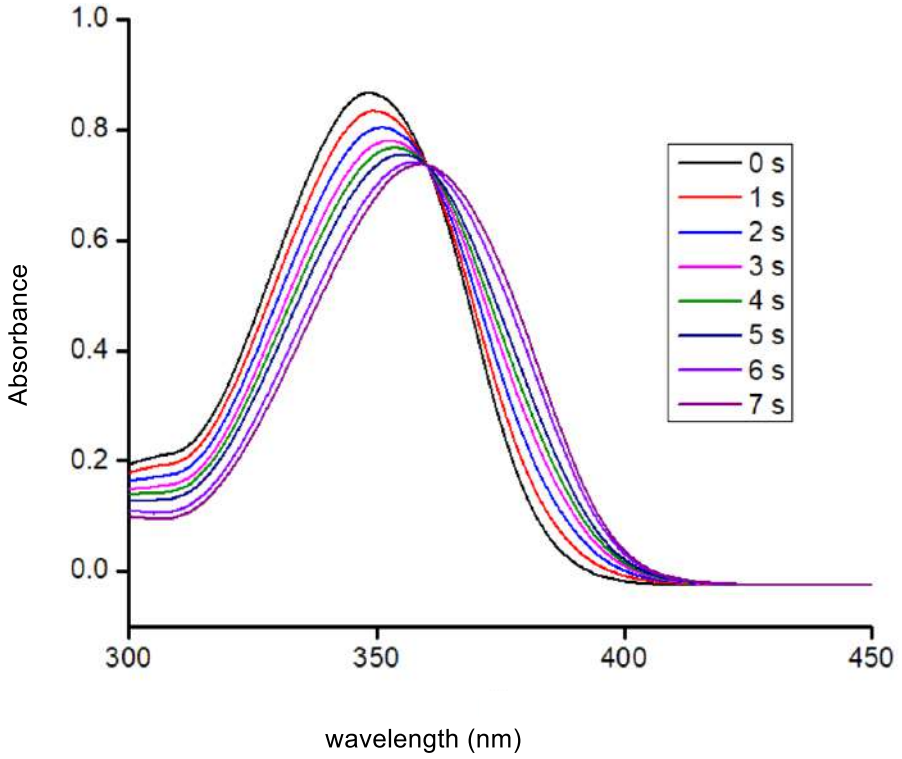

Figure 4.46. UV-Vis spectral changes for **1a** (25 μM) upon irradiation with 365 nm light (3 × 1 W LEDs).

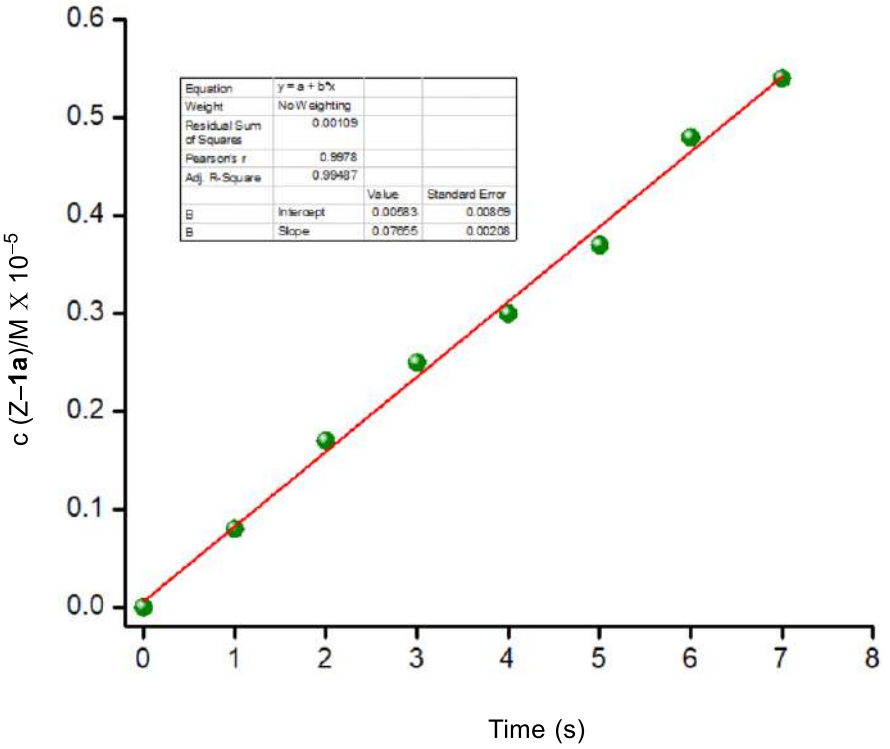

Figure 4.47. Concentration vs. time plot for the formation of *Z*–**1a** during the irradiation at 365 nm using (3 × 1 W LEDs).

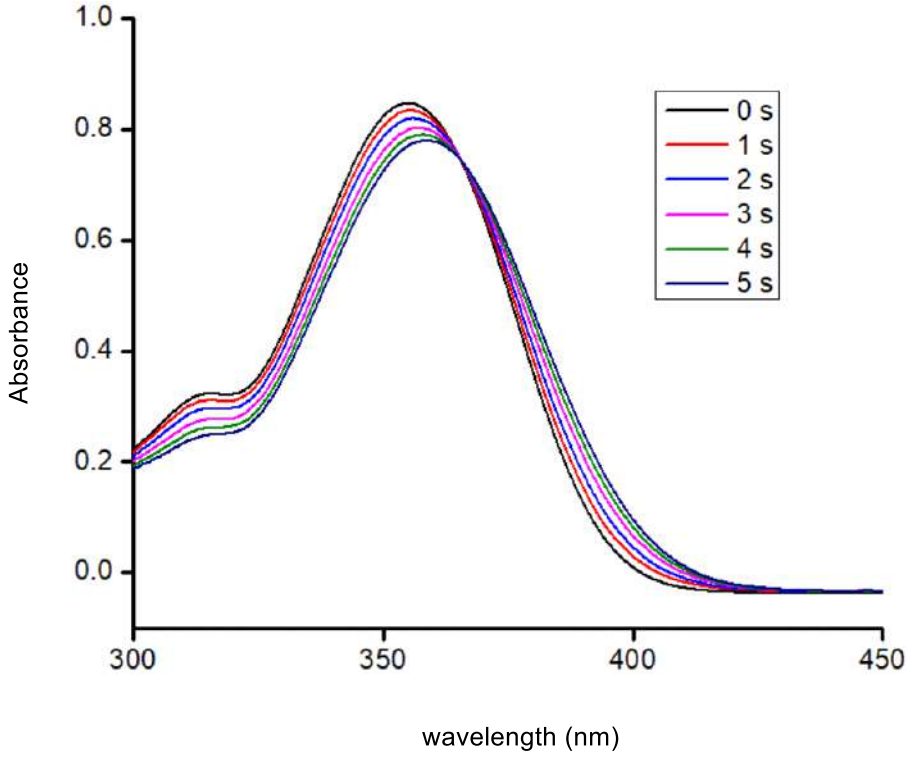

Figure 4.48. UV-Vis spectral changes for **1b** (25 μM) upon irradiation with 365 nm light (3 × 1 W LEDs).

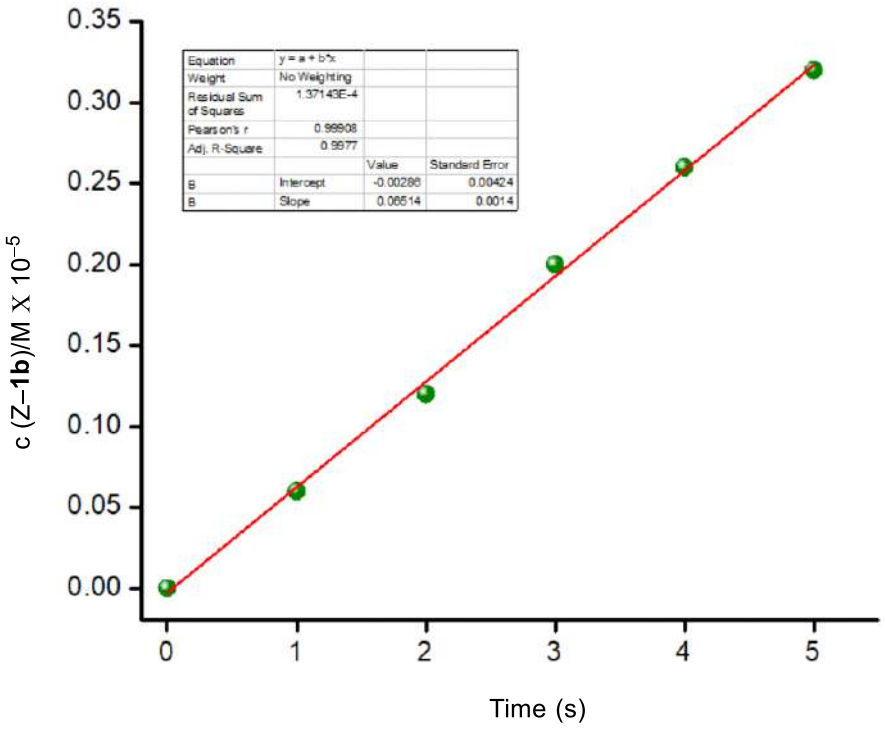

Figure 4.49. Concentration vs. time plot for the formation of *Z*–**1b** during the irradiation at 365 nm using (3 × 1 W LEDs).

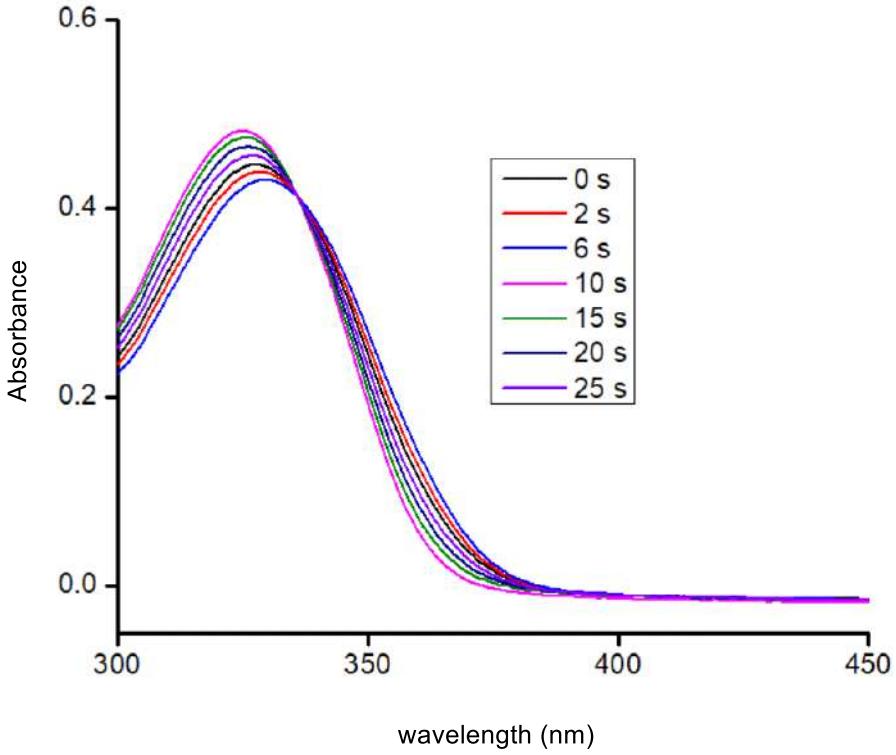

Figure 4.50. UV-Vis spectral changes for **1c** (25 μM) upon irradiation with 365 nm light (3 × 1 W LEDs).

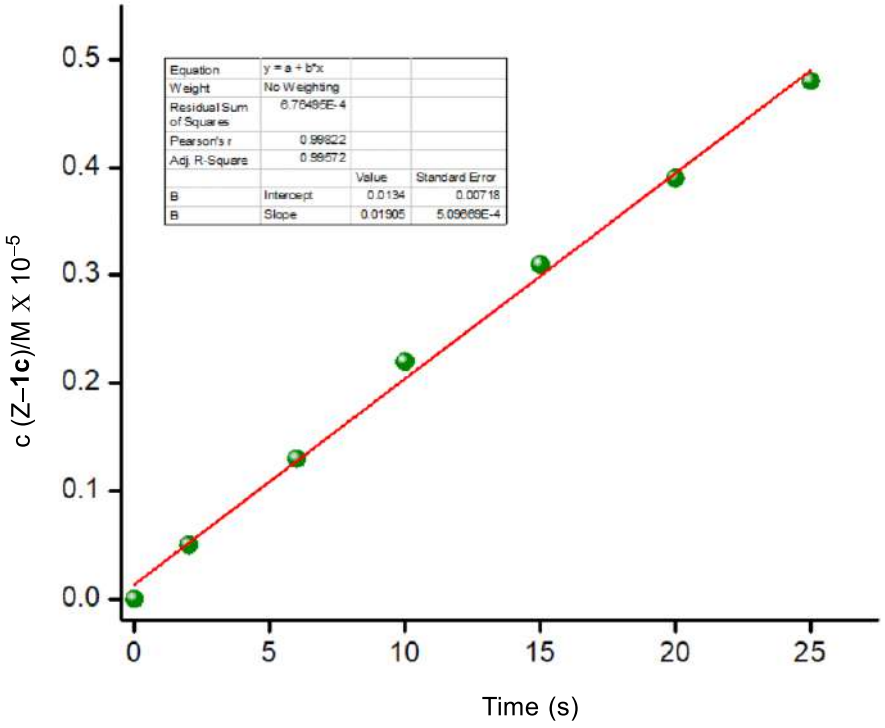

Figure 4.51. Concentration vs. time plot for the formation of *Z*–**1c** during the irradiation at 365 nm using (3 × 1 W LEDs).

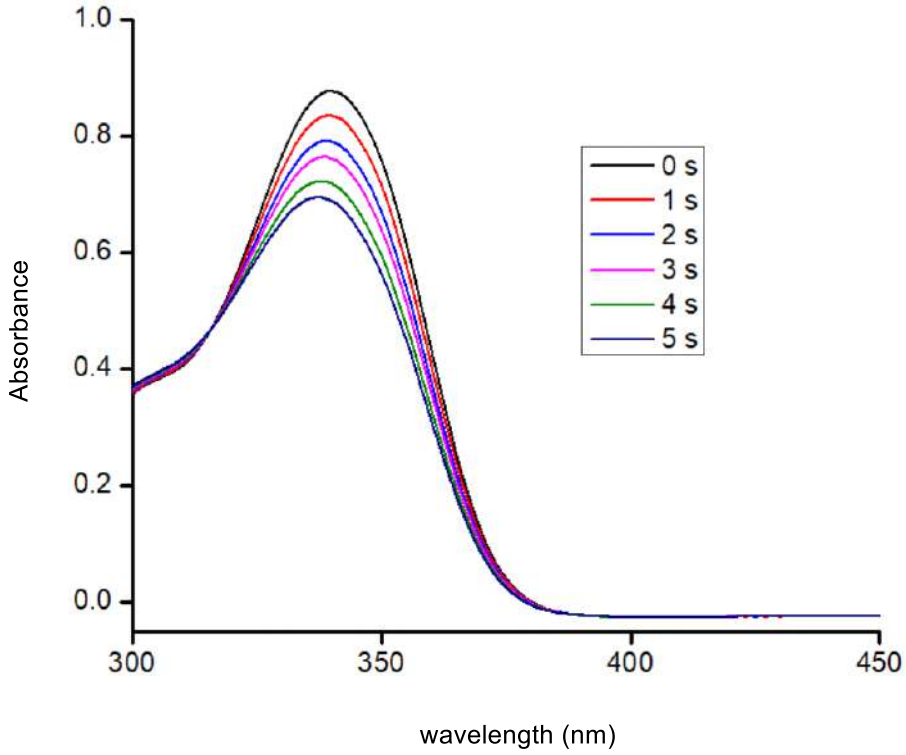

Figure 4.52. UV-Vis spectral changes for **1d** (25 μM) upon irradiation with 365 nm light (3 × 1 W LEDs).

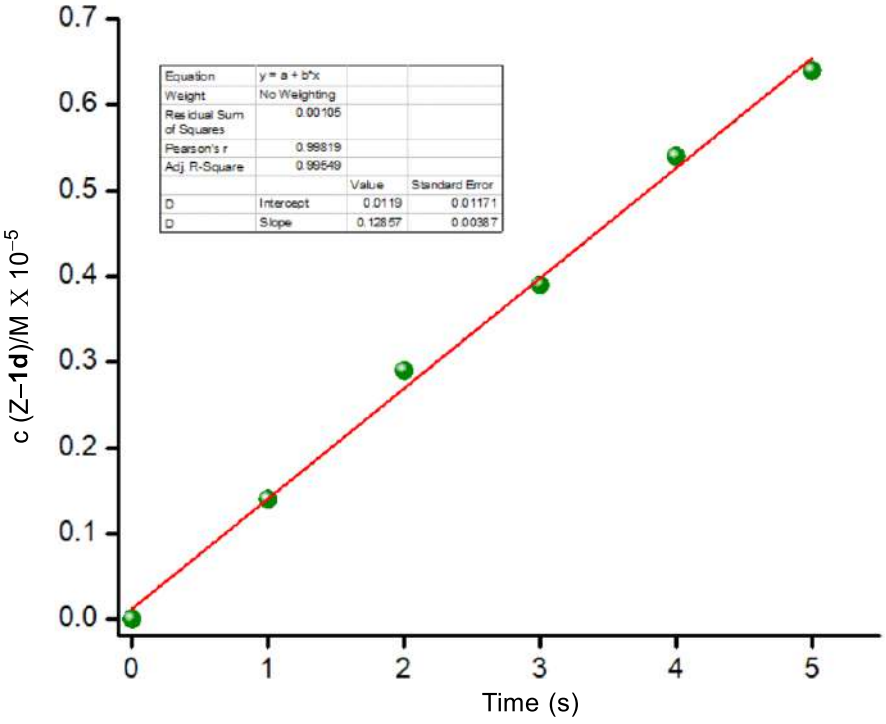

Figure 4.53. Concentration vs. time plot for the formation of *Z*–**1d** during the irradiation at 365 nm using (3 × 1 W LEDs).

4.4.7. X-Ray Crystallographic Studies

4.4.7.1. General procedure for crystallization

4.4.7.1.1. Procedure for **1a**–*E*

The solution of **1a**–*E* (10 mg) in acetonitrile was heated in a 5 mL of glass vial and then filtered to separate any undissolved components. The solution was then left in a stable place to evaporate slowly. After few days, colourless sheet-like crystalline material precipitated from the vial. Suitable crystals were chosen for the X-ray measurement.

4.4.7.1.2. Procedure for **1a**–*Z*

The solution of **1a**–*E* (10 mg) in $CHCl_3$ was photo irradiated in a 5 mL of glass vial at 365 nm for 1 h using three 1W LEDs to photo-isomerize the sample to **1a**–*Z* form. This photo isomerized sample was then left in a stable place to evaporate slowly. After few days, colourless needle-like crystalline material precipitated from the vial. Suitable crystals were chosen for the X-ray measurement.

4.4.7.2. X-ray Single Crystal Diffraction Analysis

The single-crystal X-ray diffraction (SCXRD) analysis of compounds **1a**–*E* and **1a**–*Z* was performed on a Bruker Smart Apex Duo diffractometer using Mo Kα radiation (λ = 0.71073Å). The crystal structures were solved using intrinsic methods and then refined by full-matrix least-squares against F^2 using all data by using SHELXL-2014/7 built in the Apex-3 package[22] The crystallographic refinement data for compounds **1a**–*E* and **1a**–*Z* are listed in (Table 4.2). All the non-hydrogen atoms were refined anisotropically if not stated otherwise. Hydrogen atoms were constructed in geometric positions to their parent atoms.[23] Some of the atom positions (CF_3 group) disordered sites and their occupancies were modeled using the different crystallographic constrain commands. The DIAMOND-3.1 and Mercury software were used to describe the bond length, bond angles, and various structural illustrations of compound **1a**–*E* (Table 4.3) and **1a**–*Z* (Table 4.4), respectively.

Table 4.2. Crystallographic data for **1a**–*E* and **1a**–*Z* at 100 K.

Crystallographic details	**1a**–*E*	**1a–***Z*
Chemical formula	$C_{14}H_{12}F_3N_3O$	$C_{14}H_{12}F_3N_3O$

Formula weight (g/mol)	295.27	295.27
Temperature	100(2)K	100(2)K
Crystal system	Orthorhombic	Orthorhombic
Space group	$P2_12_12_1$	$Pca2_1$
a (Å); α (°)	7.5541(4); 90	15.182(5); 90
b (Å); β (°)	11.0830(7); 90	13.838(4); 90
c (Å); γ (°)	15.9202(10); 90	6.809(2); 90
V (Å^3); Z	1332.87(14); 4	1430.5(7); 4
ρ (calc.) g cm^{-3}	1.471	1.366
μ(Mo K$_\alpha$) mm^{-1}	0.124	0.116
2θ$_{max}$ (°)	56.6	49.98
R(int)	0.1065	0.3576
Completeness to θ	99.9	99.2
Data / param.	3310/192	2431/167
GOF	1.047	1.117
R1 [F>4σ(F)]	0.0502	0.1617
wR2 (all data)	0.1199	0.4256
max. peak/hole (e.Å^{-3})	0.379/-0.251	0.286/-0.307

Table 4.3. Selected bond lengths [Å] and angles [°] for **1a**–*E* at 100 K.

Atom 1	Atom 2	Bond length
F3	C8	1.336(4)
F1	C8	1.344(4)
O1	C2	1.357(4)
O1	C1	1.436(4)
F2	C8	1.336(4)
N2	N3	1.352(3)
N2	C7	1.276(4)
N1	C6	1.341(4)
N1	C2	1.333(4)
N3	H100	0.879
N3	C1P	1.376(4)
C5P	H5P	0.95
C5P	C4P	1.390(4)
C5P	C6P	1.375(4)
C2P	H2P	0.95
C2P	C1P	1.397(4)
C2P	C3P	1.381(4)
C1P	C6P	1.405(5)
C6	C7	1.468(4)
C6	C5	1.393(5)

C3P	H3P	0.95
C3P	C4P	1.395(5)
C7	H7	0.95
C4P	C8	1.471(4)
C6P	H6P	0.95
C2	C3	1.390(5)
C3	H3	0.95
C3	C4	1.382(4)
C4	H4	0.95
C4	C5	1.377(4)
C5	H5	0.95
C1	H1A	0.981
C1	H1B	0.98
C1	H1C	0.98

Table 4.4. Selected bond lengths [Å] and angles [°] for **1a**–*Z* at 100 K.

Atom 1	Atom 2	Bond length
O	C6	1.27(1)
O	C00H	1.42(2)
N2	C1	1.29(2)
N2	N1	1.34(2)
C1	H006	0.95
C1	C2	1.41(1)
C1P	C2P	1.39(2)
C1P	C6P	1.39(2)
C1P	C7	1.46(3)
C2P	H2P	0.95
C2P	C3P	1.39(1)
C3P	H3P	0.95
C3P	C4P	1.39(1)
C4P	C5P	1.39(1)
C4P	N1	1.36(1)
C5P	H5P	0.95
C5P	C6P	1.39(2)
C6P	H6P	0.95
N1	H1	0.88
C2	C3	1.39(1)
C2	N3	1.390(9)
C3	H2	0.951
C3	C4	1.39(1)
C4	H3	0.95
C4	C5	1.39(1)
C5	H4	0.949
C5	C6	1.39(1)
C6	N3	1.39(1)
C00H	H00A	0.98
C00H	H00B	0.98

C00H	H00C	0.98
C7	F1	1.35(4)
C7	F2	1.31(5)
C7	F3	1.30(4)

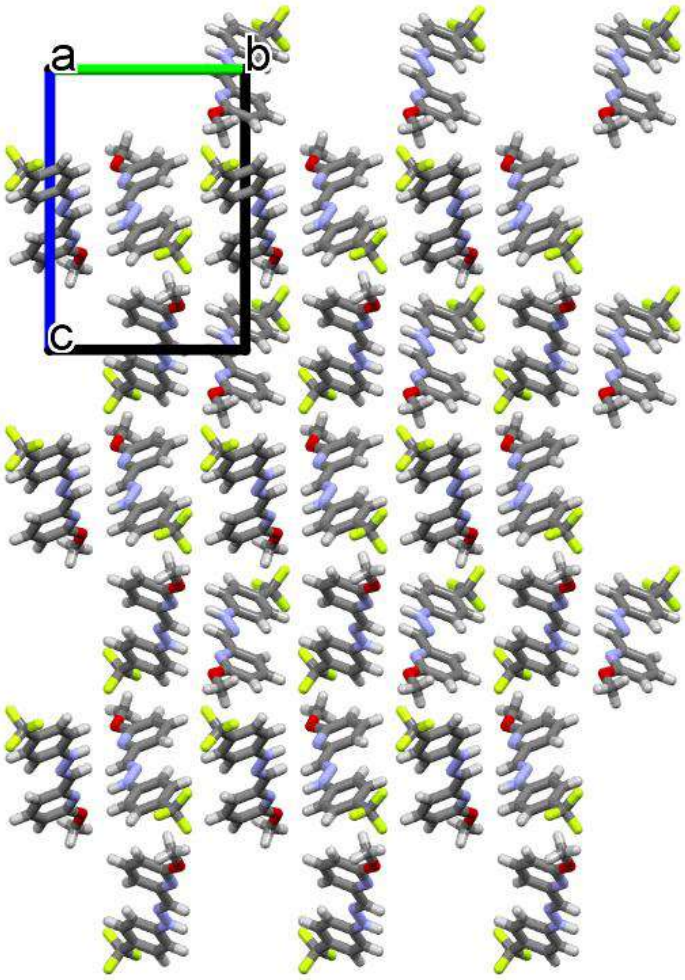

Figure 4.54. The crystal packing diagram of **1a–***E* viewing direction of 'a' axis at 100 K (CCDC = 2102642).

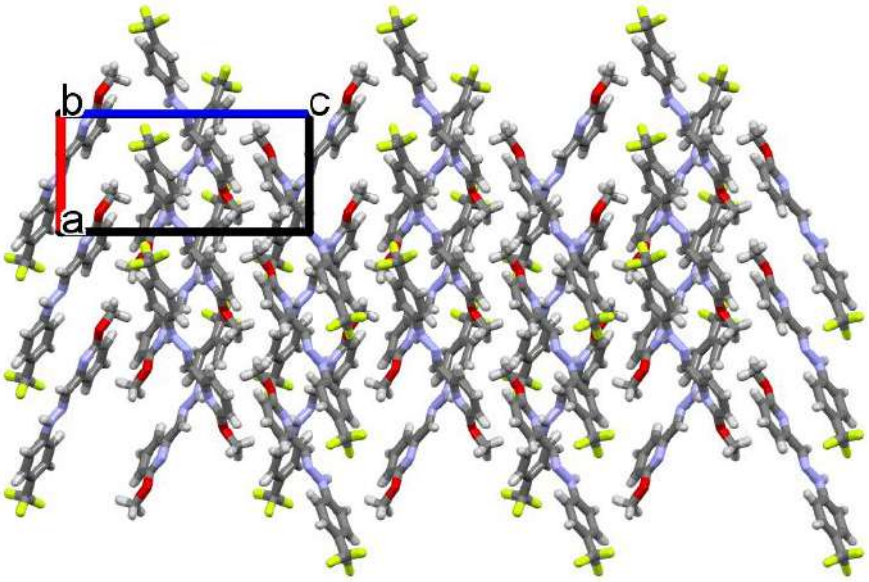

Figure 4.55. The crystal packing diagram of **1a–***E* viewing direction of 'b' axis at 100 K.

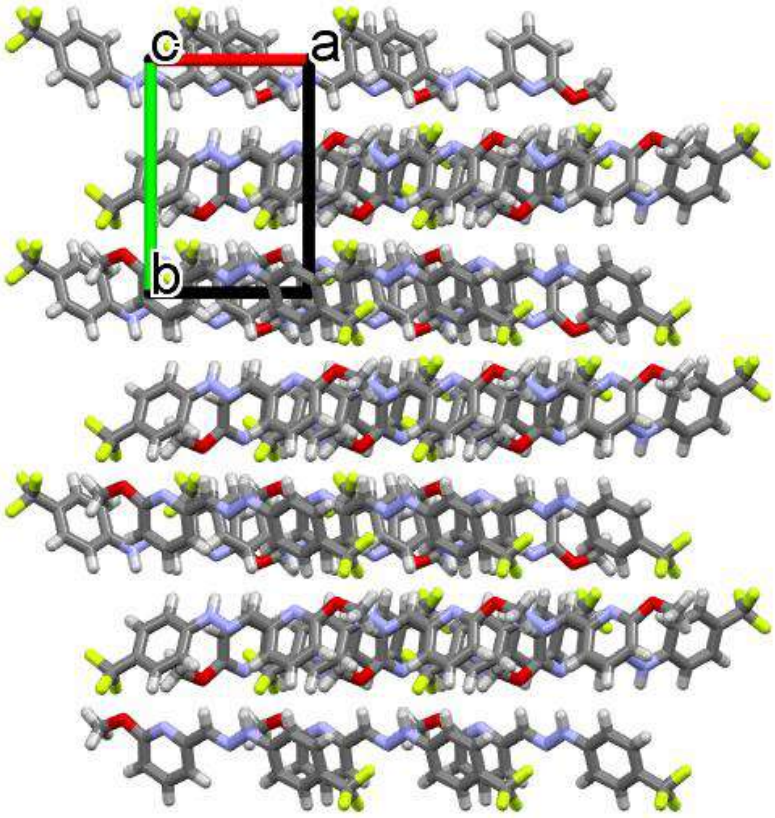

Figure 4.56. The crystal packing diagram of **1a–***E* viewing direction of 'c' axis at 100 K.

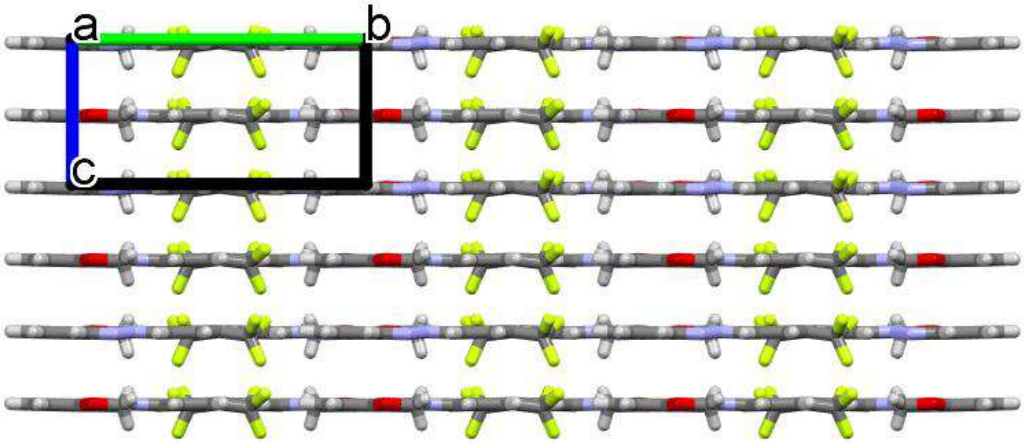

Figure 4.57. The crystal packing diagram of **1a–*Z*** viewing direction of 'a' axis at 100 K.

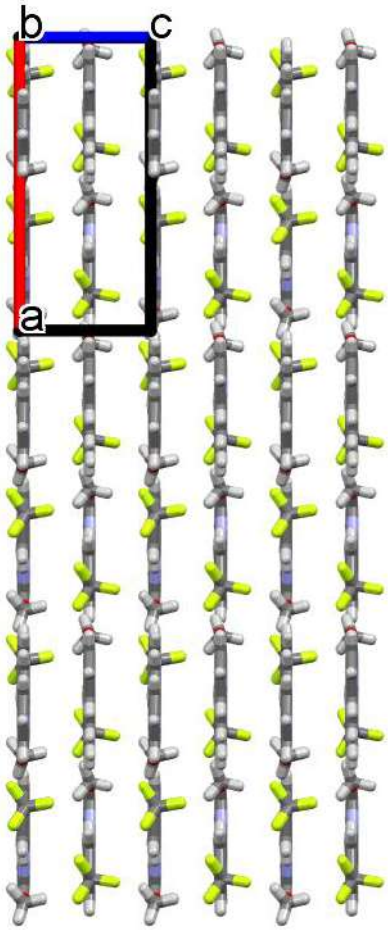

Figure 4.58. The crystal packing diagram of **1a–*Z*** viewing direction of 'b' axis at 100 K.

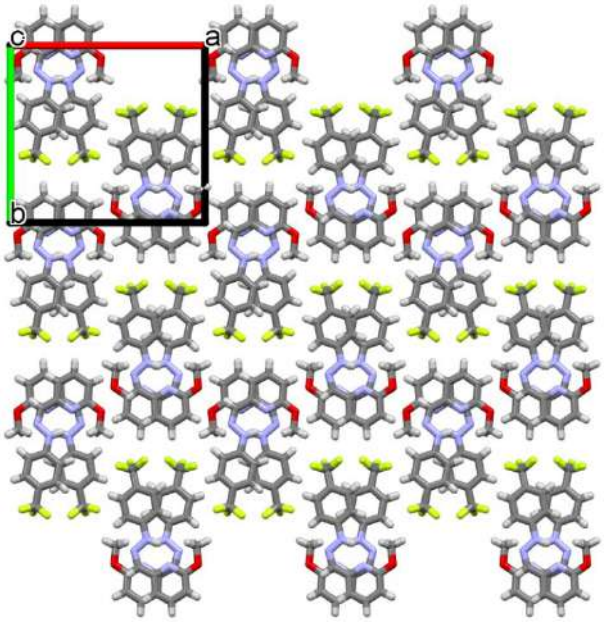

Figure 4.59. The crystal packing diagram of **1a–*Z*** viewing direction of 'c' axis at 100 K (CCDC = 2102641).

4.4.8. Theoretical Calculations

To get an idea about the conformation of [(**1a**)$_2$+Cl$^-$], several initial geometries of the complex were generated using the CONFLEX 8 software package using MMFF94s force field. The calculation provided 10319 conformers. The Boltzmann population of the highest populated conformation (**Conf-1**) was 45.51% (Figure 4.60A). The populations of second to tenth highest conformers (**Conf-2**–**Conf-10**) were 9.40%, 6.20%, 5.77%, 2.42%, 2.34%, 9.38%, 9.37%, 2.54%, and 2.45%, respectively (Figure 4.60B–J).

Among the several conformations, the highest Boltzmann populated structure was used for geometry optimization. The geometry optimization was carried out by Gaussian 09 program package using B3LYP functional and 6-311++G(d,p) basis set. The geometry optimized structure is given in the manuscript. For all structures (i.e., free receptors and anionic complexes), the vibrational frequency calculation during the geometry optimization shows no imaginary frequencies, which indicates that all optimized structures are ground state minima.

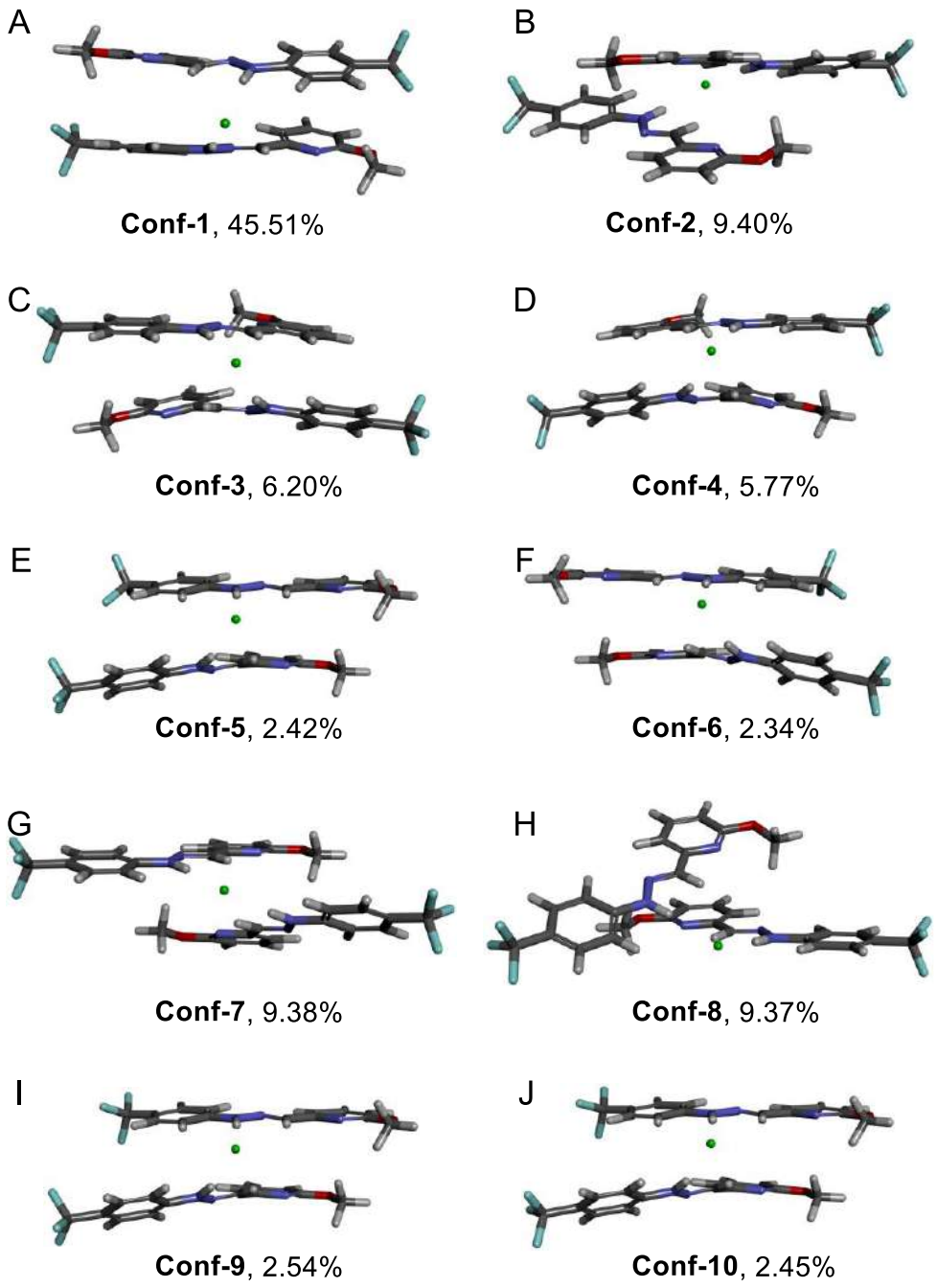

Figure 4.60. Initial geometries **Conf-1**–**Conf-10** (**A–J**) for [(**1a**)$_2$+Cl$^-$], optimized by CONFLEX 8 software using MMFF94s force field.

Figure 4.61. The geometry optimized structures of **1a**.

The Gaussian 09 program was used to calculate the zero-point energy (ZPE) and basis set superposition error (BSSE) corrected bonding energy of [(**1a**)$_2$+Cl$^-$], which was used for the calculation of binding energy (*BE*) using the following equations.

$$BE = [HF_{[\mathbf{M}+Cl^-]} + ZPE_{[\mathbf{M}+Cl^-]} + BSSE_{[\mathbf{M}+Cl^-]}] - 2 \times [HF_{\mathbf{M}} + ZPE_{\mathbf{M}}] - [HF_{Cl^-}] \qquad \text{Equation S6}$$

where, M is the receptor (i.e. **1a**), $HF_{[\mathbf{M}+Cl^-]}$ = electronic energy of [(**1a**)$_2$+Cl$^-$] complex, $ZPE_{[\mathbf{M}+Cl^-]}$ = zero point energy of [(**1a**)$_2$+Cl$^-$] complex, $BSSE_{[\mathbf{M}+Cl^-]}$ = BSSE of [(**1a**)$_2$+Cl$^-$] complex, $HF_{\mathbf{M}}$ = electronic energy of the receptor M, $ZPE_{\mathbf{M}}$ = zero point energy of the receptor **M**, HF_{Cl^-} = electronic energy of anion Cl$^-$.

The structures (i.e., free receptor and the complex), the vibrational frequency calculation during the geometry optimization, shows no imaginary frequencies, which indicates that all optimized structures are ground state minima.

Table 4.5. The electronic energy (HF), zero point energy (ZPE), basis set superposition error (BSSE) corrected energy (in Hartree unit) for all structures and complexes are calculated at the DFT B3LYP/6-311++G(d,p) level of theory.

Structures	Energy values
$HF_{[\mathbf{M}+Cl^-]}$ (in Hartree)	–2620.3960035
$ZPE_{[\mathbf{M}+Cl^-]}$ (in Hartree)	0.4877623
$BSSE_{[\mathbf{M}+Cl^-]}$ (in Hartree)	0.0024460
$HF_{\mathbf{M}}$ (in Hartree)	–1080.0059807
$ZPE_{\mathbf{M}}$ (in Hartree)	0.2431879
HF_{Cl^-} (in Hartree)	–460.2522333
BE (in Hartree)	–0.1279762
BE (in kcal/mol)	–80.3062410

Table 4.6. Atomic coordinates of the optimized structure of lowest energy conformation obtained for **1a** from DFT B3LYP/6-311++G(d,p) geometry optimization.

Charge = 0, Multiplicity = 1

Atom #	Atom Type	x	y	z
1	C	-4.160811	-0.063427	-0.037731

2	C	-3.780998	-1.407188	-0.033293
3	C	-2.439014	-1.754255	-0.030652
4	C	-1.448738	-0.758654	-0.027696
5	C	-1.829703	0.591713	-0.030227
6	C	-3.175678	0.927165	-0.033309
7	N	-0.115950	-1.145150	-0.026624
8	N	0.889895	-0.254940	-0.022160
9	C	2.092492	-0.704330	-0.012588
10	C	3.258013	0.181963	-0.008268
11	C	3.158613	1.573124	-0.019245
12	C	4.338655	2.317356	-0.013694
13	C	5.562848	1.670701	0.002261
14	C	5.552553	0.265876	0.012411
15	N	4.447532	-0.460477	0.007250
16	O	6.756068	-0.349178	0.028353
17	C	6.774656	-1.781275	0.039622
18	H	0.099558	-2.138062	-0.020098
19	H	2.315287	-1.776276	-0.006721
20	F	-5.866251	1.475310	-0.626472
21	C	-5.609585	0.311854	0.017570
22	F	-6.051606	0.482191	1.294577
23	F	-6.407946	-0.632908	-0.534201
24	H	-4.535485	-2.183666	-0.040618
25	H	-2.153959	-2.801292	-0.033596
26	H	-1.068156	1.358310	-0.032222
27	H	-3.462262	1.971752	-0.040167
28	H	2.186506	2.046256	-0.031767
29	H	4.298860	3.400877	-0.021932
30	H	6.504783	2.202795	0.007112
31	H	7.829000	-2.051746	0.051064

32	H	6.271865	-2.171354	0.926889
33	H	6.287535	-2.185269	-0.850139

Table 4.7. Atomic coordinates of the optimized structure of lowest energy conformation obtained for [(**1a**)$_2$+Cl$^-$] complex from DFT B3LYP/6-311++G(d,p) geometry optimization.

Charge = –1, Multiplicity = 1

Atom #	Atom Type	x	y	z
1	C	6.213735	0.475145	1.461509
2	C	6.025668	1.581765	0.627693
3	C	4.750429	2.017346	0.302139
4	C	3.624037	1.341549	0.807961
5	C	3.813954	0.223783	1.646755
6	C	5.092988	-0.199202	1.963111
7	N	2.333351	1.728110	0.519816
8	N	2.087522	2.785929	-0.264004
9	C	0.853259	3.086415	-0.490530
10	C	0.505167	4.226772	-1.335948
11	C	1.458036	5.059341	-1.935218
12	C	1.012450	6.117313	-2.722871
13	C	-0.347742	6.328854	-2.900543
14	C	-1.220403	5.438241	-2.257324
15	N	-0.821930	4.428741	-1.504864
16	O	-2.549685	5.647242	-2.434688
17	C	-3.449368	4.739179	-1.786044
18	H	1.546045	1.182570	0.923014
19	H	0.026769	2.512697	-0.069144
20	F	7.681488	-0.631491	2.965054
21	C	7.586977	-0.023449	1.754115
22	F	8.521481	0.964311	1.740721
23	F	8.026148	-0.950226	0.846407

24	H	6.885234	2.112559	0.235740
25	H	4.606390	2.876797	-0.337160
26	H	2.943956	-0.290995	2.039295
27	H	5.224098	-1.056408	2.612502
28	H	2.510225	4.867122	-1.777258
29	H	1.728327	6.778733	-3.199883
30	H	-0.741787	7.136429	-3.503378
31	H	-3.285662	3.714960	-2.125808
32	H	-3.323859	4.770552	-0.702106
33	H	-4.446131	5.078742	-2.064325
34	C	-6.214650	-0.476851	1.460867
35	C	-5.094200	0.197857	1.962649
36	C	-3.814979	-0.224580	1.646311
37	C	-3.624573	-1.342136	0.807350
38	C	-4.750665	-2.018299	0.301353
39	C	-6.026096	-1.583268	0.626892
40	N	-2.333714	-1.728144	0.519239
41	N	-2.087392	-2.785642	-0.264860
42	C	-0.852984	-3.085572	-0.491331
43	C	-0.504329	-4.225537	-1.337044
44	C	-1.456786	-5.058286	-1.936717
45	C	-1.010669	-6.115848	-2.724622
46	C	0.349632	-6.326811	-2.902147
47	C	1.221852	-5.436060	-2.258521
48	N	0.822870	-4.426943	-1.505815
49	O	2.551240	-5.644502	-2.435726
50	C	3.450474	-4.736352	-1.786576
51	H	-1.546671	-1.182395	0.922630
52	H	-0.026772	-2.511645	-0.069684
53	F	-8.522238	-0.966915	1.739842

54	C	-7.588100	0.021189	1.753445
55	F	-8.027543	0.947928	0.845834
56	F	-7.682927	0.629027	2.964459
57	H	-5.225685	1.054915	2.612158
58	H	-2.945209	0.290477	2.038991
59	H	-4.606245	-2.877595	-0.338068
60	H	-6.885429	-2.114342	0.234806
61	H	-2.509075	-4.866519	-1.778868
62	H	-1.726216	-6.777399	-3.201947
63	H	0.744079	-7.134049	-3.505170
64	H	4.447411	-5.075449	-2.064797
65	H	3.286458	-3.712065	-2.125981
66	H	3.324775	-4.768180	-0.702673
67	Cl	-0.000517	0.000325	1.820746

4.5. NMR Spectra

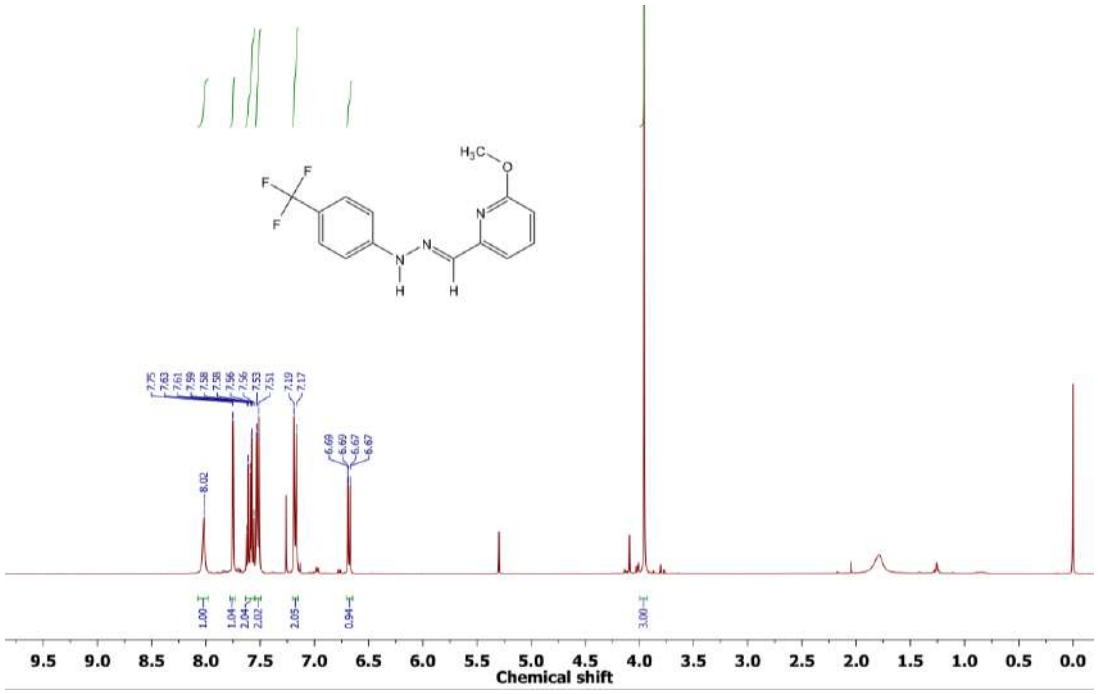

Figure 4.62. ^{1}H NMR spectrum (400 MHz) of **1a** in $CDCl_3$ at room temperature.

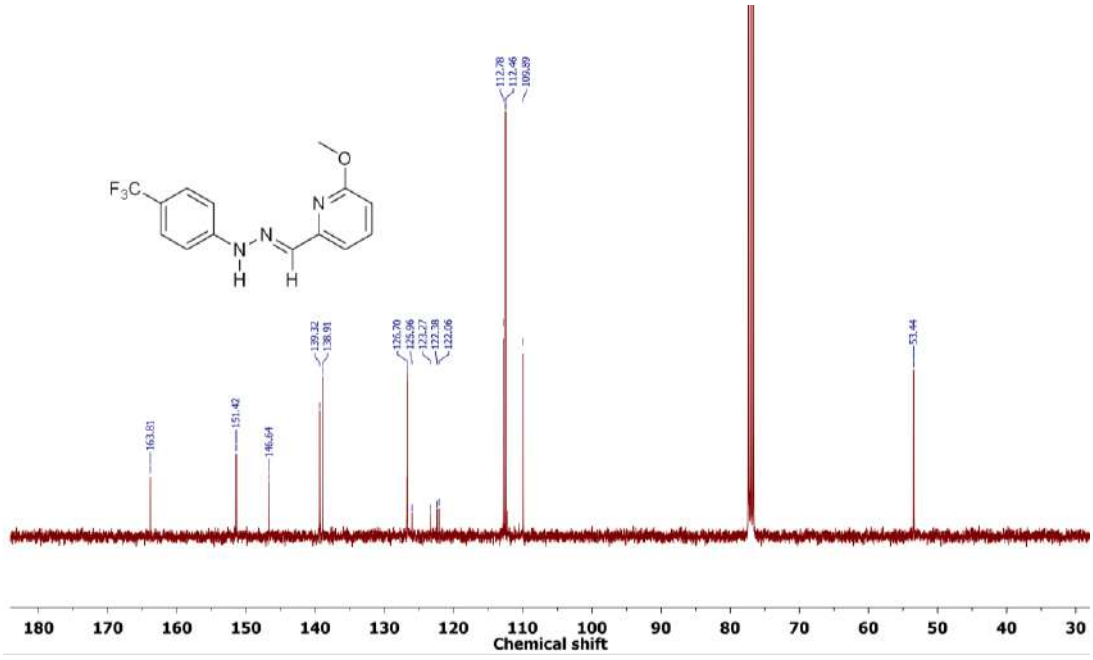

Figure 4.63. ^{13}C NMR spectrum (101 MHz) of **1a** in $CDCl_3$ at room temperature.

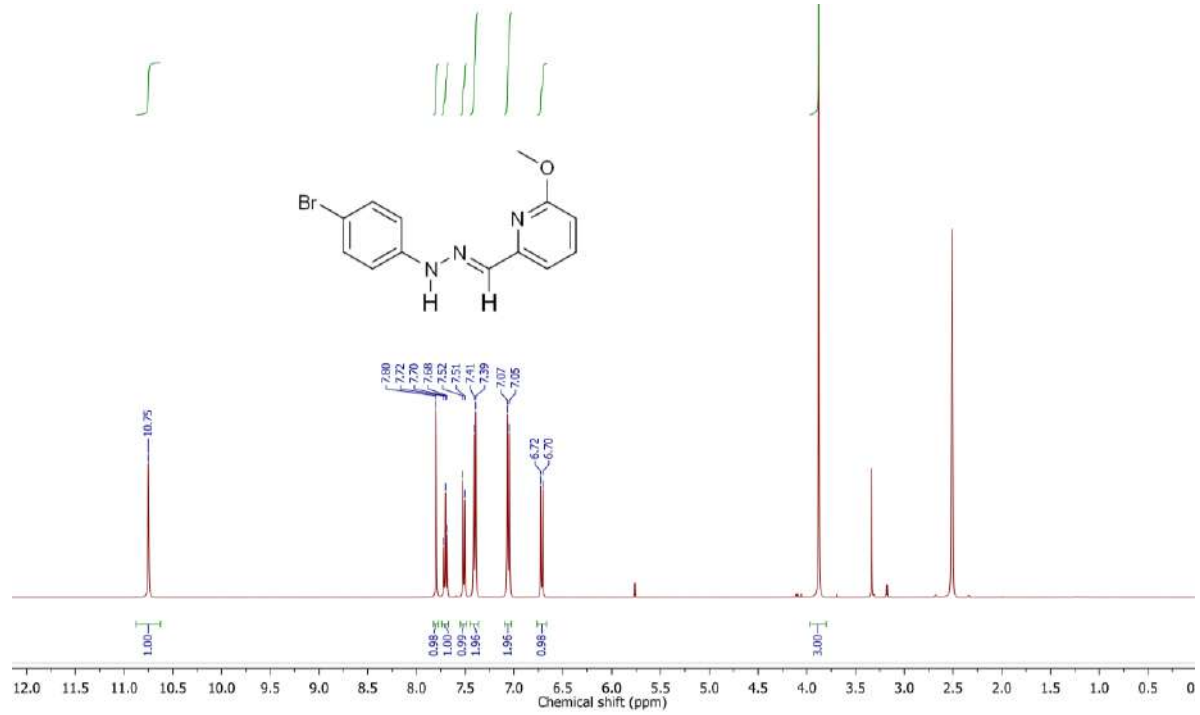

Figure 4.64. ^{1}H NMR spectrum (400 MHz) of **1b** in DMSO-d_6 at room temperature.

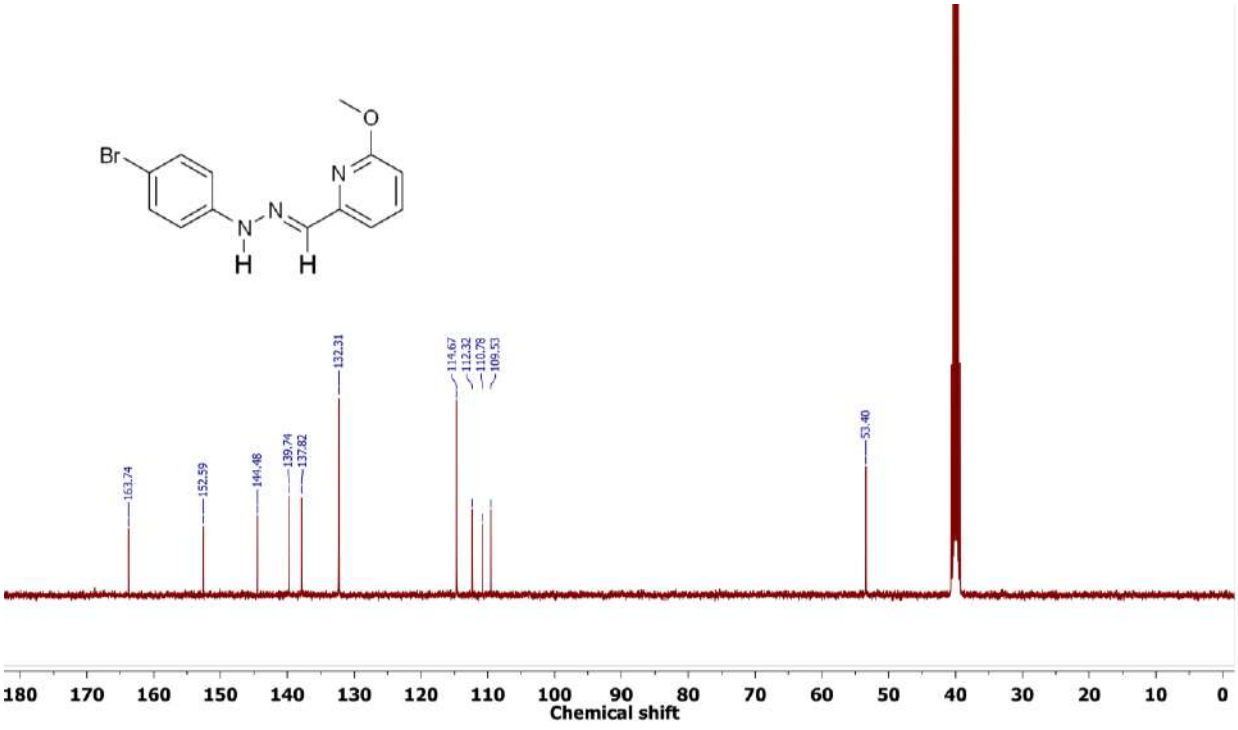

Figure 4.65. ^{13}C NMR spectrum (101 MHz) of **1b** in DMSO-d_6 at room temperature.

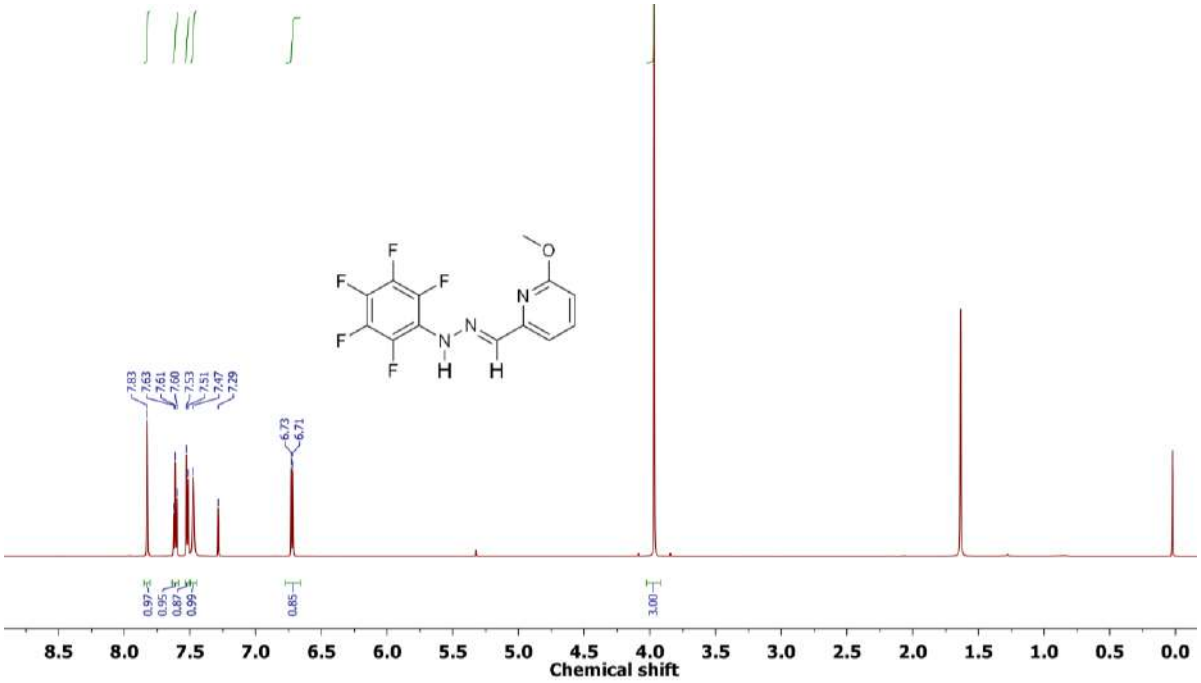

Figure 4.66. ^{1}H NMR spectrum (400 MHz) of **1c** in $CDCl_3$ at room temperature.

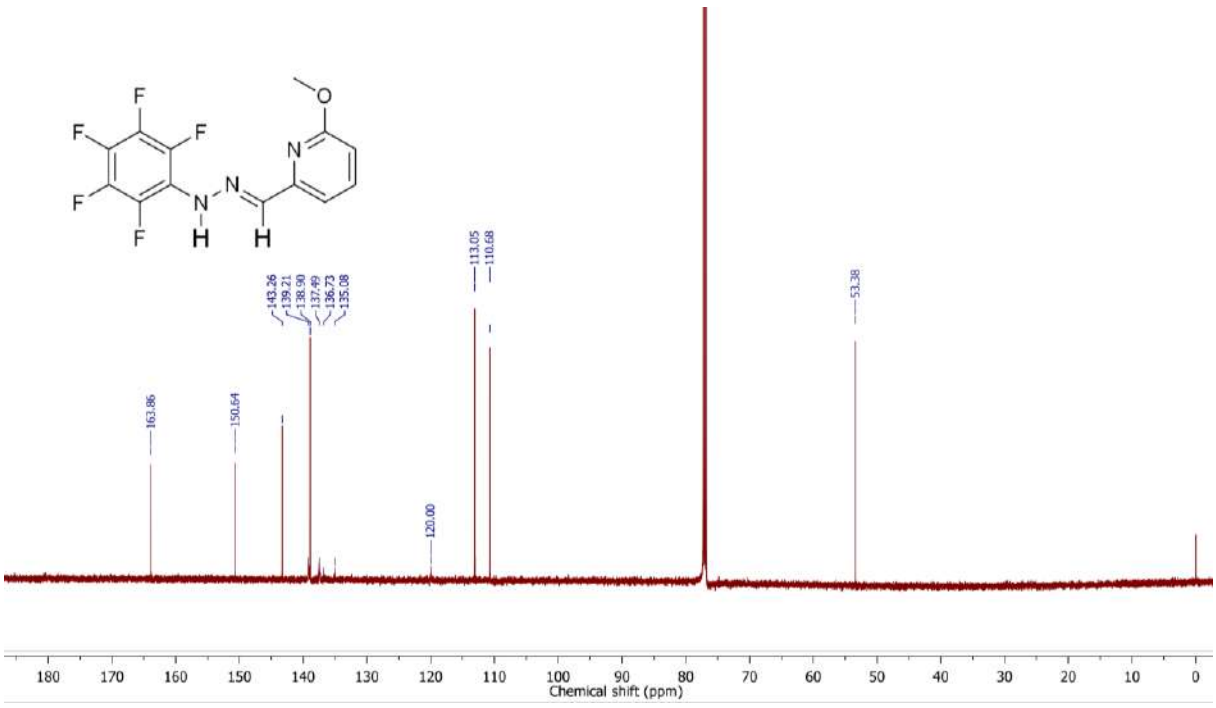

Figure 4.67. ^{13}C NMR spectrum (101 MHz) of **1c** in $CDCl_3$ at room temperature.

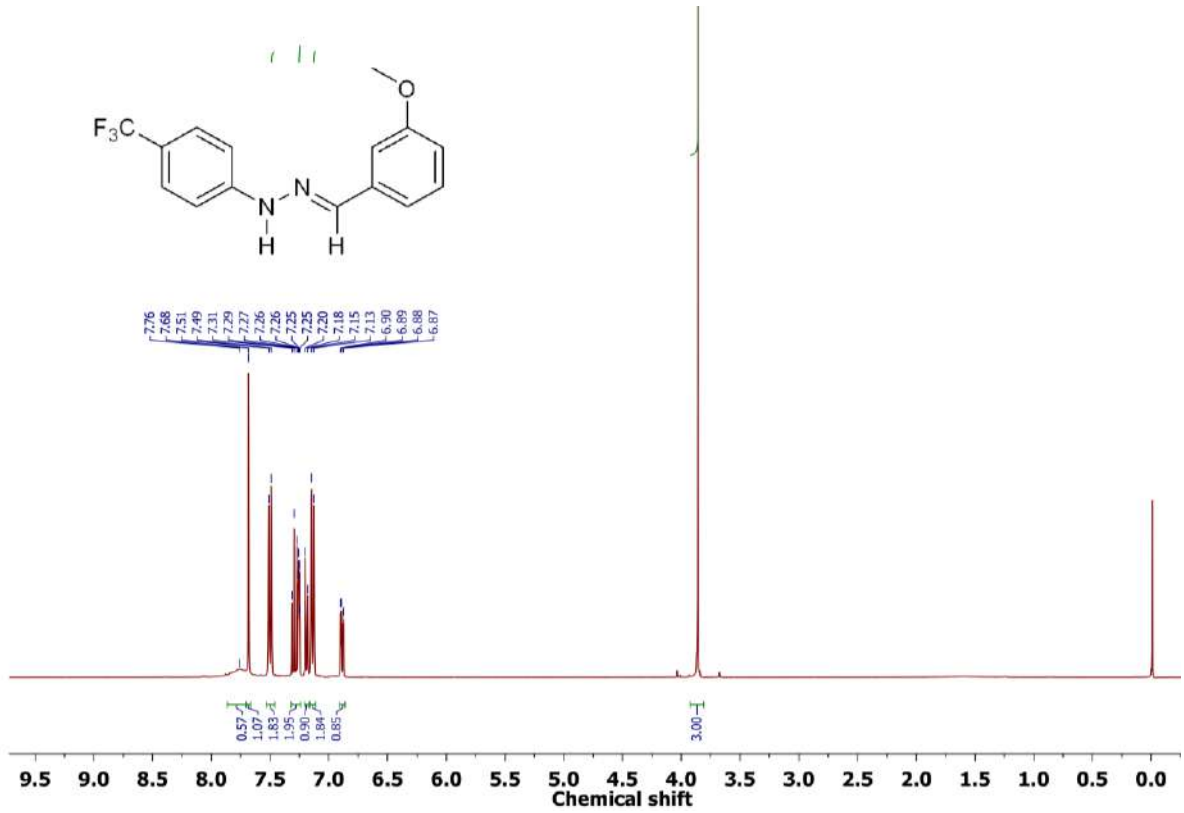

Figure 4.68. ^{1}H NMR spectrum (400 MHz) of **1d** in $CDCl_3$ at room temperature.

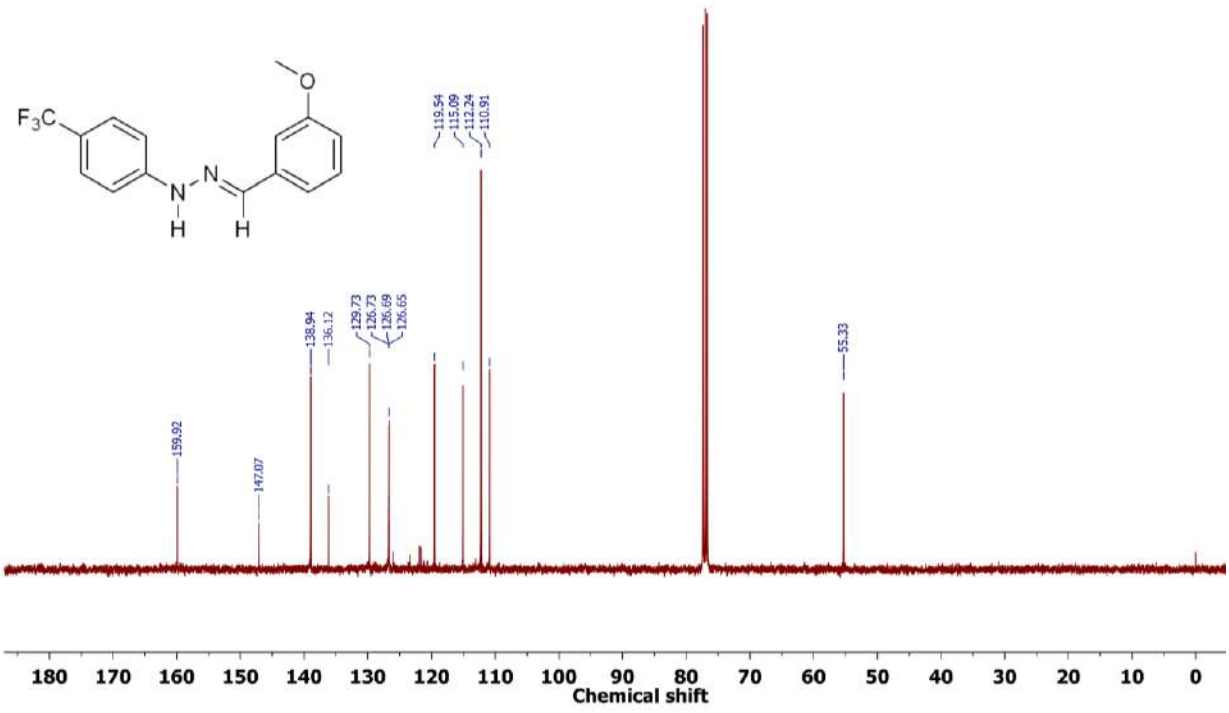

Figure 4.69. ^{13}C NMR spectrum (101 MHz) of **1d** in $CDCl_3$ at room temperature.

4.6. References.

[1] (a) N. Busschaert, S.-H. Park, K.-H. Baek, Y. P. Choi, J. Park, E. N. W. Howe, J. R. Hiscock, L. E. Karagiannidis, I. Marques, V. Félix, W. Namkung, J. L. Sessler, P. A. Gale, I. Shin, *Nat. Chem.* **2017**, *9*, 667-675; (b) K. J. Winstanley, S. J. Allen, D. K. Smith, *Chem. Commun.* **2009**, 4299-4301; (c) A. Vargas, D. Emery, J. Mareda, P. Metrangolo, G. Resnati, S. Matile, *Angew. Chem. Int. Ed.* **2011**, *50*, 11675-11678; (d) T. Saha, A. Gautam, A. Mukherjee, M. Lahiri, P. Talukdar, *J. Am. Chem. Soc.* **2016**, *138*, 16443-16451; (e) H. Valkenier, L. W. Judd, H. Li, S. Hussain, D. N. Sheppard, A. P. Davis, *J. Am. Chem. Soc.* **2014**, *136*, 12507-12512; (f) X. Wu, E. N. W. Howe, P. A. Gale, *Acc. Chem. Res.* **2018**, *51*, 1870-1879; (g) A. Vargas Jentzsch, S. Matile, *J. Am. Chem. Soc.* **2013**, *135*, 5302-5303.

[2] J. T. Davis, O. Okunola, R. Quesada, *Chem. Soc. Rev.* **2010**, *39*, 3843-3862.

[3] (a) I. F. Tannock, D. Rotin, *Cancer Res.* **1989**, *49*, 4373-4384; (b) W. Van Rossom, D. J. Asby, A. Tavassoli, P. A. Gale, *Org. Biomol. Chem.* **2016**, *14*, 2645-2650; (c) N. Busschaert, C. Caltagirone, W. Van Rossom, P. A. Gale, *Chem. Rev.* **2015**, *115*, 8038-8155; (d) J. A. Malla, R. M. Umesh, S. Yousf, S. Mane, S. Sharma, M. Lahiri, P. Talukdar, *Angew. Chem. Int. Ed.* **2020**, *59*, 794-7952; (e) S. B. Salunke, J. A. Malla, P. Talukdar, *Angew. Chem. Int. Ed.* **2019**, *58*, 5354-5358; (f) J. A. Malla, V. K. Sharma, M. Lahiri, P. Talukdar, *Chem. Eur. J.* **2020**, *26*, 11910-11910.

[4] M. R. Banghart, M. Volgraf, D. Trauner, *Biochemistry* **2006**, *45*, 15129-15141.

[5] J. A. Peterson, C. Wijesooriya, E. J. Gehrmann, K. M. Mahoney, P. P. Goswami, T. R. Albright, A. Syed, A. S. Dutton, E. A. Smith, A. H. Winter, *J. Am. Chem. Soc.* **2018**, *140*, 7343-7346.

[6] I. Aprahamian, *Chem. Commun.* **2017**, *53*, 6674-6684.

[7] H. Qian, S. Pramanik, I. Aprahamian, *J. Am. Chem. Soc.* **2017**, *139*, 9140-9143.

[8] (a) X. Su, I. Aprahamian, *Chem. Soc. Rev.* **2014**, *43*, 1963-1981; (b) H. Miyaji, J. L. Sessler, *Angew. Chem. Int. Ed.* **2001**, *40*, 154-157; (c) E. V. Anslyn, *J. Org. Chem.* **2007**, *72*, 687-699; (d) M. Kumaravel, J. T. Mague, M. S. Balakrishna, *Chem. Sci.* **2017**, *129*, 471-481; (e) Y.-H. Qiao, H. Lin, H.-K. Lin, *J. Incl. Phenom. Macrocycl. Chem.* **2007**, *59*, 211-215; (f) N. Chakraborty, A. Chakraborty, S. Das, *Can. J. Chem.* **2020**, *98*, 779-786; (g) H. Wang, S. Fang, G. Wu, Y. Lei, Q. Chen, H. Wang, Y. Wu, C. Lin, X. Hong, S. K. Kim, J. L. Sessler, H. Li, *J. Am. Chem. Soc.* **2020**, *142*, 20182-20190; (h) C.-Y. Chen, T.-P. Lin, C.-K. Chen, S.-C. Lin, M.-C. Tseng, Y.-S. Wen, S.-S. Sun,

J. Org. Chem. **2008**, *73*, 900-911; (i) D. Singhal, N. Gupta, A. K. Singh, *Mater Sci. Eng. C. Mater Biol. Appl.* **2016**, *58*, 548-557.

[9] (a) B. Shao, I. Aprahamian, *Chem.* **2020**, *6*, 2162-2173; (b) B. Shao, I. Aprahamian, *ChemistryOpen* **2020**, *9*, 191-194; (c) I. Aprahamian, *ACS Cent. Sci.* **2020**, *6*, 347-358; (d) I. Aprahamian, *Chem. Commun.* **2017**, *53*, 6674-6684.

[10] C. A. Lipinski, F. Lombardo, B. W. Dominy, P. J. Feeney, *Adv. Drug Deliv. Rev.* **1997**, *23*, 3-25.

[11] Marvin 5.8.0, *ChemAxon*, **2012**, *(http://www.chemaxon.com).*

[12] http://app.supramolecular.org/bindfit/, (accessed July **2017**).

[13] A. Roy, T. Saha, M. L. Gening, D. V. Titov, A. G. Gerbst, Y. E. Tsvetkov, N. E. Nifantiev, P. Talukdar, *Chem. Eur. J.* **2015**, *21*, 17445-17452.

[14] D. Mondal, A. Sathyan, S. V. Shinde, K. K. Mishra, P. Talukdar, *Org. Biomol. Chem.* **2018**, *16*, 8690-8694.

[15] N. Busschaert, M. Wenzel, M. E. Light, P. Iglesias-Hernández, R. Pérez-Tomás, P. A. Gale, *J. Am. Chem. Soc.* **2011**, *133*, 14136-14148.

[16] D. Mondal, A. Sathyan, S. V. Shinde, K. K. Mishra, P. Talukdar, *Org. Biomol. Chem.* **2018**, *16*, 8690-8694.

[17] T. Saha, M. S. Hossain, D. Saha, M. Lahiri, P. Talukdar, *J. Am. Chem. Soc.* **2016**, *138*, 7558-7567.

[18] (a) S. O. H. Goto, N. Nakayama, K. Ohta, CONFLEX 8, *CONFLEX Corporation, Tokyo, Japan*, **2012**; (b) H. Goto, E. Osawa, *J. Am. Chem. Soc.* **1989**, *111*, 8950-8951.

[19] M. J. Frisch, G. W. Trucks, H. B. Schlegel, G. E. Scuseria, M. A. Robb, J. R. Cheeseman, G. Scalmani, V. Barone, B. Mennucci, G. A. Petersson, H. Nakatsuji, M. Caricato, X. Li, H. P. Hratchian, A. F. Izmaylov, J. Bloino, G. Zheng, J. L. Sonnenberg, M. Hada, M. Ehara, K. Toyota, R. Fukuda, J. Hasegawa, M. Ishida, T. Nakajima, Y. Honda, O. Kitao, H. Nakai, T. Vreven, J. A. Montgomery, J. E. Peralta, F. Ogliaro, M. Bearpark, J. J. Heyd, E. Brothers, K. N. Kudin, V. N. Staroverov, T. Keith, R. Kobayashi, J. Normand, K. Raghavachari, A. Rendell, J. C. Burant, S. S. Iyengar, J. Tomasi, M. Cossi, N. Rega, J. M. Millam, M. Klene, J. E. Knox, J. B. Cross, V. Bakken, C. Adamo, J. Jaramillo, R. Gomperts, R. E. Stratmann, O. Yazyev, A. J. Austin, R. Cammi, C. Pomelli, J. W. Ochterski, R. L. Martin, K. Morokuma, V. G. Zakrzewski, G. A. Voth, P. Salvador, J. J. Dannenberg, S. Dapprich, A. D. Daniels, O. Farkas, J. B. Foresman, J. V. Ortiz, J. Cioslowski, D. J. Fox, Gaussian 09, Revision B.01; Gaussian, Inc.: Wallingford, CT, 2010.

[20] A. D. McLean, G. Chandler, *J. Chem. Phys.* **1980**, *72*, 5639-5648.

[21] Z. Kokan, M. J. Chmielewski, *J. Am. Chem. Soc.* **2018**, *140*, 16010-16014.

[22] G. Sheldrick, *Acta crystallographica.* **2008**, *64*, 112-122.

[23] A. Spek, *Acta Crystallographica* **2009**, *65*, 148-155.

Chapter 5

Visible-Light Phototriggered Release of an Apoptosis-Inducing Chloride Anionophore Inside the Cancer Cells

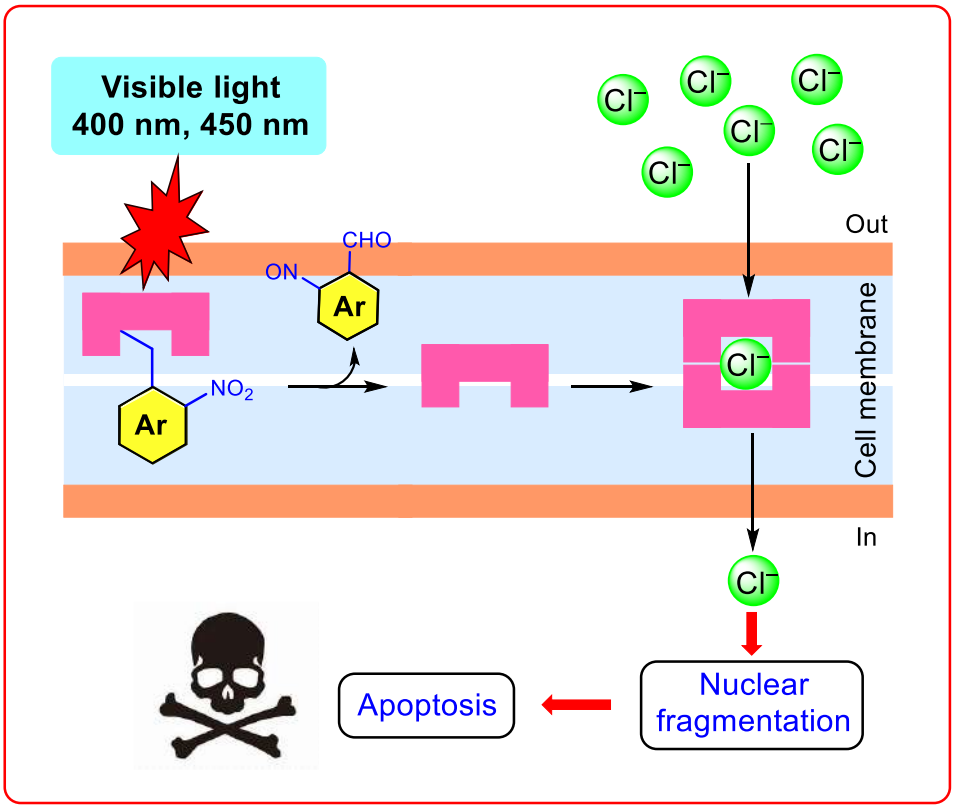

5.1. Introduction

Apoptosis is a programmed death mechanism of eukaryotic cells to eliminate unhealthy cells. A delayed or inhabited apoptosis has been known to cause autoimmune diseases or cancer. Cancer is one of the leading causes of death worldwide, and in 2018, there were 18.1 million new cases and 9.5 million cancer-related deaths around the globe. By 2040, the new cases per year are predicted to rise to 29.5 million, with the death of around 16.4 million. The traditional anticancer drugs used in chemotherapy have multiple adverse effects, including immunosuppression, neutropenic enterocolitis, anemia, infertility, etc.[1] Furthermore, these drugs usually target either specific enzymes/proteins in the cancer cells or disturb their fundamental DNA replication processes to eliminate the malignant cells.[2] Therefore, the resistance developed by the cancer cells through the activation of anti-apoptotic pathways,[3] e.g., mutation of the drug targeting sites,[4] overexpression of genes and proteins, etc.,[5] are known to curb their therapeutic applications. Dysregulation of ionic homeostasis, particularly for calcium,[6] potassium,[7] and chloride,[8] are known to be closely related to the onset of apoptosis. Various natural and artificial chloride transporters are known to perturb the chloride ion homeostasis and lead to apoptosis-mediated cell death inside the cancer cells. These include Prodigiosin,[9] tambjamine,[10] calix[4]pyrroles,[11] urea/thioureas,[12] bis-sulfonamides,[13] and squaramides,[14] etc. Unlike binding to the specific enzymes or proteins, these molecules function in the lipid membrane and they hence can overcome the resistance issues related to the mutations and overexpression of genes and proteins in cancer cells. However, the undesired cytotoxicity to normal cells can delimit their applications in anticancer therapy. In this regard, many stimulus-responsive ion transport systems have been reported to selectively activate these systems inside the cancer cells without affecting the normal healthy cells. The stimuli include the use of pH,[15] enzymes,[16] ligand,[17] light[18] and others,[19] etc. However, very few stimuli-responsive ion transport systems are known to be selectively activated inside the cancer cells.[20] Light-responsive ion transport systems, in particular, are important targets because of their Spatio-temporal control, remote addressability, and less cytotoxicity.[21] In our previous chapters 2nd, 3rd and 4th, we demonstrated photoswitchable ion transport systems based on azobenzene, acylhydrazone and phenylhydrazone photoswitches. All the three systems showed efficient photoswitchable ion transport activity across the lipid bilayer membrane and we were successful in achieving the stability of the excited state in case of the acylhydrazone photosystem, which was considered to be the main drawback associated with the azobenzene photoswitch for the potential biological applications demonstrated in the 2nd chapter. In chapter

3rd, we tried to enhance the excitation wavelength using a closely related phenylhydrazone photoswitch with similar thermally stabilized excited state as acylhydrazones. However, use of acid as a stimulus for reverse isomerization limits its biological applications. Photocages like *o*-nitrobenzyl (*O*NB) are versatile molecules that offer a way to generate a covalently linked active substrate with the help of external electromagnetic radiations, [22] and they have been used for either delivery [23] or activation [24] of anticancer drugs inside the cancer cells. Recently, our group introduced an *O*NB-linked N-aryl-1*H*-indole-2-carboxamide procarrier **1**, which in the presence of external electromagnetic radiations generates an active anion carrier **1′** inside the artificial liposomes and cancer cells (Figure 5.1). Although the procarrier molecule showed photoactivation inside the cancer cells, the as-synthesized active transporter **1′** did not show any cell toxicity due to the precipitation issues, and hence the detailed mechanism of apoptosis could not be evaluated. Lipophilicity of the active compound (logP = 3.9) was considered as the main reason for this inactive behavior because, as per Lipinski's rule, the ionophores must possess optimum lipophilicity for better transmembrane transport.[25] Moreover, harmful UV radiations (λ = 365 nm) were used for photoactivation purposes. The ultraviolet radiations possess limited cellular penetration, restricting their photocaging studies to the cells or tissue slices.[26] Moreover, the exposure of the cells to ultraviolet radiation can lead to phototoxic cell damage or death.[26]

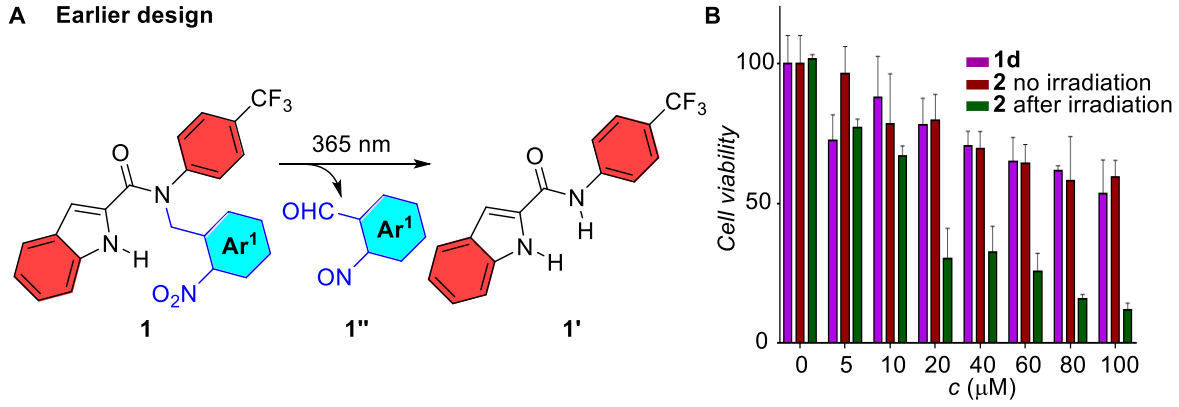

Figure 5.1. Schematic representation of earlier design of *o*-nitrobenzyl-linked indole-2-carboxamide-based photocleavable ion transporters (**A**). Cell viability of **1′** and **1** upon photoirradiation in MCF 7 cells. (**B**).

In the modified design, we improved the lipophilicity of the active transporters by incorporating different aromatic moieties at position-3 of the indole ring to generate a set of modified active carriers **2′**–**5′** (Figure 5.2A). The improved lipophilicity was expected to enhance their ion transport property and the cellular toxicity. Secondly, to improve the photocleavable absorption wavelength of the procarriers, we modified the *O*NB photocleavable

protecting group with different electron-donating groups to generate a set of modified procarriers **5a**–**5e** (Figure 5.2A). The incorporation of electron-donating groups to the *O*NB group is well known to red-shift its absorption wavelength.[27] So, the incorporation of electron-donating groups like *N*, *N* dimethyl was expected to enhance the absorption wavelength of the procarrier and hence can be activated inside the cancer cells at higher wavelengths of electromagnetic radiations (Figure 5.2B).

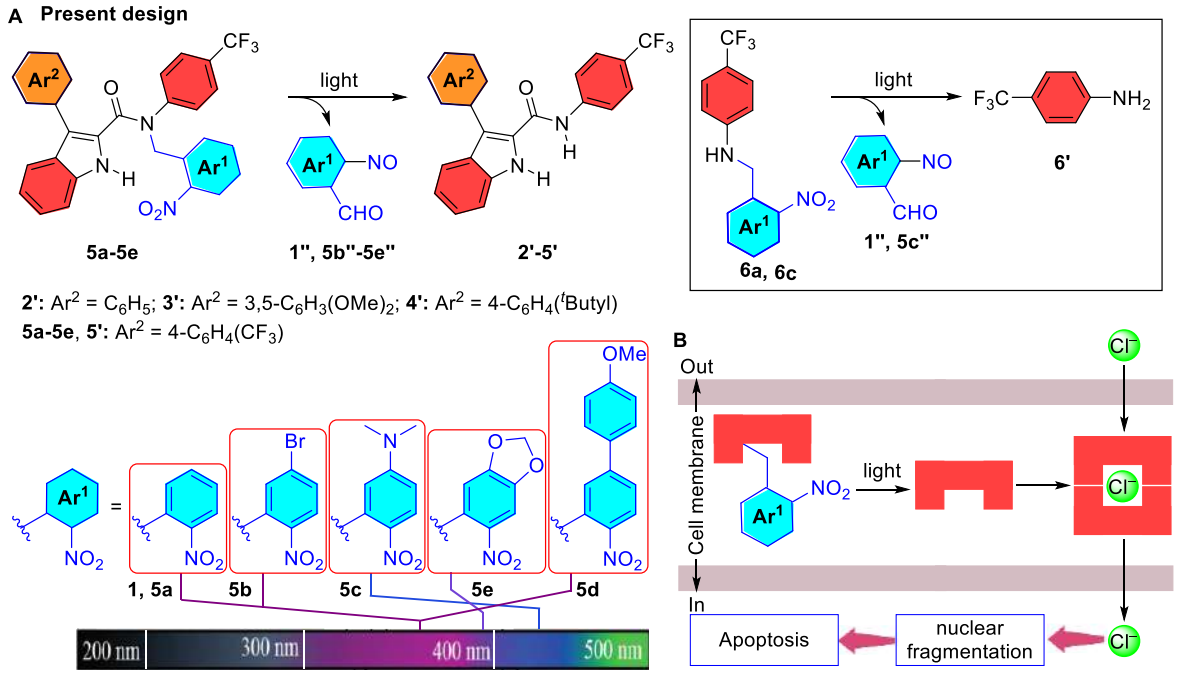

Figure 5.2. Schematic representation of present design of *o*-nitrobenzyl-linked indole-2-carboxamide based photocleavable ion transporters showing chemical structures of procarreiers **5a**–**5e**, active transporters **2′**–**5′** and amine-based control compounds **6a** and **6c** (**A**). Graphical representation of phototriggered release of an active anion carrier **5′** from *O*NB-protected procarriers **5a**–**5e** to induce chloride-mediated apoptosis inside the cancer cells (**B**).

5.2. Results and discussion

5.2.1. Synthesis

The overall synthesis of the active compounds, intermediate amines, and protected carriers is shown in Scheme 5.1. To synthesize the active transporters **2′**–**5′**, 3-iodo-2-indole carboxylic acid **8**, which itself was synthesized from indole-2-carboxylic acid using the reported literature[28] was coupled with 4-trifluoromethyl aniline to furnish the amide derivative **9**. Compound **9** was then coupled with different aryl boronic acids using Suzuki coupling reaction in the presence of $Pd(PPh_3)_4$ as the catalyst to synthesize the desired active transporters **2′**–**5′** in excellent yields. To synthesize the ONB-protected compounds **5a**–**5e** based on the free

compound **5′**, initially, the ONB based amine compounds **6a**–**6e** were synthesized by coupling 4-trifluoromethyl aniline **6′** with different nitrobenzaldehyde compounds **10a**–**10e**. This reaction was done in two steps: (i) coupling of nitrobenzaldehyde derivatives **10a**–**10e** with 4-trifluoromethylaniline **6′** in dichloromethane under reflux condition in the presence of pyrrolidine as a catalyst and 3-4 Å molecular sieves to give the imine intermediates. (ii) In situ reductions of imine compounds using sodium borohydride in methanol to furnish the desired amines **6a**–**6e**. Meanwhile, 3-iodo-2-indolecarboxylate **13** was coupled with 4-trifluoromethylphenyl boronic acid following a Suzuki coupling conditions in the presence of $Pd(PPh_3)_4$ as the catalyst to obtain methyl 3-(4-(trifluoromethyl)phenyl)-1*H*-indole-2-carboxylate **14**. This ester-based compound **14** was subsequently hydrolysed using aqueous sodium hydroxide in the 1:1 mixture of methanol and

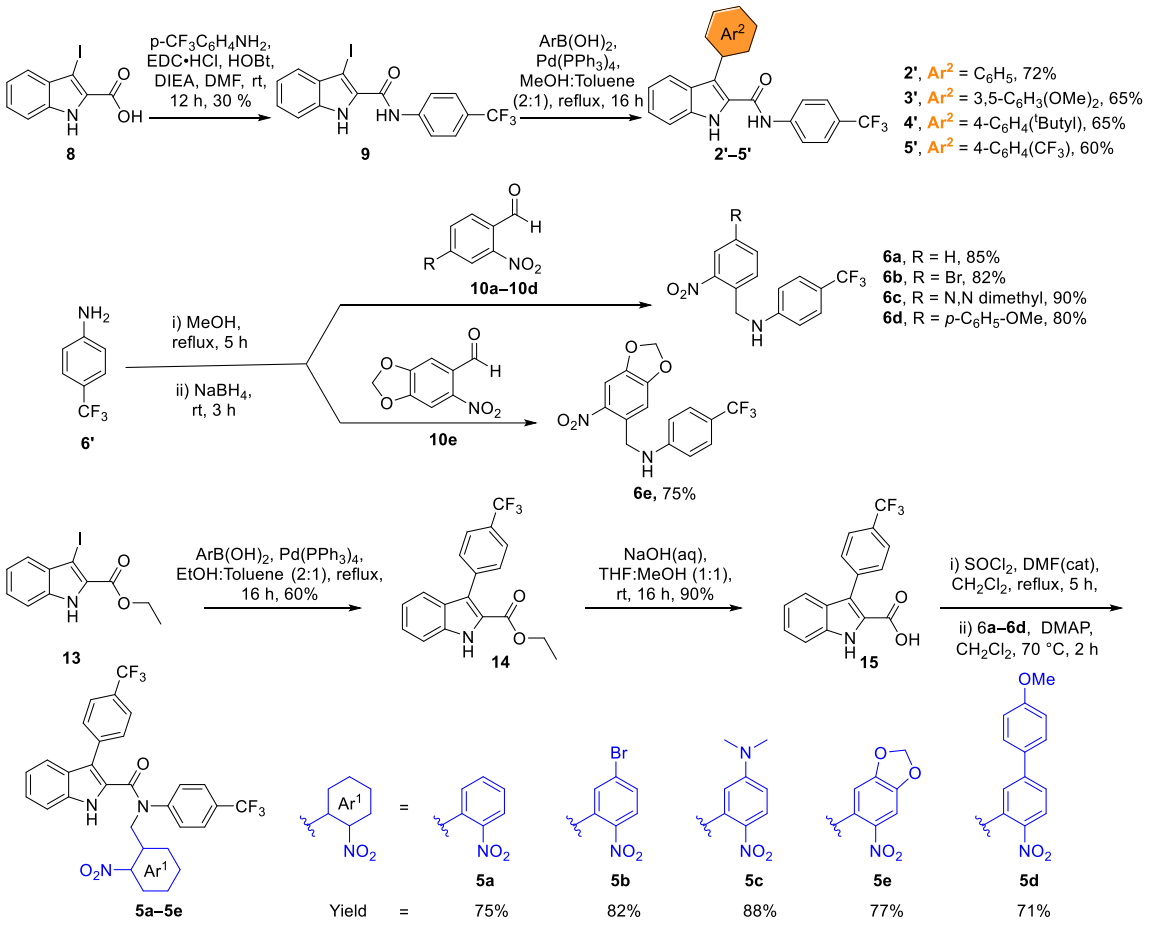

Scheme 5.1. Chemical synthesis of anionophores **2′–5′**, amine derivatives **6a–6e** and *O*NB protected compounds **5a–5d**

tetrahydrofuran for 24 h at rt to get the acid derivative **15**. Finally, the acid **15** was coupled with different amines **6a**–**6e** in dichloromethane under reflux conditions using triethylamine as the base to furnish the desired *O*NB protected compounds **5a**–**5e** in 71–88% yield.

5.2.2. Chloride binding studies

The initial evidence of Cl^- binding by the receptors **2′**–**5′** was confirmed by performing the ^1H NMR titration studies in acetonitrile–d_3. Fresh samples of the receptors **2′**–**5′** were prepared in the clean NMR tubes, and ^1H NMR for each sample was recorded. After that, tetrabutylammonium chloride (TBACl), in increasing equivalents, was added to the samples, and ^1H NMR was recorded after each addition. A significant downfield shifts of indole–N–H_1, amide–N–H_2 and C_{Ar}–H_3 protons were observed, indicating the involvement of these protons in hydrogen bonding through indole–N–H_1···Cl^-, amide–N–H_2···Cl^- and C_{Ar}–H_3···Cl^- non-covalent interactions (Figure 5.3A, 5.15, 5.17, and 5.19). The BindFit program[29] yielded a 1:1 (Host : Guest) binding stoichiometry with the binding constant values of ($K_{a(1:1)}$/Cl^-) of 717 ± 42 M^{-1} for **5′**, 280 ± 8 M^{-1} for **2′**, 292 ± 14 M^{-1} for **3′**, and 172 ± 10 M^{-1} for **4′**, respectively (Figure 5.3B, 5.16, 5.18, 5.20, and Table 1), with the binding affinity sequence of **5′** > **3′** > **2′** > **4′**. Moreover, *O*NB protected compound 5c upon titration with TBACl does not furnish any significant chemical shift change in H_1 proton (Figure 5.4 A). The binding constant value was

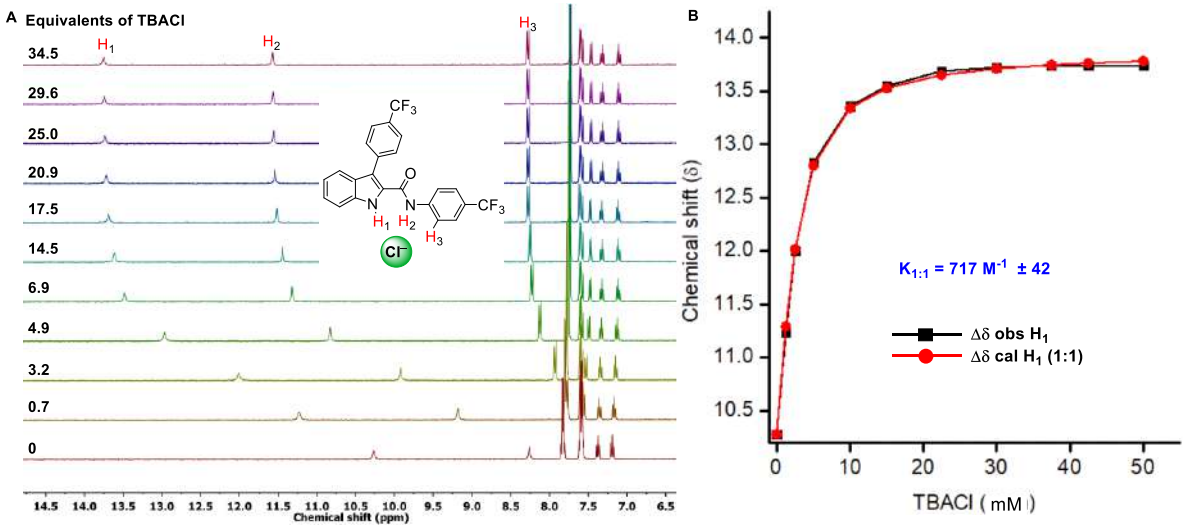

Figure 5.3. ^1H NMR titration spectra for **5′** (0.0025 M) with stepwise addition of TBACl in CD_3CN. The equivalents of added TBACl are shown on the stack spectra (**A**). The plot of chemical shift (δ) of H_1 protons *vs* TBACl added, fitted to 1:1 binding model of *BindFit* 0.5. The binding constant obtained is the mean of the three independent experiments. http://app.supramolecular.org/bindfit/view/ce336a99-7e4b-4920-84c3-82c3a793b9d5-(**5′** with TBACl) (**B**).

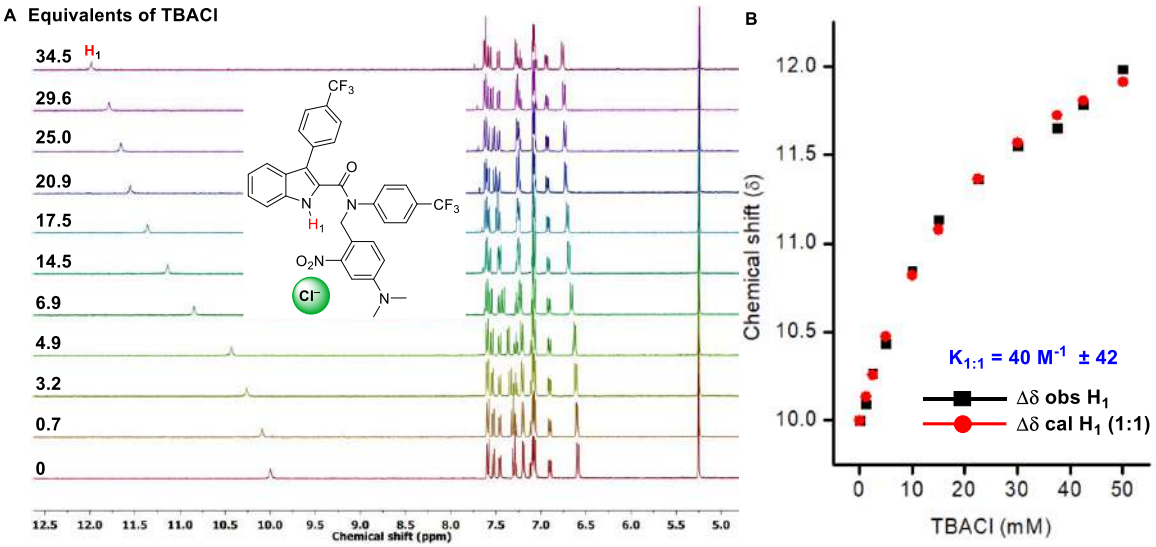

Figure 5.4. ^{1}H NMR titration spectra for **5c** (0.0025 M) with stepwise addition of TBACl in CD_3CN. The equivalents of added TBACl are shown on the stack spectra (A). The plot of chemical shift (δ) of H_1 protons *vs* TBACl added, fitted to 1:1 binding model of *BindFit* 0.5. The binding constant obtained is the mean of the three independent experiments. http://app.supramolecular.org/bindfit/view/ff0a2125-8cbc-4f4e-8636-00f3dc319ef5- (**5c** with TBACl).

found to be only 40 ± 6 M^{-1} (Figure 5.4 B). These results suggest that proton H_2 is important for creating an anion binding site in the active receptor molecule and protection of which with a photocleavable group greatly decreases the anion binding affinity.

5.2.3. Single crystal X-Ray analysis

The single-crystal X–ray diffraction analysis provides direct evidence of chloride binding to **5′** and reveals the formation of **5′**·Cl^- complex in 1:1 binding mode (Figure 5.5B). The chloride anion interacts with molecule **5′** through indole N–H_1, amide N–H_2 and C_{Ar}–H_3 hydrogen bonding interactions.with $H_1\cdots Cl^-$ distance of 2.18 Aº, $H_2\cdots Cl^-$ distance of 2.34 Aº, and $H_3\cdots Cl^-$ distance of 2.79 Aº, respectively.

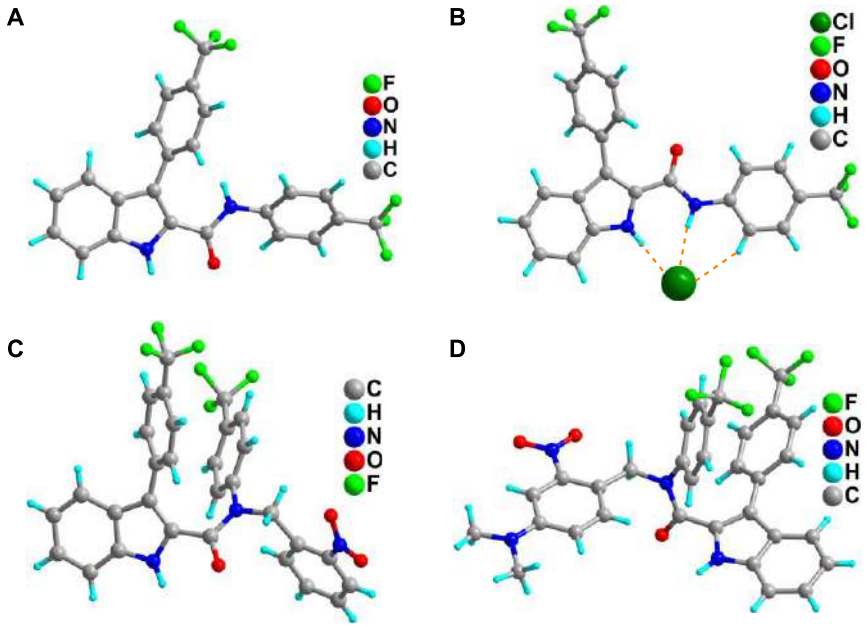

Figure 5.5. Single crystal X-ray structure of carrier **5′** (**A**), **5′**:Cl^- (**B**), Note: The tetrabutylammonium cation was omitted for clarity. *O*NB protected compounds **5b** (**C**) and **5C** (**D**), respectively.

5.2.4. Ion transport activity studies

The anion recognition properties of active compounds **2′**–**5′** prompted us to check the ion transport properties across artificial liposomes (LUVs). In order to do that, vesicles entrapping with 8-hydroxypyrene-1,3,6-trisulfonate (HPTS, pK_a = 7.2) dye were prepared from egg-yolk phosphatidylcholine (EYPC) lipid.[30] After that, a pH gradient, (ΔpH = 0.8) was created across the vesicular membrane by using NaOH in the extravesicular medium. The collapse of the pH gradient upon the addition of compounds **2′**–**5′** and previously reported active compound **1′** was monitored by measuring the fluorescence intensity of HPTS at λ_{em} = 510 nm (λ_{ex} = 450 nm). Eventually, the vesicles were collapsed by adding Triton X−100 to get the maximum fluorescence intensity. The Comparison of ion transport activity at an identical concentration of 0.2 μM provided the activity sequence: **5** > **3′** > **2′** > **1′** > **4′**, respectively (Figure 5.6A). The Hill analysis of the dose−response plots of the compounds **2′**, **3′**, **5′** and **1′** provided the EC_{50} values of 0.132 ± 0.015 μM, 0.113 ± 0.012 μM , 0.051 ± 0.008 μM, and 0.184 ± 0.018 μM for the compounds **5′**, **2′**, **3′**, and **1′**, respectively (Figure 5.21, 5.22, 5.23, 5.25 and Table 1), and the Hill coefficient *n* comes out to be ~ 2, which indicates that two receptor molecules are involved in forming the active transport system during the ion transport process. The Hill analysis could not be evaluated for **4′** due to its precipitation observed at higher concentrations in the buffer (Figure 5.24). The compounds **2′**, **3′** and **5′** showed better ion transport activity

than **1′**, with **5′** showing almost 4–fold increment in ion transport activity compared to **1′**. The incorporation of an aromatic moiety to the indole ring increases the hydrophobicity of the transporters, which on the other hand, increased the membrane permeability, and eventually, ion transport activity was enhanced. Among the modified anionophores **2′–5′**, **5′** showed better transport activity, likely due to two CF_3 groups, which are known to increase the membrane permeability and binding affinity of the ionophores.

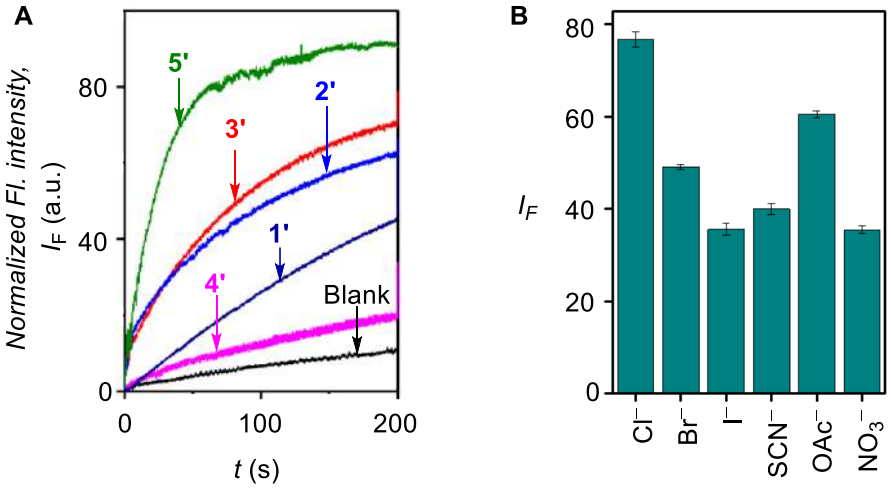

Figure 5.6. Activity comparison of **2′–5′** and **1′** (0.2 μM each) across EYPC–LUVs⊃HPTS (**A**). Anion selectivity of **5‘** (0.2 μM) across EYPC–LUVs⊃HPTS, (**B**).

Table 5.1. Summary of pK_a (indole-N–H$_1$), logP, K_a (M^{-1}), EC_{50} (μM), and Hill coefficient (*n*) values of compounds **2′–5′** and **1′**.

Comp.	**logP[a]**	**p*K*$_a$[a]**	***K*$_a$[b] (M^{-1})/ Cl^-**	***E*C$_{50}$ (μM)**	***n***
5′	6.49	11.81	717 ± 42	0.051 ± 0.008	2.1 ± 0.3
2′	5.61	15.80	280 ± 8	0.132 ± 0.015	2.2 ± 0.4
3′	5.29	11.68	292 ± 14	0.113 ± 0.012	2.6 ± 0.4
4′	7.15	11.84	172 ± 10	-[c]	-[c]
1′	3.96	11.76	599	0.184 ± 0.018	2.7 ± 0.3

[a] The logP and pK_a values were calculated using the Calculator plugin of the MarvinSketch program. [b] Association constants were obtained using *Bindfit* program based on the 1:1 binding model for N–H protons. [c] Could not be determined due to the precipitation of the compound at higher concentrations.

Chloride leakage studies

In order to check the transport of Cl^- ion, the transport activity of the highest active compound in the HPTS assay **5′** was monitored across EYPC-LUVs⊃lucigenin.[31] Vesicles were prepared by entrapping the lucigenin dye and $NaNO_3$ salt, and subsequently, a Cl^-/NO_3^- gradient was created across the vesicular membrane using NaCl in the external media solution. The transport of Cl^- ions by **5′** was measured by recording the change in the the fluorescence intensity of intravesicular lucigenin dye at λ_{em} = 535 nm (λ_{ex} = 455 nm). A significant decrease in the fluorescence intensity of the lucigenin dye was observed upon the addition of transporter **5′**. The dose-dependent chloride transport activity of **5′** is shown in Figure 5.7A. The Hill analysis provided the EC_{50} value of 0.870 ± 0.065 μM and *n* value of ~ 2, indicating the involvement of two receptor molecules for driving the ion transport process (Figure 5.26).

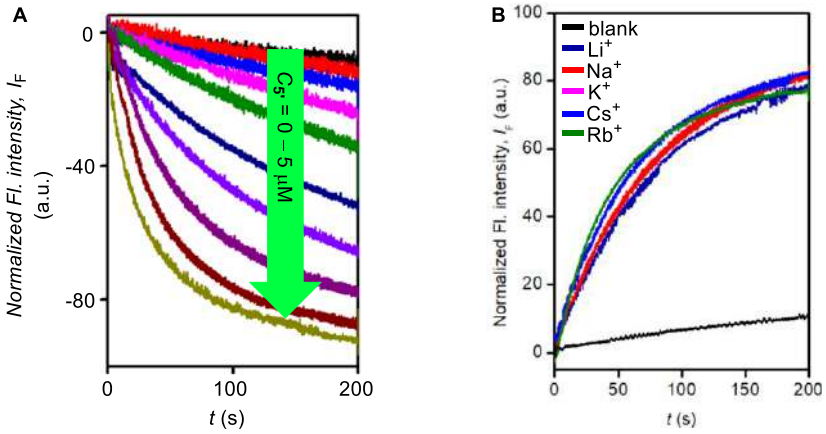

Figure 5.7. Concentration-dependent activity of compound **5′** across EYPC–LUVs⊃lucigenin (**A**). Cation selectivity of **5′** (340 nM) measured by varying external cations (M^+ = Li^+, Na^+, K^+, Rb^+, Cs^+) across EYPC-LUVs⊃HPTS (**B**).

Ion selectivity and mechanism of ion transport

Mechanistically, the disruption of the pH gradient across EYPC-LUVs⊃HPTS based vesicles can occur through the following different modes: (a) H^+/X^- symport, (b) OH^-/X^- antiport, (c)

H^+/M^+ antiport, or (d) OH^-/M^+ symport. In order to get the insights of the possible mechanistic way among the above different possible ways, the ion transport activity of **5′** was monitored across EYPC-LUVs⊃HPTS using intracellular NaCl and an iso-osmolar extravesicular M^+/Cl^- salt (where, M^+ = Li^+, Na^+, K^+, Rb^+, and Cs^+). Changing the extravesicular cations did not change the ion transport activity of the **5′** (Figure 5.7B) and hence, discards the H^+/M^+ antiport or OH^-/M^+ symport ion transport mechanisms.[32] However, changing the extravesicular Na^+/X^- salt (X^- = Cl^-, Br^-, I^-, SCN^-, OAc^-, and NO_3^-) made a significant change in the ion transport activity (Figure 5.6B), indicating the role of anions in an overall transport process, and hence indicates that the ion transport process can occur through either OH^-/X^- antiport or H^+/X^- symport mode.

The anion antiport process was eventually manifestly confirmed through chloride–based Ion-Selective Electrode (ISE) studies. Vesicles were prepared by entrapping with KCl (300 mM) and placed in potassium gluconate solution (300 mM, Figure 3E). The Cl^- efflux using chloride sensitive iion-selectiveelectrode (ISE) was monitored in the presence and absence of valinomycin and monensin. No noticeable change was observed in the Cl^- efflux by **5′** in the presence of monensin (Figure 5.8A), but, on the other hand, a significant increase in the Cl^- efflux by **5′** was observed in the presence of valinomycin (Figure 5.8B). The synergistic cooperative effect of the valinomycin with the anionophore **5′** indicates the occurrence of an [33] electrogenic mode of ion transport and thus, validates the operation of an anion antiport mechanism for the ion transport process. Additionally, the evidence of the carrier mode of ion transport by **5′** was obtained by performing the classic U-tube experiment.[12a, 34] Significant chloride transport was observed from one of the arms of the U-tube (source arm,

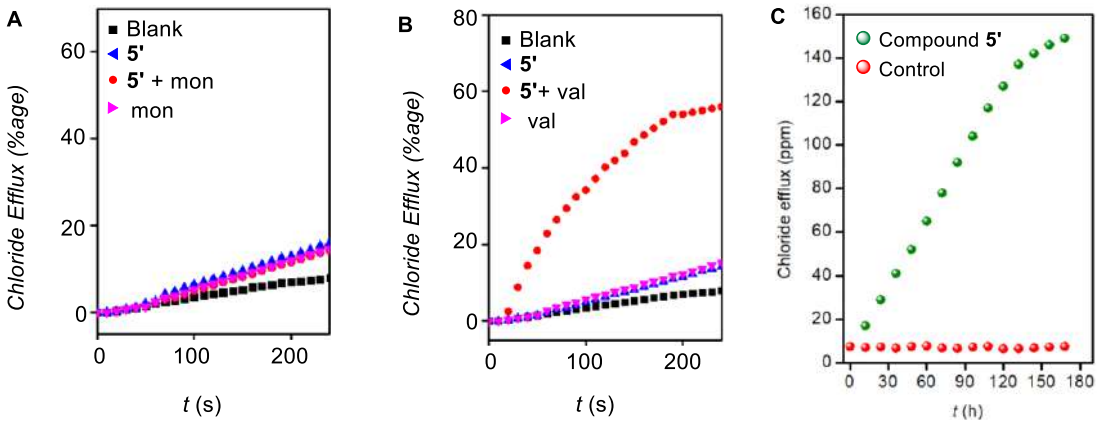

Figure 5.8. Chloride efflux of **5′** with and without Monensin (**A**), and with and without Valinomycin (**B**). Change of chloride ion concentration in a U-tube experiment with and without compound **5′** (1.0 mM) (**C**).

containing 500 mM NaCl) to the other arm (receiver arm, containing 500 mM $NaNO_3$) using chloride selective electrode (Figure 5.8C).

5.2.5. Photocleavable studies

Initially, the UV–Vis absorption studies of the *O*NB–protected compounds **5a**–**5e** were performed in acetonitrile. The UV–Vis absorption spectrum of the compounds is shown in Figure 5.9A. The absorption spectra of **5a**, **5b**, **5d** and **5e**, displayed λ_{max} centered around 310 nm with the UV bands of **5a**, **5b** and **5e** extended up to the wavelength of 385 nm, whereas, **5d** up to 408 nm, and on the other hand, The absorption spectra of **5c** displayed λ_{max} of 410 nm and the UV band is extended up to 500 nm. This gives an idea about the wavelength of the external source needed to photolyze these compounds, and among all the compounds, compound **5c** was expected to photolyze at a higher wavelength.

After getting an idea about the UV–Vis absorption wavelength, the photocleavable studies of **5a**–**5e** were performed at 365 nm and 400 nm using LEDs as the external source of light. The photolytic studies were performed using ^{1}H NMR studies in DMSO-d_6. The solutions of **5a**–**5e** were prepared in DMSO-d_6, and ^{1}H NMR was recorded before any photoirradiation. After that, each sample was irradiated at 365 nm using (3 × 1 W LEDs) and 400 nm using (1 × 8 W LEDs) respectively, at different intervals of time, and ^{1}H NMR was recorded after each

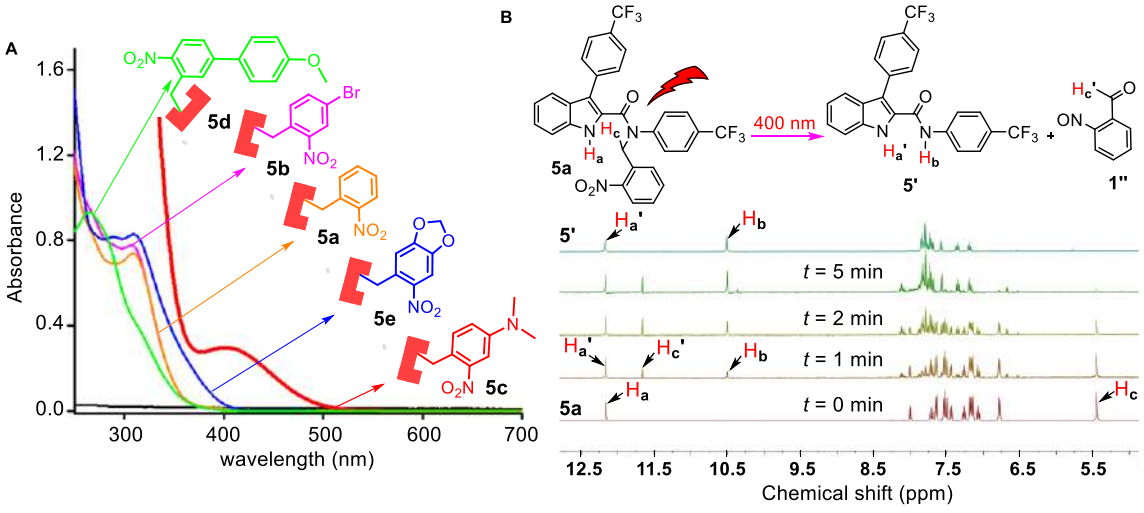

Figure 5.9. UV-Visible absorption spectrum of *O*NB protected procarrier compounds **5a–5e** (**A**). Phototriggered release of an active carrier **5′** from *O*NB protected procarrier **5a** monitored by ^{1}H NMR studies recorded in DMSO-d_6 photoirradiated using 365 nm LEDs at different intervals of time (**B**).

irradiation. The ^{1}H NMR spectra of the protected compounds, photoirradiated samples, and the non-protected compound **5′** were staked and compared. All of the compounds showed efficient photocleavable properties to generate the active compound **5′**, and the corresponding nitrosobenzaldehyde byproduct at 365 nm and 400 nm, respectively (Figure 5.27–5.36). The photolytic studies of **5a** at 400 nm are shown in Figure 5.9B. Furthermore, as indicated by the UV–Vis absorbtion spectrum, the photocleavable studies of **5c** were aslo performed at 450 nm of light. The sample of **5c** (10 μM) in the mixture of Methanol:Acetonitrile:Water (2:2:1) was photoirradiated at 450 nm for 2 h using (3 × 1 W LEDs). The mass spectroscopic data provided peaks at m/z = 449.1090 and 179.0821, corresponding to **5′** and 4-dimethylamino-2-nitrosobenzaldehyde byproduct in the solution (Figure 5.39).

5.2.6. Photocleavable ion transport studies

After successful photolytic studies of **5a**–**5e**, the compounds were subjected to phototriggered ion transport studies, and it was done through EYPC-LUVs⊃HPTS.[35] Vesicles containing **5a**–**5e** were photoirridiated at 365 nm, 400 nm, and 450 nm for different time intervals, and each time ion transport activity was monitored. A significant increment in ion transport activity was observed after each irradiation process. The ion transport activities obtained were compared by setting the ion transport activity of the blank sample as 0, and to that of active compound **5′** as 100%. The non-photoirradiated samples of **5a**–**5e** did not show any activity at these concentrations. Efficient photoactivation was achieved within one minute of photoirradiation of the samples (Figure 5.10, 5.41, 5.42, 5.43, and 5.44). Moreover, 1% of DMSO photoirradiating for five minutes did not furnish any activity, which confirms that the photoirradiation of the vesicles does not destroy the integrity of vesicles. Furthermore, compounds **5a**, **5b**, **5d**, and **5e** did not show any photoactivation at 450 nm, and on the other hand, efficient photoactivation was achieved for **5c** at 450 nm. This indicates that compound **5c** can be photoactivated at a higher wavelength of 450 nm. The increment in the activity of **5a**–**5e** upon photoirradiation at different wavelengths indicates the photocleavage of these compounds inside the lipid vesicles generating the active compound **5′**, which drives the ion transport across the lipid bilayer membrane.

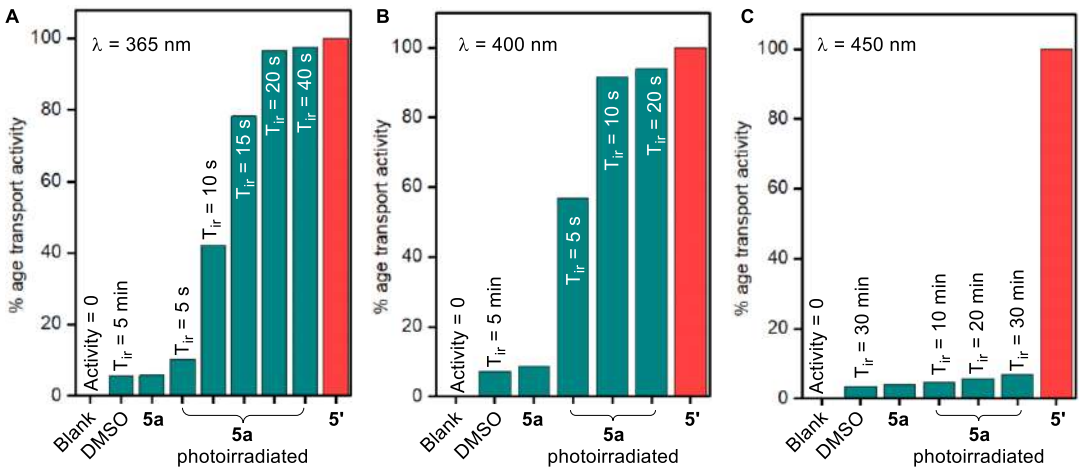

Figure 5.10. Normalized ion transport activity data upon photoirradiation of **5a** at 365 nm (**A**), at 400 nm (**B**) and at 450 nm (**C**) for different time intervals.

5.2.7. Geometry Optimization and Binding Energy Calculation

To obtain the geometry of [(**5′**)$_2$+Cl$^-$] complex, the DFT calculation studies were performed. The initial coordinates for the calculations were obtained by using CONFLEX 8 software program[36], which gives several conformational structures with almost equal populations (Figure S50). Subsequently, highest Boltzmann populated structure was taken for further geometry optimization by Gaussian 09 program[37] using a B3LYP functional and 6-31G(d,p) basis set.[38] The geometry optimized structure of [(**5′**)$_2$+Cl$^-$] complex showed that the two receptor molecules are oriented orthogonally to each other for proper binding of the chloride ion (Figure 5.11). The structure confirmed that each receptor participates in the Chloride recognition through indole-N–H$_1$···Cl$^-$ (H$_1$···Cl$^-$ = 2.42 Å), amide-N–H$_2$···Cl$^-$ (H$_2$···Cl$^-$ = 2.42 Å) and C$_{Ar}$–H$_3$···Cl$^-$ (H$_3$···Cl$^-$ = 2.80 Å), hydrogen bonding interactions. Further, calculations yield the binding energy of –47.89 kcal mol^{-1} for the [(**5′**)$_2$+Cl$^-$] complex.

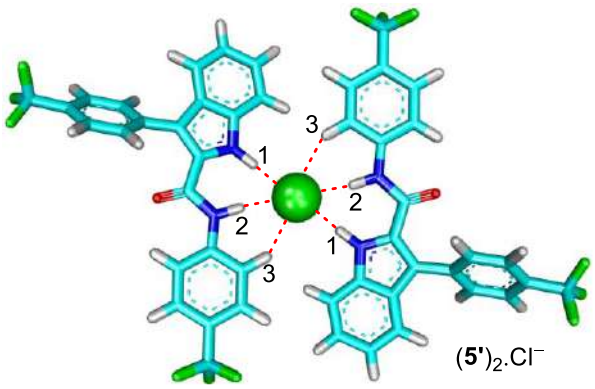

Figure 5.11. The geometry–optimized structure of [(**5′**)$_2$+Cl$^-$] complex. The hydrogen bonding interactions of different protons with the chloride anion are also shown as red dotted lines.

5.2.8. Cellular viability and photo triggered cell death

After the detailed ion transport studies, the highest active compound **5′** was subjected to biological studies. Initially, the viability of MCF-7 cells (human breast cancer cells) was monitored using the standard MTT assay after the cells were incubated with **5′** (0–20 μM each) for 24 h.[39] Significant cytotoxicity was seen for **5′** with IC_{50} value of 4.5 μM (Figure 5.12).

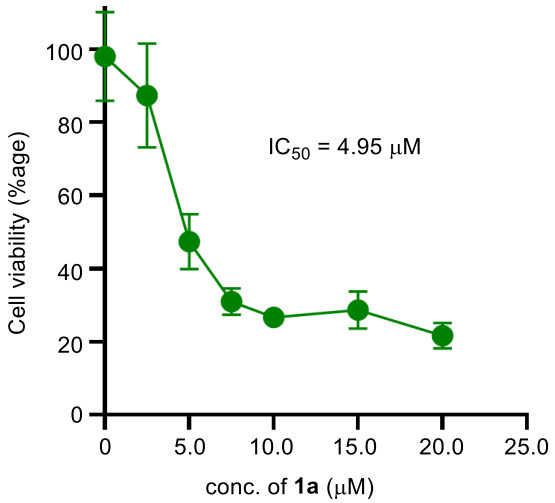

Figure 5.12. Cell viability of MCF-7 cells incubated with different concentrations of **5′** (0–20 μm each) for 24 hours.

Now, in order to check the phototriggered activation of the protected compounds **5a–5e** inside the cancer cells by the application of external electromagnetic radiations, MCF-7 cells were incubated with the compounds **5a**–**5e** in two different cell plates for 4 h. One of the cell plates containing the compounds was photoirradiated with 400 nm of light using (1 × 8 W LED) for 20 minutes, and the other containing the same compounds was not photoirradiated. The cell plates were then kept further in the incubator for 20 h and monitored using the standard MTT assay. A significant amount of cell death was observed for the cells which were photoirradiated compared to the non-photoirradiated cells (Figure 5.13A). The photoirradiated control cells, which do not contain the compounds **5a**–**5e**, did not show any cytotoxicity, which indicates that the light itself does not contribute to the cell death. Furthermore, in order to check the effect of *in situ* generated byproduct *o*-nitrosobenzaldehyde **1′′**, compound **6a** was used. This compound generates the same *o*-nitrosobenzaldehyde byproduct **1′′** as generated by the photoirradiation of **5a** along with 4-Trifluoromethylaniline **6′** while photoirradiation at 400 nm of light (Figure 5.37). The commercial 4-trifluoromethylaniline **6′** did not show any cytotoxicity in the MCF-7 cells, and hence, any cytotoxicity from the compound **6a** in the

presence of 400 nm of light was expected to be the outcome of the *o*-nitrosobenzaldehyde byproduct **1′′**. However, no significant cytotoxicity was generated for **6a** after photoirradiation compared to compound **5a**, which generates a similar by-product along with the active transporter **5′** (Figure 5.13C). This result suggests that the cytotoxicity generated in the case of compound **5a** in the presence of light is due to the formation of the active transporter **5′** and hence established our proposition of inducing the cell death by photoactivating the Cl^- transport in cancer cells.

After successfully photoactivating the compounds **5a**–**5e** inside the MCF-7 cells by photoirradiation at 400 nm, the photoactivation of these compounds was checked at 450 nm of electromagnetic radiations. In order to achieve this, MCF-7 cells were incubated with the compounds **5a**–**5e** in two different cell plates for 4 h. One of the cell plates containing the compounds **5a**–**5e** was photoirradiated with 450 nm of light using (3 × 1 W LEDs) for 2 h, and the other cell plate containing the same compounds was not photoirradiated. The cell plates were then kept in the incubator for 20 more h and monitored using the standard MTT assay. Significant cytotoxicity was observed only in the case of the cells incubated with the procarrier **5c** (Figure 5.13B). The photoactivation of only the procarrier **5c** at 450 nm inside the MCF-7 cells compared to the other compounds was rationally expected due to the presence of the UV-Vis absorption band at this wavelength and its photoactivation inside the artificial liposomes in the HPTS assay. The photoirradiated control cells which does not contain the procarrier compounds were completely viable. Furthermore, in order to check the effect of *in situ* generated byproduct *N*, *N* dimethyl *o*-nitrosobenzaldehyde **5c′′**, compound **6c** was used. This compound generates the same *N*, *N* dimethyl *o*-nitrosobenzaldehyde byproduct **5c′′** as generated by the photoirradiation of **5c** along with 4-Trifluoromethylaniline **6′′** while photoirradiation at 450 nm of light (Figure 5.38). As commercial 4-Trifluoromethylaniline **6′** did not show any cell death, and hence, any cytotoxity from **6c** in the presence of 450 nm of light would be because of the byproduct 4-dimethylamino-2-nitrobenzaldehyde **5c′′**. No significant cytotoxicity was observed for **6c** under 450 nm of light compared to the procarrier **5c,** which generates the same byproduct along with the active transporter **5′** (Figure 5.13D). This result confirms that the cytotoxicity for **5a** under the 450 nm of light is because of the formation of the active transporter **5′**.

Chloride-mediated apoptotic cell death

The chloride-mediated apoptosis is a well-studied cellular process, and in order to see the effect of the chloride ion transport in the process of cell death, the cell viability for **5′** was checked using the culture medium in the absence of presence of chloride. Two different types of HBSS (Hanks balanced salt solution) solutions were used as the extracellular media. One containing the Cl^- ions and another without the Cl^- ions. The MCF7 cells were suspended in both of these media and incubated with compound **5′** at different concentrations. Expectedly, the transporter **5′** showed more cell death with the HBSS solution containing the Cl^- ions compared to that solution, which does not contain the Cl^- ions (Figure 5.14A) and hence indicates the chloride-mediated cell death.[11, 20b, 40]

In order to identify the mode of cell death, the immunoblot studies were carried out for both **5′** treated cells and control cells (Figure 5.14B). In the intrinsic apoptotic pathway of apoptosis, The formation of the cytochrome c/Apaf-1 complex activates different caspases, including caspase 2 pathway. We analyzed the caspase 2 protein expressions by immunoblotting, and it was observed that cells treated with **5′** showed higher protein levels of caspase 2. Cleaved poly (ADP-ribose) polymerase (PARP-1) is also the apoptotic marker, and PARP-1 cleavage is known to prevent DNA repair to facilitate the apoptosis. We observed degradation for the full-length PARP-1 (116 kDa) with a concomitant increase of cleaved PARP-1 (86 kDa) upon the immunoblot analysis of MCF7 cells when incubated with **5′**. These results confirmed that the treatment of compound **5′** makes the cells susceptible to Furthermore, apoptosis is generally

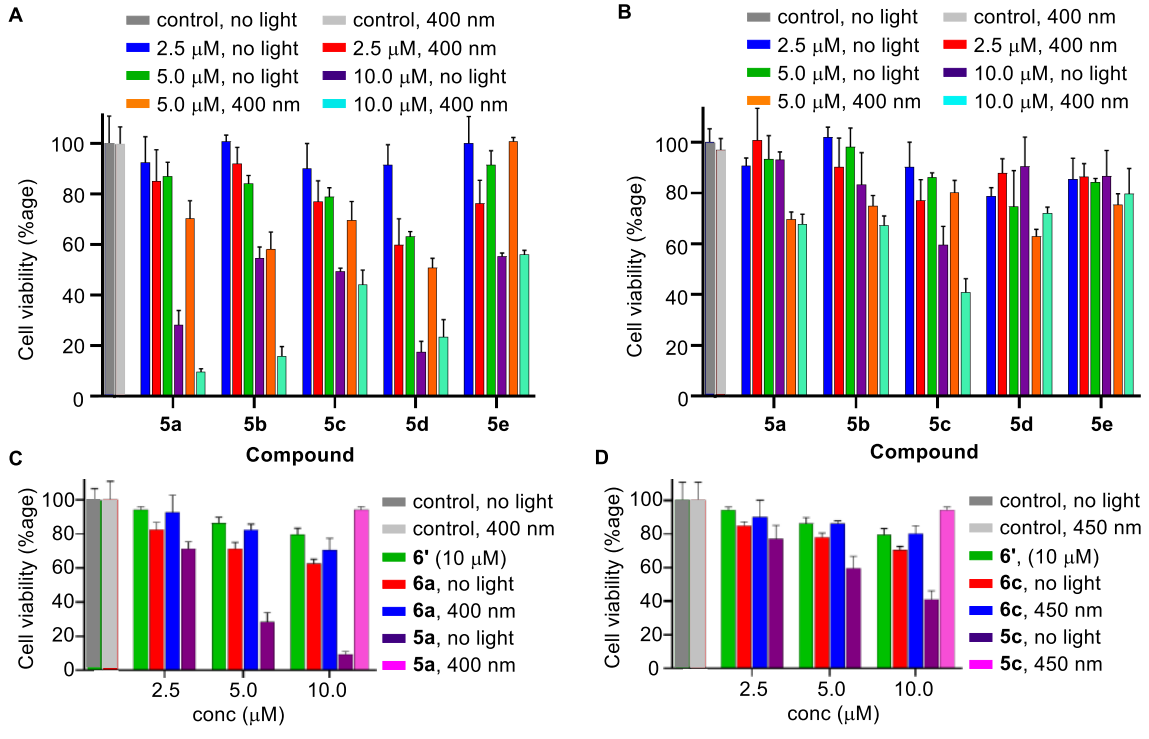

Figure 5.13. Cell viability using **5a–5e** for 24 h in MCF 7 cells in the absence of light and upon photoirradiation at 400 nm for 20 min using (1 × 8 W LED). (**A**). Cell viability obtained from MTT assay upon addition of **5a–5e** for 24 h in MCF 7 cells in the absence of light and upon photoirradiation at 450 nm for 2 h using (3 × 1 W LED) (**B**). Cell viability using **6a** and **5a** for 24 h in MCF 7 cells in the absence of light and upon photoirradiation at 400 nm for 20 min using (1 × 8 W LED) and Cell viability of **6′** (**C**). Cell viability using **6c** and **5c** for 24 h in MCF 7 cells in the absence of light and upon photoirradiation at 450 nm for 2 h using (1 × 8 W LED) and Cell viability upon addition of **6** (**D**).

induced after the initiation of high-intensity DNA damage inside the cells. To confirm the DNA damage, **5′** treated cells were also checked for the various DNA damage markers such as pRPA,[41] a single-strand DNA break marker and γH2AX,[42] a double-strand undergo apoptotic way of cell death.break marker. It was observed that **5′** treated cells showed higher protein expressions of activated pRPA, not the γH2AX. These results overall confirmed that **5′** causes DNA damage through a single-stranded DNA break which eventually induces apoptosis to the cells.

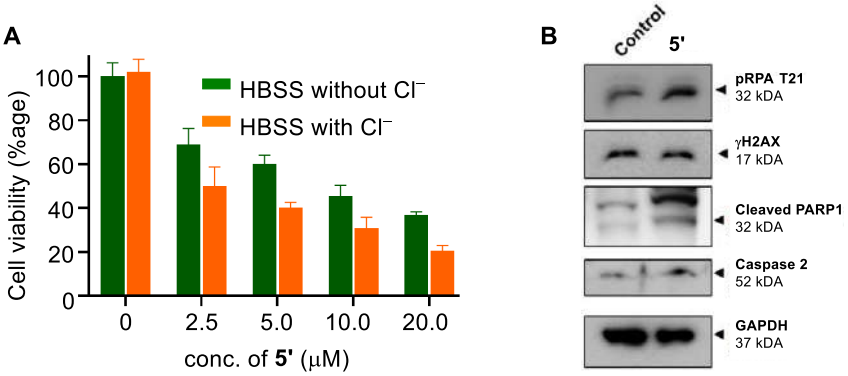

Figure 5.14. Cell viability in the presence and absence of Cl^- ions incubated with **5′** at different concentrations (**A**). Immunoblot assay for active caspase 2, expression of cleaved PARP-1 and degradation of full length PARP-1, expression of pRPA and γH2AX proteins in MCF7 cells, after 24 h incubation with 0 μM and 10 μM of **5′** (**B**).

5.3. Conclusion

In conclusion, we have successfully modified the previously studied indole-2-carboxamide ion carrier **1′** by incorporating different aromatic moieties to generate the new set of ion carriers **2′–5′** with efficient ion transport activities. The highest active compound **5′** showed an almost four-fold increment in the transport activity as compared to the previously studied **1′**. The chloride binding studies were confirmed by ^{1}H NMR titration studies, and the direct proof of chloride binding of **5′** was obtained by solid-state X-ray crystallographic studies. The highest active compound **5′** furnished the EC_{50} value of 0.05 μM with a Hill coefficient *n* value of ~ 2,

indicating the involvement of two receptors in the formation of an active ion transport system to drive the ion transport across the membrane. Detailed mechanistic studies of ion transport confirmed the operation of an anion antiport mechanism. The active transport **5′** showed efficient cytotoxicity inside the MCF-7 breast cancer cells. The procarriers **5a–5e** can be activated upon photoirradiation at 400 nm inside the cancer cells. Moreover, by virtue of the modified *o*-nitrobenzyl photocleavable groups, the procarrier **5c** can also be activated at 450 nm. This utilization of higher wavelength electromagnetic radiations is highly desirable for potential biological applications.

5.4. Experimental details

5.4.1. General Methods

All reagents and solvents for synthesis were purchased from different commercial sources (Sigma-Aldrich and Spectrochem), and used without further purification. The column chromatography was carried out using Merck silica (100-200 mesh size). The thin layer chromatography was performed on E. Merck silica gel 60-F254 plates. Egg yolk phosphatidylcholine (EYPC) as a solution of chloroform (25 mg/mL), mini extruder, polycarbonate membrane of 100 nm and 200 nm were purchased from Avanti Polar Lipid. HEPES, HPTS, lucigenin, NaOH, Sephadex G-50, Triton X-100, valinomycin and all inorganic salts were obtained as molecular biology grade from Sigma Aldrich.

5.4.2. Physical Measurements

All the NMR spectra were recorded on a 400 MHz spectrophotometer. The residual solvent signals were considered as an internal reference (δ_H = 7.26 ppm for $CDCl_3$, δ_H = 2.50 for DMSO-d_6, and δ_H = 1.94 for CD_3CN) to calibrate spectra. The chemical shifts were reported in ppm. Following abbreviations were used to indicate multiplicity patterns m: multiplet, s: singlet, d: doublet, t: triplet, q: triplet, dd: doublet of doublets, td: triplet of doublets, ddd: doublet of doublet of doublets,.Coupling constants were measured in Hz. Infra-red (IR) spectra were measured in cm^{-1} using FT–IR spectrophotometer. High-resolution mass spectra (HRMS) were recorded on an electrospray ionization time-of-flight (ESI-TOF) mass spectrometer. Fluorescence experiments were recorded on a Fluoromax-4 instrument from Horriba equipped with an injector port and magnetic stirrer. All buffer solutions were prepared in the autoclaved water. Adjustment of pH of buffer solutions was made using pH meter purchased from Hanna instruments. The extravesicular dye was removed by performing gel chromatography using Sephadex G-50. The fluorescence data were processed using OriginPro 8.5. ChemBio Draw

15 Ultra software was used for drawing structures and processing figures. UV-Vis spectra were recorded on a Shimadzu UV-2600 UV-Vis spectrophotometer. Chloride ion efflux was measured using Thermo Scientific Orion Chloride ion plus ISE connected to a Fisherbrand AB 250 ph/ISE meter for recording chloride concentration in ppm. The single-crystal X-ray diffraction (SCXRD) analysis was performed on a Bruker Smart Apex Duo diffractometer using Mo Kα radiation (λ = 0.71073Å). The crystal structures were solved using intrinsic methods and then refined by full-matrix least-squares against F^2 using all data by using SHELXL-2014/7 built in the Apex-3 package.

5.4.3. Synthetic procedures

3-iodo-*N*-(4-(trifluoromethyl)phenyl)-1H-indole-2-carboxamide (9): In a 25 mL round bottom flask, 3-iodo-1H-indole-2-carboxylic acid **8** (1.0 g, 1 eq), which itself was synthesized using the reported literature[S1], EDC·HCl (998 mg, 1.5 eq) and HOBt (611 mg, 1.3 eq) were dissolved in DMF (10 mL). The resulted solution was stirred at room temperature for 30 min. After 30 min, *4-(trifluoromethyl)aniline* (841 mg, 1.5 eq) and *N*, *N*-diisopropylethylamine (585 mg, 1.3 eq) were added. The reaction was kept to stirr at room temperature for an additional 12 h. After completion of the reaction, the reaction mixture was extracted with ethyl acetate (3 × 20 mL), washed with brine (2 × 20 mL), the organic layer was dried over Na_2SO_4 and concentrated under reduced pressure. The crude product was purified by column chromatography over 100-200 mesh silica gel (*Eluent*: EtOAc : petroleum ether 1:10 v/v) to furnish **9** as white solid (450 mg, 30%). **^{1}H NMR (400 MHz, Chloroform-*d*):** δ 9.80 (s, 1H), 9.21 (s, 1H), 7.87 (d, *J* = 8.4 Hz, 2H), 7.67 (d, *J* = 8.5 Hz, 2H), 7.52 (d, *J* = 8.1 Hz, 1H), 7.46 – 7.37 (m, 2H), 7.31 – 7.26 (m, 1H); **^{13}C NMR (101 MHz, DMSO-d6):** δ 162.2, 137.9, 127.5, 127.2, 125.1, 122.6, 120.7, 113.1, 108.2, 52.3.; **IR (Neat, ν/cm^{-1}):** 3750, 3307, 1654, 1530, 1408, 1320, 1233, 1100, 830, 743; **HRMS (ESI):** Calc. for $C_9H_{12}N_2OH^+$ $[M+H]^+$: 165.1022, found 165.1028.

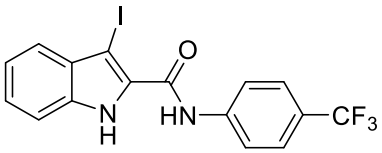

$C_{16}H_{10}F_3IN_2O$
Mol. Wt.: 430.16

General procedure for synthesizing the compounds (2′-5′)

General method A: In a 25 mL round bottom flask, 3-iodo-*N*-(4-(trifluoromethyl)phenyl)-1H-indole-2-carboxamide **9** (100 mg, 1.0 eq), and an appropriate aromatic boronic anhydride (1.0 eq) were degassed using nitrogen in a mixture of ethanol and toluene (2:1, 30mL) for 30 min. After that tetrakis triphenylphosphine palladium 0 (13mg, 0.05 eq) and aqueous sodium nitrate solution (1 mL of 2 N solution) were added and the reaction mixture was refluxed using oil

bath for 16 h. After the completion of the reaction, monitored through TLC, the reaction mixture was filtered through celite and volatiles were evaporated under high vaccum using Rota evaporator. The mixture was extracted with ethylacetate (3 × 20 mL), washed with brine (2 × 20 mL), dried on anhydrous sodium sulfate and purified through column chromatography using 100-200 mesh silica gel to furnish the desired compounds **2′-5′**.

3-phenyl-N-(4-(trifluoromethyl)phenyl)-1H-indole-2-carboxamide (2′): Synthesized by

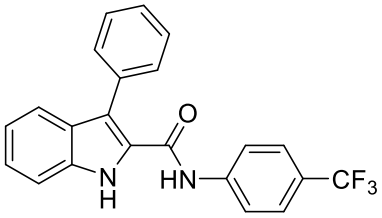

$C_{22}H_{15}F_3N_2O$
Mol. Wt.: 380.37

reacting 3-iodo-N-(4-(trifluoromethyl)phenyl)-1H-indole-2-carboxamide **9** (100 mg, 1.0 eq) with phenylboronic acid (42 mg, 1.5 eq). The crude product was purified by column chromatography over 100-200 mesh silica gel (*Eluent*: EtOAc : petroleum ether 1:9 v/v) to furnish **2′** as white solid (63 mg, 72%); **^{1}H NMR (400 MHz, $CDCl_3$):** δ 9.52 (s, 1H), 7.88 (s, 1H), 7.68 – 7.60 (m, 5H), 7.51 (d, *J* = 7.6 Hz, 4H), 7.41 – 7.35 (m, 1H), 7.33 (d, *J* = 8.5 Hz, 2H), 7.17 (t, *J* = 8.0 Hz, 1H); **^{13}C NMR (101 MHz, $CDCl_3$):** δ 159.8 , 140.6 , 135.4 , 133.2 , 130.9 , 129.6 , 128.9 , 128.2 ,126.0 (q, *J* = 272.2 Hz), 126.30(q, *J* = 3.9 Hz), 126.2 , 126-125 (q, *J* = 32.3 Hz), 125.7 , 121.1 , 118.8 , 111.9; **IR (Neat, ν/cm^{-1}):** 3402, 3312, 1690, 1655, 1600, 1532, 1447, 1408, 1318, 1237, 1187, 1162, 1100, 1064; **HRMS (ESI):** Calc. for $C_{22}H_{16}F_3N_2O$ $[M+H]^+$: 381.1029 found 381.1029.

3-(3,5-dimethoxyphenyl)-N-(4-(trifluoromethyl)phenyl)-1H-indole-2-carboxamide (3′):

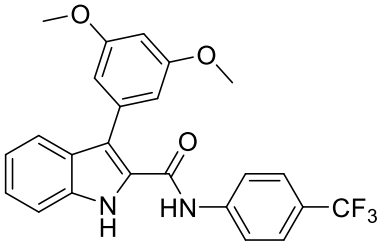

$C_{24}H_{19}F_3N_2O_3$
Mol. Wt.: 440.42

Synthesized by reacting 3-iodo-N-(4-(trifluoromethyl)phenyl)-1H-indole-2-carboxamide **9** (100 mg, 1.0 eq) with (3,5-dimethoxyphenyl)boronic acid (63 mg, 1.5 eq). The mixture was purified by column chromatography over 100-200 mesh silica gel (*Eluent*: EtOAc : petroleum ether 2:8 v/v) to furnish **3′** as white (66 mg, 65%); **^{1}H NMR (400 MHz, $CDCl_3$):** δ 9.71 (s, 1H), 8.16 (s, 1H), 7.58 – 7.47 (m, 4H), 7.44 – 7.34 (m, 3H), 7.22 – 7.08 (m, 4H), 4.03 (s, 3H), 3.90 (s, 3H); **^{13}C NMR (101 MHz, $CDCl_3$):** δ 159.8, 149.8, 149.5, 140.6, 135.4, 128.4, 126.4, 126.1, 126.3 (q, *J* = 3.9 Hz), 125.7 (q, *J* = 32.3 hz), 125.6, 125.2, 123.15, 122.68 (q, *J* = 272 hz), 121.1, 121.0, 119.3, 118.9, 113.6, 111.9, 111.9, 56.1; **IR (Neat, ν/cm^{-1}):** 3402, 3306, 1689, 1657, 1601, 1531, 1449, 1407, 1320, 1235, 1186, 1162, 1097, 1064; **HRMS (ESI):** Calc. for $C_{24}H_{20}F_3N_2O_3$ $[M+H]^+$: 441.1420 found 441.1426.

3-(4-(tert-butyl)phenyl)-N-(4-(trifluoromethyl)phenyl)-1H-indole-2-carboxamide (4′):

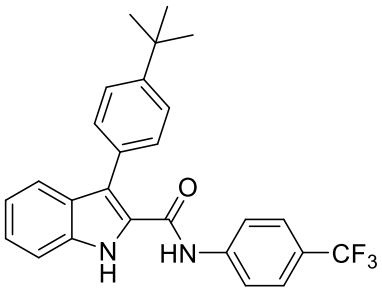

$C_{26}H_{23}F_3N_2O$
Mol. Wt.: 436.47

Synthesized by reacting 3-iodo-N-(4-(trifluoromethyl)phenyl)-1H-indole-2-carboxamide **9** (100 mg, 1.0 eq) with (4-(tert-butyl)phenyl)boronic acid (62 mg, 1.5 eq). The mixture was purified by column chromatography over 100-200 mesh silica gel (*Eluent*: EtOAc : petroleum ether 1:9 v/v) to furnish **4′** as white solid (65 mg, 65%). **^{1}H NMR (400 MHz, $CDCl_3$):** δ 9.41 (s, 1H), 7.91 (s, 1H), 7.68 (d, *J* = 8.3 Hz, 2H), 7.59 – 7.49 (m, 6H), 7.40 (t, *J* = 7.6 Hz, 1H), 7.30 (d, *J* = 7.6 Hz, 2H), 7.19 (t, *J* = 7.5 Hz, 1H), 1.49 (s, 9H); **^{13}C NMR (101 MHz, Chloroform-d):** δ 159.8, 152.4, 140.6, 135.4, 130.6, 130.0, 128.3, 126.5, 126.38, 126.24 (q, *J* = 3.9 Hz), 125.9 (q, *J* = 32.3 Hz), 125.6, 122.6(q, *J* = 272 hz), 121.3, 121.0, 119.6, 118.7, 111.8, 34.9, 31.3; **IR (Neat, ν/cm^{-1}):** 3405, 3310, 1688, 1657, 1599, 1533, 1447, 1409, 1318, 1235, 1189, 1162, 1099, 1068; **HRMS (ESI):** Calc. for $C_{26}H_{24}F_3N_2O$ $[M+H]^+$: 437.1835 found 437.1836.

***N*,3-bis(4-(trifluoromethyl)phenyl)-1H-indole-2-carboxamide (5′):** Synthesized by reacting 3-iodo-N-(4-(trifluoromethyl)phenyl)-1H-indole-2-carboxamide **9** (100 mg, 1.0 eq) with 4-trifluoromethyl phenylboronic acid (66 mg, 1.5 eq). The crude product was purified by column chromatography over 100-200 mesh silica gel (*Eluent*: EtOAc : petroleum ether 1:9 v/v) to furnish **5′** as white solid (62 mg, 60%). **^{1}H NMR (400 MHz, $CDCl_3$):** δ 9.79 (s, 1H), 7.91 (d, *J* = 8.0 Hz, 2H), 7.78 (d, *J* = 8.0 Hz, 2H), 7.63 (s, 1H), 7.57 – 7.47 (m, 4H), 7.40 (t, J = 7.6 Hz, 1H), 7.35 (d, *J* = 8.5 Hz, 2H), 7.20 (t, *J*= 7.5 Hz, 1H); **^{13}CNMR (101 MHz, Chloroform-d):** δ 140.3, 135.5, 131.4, 130.9 (q, *J* = 272.2 Hz), 127.9, 126.64, 126.61, 126.57, 126.53, 126.49, 126.47, 126.2 (q, *J* = 272.2 Hz), 126.1, 125.1 (q, *J* = 32.3 Hz), 122.5 (q, *J* = 32.3 Hz), 120.7, 119.1, 117.7; **IR (Neat, ν/cm^{-1}):** 3402, 3310, 1687, 1657, 1599, 1531, 1447, 1407, 1318, 1235, 1186, 1162, 1099, 1064; **HRMS (ESI):** Calc. for $C_{23}H_{15}F_6N_2O$ $[M+H]^+$: 449.1083 found 449.1078.

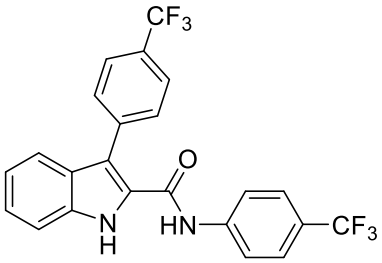

$C_{23}H_{14}F_6N_2O$
Mol. Wt.: 448.36

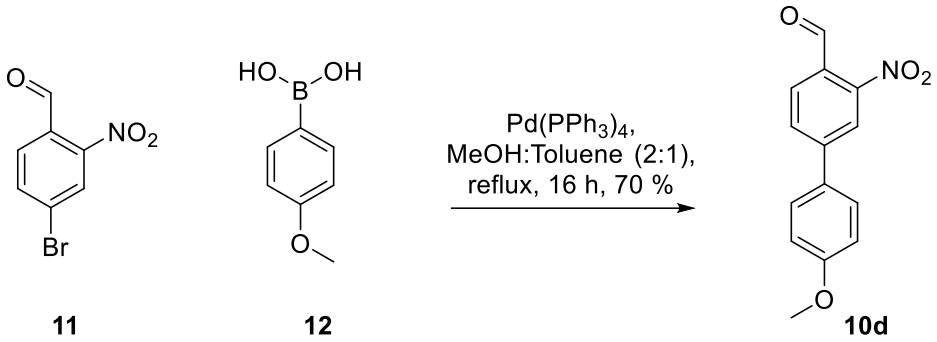

11 **12** **10d**

Scheme 5.2. Chemical synthesis for the compound **10d**.

ii. General procedure for synthesizing the compound 10d

In a 25 mL round bottom flask, (4-methoxyphenyl)boronic acid **12** (264 mg, 2 eq), and 4-bromo-2-nitrobenzaldehyde **11** (200mg, 1 eq) were degassed using nitrogen in a mixture of Methanol and toluene (2:1, 20 mL) for 30 min. After that tetrakis triphenylphosphine palladium 0 (50mg, 0.5 eq) and aqueous sodium nitrate solution (2 mL of 2 N solution) was added and the reaction mixture was refluxed using oil bath for 16 h. After the completion of the reaction, the mixture was filtered through celite and volatiles were evaporated under high vaccum using Rota evaporator. The crude mixture was extracted with ethylacetate (3 × 20 mL), washed with brine (2 × 20 mL), dried on.anhydrous sodium sulfate and purified through column chromatography using 100-200 mesh silica gel(*Eluent*: EtOAc : petroleum ether 2:8 v/v) to furnish the desired compound **10d** as white solid (156 mg, 70%). **^{1}H NMR (400 MHz, Chloroform-d):** δ 10.41 (s, 1H), 8.23 (s, 1H), 8.01 (d, *J* = 8.1 Hz, 1H), 7.92 (d, *J* = 8.0 Hz, 1H), 7.60 (d, *J* = 8.7 Hz, 2H), 7.03 (d, *J* = 8.7 Hz, 2H); **^{13}C NMR (101 MHz, Chloroform-d):** δ 187.8,16.0, 150.5, 146.9, 131.2, 130.3, 128.6, 122.1, 114.9, 55.5; **IR (Neat, v/cm^{-1}):** 2362, 1725, 1682, 1600, 1514, 1443, 1398, 1346, 1302, 1275, 1245; **HRMS (ESI):** Calc. for $C_{14}H_{12}NO_4$ $[M+H]^+$: 258.076 found 258.0775.

iii. General procedure for synthesizing the amine derivatives 6a-6e

General method B: In a 25 mL round bottom flask, a solution of 4-(trifluoromethyl) aniline **6′** (100 mg, 1.0 eq), pyrolidine (10 mg, 2 eq), molecular sieves 4 A˚ (1.0 gram), and an appropriate benzaldehyde **10a-10e** (1.0 eq) were refluxed in dry dichloromethane for 16 h. The reaction mixture was allowed to cool to room temperature and solvent was removed. Subsequently, the crude product was redissolved in dry methanol (20 mL) and $NaBH_4$ (4.0 eq) was added to the reaction mixture and stirred for extra 3 h at room temperature. After the completion of the reaction, monitored through TLC, the solvent was evaporated under reduced

pressure using rota evaporator. The residue was dissolved in ethyl acetate (30 mL), and water (15 mL) was added. The crude product was extracted in ethyl acetate (3 × 20 mL). The organic layer was washed with water (2 × 10 mL) and brine (2 × 10 mL), dried over Na_2SO_4 and filtered. The filtrate was concentrated under reduced pressure. The purification of the crude product was done using either100-200 mesh silica gel or neutral alumunium oxide column chromatography to furnish the desired compounds **6a–6e**.

***N*-(2-nitrobenzyl)-4-(trifluoromethyl)aniline (6a):** Synthesized by reacting 4-trifluoromethyl aniline **6′** (100mg, 1.0 eq) with *ortho*-nitrobenzaldehyde **10a** (94mg, 1.0 eq). The crude product was purified by column chromatography over 100-200 mesh silica gel (*Eluent*: EtOAc : petroleum ether 1:9 v/v) to furnish **6a** as a yellow oil (155 mg, 85%). **^{1}H NMR (400 MHz, Chloroform-d):** δ 8.11 (d, *J* = 7.8 Hz, 1H), 7.63 – 7.57 (m, 2H), 7.46 (ddd, *J* = 6.4, 5.8, 3.1 Hz, 1H), 7.38 (d, *J* = 8.8 Hz, 2H), 6.58 (t, *J* = 5.7 Hz, 2H), 4.79 (d, *J* = 6.1 Hz, 2H), 4.71 (d, *J* = 5.7 Hz, 1H).

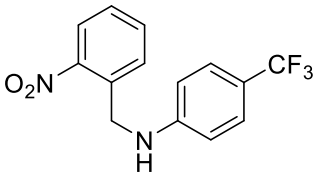

$C_{14}H_{11}F_3N_2O_2$
Mol. Wt.: 296.24

***N*-(4-bromo-2-nitrobenzyl)-4-(trifluoromethyl)aniline (6b):** Synthesized by reacting 4-trifluoromethyl aniline **6′** (100mg, 1.0 eq) with *4*-bromo-*2*-nitrobenzaldehyde **10b** (142mg, 1.0 eq). The crude product was purified by column chromatography over 100-200 mesh silica gel (*Eluent*: EtOAc : petroleum ether 2:8 v/v) to furnish **6b** as reddish solid (190 mg, 82%). **^{1}H NMR (400 MHz, Chloroform-*d*):** δ 8.25 (s, 1H), 7.70 (d, *J* = 8.3 Hz, 1H), 7.49 (d, *J* = 8.4 Hz, 1H), 7.39 (d, *J* = 8.7 Hz, 2H), 6.56 (d, *J* = 8.7 Hz, 2H), 4.74 (d, *J* = 5.8 Hz, 2H), 4.69 (s, 1H); **^{13}C NMR (101 MHz, Chloroform-*d*):** δ 149.5, 148.5, 136.9, 133.8, 131.0, 128.4, 126.8 (q, *J*= 3.9 hz), 126.1 (q, *J* = 272 hz)), 121.5,120.25 (q, *J* = 32.3), 112.20, 45.2; **IR (Neat, ν/cm^{-1}):** 3449, 2361, 1661, 1533, 1464, 1443, 1409, 1322, 1275, 1248; **HRMS (ESI):** Calc. for $C_{14}H_{11}BrF_3N_2O_2$ $[M+H]^+$: 374.9950 found 374.9938.

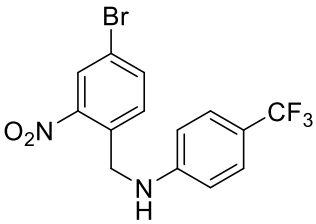

$C_{14}H_{10}BrF_3N_2O_2$
Mol. Wt.: 375.14

***N,N*-dimethyl-3-nitro-4-(((4-(trifluoromethyl)phenyl)amino)methyl)aniline (6c):**

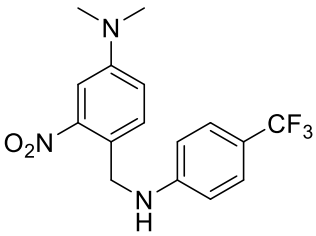

$C_{16}H_{16}F_3N_3O_2$
Mol. Wt.: 339.31

Synthesized by reacting 4-trifluoromethyl aniline **6′** (100 mg, 1.0 eq) with 4-(dimethylamino)-2-nitrobenzaldehyde **10c** (120 mg, 1.0 eq). The crude product was purified by column chromatography over neutral alumunium oxide (*Eluent*: EtOAc : petroleum ether 1:9 v/v) to furnish **6c** as red solid (189 mg, 90%). **^{1}H NMR (400 MHz, Chloroform-*d*):** δ 7.41 – 7.29 (m, 4H), 6.85 (dd, *J* = 8.7, 2.8 Hz, 1H), 6.68 – 6.51 (m, 2H), 4.62 (d, *J* = 15.0 Hz, 3H), 3.00 (s, 6H); **^{13}C NMR (101 MHz, Chloroform-*d*):** δ 150.2, 150.0, 130.8, 126.6 (q *J*= 3.9 hz),126.2 (q, *J* = 272 hz), 120.4, 119.3 (q, *J* = 32.3 hz), 116.7, 112.1, 107.9, 44.9, 40.2; **IR (Neat, ν/cm^{-1}):** 3447, 2360, 1661, 1533, 1466, 1442, 1409, 1321, 1277, 1249; **HRMS (ESI):** Calc. for $C_{16}H_{17}F_3N_2O_2$ $[M+H]^+$: 340.1267 found 340.1235.

***N*-((4'-methoxy-3-nitro-[1,1'-biphenyl]-4-yl)methyl)-4-(trifluoromethyl)aniline (6d):**

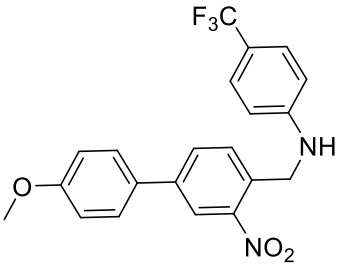

$C_{21}H_{17}F_3N_2O_3$
Mol. Wt.: 402.37

Synthesized by reacting 4-trifluoromethyl aniline **6′** (100 mg, 1.0 eq) with 4'-methoxy-3-nitro-[1,1'-biphenyl]-4-carbaldehyde **10d** (160mg, 1.0 eq).The crude product was purified by column chromatography over 100-200 mesh silica gel: (*Eluent*: EtOAc : petroleum ether 2:8 v/v) to furnish **6d** as white solid (199 mg, 80%). **^{1}H NMR (400 MHz, Chloroform-*d*):** δ 8.27 (s, 1H), 7.74 (dd, *J* = 8.1, 1.9 Hz, 1H), 7.60 (d, *J* = 8.1 Hz, 1H), 7.53 (d, *J* = 8.7 Hz, 2H), 7.38 (d, *J* = 8.5 Hz, 2H), 6.99 (d, *J* = 8.9 Hz, 2H), 6.60 (d, *J* = 8.5 Hz, 2H), 4.78 (s, 2H), 4.71 (s, 1H), 3.85 (s, 3H); **^{13}C NMR (101 MHz, Chloroform-*d*):** δ 160.1, 149.9, 141.5, 132.4, 131.6, 130.5, 130.1, 128.20, 126.8 (q, *J* = 3.9 hz), 126.2 (q, *J* = 272 hz), 123.3, 119.8 (q, *J* = 32.3 hz), 114.6, 112.2, 55.5, 45.3; **.IR (Neat, ν/cm^{-1}):** 3449, 2359, 1660, 1533, 1464, 1445, 1407, 1322, 1277, 1248; **HRMS (ESI):** Calc. for $C_{21}H_{18}F_3N_2O_3$ $[M+H]^+$: 403.1264 found 403.1270.

***N*-((6-nitrobenzo[d][1,3]dioxol-5-yl)methyl)-4-(trifluoromethyl)aniline (6e):** Synthesized by reacting 4-trifluoromethyl aniline **6′** (100 mg, 1.0 eq) with 6-nitrobenzo[d][1,3]dioxole-5-carbaldehyde **10e** (121 mg, 1.0 eq).The crude product was purified by column chromatography over 100-200 mesh silica gel (*Eluent*: EtOAc : petroleum ether 2:8 v/v) to furnish **6e** as white solid (158 mg, 75%). **^{1}H NMR (400 MHz, Chloroform-*d*):** δ 7.65 (s, 1H), 7.39 (d, *J* = 8.4 Hz, 2H), 7.02

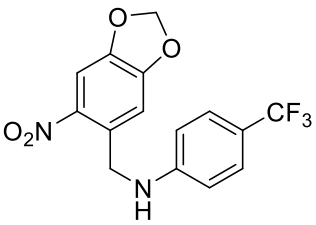

$C_{15}H_{11}F_3N_2O_4$
Mol. Wt.: 340.25

(s, 1H), 6.57 (d, *J* = 8.4 Hz, 2H), 6.10 (s, 2H), 4.73 (s, 3H); **^{13}C NMR (101 MHz, Chloroform-*d*):** δ 152.8, 149.8, 141.8, 132.7, 126.8 (q, *J*= 3.9 hz) , 123.5 (q, *J* = 272 hz), 119.9 (q, *J* = 32.3 hz), 112.2, 108.2, 106.3, 103.1, 46.0; **IR (Neat, ν/cm^{-1}):** 3449, 2363, 1659, 1531, 1464, 1443, 1410, 1322, 1277, 1246; **HRMS (ESI):** Calc. for $C_{15}H_{12}F_3N_2O_4$ $[M+H]^+$: 341.0743 found 341.0750.

Ethyl 3-(4-(trifluoromethyl)phenyl)-1H-indole-2-carboxylate (14): In a 25 mL round bottom flask, ethyl 3-iodo-1H-indole-2-carboxylate **13** (1g, 1 eq), and 4-trifluoromethyl phenylboronic acid (1.5g, 1.0 eq) were degassed using nitrogen in a mixture of ethanol and toluene (2:1, 40 mL) for 30 min. After that tetrakis triphenylphosphine palladium 0 (183mg, 0.5 eq) and aqueous sodium nitrate solution (5 mL of 2 N solution) was added and the reaction mixture was refluxed using oil bath for 16 h. After the completion of the reaction, monitored through TLC, the reaction mixture was filtered through celite and volatiles were evaporated under high vaccum using rota evaporator. The crude mixture was extracted with ethylacetate (3 × 30 mL), washed with brine (2 × 20 mL), dried on.anhydrous sodium sulfate and purified through column chromatography using 100-200 mesh silica gel (*Eluent*: EtOAc : petroleum ether 1:10 v/v) to furnish the desired compound **14** as white solid (636 mg, 60%).**^{1}H NMR (400 MHz, Chloroform-d):** δ 9.11 (s, 1H), 7.74 – 7.65 (m, 4H), 7.58 (d, J = 8.2 Hz, 1H), 7.47 (d, J = 8.4 Hz, 1H), 7.42 – 7.35 (m, 1H), 7.22 – 7.13 (m, 1H), 4.30 (q, J = 7.1 Hz, 2H), 1.24 (t, J = 7.1 Hz, 3H); **^{13}C NMR (101 MHz, Chloroform-*d*):** δ 161.7, 137.5, 135.7, 131.05 , 129.4 (q, *J*= 32.3 hz), 127.6, 126.1, 125.8 (q, *J* = 272 hz), 124.8 (q, *J* = 3.9 hz) , 123.1, 122.6, 121.4, 121.3, 111.9, 61.2, 14.1;.**IR (Neat, ν/cm^{-1}):** 3323, 1679, 165, 1549, 1502, 1450, 1303, 1318; **HRMS (ESI):** Calc. for $C_{18}H_{15}F_3NO_2$ $[M+H]^+$: 334.1049, found 334.1048

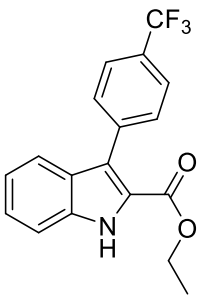

$C_{18}H_{14}F_3NO_2$
Mol. Wt.: 333.31

3-(4-(trifluoromethyl)phenyl)-1H-indole-2-carboxylic acid (15): A suspension of **14** (600 mg) in a solution of aqueous NaOH (10 mL, 2N), tetrahydrofuran (10 mL) and MeOH (10 mL) was stirred at rt for 24 h. After that, the solvent was removed under reduced pressure using rota evaporator. The pH of the solution was adjusted to 1 with concentrated HCl and the crude product was then extracted with EtOAc (2 x 50 mL) and the combined organic phase was washed with brine (2 x 30 mL). It was then dried over Na_2SO_4, and solvent was removed under vacuum using rota evaporator. The crude

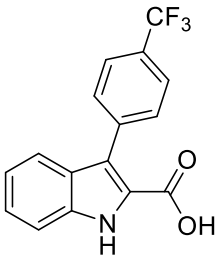

$C_{16}H_{10}F_3NO_2$
Mol. Wt.: 305.25

product was purified by column chromatography using 100-200 mesh silica gel (*Eluent*: MeOH : $CHCl_3$ 1:9 v/v) to get **15** as white solid (494 mg, 90%). **^{1}H NMR (400 MHz, DMSO-*d*$_6$):** δ 13.04 (s, 1H), 12.00 (s, 1H), 7.79 (d, *J* = 8.4 Hz, 2H), 7.73 (d, *J* = 8.2 Hz, 2H), 7.50 (t, J = 8.8 Hz, 2H), 7.31 (t, J = 7.2 Hz, 1H), 7.10 (t, J = 7.6 Hz, 1H); **^{13}C NMR (101 MHz, DMSO-*d*$_6$):** δ 163.0, 138.8, 136.4, 131.6, 127.6 (q, *J* = 32.4), 127.0, 126.3 (q, *J* = 32.4), 125.4, 125.08, 125.8, 124.58, 121.2, 120.6 (q, *J* = 3.9), 113.2; **.IR (Neat, ν/cm^{-1}):** 3459, 1724, 1662, 1615, 1553, 1532, 1512, 1463, 1402**. HRMS (ESI):** Calc. for $C_{16}H_{11}F_3NO_2$ $[M+H]^+$: 306.0736, 306.0756

iv. General procedure for synthesizing the protecting indole derivatives (5a-5e)

General method C: To a solution of 3-(4-(trifluoromethyl)phenyl)-1H-indole-2-carboxylic acid **15** (200 mg, 2.0 eq) in CH_2Cl_2 (15 mL), thionyl chloride (779 mg, 20.0 eq) and 2 drops of DMF were added. The reaction mixture was refluxed using oil bath for 6 h. The excess of thionyl chloride and solvent was then evaporated to dryness in *vacuo* to give 3-(4-(trifluoromethyl)phenyl)-1H-indole-2-carbonyl chloride. The residue was dissolved in dry dichloromethane (10 mL). To this solution, amine derivatives **6a–6e** (1.0 eq) in dichloromethane (5 mL) were added dropwise followed by the addition of triethylamine (50 mg, 1.5 eq). The reaction mixture was heated at 70 °C and stirred for 2 h. After the completion of the reaction, water was added and extracted with CH_2Cl_2 (3 × 10 mL). The organic phase was washed brine (2 × 10 mL) and then dried over Na_2SO_4, and concentrated under reduced pressure. The crude product was purified by either by 100-200 mesh silica gel or basic aluminium oxide column chromatography to give the desired protected compounds compound **5a**–**5e**.

***N*-(2-nitrobenzyl)-N,3-bis(4-(trifluoromethyl)phenyl)-1H-indole-2-carboxamide (5a):**

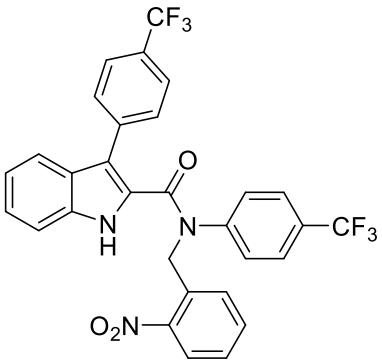

$C_{30}H_{19}F_6N_3O_3$
Mol. Wt.: 583.49

Synthesized by reacting 3-(4-(trifluoromethyl)phenyl)-1H-indole-2-carboxylic acid **15** (200 mg, 2.0 eq) with *N*-(2-nitrobenzyl)-4-(trifluoromethyl)aniline **6a** (97 mg, 1.0 eq). The crude product was purified by column chromatography over 100-200 mesh silica gel (*Eluent*: EtOAc : petroleum ether 3:7 v/v) to furnish **5a** as white solid (286 mg, 75%). **^{1}H NMR (400 MHz, Chloroform-*d*):** δ 9.29 (s, 1H), 7.98 (d, *J* = 8.2 Hz, 1H), 7.59 – 7.54 (m, 1H), 7.51 (d, *J* = 7.8 Hz, 3H), 7.41 (q, *J* = 7.5, 6.7 Hz, 3H), 7.35 – 7.29 (m, 1H), 7.13 (t, *J* = 8.0 Hz, 1H),

7.06 (dd, *J* = 12.6, 8.2 Hz, 4H), 6.52 (d, *J* = 8.4 Hz, 2H), 5.48 (s, 2H); **^{13}C NMR (101 MHz, Chloroform-*d*):** δ 165.0, 148.1, 144.5, 137.3, 135.9, 133.4, 129.8, 129.4 (q, *J* = 272 hz), 129.1, 128.5,128.1 (q, *J* = 32.3 hz), 126.1, 126.1, 125.6, 125.5, 125.3, 125.3,124.8 (q, *J* = 272 hz), 122.8 (q, *J* = 32.3 hz), 121.5, 120.4, 111.9, 50.7; **IR (Neat, ν/cm^{-1}):** 3316, 2361, 1661, 1608, 1549, 1531, 1498, 1481; **HRMS (ESI):** Calc. for $C_{30}H_{20}F_6N_3O_3$ $[M+H]^+$: 584.1403 found 584.1406.

***N*-(4-bromo-2-nitrobenzyl)-N,3-bis(4-(trifluoromethyl)phenyl)-1H-indole-2-carboxamide (5b):** Synthesized by reacting 3-(4-(trifluoromethyl)phenyl)-1H-indole-2-carboxylic acid **15** (200 mg, 2.0 eq) with N-(4-bromo-2-nitrobenzyl)-4-(trifluoromethyl)aniline **6b** (122 mg, 1.0 eq).The crude product was purified by column chromatography over 100-200 silica gel (*Eluent*: EtOAc : petroleum ether 3:7 v/v) to furnish **5b** as reddish solid (355 mg, 82%). **^{1}H NMR (400 MHz, Chloroform-*d*):** δ 9.31 (s, 1H), 8.09 (d, *J* = 2.0 Hz, 1H), 7.65 (d, *J* = 8.4 Hz, 1H), 7.52 (d, *J* = 8.0 Hz, 2H), 7.45 – 7.30 (m, 4H), 7.13 (t, *J* = 7.6 Hz, 1H), 7.06 (d, *J* = 8.2 Hz, 4H), 6.51 (d, *J* = 8.4 Hz, 2H), 5.41 (s, 2H); **^{13}C NMR (101 MHz, Chloroform-*d*):** δ 164.9, 144.2, 137.2, 136.2, 135.8, 130.6, 130.6, 129.7, 129.4 (q, *J*= 32.3 hz), 128.0, 127.9 (q, *J* = 32.5), 126.1, 125.8, 125.5, 125.5, 125.4, 125.4, 125.4, 124.7 (q, *J* = 272 hz), 121.5, 120.4, 119.3 (q, *J* = 272 hz), 111.8, 50.2; .**IR (Neat, ν/cm^{-1}):** 3315, 2359, 1659, 1607, 1548, 1530, 1498, 1480; **HRMS (ESI):** Calc. for $C_{30}H_{19}BrF_6N_3O_3$ $[M+H]^+$: 662.0508 found 662.0505.

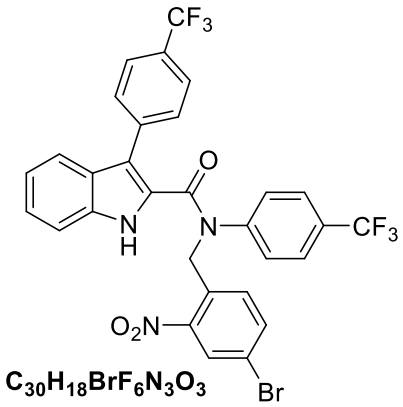

$C_{30}H_{18}BrF_6N_3O_3$
Mol. Wt.: 662.04

***N*-(4-(dimethylamino)-2-nitrobenzyl)-N,3-bis(4-(trifluoromethyl)phenyl)-1H-indole-2-carboxamide (5c):** Synthesized by reacting 3-(4-(trifluoromethyl)phenyl)-1H-indole-2-carboxylic acid **15** (200 mg, 2.0 eq) with *N*,*N*-dimethyl-3-nitro-4-(((4-(trifluoromethyl)phenyl)amino)methyl) aniline **6c** (111 mg, 1.0 eq). The crude product was purified by column chromatography over basic alumunium oxide (*Eluent*: EtOAc : petroleum ether 3:7 v/v) to furnish **5c** as red solid (360 mg, 88%). **^{1}H NMR (400 MHz, Chloroform-*d*):** δ 9.55 (s, 1H), 7.50 (d, *J* = 8.1 Hz, 2H), 7.39 (t, *J* = 8.2 Hz, 2H), 7.31 – 7.25 (m, 2H), 7.15 – 7.05 (m, 4H), 7.01 (d, *J* = 8.4 Hz, 2H), 6.73 (dd, *J* = 8.8, 2.8 Hz, 1H), 6.47 (d,

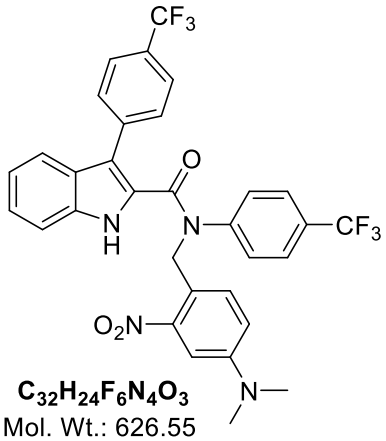

$C_{32}H_{24}F_6N_4O_3$
Mol. Wt.: 626.55

J = 8.3 Hz, 2H), 5.37 (s, 2H), 2.93 (s, 6H); **^{13}C NMR (101 MHz, Chloroform-*d*):** δ 164.9, 149.8, 144.5, 137.4, 135.8, 130.5, 129.7, 129.1 (q, *J* = 272 hz), 128.8 (q, *J* = 272 hz), 126.7, 126.0, 125.5 (q, *J* = 32.3 hz), 125.8, 125.3, 125.0, 122.8 (q, *J* = 323.3 hz), 121.2, 120.2, 117.8, 117.1, 116.0, 111.9, 107.3, 49.8, 40.0; **IR (Neat, ν/cm^{-1}):** 3316, 2360, 1660, 1607, 1549, 1532, 1498, 1483; **HRMS (ESI):** Calc. for $C_{32}H_{25}F_6N_4O_3$ $[M+H]^+$: 627.1825 found 627.1826.

***N*-((4'-methoxy-3-nitro-[1,1'-biphenyl]-4-yl)methyl)-*N*,3-bis(4-(trifluoromethyl)phenyl)-1H-indole-2-carboxamide (5d)**: Synthesized by reacting 3-(4-(trifluoromethyl)phenyl)-1H-indole-2-carboxylic acid **15** (200 mg, 2.0 eq) with N-((4'-methoxy-3-nitro-[1,1'-biphenyl]-4-yl)methyl)-4-(trifluoromethyl)aniline **6d** (131 mg, 1.0 eq). The crude product was purified by column chromatography over 100-200 mesh silica gel (*Eluent*: EtOAc : petroleum ether 3:7 v/v) to furnish **5d** as white solid (320 mg, 71%). **^{1}H NMR (400 MHz, Chloroform-*d*):** δ 9.69 (s, 1H), 8.10 (s, 1H), 7.65 (d, *J* = 8.2 Hz, 1H), 7.51 (d, *J* = 8.1 Hz, 3H), 7.44 – 7.33 (m, 4H), 7.28 (d, *J* = 6.9 Hz, 1H), 7.07 (td, *J* = 14.6, 13.4, 8.1 Hz, 5H), 5.52 (s, 2H), 3.82 (s, 3H); **^{13}C NMR (101 MHz, Chloroform-*d*):** δ 165.2, 160.2, 148.7, 144.5, 137.3, 135.9, 131.0, 129.8, 129.4, 128.1, 126.21 , 125.7, 125.5, 125.3, 122.9, 121.4, 120.4, 118.2, 114.6, 111.9, 55.4, 50.7; **IR (Neat, ν/cm^{-1}):** 3315, 2359, 1659, 1604, 1549, 1530, 1497, 1481; **HRMS (ESI):** Calc. for $C_{37}H_{26}F_6N_3O_4$ $[M+H]^+$: 690.1822 found 690.1816.

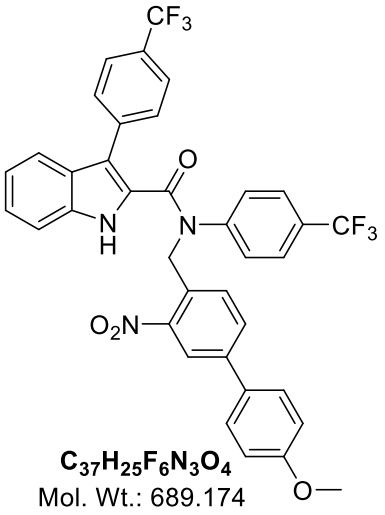

***N*-((6-nitrobenzo[d][1,3]dioxol-5-yl)methyl)-N,3-bis(4-(trifluoromethyl)phenyl)-1H-indole-2-carboxamide (5e):** Synthesized by reacting 3-(4-(trifluoromethyl)phenyl)-1H-indole-2-carboxylic acid **15** (200 mg, 2.0 eq) with N-((6-nitrobenzo[d][1,3]dioxol-5-yl)methyl)-4-(trifluoromethyl)aniline **6e** (111 mg, 1.0 eq). The crude product was purified by column chromatography over 100-200 mesh silica gel (*Eluent*: EtOAc : petroleum ether 3:7 v/v) to furnish **5e** as white solid (316 mg, 77%). **^{1}H NMR (400 MHz, Chloroform-*d*):** δ 9.60 (s, 1H), 7.53 (d, *J* = 8.0 Hz, 2H), 7.48 (s, 1H), 7.39 (dd, *J* = 15.9, 8.2 Hz, 2H), 7.32 – 7.27 (m, 1H), 7.14 – 7.03 (m, 5H), 6.95 (s, 1H), 6.53 (d, *J* = 8.3 Hz, 2H), 6.02 (s, 2H), 5.48 (s, 2H);**^{13}C NMR (101 MHz, Chloroform-*d*):** δ 165.2, 152.3, 147.2, 144.4, 137.2, 135.8, 129.7,129.4 (q, *J* = 32.3 hz), 129.2, 128.1 (q, *J* = 323 hz) , 126.1, 126.0, 125.5, 125.4, 125.3, 124.7 (q, *J* = 272

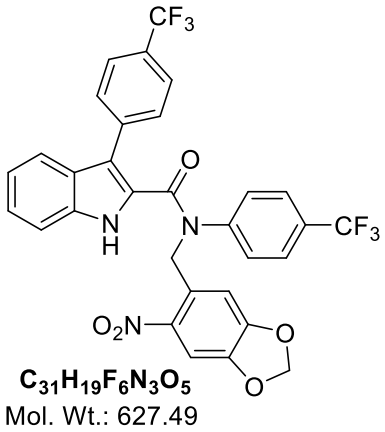

hz), 122.0 (q, *J* = 272 hz), 121.4, 120.3, 111.8, 107.4, 106.0, 103.1, 51.1; .**IR (Neat, ν/cm^{-1}):** 3316, 2361, 1660, 1606, 1551, 1531, 1497, 1481; **HRMS (ESI):** Calc. for $C_{31}H_{20}F_6N_3O_5$ $[M+H]^+$: 628.1301 found 628.1323.

5.4.4. Chloride Binding by ^{1}H NMR titration studies

^{1}H NMR titration was carried out at room temperature on Bruker 400 MHz spectrometer. The residual solvent signal (CD_3CN, δ_H = 1.94) was considered as an internal reference to calibrate spectra. Both the TBACl salt and receptor were dried in high vacuum before use. The titrations were performed by addition of aliquots from the tetrabutylammonium chloride (TBACl) solution (1 M in CD_3CN) to the solution of either **2′**, **3′**, **4′** or **5′** (0.0025 M in CD_3CN). All NMR data were processed using MestReNova 6.0 and collected data were fitted in different binding modes using *BindFit* 0.5.

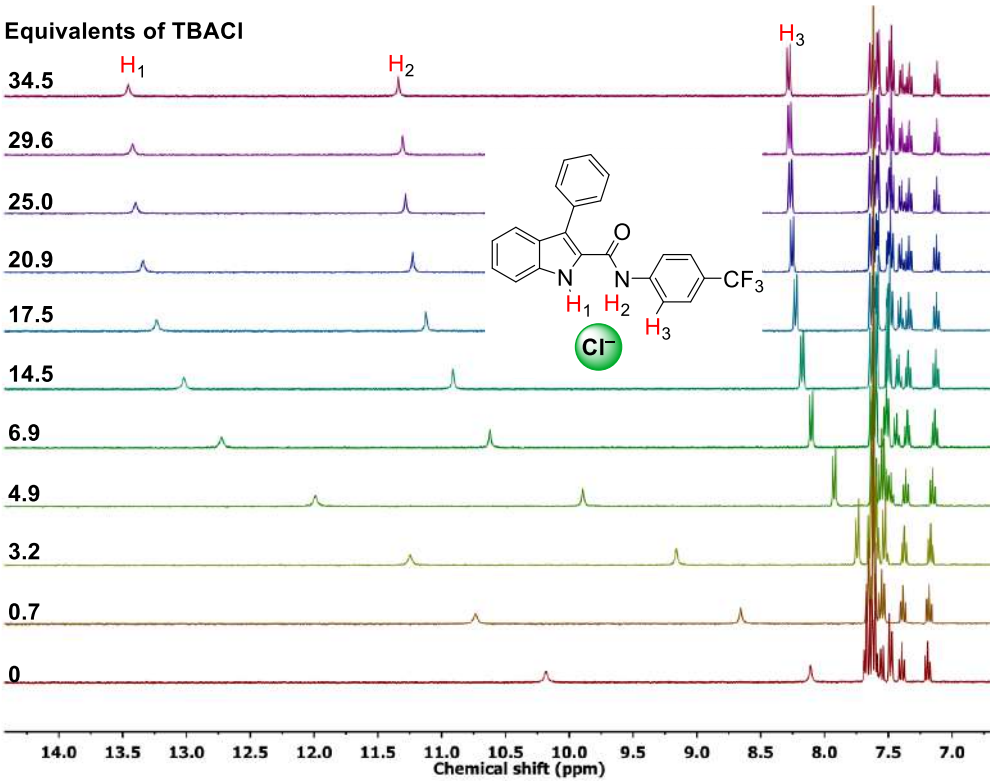

Figure 5.15. ^{1}H NMR titration spectra for **2′** (0.0025 M) with stepwise addition of TBACl in CD_3CN. The equivalents of added TBACl are shown on the stack spectra.

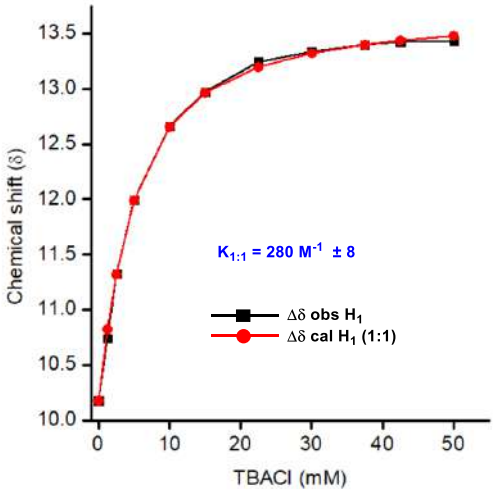

Figure 5.16. The plot of chemical shift (δ) of H_1 protons *vs* concentration of TBACl added, fitted to 1:1 binding model of *BindFit* 0.5. The binding constant obtained is the mean of the three independent experiments. http://app.supramolecular.org/bindfit/view/d7a4d498-42d8-471b-aaa5-b9c45bcc017c-(**2′** with TBACl).

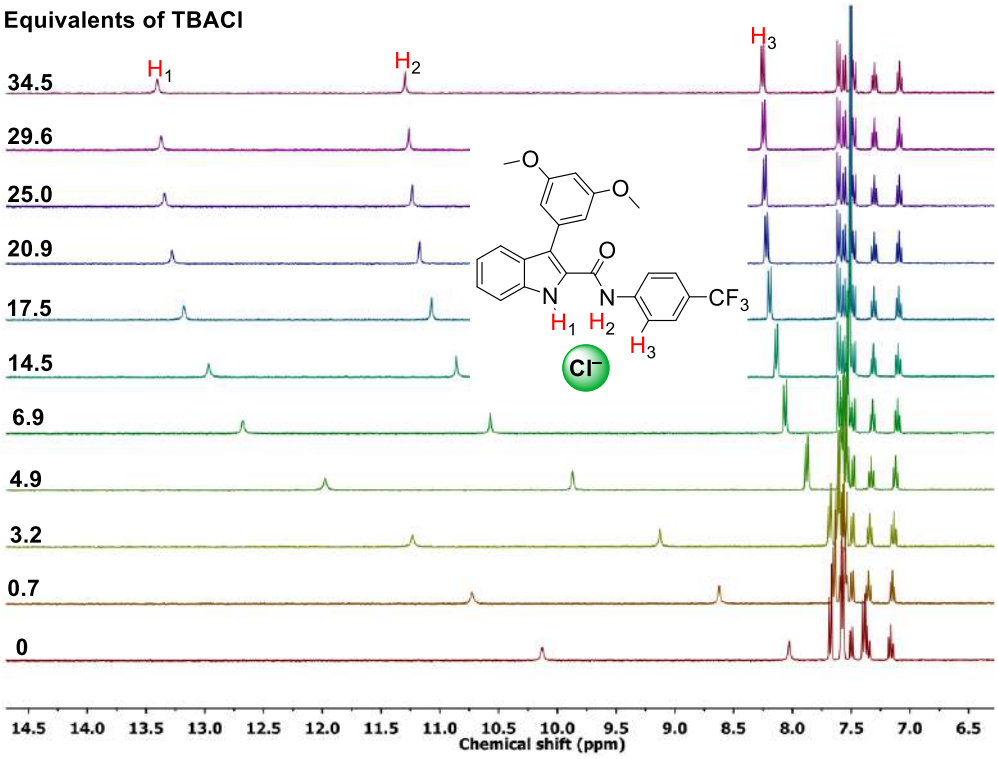

Figure 5.17. ^{1}H NMR titration spectra for **3′** (0.0025 M) with stepwise addition of TBACl in CD_3CN. The equivalents of added TBACl are shown on the stack spectra.

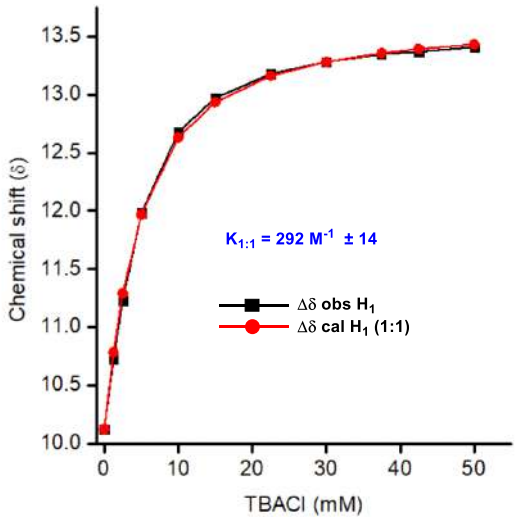

Figure 5.18. The plot of chemical shift (δ) of H_1 protons *vs* concentration of TBACl added, fitted to 1:1 binding model of *BindFit* 0.5. The binding constant obtained is the mean of the three independent experiments. http://app.supramolecular.org/bindfit/view/9ac3650e-7e13-40c1-806a-7dfc79e66a9e-(**3′** with TBACl).

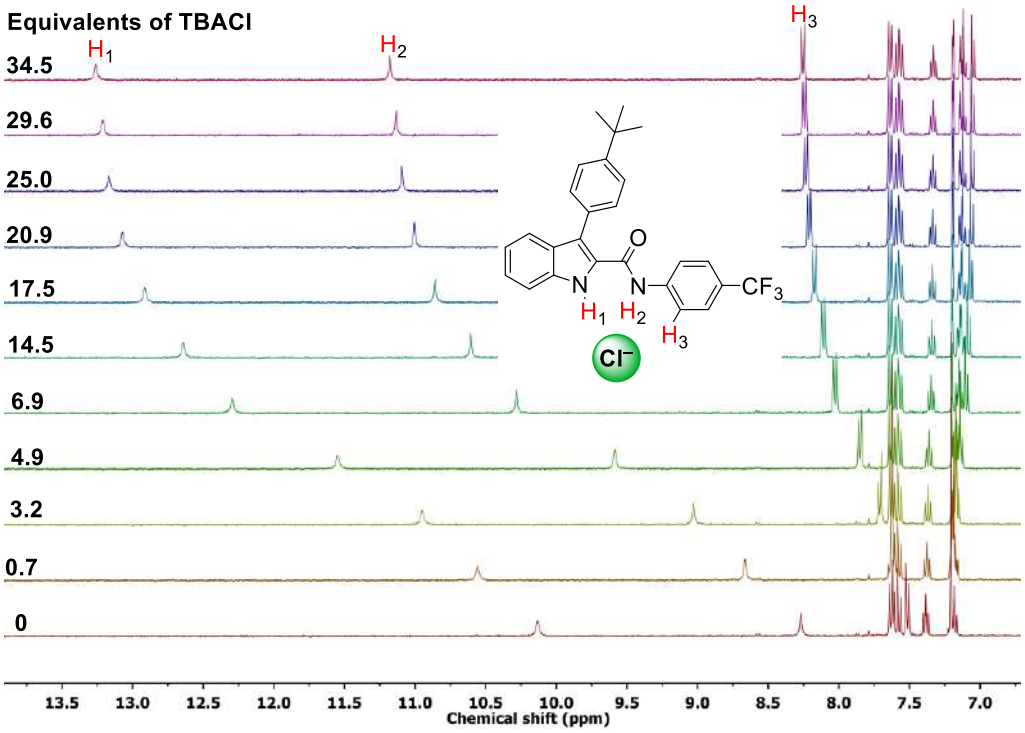

Figure 5.19. ^1H NMR titration spectra for **4′** (0.0025 M) with stepwise addition of TBACl in CD_3CN. The equivalents of added TBACl are shown on the stack spectra.

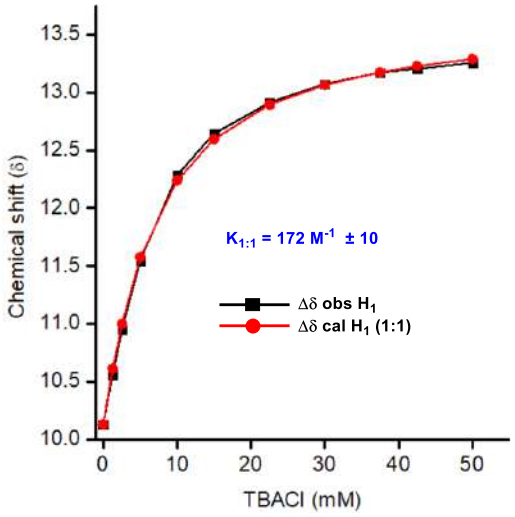

Figure 5.20. The plot of chemical shift (δ) of H_1 protons *vs* concentration of TBACl added, fitted to 1:1 binding model of *BindFit* 0.5. The binding constant obtained is the mean of the three independent experiments. http://app.supramolecular.org/bindfit/view/e2dc3df0-df1a-4bd9-8d38-55abce32c6e0-(**4′** with TBACl).

5.4.5. Ion Transport Studies

Ion transporting activity studies across EYPC-LUVs⊃HPTS

The ion transport studies were performed according to the procedures reported in the previous chapters.

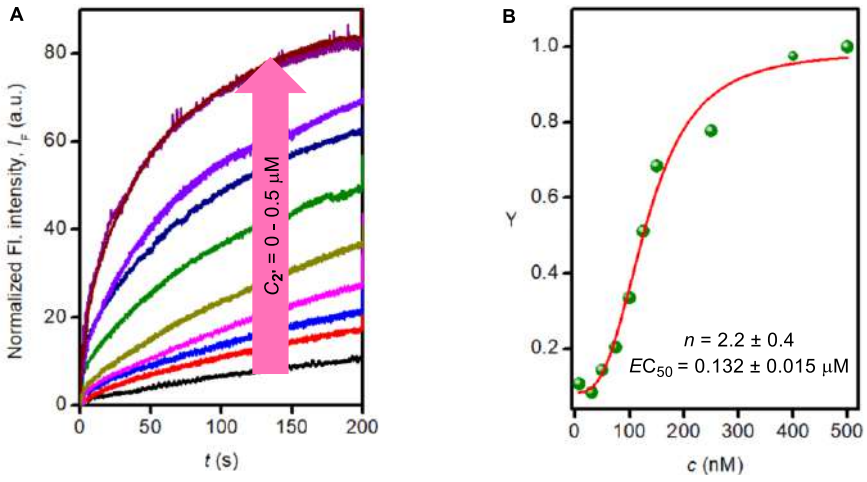

Figure 5.21. Concentration dependent activity of **2′** across EYPC-LUVs⊃HPTS (**A**). Dose-response plot of **2′** at 280 s after addition of compound (**B**).

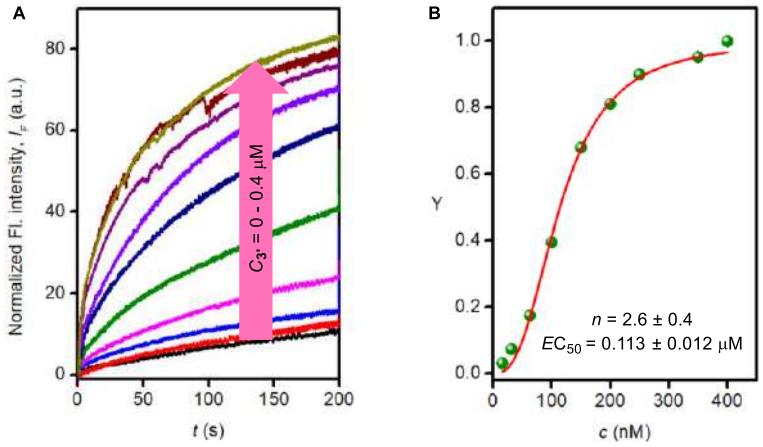

Figure 5.22. Concentration dependent activity of **3′** across EYPC-LUVs⊃HPTS (**A**). Dose-response plot of **3′** at 280 s after addition of compound (**B**).

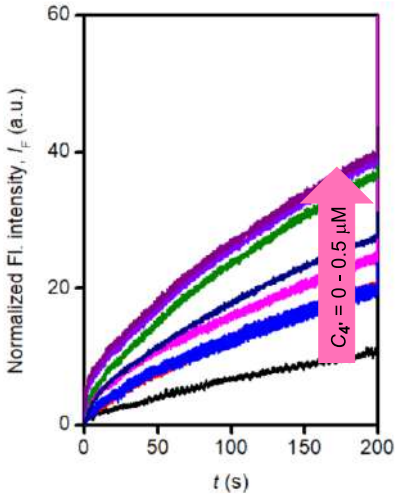

Figure 5.23. Concentration dependent activity of **4′** across EYPC-LUVs⊃HPTS (**A**). Dose-response plot of **4′** at 280 s after addition of compound (**B**).

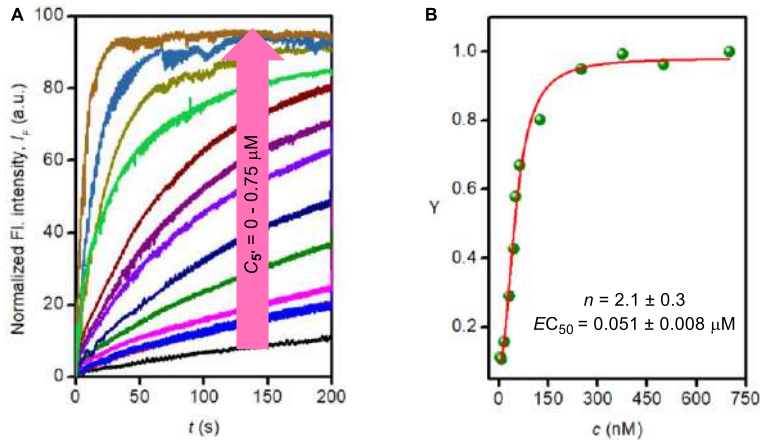

Figure 5.24. Concentration dependent activity of **5′** across EYPC-LUVs⊃HPTS (**A**). Dose-response plot of **5′** at 280 s after addition of compound (**B**).

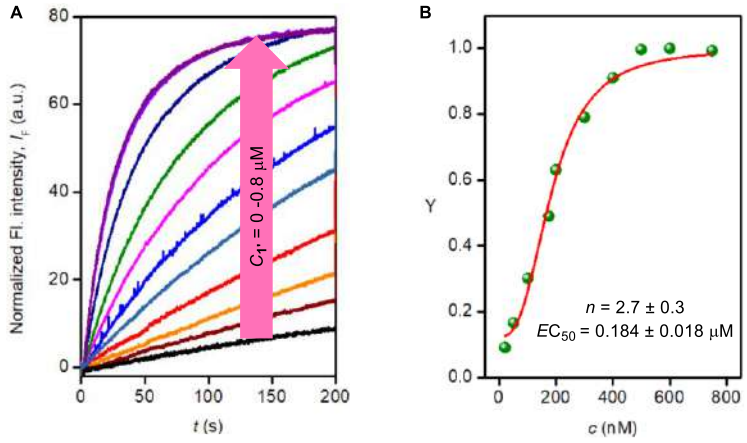

Figure 5.25. Concentration dependent activity of **1′** across EYPC-LUVs⊃HPTS (**A**). Dose-response plot of **1′** at 280 s after addition of compound (**B**).

Chloride transport activity across EYPC-LUVs⊃lucigenin vesicles

The ion transport studies were performed according to the procedures reported in the previous chapters.

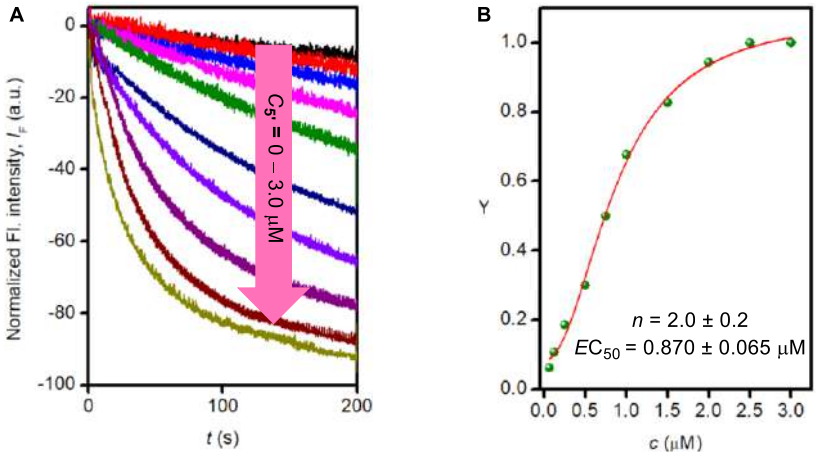

Figure 5.26. Concentration-dependent activity of **5′** across EYPC-LUVs⊃Lucigenin (**A**). Dose-response plot of **5′** at 280 s after addition of compound (**B**).

5.4.6. Photoresponsive studies

UV-Vis absorbtion studies

Photoisomerization studies of compounds **5a**–**5e**, were carried out in CH_3CN. Initially, stock solutions of these compounds (2 mM in CH_3CN) were prepared in different vials and covered with an aluminum foil.

In a 2 mL UV cuvette, was placed 1900 μL of CH_3CN and 100 μL of either **5a**, **5b**, **5c**, **5d** or **5e**, was added to get the final concentration of 100 μM.

The cuvette was placed in a UV-Vis spectrometer, and the UV-Vis spectrum was recorded.

Photolytic Studies

Assessment of photolysis of procarriers 5a-5e using ^{1}H NMR spectroscopy by irradiation at 356 nm or 400 nm: In a clean and dry NMR tube, the solution of procarriers **5a-5e** were taken in DMSO-d_6 (2 mM in 0.5 mL). The ^{1}H NMR spectrum of each sample were recorded first (t = 0 min). Then, the NMR tubes were kept in the photoreactor and irradiated with either UV light (3 × 1 Watt LEDs, λ = 365 nm) or visible light (8 × 1 Watt LEDs, λ = 400 nm) for different time intervals, and ^{1}H NMR spectrum of the irradiated samples were recorded at the end of each irradiation. All ^{1}H NMR spectra were processed using MestReNova 6.0 by considering residual solvent peak as an internal reference. Upon photoirradiation, the appearance and disappearance of the different proton peak signals were monitored by stacking all calibrated spectra. The photolytic conversion of procarriers **5a–5e** to carrier **5′** were confirmed by comparing the ^{1}H NMR spectra with as synthesized **5′**.

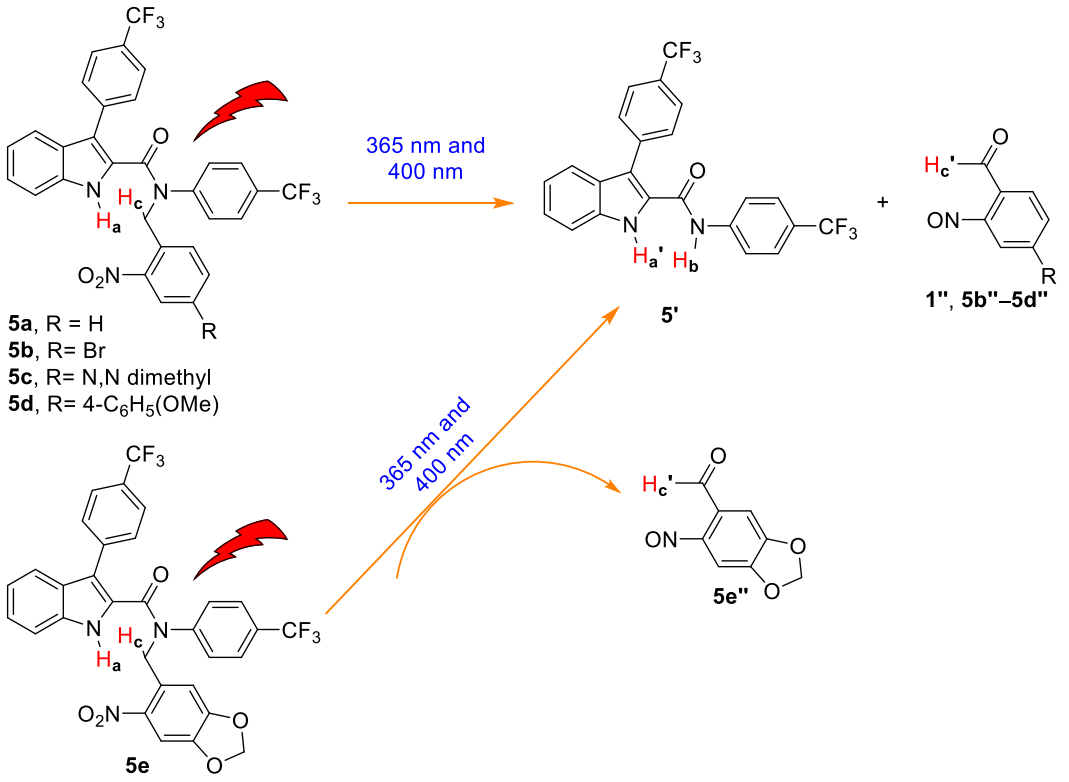

Scheme 5.3. Schematic representation of the photocleavage of procarriers **5a–5e**.

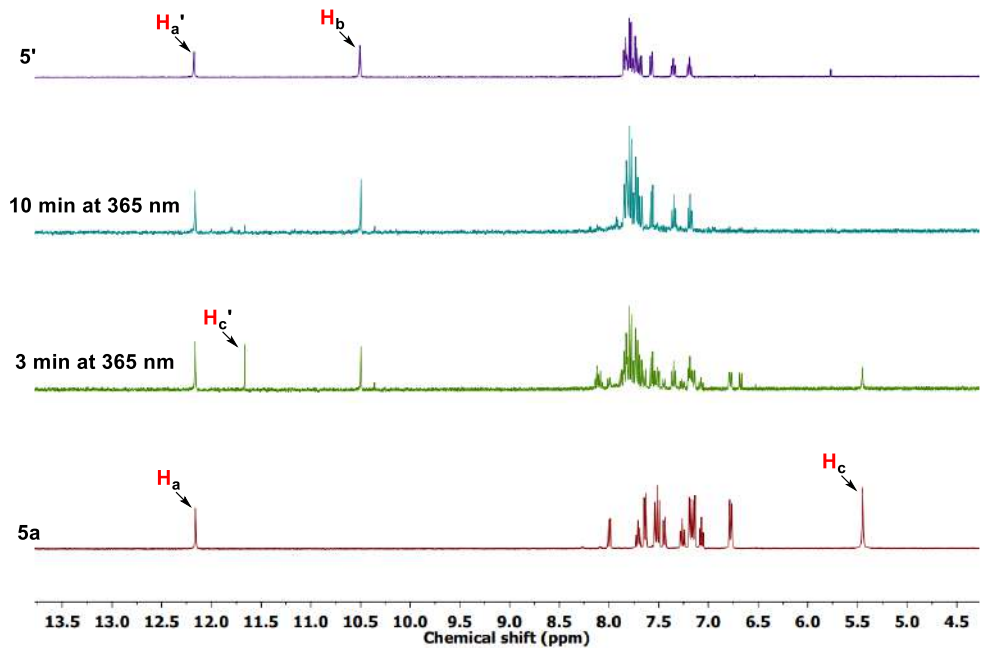

Figure 5.27. Photocleavable studies of procarrier **5a** to release indole carboxamide **5′** monitored by ^{1}H NMR in DMSO-d_6 recorded at different time intervals upon irradiation at 365 nm of electromagnetic radiations.

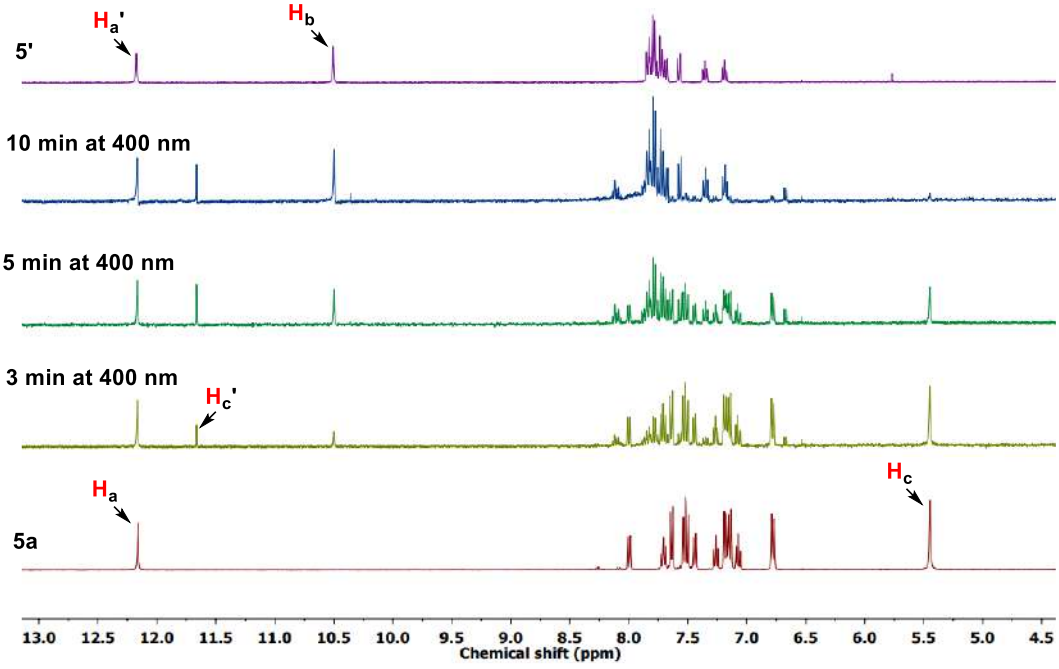

Figure 5.28. Photocleavable studies of procarrier **5a** to release indole carboxamide **5′** monitored by ^{1}H NMR in DMSO-d_6 recorded at different time intervals upon irradiation at 400 nm of electromagnetic radiations.

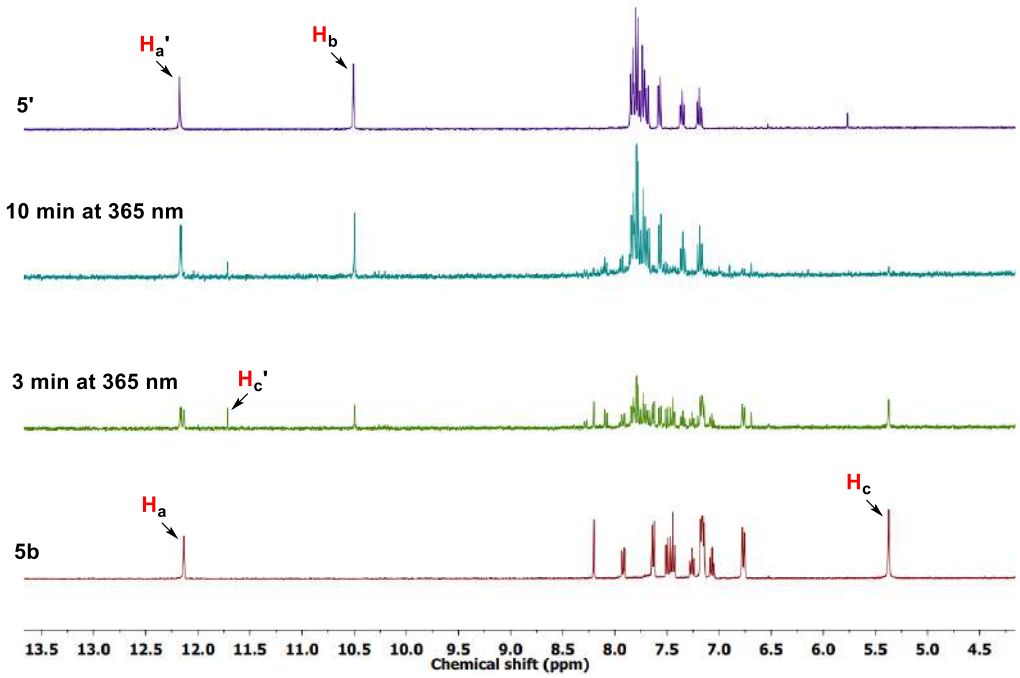

Figure 5.29. Photocleavable studies of procarrier **5b** to release indole carboxamide **5′** monitored by ^{1}H NMR in DMSO-d_6 recorded at different time intervals upon irradiation at 365 nm of electromagnetic radiations.

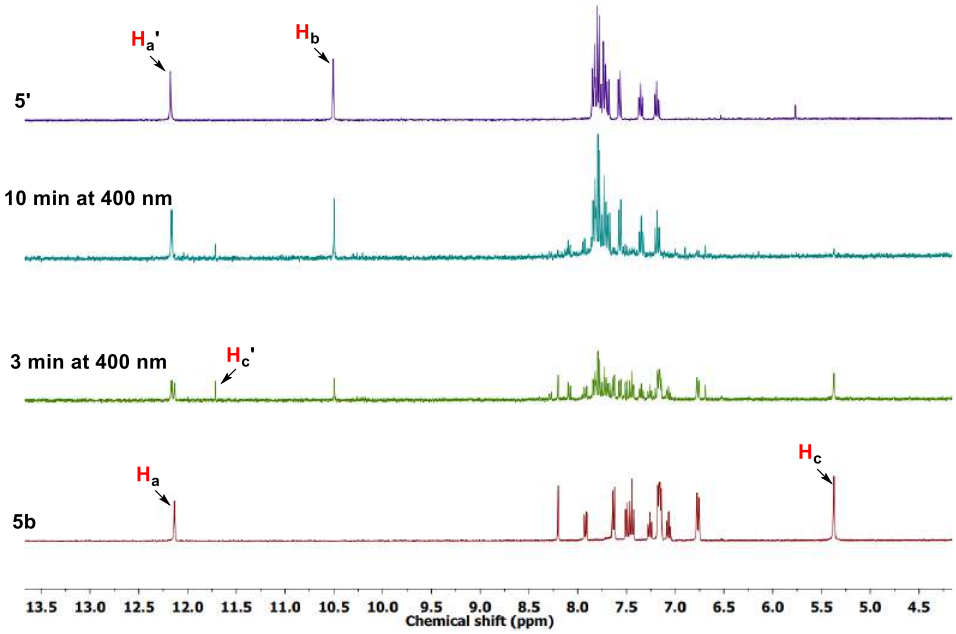

Figure 5.30. Photocleavable studies of procarrier **5b** to release indole carboxamide **5′** monitored by ^{1}H NMR in DMSO-d_6 recorded at different time intervals upon irradiation at 400 nm of electromagnetic radiations.

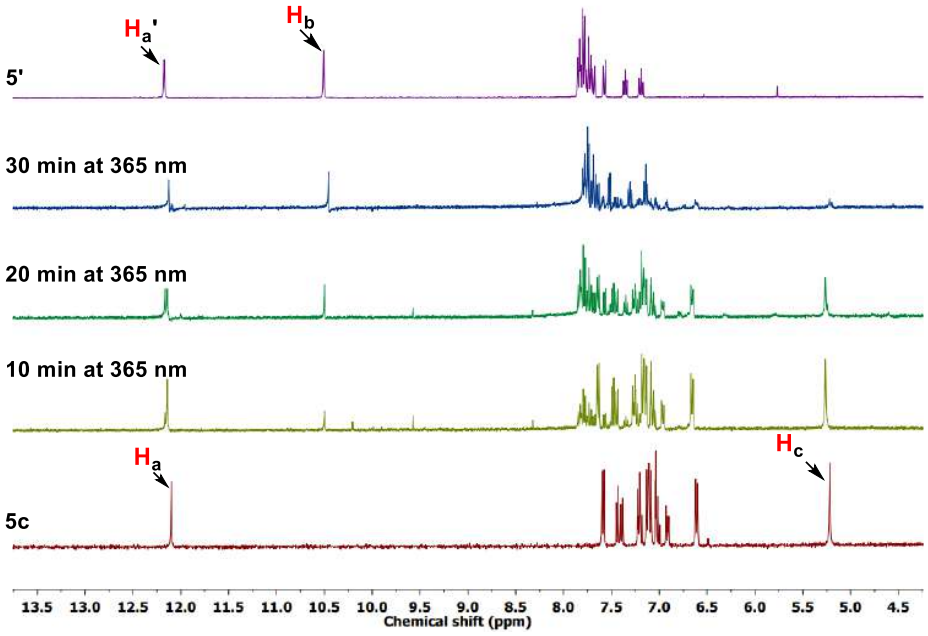

Figure 5.31. Photocleavable studies of procarrier **5c** to release indole carboxamide **5′** monitored by ^{1}H NMR in DMSO-d_6 recorded at different time intervals upon irradiation at 365 nm of electromagnetic radiations.

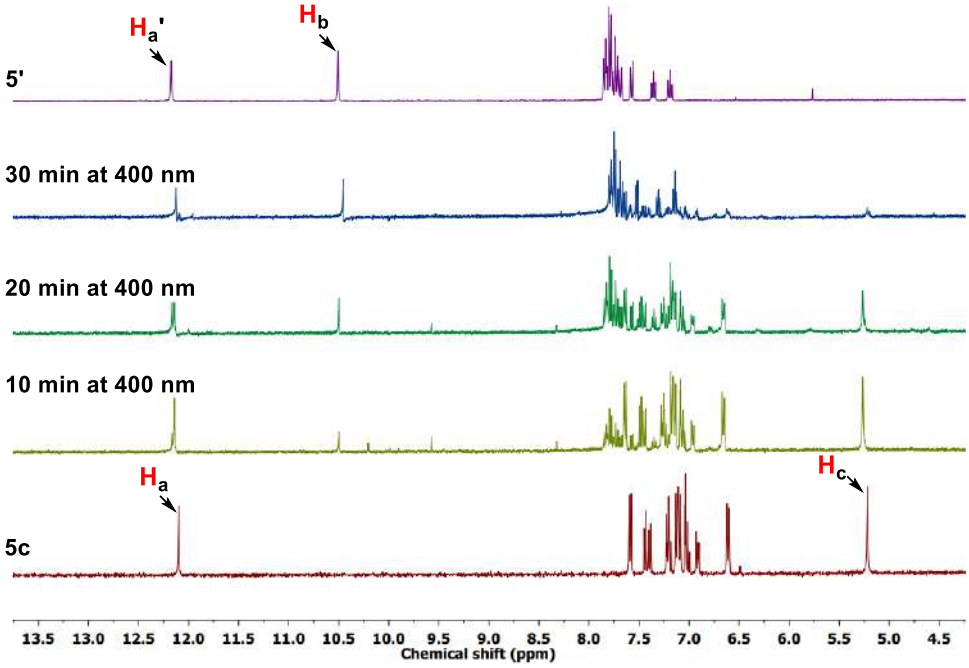

Figure 5.32. Photocleavable studies of procarrier **5c** to release indole carboxamide **5′** monitored by ^{1}H NMR in DMSO-d_6 recorded at different time intervals upon irradiation at 400 nm of electromagnetic radiations.

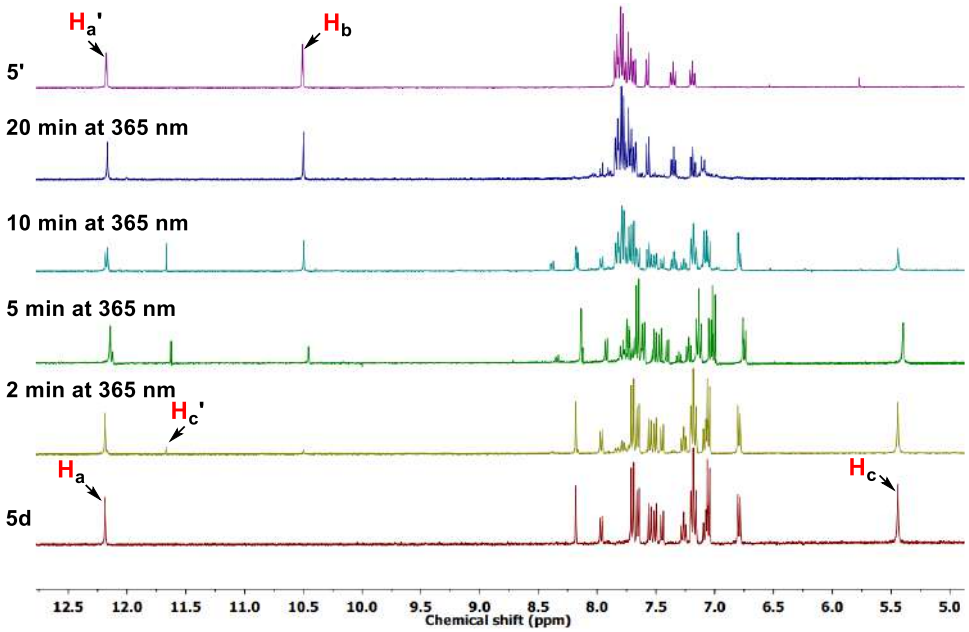

Figure 5.33. Photocleavable studies of procarrier **5d** to release indole carboxamide **5′** monitored by ^{1}H NMR in DMSO-d_6 recorded at different time intervals upon irradiation at 365 nm of electromagnetic radiations.

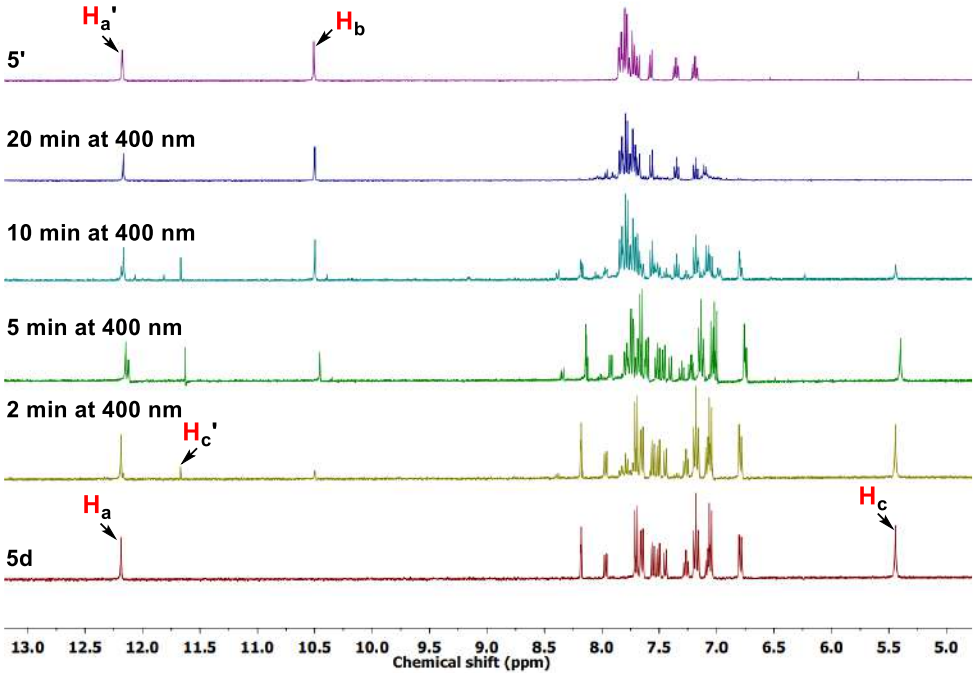

Figure 5.34. Photocleavable studies of procarrier **5d** to release indole carboxamide **5′** monitored by ^{1}H NMR in DMSO-d_6 recorded at different time intervals upon irradiation at 400 nm of electromagnetic radiations.

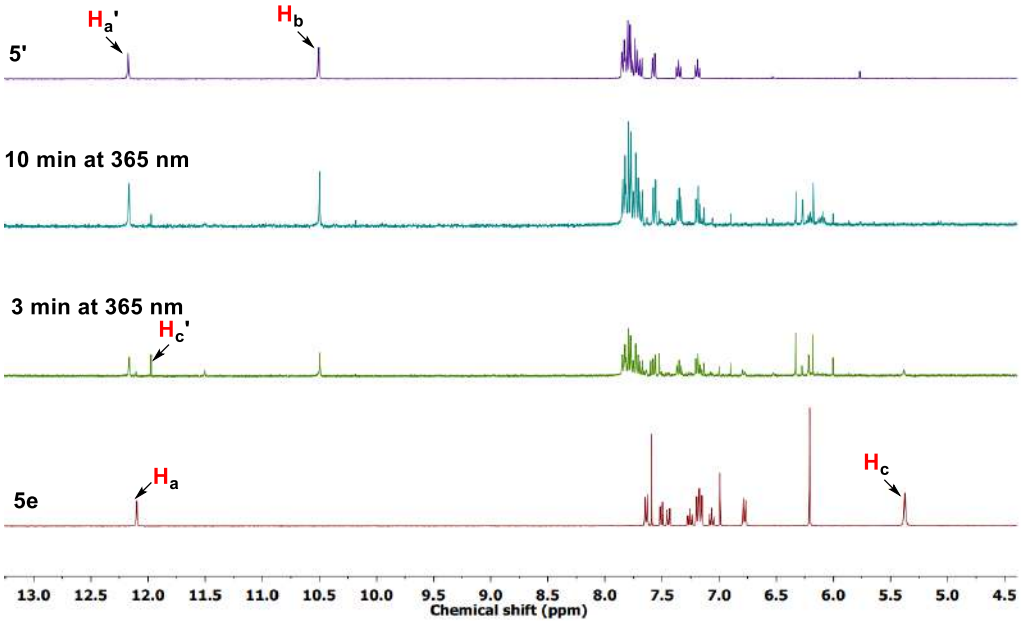

Figure 5.35. Photocleavable studies of procarrier **5e** to release indole carboxamide **5′** monitored by ^{1}H NMR in DMSO-d_6 recorded at different time intervals upon irradiation at 365 nm of electromagnetic radiations.

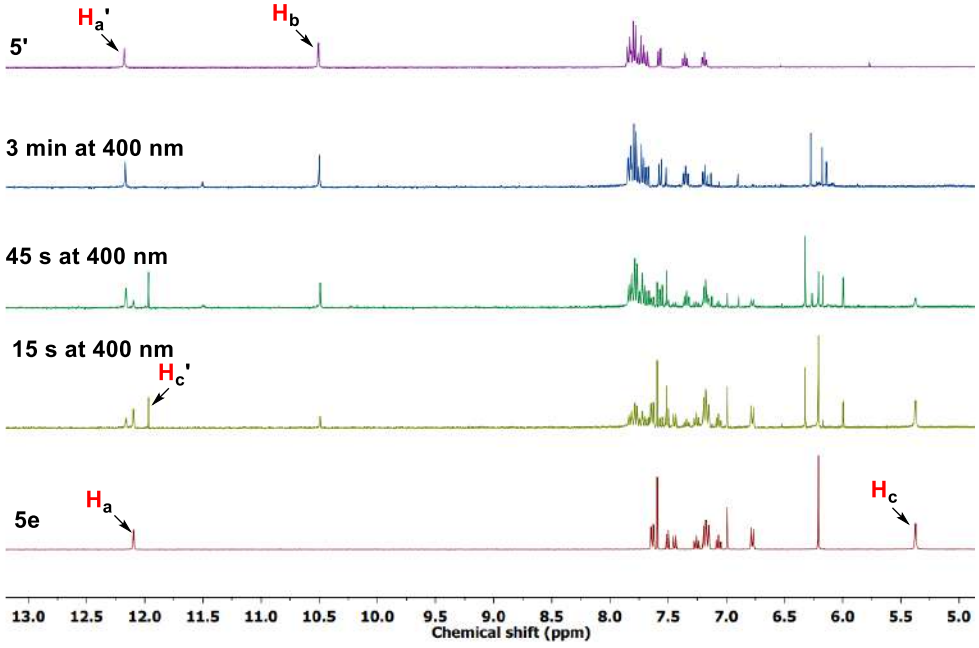

Figure 5.36. Photocleavable studies of procarrier **5e** to release indole carboxamide **5′** monitored by ^{1}H NMR in DMSO-d_6 recorded at different time intervals upon irradiation at 400 nm of electromagnetic radiations.

Assessment of photolysis of Control compounds 6a and 6c using ^{1}H NMR spectroscopy by irradiation at 400 nm or 450 nm: In a clean and dry NMR tube, the solution of compounds **6a** or **6c** were taken in DMSO-d_6 (2 mM in 0.5 mL). The ^{1}H NMR spectrum was recorded first (at t = 0 min). Then, the sample **6a** was photoirradiated with UV light (3 × 1 Watt LEDs, λ =

365 nm) and **6c** with visible light (8 × 1 Watt LEDs, λ = 400 nm) for different time intervals, and ^{1}H NMR spectrum of the irradiated samples were recorded at the end of each irradiation. All ^{1}H NMR spectra were processed using MestReNova 6.0 by considering residual solvent peak as an internal reference. Upon photoirradiation, the appearance and disappearance of the different proton peak signals were monitored by stacking all calibrated spectra. The photolytic conversion of compounds **6a** and **6c** to the corresponding 4-trifluoromethylaniline **6′** was confirmed by comparing the ^{1}H NMR spectra with the commercially available 4-trifluoromethylaniline **6′**.

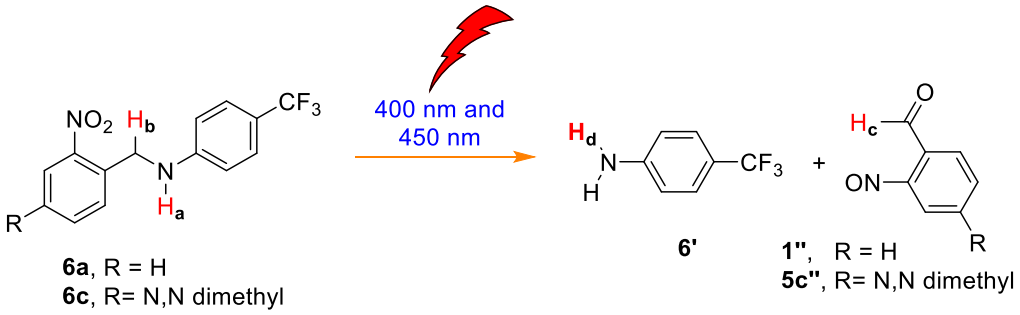

Scheme 5.4. Schematic representation of the photocleavage of intermediates **6a** and **6c**.

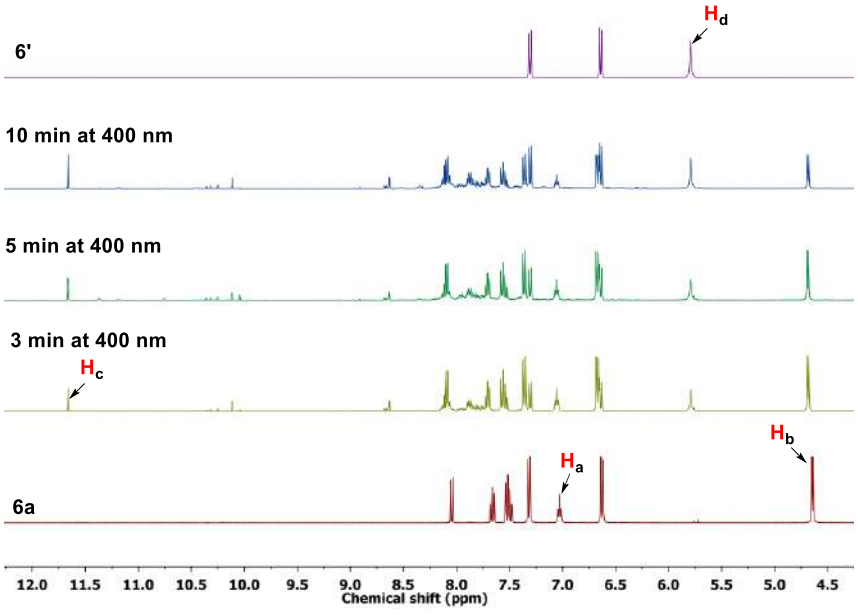

Figure 5.37. Photocleavage of compound **6a** by 400 nm visible light at different time intervals.

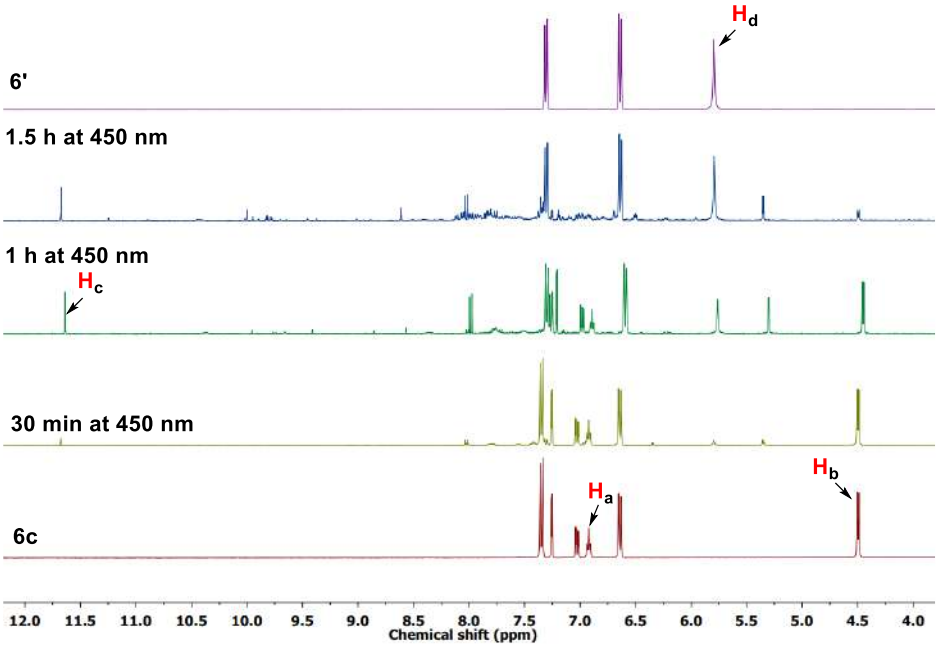

Figure 5.38. Photocleavage of compound **6c** by 450 nm visible light at different time intervas.

Assessment of photolysis of procarrier 5c using mass spectrometric studies by irradiation at 450 nm: The solution of **5c** (10 μM, 2 mL in MeOH:ACN:H_2O (2:2:1)) was photoirradiated at 450 nm using (3 × 1 Watt LEDs) for 2 h in a 4 mL cuvette. After photoirradiation the sample was subjected to ESI-MS studies. The ESI-MS data confirms the photocleavage of protected compound **5c** into the active carrier **5′** and corresponding *N*, *N* dimethyl nitrosobenzaldehye byproduct.

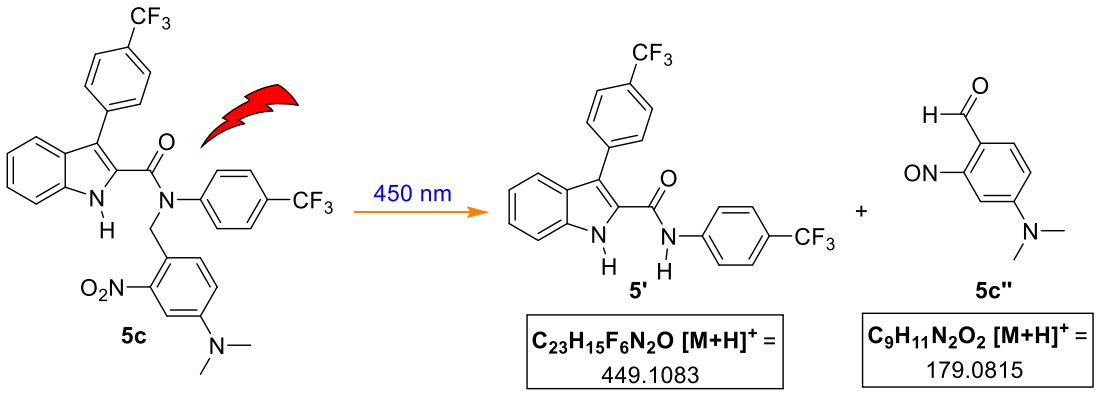

Scheme 5.5. Schematic representation of the photocleavage of **5c** at 450 nm.

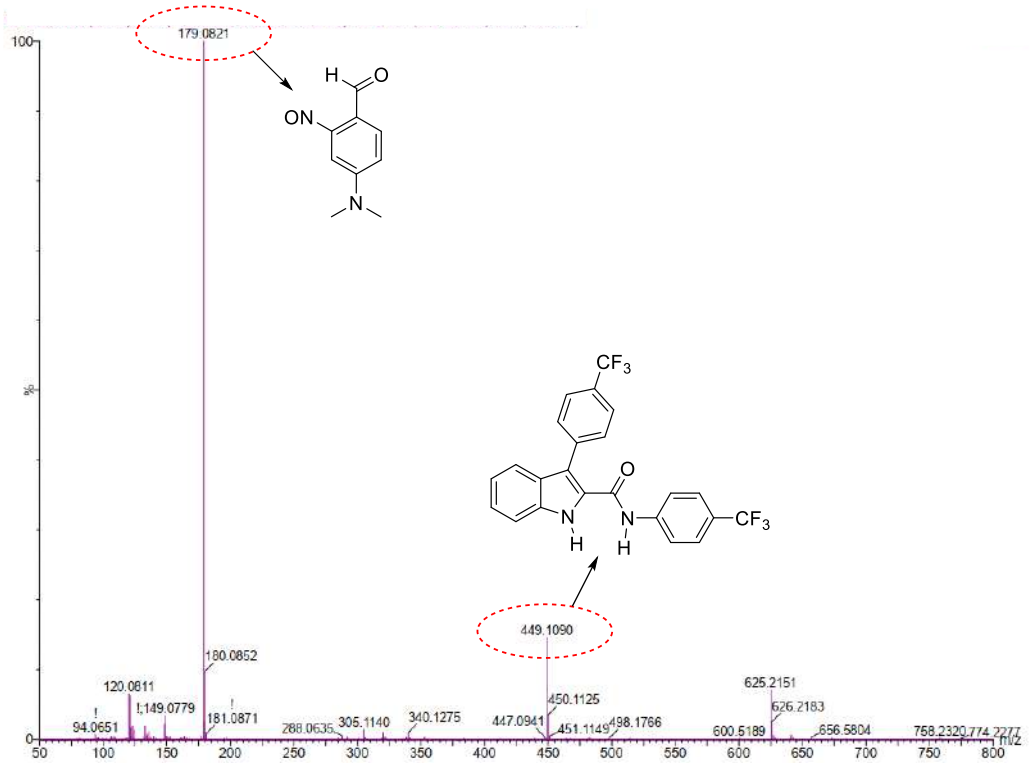

Figure 5.39. ESI-MS spectrum of **5c** recorded after irradiation at 450 nm using (3 × 1 Watt LEDs) for 2 h in a mixture of MeOH:ACN:H_2O (2:2:1).

5.4.7. Phototriggered ion transport across EYPC-LUVs⊃HPTS

Preparation of HEPES buffer and stock solutions: The HEPES buffer of pH = 7.0 was prepared by dissolving an appropriate amount of solid HEPES (10 mM) and NaCl (100 mM) in autoclaved water. The pH was adjusted to 7.0 by addition aliquots from 0.5 M NaOH solution using pH meter. The stock solutions of carrier **5′**, procarriers **5a–5e**, Control compounds **6a** and **6c**, and commercial 4-Trifluoroaniline **6′** were prepared using HPLC grade DMSO.

Preparation of EYPC-LUVs⊃HPTS: The vesicles were prepared by the following protocol as stated above.

Phototriggered activation and ion transport assay in LUVs: In clean and dry fluorescence cuvette, 1975 μL HEPES buffer (10 mM HEPES, 100 mM NaCl, pH = 7.0) and 25 μL EYPC-LUVs⊃HPTS vesicles were placed. To this suspension, procarriers **5a–5e** (20 μL as DMSO solution) were added to get the final concentration of 200 nM. The suspension with either of the procarriers **5a–5e** were then photoirradiated with either 365 nm wavelength (using 3 × 1 W LEDs) or 400 nm wavelength (using 1 × 8 W LED) or 450 nm wavelength (using three 1 W

LEDs) for different time intervals. Similarly, control compounds **6a** and **6c** were added to get the similar concentration of 200 nM. The vesicles containing **6a** were irradiated with light of 400 nm wavelength (using 1 × 8 W LED) and the vesicles containing **6c** were irradiated with light of 450 nm wavelength (using 3 × 1 W LEDs). Each irradiated sample was then placed in the fluorescence instrument equipped with a magnetic stirrer. The fluorescence intensity of HPTS at λ_{em} = 510 nm (λ_{ex} = 450 nm) of each sample was monitored as a course of time *t*. At *t* = 100 s, a pH gradient was created by the addition of 20 μL NaOH (0.5 M). Finally, at *t* = 300 s vesicles were lysed by the addition of 10% Triton X-100 (25 μL) to get the complete destruction of the applied pH gradient. Each, time-dependent fluorescence data was normalized using Equation S2. A sample containing 1975 μL HEPES buffer (10 mM HEPES, 100 mM NaCl, pH = 7.0), 25 μL EYPC-LUVs⊃HPTS and 20 μL DMSO was also subjected to 5 min irradiation with same LEDs. The ion transport activity of this sample was measured by adding 20 μL NaOH (0.5 M) at *t* = 100 s of the kinetics experiment, and this data was used as a control data. The time axis was normalized according to Equation S1. The time-dependent data were normalized to percent change in fluorescence intensity using Equation S2.

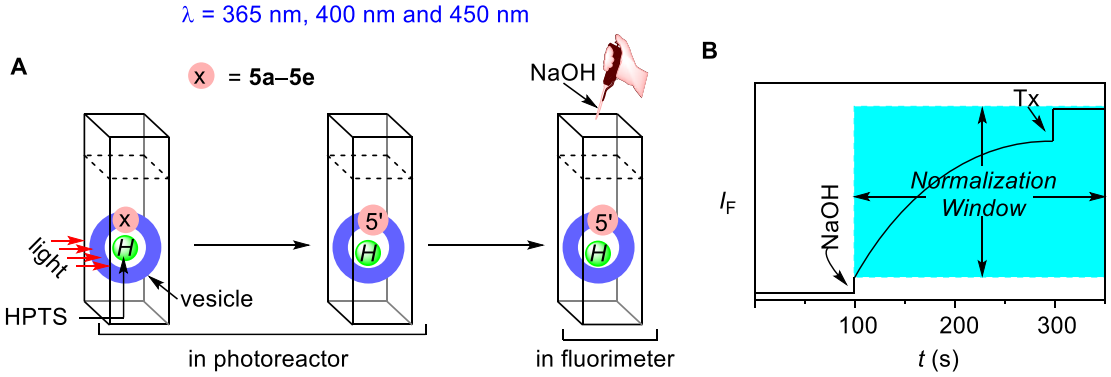

Figure 5.40. Description of the phototriggered release of an active transporter **5′** in the presence of unilamellar vesicles followed by ion transport measurement (**A**). Illustration of ion transport kinetics showing normalization window (**B**).

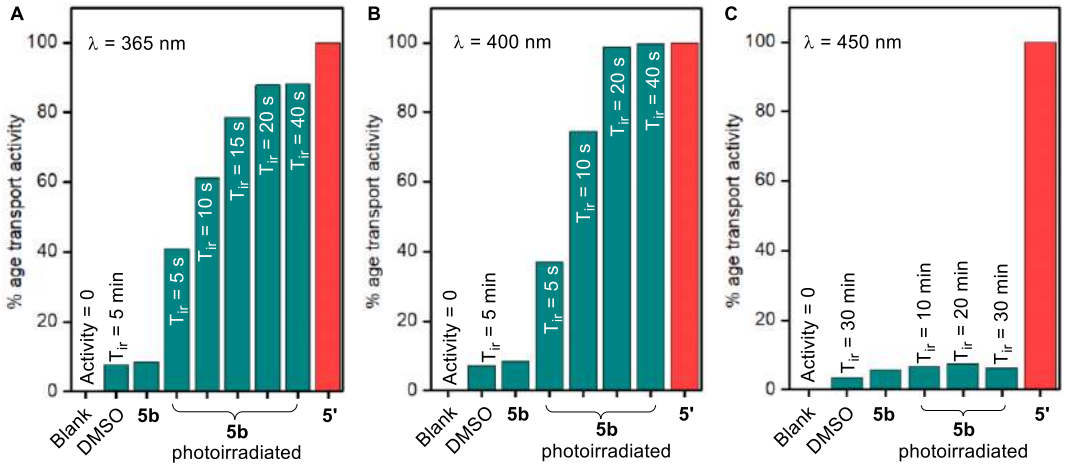

Figure 5.41. Normalized ion transport activity data upon photoirradiation of **5b** at 365 nm (**A**), at 400 nm (**B**) and at 450 nm (**C**) for different time intervals.

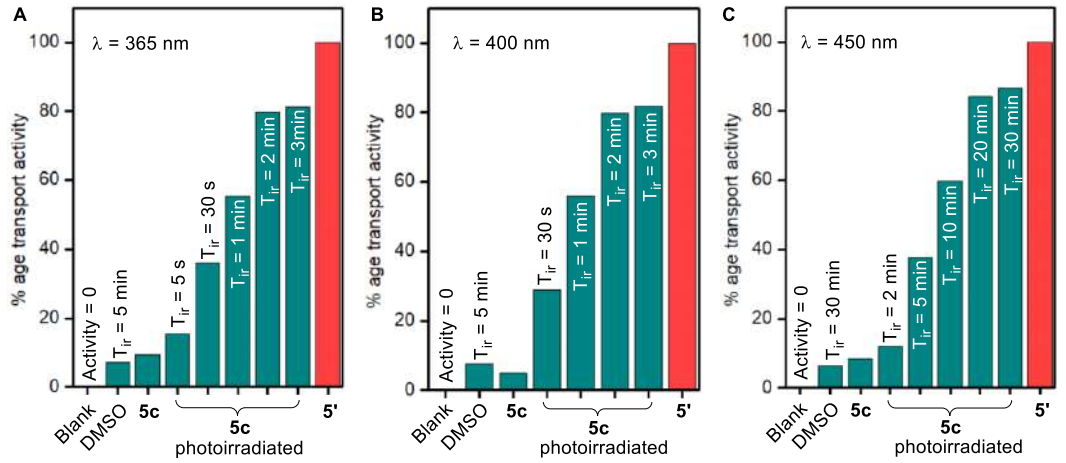

Figure 5.42. Normalized ion transport activity data upon photoirradiation of **5c** at 365 nm (**A**), at 400 nm (**B**) and at 450 nm (**C**) for different time intervals.

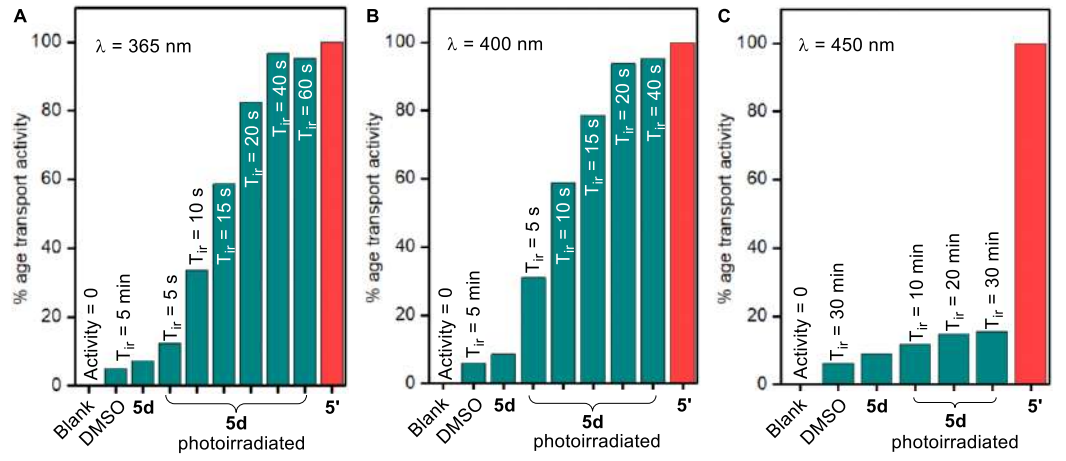

Figure 5.43. Normalized ion transport activity data upon photoirradiation of **5d** at 365 nm (**A**), at 400 nm (**B**) and at 450 nm (**C**) for different time intervals.

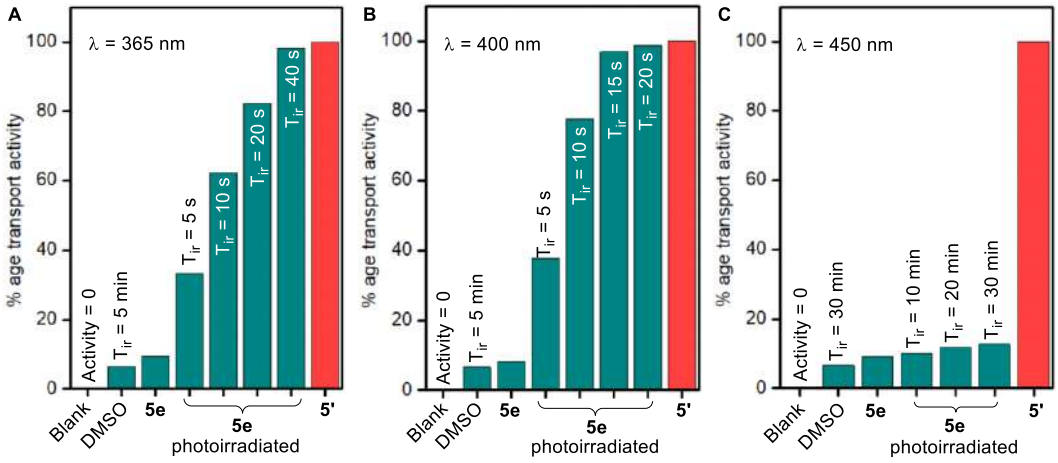

Figure 5.44. Normalized ion transport activity data upon photoirradiation of **5e** at 365 nm (**A**), at 400 nm (**B**) and at 450 nm (**C**) for different time intervals.

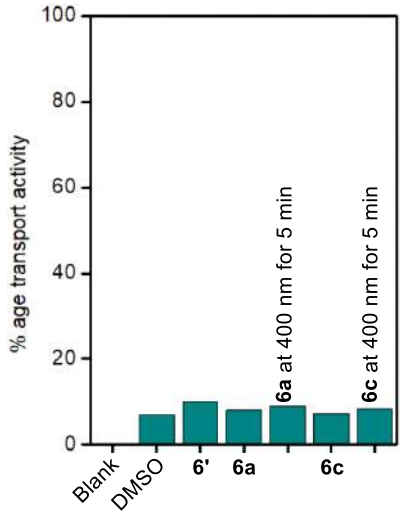

Figure S45. Normalized ion transport activity data upon photoirradiation of **6′** (200nM), **6a** (200nM), photoirradiated **6a** (200nM) at 400 nm, **6c** (200nM), and photoirradiated **6c** (200nM) at 450 nm, respectively.

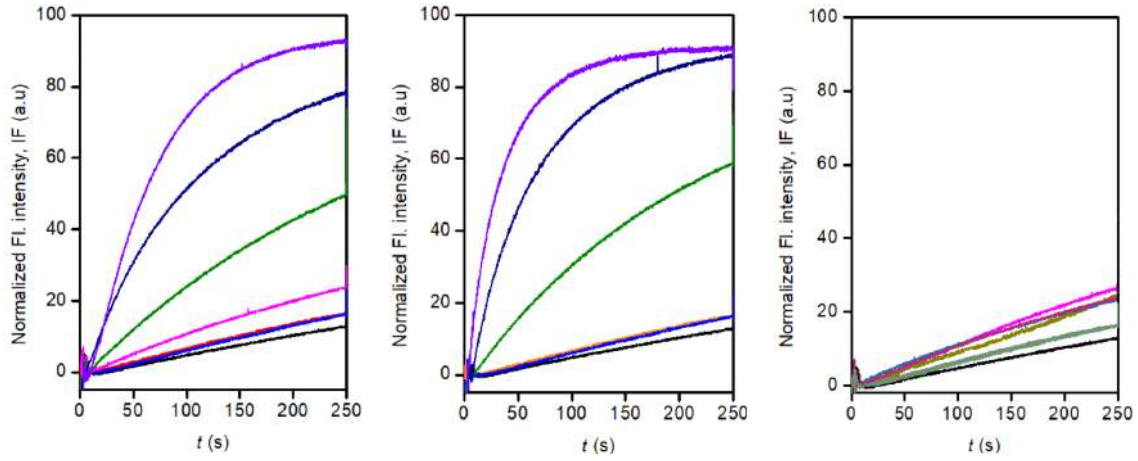

Figure 5.46. Ion transport activity data upon photoirradiation of **5a** at 365 nm (0 - 40 s) (**A**), at 400 nm (0 – 20 s) (**B**) and at 450 nm (0 – 30 min) (**C**), respectively.

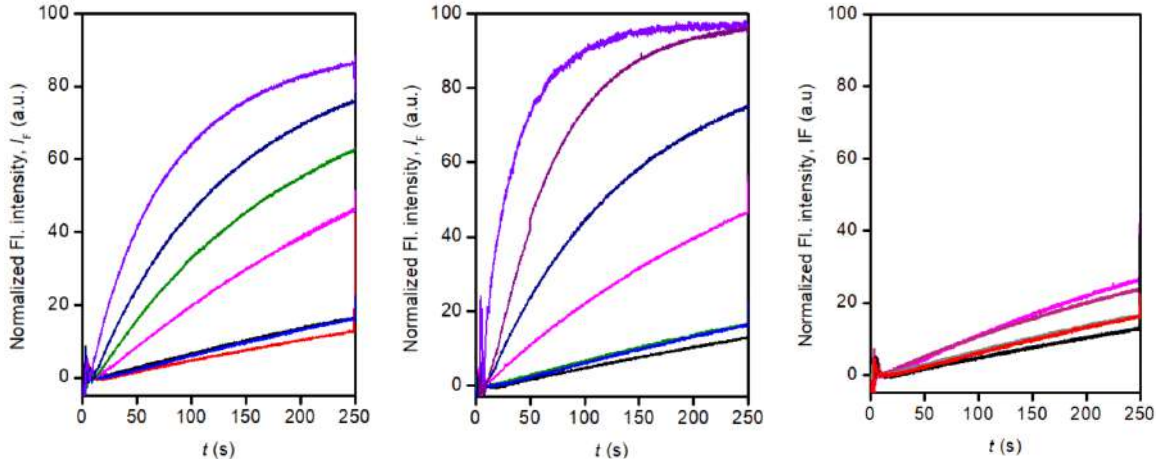

Figure 5.47. Ion transport activity data upon photoirradiation of **5b** at 365 nm (0 - 40 s) (**A**), at 400 nm (0 – 40 s) (**B**) and at 450 nm (0 – 30 min) (**C**), respectively.

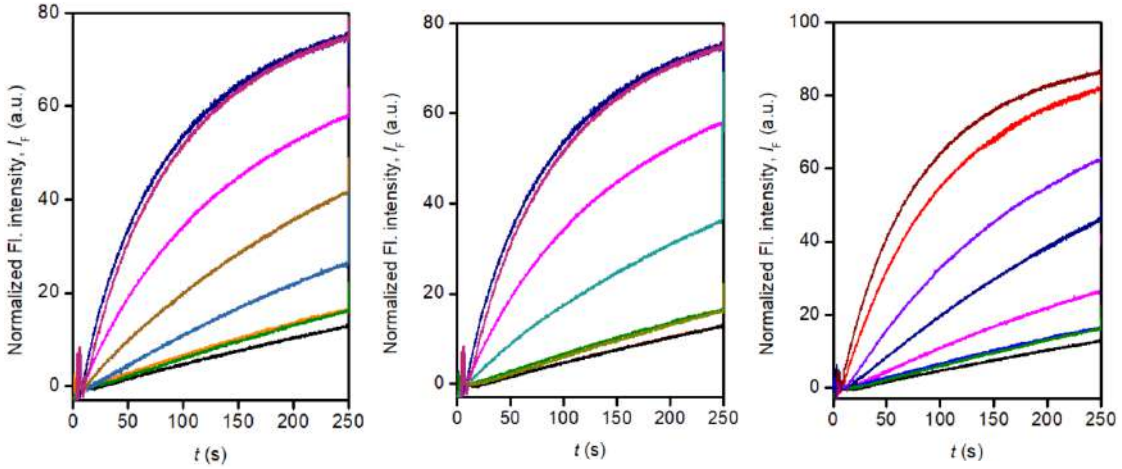

Figure 5.48. Ion transport activity data upon photoirradiation of **5c** at 365 nm (0 – 3 min) (**A**), at 400 nm (0 – 3 min) (**B**) and at 450 nm (0 – 30 min) (**C**), respectively.

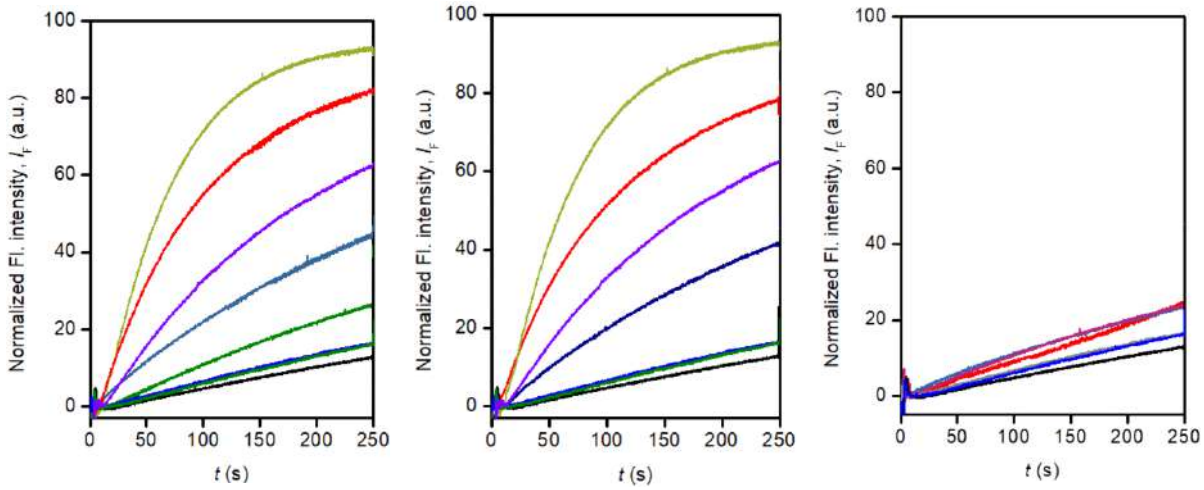

Figure 5.49. Ion transport activity data upon photoirradiation of **5d** at 365 nm (0 - 40 s) (**A**), at 400 nm (0 – 40 s) (**B**) and at 450 nm (0 – 30 min) (**C**), respectively.

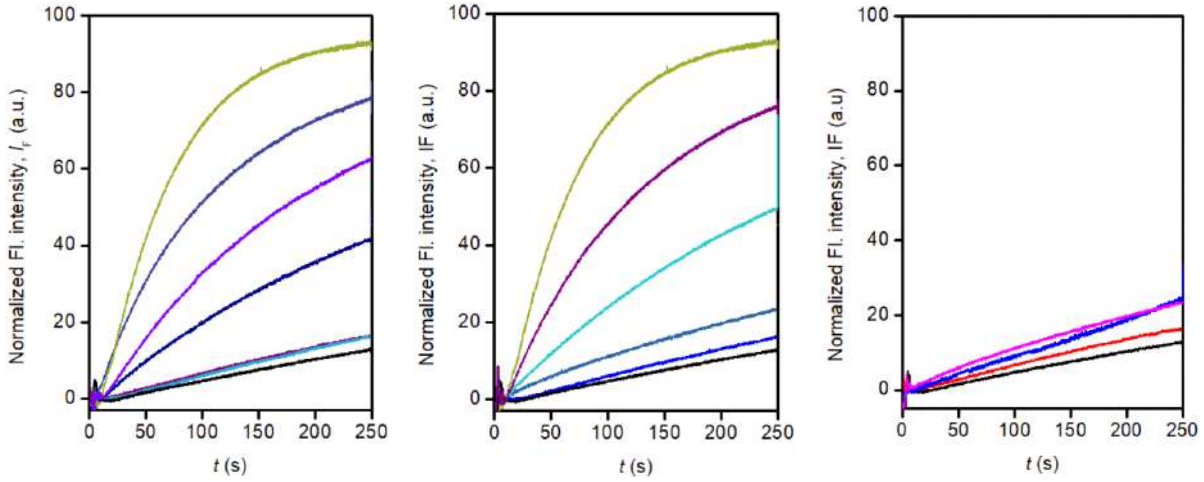

Figure 5.50. Ion transport activity data upon photoirradiation of **5e** at 365 nm (0 - 40 s) (**A**), at 400 nm (0 – 20 s) (**B**) and at 450 nm (0 – 30 min) (**C**), respectively.

5.4.8. Biological Studies (done in collaboration with Dr. Virender Kumar Sharma and Dr. Mayurika Lahiri from biological department of IISER Pune)

A. Cell culture protocol: The MCF 7 cells were grown in High Glucose Dulbecco's Modified Eagle Medium (DMEM; Invitrogen or Lonza) containing 10% fetal bovine serum (FBS; Invitrogen), 2 mM L-glutamine (Invitrogen) and 100 units/mL penicillin-streptomycin (Invitrogen). Cells were maintained in 100 mm tissue culture treated dishes (Corning) at 37 °C in humidified 5% CO_2 incubator (Thermo Scientific).

B. MTT-based cytotoxicity assay: The cells were dispersed in a 96-well flat bottom tissue culture treated plates (Corning) at density of 10^4 cells/well (per 100 µL) and incubated at 37 ^oC in a 5% CO_2 incubator for 24 h. Compounds were added to each well in different

concentration by maintaining maximum amount of DMSO at 2 µL and incubated for 24 h. DMEM solution containing compounds in each well were replaced with 110 µL of MTT-DMEM mixture (0.5 mg MTT/mL of DMEM) and incubated for 4 h in identical condition. After 4 h, the MTT solution was removed and to dissolve the formazan crystals 100 µL of DMSO was added to each well. The absorbance was recorded in a microplate reader (Varioskan Flash) at the wavelength of 570 nm. All experiments were performed in triplicates, and the relative cell viability (%) was expressed as a percentage of untreated cells (Figure S19).

C. Phototriggered activation in cells: The cells were dispersed in a 96-well flat bottom tissue culture treated plates (Corning) at density of 10^4 cells/well (per 100 µL) and incubated at 37 ^oC in a 5% CO_2 incubator for 24 h. Compound **5a**, **5b**, **5c**, **5d**, and **5e** were added to each well in different concentration by maintaining maximum amount of DMSO at 2 µL and incubated for 4 h. Then, the whole cell plate covered with aluminium foil was irradiated for either 20 minutes at 400 nm (using 1 × 8 W LEDs) or for 2 h at 450 nm (using 3 ×1 W LEDs) in two separate experiments for the two different wavelengths. The cell plate was then kept back in the incubator for another 20 h. Finally, the normal protocol for the MTT assay was followed.

D. Cytotoxicity of the *o*-nitrosobenzaldehyde byproducts 1″ and 5c″ : To evaluate the cytotoxicity of the *o*-nitrosobenzaldehyde byproducts **1″** and **5c″** generated during the photocleavage of the procarriers **5a** and **5c** during photoirradiation at 400 nm and 450 nm, respectively, the amine derivatives **6a** and **6c** were used for cell viability studies under similar irradiation conditions. The compounds **6a** and **6c** furnish **1″** and **5c″** byproducts along with 4-trifluoromethylaniline **6′** under photoirradiation at 400 nm and 450 nm respectively. The commercially available 4-trifluoromethylaniline **6′** did not showed any cellular toxicity. So, any toxicity for the photoirradiated samples **6a** or **6c** would be mainly due to the formation of *o*-nitrosobenzaldehyde byproducts **1″** and **5c″**, respectively.

Cell viability: The cells were dispersed in a 96-well flat bottom tissue culture treated plates (Corning) at density of 10^4 cells/well (per 100 µL) and incubated at 37 ^oC in a 5% CO_2 incubator for 24 h. Compound **6a** and **6c** were added to each well in different concentration by maintaining maximum amount of DMSO at 1.5 µL and incubated for 4 h. Then the whole cell plate covered with aluminium foil containing **6a** was irradiated for 20 minutes at 400 nm (using 1 × 8 W LEDs) and the cell plate containing **6c** was irradiated for 2 h at 450 nm (using 3 ×1 W LEDs). The cell plates for two separate experiments were then kept back in the incubator for another 20 h. Then normal protocol for the MTT assay was followed. The obtained data from

the cell plates containing **6a** was compared with that of procarrier compound **6a** photoactivated at 400 nm and the obtained data from the cell plates containing **6c** was compared with that of procarrier compound **6c** photoactivated at 450 nm.

E. Chloride mediated cell death studies

HBSS buffer solution. Hank's balanced salt solution (HBSS with Cl^-) was prepared with the following compositions: 136.9 mM NaCl, 5.5 mM KCl, 0.34 mM Na_2HPO_4, 0.44 mM KH_2PO_4, 0.81 mM $MgSO_4$, 1.25 mM $CaCl_2$, 5.5 mM D-glucose, 4.2 mM $NaHCO_3$ and 10 mM HEPES (pH 7.4). Chloride free HBSS was prepared by mixing 136.9 mM Na-gluconate, 5.5 mM K-gluconate, 0.34 mM Na_2HPO_4, 0.44 mM KH_2PO_4, 0.81 mM $MgSO_4$, 1.25 mM Ca-gluconate, 5.5 mM D-glucose, 4.2 mM $NaHCO_3$ and 10 mM HEPES (pH 7.4).

Cells were dispersed in a 96-well flat bottom tissue culture treated plates (Corning) at density of 104 cells/well (per 100 μL) and incubated at 37 ^oC in 5% CO_2 for 16 h. Cellular media was replaced by HBSS buffer (either with Cl^- or without Cl^-) containing 10% FBS. Compounds were added to each well in different concentration by maintaining maximum amount of DMSO at 2 μL and incubated for 24 h. HBSS buffer solution of compounds in each well was replaced by 110 μL of MTT-DMEM mixture (0.5 mg MTT/mL of DMEM) and incubated for 4 h in identical condition. Remaining MTT solution was removed after 4 h and 100 μL of DMSO was added in each well to dissolve the formazan crystals. The absorbance was recorded in a microplate reader (Varioskan Flash) at the wavelength of 570 nm.

F. Immunoblot analysis

Cells were seeded at a density of 6×10^5 cells per well in 6-well tissue culture treated plates (Corning) and maintained at 37 °C for 16 h. Cells were then treated with **5′** by direct addition of drug to the culture medium for 24 h at different concentration (0, 10, 20 and 40 μM). Control cells were treated with equivalent volume of DMSO. After 24 h treatment, medium containing **5′** was aspirated and cells were washed once with 1X phosphate buffered saline (PBS; PAN-Biotech GmbH). Cells were lysed in sample buffer containing 60 mM Tris (pH 6.8), 6% glycerol, 2% sodium dodecyl sulphate (SDS), 0.1 M dithiothreitol (DTT) and 0.006% bromophenol blue and lysates were stored at – 40 °C.

Cell lysates were resolved using sodium dodecyl sulphate polyacrylamide gel electrophoresis (SDS-PAGE) and transferred to Immobilon-P polyvinylidene difluoride (PVDF) membrane (Millipore). Blocking was performed in 5% (w/v) skimmed milk (SACO

Foods, USA) prepared in 1X Tris buffered saline containing 0.1% Tween 20 (1X TBS-T) for 1 h at room temperature. Blots were incubated for 16 h at room temperature at 4 °C in primary antibody solution. Following washes, blots were incubated with peroxidase conjugated secondary antibody solution prepared in 5% (w/v) skimmed milk in 1X TBS-T for 1 h at room temperature following which blots were developed using Immobilon Western Detection Reagent kit (Millipore) and visualized using ImageQuant LAS 4000 (GE Healthcare)

5.4.9. X-Ray Crystallographic Studies

Single Crystal X-ray Diffraction Analysis

The single-crystal X-ray diffraction (SCXRD) analysis of all the compounds was performed on a Bruker Smart Apex Duo diffractometer using Mo Kα radiation (λ = 0.71073Å). The crystal structures were solved using intrinsic methods and then refined by full-matrix least-squares against F^2 using all data by using SHELXL-2014/7 built in the Apex-3 package.[S7] The crystallographic refinement data for different compounds are listed below in different Tables. All the non-hydrogen atoms were refined anisotropically if not stated otherwise. Hydrogen atoms were constructed in geometric positions to their parent atoms. [S8] The DIAMOND-3.1 and Mercury software were used to describe the bond length, bond angles, and various structural illustrations of compound.

Crystallization for 5′

5′ (10mg) in 2 mL of acetonitrile was shortly heated and the solution was filtered through a cotton plug to seperate any undissolved compound. Suitable crystals for X-ray analysis were obtained by slow evaporation of the solovant.

Table 5.2. Crystallographic data of **5′** at 100 K.

Crystallographic details	**5′**
Chemical formula	$C_{23}H_{14}F_6N_2O$
Formula weight (g/mol)	448.36
Temperature	100(2)K
Crystal system	Triclinic
Space group	*P-1*
a (Å); α (°)	7.6045(15); 76.190(6)
b (Å); β (°)	9.8170(19); 74.705(6)
c (Å); γ (°)	14.024(3); 74.570(6)

V (Å^3); Z	957.3(3); 2
ρ (calc.) g cm^{-3}	1.555
μ(Mo K$_\alpha$) mm^{-1}	0.137
2θ$_{max}$ (°)	56.60
R(int)	0.0540
Completeness to θ	99.7
Data / param.	4748/290
GOF	1.054
R1 [F>4σ(F)]	0.0504
wR2 (all data)	0.1404
max. peak/hole (e.Å^{-3})	0.487/-0.547

Table 5.3. Selected bond lengths [Å] for **5′** at 100 K.

Type of bond	Bond length	Type of bond	Bond length
F3-C12	1.326(2)	F5-C23	1.339(2)
F4-C23	1.344(2)	O1-C16	1.230(2)
F6-C23	1.344(2)	F1-C12	1.340(3)
N1-C6	1.365(2)	N1-C7	1.382(2)
N1-H1	0.88	N2-C16	1.364(2)
N2-C18	1.417(2)	N2-H2	0.88
F2-C12	1.314(3)	C6-C1	1.399(3)
C6-C5	1.419(2)	C16-C7	1.476(3)
C5-C4	1.411(3)	C5-C8	1.428(3)
C7-C8	1.388(2)	C13-C14	1.384(3)
C13-C11	1.390(3)	C13-C12	1.504(2)
C15-C14	1.397(2)	C15-C9	1.397(3)
C15-H15	0.95	C9-C10	1.398(3)
C9-C8	1.490(2)	C18-C17	1.395(3)
C18-C19	1.398(3)	C14-H14	0.95
C17-C22	1.388(3)	C17-H17	0.95
C11-C10	1.391(2)	C11-H11	0.95
C10-H10	0.95	C1-C2	1.374(3)

C1-H1A	0.95	C4-C3	1.381(3)
C4-H4	0.95	C2-C3	1.413(3)
C2-H2A	0.95	C22-C21	1.394(3)
C22-H22	0.95	C19-C20	1.398(3)
C19-H19	0.95	C3-H3	0.95
C21-C20	1.378(3)	C21-C23	1.491(3)
C20-H20	0.95		

Table 5.4. Selected bond angles [°] for **5′** at 100 K.

Type of bond	Bond angle	Type of bond	Bond angle
C6-N1-C7	109.45(14)	C6-N1-H1	125.3
C7-N1-H1	125.3	C16-N2-C18	125.25(15)
C16-N2-H2	117.4	C18-N2-H2	117.4
N1-C6-C1	130.20(16)	N1-C6-C5	107.49(16)
C1-C6-C5	122.31(17)	O1-C16-N2	122.23(17)
O1-C16-C7	120.64(16)	N2-C16-C7	117.13(15)
C4-C5-C6	118.93(17)	C4-C5-C8	133.56(16)
C6-C5-C8	107.51(15)	N1-C7-C8	109.34(16)
N1-C7-C16	115.84(15)	C8-C7-C16	134.71(17)
C14-C13-C11	120.51(16)	C14-C13-C12	120.32(17)
C11-C13-C12	119.17(16)	C14-C15-C9	120.41(16)
C14-C15-H15	119.8	C9-C15-H15	119.8
C15-C9-C10	118.79(16)	C15-C9-C8	121.62(16)
C10-C9-C8	119.51(16)	C17-C18-C19	119.91(17)
C17-C18-N2	121.48(17)	C19-C18-N2	118.57(16)
C7-C8-C5	106.20(15)	C7-C8-C9	130.19(17)
C5-C8-C9	123.61(15)	C13-C14-C15	119.86(17)
C13-C14-H14	120.1	C15-C14-H14	120.1
C22-C17-C18	119.37(17)	C22-C17-H17	120.3

C18-C17-H17	120.3	C13-C11-C10	119.52(17)
C13-C11-H11	120.2	C10-C11-H11	120.2
C11-C10-C9	120.90(17)	C11-C10-H10	119.6
C9-C10-H10	119.6	C2-C1-C6	117.30(17)
C2-C1-H1A	121.3	C6-C1-H1A	121.3
C3-C4-C5	118.61(17)	C3-C4-H4	120.7
C5-C4-H4	120.7	C1-C2-C3	121.70(18)
C1-C2-H2A	119.2	C3-C2-H2A	119.2
C17-C22-C21	120.34(17)	C17-C22-H22	119.8
C21-C22-H22	119.8	C18-C19-C20	120.44(17)
C18-C19-H19	119.8	C20-C19-H19	119.8
C4-C3-C2	121.16(17)	C4-C3-H3	119.4
C2-C3-H3	119.4	C20-C21-C22	120.87(18)
C20-C21-C23	120.71(18)	C22-C21-C23	118.42(17)
F2-C12-F3	107.72(18)	F2-C12-F1	106.73(19)
F3-C12-F1	104.34(16)	F2-C12-C13	112.50(16)
F3-C12-C13	113.12(16)	F1-C12-C13	111.88(17)
C21-C20-C19	119.06(18)	C21-C20-H20	120.5
C19-C20-H20	120.5	F5-C23-F4	105.95(17)
F5-C23-F6	106.09(17)	F4-C23-F6	105.76(16)
F5-C23-C21	112.85(16)	F4-C23-C21	113.76(17)
F6-C23-C21	111.82(18)		

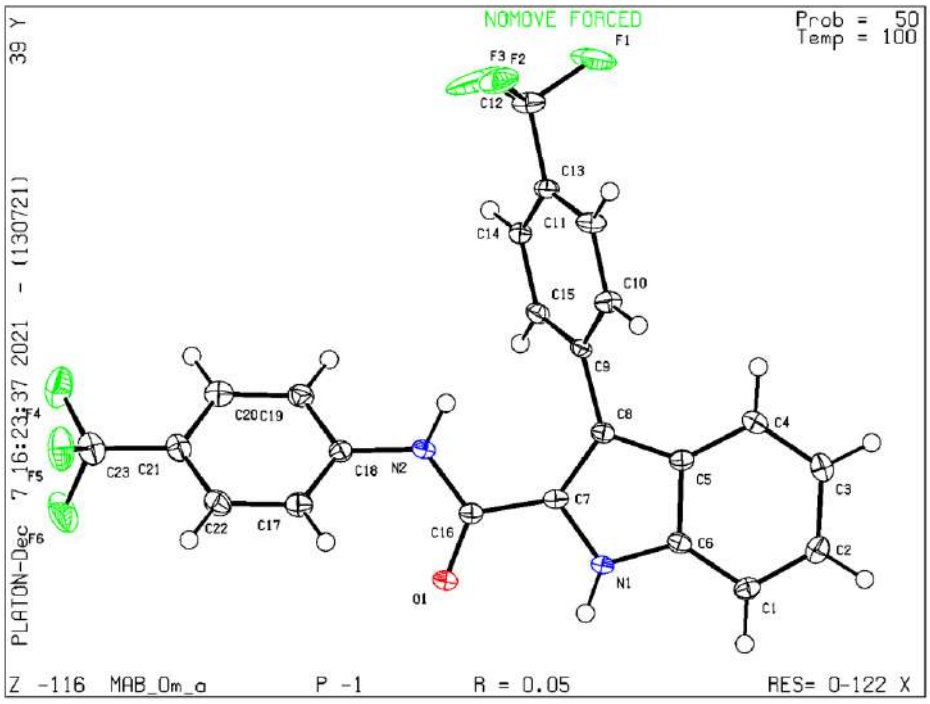

Figure 5.51. ORTEP diagram of **5′**. Ellipsoids are drawn at 50% probability.

Crystallization for 5′·Cl⁻

5′ (10mg) and TBACl in 2 mL of acetonitrile, in a ratio of **5′**:TBACl of 1:3 and 1:6 in two different glass vilas were shortly heated and the solution was filtered through a cotton plug to seperate any undissolved compound. Suitable crystals for X-ray analysis were obtained by slow evaporation of one of the sample containing **5′**:TBACl in a ratio of 1:6.

Table 5.5. Crystallographic data of **5′·Cl⁻** at 100 K.

Crystallographic details	**5′.Cl**
Chemical formula	$C_{39}H_{50}ClF_6N_3O$
Formula weight (g/mol)	726.27
Temperature	100(2)K
Crystal system	Monoclinic
Space group	*P1 21/c 1*
a (Å); α (°)	24.4975(12); 90
b (Å); β (°)	8.6281(5); 106.476(2)
c (Å); γ (°)	18.2798(9); 90
V (Å^3); Z	3705.1(3); 4
ρ (calc.) g cm^{-3}	1.302

μ(Mo K_α) mm^{-1}	0.168
$2\theta_{max}$ (°)	50.06
R(int)	0.1637
Completeness to θ	100
Data / param.	6538/456
GOF	1.045
R1 [F>4σ(F)]	0.0575
wR2 (all data)	0.1095
max. peak/hole ($e.Å^{-3}$)	0.259/-0.280

Table 5.6. Selected bond lengths [Å] for **5′·Cl⁻** at 100 K

Type of bond	Bond length	Type of bond	Bond length
F5-C22	1.346(3)	F3-C23	1.350(3)
F6-C22	1.345(3)	F4-C22	1.337(3)
O1-C15	1.226(3)	F2-C23	1.333(3)
F1-C23	1.331(3)	N1-C13	1.369(3)
N1-C14	1.387(3)	N1-H1	0.88
N2-C15	1.367(3)	N2-C16	1.407(3)
N2-H2	0.88	N1A-C5A	1.517(3)
N1A-C13A	1.521(3)	N1A-C9A	1.523(3)
N1A-C1A	1.524(3)	C21-C20	1.382(4)
C21-C16	1.390(4)	C21-H21	0.95
C20-C19	1.386(4)	C20-H20	0.95
C15-C14	1.475(4)	C14-C7	1.384(4)
C13A-C14A	1.515(3)	C13A-H13A	0.99
C13A-H13B	0.99	C6-C1	1.380(4)
C6-C5	1.384(4)	C6-H6	0.95
C19-C18	1.382(4)	C19-C22	1.489(4)
C8-C13	1.405(4)	C8-C9	1.407(4)
C8-C7	1.438(4)	C5-C4	1.389(4)
C5-H5	0.95	C5A-C6A	1.514(4)

C5A-H5A1	0.99	C5A-H5A2	0.99
C9A-C10A	1.516(4)	C9A-H9A1	0.99
C9A-H9A2	0.99	C17-C18	1.372(4)
C17-C16	1.401(4)	C17-H17	0.95
C10A-C11A	1.530(4)	C10A-H10A	0.99
C10A-H10B	0.99	C1A-C2A	1.520(4)
C1A-H1A1	0.99	C1A-H1A2	0.99
C12A-C11A	1.519(4)	C12A-H12A	0.98
C12A-H12B	0.98	C12A-H12C	0.98
C4-C3	1.389(4)	C4-C7	1.477(4)
C14A-C15A	1.523(4)	C14A-H14A	0.99
C14A-H14B	0.99	C1-C2	1.381(4)
C1-C23	1.491(4)	C13-C12	1.396(4)
C18-H18	0.95	C15A-C16A	1.518(4)
C15A-H15A	0.99	C15A-H15B	0.99
C11A-H11A	0.99	C11A-H11B	0.99
C3-C2	1.389(4)	C3-H3	0.95
C2A-C3A	1.525(4)	C2A-H2A1	0.99
C2A-H2A2	0.99	C12-C11	1.372(4)
C12-H12	0.95	C9-C10	1.377(4)
C9-H9	0.95	C2-H2A	0.95
C11-C10	1.404(4)	C11-H11	0.95
C10-H10	0.95	C3A-C4A	1.510(4)
C3A-H3A1	0.99	C3A-H3A2	0.99
C6A-C7A	1.515(4)	C6A-H6A1	0.99
C6A-H6A2	0.99	C4A-H4A1	0.98
C4A-H4A2	0.98	C4A-H4A3	0.98
C8A-C7A	1.520(4)	C8A-H8A1	0.98
C8A-H8A2	0.98	C8A-H8A3	0.98

C16A-H16A	0.98	C16A-H16B	0.98
C16A-H16C	0.98	C7A-H7A1	0.99
C7A-H7A2	0.99		

Table 5.7. Selected bond angles [°] for **5′·Cl⁻** at 100 K.

Type of bond	Bond angle	Type of bond	Bond angle
C13-N1-C14	109.2(2)	C13-N1-H1	125.4
C14-N1-H1	125.4	C15-N2-C16	127.4(2)
C15-N2-H2	116.3	C16-N2-H2	116.3
C5A-N1A-C13A	111.44(19)	C5A-N1A-C9A	105.87(19)
C13A-N1A-C9A	111.3(2)	C5A-N1A-C1A	111.5(2)
C13A-N1A-C1A	105.71(19)	C9A-N1A-C1A	111.08(19)
C20-C21-C16	120.2(3)	C20-C21-H21	119.9
C16-C21-H21	119.9	C21-C20-C19	120.4(3)
C21-C20-H20	119.8	C19-C20-H20	119.8
O1-C15-N2	122.8(2)	O1-C15-C14	121.0(2)
N2-C15-C14	116.1(2)	C7-C14-N1	109.1(2)
C7-C14-C15	128.2(2)	N1-C14-C15	122.7(2)
C14A-C13A-N1A	116.7(2)	C14A-C13A-H13A	108.1
N1A-C13A-H13A	108.1	C14A-C13A-H13B	108.1
N1A-C13A-H13B	108.1	H13A-C13A-H13B	107.3
C1-C6-C5	119.4(3)	C1-C6-H6	120.3
C5-C6-H6	120.3	C18-C19-C20	119.4(3)
C18-C19-C22	121.3(3)	C20-C19-C22	119.3(3)
C13-C8-C9	118.8(3)	C13-C8-C7	107.4(2)
C9-C8-C7	133.8(3)	C6-C5-C4	121.3(3)
C6-C5-H5	119.3	C4-C5-H5	119.3
C6A-C5A-N1A	116.4(2)	C6A-C5A-H5A1	108.2
N1A-C5A-H5A1	108.2	C6A-C5A-H5A2	108.2

N1A-C5A-H5A2	108.2	H5A1-C5A-H5A2	107.3
C10A-C9A-N1A	115.7(2)	C10A-C9A-H9A1	108.4
N1A-C9A-H9A1	108.4	C10A-C9A-H9A2	108.4
N1A-C9A-H9A2	108.4	H9A1-C9A-H9A2	107.4
C18-C17-C16	120.2(3)	C18-C17-H17	119.9
C16-C17-H17	119.9	C9A-C10A-C11A	110.4(2)
C9A-C10A-H10A	109.6	C11A-C10A-H10A	109.6
C9A-C10A-H10B	109.6	C11A-C10A-H10B	109.6
H10A-C10A-H10B	108.1	C21-C16-C17	119.0(2)
C21-C16-N2	124.6(2)	C17-C16-N2	116.4(2)
C2A-C1A-N1A	116.0(2)	C2A-C1A-H1A1	108.3
N1A-C1A-H1A1	108.3	C2A-C1A-H1A2	108.3
N1A-C1A-H1A2	108.3	H1A1-C1A-H1A2	107.4
C11A-C12A-H12A	109.5	C11A-C12A-H12B	109.5
H12A-C12A-H12B	109.5	C11A-C12A-H12C	109.5
H12A-C12A-H12C	109.5	H12B-C12A-H12C	109.5
C3-C4-C5	118.2(2)	C3-C4-C7	120.8(2)
C5-C4-C7	120.8(2)	C13A-C14A-C15A	108.8(2)
C13A-C14A-H14A	109.9	C15A-C14A-H14A	109.9
C13A-C14A-H14B	109.9	C15A-C14A-H14B	109.9
H14A-C14A-H14B	108.3	C6-C1-C2	120.6(3)
C6-C1-C23	119.7(3)	C2-C1-C23	119.6(3)
N1-C13-C12	129.4(3)	N1-C13-C8	107.9(2)
C12-C13-C8	122.7(3)	C17-C18-C19	120.8(3)
C17-C18-H18	119.6	C19-C18-H18	119.6
C14-C7-C8	106.4(2)	C14-C7-C4	129.5(3)
C8-C7-C4	123.9(2)	C16A-C15A-C14A	112.6(2)
C16A-C15A-H15A	109.1	C14A-C15A-H15A	109.1
C16A-C15A-H15B	109.1	C14A-C15A-H15B	109.1

H15A-C15A-H15B	107.8	C12A-C11A-C10A	113.4(2)
C12A-C11A-H11A	108.9	C10A-C11A-H11A	108.9
C12A-C11A-H11B	108.9	C10A-C11A-H11B	108.9
H11A-C11A-H11B	107.7	C4-C3-C2	121.1(3)
C4-C3-H3	119.5	C2-C3-H3	119.5
C1A-C2A-C3A	109.7(2)	C1A-C2A-H2A1	109.7
C3A-C2A-H2A1	109.7	C1A-C2A-H2A2	109.7
C3A-C2A-H2A2	109.7	H2A1-C2A-H2A2	108.2
C11-C12-C13	117.1(3)	C11-C12-H12	121.5
C13-C12-H12	121.5	C10-C9-C8	118.6(3)
C10-C9-H9	120.7	C8-C9-H9	120.7
C1-C2-C3	119.4(3)	C1-C2-H2A	120.3
C3-C2-H2A	120.3	C12-C11-C10	121.6(3)
C12-C11-H11	119.2	C10-C11-H11	119.2
F4-C22-F6	106.6(2)	F4-C22-F5	105.8(2)
F6-C22-F5	105.5(2)	F4-C22-C19	113.2(2)
F6-C22-C19	112.5(2)	F5-C22-C19	112.6(2)
C9-C10-C11	121.2(3)	C9-C10-H10	119.4
C11-C10-H10	119.4	C4A-C3A-C2A	113.6(2)
C4A-C3A-H3A1	108.8	C2A-C3A-H3A1	108.8
C4A-C3A-H3A2	108.8	C2A-C3A-H3A2	108.8
H3A1-C3A-H3A2	107.7	F1-C23-F2	107.0(3)
F1-C23-F3	105.4(2)	F2-C23-F3	105.1(2)
F1-C23-C1	113.3(2)	F2-C23-C1	114.0(3)
F3-C23-C1	111.3(2)	C5A-C6A-C7A	109.5(2)
C5A-C6A-H6A1	109.8	C7A-C6A-H6A1	109.8
C5A-C6A-H6A2	109.8	C7A-C6A-H6A2	109.8
H6A1-C6A-H6A2	108.2	C3A-C4A-H4A1	109.5
C3A-C4A-H4A2	109.5	H4A1-C4A-H4A2	109.5

C3A-C4A-H4A3	109.5	H4A1-C4A-H4A3	109.5
H4A2-C4A-H4A3	109.5	C7A-C8A-H8A1	109.5
C7A-C8A-H8A2	109.5	H8A1-C8A-H8A2	109.5
C7A-C8A-H8A3	109.5	H8A1-C8A-H8A3	109.5
H8A2-C8A-H8A3	109.5	C15A-C16A-H16A	109.5
C15A-C16A-H16B	109.5	H16A-C16A-H16B	109.5
C15A-C16A-H16C	109.5	H16A-C16A-H16C	109.5
H16B-C16A-H16C	109.5	C6A-C7A-C8A	112.1(2)
C6A-C7A-H7A1	109.2	C8A-C7A-H7A1	109.2
C6A-C7A-H7A2	109.2	C8A-C7A-H7A2	109.2
H7A1-C7A-H7A2	107.9		

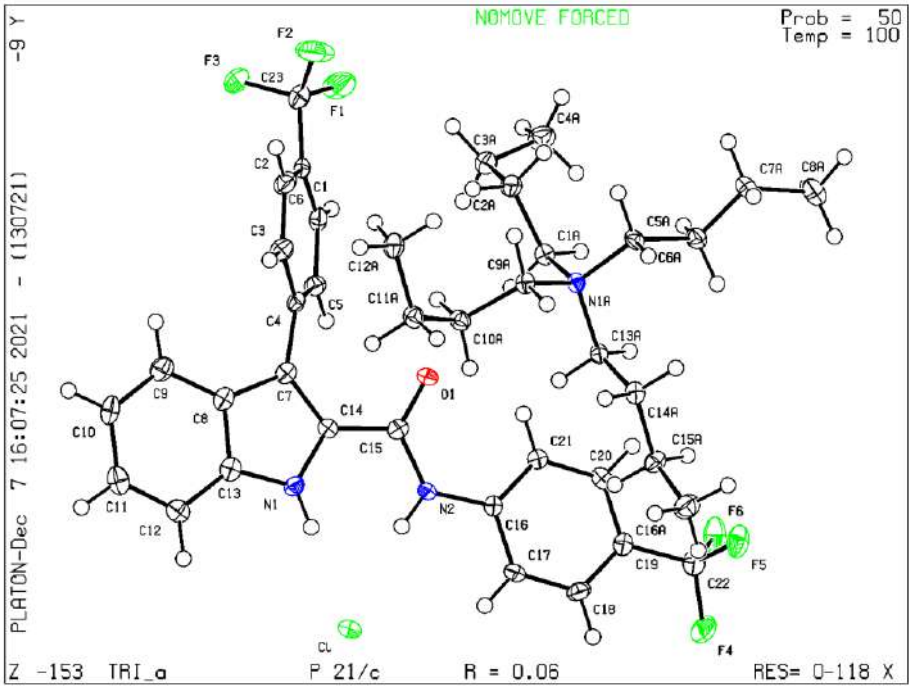

Figure 5.52. ORTEP diagram of **5′** co-crystalized TBACl. Ellipsoids are drawn at 50% probability.

Crystallization for 5c

5c (10 mg) in 2 mL of acetonitrile was shortly heated and the solution was filtered through a cotton plug to seperate any undissolved compound. Suitable crystals for X-ray analysis were obtained by slow evaporation of the solovant.

Table 5.8. Crystallographic data of **5c** at 100 K.

Crystallographic details	**5c**
Chemical formula	$C_{32}H_{24}F_6N_4O_3$
Formula weight (g/mol)	626.55
Temperature	100(2)K
Crystal system	Triclinic
Space group	*P-1*
a (Å); α (°)	10.851(2); 81.019(8)
b (Å); β (°)	11.560(2); 72.671(9)
c (Å); γ (°)	11.920(2); 78.352(9)
V (Å^3); Z	1390.6(5); 2
ρ (calc.) g cm^{-3}	1.496
μ(Mo K$_\alpha$) mm^{-1}	1.076
2θ$_{max}$ (°)	131.54
R(int)	0.0455
Completeness to θ	97.1
Data / param.	4677/409
GOF	1.073
R1 [F>4σ(F)]	0.0604
wR2 (all data)	0.1506
max. peak/hole (e.Å^{-3})	1.121/-0.961

Table 5.9. Selected bond lengths [Å] for **5c** at 100 K.

Type of bond	**Bond length**	**Type of bond**	**Bond length**
F6-C23	1.348(3)	F4-C23	1.343(3)
F5-C23	1.342(3)	O1-C16	1.233(3)
F1-C15	1.284(4)	F2-C15	1.312(4)
N1-C8	1.365(3)	N1-C5	1.375(3)
N1-H1	0.88	N2-C16	1.360(4)
N2-C17	1.437(4)	N2-C24	1.475(3)
O2-N4	1.212(3)	N4-O3	1.218(3)
N4-C30	1.468(4)	N3-C28	1.376(4)

N3-C31	1.447(4)	N3-C32	1.453(4)
F3-C15	1.344(4)	C7-C8	1.377(4)
C7-C6	1.448(4)	C7-C9	1.472(4)
C25-C26	1.393(4)	C25-C30	1.407(4)
C25-C24	1.518(4)	C16-C8	1.490(4)
C17-C18	1.384(4)	C17-C22	1.397(4)
C6-C1	1.404(4)	C6-C5	1.408(4)
C9-C10	1.392(4)	C9-C14	1.403(4)
C20-C21	1.389(4)	C20-C19	1.389(4)
C20-C23	1.495(4)	C26-C27	1.374(4)
C26-H26	0.95	C10-C11	1.376(4)
C10-H10	0.95	C30-C29	1.385(4)
C18-C19	1.383(4)	C18-H18	0.95
C27-C28	1.403(4)	C27-H27	0.95
C5-C4	1.396(4)	C19-H19	0.95
C11-C12	1.387(4)	C11-H11	0.95
C28-C29	1.398(4)	C29-H29	0.95
C4-C3	1.377(4)	C4-H4	0.95
C22-C21	1.383(4)	C22-H22	0.95
C21-H21	0.95	C13-C14	1.381(4)
C13-C12	1.392(4)	C13-H13	0.95
C14-H14	0.95	C1-C2	1.372(4)
C1-H1A	0.95	C12-C15	1.484(4)
C3-C2	1.400(4)	C3-H3	0.95
C24-H24A	0.99	C24-H24B	0.99
C2-H2	0.95	C32-H32A	0.98
C32-H32B	0.98	C32-H32C	0.98
C31-H31A	0.98	C31-H31B	0.98
C31-H31C	0.98		

Table 5.10. Selected bond angles [°] for **5c** at 100 K.

Type of bond	Bond angle	Type of bond	Bond angle
C8-N1-C5	108.9(2)	C8-N1-H1	125.5
C5-N1-H1	125.5	C16-N2-C17	124.3(2)
C16-N2-C24	117.6(2)	C17-N2-C24	117.8(2)
O2-N4-O3	121.4(2)	O2-N4-C30	119.3(2)
O3-N4-C30	119.3(2)	C28-N3-C31	119.4(2)
C28-N3-C32	119.1(2)	C31-N3-C32	118.1(2)
C8-C7-C6	105.8(2)	C8-C7-C9	126.0(2)
C6-C7-C9	128.1(2)	C26-C25-C30	114.3(2)
C26-C25-C24	120.8(2)	C30-C25-C24	124.8(2)
O1-C16-N2	122.0(2)	O1-C16-C8	120.2(2)
N2-C16-C8	117.8(2)	C18-C17-C22	119.5(3)
C18-C17-N2	119.3(2)	C22-C17-N2	121.1(2)
C1-C6-C5	118.1(2)	C1-C6-C7	135.1(3)
C5-C6-C7	106.7(2)	C10-C9-C14	118.2(3)
C10-C9-C7	119.6(2)	C14-C9-C7	122.2(2)
N1-C8-C7	110.4(2)	N1-C8-C16	118.0(2)
C7-C8-C16	131.5(2)	C21-C20-C19	120.0(3)
C21-C20-C23	119.0(3)	C19-C20-C23	120.9(3)
C27-C26-C25	123.4(3)	C27-C26-H26	118.3
C25-C26-H26	118.3	C11-C10-C9	121.3(3)
C11-C10-H10	119.3	C9-C10-H10	119.3
C29-C30-C25	123.7(3)	C29-C30-N4	115.3(2)
C25-C30-N4	121.0(2)	C19-C18-C17	120.4(3)
C19-C18-H18	119.8	C17-C18-H18	119.8
C26-C27-C28	121.5(3)	C26-C27-H27	119.3
C28-C27-H27	119.3	N1-C5-C4	129.4(3)

N1-C5-C6	108.1(2)	C4-C5-C6	122.5(2)
C18-C19-C20	120.0(3)	C18-C19-H19	120.0
C20-C19-H19	120.0	C10-C11-C12	120.0(3)
C10-C11-H11	120.0	C12-C11-H11	120.0
N3-C28-C29	121.5(2)	N3-C28-C27	121.8(3)
C29-C28-C27	116.7(2)	C30-C29-C28	120.5(2)
C30-C29-H29	119.8	C28-C29-H29	119.8
C3-C4-C5	117.7(3)	C3-C4-H4	121.1
C5-C4-H4	121.1	C21-C22-C17	120.2(3)
C21-C22-H22	119.9	C17-C22-H22	119.9
C22-C21-C20	119.8(3)	C22-C21-H21	120.1
C20-C21-H21	120.1	C14-C13-C12	120.0(3)
C14-C13-H13	120.0	C12-C13-H13	120.0
C13-C14-C9	120.7(3)	C13-C14-H14	119.6
C9-C14-H14	119.6	C2-C1-C6	119.2(3)
C2-C1-H1A	120.4	C6-C1-H1A	120.4
C11-C12-C13	119.7(3)	C11-C12-C15	120.4(3)
C13-C12-C15	119.8(3)	C4-C3-C2	120.6(3)
C4-C3-H3	119.7	C2-C3-H3	119.7
N2-C24-C25	112.7(2)	N2-C24-H24A	109.1
C25-C24-H24A	109.1	N2-C24-H24B	109.1
C25-C24-H24B	109.1	H24A-C24-H24B	107.8
F5-C23-F4	107.0(2)	F5-C23-F6	105.6(2)
F4-C23-F6	105.4(2)	F5-C23-C20	113.2(2)
F4-C23-C20	113.2(2)	F6-C23-C20	111.8(2)
C1-C2-C3	121.7(3)	C1-C2-H2	119.1
C3-C2-H2	119.1	N3-C32-H32A	109.5
N3-C32-H32B	109.5	H32A-C32-H32B	109.5
N3-C32-H32C	109.5	H32A-C32-H32C	109.5

H32B-C32-H32C	109.5	F1-C15-F2	108.5(3)
F1-C15-F3	104.6(4)	F2-C15-F3	102.8(3)
F1-C15-C12	113.0(3)	F2-C15-C12	114.4(3)
F3-C15-C12	112.6(3)	N3-C31-H31A	109.5
N3-C31-H31B	109.5	H31A-C31-H31B	109.5
N3-C31-H31C	109.5	H31A-C31-H31C	109.5
H31B-C31-H31C	109.5		

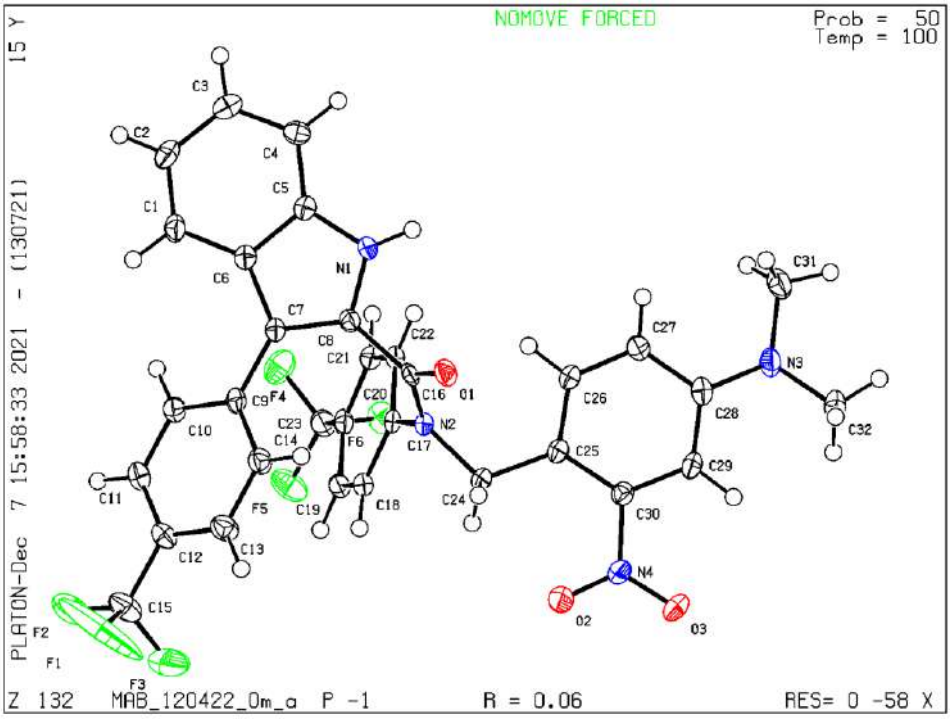

Figure 5.53. ORTEP diagram of **5c**. Ellipsoids are drawn at 50% probability.

Crystallization for 5a

5a (10 mg) in 2 mL of acetonitrile was shortly heated and the solution was filtered through a cotton plug to seperate any undissolved compound. Suitable crystals for X-ray analysis were obtained by slow evaporation of the solovant.

Table 5.11. Crystallographic data of **2a** at 100 K.

Crystallographic details	**2a**
Chemical formula	$C_{30}H_{19}F_6N_3O_3$

Formula weight (g/mol)	585.48
Temperature	100(2)K
Crystal system	Monoclinic
Space group	*P 1 21/c 1*
a (Å); α (°)	19.6161(11); 90
b (Å); β (°)	18.8098(10); 94.641(2)
c (Å); γ (°)	8.1114(5); 90
V ($Å^3$); Z	2983.1(3); 4
ρ (calc.) g cm^{-3}	1.299
μ(Mo K_α) mm^{-1}	0.110
$2\theta_{max}$ (°)	50.04
R(int)	0.0761
Completeness to θ	99.6
Data / param.	5253/343
GOF	2.088
R1 [F>4σ(F)]	0.1755
wR2 (all data)	0.5122
max. peak/hole (e.$Å^{-3}$)	1.717/-0.995

Table 5.12. Selected bond lengths [Å] for **2a** at 100 K.

Type of bond	**Bond length**	**Type of bond**	**Bond length**
C22-C23	1.39	C22-C27	1.39
C22-C28	1.674(12)	C23-N3	1.233(16)
C23-C24	1.39	C24-C25	1.39
C24-H24	0.95	C25-C26	1.39
C25-H25	0.95	C26-C27	1.39
C26-H26	0.95	C27-H27	0.95
N1-C8	1.351(8)	N1-C5	1.420(5)
N1-C28	1.455(9)	C2-C3	1.39
C2-C7	1.39	C2-C1	1.436(6)
C3-C4	1.39	C3-H3	0.95
C4-C5	1.39	C4-H4	0.95
C5-C6	1.39	C6-C7	1.39

C6-H6	0.95	C7-H7	0.95
O1-C8	1.229(7)	C16-C17	1.39
C16-C21	1.39	C16-C30	1.476(7)
C17-C18	1.39	C17-H17	0.95
C18-C19	1.39	C18-H18	0.95
C19-C20	1.39	C19-C29	1.466(15)
C20-C21	1.39	C20-H20	0.95
C21-H21	0.95	N2-C15	1.360(7)
N2-C9	1.384(8)	N2-H2	0.88
F1-C1	1.310(11)	C14-C13	1.384(9)
C14-C15	1.394(9)	C14-H14	0.95
F2-C1	1.475(13)	F3-C1	1.174(11)
C30-C9	1.355(9)	C30-C10	1.437(8)
C8-C9	1.504(9)	C28-H28A	0.99
C28-H28B	0.99	O2-N3	1.348 (16)
N3-O3	1.414(16)	C10-C15	1.399(8)
C10-C11	1.424(9)	C13-C12	1.406(9)
C13-H13	0.95	C12-C11	1.346(9)
C12-H12	0.95	C11-H11	0.95
F4-C29	1.241(18)	F5-C29	1.49(4)
F6-C29	1.15(3)		

Table 5.13. Selected bond angles [°] for **2a** at 100 K.

Type of bond	Bond angle	Type of bond	Bond angle
C23-C22-C27	120.0	C23-C22-C28	120.2(6)
C27-C22-C28	119.7(5)	N3-C23-C24	119.4(9)
N3-C23-C22	120.6(9)	C24-C23-C22	120.0
C25-C24-C23	120.0	C25-C24-H24	120.0
C23-C24-H24	120.0	C24-C25-C26	120.0

C24-C25-H25	120.0	C26-C25-H25	120.0
C25-C26-C27	120.0	C25-C26-H26	120.0
C27-C26-H26	120.0	C26-C27-C22	120.0
C26-C27-H27	120.0	C22-C27-H27	120.0
C8-N1-C5	124.2(5)	C8-N1-C28	116.7(5)
C5-N1-C28	118.9(5)	C3-C2-C7	120.0
C3-C2-C1	120.3(5)	C7-C2-C1	119.7(5)
C4-C3-C2	120.0	C4-C3-H3	120.0
C2-C3-H3	120.0	C3-C4-C5	120.0
C3-C4-H4	120.0	C5-C4-H4	120.0
C6-C5-C4	120.0	C6-C5-N1	119.5(3)
C4-C5-N1	120.5(3)	C5-C6-C7	120.0
C5-C6-H6	120.0	C7-C6-H6	120.0
C6-C7-C2	120.0	C6-C7-H7	120.0
C2-C7-H7	120.0	C17-C16-C21	120.0
C17-C16-C30	120.0(4)	C21-C16-C30	119.8(4)
C16-C17-C18	120.0	C16-C17-H17	120.0
C18-C17-H17	120.0	C19-C18-C17	120.0
C19-C18-H18	120.0	C17-C18-H18	120.0
C18-C19-C20	120.0	C18-C19-C29	114.6(14)
C20-C19-C29	125.3(14)	C19-C20-C21	120.0
C19-C20-H20	120.0	C21-C20-H20	120.0
C20-C21-C16	120.0	C20-C21-H21	120.0
C16-C21-H21	120.0	C15-N2-C9	108.4(5)
C15-N2-H2	125.8	C9-N2-H2	125.8
C13-C14-C15	115.8(6)	C13-C14-H14	122.1
C15-C14-H14	122.1	C9-C30-C10	105.7(5)
C9-C30-C16	129.1(5)	C10-C30-C16	125.1(5)
O1-C8-N1	121.5(6)	O1-C8-C9	119.4(5)

N1-C8-C9	119.1(5)	C30-C9-N2	110.5(5)
C30-C9-C8	132.3(5)	N2-C9-C8	117.2(5)
F3-C1-F1	114.1(9)	F3-C1-C2	119.1(9)
F1-C1-C2	116.8(8)	F3-C1-F2	100.0(11)
F1-C1-F2	91.6(8)	C2-C1-F2	109.6(8)
N1-C28-C22	108.8(7)	N1-C28-H28A	109.9
C22-C28-H28A	109.9	N1-C28-H28B	109.9
C22-C28-H28B	109.9	H28A-C28-H28B	108.3
C23-N3-O2	136.1(12)	C23-N3-O3	131.7(13)
O2-N3-O3	91.3(13)	C15-C10-C11	118.5(5)
C15-C10-C30	107.5(5)	C11-C10-C30	134.0(6)
N2-C15-C14	128.7(6)	N2-C15-C10	107.9(5)
C14-C15-C10	123.4(5)	C14-C13-C12	121.9(6)
C14-C13-H13	119.0	C12-C13-H13	119.0
C11-C12-C13	121.8(6)	C11-C12-H12	119.1
C13-C12-H12	119.1	C12-C11-C10	118.5(6)
C12-C11-H11	120.7	C10-C11-H11	120.7
F6-C29-F4	110.(2)	F6-C29-C19	122.(2)
F4-C29-C19	117.8(12)	F6-C29-F5	98.9(17)
F4-C29-F5	97.(2)	C19-C29-F5	106.(2)

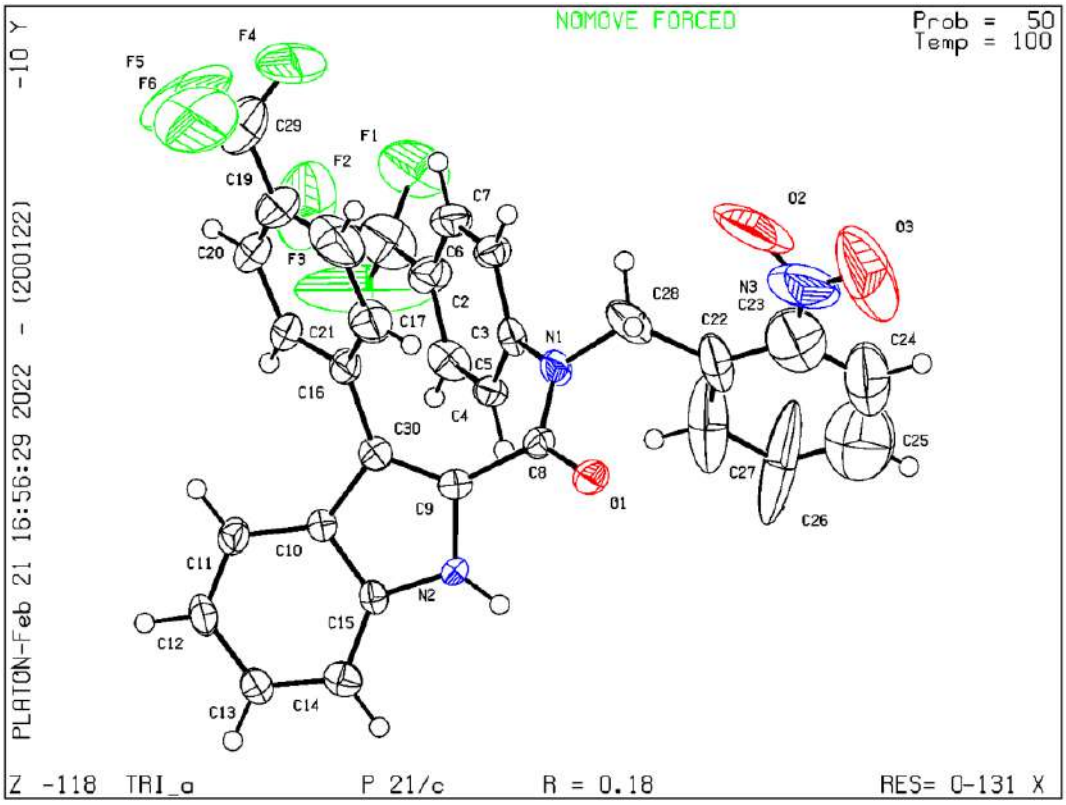

Figure 5.54. ORTEP diagram of **5a**. Ellipsoids are drawn at 50% probability.

Crystallization for 5d

5d (10mg) in 2 mL of acetonitrile was shortly heated and the solution was filtered through a cotton plug to seperate any undissolved compound. Suitable crystals for X-ray analysis were obtained by slow evaporation of the solovant.

Table 5.14. Crystallographic data of **5d** at 100 K.

Crystallographic details	**5d**
Chemical formula	$C_{37}H_{25}F_6N_3O_4$
Formula weight (g/mol)	689.60
Temperature	100(2)K
Crystal system	Monoclinic
Space group	*P 1 21 1*
a (Å); α (°)	11.639(5); 90
b (Å); β (°)	14.954(7); 98.594(11)
c (Å); γ (°)	18.483(8); 90
V (Å^3); Z	3181.(2); 4

ρ (calc.) g cm^{-3}	1.440
μ(Mo K_α) mm^{-1}	0.118
$2\theta_{max}$ (°)	49.54
R(int)	0.1464
Completeness to θ	99.8
Data / param.	10653/903
GOF	0.954
R1 [F>4σ(F)]	0.0657
wR2 (all data)	0.1689
max. peak/hole (e.$Å^{-3}$)	0.321/-0.336

Table 5.15. Selected bond lengths [Å] for **5d** at 100 K.

Type of bond	Bond length	Type of bond	Bond length
F1-C22	1.343(12)	F2-C22	1.343(11)
F3-C22	1.355(11)	F4-C38	1.355(11)
F5-C38	1.334(11)	F6-C38	1.325(12)
F7-C60	1.343(14)	F8-C60	1.337(12)
F9-C60	1.334(13)	F10-C75	1.343(14)
F11-C75	1.342(12)	F12-C75	1.355(12)
O5-C40	1.382(11)	O5-C39	1.448(10)
O4-C23	1.245(10)	O7-N4	1.234(9)
O8-C01O	1.243(10)	O6-N4	1.242(9)
O3-N1	1.231(9)	O1-C2	1.362(10)
O1-C1	1.437(11)	O2-N1	1.224(10)
N4-C51	1.463(11)	N1-C10	1.476(12)
N6-C61	1.373(12)	N6-C64	1.398(11)
N6-H6	0.88	N2-C23	1.377(11)
N2-C16	1.426(11)	N2-C14	1.487(11)
N5-C01O	1.372(12)	N5-C54	1.434(11)
N5-C52	1.471(11)	N3-C27	1.359(11)
N3-C24	1.384(11)	N3-H3	0.88

C34-C37	1.380(12)	C34-C33	1.387(12)
C34-H34	0.95	C61-C62	1.377(12)
C61-C01O	1.477(13)	C10-C13	1.392(12)
C10-C9	1.406(11)	C33-C32	1.397(13)
C33-H33	0.95	C37-C36	1.388(14)
C37-C38	1.476(13)	C32-C35	1.399(13)
C32-C25	1.479(13)	C51-C47	1.388(11)
C51-C100	1.408(12)	C54-C55	1.389(13)
C54-C57	1.393(13)	C17-C16	1.390(14)
C17-C19	1.394(13)	C17-H17	0.95
C45-C43	1.391(12)	C45-C44	1.404(13)
C45-C46	1.481(12)	C69-C70	1.390(12)
C69-C72	1.405(11)	C69-C62	1.480(13)
C62-C63	1.440(13)	C19-C21	1.393(12)
C19-H19	0.95	C22-C21	1.489(13)
C23-C24	1.474(13)	C21-C20	1.372(14)
C59-C56	1.361(13)	C59-C58	1.410(13)
C59-C60	1.477(13)	C14-C13	1.531(12)
C14-H14A	0.99	C14-H14B	0.99
C44-C42	1.377(12)	C44-H44	0.95
C70-C71	1.396(12)	C70-H70	0.95
C18-C20	1.392(13)	C18-C16	1.394(12)
C18-H18	0.95	C46-C48	1.386(12)
C46-C47	1.389(12)	C27-C28	1.410(13)
C27-C26	1.417(12)	C74-C73	1.385(13)
C74-C71	1.391(12)	C74-C75	1.476(14)
C13-C12	1.377(13)	C6-C7	1.392(13)
C6-C5	1.392(11)	C6-H6A	0.95
C26-C31	1.410(12)	C26-C25	1.427(12)

C12-C11	1.390(12)	C12-H12	0.95
C8-C9	1.375(13)	C8-C11	1.400(13)
C8-C7	1.490(12)	C24-C25	1.391(12)
C55-C56	1.394(12)	C55-H55	0.95
C11-H11	0.95	C5-C2	1.390(13)
C5-H5	0.95	C66-C65	1.383(13)
C66-C67	1.411(13)	C66-H66	0.95
C40-C41	1.370(13)	C40-C42	1.400(12)
C42-H42	0.95	C36-C35	1.396(13)
C36-H36	0.95	C9-H9	0.95
C64-C65	1.383(14)	C64-C63	1.415(12)
C7-C4	1.389(14)	C52-C100	1.508(12)
C52-H52A	0.99	C52-H52B	0.99
C65-H65	0.95	C2-C3	1.373(13)
C43-C41	1.402(12)	C43-H43	0.95
C100-C49	1.391(13)	C28-C29	1.389(13)
C28-H28	0.95	C71-H71	0.95
C30-C31	1.366(13)	C30-C29	1.411(13)
C30-H30	0.95	C4-C3	1.395(12)
C4-H4	0.95	C58-C57	1.388(12)
C58-H58	0.95	C63-C68	1.403(12)
C72-C73	1.363(12)	C72-H72	0.95
C56-H56	0.95	C47-H47	0.95
C68-C67	1.372(14)	C68-H68	0.95
C41-H41	0.95	C48-C49	1.388(12)
C48-H48	0.95	C31-H31	0.95
C57-H57	0.95	C67-H67	0.95
C73-H73	0.95	C49-H49	0.95
C35-H35	0.95	C20-H20	0.95

C3-H3A	0.95	C29-H29	0.95
C1-H1A	0.98	C1-H1B	0.98
C1-H1C	0.98	C39-H39A	0.98
C39-H39B	0.98	C39-H39C	0.98

Table 5.16. Selected bond angles [°] for **5d** at 100 K.

Type of bond	Bond angle	Type of bond	Bond angle
C40-O5-C39	115.6(8)	C2-O1-C1	117.8(8)
O7-N4-O6	122.6(8)	O7-N4-C51	118.7(7)
O6-N4-C51	118.7(8)	O2-N1-O3	125.4(9)
O2-N1-C10	117.7(8)	O3-N1-C10	116.9(8)
C61-N6-C64	109.0(7)	C61-N6-H6	125.5
C64-N6-H6	125.5	C23-N2-C16	124.1(8)
C23-N2-C14	115.8(7)	C16-N2-C14	120.0(7)
C01O-N5-C54	124.0(8)	C01O-N5-C52	115.8(8)
C54-N5-C52	120.1(8)	C27-N3-C24	109.2(7)
C27-N3-H3	125.4	C24-N3-H3	125.4
C37-C34-C33	119.8(9)	C37-C34-H34	120.1
C33-C34-H34	120.1	N6-C61-C62	110.0(9)
N6-C61-C01O	117.1(8)	C62-C61-C01O	132.7(9)
C13-C10-C9	121.8(9)	C13-C10-N1	121.8(8)
C9-C10-N1	116.3(8)	C34-C33-C32	121.1(9)
C34-C33-H33	119.5	C32-C33-H33	119.5
C34-C37-C36	120.7(9)	C34-C37-C38	119.1(9)
C36-C37-C38	120.2(9)	C33-C32-C35	118.2(9)
C33-C32-C25	122.2(9)	C35-C32-C25	119.4(9)
C47-C51-C100	123.2(9)	C47-C51-N4	117.1(8)
C100-C51-N4	119.5(8)	C55-C54-C57	119.8(9)
C55-C54-N5	120.4(9)	C57-C54-N5	119.9(9)

F6-C38-F5	107.0(8)	F6-C38-F4	105.6(9)
F5-C38-F4	104.6(8)	F6-C38-C37	113.0(9)
F5-C38-C37	114.1(9)	F4-C38-C37	111.9(8)
C16-C17-C19	120.6(9)	C16-C17-H17	119.7
C19-C17-H17	119.7	C43-C45-C44	118.1(9)
C43-C45-C46	121.6(9)	C44-C45-C46	120.3(8)
C70-C69-C72	117.8(9)	C70-C69-C62	122.1(8)
C72-C69-C62	120.1(8)	C61-C62-C63	106.6(8)
C61-C62-C69	129.2(9)	C63-C62-C69	124.1(8)
C21-C19-C17	119.3(9)	C21-C19-H19	120.4
C17-C19-H19	120.4	F1-C22-F2	106.3(9)
F1-C22-F3	106.0(8)	F2-C22-F3	107.1(8)
F1-C22-C21	112.4(8)	F2-C22-C21	112.7(9)
F3-C22-C21	111.9(9)	O4-C23-N2	119.6(8)
O4-C23-C24	119.3(9)	N2-C23-C24	121.0(8)
C20-C21-C19	120.1(9)	C20-C21-C22	120.5(9)
C19-C21-C22	119.3(9)	C56-C59-C58	120.5(9)
C56-C59-C60	121.5(10)	C58-C59-C60	117.9(9)
N2-C14-C13	111.9(8)	N2-C14-H14A	109.2
C13-C14-H14A	109.2	N2-C14-H14B	109.2
C13-C14-H14B	109.2	H14A-C14-H14B	107.9
C42-C44-C45	121.3(9)	C42-C44-H44	119.3
C45-C44-H44	119.3	C69-C70-C71	121.3(8)
C69-C70-H70	119.3	C71-C70-H70	119.3
C20-C18-C16	119.4(10)	C20-C18-H18	120.3
C16-C18-H18	120.3	C48-C46-C47	117.7(8)
C48-C46-C45	121.0(8)	C47-C46-C45	121.2(8)
C17-C16-C18	119.5(9)	C17-C16-N2	119.9(8)
C18-C16-N2	120.6(9)	N3-C27-C28	129.9(9)

N3-C27-C26	108.0(8)	C28-C27-C26	122.0(9)
C73-C74-C71	120.0(9)	C73-C74-C75	120.6(9)
C71-C74-C75	119.3(9)	C12-C13-C10	117.0(8)
C12-C13-C14	120.9(8)	C10-C13-C14	122.0(9)
C7-C6-C5	121.1(9)	C7-C6-H6A	119.4
C5-C6-H6A	119.4	C31-C26-C27	118.8(9)
C31-C26-C25	133.9(9)	C27-C26-C25	107.3(8)
C13-C12-C11	121.7(9)	C13-C12-H12	119.2
C11-C12-H12	119.2	C9-C8-C11	117.8(8)
C9-C8-C7	121.4(9)	C11-C8-C7	120.7(9)
N3-C24-C25	109.2(8)	N3-C24-C23	115.1(8)
C25-C24-C23	135.1(9)	C54-C55-C56	119.6(9)
C54-C55-H55	120.2	C56-C55-H55	120.2
O8-C01O-N5	119.4(9)	O8-C01O-C61	119.8(9)
N5-C01O-C61	120.6(8)	C12-C11-C8	121.0(10)
C12-C11-H11	119.5	C8-C11-H11	119.5
C2-C5-C6	119.2(9)	C2-C5-H5	120.4
C6-C5-H5	120.4	C24-C25-C26	106.2(8)
C24-C25-C32	130.4(8)	C26-C25-C32	123.3(8)
C65-C66-C67	120.2(10)	C65-C66-H66	119.9
C67-C66-H66	119.9	C41-C40-O5	126.1(9)
C41-C40-C42	121.0(9)	O5-C40-C42	112.9(9)
C44-C42-C40	119.2(10)	C44-C42-H42	120.4
C40-C42-H42	120.4	C37-C36-C35	119.3(9)
C37-C36-H36	120.4	C35-C36-H36	120.4
C8-C9-C10	120.4(9)	C8-C9-H9	119.8
C10-C9-H9	119.8	C65-C64-N6	129.9(9)
C65-C64-C63	123.2(9)	N6-C64-C63	107.0(9)
C4-C7-C6	119.1(9)	C4-C7-C8	118.7(9)

C6-C7-C8	122.2(9)	N5-C52-C100	111.9(7)
N5-C52-H52A	109.2	C100-C52-H52A	109.2
N5-C52-H52B	109.2	C100-C52-H52B	109.2
H52A-C52-H52B	107.9	C66-C65-C64	117.3(9)
C66-C65-H65	121.4	C64-C65-H65	121.4
O1-C2-C3	115.9(9)	O1-C2-C5	124.3(9)
C3-C2-C5	119.9(9)	C45-C43-C41	121.1(10)
C45-C43-H43	119.5	C41-C43-H43	119.5
C49-C100-C51	115.1(9)	C49-C100-C52	121.6(8)
C51-C100-C52	123.2(9)	C29-C28-C27	116.9(10)
C29-C28-H28	121.6	C27-C28-H28	121.6
C74-C71-C70	119.1(9)	C74-C71-H71	120.5
C70-C71-H71	120.5	C31-C30-C29	121.0(9)
C31-C30-H30	119.5	C29-C30-H30	119.5
C7-C4-C3	119.4(10)	C7-C4-H4	120.3
C3-C4-H4	120.3	C57-C58-C59	118.8(9)
C57-C58-H58	120.6	C59-C58-H58	120.6
C68-C63-C64	118.6(9)	C68-C63-C62	133.9(9)
C64-C63-C62	107.4(8)	C73-C72-C69	121.3(9)
C73-C72-H72	119.4	C69-C72-H72	119.4
C59-C56-C55	120.7(9)	C59-C56-H56	119.7
C55-C56-H56	119.7	C51-C47-C46	120.0(8)
C51-C47-H47	120.0	C46-C47-H47	120.0
C67-C68-C63	118.1(9)	C67-C68-H68	120.9
C63-C68-H68	120.9	C40-C41-C43	119.2(9)
C40-C41-H41	120.4	C43-C41-H41	120.4
C46-C48-C49	121.8(9)	C46-C48-H48	119.1
C49-C48-H48	119.1	C30-C31-C26	119.6(9)
C30-C31-H31	120.2	C26-C31-H31	120.2

C58-C57-C54	120.6(9)	C58-C57-H57	119.7
C54-C57-H57	119.7	C68-C67-C66	122.5(9)
C68-C67-H67	118.7	C66-C67-H67	118.7
C72-C73-C74	120.5(9)	C72-C73-H73	119.8
C74-C73-H73	119.8	C48-C49-C100	122.1(9)
C48-C49-H49	119.0	C100-C49-H49	119.0
C36-C35-C32	120.9(10)	C36-C35-H35	119.5
C32-C35-H35	119.5	C21-C20-C18	121.0(9)
C21-C20-H20	119.5	C18-C20-H20	119.5
C2-C3-C4	121.2(10)	C2-C3-H3A	119.4
C4-C3-H3A	119.4	F9-C60-F8	105.8(10)
F9-C60-F7	104.5(9)	F8-C60-F7	105.6(9)
F9-C60-C59	113.4(10)	F8-C60-C59	112.9(9)
F7-C60-C59	113.8(10)	C28-C29-C30	121.7(10)
C28-C29-H29	119.2	C30-C29-H29	119.2
F11-C75-F10	105.4(10)	F11-C75-F12	106.2(9)
F10-C75-F12	105.7(10)	F11-C75-C74	113.1(10)
F10-C75-C74	113.5(10)	F12-C75-C74	112.4(10)
O1-C1-H1A	109.5	O1-C1-H1B	109.5
H1A-C1-H1B	109.5	O1-C1-H1C	109.5
H1A-C1-H1C	109.5	H1B-C1-H1C	109.5
O5-C39-H39A	109.5	O5-C39-H39B	109.5
H39A-C39-H39B	109.5	O5-C39-H39C	109.5
H39A-C39-H39C	109.5	H39B-C39-H39C	109.5

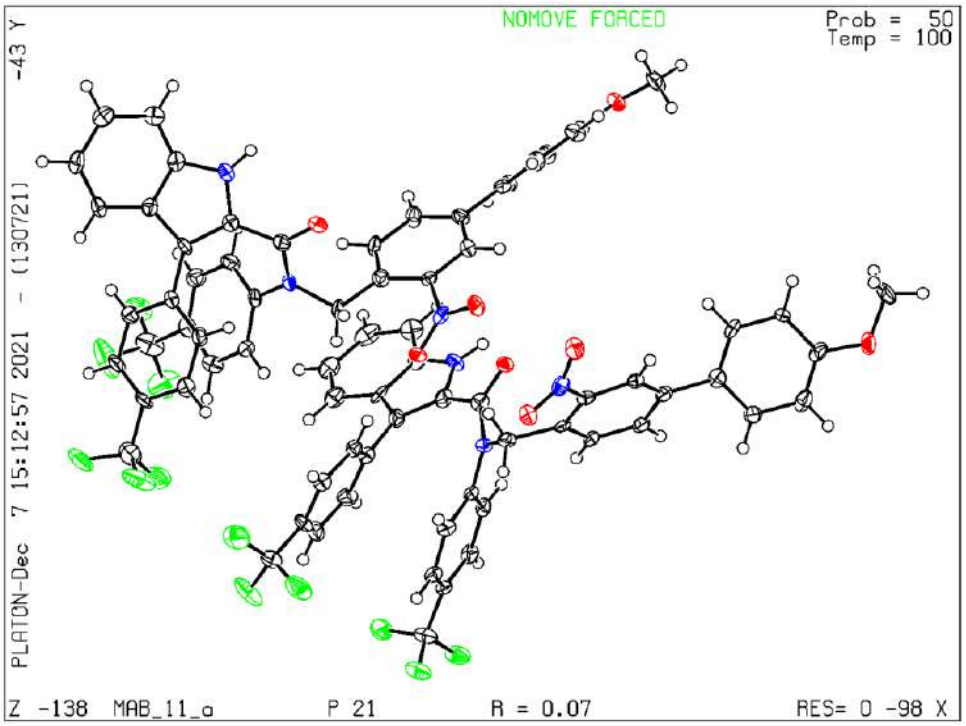

Figure 5.55. ORTEP diagram of **5d**. Ellipsoids are drawn at 50% probability.

Crystallization for 7e

7e (10 mg) in 2 mL of acetonitrile was shortly heated and the solution was filtered through a cotton plug to seperate any undissolved compound. Suitable crystals for X-ray analysis were obtained by slow evaporation of the solovant.

Table 5.17. Crystallographic data of **7e** at 100 K.

Crystallographic details	**7e**
Chemical formula	$C_{15}H_{11}F_3N_2O_4$
Formula weight (g/mol)	340.26
Temperature	100(2)K
Crystal system	Monoclinic
Space group	*P 1 21/n 1*
a (Å); α (°)	8.3389(15); 90
b (Å); β (°)	5.3319(10); 92.827(6)
c (Å); γ (°)	30.853(5); 90
V (Å^3); Z	1370.1(4); 4
ρ (calc.) g cm^{-3}	1.650
μ(Mo K$_\alpha$) mm^{-1}	0.147

$2\theta_{max}$ (°)	49.64
R(int)	0.0690
Completeness to θ	99.3
Data / param.	2344/217
GOF	1.060
R1 [F>4σ(F)]	0.0423
wR2 (all data)	0.1159
max. peak/hole (e.Å^{-3})	0.429/-0.449

Table 5.18. Selected bond lengths [Å] for **7e** at 100 K.

Type of bond	Bond length	Type of bond	Bond length
F1-C1	1.344(3)	F2-C1	1.352(3)
F3-C1	1.332(3)	O4-C13	1.376(3)
O4-C15	1.432(3)	O3-C14	1.361(3)
O3-C15	1.441(3)	O2-N2	1.236(3)
O1-N2	1.231(3)	N2-C10	1.456(3)
N1-C7	1.379(3)	N1-C8	1.452(3)
N1-H1	0.88	C3-C6	1.380(3)
C3-C2	1.390(3)	C3-H3	0.95
C4-C5	1.381(3)	C4-C2	1.392(3)
C4-H4	0.95	C5-C7	1.399(3)
C5-H5	0.95	C7-C6	1.401(3)
C2-C1	1.486(4)	C6-H6	0.95
C10-C9	1.406(3)	C10-C11	1.407(3)
C13-C11	1.357(4)	C13-C14	1.380(4)
C9-C12	1.405(3)	C9-C8	1.529(3)
C14-C12	1.369(4)	C11-H11	0.95
C12-H12	0.95	C8-H8A	0.99
C8-H8B	0.99	C15-H15A	0.99
C15-H15B	0.99		

Table 5.19. Selected bond angles [°] for **7e** at 100 K.

Type of bond	Bond angle	Type of bond	Bond angle
C13-O4-C15	105.71(19)	C14-O3-C15	105.8(2)
O1-N2-O2	121.9(2)	O1-N2-C10	119.6(2)
O2-N2-C10	118.5(2)	C7-N1-C8	121.9(2)
C7-N1-H1	119.1	C8-N1-H1	119.1
C6-C3-C2	120.8(2)	C6-C3-H3	119.6
C2-C3-H3	119.6	C5-C4-C2	119.9(2)
C5-C4-H4	120.0	C2-C4-H4	120.0
C4-C5-C7	121.1(2)	C4-C5-H5	119.5
C7-C5-H5	119.5	N1-C7-C5	120.0(2)
N1-C7-C6	121.5(2)	C5-C7-C6	118.6(2)
C3-C2-C4	119.4(2)	C3-C2-C1	119.4(2)
C4-C2-C1	121.0(2)	C3-C6-C7	120.2(2)
C3-C6-H6	119.9	C7-C6-H6	119.9
C9-C10-C11	123.4(2)	C9-C10-N2	121.5(2)
C11-C10-N2	115.2(2)	C11-C13-O4	128.3(2)
C11-C13-C14	121.7(2)	O4-C13-C14	110.0(2)
C12-C9-C10	117.6(2)	C12-C9-C8	117.7(2)
C10-C9-C8	124.7(2)	O3-C14-C12	127.0(2)
O3-C14-C13	110.4(2)	C12-C14-C13	122.6(2)
C13-C11-C10	116.3(2)	C13-C11-H11	121.8
C10-C11-H11	121.8	C14-C12-C9	118.4(2)
C14-C12-H12	120.8	C9-C12-H12	120.8
N1-C8-C9	114.6(2)	N1-C8-H8A	108.6
C9-C8-H8A	108.6	N1-C8-H8B	108.6
C9-C8-H8B	108.6	H8A-C8-H8B	107.6
F3-C1-F1	106.8(2)	F3-C1-F2	106.0(2)
F1-C1-F2	104.9(2)	F3-C1-C2	113.5(2)

F1-C1-C2	113.0(2)	F2-C1-C2	111.9(2)
O4-C15-O3	108.0(2)	O4-C15-H15A	110.1
O3-C15-H15A	110.1	O4-C15-H15B	110.1
O3-C15-H15B	110.1	H15A-C15-H15B	108.4

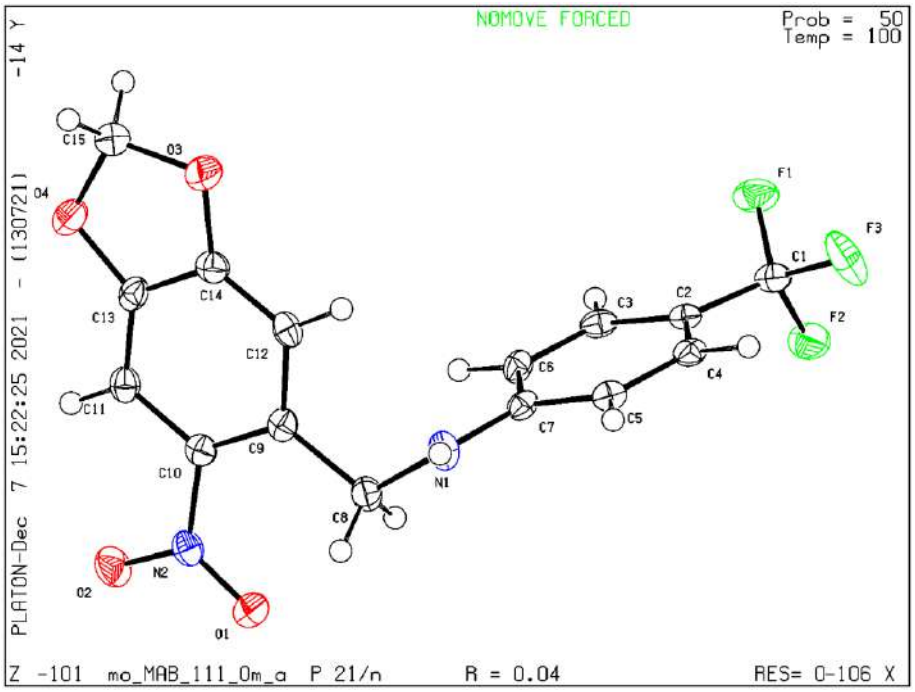

Figure 5.56. ORTEP diagram of **7e**. Ellipsoids are drawn at 50% probability.

5.4.10. Geometry optimization and binding energy calculations

To get an idea about the conformation of [(**5′**)$_2$+Cl$^-$], several initial geometries of the complex were generated using the CONFLEX 8[S9] software packageS9 using MMFF94s force field. The Boltzmann population of the geometries (Conf-1–Conf-9) obtained were 7.53%, 7.41%, 7.28%, 6.99%, 6.93%, 6.88%, 6.86%, 6.81%, and 6.78%, respectively (Figure S57A–I).

Among the several conformations, the highest Boltzmann populated structure was used for geometry optimization. The geometry optimization was carried out by Gaussian 09 programS10 package[S10] using B3LYP functional and 6-311++G(d,p) basis set.[S11] The structures (i.e., free receptor and the complex), the vibrational frequency calculated during the geometry optimization, shows no imaginary frequencies, which indicates that all optimized structures are ground state minima.

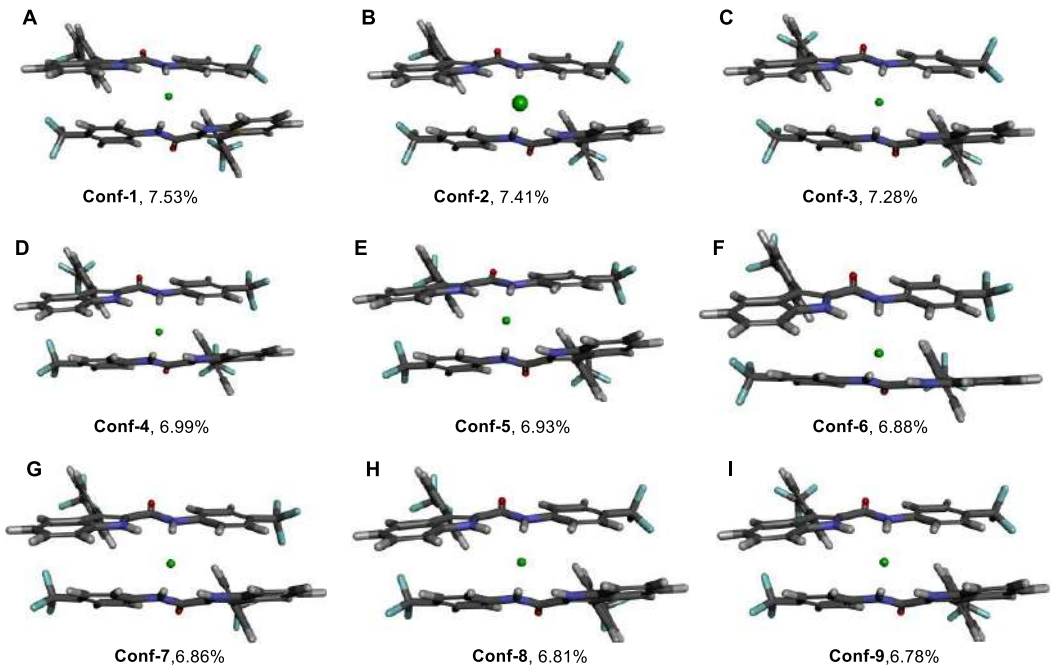

Figure 5.57. Initial geometries **Conf-1**–**Conf-9** (**A**–**I**) for [(**5′**)$_2$+Cl$^-$], optimized by CONFLEX 8 software using MMFF94s force field.

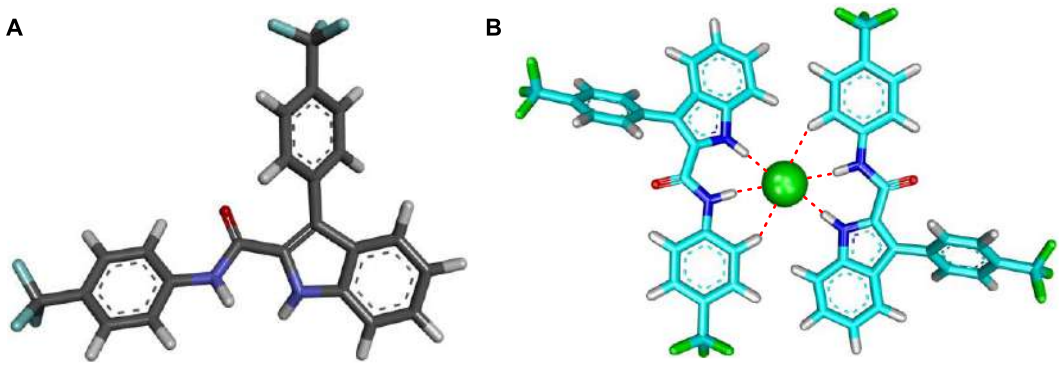

Figure 5.58. The geometry optimized structures of **5′** (**A**) and [(**5′**)$_2$ + Cl$^-$] (**B**).

The Gaussian 09 program was used to calculate the zero point energy (ZPE) and basis set superposition error (BSSE)[S3, S4] corrected bonding energy of [(**5′**)$_2$ + Cl$^-$] complex which was used for the calculation of binding energy (*BE*) using the following equations.

$$BE = [HF_{[M+X^-]} + ZPE_{[M+X^-]} + BSSE_{[M+X^-]}] - 2\times[HF_{\mathbf{M}} + ZPE_{\mathbf{M}}] - [HF_{Cl^-}] \qquad \text{Eq. S6}$$

where, $HF_{[M+X^-]}$ = electronic energy of [(**5′**)$_2$ + Cl$^-$] complex, $ZPE_{[M+X^-]}$ = zero point energy of [(**5′**)$_2$ + Cl$^-$] complex, $BSSE_{[M+X^-]}$ = BSSE of [(**5′**)$_2$ + Cl$^-$] complex, $HF_{\mathbf{M}}$ = electronic energy of the receptor **5′**, $ZPE_{\mathbf{M}}$ = zero point energy of the receptor **5′**, and HF_{Cl^-} = electronic energy of Cl$^-$.

Table 5.20. The electronic energy (HF), zero point energy (ZPE), basis set superposition error (BSSE) corrected energy (in Hartree unit) for all structures and complexes are calculated at the DFT B3LYP/6-31G(d,p) level of theory.

Structures	Energy
$HF_{[M+X^-]}$ (in Hartree)	–3797.8350322
$ZPE_{[M+X^-]}$ (in Hartree)	0.6579637
$BSSE_{[M+X^-]}$ (in Hartree)	0.014174845
$HF_{\mathbf{M}}$ (in Hartree)	–1668.7285333
$ZPE_{\mathbf{M}}$ (in Hartree)	0.3285074
HF_{Cl^-} (in Hartree)	–460.2522333
BE (in Hartree)	–0.11060852
BE (in kcal/mol)	–69.40784487

Table 5.21. Atomic coordinates of the optimized structure of lowest energy conformation obtained for **5′** from DFT B3LYP/6-31G(d,p) geometry optimization.

Charge = 0, Multiplicity = 1

Atom #	Atom Type	x	y	Z
1	C	4.178121	4.473606	-0.249254
2	C	3.146254	5.430315	-0.145169
3	C	1.819768	5.046721	0.001966
4	C	1.550875	3.675053	0.055182
5	C	2.574744	2.696019	-0.009324
6	C	3.906257	3.114773	-0.189143
7	N	0.341757	3.010861	0.149915
8	C	0.585015	1.636102	0.226686
9	C	1.943799	1.399818	0.109887
10	C	2.644560	0.102496	0.058379
11	C	3.800439	-0.100206	0.831266
12	C	4.492097	-1.307094	0.781353

13	C	4.039258	-2.335915	-0.046733
14	C	2.890785	-2.150207	-0.820806
15	C	2.203801	-0.942702	-0.768911
16	C	-0.530638	0.676347	0.409820
17	O	-0.393944	-0.403206	0.967843
18	N	-1.738178	1.140519	-0.100342
19	C	-2.999711	0.518699	-0.064576
20	C	-4.036966	1.125388	-0.793500
21	C	-5.313806	0.580884	-0.793552
22	C	-5.578198	-0.581331	-0.063970
23	C	-4.548742	-1.185961	0.660007
24	C	-3.263705	-0.650969	0.666662
25	C	-6.971898	-1.138706	-0.016525
26	F	-6.975460	-2.473297	0.195484
27	F	-7.644612	-0.907077	-1.167753
28	F	-7.705305	-0.583425	0.978948
29	F	4.033736	-4.664276	-0.478805
30	C	4.820713	-3.616022	-0.149653
31	F	5.442285	-3.922255	1.011624
32	F	5.785927	-3.539357	-1.098261
33	H	5.201539	4.810805	-0.380830
34	H	3.392857	6.486596	-0.191575
35	H	1.023400	5.782351	0.064268
36	H	4.704308	2.385142	-0.277920
37	H	-0.484349	3.434199	0.547824
38	H	4.142844	0.686312	1.495750
39	H	5.374111	-1.456051	1.394694
40	H	2.535809	-2.951550	-1.459361
41	H	1.317604	-0.805556	-1.378470
42	H	-1.673116	1.941617	-0.713737

43	H	-3.837943	2.027201	-1.367583
44	H	-6.103740	1.052711	-1.367466
45	H	-4.747906	-2.093515	1.219340
46	H	-2.465002	-1.129753	1.213632

Table 5.22. Atomic coordinates of the optimized structure of lowest energy conformation obtained for [(**5′**)$_2$ + Cl^-] complex from DFT B3LYP/6-31G(d,p) geometry optimization.

Charge = 0, Multiplicity = 1

Atom #	Atom Type	x	y	Z
1	C	4.560768	-4.869606	1.561212
2	C	4.489207	-3.486969	1.849233
3	C	3.306080	-2.780033	1.696036
4	C	2.182860	-3.493130	1.249238
5	C	2.224340	-4.886351	0.974099
6	C	3.447759	-5.571062	1.125402
7	N	0.915292	-3.050383	0.988834
8	C	0.133223	-4.105706	0.551382
9	C	0.907888	-5.269602	0.532036
10	C	0.545879	-6.645836	0.139849
11	C	0.908284	-7.721591	0.969371
12	C	0.639888	-9.038779	0.604974
13	C	0.000000	-9.309045	-0.605498
14	C	-0.370114	-8.250829	-1.442943
15	C	-0.099925	-6.939148	-1.073941
16	C	-1.313614	-3.978048	0.234757
17	O	-1.994386	-4.975982	-0.000837
18	N	-1.826829	-2.696070	0.218050
19	C	-3.153032	-2.311938	-0.040019
20	C	-3.419974	-0.928218	-0.053308

21	C	-4.702338	-0.456768	-0.293137
22	C	-5.749910	-1.354058	-0.529705
23	C	-5.488129	-2.725431	-0.520266
24	C	-4.206129	-3.213118	-0.280720
25	C	-7.143960	-0.845548	-0.726921
26	F	-7.909615	-1.706297	-1.441846
27	F	-7.167829	0.344148	-1.375185
28	F	-7.794044	-0.647302	0.450794
29	F	-1.354863	-10.853657	-1.787238
30	C	-0.234847	-10.725308	-1.036729
31	F	-0.359556	-11.568617	0.016540
32	F	0.786894	-11.207086	-1.792583
33	H	5.508317	-5.387105	1.680689
34	H	5.379259	-2.967790	2.192927
35	H	3.244523	-1.717833	1.910147
36	H	3.517048	-6.629838	0.896253
37	H	0.625106	-2.076034	1.117645
38	H	1.387249	-7.517473	1.921328
39	H	0.915096	-9.854167	1.265480
40	H	-0.875255	-8.457195	-2.380671
41	H	-0.400614	-6.126393	-1.723099
42	H	-1.205917	-1.908379	0.404280
43	H	-2.606144	-0.232124	0.124820
44	H	-4.886439	0.612628	-0.301161
45	H	-6.294223	-3.426457	-0.709820
46	H	-4.007224	-4.273855	-0.281044
47	C	-4.560768	4.869606	1.561212
48	C	-4.489207	3.486969	1.849233
49	C	-3.306080	2.780033	1.696036
50	C	-2.182860	3.493130	1.249238

51	C	-2.224340	4.886351	0.974099
52	C	-3.447759	5.571062	1.125402
53	N	-0.915292	3.050383	0.988834
54	C	-0.133223	4.105706	0.551382
55	C	-0.907888	5.269602	0.532036
56	C	-0.545879	6.645836	0.139849
57	C	-0.908284	7.721591	0.969371
58	C	-0.639888	9.038779	0.604974
59	C	0.000000	9.309045	-0.605498
60	C	0.370114	8.250829	-1.442943
61	C	0.099925	6.939148	-1.073941
62	C	1.313614	3.978048	0.234757
63	O	1.994386	4.975982	-0.000837
64	N	1.826829	2.696070	0.218050
65	C	3.153032	2.311938	-0.040019
66	C	3.419974	0.928218	-0.053308
67	C	4.702338	0.456768	-0.293137
68	C	5.749910	1.354058	-0.529705
69	C	5.488129	2.725431	-0.520266
70	C	4.206129	3.213118	-0.280720
71	C	7.143960	0.845548	-0.726921
72	F	7.167829	-0.344148	-1.375185
73	F	7.794044	0.647302	0.450794
74	F	7.909615	1.706297	-1.441846
75	F	1.354863	10.853657	-1.787238
76	C	0.234847	10.725308	-1.036729
77	F	0.359556	11.568617	0.016540
78	F	-0.786894	11.207086	-1.792583
79	H	-5.508317	5.387105	1.680689
80	H	-5.379259	2.967790	2.192927

81	H	-3.244523	1.717833	1.910147
82	H	-3.517048	6.629838	0.896253
83	H	-0.625106	2.076034	1.117645
84	H	-1.387249	7.517473	1.921328
85	H	-0.915096	9.854167	1.265480
86	H	0.875255	8.457195	-2.380671
87	H	0.400614	6.126393	-1.723099
88	H	1.205917	1.908379	0.404280
89	H	2.606144	0.232124	0.124820
90	H	4.886439	-0.612628	-0.301161
91	H	6.294223	3.426457	-0.709820
92	H	4.007224	4.273855	-0.281044
93	Cl	0.000000	0.000000	1.117645

5.4.11. NMR spectra

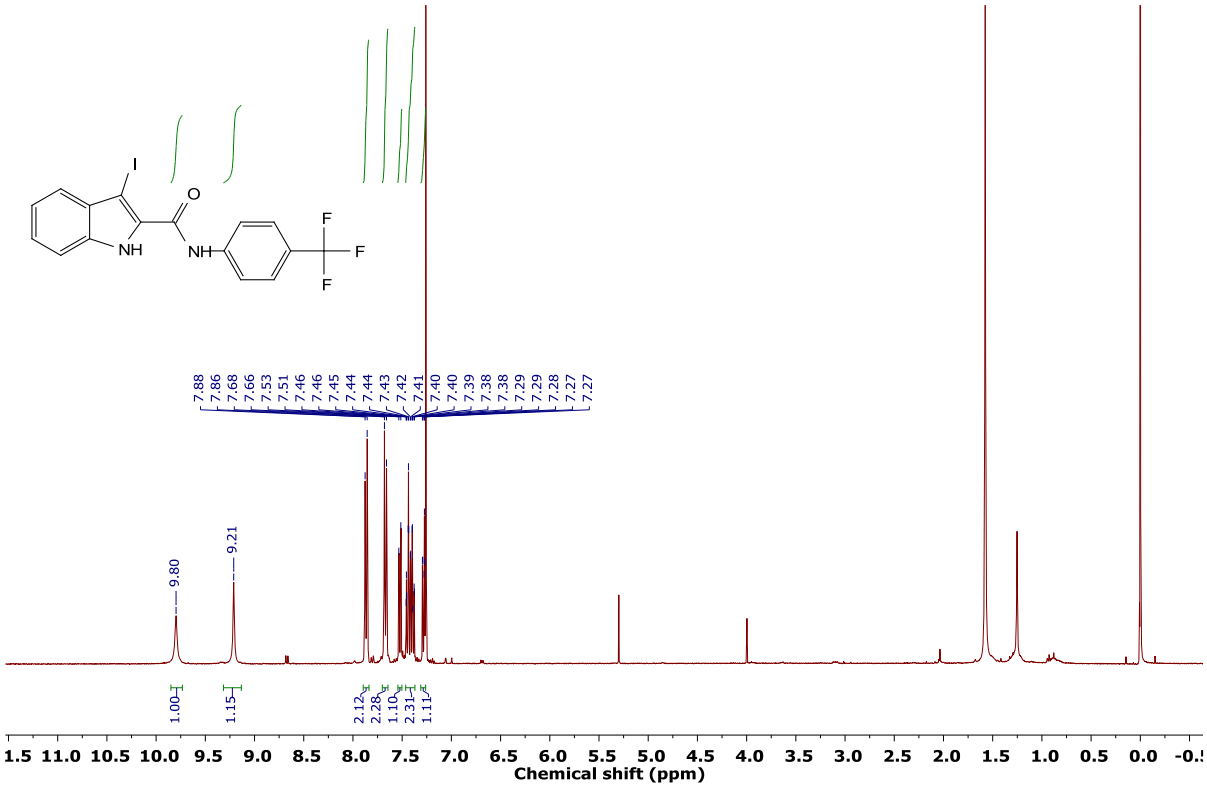

Figure 5.59. ^{1}H NMR spectrum (400 MHz) of **4** in $CDCl_3$ at room temperature.

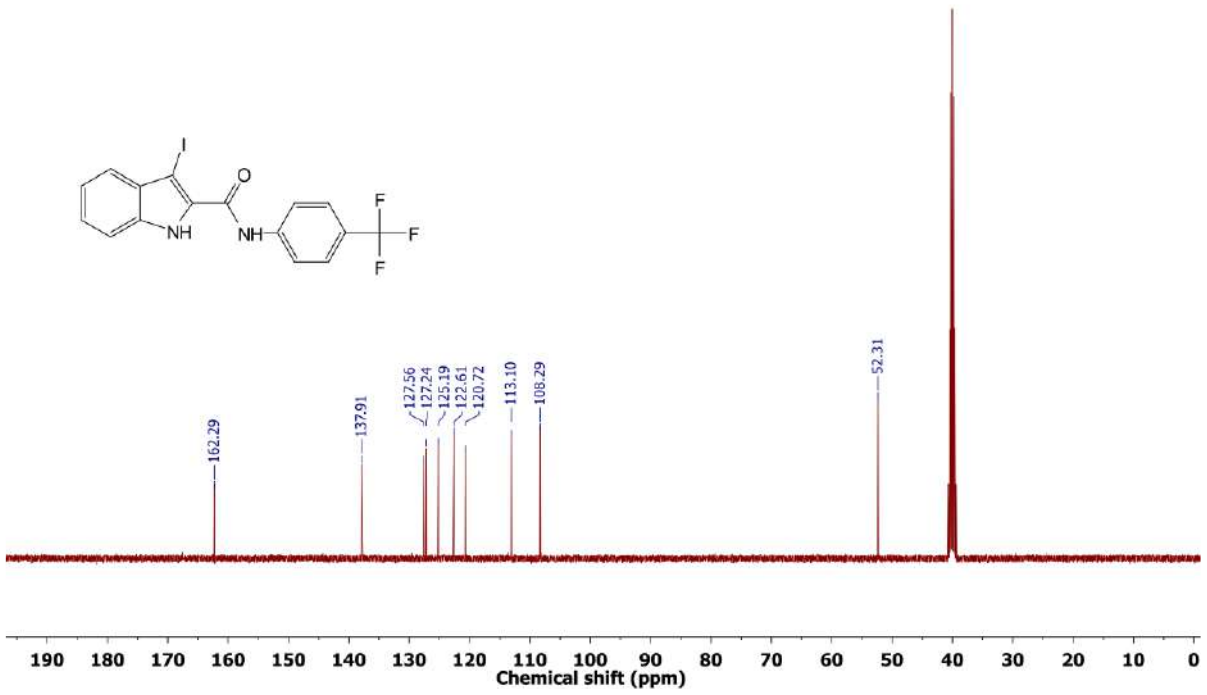

Figure 5.60. ^{13}C NMR spectrum (101 MHz) of **4** in $CDCl_3$ at room temperature.

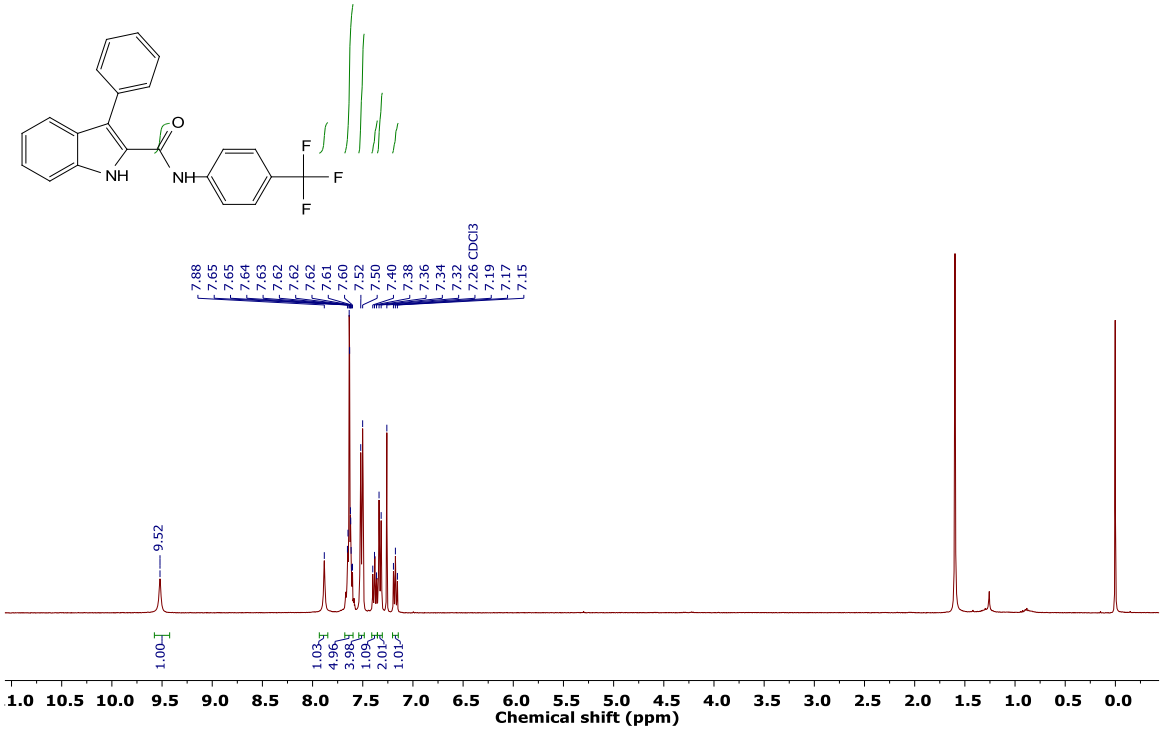

Figure 5.61. ^{1}H NMR spectrum (400 MHz) of **2′** in $CDCl_3$ at room temperature.

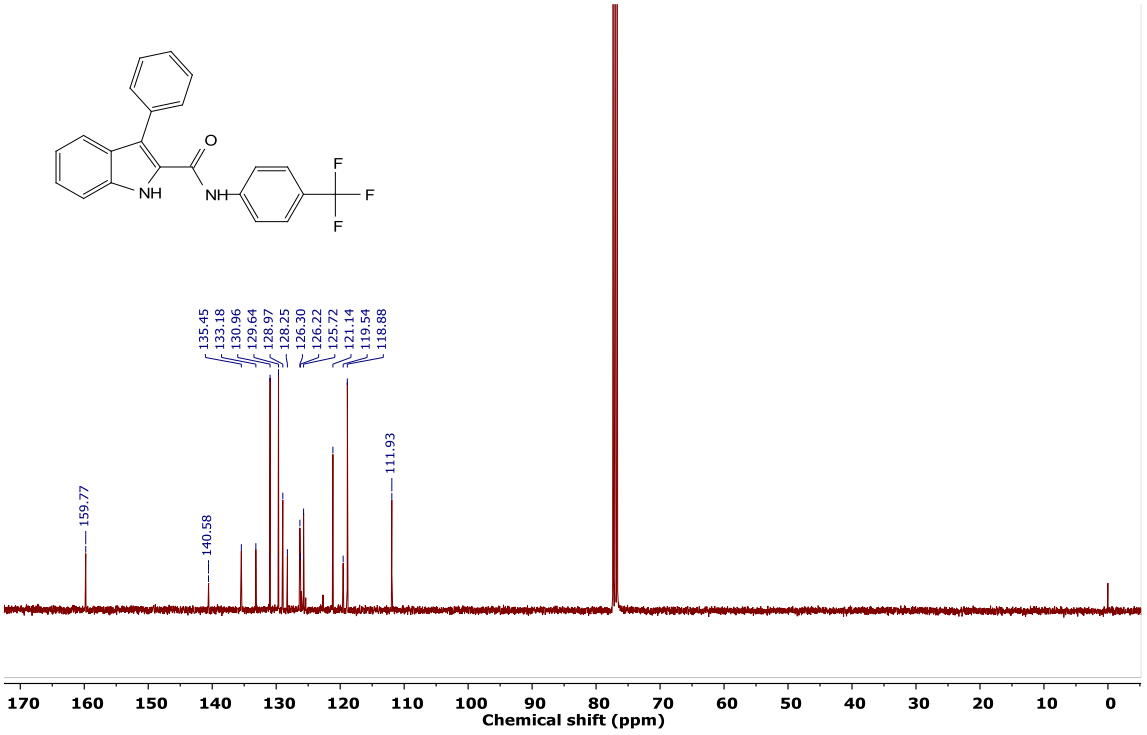

Figure 5.62. ^{13}C NMR spectrum (101 MHz) of **2′** in $CDCl_3$ at room temperature.

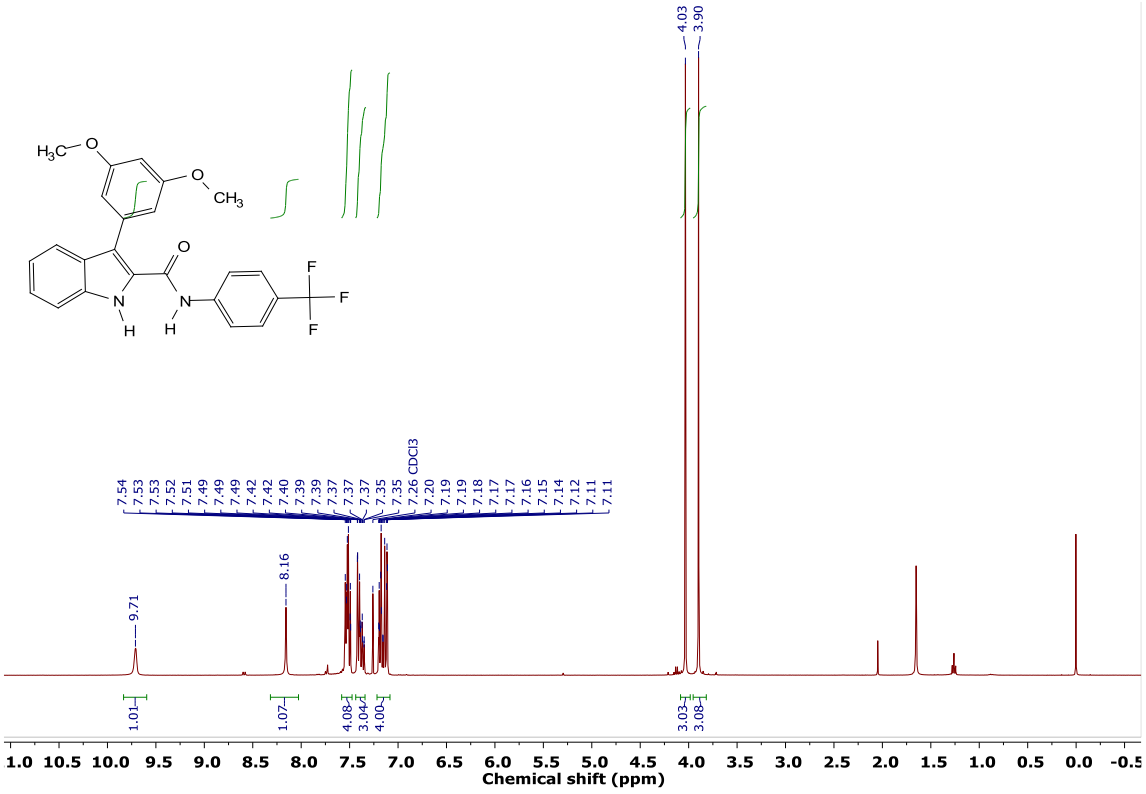

Figure 5.63. ^{1}H NMR spectrum (400 MHz) of **3′** in $CDCl_3$ at room temperature.

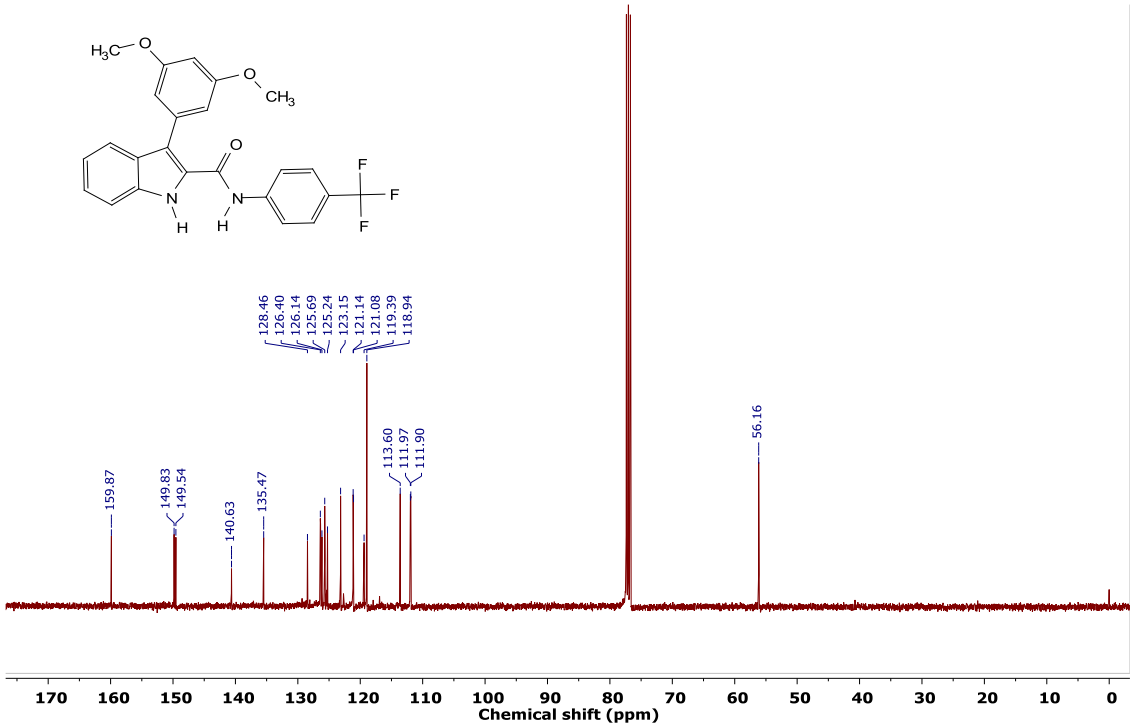

Figure 5.64. ^{13}C NMR spectrum (101 MHz) of **3′** in $CDCl_3$ at room temperature.

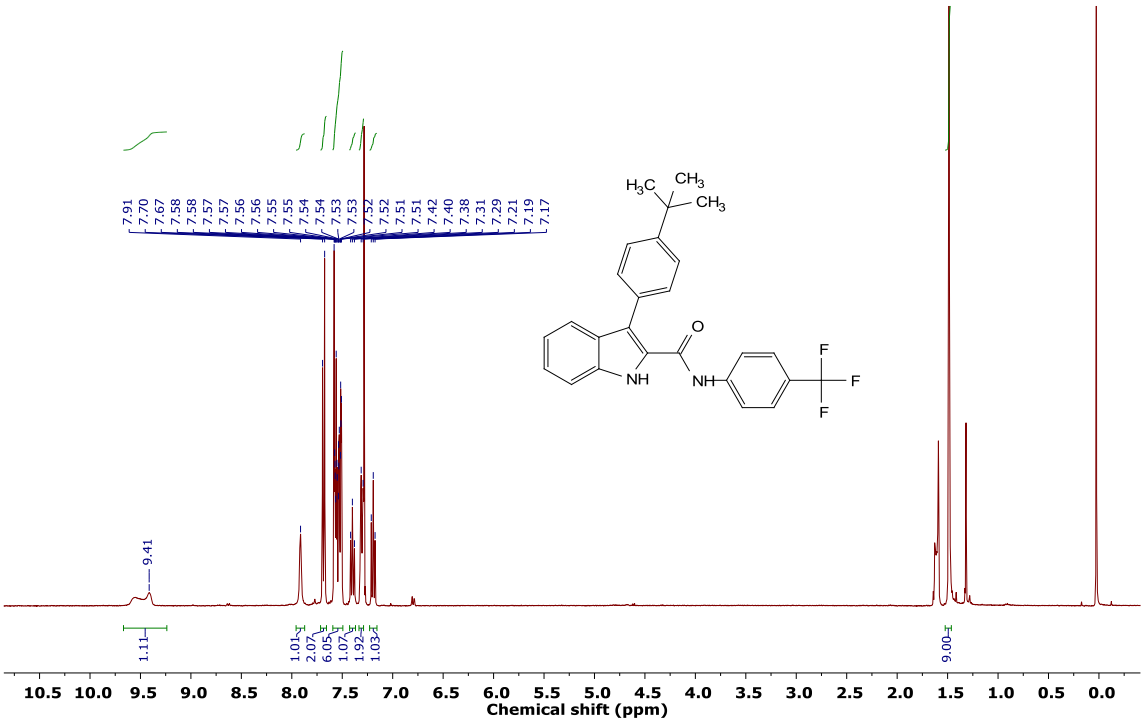

Figure 5.65. ^{1}H NMR spectrum (400 MHz) of **4′** in $CDCl_3$ at room temperature.

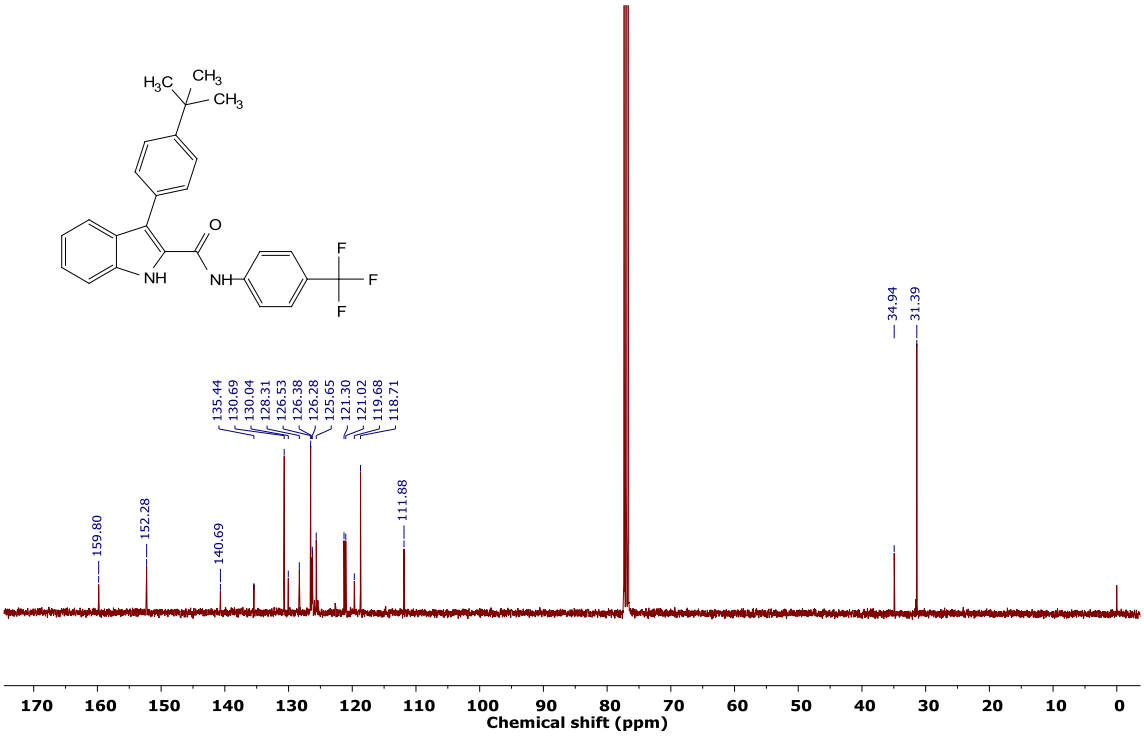

Figure 5.66. ^{13}C NMR spectrum (101 MHz) of **4′** in $CDCl_3$ at room temperature.

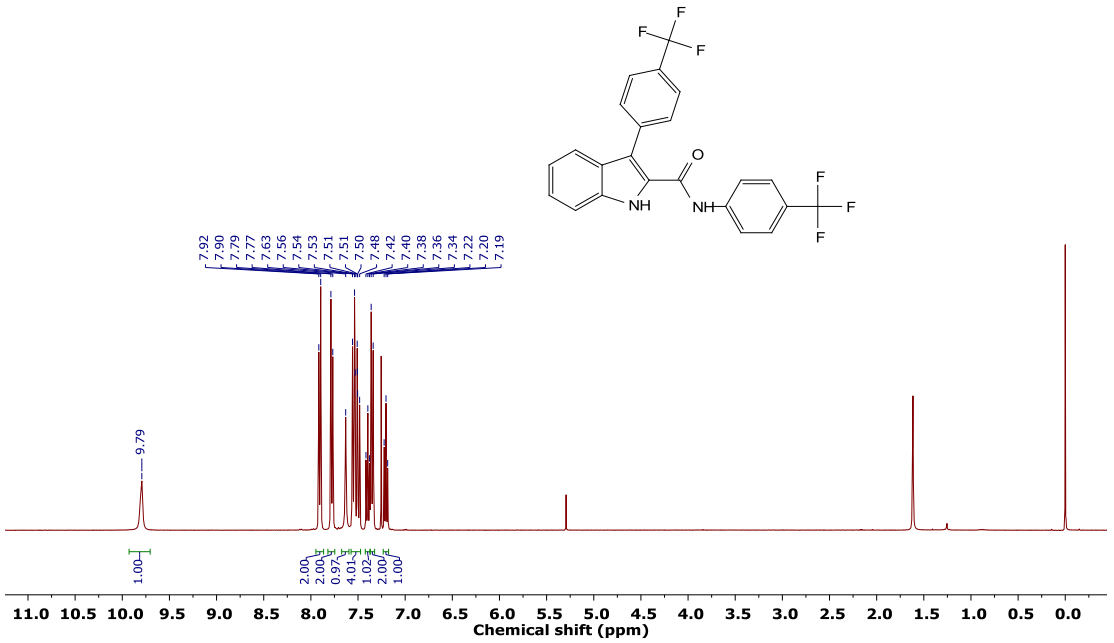

Figure 5.67. ^{1}H NMR spectrum (400 MHz) of **5′** in $CDCl_3$ at room temperature.

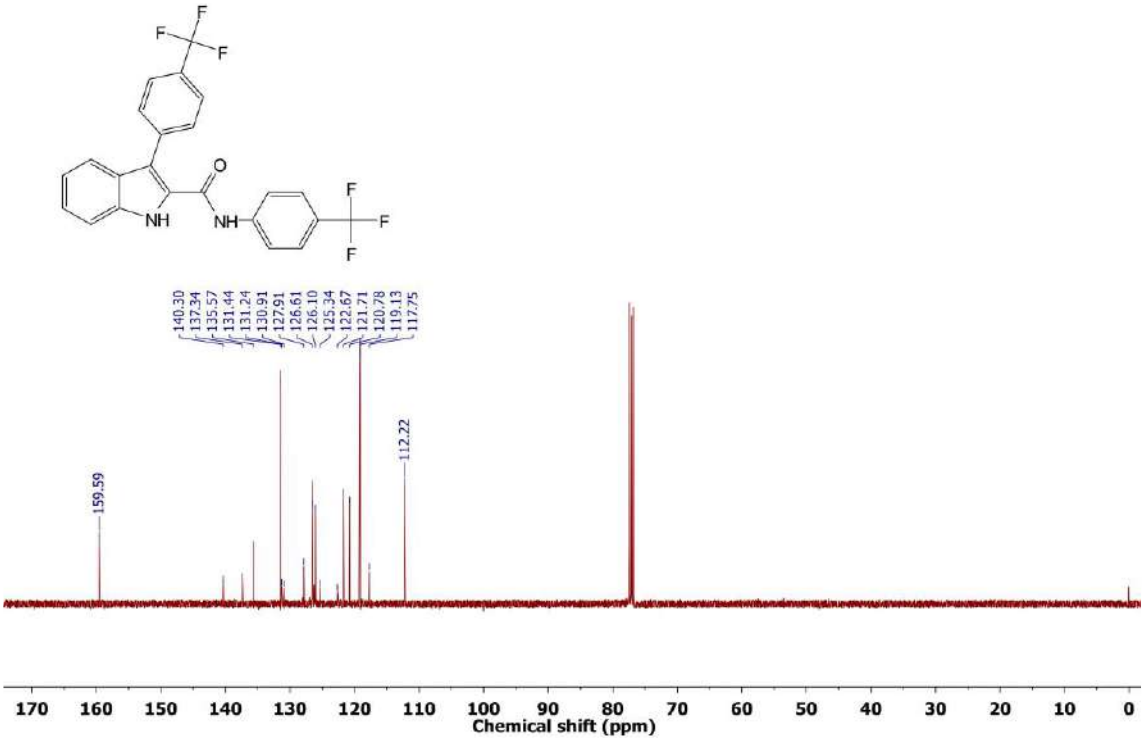

Figure 5.68. ^{13}C NMR spectrum (101 MHz) of **5′** in $CDCl_3$ at room temperature.

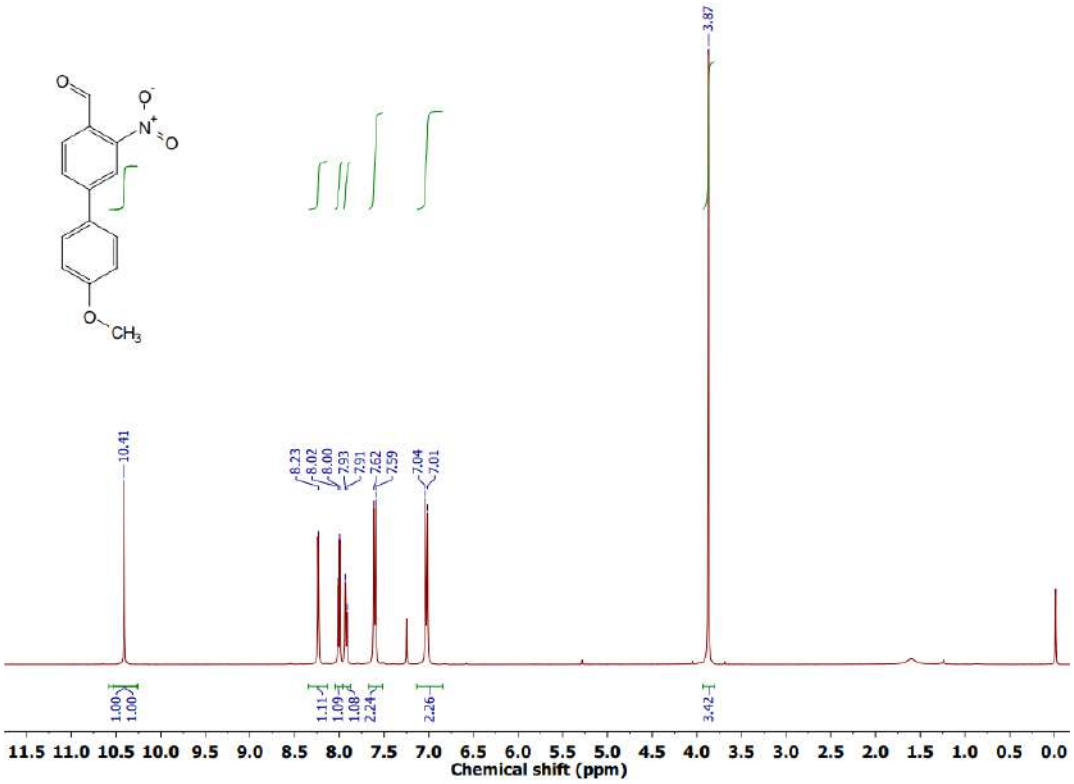

Figure 5.69. ^{1}H NMR spectrum (400 MHz) of **6d** in $CDCl_3$ at room temperature.

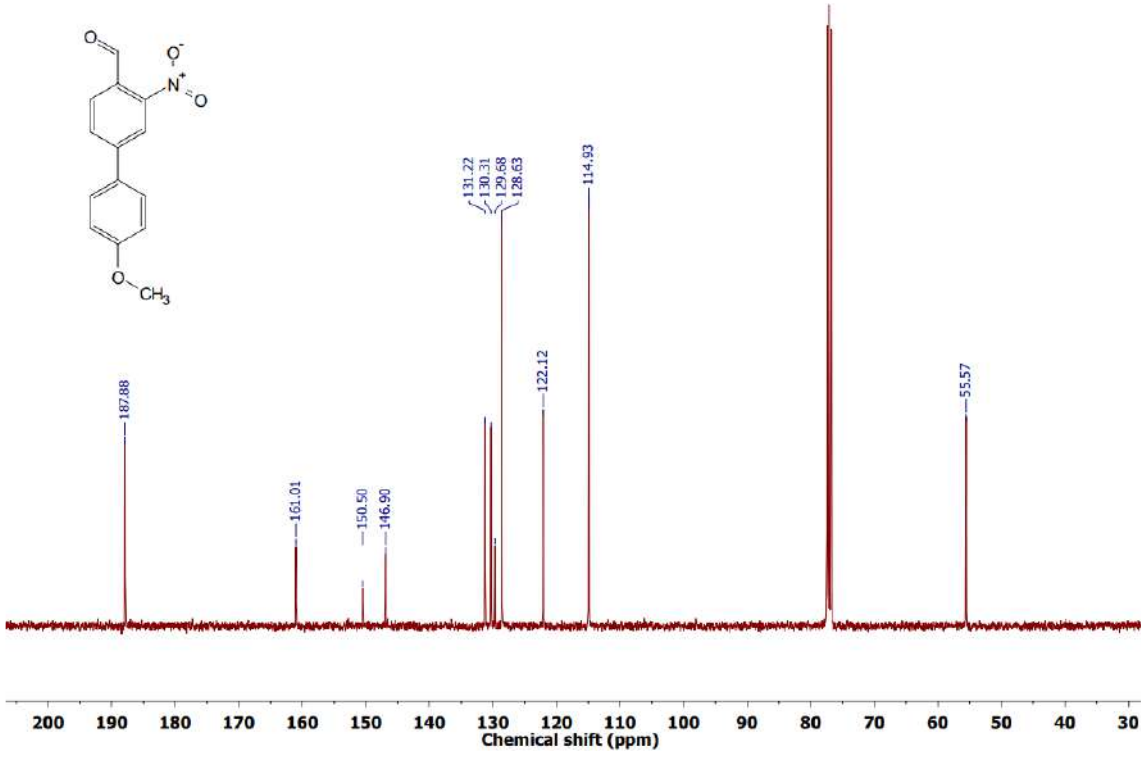

Figure 5.70. ^{13}C NMR spectrum (101 MHz) of **6d** in $CDCl_3$ at room temperature.

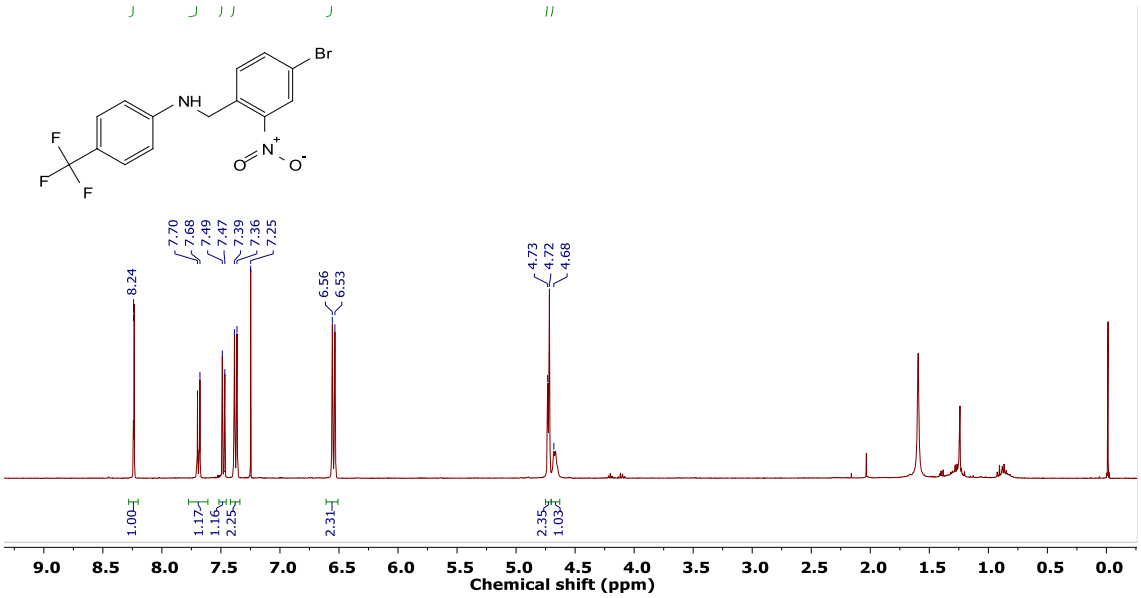

Figure 5.71. ^{1}H NMR spectrum (400 MHz) of **7b** in $CDCl_3$ at room temperature.

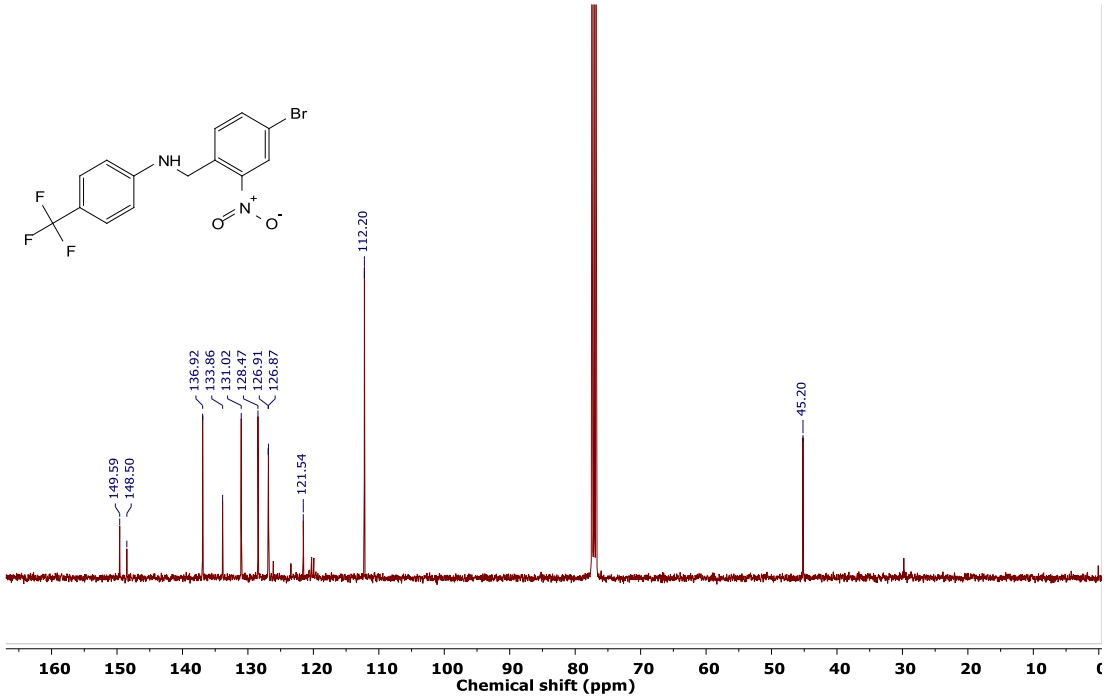

Figure 5.72. ^{13}C NMR spectrum (101 MHz) of **7b** in $CDCl_3$ at room temperature.

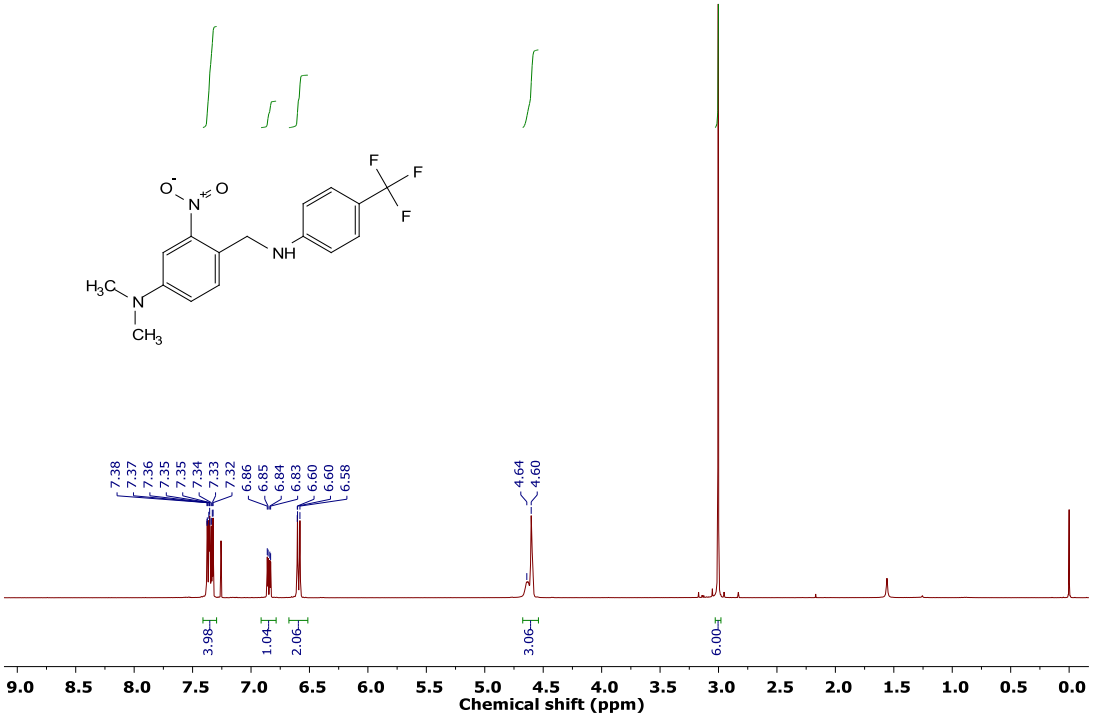

Figure 5.73. ^{1}H NMR spectrum (400 MHz) of **7c** in $CDCl_3$ at room temperature.

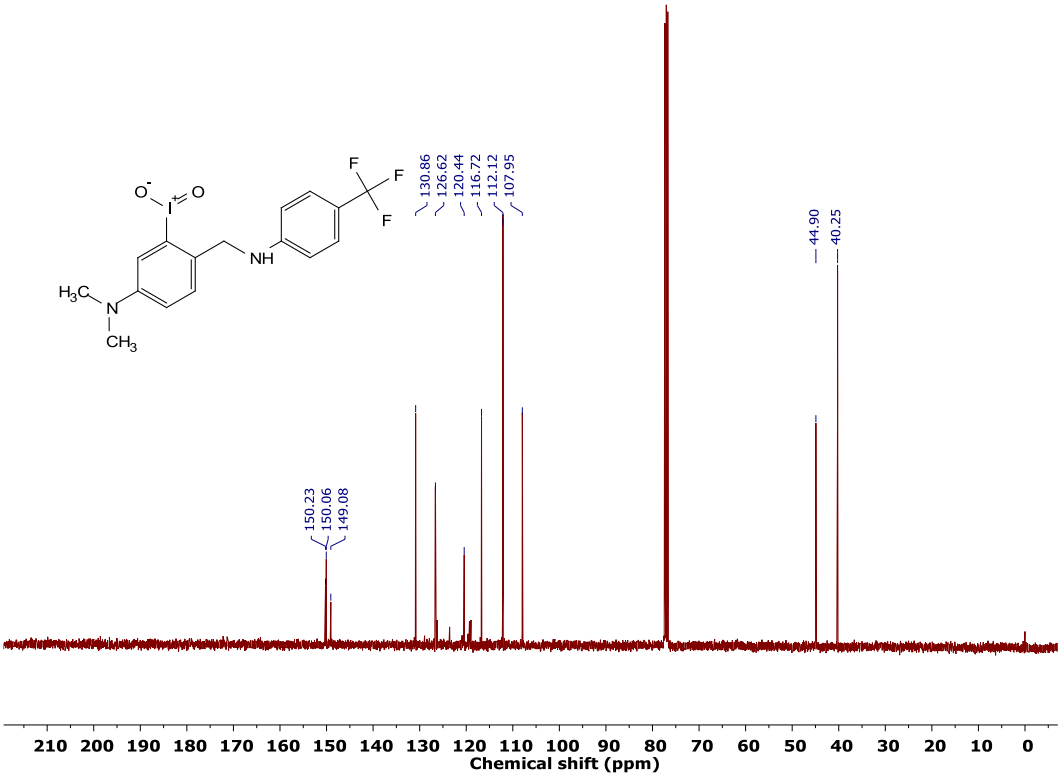

Figure 5.74. ^{13}C NMR spectrum (101 MHz) of **7c** in $CDCl_3$ at room temperature.

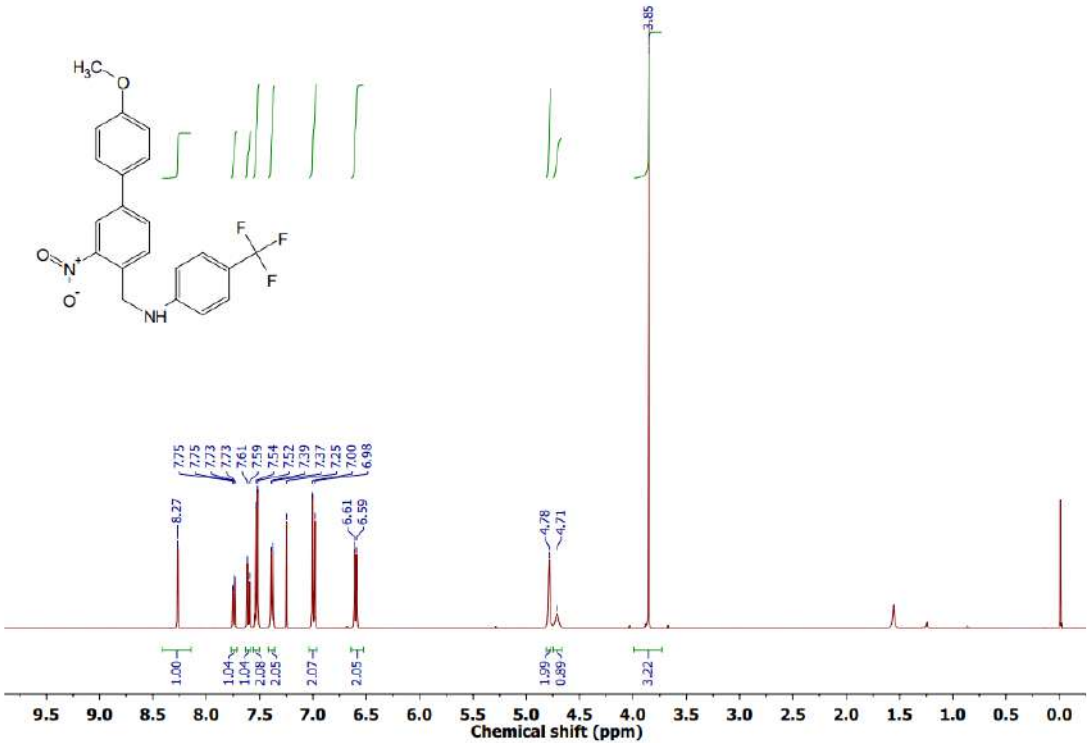

Figure 5.75. ^{1}H NMR spectrum (400 MHz) of **7d** in $CDCl_3$ at room temperature.

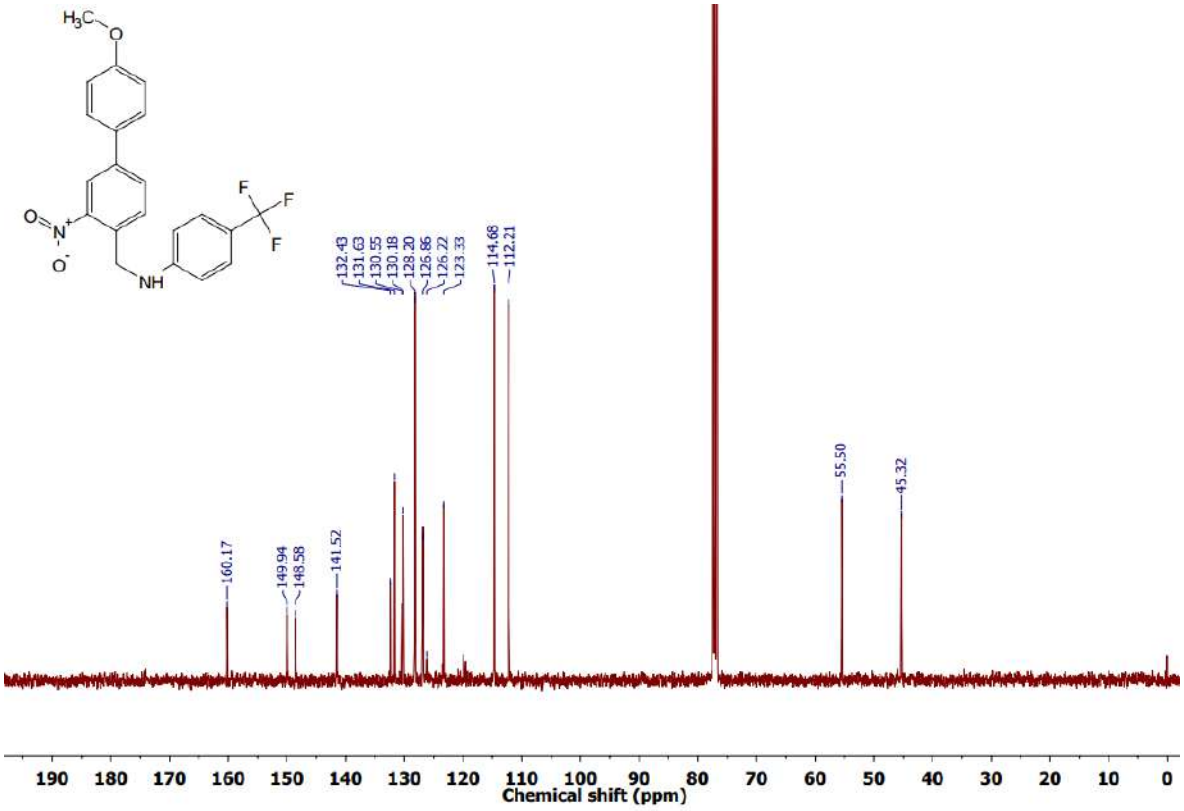

Figure 5.76. ^{13}C NMR spectrum (101 MHz) of **7d** in $CDCl_3$ at room temperature.

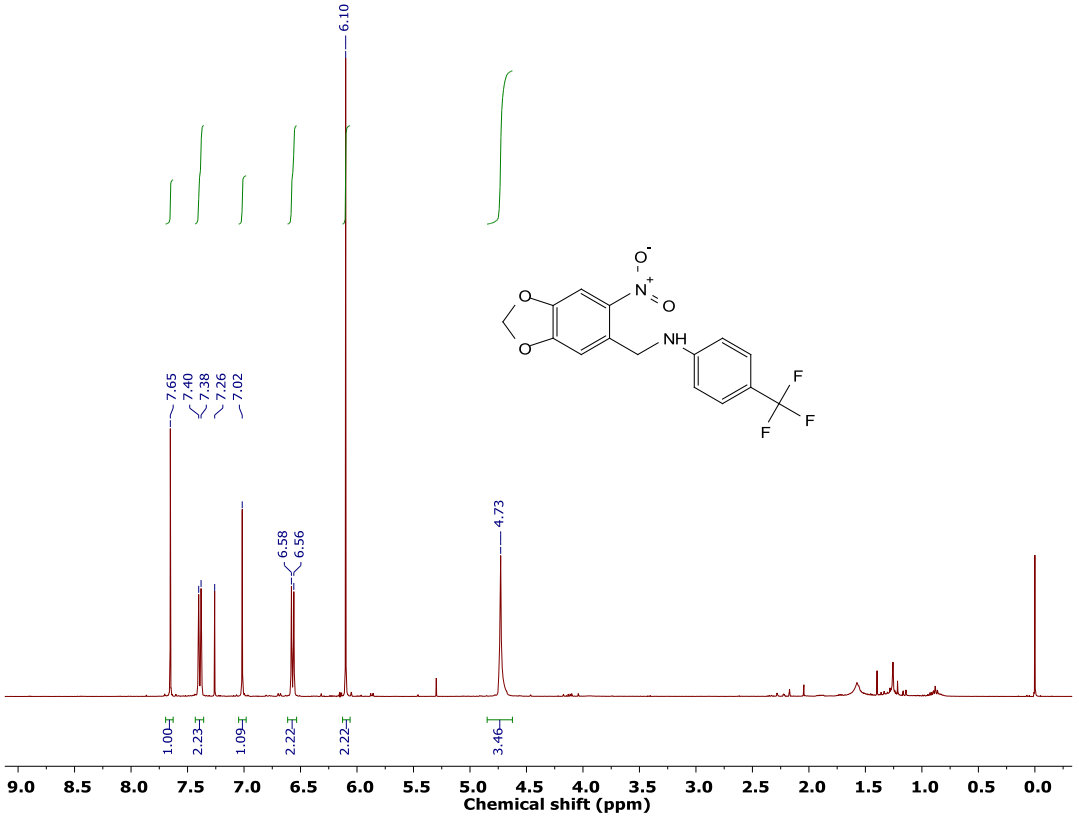

Figure 5.77. ^{1}H NMR spectrum (400 MHz) of **7e** in $CDCl_3$ at room temperature.

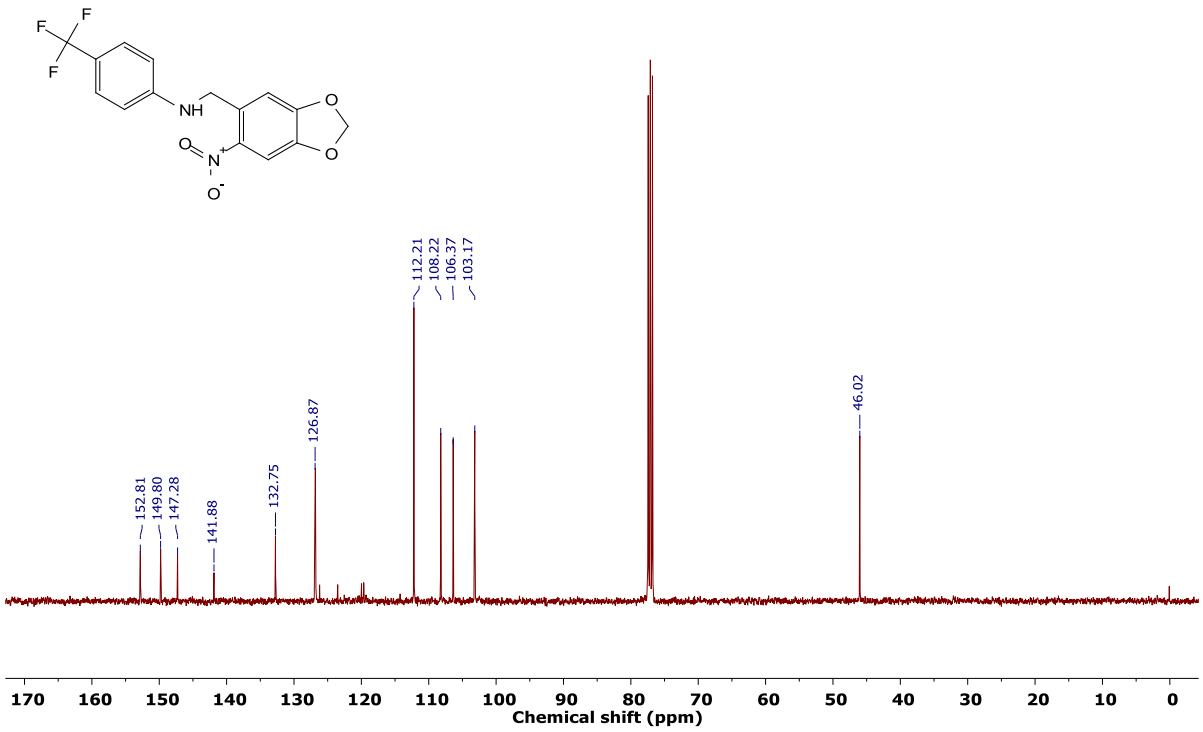

Figure 5.78. ^{13}C NMR spectrum (101 MHz) of **7e** in $CDCl_3$ at room temperature.

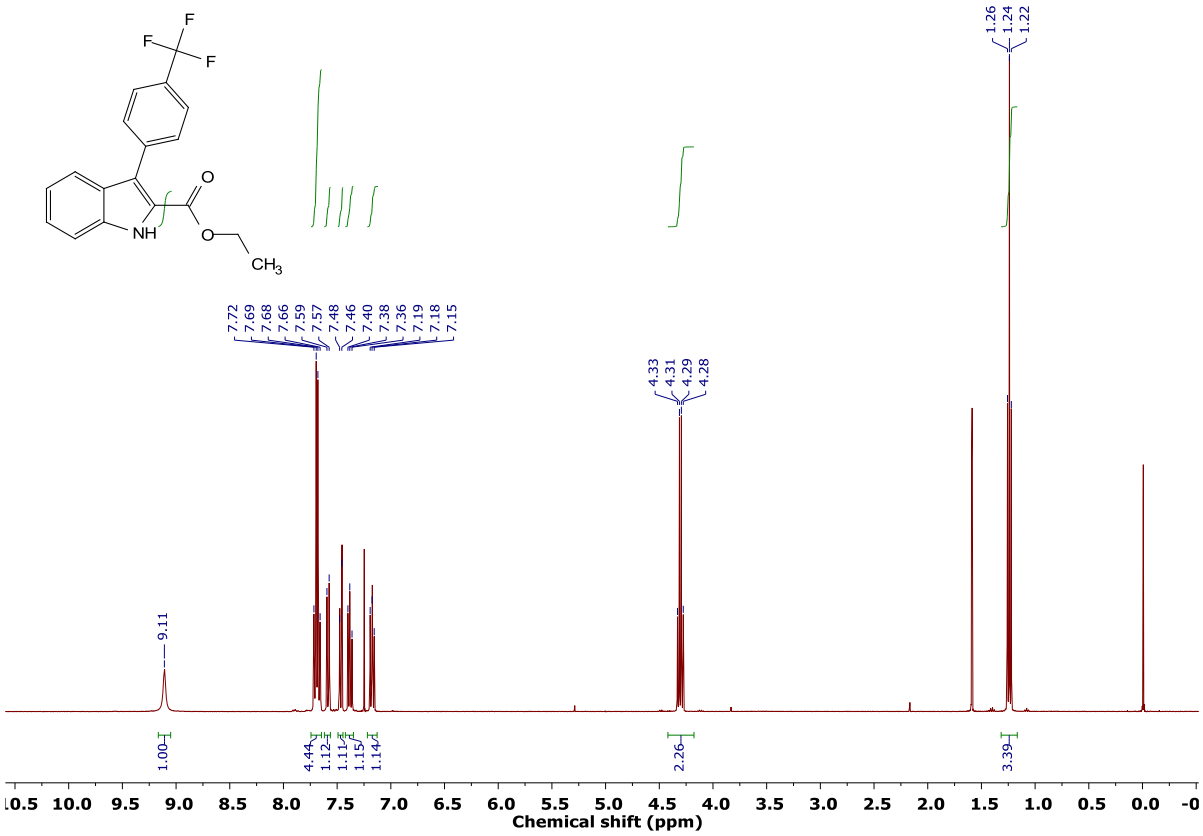

Figure 5.79. ^{1}H NMR spectrum (400 MHz) of **11** in $CDCl_3$ at room temperature.

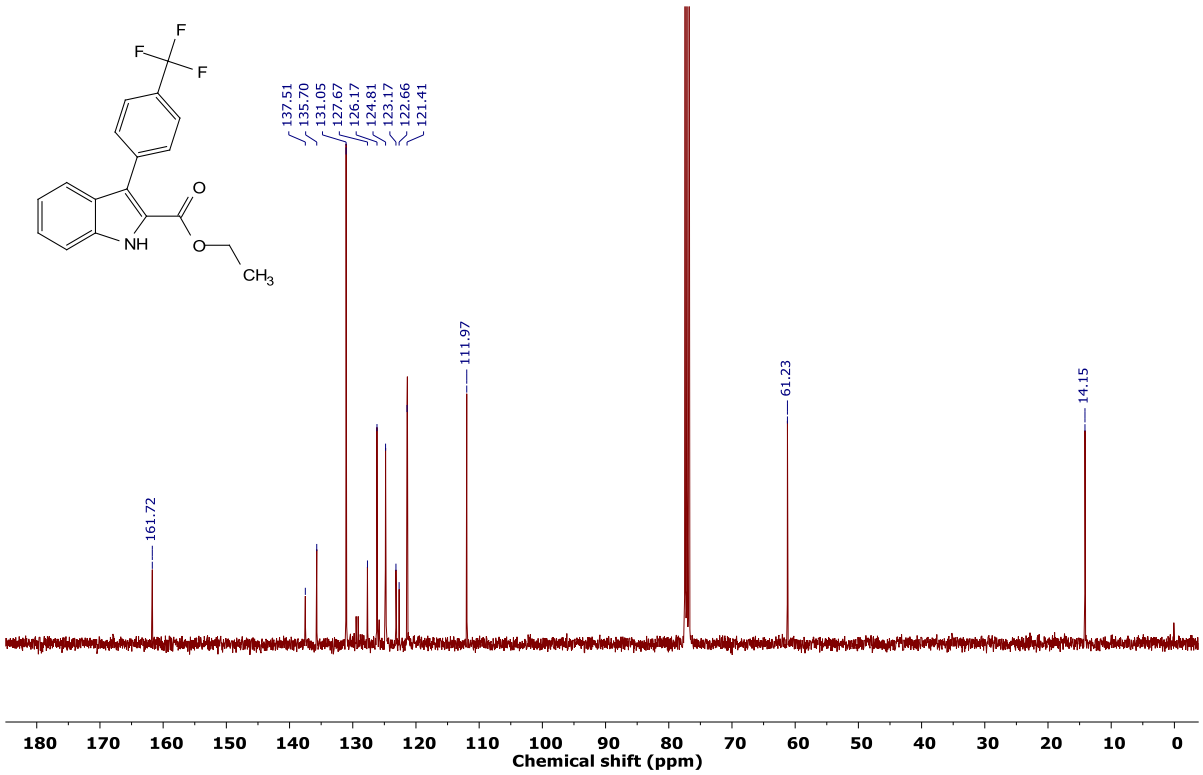

Figure 5.80. ^{13}C NMR spectrum (101 MHz) of **11** in $CDCl_3$ at room temperature.

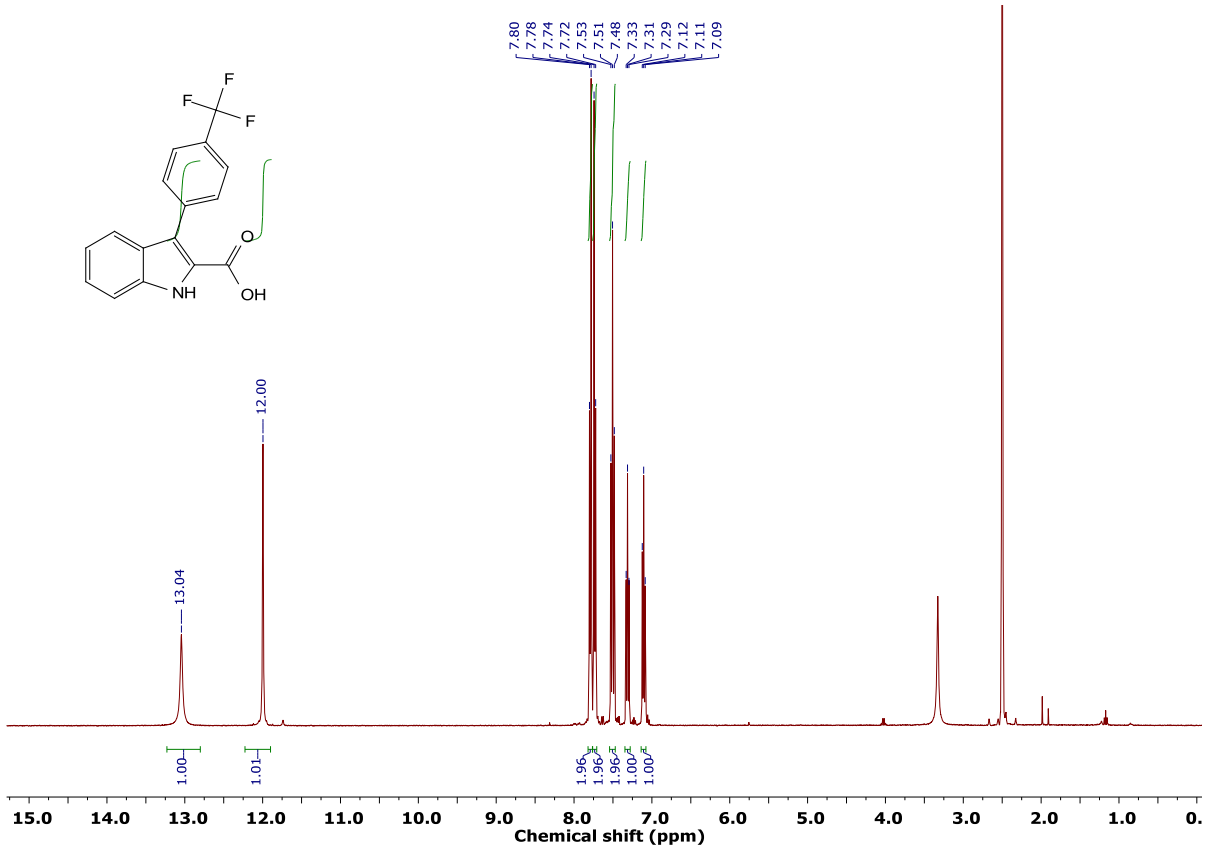

Figure 5.81. ^{1}H NMR spectrum (400 MHz) of **12** in DMSO-d_6 at room temperature.

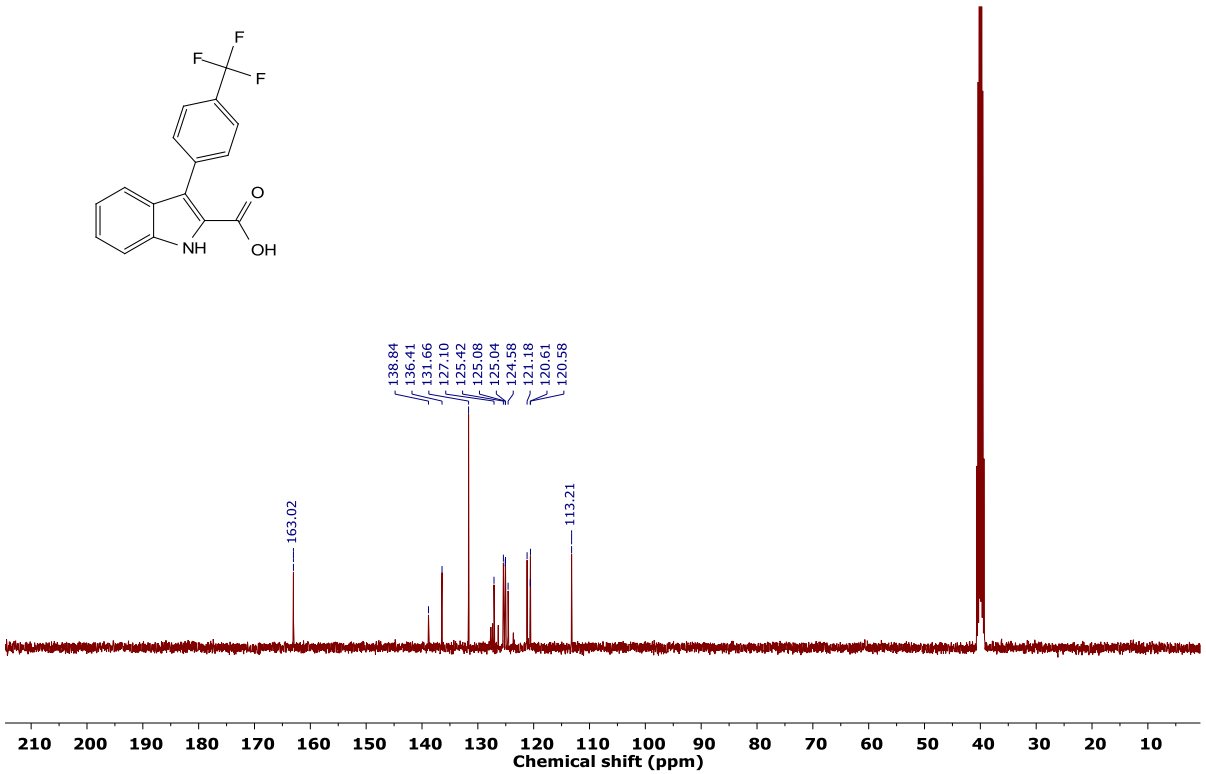

Figure 5.82. ^{13}C NMR spectrum (101 MHz) of **12** in DMSO-d_6 at room temperature.

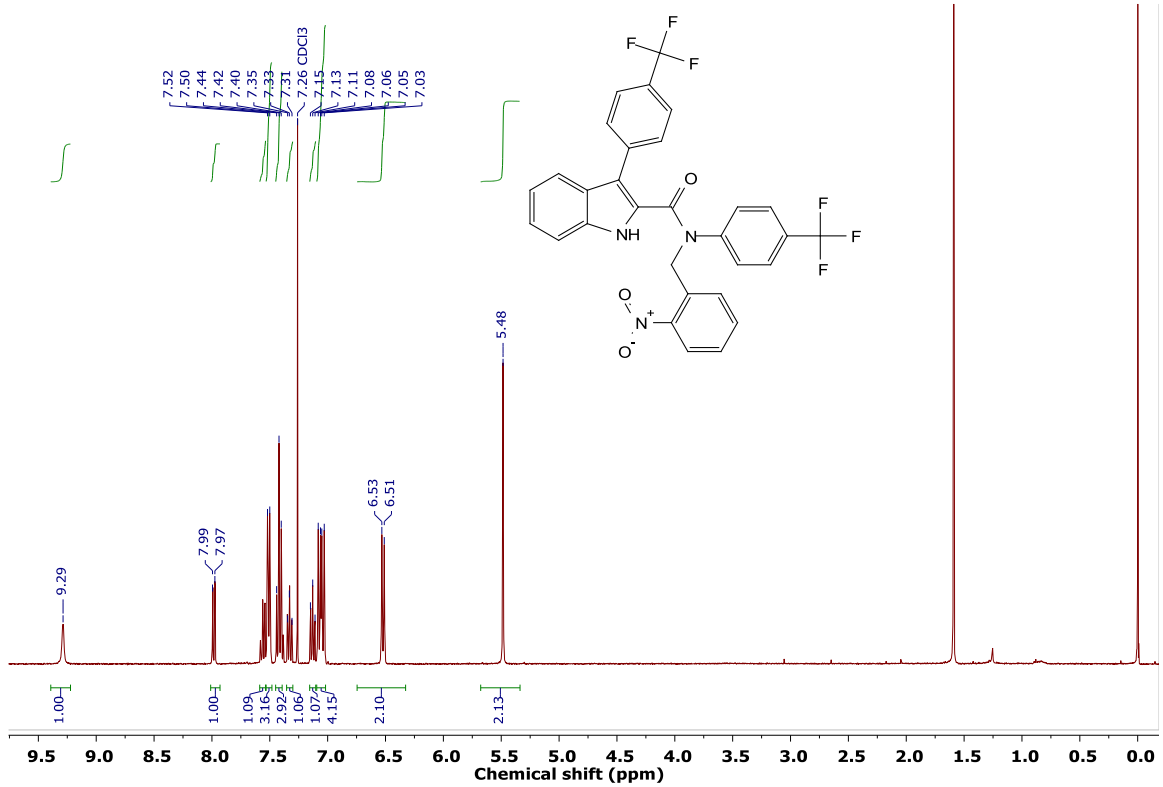

Figure 5.83. ^{1}H NMR spectrum (400 MHz) of **5a** in $CDCl_3$ at room temperature.

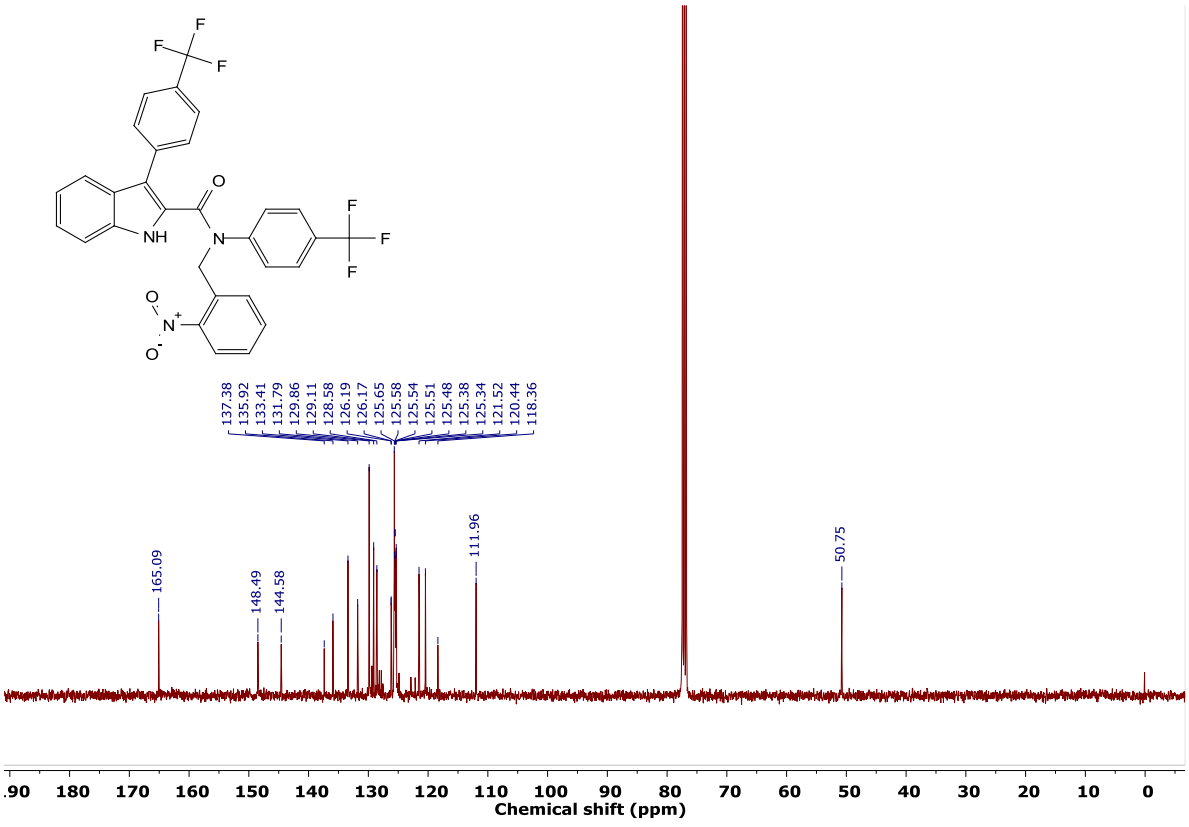

Figure 5.84. ^{13}C NMR spectrum (101 MHz) of **5a** in $CDCl_3$ at room temperature.

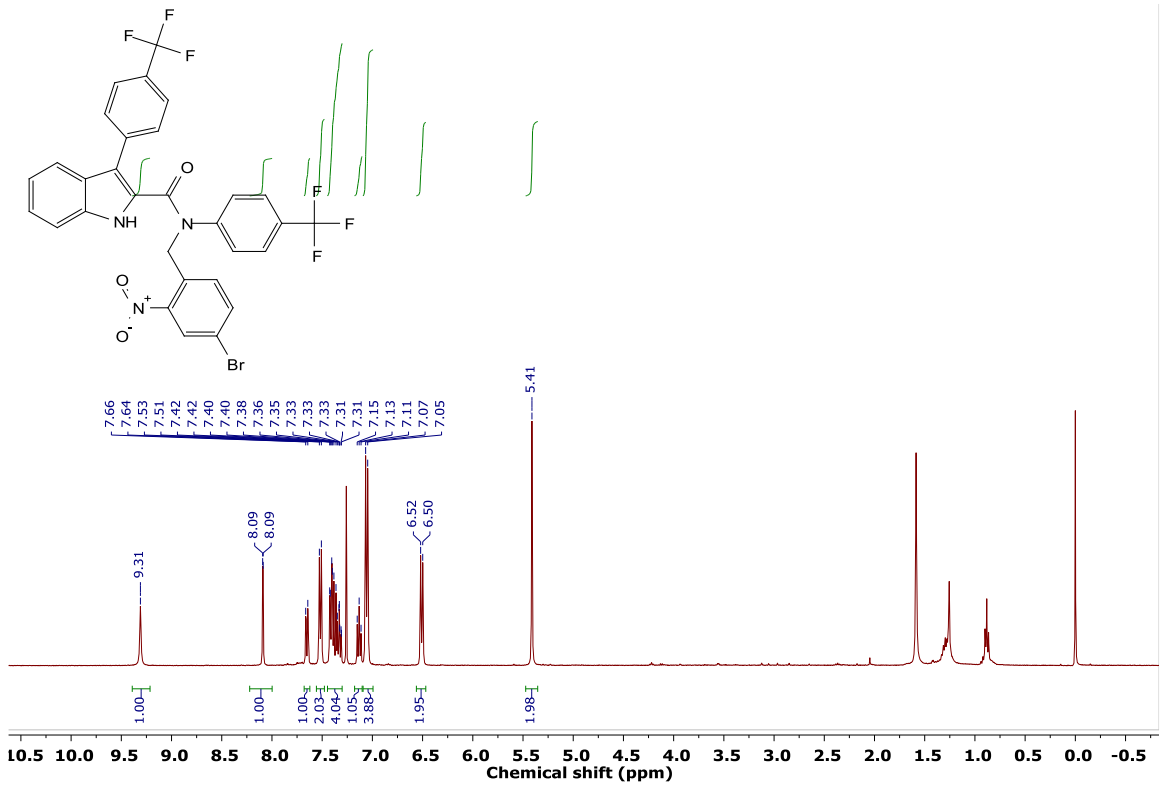

Figure 5.85. ^{1}H NMR spectrum (400 MHz) of **5b** in $CDCl_3$ at room temperature.

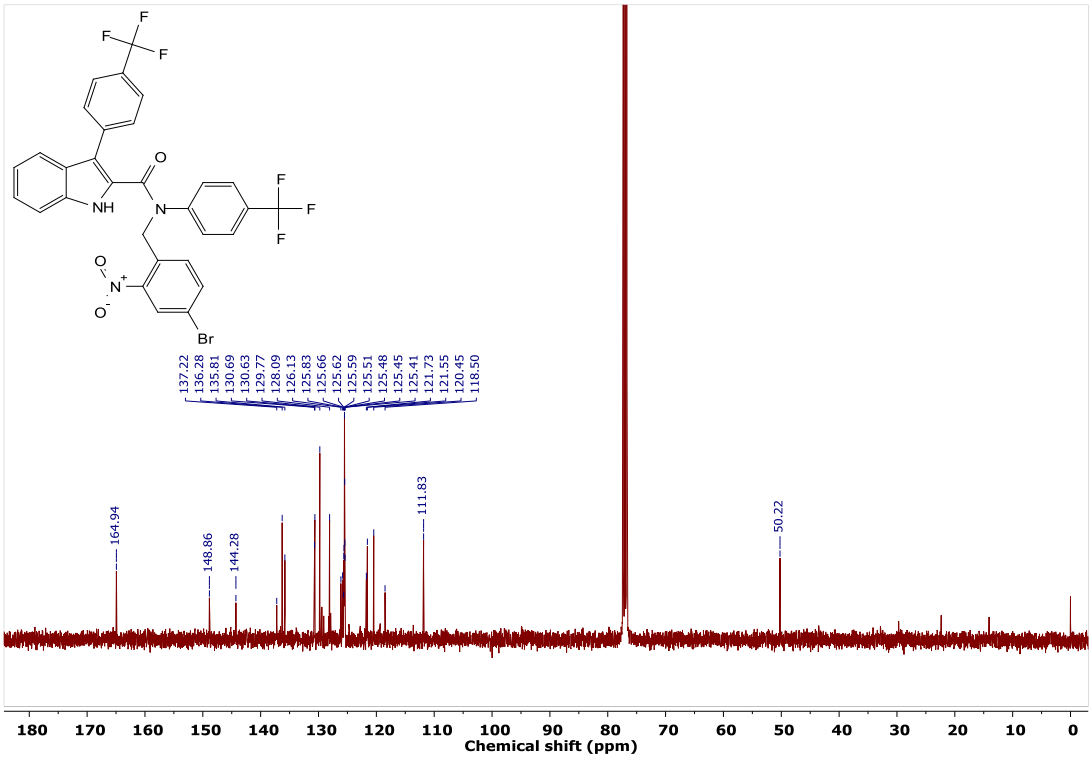

Figure 5.86. ^{13}C NMR spectrum (101 MHz) of **5b** in $CDCl_3$ at room temperature.

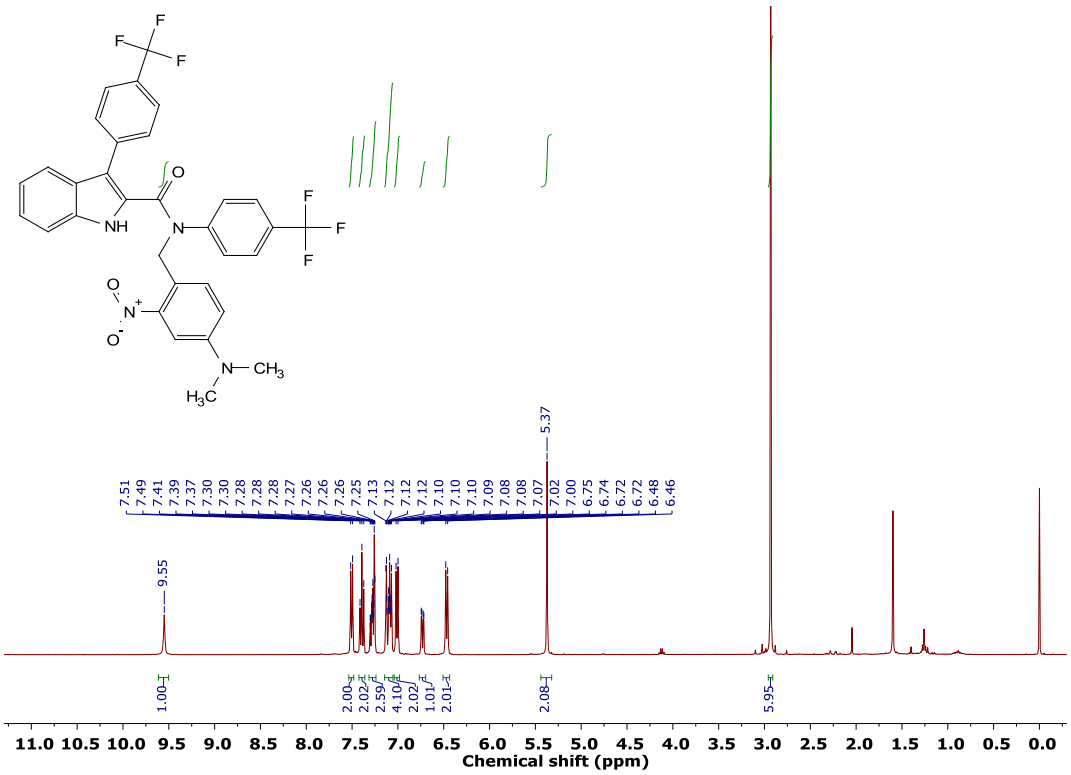

Figure 5.87. ^{1}H NMR spectrum (400 MHz) of **5c** in $CDCl_3$ at room temperature.

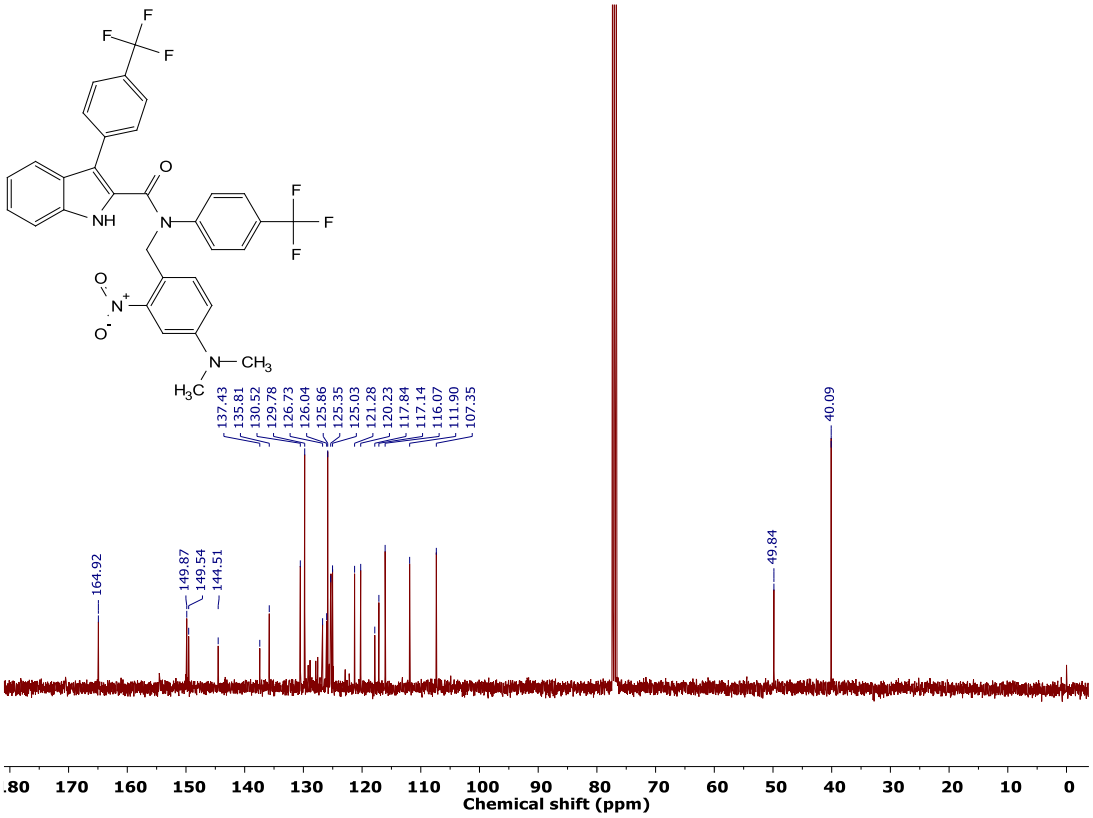

Figure 5.88. ^{13}C NMR spectrum (101 MHz) of **5c** in $CDCl_3$ at room temperature.

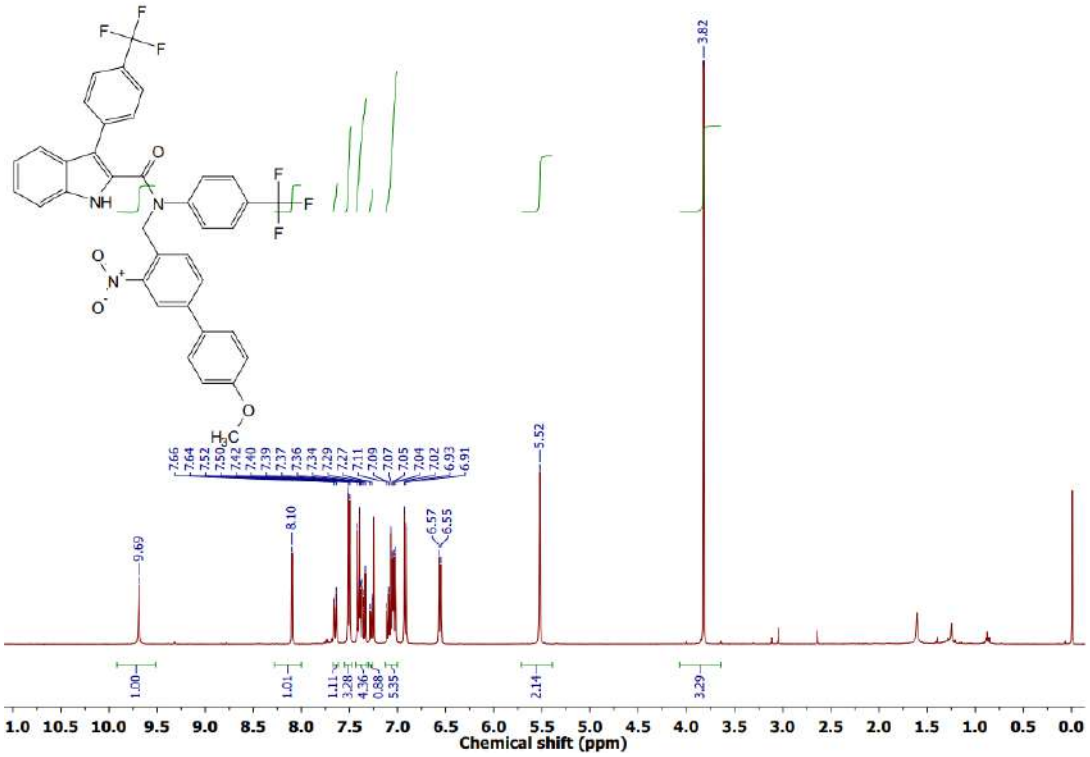

Figure 5.89. ^{1}H NMR spectrum (400 MHz) of **5d** in $CDCl_3$ at room temperature.

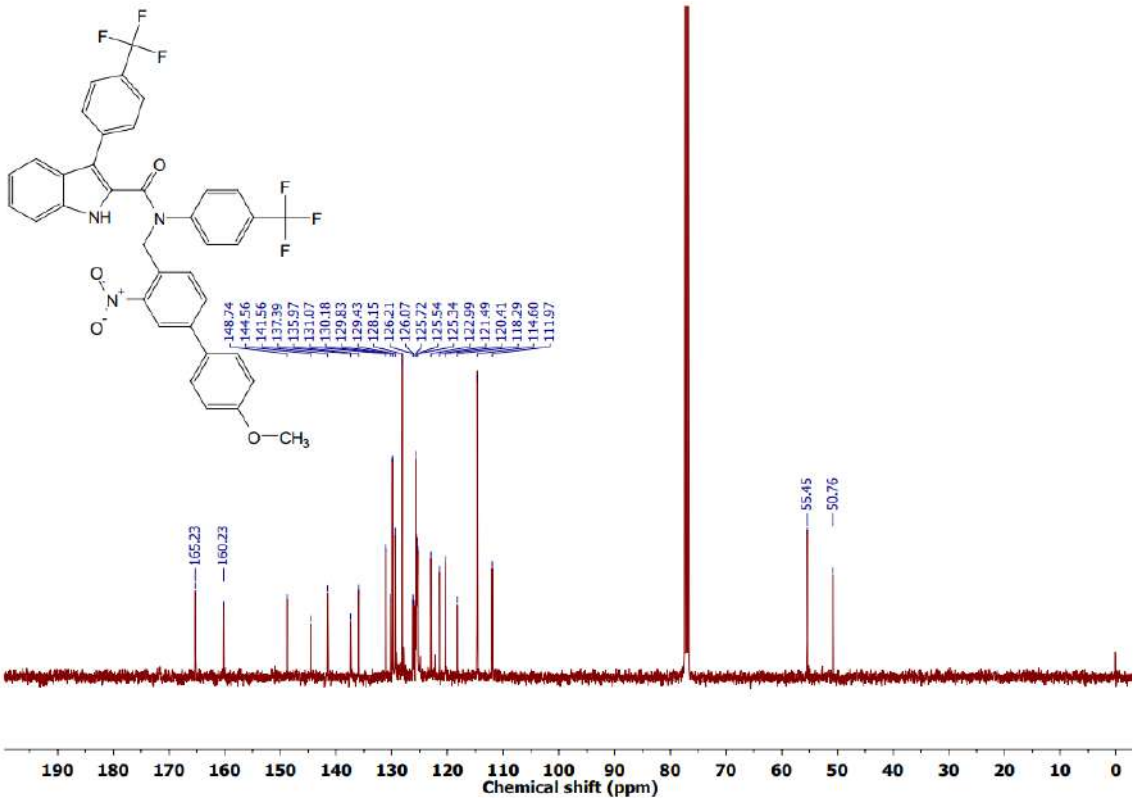

Figure 5.90. ^{13}C NMR spectrum (101 MHz) of **5d** in $CDCl_3$ at room temperature.

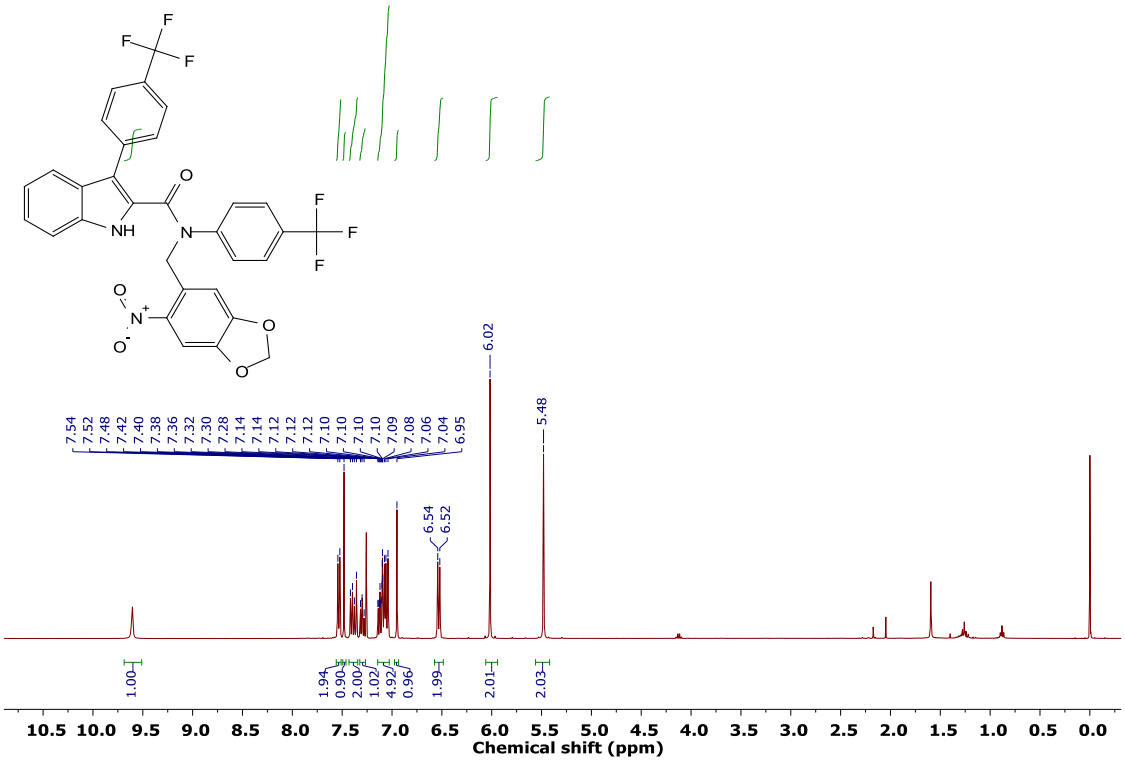

Figure 5.91. ^{1}H NMR spectrum (400 MHz) of **5e** in $CDCl_3$ at room temperature.

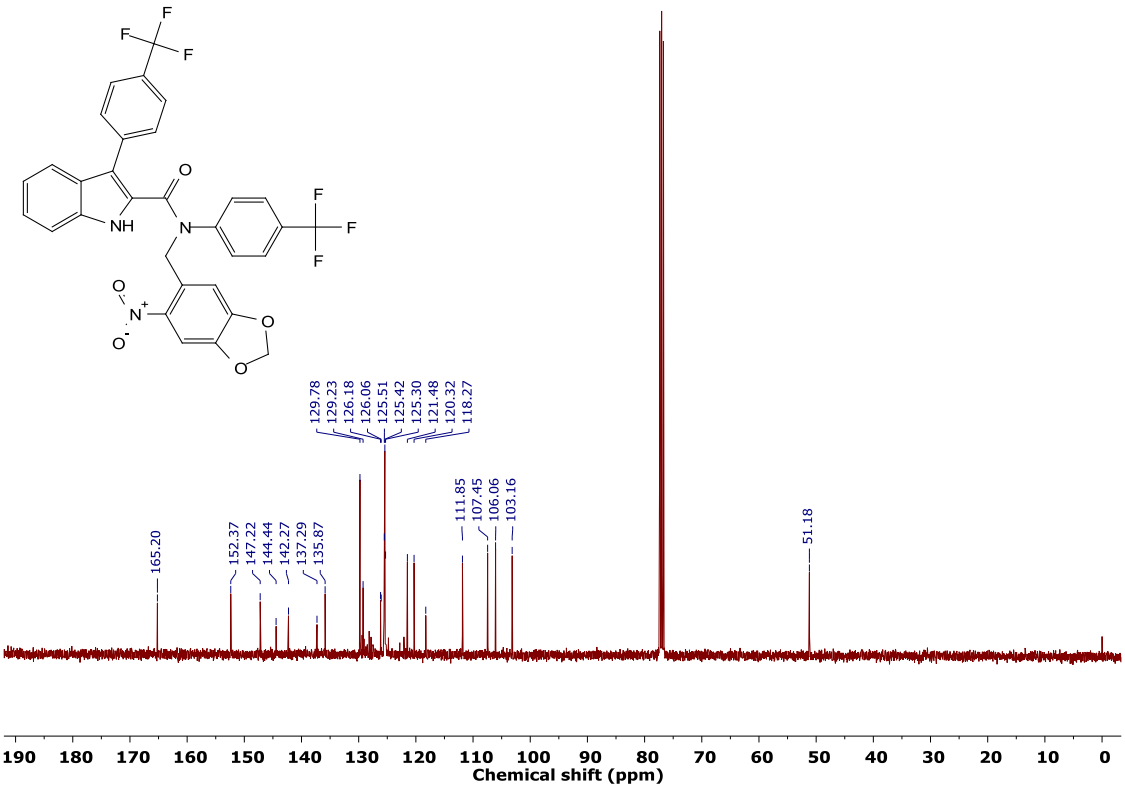

Figure 5.92. ^{13}C NMR spectrum (101 MHz) of **5e** in $CDCl_3$ at room temperature.

5.4.12. References

[1] (a) M. L. Davila, *Curr. Opin. Gastroenterol* **2006**, *22*, 44-47; (b) D. J. Franklin, L. Packel, *Arch. Phys. Med. Rehabil.* **2006**, *87*, 91-93; (c) M. Brydøy, S. D. Fosså, O. Dahl, T. Bjøro, *Acta. Oncologica.* **2007**, *46*, 480-489.

[2] (a) M. Ogawa, *Nippon rinsho.* **1997**, *55*, 1017-1023; (b) M. Montaño-Samaniego, D. M. Bravo-Estupiñan, O. Méndez-Guerrero, E. Alarcón-Hernández, M. Ibáñez-Hernández, *Front. Oncol.* **2020**, *10*.

[3] W. R. Sellers, D. E. Fisher, *J. Clin. Invest.* **1999**, *104*, 1655-1661.

[4] (a) J. M. Brown, L. D. Attardi, *Nat. Rev. Cancer* **2005**, *5*, 231-237; (b) L. Portt, G. Norman, C. Clapp, M. Greenwood, M. T. Greenwood, *Biochim Biophys Acta.* **2011**, *1813*, 238-259.

[5] R. S. Y. Wong, *Clin. Cancer Res.* **2011**, *30*.

[6] J. M. Lee, F. M. Davis, S. J. Roberts-Thomson, G. R. Monteith, *Am. J. Physiol. Cell Physiol.* **2011**, *301*, 969-976.

[7] R. S. Frey, A. B. Malik, *Am. J. Physiol. Lung Cell Mol. Physiol.* **2004**, *286*, 1-3.

[8] (a) L. Yu, X. H. Jiang, Z. Zhou, L. L. Tsang, M. K. Yu, Y. W. Chung, X. H. Zhang, A. M. Wang, H. Tang, H. C. Chan, *PLoS One* **2011**, *6*, e17322-e17322; (b) M. D. Davis, J. J. Clemens, T. L. Macdonald, K. R. Lynch, *J. Biol. Chem.* **2005**, *280*, 9833-9841.

[9] R. Pérez-Tomás, B. Montaner, E. Llagostera, V. Soto-Cerrato, *Biochem. Pharmacol.* **2003**, *66*, 1447-1452.

[10] P. Manuel-Manresa, L. Korrodi-Gregório, E. Hernando, A. Villanueva, D. Martínez-García, A. M. Rodilla, R. Ramos, M. Fardilha, J. Moya, R. Quesada, V. Soto-Cerrato, R. Pérez-Tomás, *Mol. Cancer Ther.* **2017**, *16*, 1224-1235.

[11] S. K. Ko, S. K. Kim, A. Share, V. M. Lynch, J. Park, W. Namkung, W. Van Rossom, N. Busschaert, P. A. Gale, J. L. Sessler, I. Shin, *Nat. Chem.* **2014**, *6*, 885-892.

[12] (a) N. Busschaert, M. Wenzel, M. E. Light, P. Iglesias-Hernández, R. Pérez-Tomás, P. A. Gale, *J. Am. Chem. Soc.* **2011**, *133*, 14136-14148; (b) S. J. Moore, C. J. E. Haynes, J. González, J. L. Sutton, S. J. Brooks, M. E. Light, J. Herniman, G. J. Langley, V. Soto-Cerrato, R. Pérez-Tomás, I. Marques, P. J. Costa, V. Félix, P. A. Gale, *Chem. Sci.* **2013**, *4*, 103-117.

[13] T. Saha, M. S. Hossain, D. Saha, M. Lahiri, P. Talukdar, *J. Am. Chem. Soc.* **2016**, *138*, 7558-7567.

[14] N. Busschaert, S.-H. Park, K.-H. Baek, Y. P. Choi, J. Park, E. N. W. Howe, J. R. Hiscock, L. E. Karagiannidis, I. Marques, V. Félix, W. Namkung, J. L. Sessler, P. A. Gale, I. Shin, *Nat. Chem.* **2017**, *9*, 667-675.

[15] (a) E. N. W. Howe, N. Busschaert, X. Wu, S. N. Berry, J. Ho, M. E. Light, D. D. Czech, H. A. Klein, J. A. Kitchen, P. A. Gale, *J. Am. Chem. Soc.* **2016**, *138*, 8301-8308; (b) N. Busschaert, R. B. P. Elmes, D. D. Czech, X. Wu, I. L. Kirby, E. M. Peck, K. D. Hendzel, S. K. Shaw, B. Chan, B. D. Smith, K. A. Jolliffe, P. A. Gale, *Chem. Sci.* **2014**, *5*, 3617-3626; (c) A. Roy, O. Biswas, P. Talukdar, *Chem. Comm.* **2017**, *53*, 3122-3125; (d) S. V. Shinde, P. Talukdar, *Org. Biomol. Chem.* **2019**, *17*, 4483-4490; (e) S. V. Shinde, P. Talukdar, *Angew. Chem. Int. Ed.* **2017**, *56*, 4238-4242.

[16] (a) Y. R. Choi, B. Lee, J. Park, W. Namkung, K.-S. Jeong, *J. Am. Chem. Soc.* **2016**, *138*, 15319-15322; (b) E. B. Park, K.-S. Jeong, *Chem. Commun.* **2015**, *51*, 9197-9200.

[17] (a) M. M. Tedesco, B. Ghebremariam, N. Sakai, S. Matile, *Angew. Chem. Int. Ed.* **1999**, *38*, 540-543; (b) P. Talukdar, G. Bollot, J. Mareda, N. Sakai, S. Matile, *Chem. Eur. J.* **2005**, *11*, 6525-6532; (c) T. Kiwada, K. Sonomura, Y. Sugiura, K. Asami, S. Futaki, *J. Am. Chem. Soc.* **2006**, *128*, 6010-6011; (d) G. A. Woolley, B. A. Wallace, *Biochemistry* **1993**, *32*, 9819-9825.

[18] L. Lien, D. C. J. Jaikaran, Z. Zhang, G. A. Woolley, *J. Am. Chem. Soc.* **1996**, *118*, 12222-12223.

[19] (a) Y. Kobuke, K. Ueda, M. Sokabe, *J. Am. Chem. Soc.* **1992**, *114*, 7618-7622; (b) W. Si, Z.-T. Li, J.-L. Hou, *Angew. Chem. Int. Ed.* **2014**, *53*, 4578-4581; (c) M. Fares, X. Wu, D. Ramesh, W. Lewis, P. A. Keller, E. N. W. Howe, R. Pérez-Tomás, P. A. Gale, *Angew. Chem. Int. Ed.* **2020**, *59*, 17614-17621; (d) N. Akhtar, N. Pradhan, A. Saha, V. Kumar, O. Biswas, S. Dey, M. Shah, S. Kumar, D. Manna, *Chem. Commun.* **2019**, *55*, 8482-8485.

[20] (a) I. F. Tannock, D. Rotin, *Cancer Res.* **1989**, *49*, 4373-4384; (b) W. Van Rossom, D. J. Asby, A. Tavassoli, P. A. Gale, *Org. Biomol. Chem.* **2016**, *14*, 2645-2650; (c) N. Busschaert, C. Caltagirone, W. Van Rossom, P. A. Gale, *Chem. Rev.* **2015**, *115*, 8038-8155; (d) J. A. Malla, R. M. Umesh, S. Yousf, S. Mane, S. Sharma, M. Lahiri, P. Talukdar, *Angew. Chem. Int. Ed.* **2020**, *59*, 7944-7952; (e) A. Mondal, J. A. Malla, H. Paithankar, S. Sharma, J. Chugh, P. Talukdar, *Org. Lett.* **2021**, *23*, 6131-6136; (f) J. A. Malla, V. K. Sharma, M. Lahiri, P. Talukdar, *Chem. Eur. J.* **2020**, *26*, 11910-11910.

[21] M. R. Banghart, M. Volgraf, D. Trauner, *Biochemistry*. **2006**, *45*, 15129-15141.

[22] (a) J. Zhao, S. Lin, Y. Huang, J. Zhao, P. R. Chen, *J. Am. Chem. Soc.* **2013**, *135*, 7410-7413; (b) N. Kretschy, A.-K. Holik, V. Somoza, K.-P. Stengele, M. M. Somoza, *Angew.*

Chem. Int. Ed. **2015**, *54*, 8555-8559; (c) L. Sjulson, G. Miesenböck, *Chem. Rev.* **2008**, *108*, 1588-1602.

[23] (a) S. K. Choi, M. Verma, J. Silpe, R. E. Moody, K. Tang, J. J. Hanson, J. R. Baker, *Bioorganic Med. Chem.* **2012**, *20*, 1281-1290; (b) N.-C. Fan, F.-Y. Cheng, J.-a. A. Ho, C.-S. Yeh, *Angew. Chem. Int. Ed. 2012*, **2012**, *51*, 8806-8810; (c) J. Liu, W. Bu, L. Pan, J. Shi, *Angew. Chem. Int. Ed.* **2013**, *52*, 4375-4379; (d) W. S. Shin, J. Han, R. Kumar, G. G. Lee, J. L. Sessler, J.-H. Kim, J. S. Kim, *Sci. Rep.* **2016**, *6*, 29018; (e) Y. Yang, J. Mu, B. Xing, *Wiley Interdiscip. Rev. Nanomed. Nanobiotechnol.* **2017**, *9*, e1408.

[24] (a) W. Hou, R. Liu, S. Bi, Q. He, H. Wang, J. Gu, *Molecules* **2020**, *25*, 5147; (b) G. Jalani, V. Tam, F. Vetrone, M. Cerruti, *J. Am. Chem. Soc.* **2018**, *140*, 10923-10931; (c) R. Reinhard, B. F. Schmidt, *J. Org. Chem.* **1998**, *63*, 2434-2441.

[25] C. A. Lipinski, F. Lombardo, B. W. Dominy, P. J. Feeney, *Adv. Drug Deliv. Rev.* **1997**, *23*, 3-25.

[26] J. A. Peterson, C. Wijesooriya, E. J. Gehrmann, K. M. Mahoney, P. P. Goswami, T. R. Albright, A. Syed, A. S. Dutton, E. A. Smith, A. H. Winter, *J. Am. Chem. Soc.* **2018**, *140*, 7343-7346.

[27] (a) I. Aujard, C. Benbrahim, M. Gouget, O. Ruel, J.-B. Baudin, P. Neveu, L. Jullien, *Chem. Eur. J.* **2006**, *12*, 6865-6879; (b) M. J. Hansen, W. A. Velema, M. M. Lerch, W. Szymanski, B. L. Feringa, *Chem. Soc. Rev.* **2015**, *44*, 3358-3377.

[28] L. Chacun-Lefèvre, B. Joseph, J. Merour, Synlett 2001, 2001, 848-850.

[29] http://app.supramolecular.org/bindfit/ (accessed July **2017**).

[30] A. Roy, T. Saha, M. L. Gening, D. V. Titov, A. G. Gerbst, Y. E. Tsvetkov, N. E. Nifantiev, P. Talukdar, *Chem. Eur. J.* **2015**, *21*, 17445-17452.

[31] B. L. Schottel, H. T. Chifotides, K. R. Dunbar, *Chem. Soc. Rev.* **2008**, *37*, 68-83.

[32] L. E. Bickerton, A. Docker, A. J. Sterling, H. Kuhn, F. Duarte, P. D. Beer, M. J. Langton, *Chem. Eur. J.* **2021**, *27*, 11738-11745.

[33] (a) X. Wu, E. N. W. Howe, P. A. Gale, *Acc. Chem. Res.* **2018**, *51*, 1870-1879; (b) J. T. Davis, P. A. Gale, R. Quesada, *Chem. Soc. Rev.* **2020**, *49*, 6056-6086; (c) L. Chen, S. N. Berry, X. Wu, E. N. W. Howe, P. A. Gale, *Chem.* **2020**, *6*, 61-141.

[34] (a) N. Busschaert, I. L. Kirby, S. Young, S. J. Coles, P. N. Horton, M. E. Light, P. A. Gale, *Angew. Chem. Int. Ed.* **2012**, *51*, 4426-4430; (b) P. A. Gale, C. C. Tong, C. J. E. Haynes, O. Adeosun, D. E. Gross, E. Karnas, E. M. Sedenberg, R. Quesada, J. L. Sessler, *J. Am. Chem. Soc.* **2010**, *132*, 3240-3241; (c) D. Milano, B. Benedetti, M. Boccalon, A. Brugnara, E. Iengo, P. Tecilla, *Chem. Commun.* **2014**, *50*, 9157-9160.

[35] S. B. Salunke, J. A. Malla, P. Talukdar, *Angew. Chem. Int. Ed.* **2019**, *58*, 5354-5358.

[36] (a) S. O. H. Goto, N. Nakayama, K. Ohta, *CONFLEX 8, CONFLEX Corporation*, Tokyo,Japan, **2012**; (b) H. Goto, E. Osawa, *J. Am. Chem. Soc.* **1989**, *111*, 8950-8951.

[37] M. J. Frisch, H. B. Schlegel, G. E. Scuseria, M. A. Robb, J. R. Cheeseman, G. Scalmani, V. Barone, B. Mennucci, G. A. Petersson, H. Nakatsuji, M. Caricato, X. Li, H. P. Hratchian, A. F. Izmaylov, J. Bloino, G. Zheng, J. L. Sonnenberg, M. Hada, M. Ehara, K. Toyota, R. Fukuda, J. Hasegawa, M. Ishida, T. Nakajima, Y. Honda, O. Kitao, H. Nakai, T. Vreven, J. A. Montgomery, J. E. Peralta, F. Ogliaro, M. Bearpark, J. J. Heyd, E. Brothers, K. N. Kudin, V. N. Staroverov, T. Keith, R. Kobayashi, J. Normand, K. Raghavachari, A. Rendell, J. C. Burant, S. S. Iyengar, J. Tomasi, M. Cossi, N. Rega, J. M. Millam, M. Klene, J. E. Knox, J. B. Cross, V. Bakken, C. Adamo, J. Jaramillo, R. Gomperts, R. E. Stratmann, O. Yazyev, A. J. Austin, R. Cammi, C. Pomelli, J. W. Ochterski, R. L. Martin, K. Morokuma, V. G. Zakrzewski, G. A. Voth, P. Salvador, J. J. Dannenberg, S. Dapprich, A. D. Daniels, O. Farkas, J. B. Foresman, J. V. Ortiz, J. Cioslowski, D. J. Fox, ,Gaussian 09, Revision B.01, Gaussian, Inc., Wallingford, CT, **2010**.

[38] A. D. McLean, G. Chandler, *J. Chem. Phys.* **1980**, *72*, 5639-5648.

[39] J. A. Malla, R. M. Umesh, A. Vijay, A. Mukherjee, M. Lahiri, P. Talukdar, *Chem. Sci.* **2020**, *11*, 2420-2428.

[40] (a) V. Soto-Cerrato, P. Manuel-Manresa, E. Hernando, S. Calabuig-Fariñas, A. Martínez-Romero, V. Fernández-Dueñas, K. Sahlholm, T. Knöpfel, M. García-Valverde, A. M. Rodilla, E. Jantus-Lewintre, R. Farràs, F. Ciruela, R. Pérez-Tomás, R. Quesada, *J. Am. Chem. Soc.* **2015**, *137*, 15892-15898; (b) X.H. Yu, X.Q. Hong, W.H. Chen, *J. Biol. Chem.* **2019**, *17*, 1558-1571.

[41] C. Iftode, Y. Daniely, J. A. Borowiec, *Crit. Rev. Biochem. Mol. Biol.* **1999**, *34*, 141-180.

[42] L. J. KUO, L.X. YANG, *In Vivo.* **2008**, *22*, 305-309.

Overall Conclusion:

In the overall conclusion, the fundamental objective of my doctoral research was to establish the light-responsive artificial ion carriers with an aim to selectively activate these systems inside the cancer cells for therapeutic anticancer applications. The thesis deals with the design, chemical synthesis, and characterization of light responsive biomimetic artificial ion carriers. The transport of chloride ions is known to induce chloride-mediated apoptosis inside the cancer cells. However, the traditional transporters lack selectivity and hence can damage the normal healthy tissues along with the malignant cells. Stimuli such as voltage, pH, enzymes, ligands, light, etc., have been employed for the selective activation of these systems inside the cancer cells. Light-responsive ion transport systems, in particular, are important systems because of their spatiotemporal control, remote addressability, and less cytotoxicity. We developed several light-responsive synthetic ion carriers, where electromagnetic radiations were used to control the ion transport across the lipid membrane through these systems. In chapter 2, we developed azobenzene-based light-responsive anion carriers and efficient "OFF-ON" photoreguatory ion transport activity was achieved. In chapter 3, Acylhydrazone-based photoswitches were employed to enhance the exciting state thermal stability. The

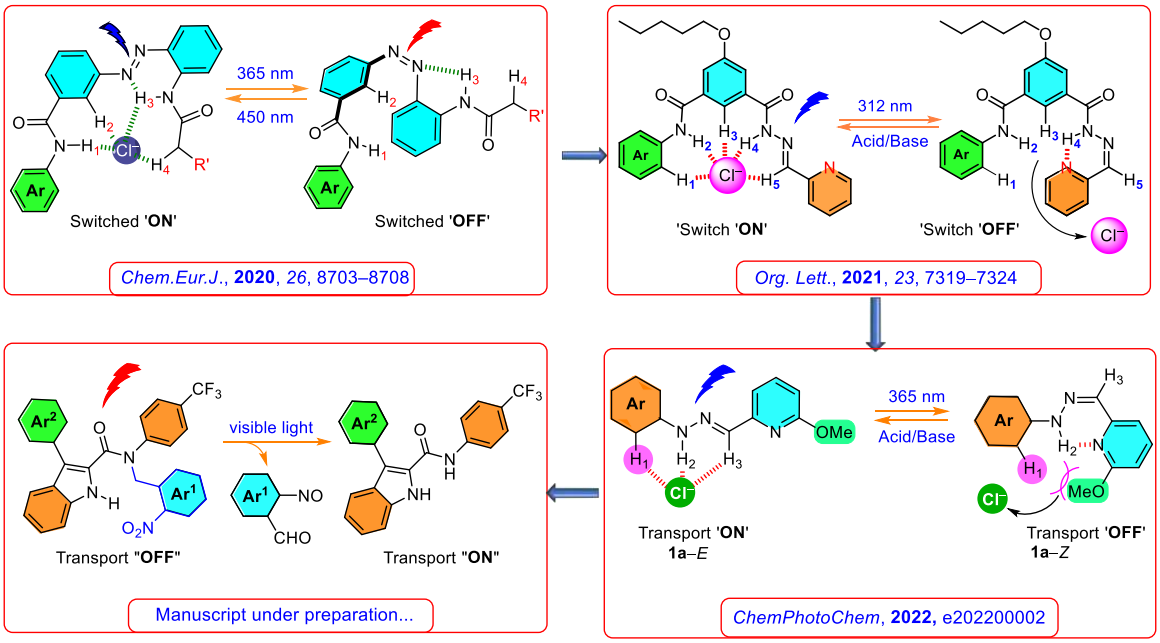

Figure: Schematic illustration of photo-responsive ion transporting systems discussed in the thesis.

reversibly-gated ion transport activity was achieved utilizing light and catalytic acid, respectively, as the external stimuli. In chapter 4, Phenylhydrazone-based photoswitches were utilized to enhance the excitation wavelength. These photoswitches function comparatively at

higher wavelengths compared to that of acylhydrazone switches. Eventually, in chapter 5, we demonstrated an o-nitrobenzyl-based photocaged ion transport systems that were selectively activated inside the cancer cells to induce chloride-mediated apoptosis utilizing the external electromagnetic radiations. However, a careful and smart optimization related to activation wavelength and significant inactivity in the 'OFF' state and activity in the 'ON' state are the important parameters to be fine-tuned for the plausible biomedical application.

Research Publications:

1. A Sandwich Azobenzene-diamide Dimer for Photoregulated Chloride Transport.

Manzoor Ahmad, Surajit Metya, Aloke Das, and Pinaki Talukdar.*

Chem. Eur. J. **2020**, *26*, 8703−8708.

2. Stimuli-Responsive Anion Transport through Acylhydrazone-Based Synthetic Anionophores.

Manzoor Ahmad, Sandip Chattopadhayay, Debashis Mondal, Thangavel Vijayakanth, and Pinaki Talukdar.*

Org. Lett. **2021**, *23*, 7319−7324.

3. Reversible Stimuli-Responsive Transmembrane Ion Transport Using Phenylhydrazone-Based Photoswitches**.**

Manzoor Ahmad, Debashis Mondal, Naveen J. Roy, Dr. Thangavel Vijayakanth, Prof. Pinaki Talukdar.*****

ChemPhotoChem **2022**, e202200002.

4. Anion Recognition through Multivalent C–H Hydrogen Bonds: Anion Induced Foldamer Formation and Transport across Phospholipid Membrane.

Debashis Mondal, **Manzoor Ahmad**, Prakash Panwaria, Avisikta Upadhyay, and Pinaki Talukdar.*

J. Org. Chem. **2022**, *87*, 10−17.

5. Molecular Self-assembly as a Tool to Construct Transmembrane Supramolecular Ion Channels.

Javid Ahmad Malla, **Manzoor Ahmad**, Prof. Pinaki Talukdar.*

Chem. Rec. **2021**, *21*, 1–14.

6. Sugar-derived oxazolone pseudotetrapeptide as γ-turn inducer and anion-selective transporter.

Sachin S. Burade, Sushil V. Pawar, Tanmoy Saha, Navanath Kumbhar, Amol S. Kotmale, **Manzoor Ahmad**, Pinaki Talukdar * and Dilip D. Dhavale. *

Beilstein J. Org. Chem. **2019**, *15*, 2419–2427.

7. Selective and Rapid Water Translocation across Self-assembled Peptide-Diol Channel via the Formation of Dual Water Array.

Debashis Mondal, Bhupendra R. Dandekar, **Manzoor Ahmad**, Abhishek Mondal, Jagannath Mondal and Pinaki Talukdar. *

Chem. Sci., **2022**, DOI: 10.1039/D2SC01737G.